Dynamical Constraints of Galaxy Clusters via Spectroscopic Observations

by

Anthony Kremin

A dissertation submitted in partial fulfillment
of the requirements for the degree of
Doctor of Philosophy
(Physics)
in the University of Michigan
2020

Doctoral Committee:

Associate Professor Christopher J. Miller, Chair
Professor August E. Evrard
Professor David Gerdes
Associate Professor Oleg Gnedin
Professor Gregory Tarlé

Anthony Kremin

kremin@umich.edu

ORCID iD: 0000-0001-6356-7424

To my parents, for working hard for many years so that
their children could have opportunities that they did not.

Acknowledgments

First and foremost, I would like to thank my advisers: Professors August Evrard, David Gerdes, and Christopher J. Miller. Their individual and collective guidance have helped to shape my research career. I entered Michigan scientifically lost, having moved away from the physics sub-field(s) I had previously worked in. They welcomed me into the group and provided me with patient guidance as I learned about spectroscopy, optical surveys, and galaxy clusters. Even as Professor Gerdes moved to other avenues of astronomical inquiry, he continued to advise me, sitting through countless boring meetings I held while working through technical issues in one analysis or another. He gave me excellent career advice and helped to guide my work along. Gus was always available to chat and offer his immense wisdom to my scientific problems. Even when my work was primarily about raw data analysis he listened and offered insightful questions and suggestions. Finally, Chris guided my scientific work from the very beginning. Starting my analysis of spectra and suggesting I write a proposal for M2FS data. He was also pivotal in helping to teach me the reduction and analysis steps. Finally, I would like to thank my remaining committee members Professors Oleg Gnedin and Greg Tarlé. Both stepped in on short notice due to scheduling constraints and I am indebted to each of them for accepting the committee roles. Greg also advised me through the DESI collision avoidance work and gave me invaluable advice on academia, grant writing, and career exploration. Oleg educated me in Extragalactic Astronomy, giving me a view of cosmology from the lens of astronomers as opposed to physicists, which was both informative and complimentary to my physics education.

I would also like to thank my undergraduate advisors: Professor Kenneth Heller (UMN), Professor Vuk Mandic (UMN), Professor Marvin Marshak, and Dr. George Redlinger (BNL). Professor Marshak gave me my first exposure to scientific research when I had very little understand of what that entailed. He managed to find a perfect project for an undergraduate freshman to begin understanding what data looks like, how to analyze it, and how to reference papers to understand what it means for a neutrino to oscillate between flavors. His encouragement and guidance are the reasons I made it to where I am today. He helped me get my foot in the door, and I will always be indebted to him for that. Professor Mandic took a chance on me by allowing a sophomore with only rudimentary programming and Linux skills to perform LIGO analysis using their large MATLAB software-stack on remote Linux servers. That is where I first learned how to truly write code, work from a command line, and operate within a large organization. Vuk also encouraged me to give presentations and taught me what it meant to produce, validate, and present a scientific finding. Finally, I want to thank Professor Kenneth Heller and Dr. George Redlinger for their additional guidance for my honors thesis on ATLAS. Thank you all.

Next, I would like to thank the United States' Department of Energy and Rackham Graduate School. This work would not have been possible without their research funding. The DOE supported the research outlined in this thesis for the majority of my time in graduate school. The University of Michigan Rackham Graduate School also offered multiple travel grants that allowed me to present my research more broadly to global communities of scientists, and a one-term fellowship that helped me to further my research more rapidly than I otherwise could have during my final year. Finally, I would like to thank the Physics Department for providing teaching positions when no research funding was available.

The funding would not have helped, however, if I did not stay in graduate school. I need to thank my family, friends, and colleagues for that. Without my fellow physics cohort, the first two years would have been far too much to handle. Through both commiseration and a sense of group resilience they helped me get by, and we even managed to have some fun and laughs from time to time. In the years after my coursework I naturally gravitated toward the cosmology and astronomy graduate students. I would like to thank those who were around me the longest: Angela Chen, Kevin Coughlin, Rutu Das, Arya Farahi, Jesse Golden-Marx, Noah Green, Stephanie Hamilton, Jessie Muir, Charles Munson, Noah Weaverdyck, and Yuanyuan Zhang, as well as all of the cosmology students I interacted with over the years. While it was valuable to have them around to ask questions or discuss difficult concepts, they were also friends and a support system. We pushed each other to learn more with our journal club and used it to stay in touch and facilitate social outings.

Last, but certainly not least, I want to thank both my immediate and extended family. To my aunts and uncles who continued to humor me with questions even when they did not understand why I was still in school or what it was useful for. And I want to thank those who asked questions because they were genuinely curious, because they

reminded me of the public interest that exists for cosmology, which is easy to forget when you are buried in a particular research problem. Those conversations helped to inspire me to keep going during challenging times. To my brother, who no doubt shaped the way I think and observe the world around me while growing up. Your interest in what I study, and your continued encouragement have meant a lot to me. And to my parents. Your love, support, help, encouragement, and understanding have meant the world to me (even if you still dont know what I actually study or research). I would not be where I am without you. Thank you.

Preface

While all of my work revolved around the central themes of spectroscopy and galaxy clusters, my projects and interests were more broad than a typical PhD dissertation. Here I have attempted to make a coherent description of my work and it's contributions to my field. A great deal of my time was spent creating tools that will enable future scientists (myself included) to produce scientific results more quickly and easily. These tools are described both in the chapters and in the appendices.

During my time at the University of Michigan, I have had the honor of working and mentoring several undergraduate students. One of whom, Efrain Segarra, helped write the original code to test DESI anticollision in python simulations. While none of that code is in use, he provided the first steps in the project outlined in Appendix A.

Fellow PhD students, especially Dr. Daniel Gifford, were instrumental in this work. Dan was the inspiration for the majority of the work and code-base in this dissertation outlines. While nearly all of the code has been re-written and the research expanded upon, his impact is clear. A small amount of his code is still used in the work outlined in Chapter 3.

Table of Contents

List of Tables

List of Figures

List of Appendices

Abstract

Galaxy Clusters are the largest gravitationally bound objects in the Universe, residing at the boundary between the expansive push of dark energy in the vacuum and the attractive pull of dark matter the fills the halo in which a cluster resides. By leveraging the power of spectroscopy, I used the three-dimensional information it provides about galaxies within these clusters to infer dynamical properties about the galaxy cluster and the underlying dark matter halo. The dynamical state and dynamic mass inferences are valuable to future cosmological studies that aim to use the unique nature of galaxy clusters and the role they play in constraining the properties of dark energy and dark matter. In this work I focus on transforming galaxy spectra into line-of-sight velocities which, when paired with projected sky locations, allow me to probe the gravitational potential of the total cluster system. I designed, targeted, acquired, reduced, and analyzed 4427 galaxy spectra from 22 galaxy clusters, of which 3054 passed my strict quality cuts. Of those that passed the cuts, 1679 were identified as cluster members based on radial-velocity phase-space cuts. The data was acquired using the Michigan-Magellan Fiber System (M2FS) multi-fiber spectrograph on the 6.5m Magellan Clay telescope. The reductions were performed using a fully-featured pipeline that I created and that I describe in this work. I also summarize the resulting dataset using spatial, redshift, magnitude, and signal-to-noise information for individual galaxies, and show that there is good agreement when comparing my re-observed redshifts with those in the literature.

To convey the amount of information contained in this dataset, I perform an analysis on one specifically selected massive cluster, Abell S1063, which was observed twice. I use two approaches for estimating cluster masses, the first is a velocity dispersion technique that takes the distribution of velocities, reduces it to a statistical measure of the width of the distribution, and maps that spread to a mass based on a model motivated in part by theory and calibrated with simulations. The second uses the velocity-radial distance information from the cluster center to identify the escape velocity edge of the cluster, which is observed as the velocity extrema in a given radial

bin. This edge is directly related to the gravitational potential and can be used to infer the total mass of the system. I compare these techniques to one another and against other mass proxies and find that the velocity dispersion measurement differs from other estimates for the system, favoring a higher mass, while the escape velocity edge technique is in good agreement with other estimates. This is expected for a galaxy cluster with substructure, which previous studies have hypothesized for this system but could not verify. I am able to visually confirm the existence of clumps using galaxies as tracers, and quantify the substructure using the Dressler-Shectman statistic, where I found a significant result with $p < 0.0001$.

Chapter 1

Introduction

1.1 Galaxy Clusters and Cosmology

Galaxy clusters are the largest gravitationally bound objects in our Universe. These structures, having formed through hierarchical formation in the recent cosmic past, are sensitive to the energy composition of the Universe in the present epoch of dark energy dominance. The pull of matter and the expansion of dark energy produce opposing forces on clusters as they continue to accrete and merge. Since the 1930's when Fritz Zwicky used galaxy clusters to propose the need for a new form of invisible matter (later termed dark matter), clusters have played an important role in probing cosmological parameters (Zwicky, 1933). While Zwicky's argument relied on dynamics and optical luminosities to indicate that luminous matter only composed a small fraction of the Coma cluster's total mass, cluster cosmology today is typically done via the comparisons of the observed halo mass function with predictions from theory or simulation. The mass function, $n(M, z)$, is the average spatial population density of halos of mass M at redshift z. In simple terms, the function represents the number of halos with a given mass, M, at a given redshift, z. $n(M, z)$ has units of number per comoving volume and depends on cosmology via both the volume element and in the strength of gravitational collapse of halos at fixed mass and redshift. In differential form the mass function can be written as:

$$\frac{dn}{d\ln M} = \frac{\bar{\rho}_{\rm m}}{M} \left| \frac{d\ln\sigma}{d\ln M} \right| f(\sigma), \tag{1.1}$$

with $\bar{\rho}_{\rm m} = \Omega_{\rm m}\rho_{\rm cr}$ being the comoving average matter density. $f(\sigma)$ is a model-dependent function of σ^2, the variance of linear cold dark matter fluctuations filtered on a mass scale, M. σ^2 is given by:

$$\sigma^2(M,a) = \int \frac{d^3k}{(2\pi)^3}\, W^2(kR)\; P_{\rm m}(k,a). \tag{1.2}$$

Here the filter function is typically that of a Fourier transformed top-hat filter, $W(y) = 3[\sin(y)/y^3 - \cos(y)/y^2]$ within radius R, and P_m is the matter power spectrum. The matter power spectrum normalization, σ_8, is found by evaluating Equation 1.2 at $8\,h^{-1}\,\mathrm{Mpc}$ and $a = 1$.

While simple in premise, studies of the halo mass function are made difficult by the fact that we cannot directly observe halo mass. Because of this, we must estimate the mass through theoretical or empirical arguments. This is typically done through the estimation of the gravitational potential or the matter density of the cluster, which are both fundamentally linked to the mass via the physics of Newtonian Mechanics and General Relativity. Clusters, which can be identified in wavelengths from the microwave to the X-ray, allow us to probe the hot intra-cluster medium (ICM), the total stellar luminosity in the galaxies, the bending of background light by the massive foreground cluster halo, and the Doppler redshifting of galaxy light due to the galaxies peculiar velocities. There have been many proposed mass estimators for galaxy clusters in the ninety years since Zwicky first performed his study, but here we will only discuss a few relevant and common probes, namely: weak gravitational lensing, strong gravitational lensing, X-ray luminosity/temperature, the thermal Sunyaev-Zel'dovich effect, velocity dispersion, Jean's equation, and the escape velocity (caustic) edge.

Figure 1.1 shows an example of the power clusters can have in constraining cosmology. On the left is an image of observed data inferred from X-ray observations under the current ΛCDMparadigm of cosmology with 70% dark energy and 30% matter today. The right figure shows the data and theoretical curves in a cosmology with no dark energy, and the agreement is visibly poor.

Figure 1.2 shows a quantitative representation of the power of galaxy clusters to probe cosmology, in this case derived from SZ mass estimates. Not only are the constraints from clusters comparable to other measurements, but they are also complimentary in the directionality of their constraints in each phase-space. Clusters are particularly good at constraining parameters related to matter, namely Ω_m and σ_8.

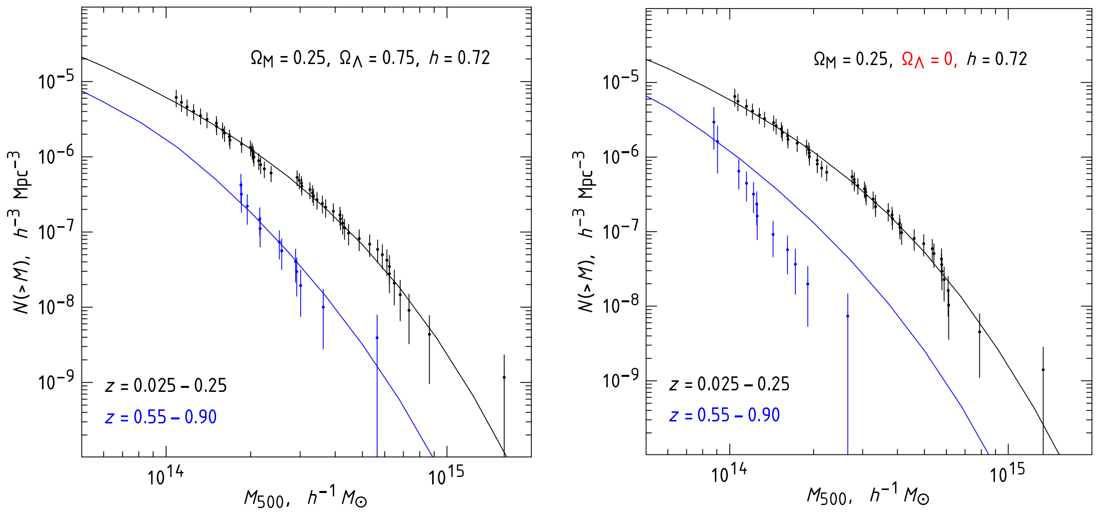

Figure 1.1 An example showing the ability of a cluster survey to discriminate between cosmologies. On the left we show measured mass functions of X-ray clusters at low (black) and high (blue) redshifts for a ΛCDMmodel. The right shows the same data with curves representing predictions in an open universe with the same amount of matter but no dark energy. Figures taken from Vikhlinin et al. (2009).

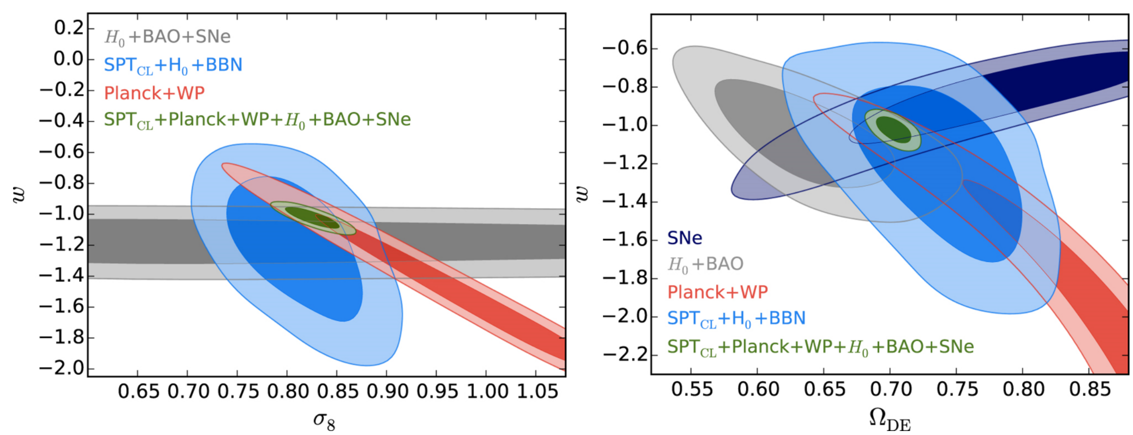

Figure 1.2 Two figures showing the unique constraining power of three powerful cosmological probes: baryon acoustic oscillations, galaxy clusters, and the cosmic microwave background when combined with a subset of big bang nucleosynthesis, H_0 measurements, and/or supernova. Note that galaxy clusters are comparably constraining, and are more constraining than other probes for cosmological parameters that are related to matter, such as Ω_m and σ_8. Figures from de Haan et al. (2016).

1.2 Estimating Masses

As stated above, we can use the physical observables and properties of galaxy clusters to estimate their masses. Through a combination of theoretical, empirical, and simulated analyses meant to understand biases and systematic uncertainties in the measurements, we are able to diagnose the expected and observed scatters in mass at fixed observable value. Each proxy has strengths and weaknesses that make it a useful contributor to the holistic picture of a galaxy cluster's mass profile, dynamic state, and physical properties. By measuring a given cluster with multiple methods we are able to test model assumptions of e.g. hydrostatic equilibrium, and identify potential biases or systematic uncertainties that may not be readily identified using a single method alone. Below we list four common observations used for estimating mass: gravitational lensing, X-ray observations, up-scattered CMB photons (SZ effect), and dynamics of member galaxies.

1.2.1 Gravitational Lensing

Gravitational lensing is a General Relativistic phenomenon that causes light to travel along geodesics in space-time that are spatially curved due to the presence of matter. In the case of clusters this is typically broken into two regimes: strong and weak lensing.

Strong lensing is caused by very dense regions, such as massive cluster cores, bending light of background galaxies so much that images are visibly distorted, magnified, and occasionally multiply imaged in different locations around the core. The magnification and shearing of the galaxies light allow strong lensing models to tightly constrain the mass that would cause such distortions. General Relativity gives precise predictions of this if we have prior knowledge of the distance to the cluster (in redshift), the distance to the background galaxies, and the distance from the cluster to the background galaxies. While accurate, this technique only works in the inner regions of the most massive clusters where such strong lensing exists.

Weak gravitational lensing is a manifestation of the same phenomena but at levels too weak to detect in individual galaxies. Instead the shear is measured statistically by looking at all background galaxies surrounding the cluster. The shapes and alignments of the galaxies should be roughly random in their orientations, but around galaxy clusters they will be preferentially aligned around the cluster's mass due to weak distortions of the background images. A non-zero tangential shear will appear in analyzing the shapes and axes, which can be mapped to a projected mass within a given radius. This can be done to large radii and gives not only a mass estimate, but mass as a function of radius. However, this can only be measured in the largest galaxy clusters where the mass is great enough for the shear to be statistically significant over the random alignments that would be there in the absence of a foreground cluster.

1.2.2 X-ray Masses

X-ray's are emitting from the intra-cluster medium (ICM) of galaxy clusters due primarily to bremsstrahlung radiation of the shock-heated gas. If we assume that the gas is in hydrostatic equilibrium, we can use thermodynamics to relate an observed temperature with mass. Typically, spherical symmetry is also assumed to simplify the calculations. If both are true, or assumed to be true, we can relate the total mass to the measured gas density and temperature profiles by (Sarazin, 1988):

$$M(r) = -\frac{r\,kT(r)}{G\mu m_{\rm p}}\left[\frac{d\ln n}{d\ln r} + \frac{d\ln T}{d\ln r}\right], \tag{1.3}$$

where $M(r)$,$T(r)$, and $n(r)$ are the mass, ICM temperature, and gas particle density within radius r, respectively. G and k are Newton's and Boltzmann's constants respectively, and $\mu m_{\rm p}$ is the mean molecular weight.

This can only be done when X-ray spectra are available, however, since a spectrum is required to infer the temperature. The luminosity on the other hand can be inferred from the integrated flux of the observed object, so long as an estimate of the redshift for the cluster is available. The absolute luminosity is also well correlated with mass, and is often used as a mass proxy.

1.2.3 Thermal Sunyaev Zel'dovich Effect Masses

The thermal SZ is related to the X-ray mass proxy in that it also probes the hot ICM. This effect measures the up-scattering of photons from the Cosmic Microwave Background (CMB) to higher energy by the hot gas in the ICM via inverse Compton scattering. While this probes the gas, it is related to mass through different powers of the gas density and temperature, so not only can we use these observations to estimate mass but we can also model the system jointly with X-ray observations to produce tighter constraints on the model parameters, and produce more accurate masses.

The greatest benefit of the SZ mass proxy is that it is nearly redshift independent.

The typical decrease in the flux of light from an object ($1/(1+z)^4$) is counteracted exactly by the increase in CMB energy density in the past. This allows us to measure a nearly redshift-complete survey of a region of the sky. The challenge, though, is that the SZ signal is small relative to the noise and is therefore hard to detect with high significance for lower mass clusters. Therefore the redshift-complete sample is mass limited, and currently restricts such surveys to the higher mass population of clusters.

1.2.4 Dynamical Masses

As Zwicky did in the 1930's, we can use galaxies as tracers of the underlying gravitational potentials in which they reside. If we solve the collisionless Boltzmann equation (CBE) under Newtonian dynamics and compute the velocity moments, we can derive the Jean's equation (Binney & Tremaine, 1987):

$$M(r) = -\frac{r\,\sigma_{\mathrm{r}}^2(r)}{G}\left[\frac{d\ln\sigma_{\mathrm{r}}^2}{d\ln r} + \frac{d\ln\nu}{d\ln r} + 2\beta\right], \tag{1.4}$$

where $\sigma_{\mathrm{r}}(r)$ is the three dimensional velocity dispersion and $\nu(r)$ is the galaxy number density. β is the velocity anisotropy parameter:

$$\beta(r) = 1 - \frac{\langle v_t^2\rangle(r)}{\langle v_r^2\rangle(r)} \tag{1.5}$$

that, as the name implies, captures the anisotropy of the velocities in the cluster. While powerful in theory this method is challenging to implement due to the number of model parameters that need to be constrained, and the difficulty in relating observed line-of-sight velocities with three-dimensional velocity dispersion while simultaneously constraining the velocity anisotropy.

With these challenges in mind and the understanding that mass should be proportional to velocity dispersion to some power, we can attempt to find a simplified power-law form to relate the velocity dispersion to mass. That is what Evrard et al. did in 2008, which they wrote in the form (Evrard et al., 2008):

$$\sigma_{\mathrm{DM}}(M,z) = \sigma_{\mathrm{DM},15}\left[\frac{h(z)M_{200c}}{10^{15}M_\odot}\right]^\alpha, \tag{1.6}$$

where $\sigma_{\mathrm{DM},15}$ is the normalization for a mass of 10^15^{-1} and h(z)=H(z)/100. They calibrated the normalization and exponent using a suite of dark matter only simulations. This relation is for a three dimensional, dark matter only velocity dispersion. They studied the bias of using galaxies as tracers and found a bias consistent with one (unbiased). They do not describe the contraction of the three dimensional velocity dispersion to observed, line-of-sight dispersions, however. Studies to determine how to appropriately use one-dimensional velocities were left to future works, such as Saro et al. (2013).

Finally, using nothing more than Newtonian mechanics, we can derive a relationship between the potential and the escape velocity for a particle at a radius, r:

$$v_{esc}^2(r) = -2\Phi(r) \tag{1.7}$$

If we then use the Poisson equation, we can relate this potential to the mass density:

$$\nabla^2\Phi(r) = 4\pi G\rho(r), \tag{1.8}$$

which if we integrate will allow us to infer a mass.

The challenge in this instance is the estimation of the escape velocity. If we assume a well sampled, spherical system then at any given radius there will be a particle traveling along the line of sight that will have the escape velocity for that orbit. If we plot line-of-sight velocities as a function of radius from the cluster center, we see the prototypical trumpet shaped caustic edge, which can be better interpreted as the escape velocity edge. Those galaxies with higher velocities will escape on short dynamical timescales, and those with smaller velocities will reside within the trumpet shaped envelope. By identifying the maximum velocity in many radial bins, we can infer the velocity profile and the potential profile, and thus the mass density at that radius. We can perform this measurement up to a statistical uncertainty due to incomplete sampling of the phase-space, for which a correction must be applied based on a normalization found in simulations. Note that in a Universe with non-zero dark energy the Poisson equation is modified to contain a cosmology dependent term, which must also be accounted for (Miller et al., 2016).

While the Jean's equation is powerful in its rigor, it contains multiple free parameters that must be constrained empirically or via simulations, and some such as the anisotropy can be difficult to jointly constrain with mass (the so-called mass-anisotropy degeneracy). The scaling relations avoid such issues by effectively taking the mean behavior, but for individual clusters this leads to larger scatter in the mass estimates. The escape edge technique, on the other hand, only requires two free parameters if we assume a mass density profile, or just one if we can fix the second to a value calibrated on simulations or constrained in empirical studies. We can make multiple measurements as a function of radius, which allows for tight constraints on mass when compared to basic scaling laws, and fewer assumptions than methods that involve the full Jean's equation.

1.3 Characterizing Mass Distributions

Masses are useful for constraining cosmological models that predict the number of halos of a given mass at a given redshift. However, for studies of the cluster astrophysics it is more useful to derive information about the radial profile of the cluster; either its mass profile or density profile. Three common models employed today are the single isothermal sphere (SIS); Navarro, Frenk and White (NFW); and Einasto density profiles (Navarro et al., 1996; Einasto, 1969).

The SIS model is useful mostly in its simplicity. It assumes a spherical collapse of a halo under isothermal conditions, which leads to the following relation between mass density and measured velocity dispersion:

$$\rho(r) = \frac{\sigma_V^2}{2\pi G r^2}. \tag{1.9}$$

This model still receives use today despite having a non-physical singularity at zero radius and showing poor fit to simulated and observed data in both the core and outskirts of the cluster, primarily because of the physical intuition that it allows for.

The most popular density profile, the NFW, was first proposed by Navarro, Frenk, and White in Navarro et al. (1996) by comparing numerous functional forms to dark matter only simulations. The profile they found to fit best is given by:

$$\rho(r) = \frac{\rho_0}{\frac{r}{R_s}\left(1 + \frac{r}{R_s}\right)^2}. \tag{1.10}$$

The two free parameters, written above as ρ_0 and R_s, are generally re-parametrized as the mass (at some fixed radius) and concentration,

$$c_{\Delta\mathrm{ref}} = \frac{R_{\Delta\mathrm{ref}}}{R_s}, \qquad M_{\Delta\mathrm{ref}} = \Delta\frac{4}{3}\pi R_{\Delta\mathrm{ref}}^3 \rho_{\mathrm{ref}}. \tag{1.11}$$

Here $R_{\Delta\mathrm{ref}}$ is defined as the distance from the center of the spherical halo at which the mean halo density drops to Δ times the critical (c) or matter (m) density of the Universe. For example $r_{200\mathrm{c}}$ is the radius at which the mean density reaches 200 times the critical density at the redshift of the halo.

The NFW vastly improves upon the SIS model, but still suffers from the singularity at zero radius. It was also later found to encounter problems when attempting to model the core and outskirts of a cluster simultaneously (Miller et al., 2016). That paper, among many others comparing mass profiles to both simulated clusters and observed clusters, found that the Einasto profile is a better functional form for fitting the full radial range of density (Einasto, 1969):

$$\rho(r) = \rho_0 \exp\left[-\left(\frac{r}{r_0}\right)^{1/n}\right]. \tag{1.12}$$

This profile not only provides a better fit, but also avoids singularities at the cluster center and integrates to a finite mass at infinite radius.

While modifications were created to form a generalized NFW that fits observed profiles more accurately, the Einasto is still the most effective in both simplicity and shape, which is why it is used in our analyses. We also provide the NFW fits for comparison with the literature where it still receives wide use.

Even the best fitting Einasto profile has shortcomings in fitting a galaxy cluster, however. It, along with the NFW and SIS and almost all proposed functional forms, assume spherical symmetry and therefore has difficulty with triaxiality and projection effects. It also assumes that the density is a smoothly decreasing function of radius, which cannot account for substructure or actively merging systems.

In the end, no two parameter (or three or four parameter generalized model) can be expected to fully encapsulate an aspheroidal, three dimensional object of unknown dynamical state. To study a cluster, an empirical radial profile is far more preferable and informative for both cosmological and astrophysical studies of individual systems.

1.4 Evidence and Impact of Substructure

In our current model of hierarchical structure formation, we expect a large fraction of galaxy clusters to be non-relaxed in their dynamics due to ongoing accretion and mergers. Large-scale numerical simulations indicate that these processes are anisotropic, occurring preferentially along filaments of the large scale structure of the universe (Colberg et al., 1998). Several decades of observations have shown that between 30 and 70 percent of all clusters contain some level of identifiable substructure, based on optical (e.g. Baier & Ziener (1977); Geller & Beers (1982); Girardi et al. (1997); Wen & Han (2013)) and X-ray (e.g. Jones & Forman (1999); Jeltema et al. (2005)) observations, as well as gravitational lensing techniques (e.g. Athreya et al. (2002);

Grillo et al. (2014)). The existence of substructure can: provide insights into the formation mechanisms of clusters, reveal the existence of dark matter (Clowe et al., 2006), probe the structure formation and expansion rate of the universe (Richstone et al., 1992; Mohr et al., 1995), and substantially affect estimates of velocity dispersion and dynamical mass (Girardi et al., 1996; Pinkney et al., 1996). For a recent review, see Biviano (2020) and references therein. A more thorough review of cluster accretion literature can be found in Feretti et al. (2002).

Substructure can be identified as smaller scale sub-clumps in strong lensing density profiles (Kneib et al., 1996; Mao & Schneider, 1998) as well as weak lensing systems (Hoekstra et al., 2000; Clowe et al., 2006; Okabe et al., 2010; Oguri et al., 2013; McCleary et al., 2015). It can also be determined using spatially resolved X-ray observations in which gas densities can be measured. These methods, however, are severely contaminated by line-of-sight structure (Hoekstra, 2003; Geller et al., 2013). While lensing and X-ray data can identify clumps and substructure in the projected density profiles, the detection of substructures using optical data is still both common and useful due to the ability to discriminate between foreground, background, and cluster galaxies using photometric or spectroscopic redshifts. Optical data can use just galaxy positions alone, just redshifts alone, or use both positions and redshifts.

Methods that use solely galaxy sky locations include the angular separations test, the density contrast test, and the symmetry test (West et al., 1988); the smoothed density-contour maps (Geller & Beers, 1982); and the two-dimensional (2D) wavelet transforms (Slezak et al., 1990; Escalera & MacGillivray, 1995; Flin & Krywult, 2006). These, like the X-ray or lensing data, suffer from the contamination of foreground and background galaxies, but are useful when spectroscopy is unavailable.

Methods that use only the galaxy redshifts typically assume Gaussianity for the individual velocity parent populations. Based on this Gaussianity, measures such as the asymmetry and tail indices (Bird & Beers, 1993), and kurtosis and skewness (West & Bothun, 1990) can be employed to both identify and quantify the sub-clustering in the one-dimensional redshift distribution. A more advanced test, based on Gaussian mixture modeling (GMM) is Kaye's mixture model (KMM) algorithm (Ashman et al., 1994; Kriessler & Beers, 1997). KMM identifies the existence of substructures by estimating the optimal number of Gaussian population distributions that best recreate a data vector with the observed values. Methods that do not assume Gaussianity include the Kruskal-Wallis Test (KW Test) of bi-modality, which quantifies the likelihood of a one dimensional vector being generated from two populations rather than one (Kruskal & Wallis, 1952). A second is the DEDICA method, which is based on an adaptive kernel and identifies specific velocity components (Pisani, 1993). When a Gaussian kernel is chosen, DEDICA reduces to a GMM.

For three dimensional data that use galaxy positions and redshifts, the Dressler-Shectman (DS) statistic is the most widely used (Dressler & Shectman, 1988). The DS statistic uses the local velocity dispersion of each galaxy with its ten (spatially) nearest neighbors and the mean velocity of that subset to compute the differences between these values and the global dispersion and mean velocity. The sum-of-squares of these differences gives an indication of how discrepant local velocities are from the global population. Other methods include the more generic Kolmogorov-Smirnov statistical test (KS Test), which determines whether two or three dimensional data belongs to a single distribution or not (Fasano & Franceschini, 1987); the three-dimensional version of both DEDICA (Pisani, 1996) and KMM (Bird, 1994) algorithms, which operate similarly to that of their one-dimensional counterparts; and the 3D wavelet transforms (Escalera & MacGillivray, 1995). Finally, a recent method utilizes the caustic technique to generate binary trees, which can be used to determine substructure via hierarchical clustering (Diaferio & Geller, 1997; Yu et al., 2015).

In addition to implications of cluster substructure to cosmology and mass estimation, there is a wealth of astrophysics that can be learned from studying non-relaxed systems. It is known empirically that galaxy cluster member galaxies differ in properties from those galaxies found in the field (isolated regions outside dense cluster environments) (e.g., Fasano et al., 2015; Girardi et al., 2015). The galaxies in the dense regions of cluster cores are observed to be redder in color, have reduced star formation, and show earlier morphological type (e.g., Gerken et al., 2004); but the dominant mechanisms driving this are still being investigated (see e.g., Treu et al. (2003) and references therein). An example of this is the identification of higher star formation rates in merging systems. It is unclear whether the enhanced star formation is caused by the process of clusters merging (as argued in e.g., Caldwell & Rose (1997); Ferrari et al. (2005)), or whether star formation is quenched in the dynamical relaxation process which decreases the star formation in clusters where there have been no recent mergers (Cohen et al., 2014). These can both be explained theoretically by either arguing that mergers cause the ejection of the inter-stellar medium (ISM) and therefore reduce star formation (i.e. quenching), or alternatively that the interaction of the intra-cluster medium (ICM) with interstellar gas induces enhanced star formation (e.g., Fujita et al., 1999; Bekki et al., 2010). To determine which is correct, increased interest has been given to post-starburst galaxies (PSBs) due to their transient nature that is attributed to rapid star formation that has recently decreased or completely ceased (Dressler & Gunn, 1983), and the fact that they can be readily identified by specific spectral features.

It is believed that in observed PSBs the star formation decreased roughly a few Myr (bluer PSBs) to a few Gyr (redder PSBs) prior to the time of emission of the light we observe, based on the lifetime of the observed stars with strong Balmer lines (Poggianti & Barbaro, 1996, 1997; Poggianti et al., 1999; Mercurio et al., 2004). By identifying the spatial and dynamical location of these PSBs, it is believed that we can determine which of the mechanisms discussed above is responsible for the differences in star formation rate between galaxies in recently merged clusters and dynamically relaxed systems (Bekki et al., 2010; Muzzin et al., 2014; Dressler et al., 2013; Lewis et al., 2002; Owen et al., 2005; Mercurio et al., 2004; Oemler et al., 2009).

Multi-wavelength data and high density spectroscopy are critical to investigating cluster substructure and cluster merging phenomena (Girardi & Biviano, 2002). Recent studies using spectra of hundreds of galaxy members show the power of such datasets in studying the structure of clusters (e.g., Owers et al., 2011; Munari et al., 2014; Girardi et al., 2015). With enough member galaxies, studies are able to investigate the substructure and dynamics as a function of star formation rate of the individual galaxies, providing critical astrophysical insights that allow us to better understand galaxy cluster formation. Such insights are important in properly understanding the systematics of these complex objects for use as cosmological probes (Czoske et al., 2002; Mercurio et al., 2004, 2008; Oemler et al., 2009; Ma et al., 2010; Girardi et al., 2015).

1.5 This Work

This dissertation will investigate galaxy clusters using the escape velocity edge technique and the velocity dispersion parameterization of Evrard et al. (2008) outlined in this chapter. I will use velocities derived from spectroscopic observations I made over the course of several years using the 6.5m Magellan-Clay telescope at Las Campanas Observatory. Chapter 2 gives an overview of spectroscopic instrumentation and goes into depth on the Michigan-Magellan Fiber System (M2FS) used for my data acquisition and the presently running Dark Energy Spectroscopic Instrument (DESI). I then describe the software pipeline I developed to reduce low resolution M2FS data into spectroscopic redshifts in Chapter 3. Chapter 4 summarizes the targets, observations, recovered data, and provides figures that summarize the complete dataset. I then use some of that data in Chapter 5 where I study the massive cluster

Abell S1063. I determine the mass using both velocity dispersion and escape velocity edge techniques, and study the dynamical state of the cluster using the well-sampled velocity phase-space. I then conclude by summarizing my dissertation in Chapter 6 and discussing future trajectories for this research and galaxy cluster spectroscopy as a field.

In Appendix A, I describe work I did for the Dark Energy Spectroscopic Instrument Collaboration creating software that is used to avoid collisions among the robotic positioners when they are moving from one location to another. In Appendix B, I provide numerous summary figures for individual galaxy clusters targeted and described in Chapter 4. Finally, in Appendix C, I provide the complete list of the data acquired as part of this dissertation, which were described in Chapter 4 and Appendix B, and used in the analysis of Chapter 5.

Chapter 2

Modern Optical Instrumentation

2.1 Introduction

The cosmic laboratories that are galaxy clusters give off radiation that spans the electromagnetic spectrum, from the microwave up to the 'hard' X-ray. This variety requires numerous instruments with capabilities to observe the huge range of photon energies, and resolve the vast range of wavelengths. In the context of this dissertation we will be focusing on the optical wavelengths, and specifically on the observation of optical spectra from visible matter (ie galaxies).

In this chapter, we will briefly discuss the evolution of optical spectroscopy in Section 2.2 before delving into detail on two modern spectroscopic instruments: the Michigan/Magellan Fiber System (M2FS) in Section 2.3 and the Dark Energy Spectroscopic Instrument (DESI) in Section 2.4. Finally we will discuss the relevance of these two "case studies" in instrumentation to the broader scope of this work in section 2.5.

Unless explicitly cited to another source, the majority of the information in Section 2.3 comes from Mateo et al. (2012) and Bailey et al. (2014). Further descriptions and information can be found in those documents. Similarly, unless cited to another source, the information in Section 2.4 comes from DESI Collaboration et al. (2016).

2.2 History of Spectroscopy

The evolution of optical spectroscopy in the past few decades has been substantial. Spectroscopy began using a single "longslit" with a prism dispersing light onto photographic plates. The slit allowed only the light along a narrow line to be passed into the prism. For point sources or unresolved objects this meant observing the spectrum of a single target with sky spectra on either side of it, or perhaps two objects if the slit was aligned correctly. For extended objects it allowed for attaining the spectral characteristics at different radial distances from the center of the object. Such spatial resolution was incredibly useful for velocity measurements via the Doppler effect. Using these techniques in the 1960's and 1970's, Vera Rubin was able to show that the velocity of galaxy outskirts was also inconsistent with the observed luminous matter (Rubin & Ford, 1970; Rubin et al., 1980). Leading to concrete evidence for Dark Matter, matter that doesn't interact electromagnetically and is therefore observable with standard astronomical tools that measure electromagnetic radiation.

Major revolutions in spectroscopy came in the 1970's with the introduction of charged-coupled devices (CCDs) and optical fibers. The CCD was invented at Bell Labs in 1969, and by 1976 it had already been utilized for ground based observing at the University of Arizona (Lesser, 2015). At roughly the same time came the introduction of optical fibers. The first instrument to utilize optical fibers was deployed in 1978 and by 1979 the MEDUSA multi-object fiber spectrograph was making observations at Steward Observatory (Hill, 1988). With improving electronics in the 1990s, these two innovations paved the way for large spectroscopic surveys and allowed for lower time losses between observations and better efficiency at capturing photons.

The challenge with slit spectroscopy is that to observe the spectrum, you need to sacrifice one direction in space in which to spread out the wavelengths of light. That precludes the ability to acquire information about the entire field of view as can be done for optical imagers. To get around this, astronomers have used the total internal reflection properties of optical fibers to capture light from the target, whose point spread function (PSF) is often smaller or equal size to the fiber diameter, and send the light to a spectrometer. In doing so they are able to increase the number of objects they can resolve since they are limited only by the width of the fibers and cladding, and the number of fibers you are able to observe with one or several spectrometers. The extreme of this is clearly to densely pack the fibers together into a dense bundle which acts almost like the pixels of a low (spatial) resolution camera (except in this case each pixel gives an entire spectrum). These Integral-Field Units are becoming more common-place with wide applications in studies of resolved, extended sources and fields with a high density of targets. See, e.g. Allington-Smith (2006), for more information.

Modern survey instruments utilize hundreds of fibers with future instruments using thousands. The typical approaches for using optical fibers for spectroscopy are plug plates and robotic positioners. Plug plates, as the name implies, use drilled plates (typically metals such as aluminum) to precisely locate where a fiber should be placed on the focal plane to observe a specific target. Holes must therefore be properly located and optical fibers inserted for each target of each field. This is a time consuming process, especially for hundreds or thousands of fibers. Methods for overcoming this include the idea of cartridges (SDSS/Boss, (York et al., 2000; Strauss et al., 2002; Gunn et al., 2006; Smee et al., 2013)) and a dual-faced rotating cube (AAOmega/2dF), (Sharp et al., 2006; Smith et al., 2004; Lewis et al., 2002). In SDSS the fibers are plugged by hand in a well lit room. The fibers in the cartridge are effectively flexible adapters that are held fixed at the other end, so that they can interface with the spectrographs. This allows the collaboration to plug cartridges even while the cartridge loaded into the telescope is being observed. The rotating AAOmega/2dF system uses a robotic hand to place all of the fibers in the correct positions on the focal plane on the back of the instrument while the data are being acquired through an identical focal plane setup on the front of the instrument. Discussion has even been made of using 4 systems in a rotating cube for multiple configurations (private communication). Finally, there is the Hectospec instrument which uses two robotic positioners to move the fibers to new locations in under 300 second using a system similar to that of 2dF (Fabricant et al., 2005). This method is highly adaptable (no need for pre-drilled plates) and fast (no hand-plugging or need for a single robotic arm to position many fibers). The drawback is the fixed patrol radii (locations where a robotic arm can carry the fiber before it is fully extended), and the lower density (the robots need space to move, so you cannot have more than two or three fibers very close together). This will be discussed further in Chapter 2.4 with regard to the Dark Energy Spectroscopic Instrument (DESI), which utilizes many robotic positioners to reduce time lost to reconfiguration.

For the two instruments that follow, M2FS has utilized the plug-plate style in order to retain the ability to observe in dense environments where the fibers must be very close together. DESI has chosen to use fixed robotic positioners. Fixed positioners have the problem of not being able to observe dense regions, but which can reconfigure very quickly (on the order of one to two minutes compared to 30 minutes for M2FS) and be scaled to much higher numbers. For example, compare the 256 fibers of M2FS with the 5000 fibers in DESI.

2.3 Michigan/Magellan Fiber System (M2FS)

2.3.1 Design Overview

The Michigan/Magellan Fiber System (M2FS) is a highly multiplexed, 256-fiber, spectroscopic instrument located at a Nasmyth focus of the Magellan/Clay telescope at the Los Campanas Observatory (LCO) in Chile. The Clay telescope is one of two identical telescopes constructed and maintained by a consortium of institutions: Carnegie Institution of Washington, University of Arizona, Harvard, Massachusetts Institute of Technology, and the University of Michigan. The Magellan Telescopes (Baade and Clay) are twin 6.5m Alt-Az telescopes located on the Cerro Manqui peak of the LCO. There are three principal foci at each telescope, two Nasmyth f/11 locations on either side of the telescope and a Cassegrain f/15 location. The mirrors are parabolic shaped borosilicate glass formed in a lightweight honeycomb structure (Shectman & Johns, 2003). With an Atmospheric Dispersion Corrector (ADC), the Nasmyth is capable of widefield imaging of 24' (30' with ADC and M2FS wide-field corrector) on the sky (Shectman & Johns, 2003; Mateo et al., 2012). M2FS consists of four major components:

1) The spectrograph (**MSpec**),

2) The mounting system (**MFib**),

3) The calibration unit (**MCal**),

4) The Wide-field correct (**WFC**);

in addition to the **fibers** themselves. Below we give an overview of each of these components.

2.3.2 Spectrograph

MSpec consists of two separate spectrographs that can be operated independently and in separate "modes." Each is differentiated with the designators "blue" and "red," though the colors hold no physical meaning and have no relation to wavelength sensitivity. Each is optimized to the same optical range of 370-950 nm. The detectors are liquid-nitrogen cooled charge-coupled detectors (CCD's) with 4096x4096 pixels made by E2V Technologies. The CCD is subdivided into 4 2k $\times$ 2k regions each controlled by its own readout. Each pixel is 15 μm in width.

As a multi-purpose instrument offered to the astronomical community to use, M2FS has a broad range of capabilities and modes. In Table 2.1, reproduced from Mateo et al. (2012), we list the filters, gratings, slits and resolutions that can be achieved with M2FS. Observations can be made in high resolution (R∼20-30k but as high as R∼52k, depending on the reference wavelength), low resolution (R∼2k, but as low as R∼200) or a medium resolution with the multiplicity varying from 5-128 fibers per spectrograph, depending on the number of spectral orders used and the specifics of the setup.

Table 2.1 Summary of the key characteristics of the M2FS instrument compared with other prominent facility instruments. Table reproduced from Mateo et al. (2012). [1] refers to Pasquini et al. (2002), and [2] refers to Fabricant et al. (2005).

	M2FS		*FLAMES (VLT)*[1]		*Hecto (MMT)*[2]	
Property	HiRes	LoRes	UVES	GIRAFFE	Spec	Spec Chelle
# of Fibers	256	256	8	132	300	240
Range (nm)	370-950		480-900	370-950	370-920	
Resolution, R	18-34k	0.2-10k	46k	7-24k	1.5-3k	32k
X- Dispersed?	Yes	No	Yes	No	No	No
Fiber Diam.	1.2”		1.0”	1.2”	1.5”	
Min. Fiber Sep.	12”		>30” (Variable)		>30” (Variable)	
Field Diam.	30 arcmin		25 arcmin		60 arcmin	
Vlimit: S/N=5, 2 hrs, 500 nm, med. Seeing	21.5 R∼20k	24 R∼2k	21	22.5 R∼7k	23.5 R∼1.5k	20.5

2.3.3 Fiber Support System

MFib, is broadly speaking the structure that holds, maintains, and organizes the fibers while idle and in operation. The apparatus organizes the fibers into two separate sets of 128 fibers, one for each spectrograph discussed above. Each set is organized and runs into the main instrumental “shoes” that mount the fibers to be imaged by the

Table 2.2 Detailed summary of the various resolutions and configurations available on the multi-purpose M2FS instrument. Table reproduced from Bailey et al. (2014).

Slit Size		**HiRes Resolution**	**MedRes Resolution**	**LoRes Resolution (600 l/mm)**	**Relative Throughput (%)**
μm	pixels				
180	12.0	18k	7.2k	1.8k	100
125	8.3	20k	8.0k	2.0k	92
95	6.3	25k [36k]	10.4k	2.6k	75
75	5.0	29k	12.1k	3.0k	61
58	3.9	32k	13.4k	3.3k	48
45	3.0	34k [52k]	14.2k	3.6k	38

spectrographs. The two shoes, just like the two spectrographs are differentiated with the names "blue" and "red." Each shoe maintains 128 fibers, giving a total of 256 optical fibers. The 128 fibers of each spectrograph are organized further into eight "tetrises" (short for tetris pieces because of the shape of the cassette that forms a "tetris"). Each tetris contains 16 fibers. Any of the 256 fibers can therefore be uniquely identified by giving the shoe ("red" "blue"), tetris number (1-8), and fiber number (1-16). For example, "r102" would identify the fiber as located where r is for "red," "1" is the tetris number, and '02' is the zero-padded numeric id of the fiber within that first tetris.

The MFib system also facilitates the placement of fibers onto the focal plane. It fixes the drilled, aluminum "plug-plate" and the WFC to the telescope. A junction box holds all of the fibers for both shoes, organized by shoe and tetris, with each fiber being identified uniquely as mentioned above. Before mounting a plug plate onto the telescope, configurations are drawn on by hand to indicate what fiber should be placed in a hole. This is how different configurations are targeted, and how targets across the focal plane are related to the list of astronomical objects under observation. Additionally, eight fibers for ensuring alignment of the plug plate relative to the sky (alignment fibers), two guide fibers used for moving the telescope as the Earth rotates, and a Shack-Hartmann Periscope are also outfitted on MFib. The Shack-Hartmann Periscope is an imager that views the central region of the field. If the field is centered on a star of sufficient brightness $9 \lesssim V \lesssim 14$, the images can be analyzed by the system to adjust the primary mirror (using pneumatic actuators) in real-time to correct for

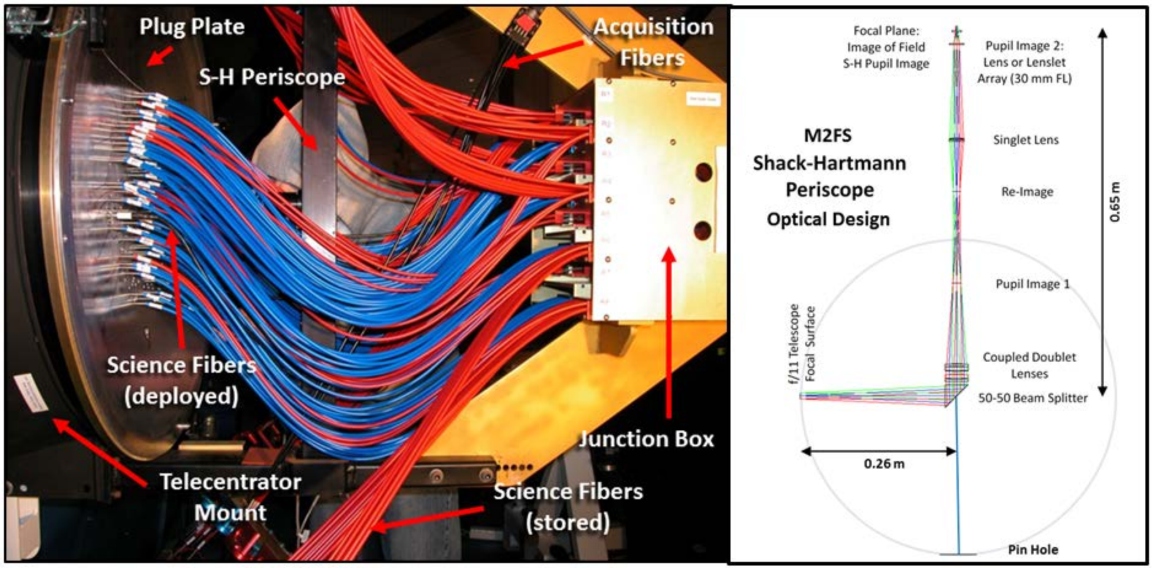

Figure 2.1 An image of the predecessor to M2FS. It shares the same fiber system as shown here. There are multiple bundled sets of fibers (in the center entering the golden box). The fibers are plugged into the focal plate to the left when observing. Those not being used are "stored" by placing them in light blocking grass material. The right shows the optical path for the Shack-Hartmann periscope peering into the middle of the focal plate. Image from Mateo et al. (2012).

changes in temperature, observing angle, etc. and reduce the point-spread function. This ensures that the maximum amount of light is focused onto the optical fiber apertures rather than being lost. If no star was selected as the center of the field, the mirrors are known to be stable with small rotations, so the operating procedure calls for the telescope operator to move to a nearby star between science observations to adjust for environmental variations of the mirror over the time of the science exposure.

2.3.4 Calibration Unit

MCal is the unit that houses the calibration lamps for the instrument. It is mounted in the secondary cage of the telescope and when deployed, covers the telescope focal surface. The cylindrical unit is approximately 2 inches long with a 4 inch in radius and weighs less than 15 lbs. It is mounted on a cantilevered arm that can be swung out via a pneumatic system from its resting location near the outer frame of the secondary cage into the optical path of the telescope. It contains lamps to calibrate both wavelength (of photons hitting a particular pixel on the ccd) and continuum (relative efficiency of a pixel in detecting light compared to others on the ccd).

For wavelength calibration, 7 Thorium-Argon lamps (ThAr) are used to fully illuminate the secondary mirror, which is propagated through the optics to the fibers and onto the CCD's. For low resolution observations; Argon, Helium, Neon, and Xenon lamps are also installed. These contain far fewer lines in the optical, making simple wavelength-pixel parametrizations easier over the broad wavelength range used. For continuum measurements, quartz filament incandescent lamps are also mounted to give a smooth signal that gives flux to all pixels illuminated by each fiber and allows for simpler "flattening."

2.3.5 Wide Field Corrector

Both Magellan telescopes were designed with 30' fields of view. However, the optics only allowed for a 24' observing window where aberrations and vignetting were not significant. The Magellan-Baade telescope was equipped with a WFC, but the Magellan-Clay was not because of issues in placement on the tertiary mirror interfering with Cassegrain observations. However, the M2FS team determined that the limitations on the design imposed by the 20-24' observing window would significantly limit the effectiveness of the instrument and designed a WFC that could be install at the Nasmyth focus for use with the M2FS instrument. The corrector increase the field of view of the instrument to the full 30' on the sky that is observable by the telescope. Designed to provide high-quality imaging (RMS fluctuations $\leq$ 0.25") across the full field. For points of reference, the typically seeing at LCO is ~0.4-1.2" (with typical "good conditions" being $\sim$ 0.6"), and the fibers have an aperture equivalent to 1.2".

2.3.6 Optical Fibers

The optical fibers have a diameter of 150μm ($\pm 3 \mu m$) and a length of 317.5 cm ($\pm 0.76 cm$). The actually light collecting size of the fiber is greater than the diameter of the fiber, however, due to the placement of a 2.2mm spherical BK7 prism in the fiber tip that allows an entrance aperture of 460μm (1.2"). The purpose of this entrance is to convert the focal ration of the Magellan beam to that desired for the exit into each spectrograph. Figure 2.3, taken from Mateo et al. (2012), shows the optical paths used to create this. Figure 2.2, again taken from Mateo et al. (2012), shows a schematic overview of how the tips were created mechanically in the lower left insert. The main image shows several of these fibers in their outer ferrules, stainless steel ends, and plastic tips. The outer ferrules are bicycle brake conduits used to provide resistance to bending and provide a preload that keeps the fibers in

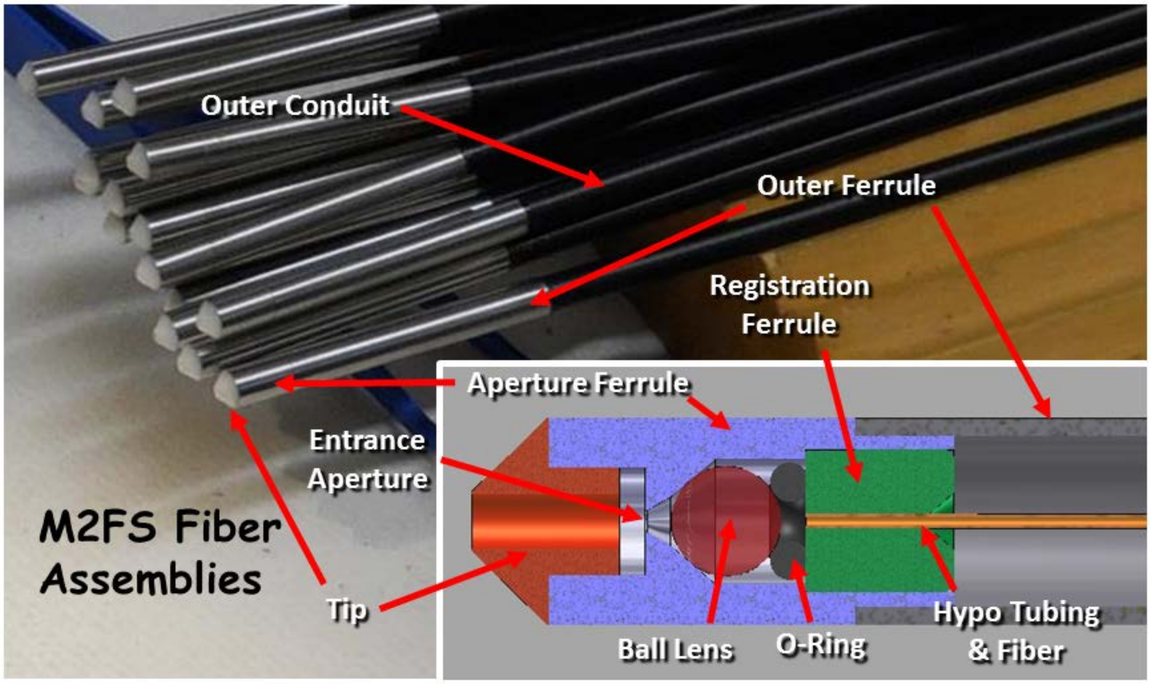

Figure 2.2 Close-up image of the M2FS fiber assemblies. The black outer ferrules provide tensile strength and protection. The metal ends give strength and resistance to strain when plugging into the metal focal plates. The plastic tips prevent damage to the glass stop that maps the focal surface. The insert in the lower right shows the interior with its spherical lens and the actual fiber size in relation to the outer ferrule. Image from Mateo et al. (2012).

place once plugged. The stainless steel ends are designed to to house the optical focal ration reduction path but held a second purpose of mitigating risks of fiber damage or assembly stresses during the repeated plugging of the fibers by hand. The plastic tips keep the stainless steel ends from scratching the telecentrator and have tapered edges to improve the ease of plugging.

The fibers are broad-spectrum multi-mode optical fibers created by Polymicro Technologies. Their attenuation at the blue end of the observing capacity is only 4.5% at 370 nm, decreasing to 1% at 520 mm, and holding attenuation values $< 1\%$ at redder wavelengths. Anti-reflective coatings applied to the fibers reduced peak reflectivity to under 2.5% with mean reflectivity under 1.5% within the observing window of 370-950 nm.

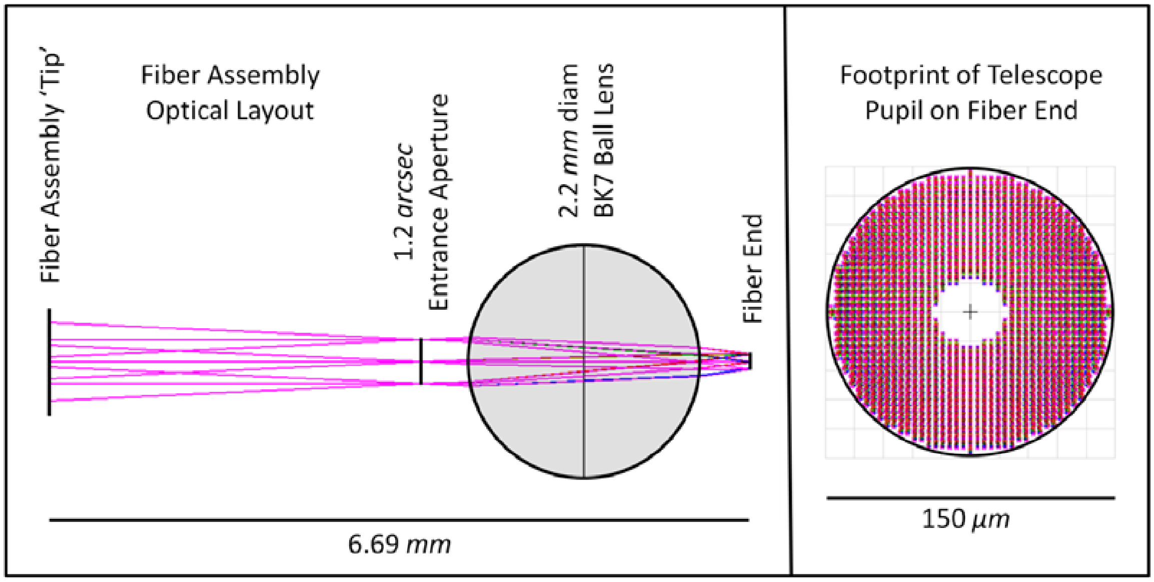

Figure 2.3 Illustration of the ball lens, which allows for a larger entrance aperture and ensures the correct focal ratio for light propagation within the fiber. Image from Mateo et al. (2012).

2.4 Dark Energy Spectroscopic Instrument (DESI)

2.4.1 Design Overview

What makes DESI unique is the 5000 fibers that the instrument contains. This is a factor of five above some of the largest present day instruments. The increase in multiplexing was no doubt achievable only because of the dedicated survey status of the instrument and the investment of hundreds of scientists and researchers, as well as a generous financial investment from the US Department of Energy. To avoid the pitfalls of managing 5000 fibers through some sort of plug plate mechanism, the survey opted to create small ($\sim mm$ sized) fixed robotic arms that will hold and move the fibers from one location to another. Because of their role in positioning the fibers, the robots are commonly referred to as positioners. Since each can run simultaneousl,y re-configurations can occur as quickly as a few seconds, while requirements based on average slew time to a new location is a reconfiguration in under 45 seconds (DESI Collaboration et al., 2016). The downside is that the positioners are fixed in place, which inherently limits the density of targets that can be achieved in a given observation. They are designed to overlap in the areas they can reach (known as patrol regions), but only partially. The fully extended fibers patrol a region of radius

6 mm. They are roughly 10.4 mm from their neighbor, allowing for 2mm of overlap between them (DESI Collaboration et al., 2016). To mitigate this, they employ a 5-pass system that enables every position on the sky to be observed a minimum of 5 times, such that new targets can be acquired that would have otherwise been too close to another target to be observed at the same time. Even so, the instrument will have difficulty in the densest regions, such as clusters (Smith et al., 2018).

DESI is a highly multiplexed instrument not only in its fibers but also in the number of spectrographs. Each fiber sends light to three optical spectrographs via a series of dichroic filters that split the incoming light in broad wavelength ranges, passing one range while reflecting the rest. There are ten such triplets that make up the spectrograph system within DESI. The instrument is intentionally compartmentalized into ten individuals "petals." This segmentation propagates to each level of the instrument, including the spectrographs such that a petal is directly tied to a specified triplet of spectrographs. The benefit of such a system is that if an issue is identified in a specific portion of the instrument, the offending petal can be identified and exchanged for a spare during engineering time to mitigate the impact to performance.

Unsurprisingly, DESI is a complex piece of machinery with many subsystems which each has its nuances. Here we will focus on several aspects most relevant to the present work and those most relevant for comparison to the Sloan Digital Sky Survey and M2FS (Mateo et al., 2012; York et al., 2000; Gunn et al., 2006; Smee et al., 2013). The relevant subsystems are:

1) The spectrographs (3×10),

2) The optical system,

3) The calibration unit, and

4) The focal plane and robotic positioners,

in addition to the optical fibers. In the following sections we give an overview of each of these components. A summary table of relevant comparison information is available in Table 2.3, which compare DESI to SDSS/Boss and to M2FS. M2FS is included to give a sense of scale for these survey instruments compared to state-of-the-art "PI instruments" around the world.

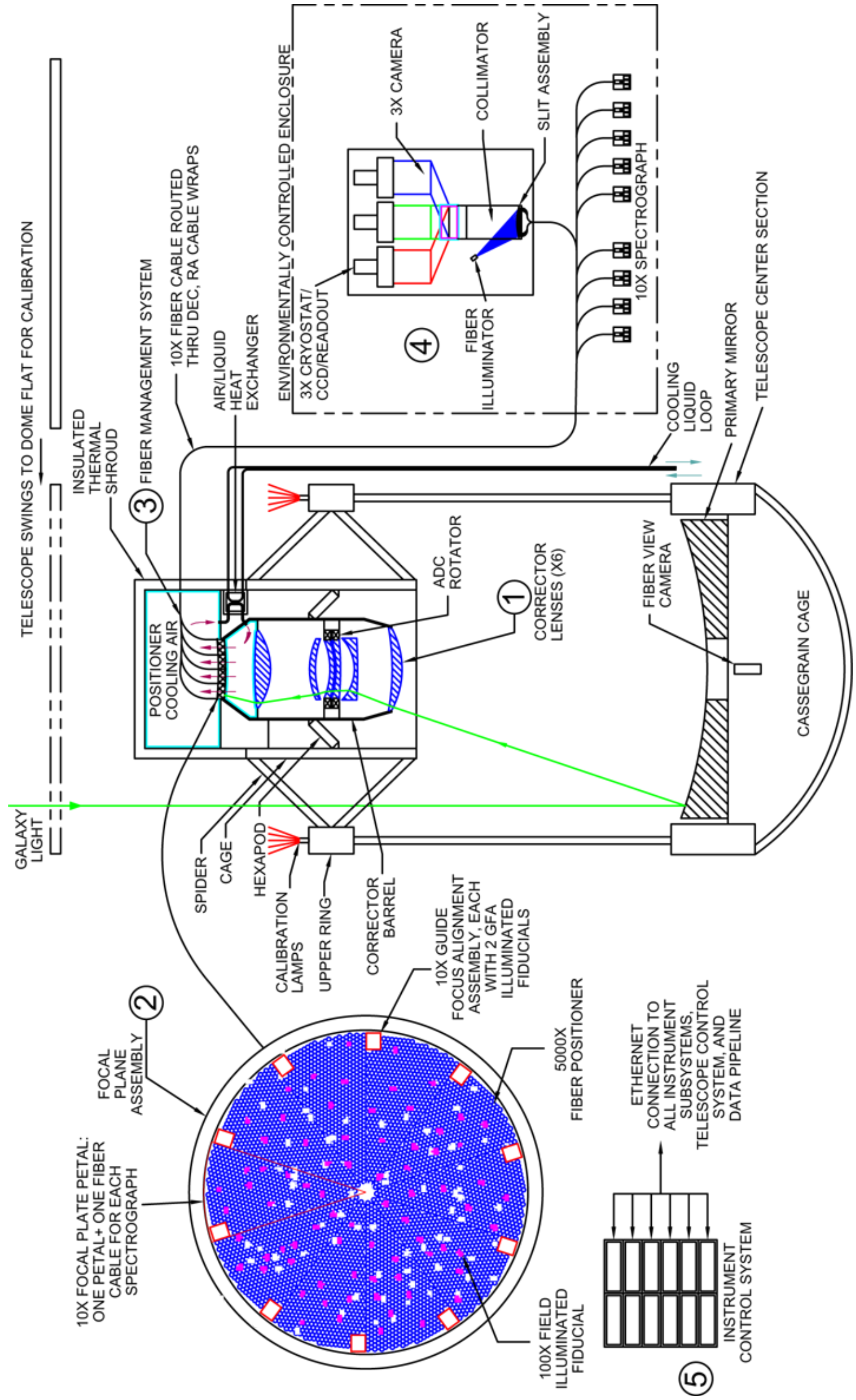

Figure 2.4 A block diagram of the entire DESI instrument. On the far left is the focal plane with blue representing science fibers and red representing illuminated fiducials used to calibrate the focal plane fiber view camera. The middle shows a cartoon of the barrel where the focal plane and cooling system sit in addition to the corrector optics. On the right is a cartoon of the spectrograph located more than 40m from the instrument itself. Image from DESI Collaboration et al. (2016).

Table 2.3 A comparison of characteristics between M2FS, SDSS/BOSS, and DESI. Information from: [1]: Mateo et al. (2012); [2]: Smee et al. (2013) and Dawson et al. (2013); and [3]: DESI Collaboration et al. (2016). [4]: In LoRes mode about 200nm is available across the CCD for any given grating angle (i.e. configuration), but the available wavelengths are in the range from 370-950nm. Higher resolutions give smaller wavelength spans.

	M2FS[1]		*SDSS*[2]		*DESI*[3]
Property	HiRes	LoRes	SDSS	BOSS	Survey
Channels	1	1	2	2	3
# of Fibers	256	256	640	1000	5000
Range (nm)	370-950[4]		380-920	365-1040	370-980
Resolution, R	18-34k	0.2-10k	1.0-2.6k	1.5-2.6k	2.0-4.1k
Fiber Diam.	1.2” (150μm)		3.0” (180μm)	2.0” (120μm)	1.5” (107μm)
Min. Fib. Sep.	12”		55”	62”	∼45”
Field Diam.	30”		3°		3.1°

2.4.2 Spectrographs

The total bandpass of the DESI is 360 nm-980 nm. To achieve such a broad range in addition to the resolutions required (see Table 2.4), three specialized spectrographs were designed. Each of the spectrographs observes roughly a third of the total bandpass, and each is has a CCD and gratings optimized to its specific wavelength range. The spectrographs are referred to by the colors they are optimized to observe: blue, red, and near-infrared. Two dichroics, one in the near-infrared and another in the red. The near-infrared is passed while the rest is reflected toward the red dichroic. The red dichroic passes the red while reflecting the shorter wavelengths to the blue spectrometer. A schematic of the light path for this system is shown in Figure 2.5. The technical specifications of the spectrometers are summarized in Table 2.4, while those of the dichroics are summarized in Table 2.5. Each dichroic is composed of fused silica flats that are coated on one side by an antireflective coating and on the other with a dichroic. As with M2FS and most modern instruments. Volume phase holographic gratings were selected as the dispersers due to their higher throughput compared to other gratings.

One note of interest in Figure 2.5 is the Fiber Back Illuminator integrated with the exposure shutter. The illuminator consists of white LED's positioned to uniformly illuminate the fibers from the spectrometer end, sending the light up to the telescope focal plane. This allows the Fiber View Camera (FVC) to detect each individual fiber and its location based on the detected points of light. This is essential for attaining the required spatial precision in positioner placement when reconfiguring for a new field.

Each spectrograph channel uses a 4k x 4k CCD with 15 μm sized pixels and four readout channels, cooled in individual cryostats. The blue CCDs were produced by the University of Arizona Imaging Technologies Lab, while the red and infrared CCDs were produced at Lawrence Berkeley National Lab (LBNL). The blue CCD has a reported read noise of < 2.9 e^- per 100 kilo-pixels per second, while the LBNL CCDs have a reported read noise of 1.8 e^- per 100,000 pixels per second.

2.4.3 Optical System

With the Mayall telescope being reserved solely for the purpose of DESI, the optical system for the telescope and the instrument are one and the same. Meaning that unlike M2FS, where a wide field corrector needed to be developed to work alongside the existing telescope optics, DESI was able to purpose build the entire optical path

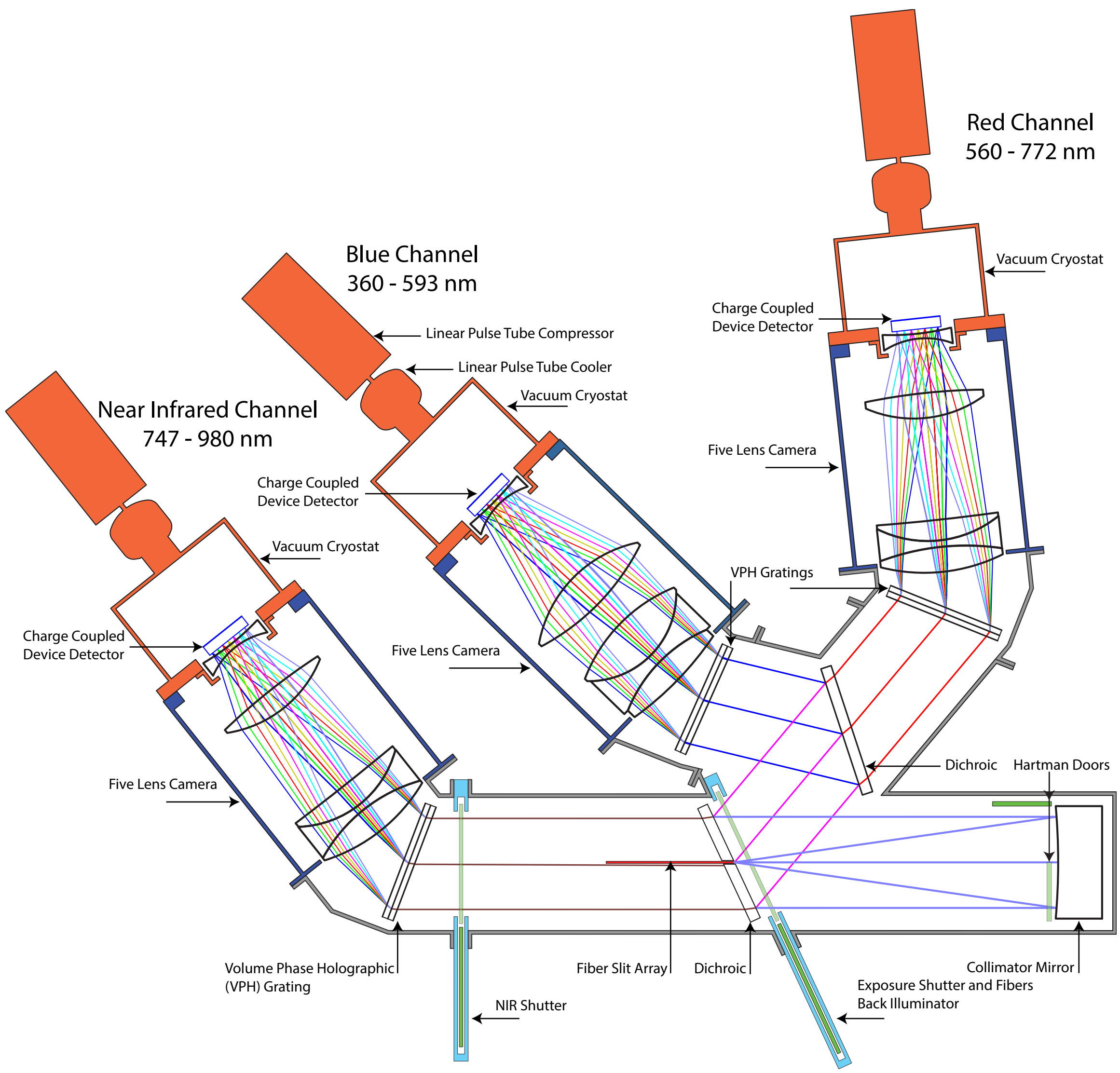

Figure 2.5 A detailed diagram of the light pathway into the three spectrographs via the two dichroics. Image from DESI Collaboration et al. (2016)

Table 2.4 DESI Spectrograph Design Specifications. The information in this table was found in DESI Collaboration et al. (2016).

Item	Current Design
Bandpass	360–980 nm
Resolution ($\lambda/\Delta\lambda$)	2,000–3,200 3,200–4,100 4,100–5,100
Number of Fibers	5,000
Fiber diameter	107 μm
Collimator f/#	3.57
Operational Temperature	+30°C
Number of spectrographs	10
Detector pixel pitch	15 μm
Spectral detector elements	4,096 pixels
Spatial detector elements	4,096 pixels
Minimum resolution elements	3.4 pixels
Fiber spacing (slit plane)	230 μm
Slit Height	120.9 mm
Number of fibers (spatial)	500
Fiber - Fiber Crosstalk	0.05–0.46%

Table 2.5 DESI Dichroic Specifications.

	NIR Pass Dichroic	Red Pass Dichroic	Throughput
Reflection Band (nm)	360–747	360–566	$> 95\%$
Transmission Band (nm)	772–980	593–747	$> 95\%$
Crossover Region R+T (nm)	747–772	566–593	$> 90\%$
Crossover Width (nm)	25	27	

(including a WFC) to enable the wide 3° field of view. Figure 2.6 shows the barrel that houses the optics, and gives a better impression of how the instrument itself is connected to the telescope. Two atmospheric dispersion correctors are inserted, in addition to lenses C1-C4 which allow the instrument to view the entire 3° field of view without significant vignetting or distortions.

2.4.4 Calibration Unit

Four calibration units are mounted on the top ring of the telescope as shown in Figure 2.7. Each unit contains multiple calibration lamps including Ar, Cd, Hg, Ne, and Xe gas discharge tubes for wavelength calibrations and a quartz iodine halogen

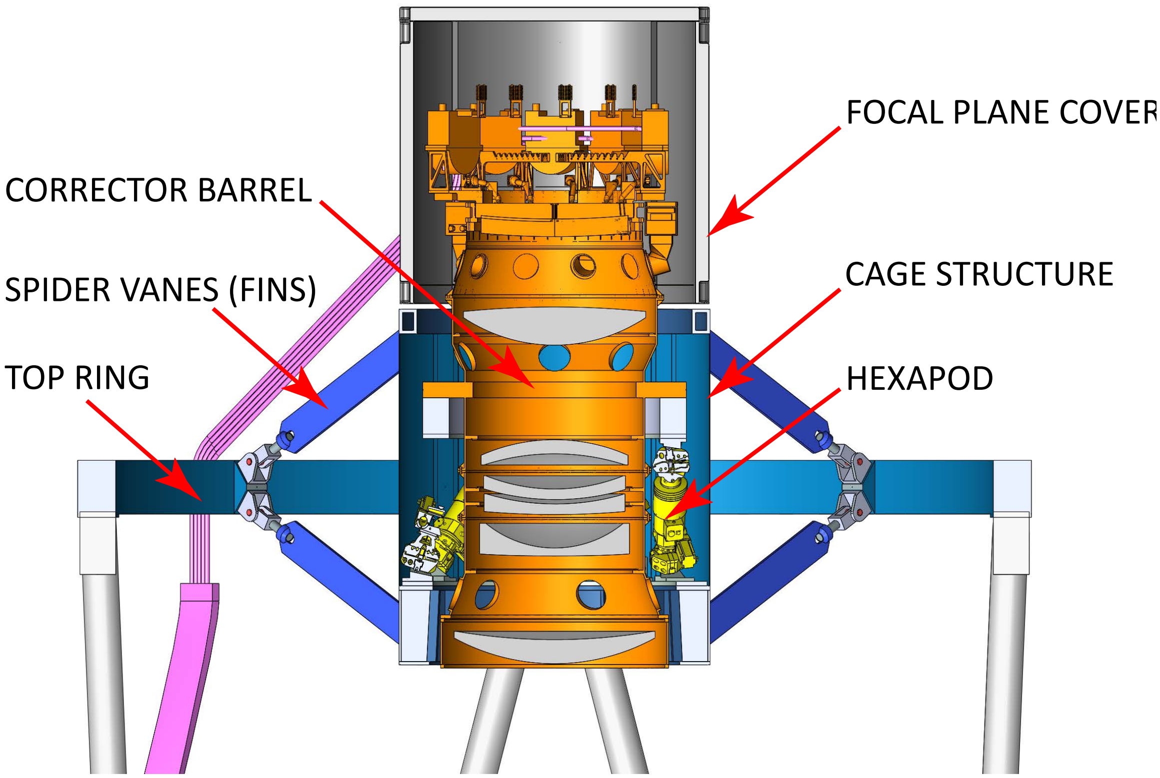

Figure 2.6 Diagram of the barrel. The central region shows the corrector optics in the optical path as light moves from the mirror below to the focal plane and fiber positioners near the top. Image from DESI Collaboration et al. (2016).

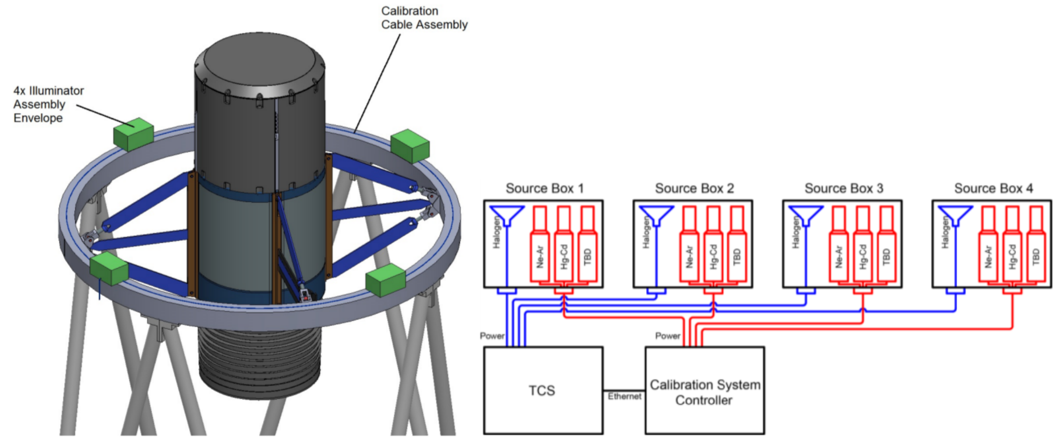

Figure 2.7 Left: Location of the calibration lamp boxes on the upper ring. Right: Schematic view of the interface of the lamp controllers to the telescope and instrument control systems. Image from DESI Collaboration et al. (2016).

continuum lamp for flat field calibrations. The placement of the units creates uniform illumination across the entire field to better than one percent.

Because of the survey nature of the DESI program, calibrations will not be taken during the night. All calibrations will be taken in the afternoon as a baseline, with sky emissions being used to monitor variations from this baseline throughout the night. Since emission lines in the sky are resolved and prevalent in the observing window, this should be sufficient given the stability expected for the spectrographs (which are single purpose and mounted in a stationary and temperature controlled environment). A minimum of 40 skies are acquired during each exposure in each petal/spectrograph (making 400 sky measurements in total).

Fiber throughput flat fielding will be done each afternoon using a flat-field screen similar to that used in photometric surveys and the quartz illuminators in the calibrations units. This helps to correct for fiber to fiber throughput variation. Main sequence F-stars will be used for spectro-photometric calibrations of the spectrometers. These stars have smooth continua and have well described model templates. This allows for accurate solutions of the flux response from counts in the detector to flux from the objects (allowing for the correction of atmospheric absorption and instrumental throughput).

Pixel-level flat calibrations will be done far less frequently, likely about once per year or after major mechanical changes. The process is involved and requires the removal of the slit heads in order to accommodate the illuminator using a flat field screen similar to what is done in many photometric surveys.

2.4.5 Focal Plane, Robotic Positioners, and Optical Fibers

The focal plate of the Dark Energy Spectroscopic Instrument is what truly makes it a revolutionary instrument. 5000 positioners are deployed in a hexagonal pattern among ten "slices" (petals) of the circular projected focal plane. The petals have slight curvature and the positioners given a slight pitch such that the fiber tips of each positioner follows the three dimensional focal surface produced by the optics of the corrector. Figure 2.8 shows the drilled aluminum petal that the positioners are placed into. Figure 2.9 shows how the positioners are placed into the petal. On the left we see a fiber in place along with the locations and appearance of the fiducials that are used for detailed calibration of fiber locations. On the right we a schematic of how the optical fibers are organized in just one of the ten petals. The discrete fibers are bundled into progressively larger sets. A complete bundle of all 500 fibers is generated with a metallic core and woven metallic threads to improve tensile strength. These bundles are roughly 40m in length and convey the light from the optical fibers to the spectrograph. The complete path is shown in the diagram in Figure 2.10.

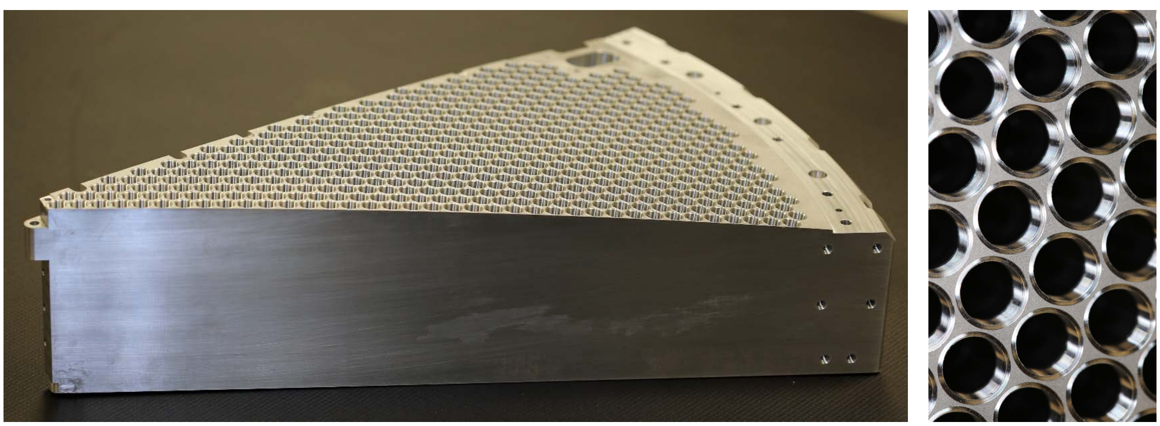

Figure 2.8 An image of the first aluminum petal. Each hole is precisely drilled at varying angles and spacings to ensure that when positioners are placed inside their fibers will follow the the focal plane of the optics. Image from DESI Collaboration et al. (2016).

The diameter of the focal plane is roughly 0. 8m, making each petal 4 cm in length. The robotic positioners consist of two rotating arms that each have a length of 3 mm, giving them a total patrol radius of 6 mm. They are located a typical center-to-center distance of 10.4 mm.

The robotic positioners consist of two brushless gear motors that each rotate about a different central axis. The motors operate at a specified angular speed determined

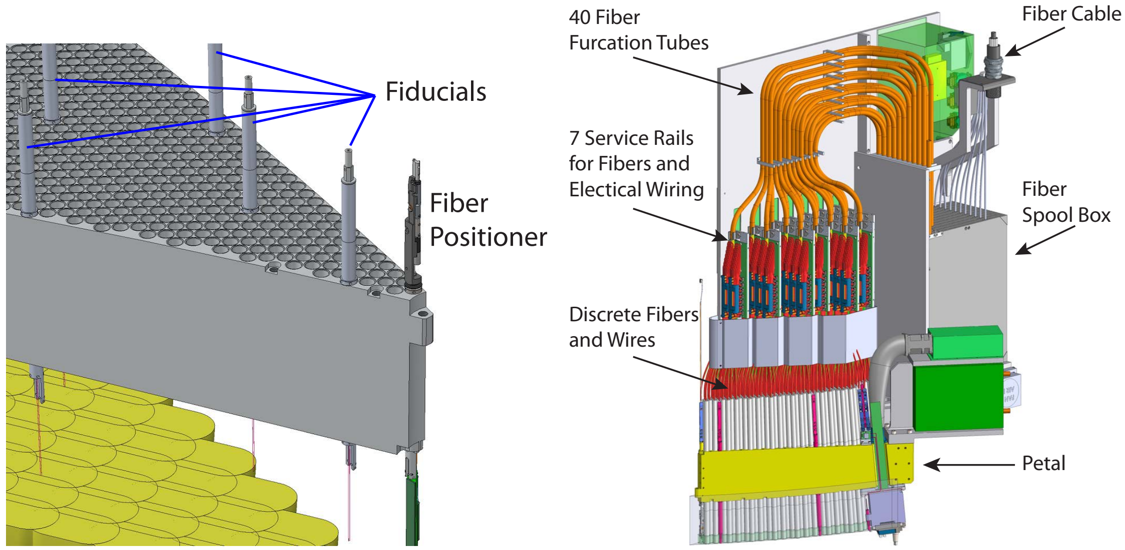

Figure 2.9 Left: Diagram showing how the fibers are be placed into the petals. Right: Illustration of a filled petal and the fiber handling required to manage 500 fibers per petal. Image from DESI Collaboration et al. (2016).

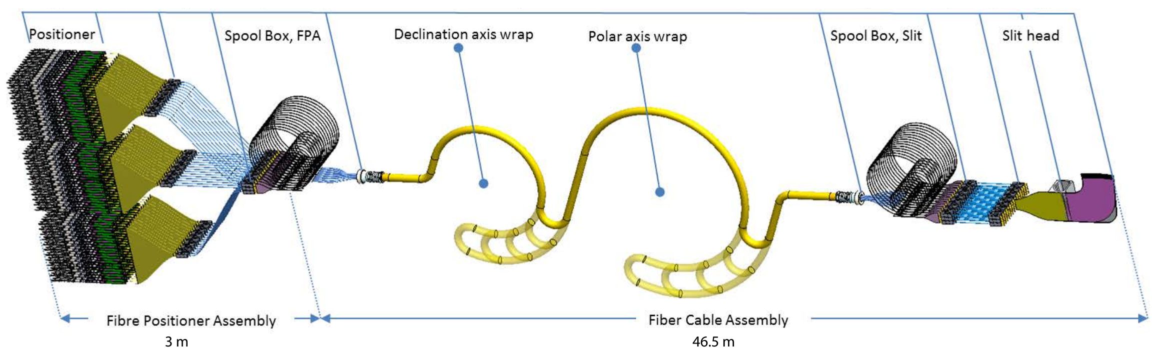

Figure 2.10 Diagram showing the fiber management and consolidation. All 5000 fibers are combined in stages into a single bundle that is strung around the telescope mount, down more than 40m to the stationary platform where the spectrographs are held. Image from DESI Collaboration et al. (2016).

by pulse-width-modulated signals. The schematic relation between them can be seen in Figure 2.11. To each motor is attached an arm to be rotated. The central motor is referred to as the theta motor and can rotate about the central axis 370° moving the inner arm (R_1 in the figure) by that angle. This allows for 10° of overlap that theoretically allows some targets in this small window to be observed from either extreme of the theta limits. The second motor is located at the end of the inner arm, such that its axis of rotation changes with movement of the theta motor. The second motor, called the phi motor, can rotate 190°. Again, there is 10° of tolerance given to the motor such that some locations have more than one potential mapping between physical space and theta-phi angular space. It rotates the outer, R_2, arm. These two rotational axes access all points in the circle of radius R1+R2 to be accessed. The optical fiber itself is located near the end of the secondary arm. It is 107 μm in diameter which corresponds to 1.5” on the sky. Designed for optimal throughput in the optical and near IR, the optical fibers were manufactured by the same company as M2FS and SDSS, Polymicro Technologies.

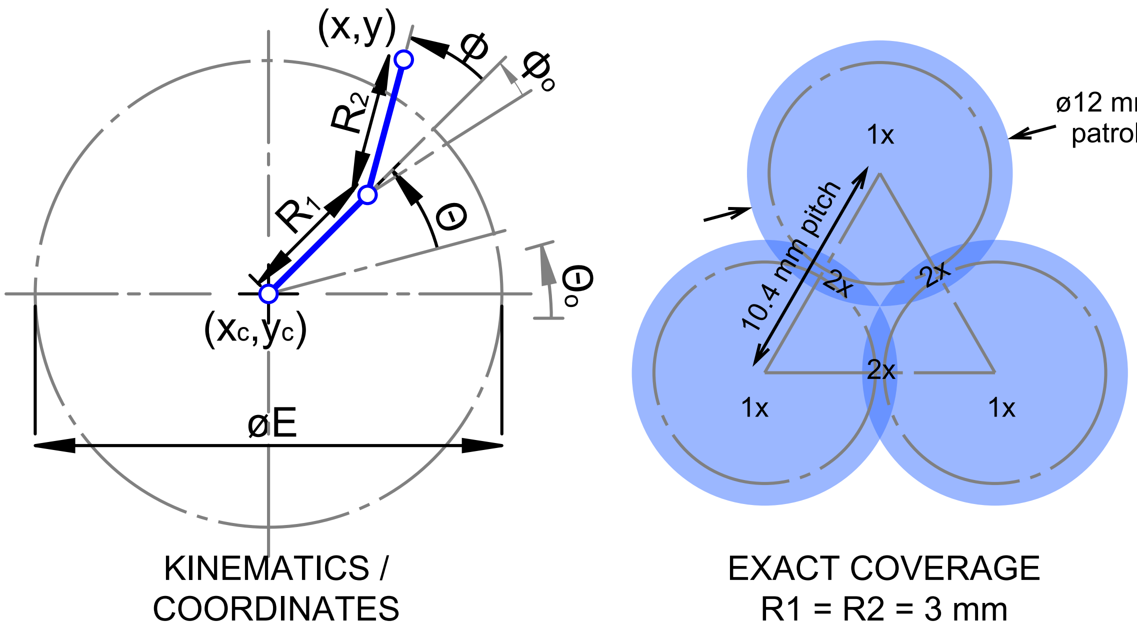

Figure 2.11 Schematic view of the fiber positioner arms and the rotational axes. The central motor rotates R1 in theta. The second motor is positioned on the end of R1 and rotates R2 in phi. These two rotational axes access all points in the circle of radius R1+R2 to be accessed. On the right shows the overlap between neighboring positioners and the relevant distance scales. Image from DESI Collaboration et al. (2016).

For each new observation, the positioners are given a set of commands from the control software for the telescope. The commands are a set of boolean values along with time durations. The boolean determines whether a motor is on or off during that prescribed time interval. The full set of intervals and corresponding motor commands should sum up to move the position from an initial location to its target location for the observation. The requirement is for this to take under 45 seconds. While it only takes a few seconds for a motor to move the fiber 180°, the challenge arises when two positioners want to move through the same vicinity at the same time. Because there is overlap in their patrol regions, collisions between the arms of neighboring positioners is possible. With 5000 positioners moving simultaneously for each observation, the likelihood of some collisions is high. Thus the set of moves given to each position needs to be checked against realistic simulations using the exact positioner and petal specifications (including manufacturer variations in lengths and sizes) such that we can position the positioner to micron accuracy in its final location for observations and ensure that no collisions would occur with a neighbor. If such a collision would occur, software has to be used to create an alternative set of moves that avoid the collision. These "collision avoidance" algorithms were one of my contributions to the DESI project. My work and the details of the software are given in Appendix A.

2.5 Relevance to this Work

The work presented in the remainder of this work utilizes the unique abilities of the M2FS instrument to perform high multiplicity studies of galaxy cluster members. We begin in Chapter 3 by detailing the a major programming endeavor to develop a nearly automated pipeline to reduce low resolution M2FS spectra. We then use that code to reduce our dataset of galaxy cluster members.

While the official DESI survey is not yet operational, initial observations are already underway. Such instruments with fixed positioner patrol radii and a regimented survey strategy that only visits each part of the sky five times are not ideal for high density studies of galaxy clusters, especially those at high redshift. Due to the large number of fibers, hand plugging is no longer possible however. In Chapter 6, we will very briefly discuss how we hope to use DESI for cluster science by leveraging its positive characteristics with other available multi-object spectrographs like M2FS for follow-up observations of dense cores.

Finally, in Appendix A we outline work on the collision avoidance system of the robotic positioners for the DESI project.

Chapter 3

M2FSreduce: A Multi-Object Spectral Reduction Pipeline

3.1 Overview

The primary objective of this dissertation was to obtain high completeness spectroscopic observations of galaxy cluster member galaxies to study their masses and dynamical state. To do so we utilized Michigan's access to the Magellan Telescopes and specifically its access to the Michigan-Magellan Fiber System (M2FS) to obtain hundreds of galaxy spectra in each of several tens of galaxy clusters. The sample will be discussed in Chapter 4. Here we first describe the development of a software pipeline used to reduce the spectroscopic data acquired using M2FS.

3.1.1 Data Reduction

Over the course of our small, targeted cluster survey we developed a Python-based data reduction pipeline to take the raw CCD (charged coupled device) images from M2FS and reduce them into calibrated spectra that we could then fit for redshifts. For analysis of the data, we worked with Prof. M. Mateo to run his M2FS *IRAF* package and reduce the data from two of the clusters, which gave us an introduction to the types and quality of the data, and what we could expect to achieve from our own reductions. Using this knowledge we were able to produce a fully functioning reduction pipeline for low-resolution M2FS data, called M2FSreduce[1] for the MDM

[1]The code can be found here once made available: `https://github.com/akremin/M2FSreduce`. The pipeline was inspired by and borrows a small amount of code from the python package *OSMOSReduce* created by Dan Gifford `https://github.com/giffordw/OSMOSreduce`

2.4m OSMOS instrument. Once the data is published, the code will also be released publicly for use by the astronomical community. This code has matured to 'pipeline' status, such that any low-res M2FS data acquired should be able to be efficiently reduced. A complete description of the code and the algorithms follows in this chapter, but first we will briefly summarize the basic steps here.

3.1.2 Overview of Pipeline Steps

1. **Bias Subtraction**: Bias images are taken as 0 second "exposures" of the CCD. This helps to capture the readout noise from the instrument. This is an additive bias that must be subtracted out. Because there can be pixel-to-pixel variation, each pixel is subtracted separately. To reduce uncertainty in the bias, the median of many 0 second exposures is found, with that being subtracted from the science and calibration images.

2. **Stitching the Image**: Each spectrograph is read out into four "images" by four different operational amplifiers. After the image specific variation (bias) is removed, the images can be combined to form the full 2048x2048 pixel CCD array (assuming 2x2 binning) for the respective spectrograph.

3. **Removing Cosmic Rays**: Cosmic rays can interact with the material in or around the CCD and produce spurious charges in a pixel of the camera. Typically they leave trails of several (even sometimes many) pixels as they travel through the CCD and interact with material. These are removed using a Python package, lacosmic[2], based on Laplacian edge detection as published in van Dokkum (2001).

4. **Extraction of Each Spectra from CCD**: 128 fibers illuminate each spectrograph's CCD. The light from the grism defines a dispersion axis roughly parallel to the CCD rows, but deviating due to the non-linearity of the optical path for each fiber based its location on the CCD. To produce one dimensional spectra, the two dimensional image of each spectra needs to be isolated, then the flux perpendicular to the dispersion direction fit or summed to give the total flux as a function of (yet to be determined) wavelength.

5. **Wavelength calibration**: There is a two step process for calibration what wavelength of light falls on a given pixel of the CCD. The first step uses low res-

[2] https://github.com/larrybradley/lacosmic

olution Argon, Neon, Helium, Mercury, and Xenon lamps to get an initial guess based on an automated cross-correlation routine. Second, a Thorium-Argon lamp exposure is used to identify significantly more emission lines distributed across the CCD. These lines are selected by-hand and matched to peaks in the spectrum by the user. After a few spectra are calibrated in this way, an automated process iterates through the remaining spectra and only returns those it is confused by to the user for correction. The pixels are fit to a fifth order polynomial to produce the wavelength. The typical RMS of the fits is between 0.3 Åand 0.5 Å.

6. **Fiber Flattening**: Because our analysis does not depend on absolute flux values, we have not implemented a spectro-photometric flattening routine. However, we do correct for differences in fiber throughput using flat-field images. Typically taken at evening or morning twilight on the dim sky, these provide truly uniform intensity to the entire focal plane. Thus any variations in the captured intensity is due to throughput. Spectral lines are smoothed over and all spectra are interpolated to the same wavelength grid. The ratio of all fibers to one reference fiber (in this case, the maximum flux fiber) are taken. These wavelength dependent ratios are then applied multiplicatively to the science fiber data to adjust for the wavelength dependent throughput variations.

7. **Sky Subtraction**: The sky is bright at redder wavelengths and the emission lines dominate the spectra unless properly removed. For this purpose a minimum of six fibers are assigned to blank locations on the sky (with typically many more unassigned fibers also being placed on blank locations). These flat-corrected and wavelength-interpolated sky fluxes are then subtracted from the science object spectra. For large emission lines found using a peak finding algorithm, the subtractions are done peak-by-peak with each being fit for a total flux and the flux being subtracted from the science fiber peak. This reduced interpolation issues with sky entering into neighboring bins and causing large negative and large positive fluxes in the resulting spectrum. Care is taken to ensure certain physical limits such as the sky must be less than sky+object. For large or poorly fit lines, the areas of the subtraction are masked and therefore not used for subsequent redshift fitting. After all lines are removed, the sky continuum is subtracted from the science spectra.

8. **Combining Science Exposures**: Each science exposure takes place over 10's of minutes and sometimes differ by an hour or more. Because variability is

inevitable each science exposure is calibrated using a calibration lamp image taken around the time of the science image. This leads to slight variation in the wavelength solutions and therefore the wavelengths of the resulting science spectra. To mitigate interpolation affects, we based our summation on the wavelengths of the central (in time) exposure. All other exposures have their flux interpolated to that wavelength grid. The masks are applied and an average of the exposures in each pixel is taken. If the pixel is masked, it is not used in the average. Note that summation and averaging are identical in most circumstances (one being a constant multiple of the other), but here we use an average because the pixel by pixel averaging naturally accounts for masked pixels.

9. **Redshift Fitting**: Finally, the combined science fluxes and wavelengths are fit to redshifts using a cross-correlation technique against luminous-red-galaxy (LRG) galaxy flux templates from SDSS (Strauss et al., 2002). The template is redshifted iteratively in small redshift increments, interpolated to the wavelength grid of the science spectra, and cross-correlated using the Pearson-r coefficient. The redshift with the maximum correlation, along with the correlation value is returned as the redshift of the cluster. This code is also publicly available as a standalone package[3], though the variant used here is still private until publication of the data[4].

3.1.3 Summary of Chapter

This chapter will proceed chronologically through the reduction steps as outlined above, and show how M2FSreduce performs these actions. A section introducing the structure and the way in which the data is organized will precede that discussion. Nearly all of the processes occur autonomously, with the exception of the wavelength calibrations.

3.2 M2FSreduce Structure

3.2.1 *quickreduce*

The main executable for the pipeline is *quickreduce.py*, which takes in three configurations files, defines three classes, and executes each reduction step. It can be called

[3] https://github.com/giffordw/zpy
[4] https://github.com/akremin/zestiPy

from a command line as an executable or from within a python interpreter as a function. Figure 3.1 shows the flow and relationship of data within the pipeline, while Figure 3.2 shows the relevant function calls used for the data reductions and their relations to one another.

3.2.2 Configuration Files

The three configuration files consist of a pipeline file, input-output file, and an observation file. The *pipeline.conf* defines what steps should be performed, what the name of the target field in question is, and a large number of optional parameters that define how the pipeline and the reduction steps will operate. The second is *io.conf*, which defines where the data, in addition to defining templates for the file structure and data naming conventions for the resulting reduced data. Finally, *obs.conf* gives the associated file numbers for each exposure type: coarse calibration, fine calibration (if a secondary calibration is used), twilight flats, science exposures, fiber maps, and bias images. It also defines what CCDs were used, what fibers were not functional, what fibers were used to replaced inoperable fibers, the configuration of the instrument, binning, etc.

3.2.3 Fielddata and Other Classes

The code *quickreduce.py* takes these configurations and uses them to define an *Observation* class, an *Instrument* class, a *Filemanager* class, and a *Fielddata* class. The final class, *Fielddata*, is what stores all of the data and all of the reduction operations to be used on the data, using the information from the other classes. Once the *Fielddata* class is defined using the other classes as inputs, *quickreduce* can run the pipeline steps requested in *pipeline.conf* by calling *Fieddata.runstep(step)*, with the appropriate keyword. The data within *Fielddata* is changed internally to it in an object oriented programming scheme.

3.2.4 Final Remarks

The general methodology for this pipeline was to enable a wide amount of control to the user about how the reduction steps would operate and how the data will be formatted and stored. In addition it allows for easy stopping and starting of the reduction process for repeat reductions of certain steps. Default values of all the pipeline parameters and instrument settings are maintained for easy use, with only a few parameters needing to be changed for a given observational need. If the instrumental state is unchanged and the reductions steps are the same, only a new *obs.conf* file needs to be generated for each new target field.

The specific names of the methods and the structure of the functions can be seen in Figure 3.2. Care was taken to make as many of the steps as possible instrument-agnostic, using *Fielddata* to manipulate the data into more generic forms that is then passed to and received from these called functions. Each reduction step will be conceptually described in the remainder of this chapter.

3.3 Bias Subtraction

Charged Coupled Devices (CCDs) are used in astronomical observations due to their low noise and high quantum efficiency ($> 95\%$). They are effectively an array of semiconductors that are assembled in a grid composed of linked rows that each form a readout path to the registers and the readout electronics at the edge of the device. Each pixel operates by absorbing a photon which releases an electron that is captured into a corresponding potential well within the pixel. However, pixel to pixel variations in zero-points can lead to different perceived electron counts in different elements. In addition there are readout differences due to the row-based readout system employed by most CCDs. To correct for pixel to pixel and row-to-row offsets, zero second "bias" images are taken. Typically 10s to 100s of bias images are acquired and a median valued "master" bias image is generated from them. With zero seconds of exposure, no photon-induced electrons and ideally no noise-induced electrons should be produced, which allows us to characterize these offsets so that we can subtract them from our other images. There are "bias columns" that also reside on each CCD. These are not exposed to photons and can therefore be used to measure and characterize the row-to-row bias inherent in that specific image. Such measurements are typically performed within a day of the observations to mitigate any potential temporal variations that could occur within the device. Figure 3.3 show two such "master" bias images, where each of the four readout regions (differentiated by their operational amplifier, or "opamp") are visible due to their bias characteristics. Figure and 3.4 shows histograms of bias values for each opamp plotted for the "red" and "blue" cameras of M2FS, respectively.

The specific implementation within M2FSreduce removes any row-to-row biases from an image based on the median of the bias pixels in that given row. The same is done for the bias frames. This gives the most realistic estimates of that variation as

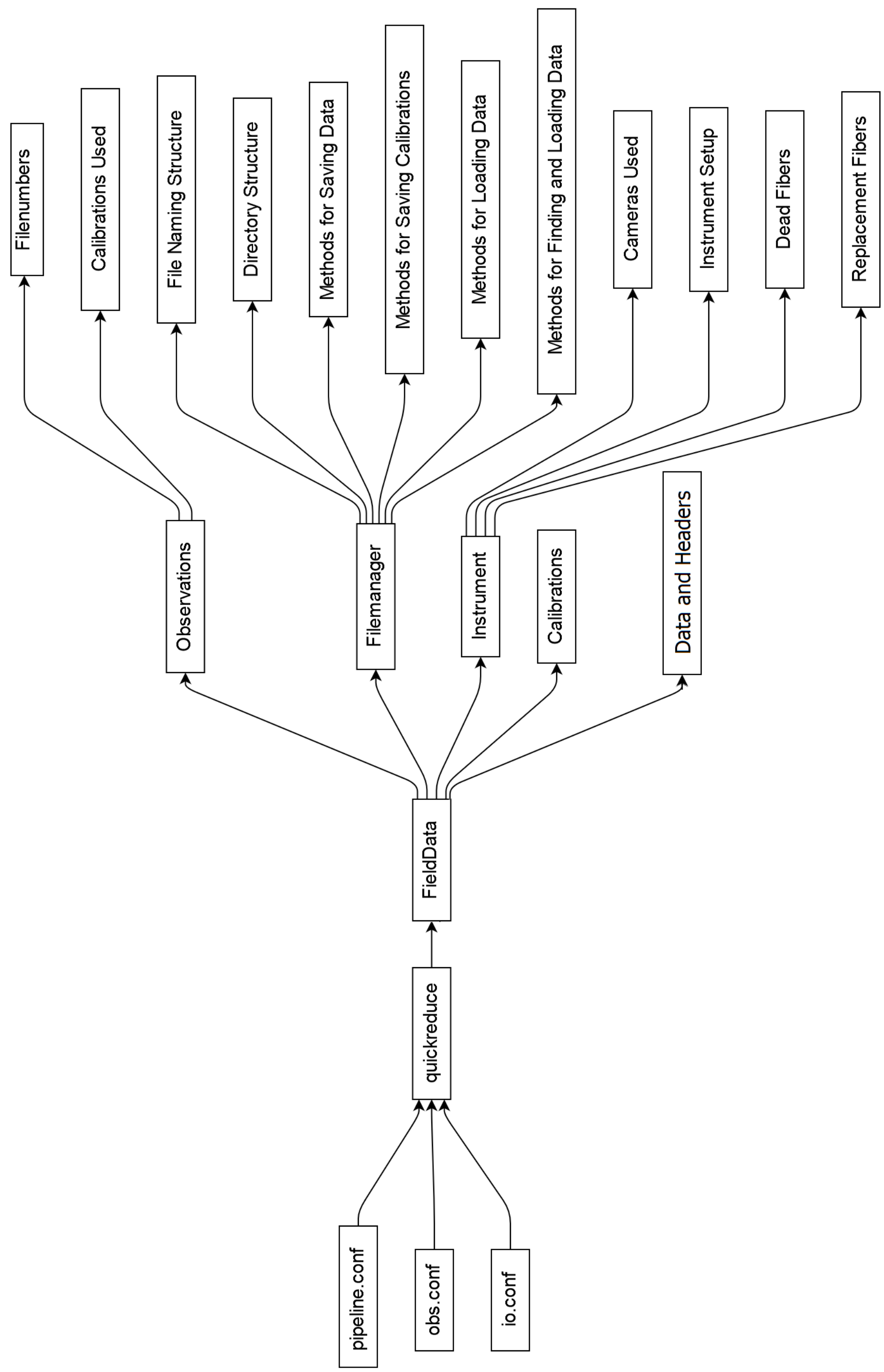

Figure 3.1 A tree diagram showing how information and data are shared within the *M2FSreduce* pipeline.

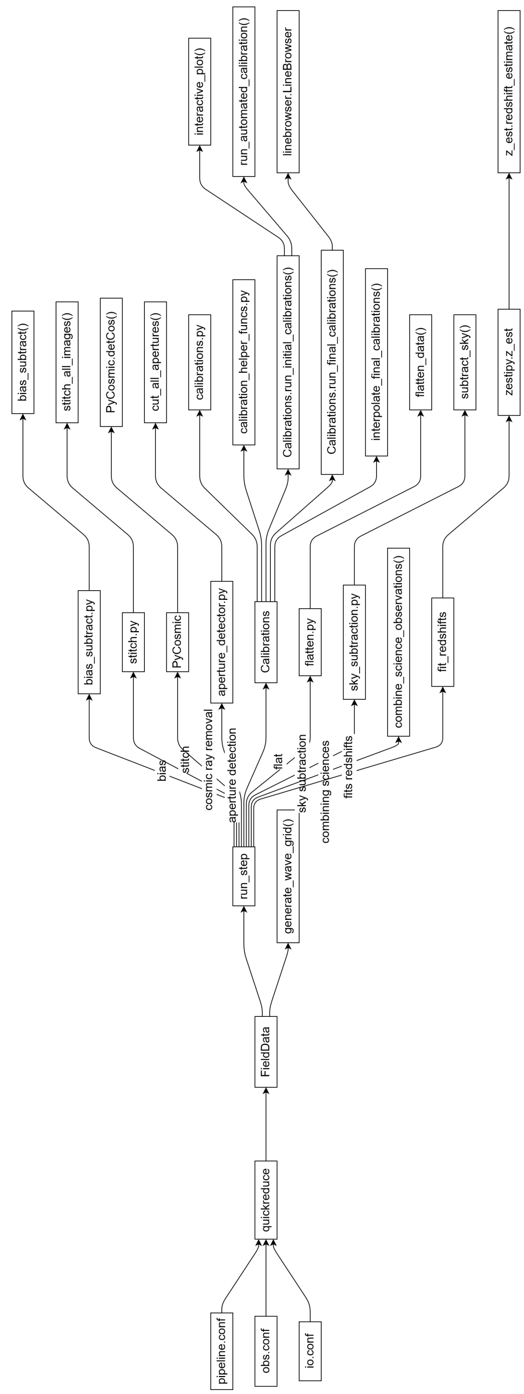

Figure 3.2 A tree diagram showing how the reduction steps in *M2FSreduce* are related for reducing the spectral data.

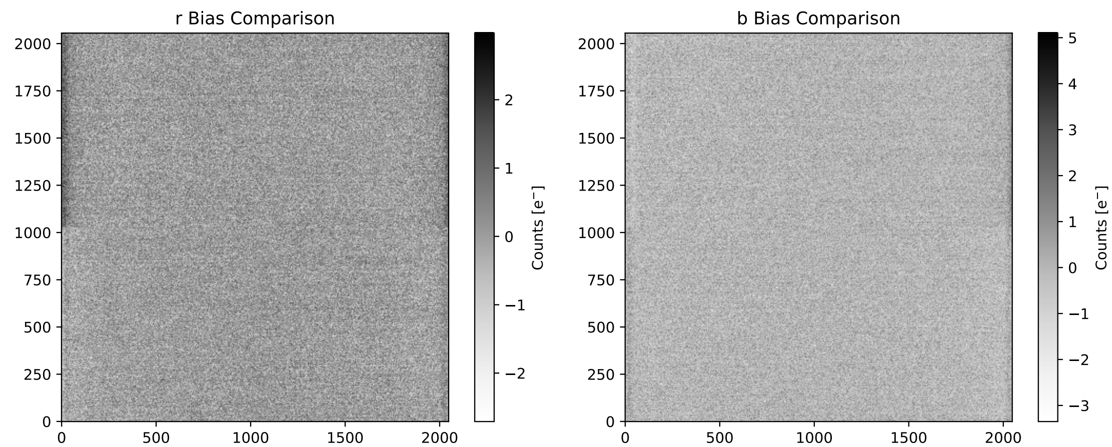

Figure 3.3 Combined bias images of all four operational amplifiers for each camera, with the red camera on the left and blue camera on the right. These master images are produced by taking the median pixel value of each pixel among hundreds of bias images. Note the structures present that could potentially affect scientific inferences if not properly accounted for.

it is captured at the precise time of the measurement of interest. After this is done, the median "master" bias is subtracted from the other images of interest to remove any residual pixel-to-pixel zero point offsets.

3.4 Combining Image Segments

Once the pixel-to-pixel and row-to-row biases are removed from the individual image segments, again broken into four based on the read opamp, the segments can be assembled into one complete image. One final step is needed to adjust for the gain of each amplifier. These affect the linear relationship between the electrons observed (and thus the photons observed, modulo small inefficiency losses) and the analog-digital units (ADUs). These are specific to a readout device and alters the number of "counts" recorded for each pixel. Without a correction we would be unable to compare the counts in one image segment to another. Figures 3.5 and 3.6 gives examples of correctly combined segments for an image exposure in cameras "red" and "blue" on the left and right, respectively. Various reflections and rotations are needed to properly combine the image segments, which are taken care of automatically within the code.

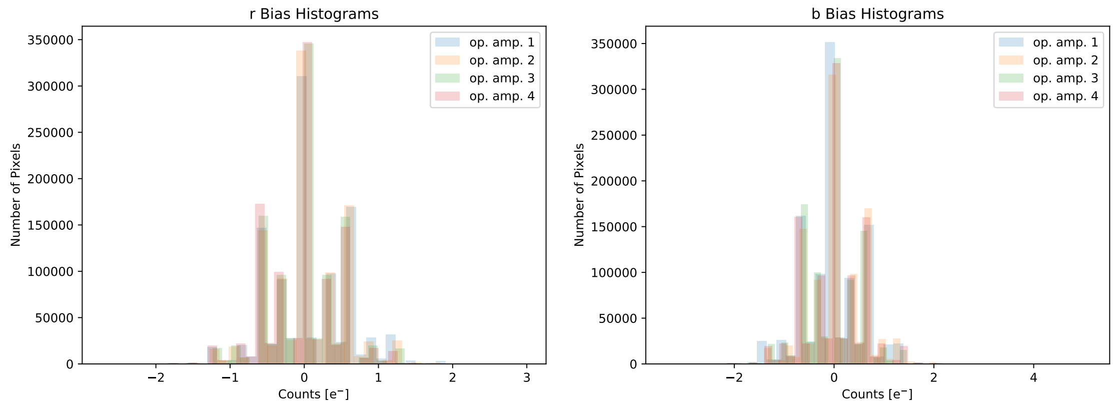

Figure 3.4 Histograms of master bias values for individual pixels in each opamp, for the red camera (left) and blue camera (right).

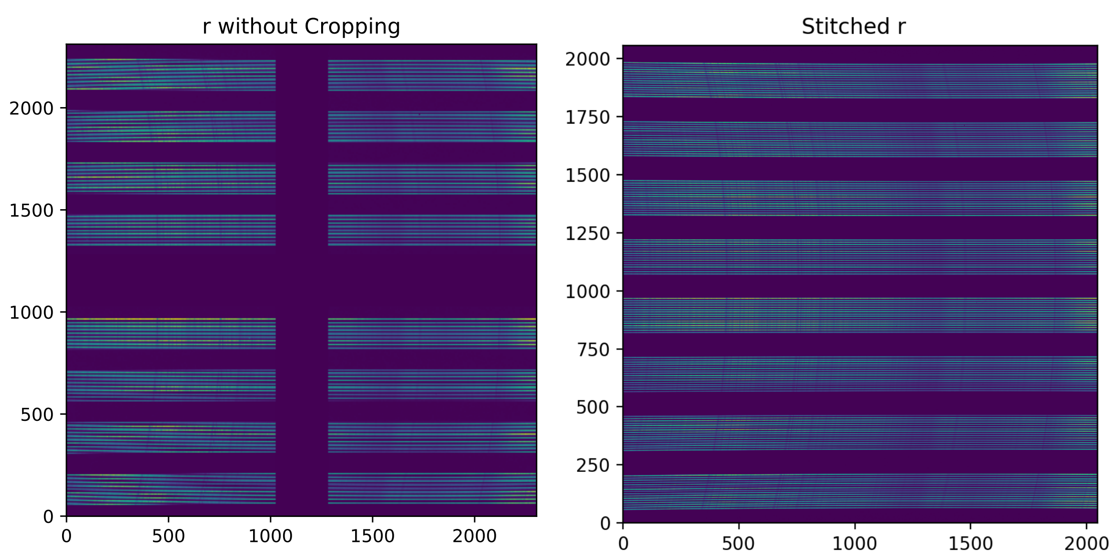

Figure 3.5 Images illustrating how the opamps (image segments) in the red CCD are correctly combined, and showing the additional columns and rows that for bias and overscan regions before removal (left) versus after removal (right).

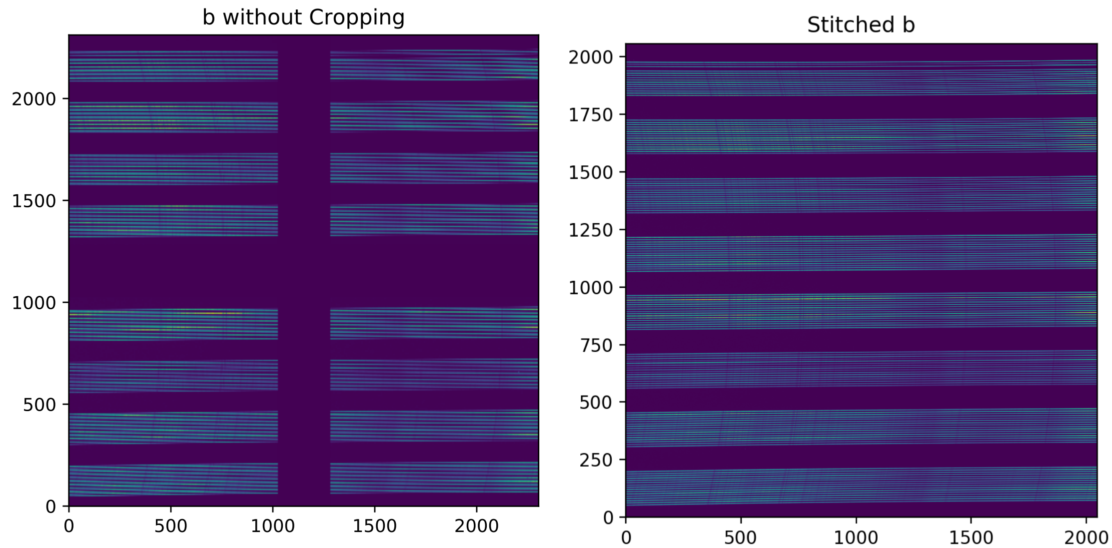

Figure 3.6 The same as Figure 3.5, except for the blue CCD.

3.5 Cosmic Ray Removal

Observations of faint objects require integration times of minutes to hours. Over this time the CCD's are exposed not only to signal photons, but also noise from the environment, atmosphere, and cosmic rays. Atmospheric flux propagates through the optical path and needs to be removed with blank sky observations after wavelength calibration. Cosmic rays, however, impinge directly onto the CCD and create sharp, bright artifacts in the raw images. Various techniques can be used to identify them, but one that has been widely used with great success is van Dokkum's Laplacian edge detection algorithm L.A. Cosmic (van Dokkum, 2001). As our reduction code is in python, we use a python implementation of the original algorithm by Larry Bradley, *lacosmic*[5], which was independently reviewed and tested prior to including in the pipeline.

While other methods typically leverage the transient nature of cosmics, L.A. Cosmic is able to identify cosmic rays in individual images without the requirement of multiple exposures. Its basic premise is that cosmic rays are very bright and appear as streaks or dots that have abrupt, discontinuous changes in counts. Thus by looking at the spatial Laplacian (in pixel space) of the image, we can identify cosmics as those with large resulting Laplacians. If we assume a two dimensional Gaussian, the Laplacian is:

[5]https://github.com/larrybradley/lacosmic

$$
\begin{aligned}
\nabla^2 f &= \frac{\partial f}{\partial x^2} + \frac{\partial f}{\partial y^2}, \quad f(x,y) = \exp\left(-\frac{r^2}{2\sigma^2}\right) \\
\implies \nabla^2 f &= \left(\frac{r^2 - 2\sigma^2}{\sigma^4}\right) \exp\left(-\frac{r^2}{2\sigma^2}\right).
\end{aligned}
\tag{3.1}
$$

If we discretize this, we find a two-dimensional filter that we can convolve with our images

$$
\nabla^2 f = \frac{1}{4} \left\{ \begin{array}{rrr} 0 & -1 & 0 \\ -1 & 4 & -1 \\ 0 & -1 & 0 \end{array} \right\}, \tag{3.2}
$$

where sigma is made to be much less than one to capture sharp pixel changes of the cosmic rays. This simple implementation has zero average and properly eliminates smoothly varying signal, but creates cross-like artifacts around identified cosmic rays. To remove this, the algorithm utilizes the comparison of multiple down-sampled versions of the image, as well as other optimizations and detailed manipulations that are described in detail in (van Dokkum, 2001).

This algorithm detects cosmic rays and saves a Boolean mask of the results to disk. In addition, it generates a "cleaned" version of the image where the masked pixels are filled with the median of all non-masked pixels within a five-by-five square centered on the masked pixel in question. The current implementation uses these cleaned images and doesn't propagate the masks into the one-dimensional spectra and one-dimensional masks. This is a priority for future improvement of the pipeline, but is not yet implemented.

Figure 3.7 shows an example from the red camera on the left and blue on the right. From top to bottom: raw image, detected cosmic rays, cosmic ray corrected image. Figure 3.8 Gives an enhanced view of three tetrises from the blue camera. You can see detection is both efficient and accurate. Notice the string of sky emission lines that are maintained, and the single science fiber emission line that was also kept intact.

3.6 Extracting Fiber Fluxes

Once the images have been corrected for cosmic rays, we can go about extracting the 128 individual spectra arranged across each CCD's surface. Figure 3.9 shows example images for the red camera (left) and blue camera (right). The red horizontal lines show the upper and lower bounds of each fiber bundle (referred to as tetrises)

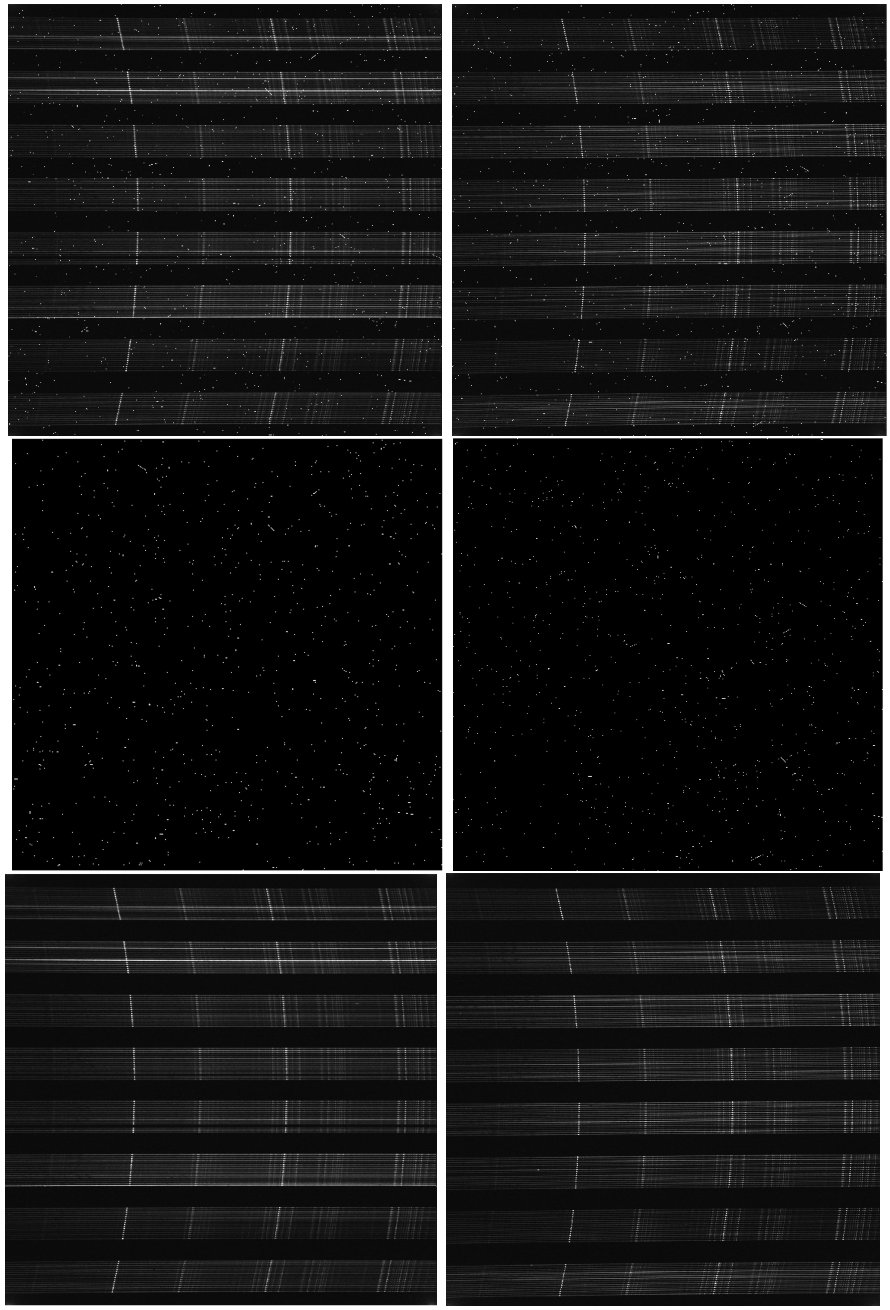

Figure 3.7 Images showing the identification and removal of cosmic rays. The left column is an example from the red camera and the right column is from the blue camera. The top row shows the uncorrected image with cosmic rays appearing as white spots and streaks in the image. The middle row is a boolean mask showing the identified location of cosmic rays. The bottom row shows the same image as in the top row, except with the identified cosmic rays being replaced by the median within a five-by-five pixel grid around each masked pixel.

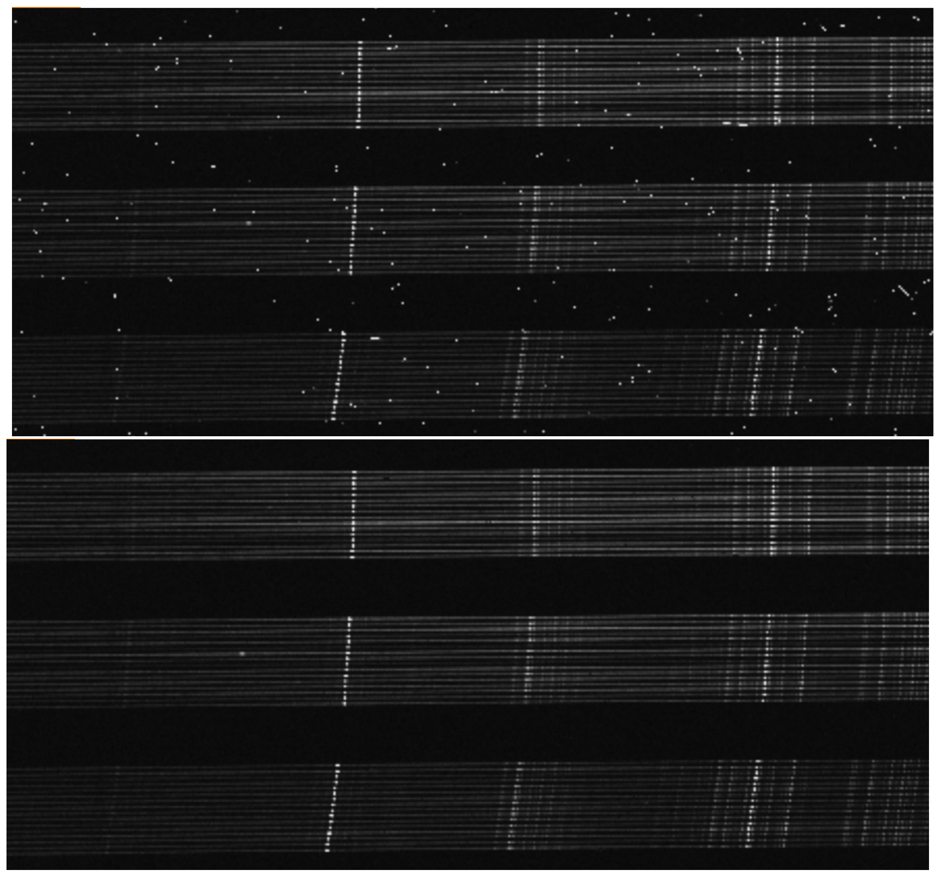

Figure 3.8 A zoomed-in view of part of the b camera image in Figure 3.7. The top image shows the exposure before the cosmic rays are removed. Cosmic rays appear as white spots and streaks in the image. The bottom image shows the image after cosmic ray removal. Note on the left-hand side in the vertical center of the image, there is a strong emission line in the spectra that was not removed, while all visible cosmic rays were. Note also that the bright sky lines in every spectra are also retained.

consisting of 16. Note that due to alignment of the fibers in the “shoe” (the container that houses all eight tetrises) at the interface with the grating assembly, in addition to CCD alignments and optical distortions, the dispersion axis of the spectra are not exactly parallel to the pixel rows of the CCD. This increases the difficulty of extracting the spectra directly. Figure 3.10 illustrates this by showing a normalized summation over the columns. Each spike is a spectrum, but there is considerable overlap between peaks due to the curvature. In any individual column, the amount of light from a neighboring fiber is far smaller, but because of the curvature, the minimum between adjacent fibers changes row location from left-hand side of the CCD to the right-hand side and leads to greater flux seen between fiber spikes in the image. Fortunately, the tetrises are well distinguished, as shown on the right hand side of Figure 3.10, where we have smoothed out the individual fibers and focus on a boolean choice of signal or no signal. This is used to extract each bundle of 16 fibers for further extraction of individual fibers.

For each of the eight tetrises, for each camera, we run a peak finding algorithm on each column (over all rows), to determine the pixel row locations of each fiber's peak flux at that specific column location on the CCD. This is done for all columns, with peak locations and distances to the minimum of the flux toward the neighbor also recorded both above and below the fiber. Special attention is paid to rejecting outliers or missing peaks in any individual column by smoothing the lower, upper, and peak locations fit as a function of column location for every fiber. Based on either location or provided dead fibers, the code also identifies the appropriate Fiber ID for each spectrum, which is critical for matching the data to the proper target. The current implementation requires the distance from the peak to the upper and lower cutoffs be the same, and constant as a function of column location. The median separation of the smoothed upper and lower distances (divided by two) is used for the cutoff location above and below the peak. Figure 3.11 shows two examples of these fiber identifications. The first demonstrates the amount of curvature in the outer tetrises and the code's ability to trace the spectra. The second shows the code's ability to identify missing or dead fibers and appropriately label the visible ones. In both instances the Fiber ID is comprised of: r/b for the red/blue camera, 1-8 for the tetris number on that camera, and 01-16 for the fiber number within that tetris and camera.

Once the fibers are extracted, there are a number of ways to convert each two dimensional spectrum into one dimension. For this, the simplest method is currently implemented where we directly sum the flux in all of the pixels in a given column.

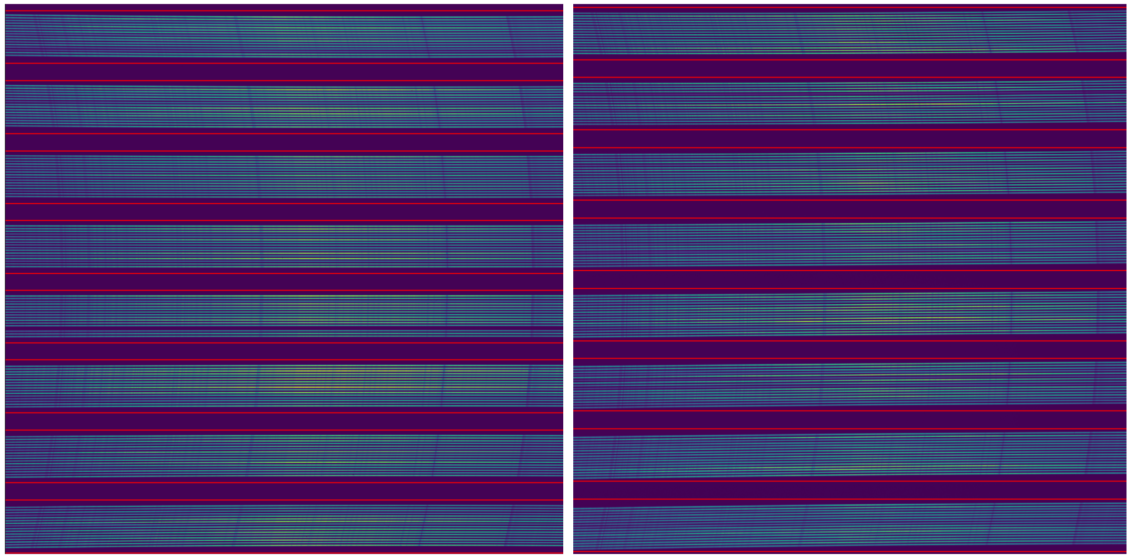

Figure 3.9 Images showing the red camera (left) and blue camera (right) of M2FS, along with red horizontal lines indicated the edges of the eight identified tetrises.

Other common methods are to fit the rows column-wise to a Gaussian or arbitrary function and integrate the fitted analytic function. The infrastructure exists to do that, but that method was not implemented.

3.7 Wavelength Calibration

3.7.1 Overview

For spectroscopic studies where absolute flux calibration is not needed, the calibration of the pixel location to wavelength value is arguably the other most important step. Without precise and accurate assignment of wavelength values to the measured counts in each pixel, the ability to measure the redshift becomes impossible. Note that due to alignment of the fibers in the "shoe" (the container that houses all eight tetrises) at the interface with the grating assembly, the dispersion axis of the spectra are not aligned in such a way that a given column location corresponds to the same wavelength for all spectra. Each fiber has its own minimum and maximum wavelength that must be individually calibrated. Because of this and the complexity of wavelength calibration in general, this step takes place in two stages:

1. **Initial Calibration**: The initial (or "coarse") calibration uses the smaller, more isolated lines of the Neon, Argon, Mercury, and Xenon lamps to fit

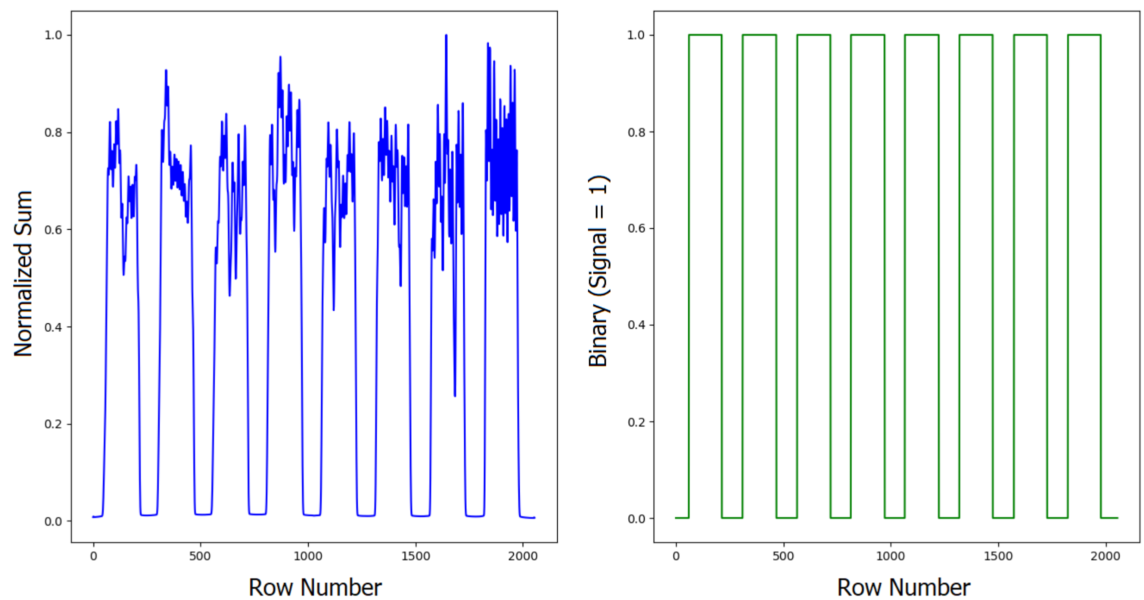

Figure 3.10 Left: Graphs showing the summation over columns of a CCD image. The spikes are caused by the flux of each individual fiber being maximum in that row, while the large amount of flux in between indicates that curvature is causing the flux maximum to change to neighboring rows as a function of column number. Right: Smoothed version of the left plot, used to identify the location of signal and thus extract each of the eight tetrises using a boolean mask on the rows.

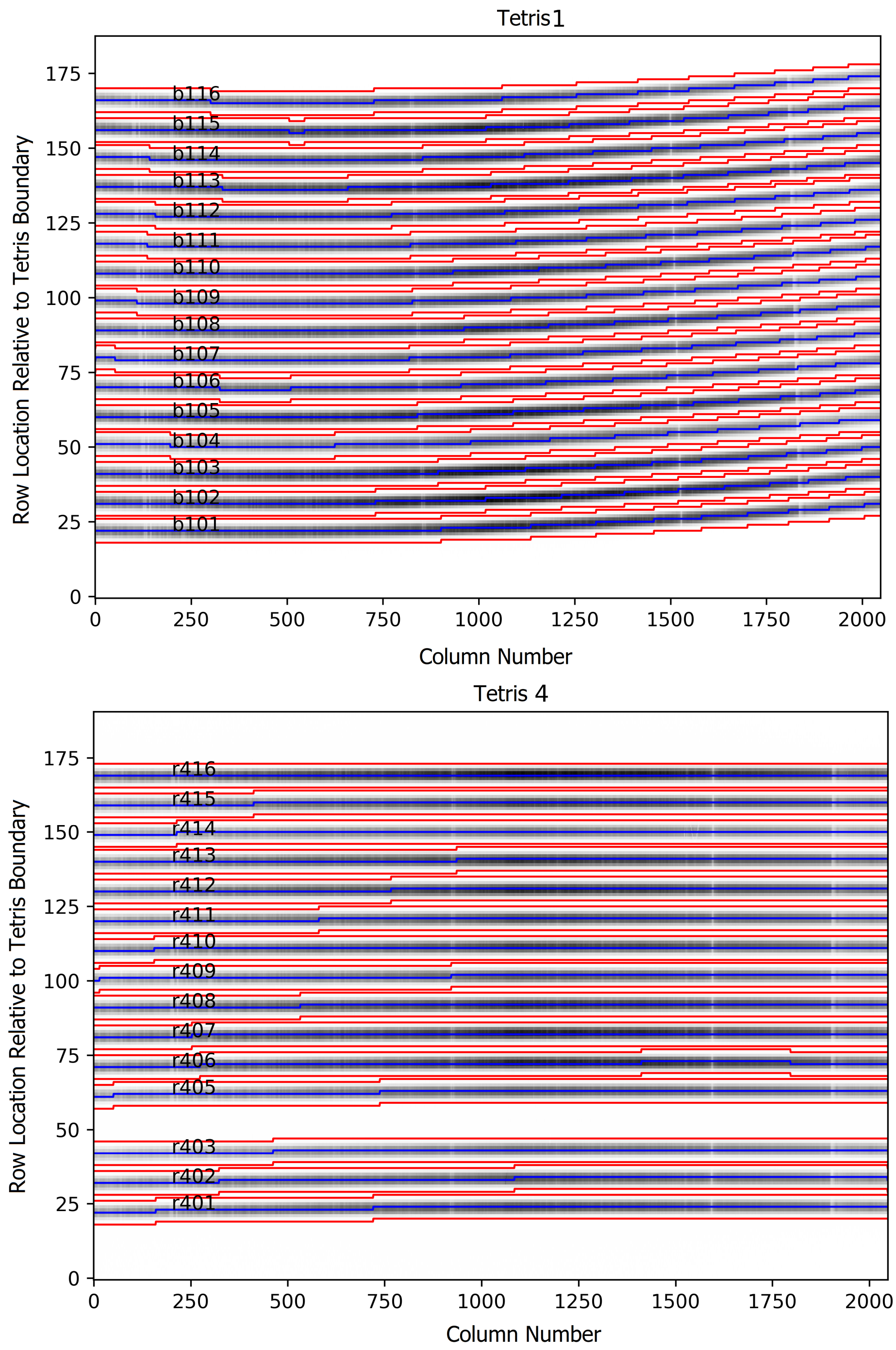

Figure 3.11 Examples showing the tracing of fibers in two different tetrises. The top is the first tetris in the blue camera and the bottom is the fourth tetris from the red camera. The color indicated flux, coming from each of the 16 fibers in the curved rows. The red lines trace the identified edges of each fiber boundary. Note the bottom image has a missing fiber, which the code identifies and properly skips in its naming assignments.

an initial quadratic function to relate pixel location with vacuum wavelength. Roughly 20-25 lines are identified and used for each spectrum in this step.

2. **Final Calibration**: The final calibration uses the much denser set of of lines provided by a Thorium-Argon lamp to calibrate a fifth-order polynomial fit for vacuum wavelength as a function of pixel location. This leverages the initial calibrations as a starting point and for initial estimates of time-evolution in the calibrations, because it is a far more difficult to fit if no prior information is known. Roughly 50-70 lines are used for each fit in this final step.

At the beginning of development, an interactive Graphical User Interface (GUI) was developed to aid in process of the initial calibrations. However, due to the volume of spectra and the time required to analyze thousands of spectra multiple times, several automated calibration codes were eventually developed. These codes were optimized to produce a high enough rate of success that the human-aided calibrations are no longer needed for this initial calibration step. While success is difficult to assess for something meant only as a starting point we can quantify the number of catastrophic failures that require additional attention, which we find to be less than one percent. Both the GUI method and the currently-implemented automated method will be discussed below.

Figure 3.12 shows a calibrated NeArHg lamp spectrum from M2FS on the bottom. In the upper plot are the lines from The National Institute of Standards and Technology (NIST) used in the calibration, broken up by the emitting atom. Because of the lack of lines in the lower half of the range (∼5700 Å), we cannot use this as our final calibration. For that we need to use Thorium-Argon lines, which densely populate the full wavelength range of interest. Figure 3.13 shows an example calibrated M2FS spectrum from a ThAr lamp along with a NIST ThAr spectrum. Note the increased density of lines and the more uniform distribution over the wavelength range of interest.

The final calibration begins by inspecting a small subset of spectra by eye through a GUI. The user either confirms or changes each match between an observed line and a corresponding calibration line. The confirmed matches are fit using a non-linear least-squares algorithm to fit wavelength as a function of pixel location to a fifth order polynomial. The code takes this set of lines, in addition to the observed offset in fitted coefficients between the preliminary and final fits, and automatically fits the complete list of fibers in an iterative manner. Once calibrations are made for a given exposure, those values are then used as input to the next calibration exposure until

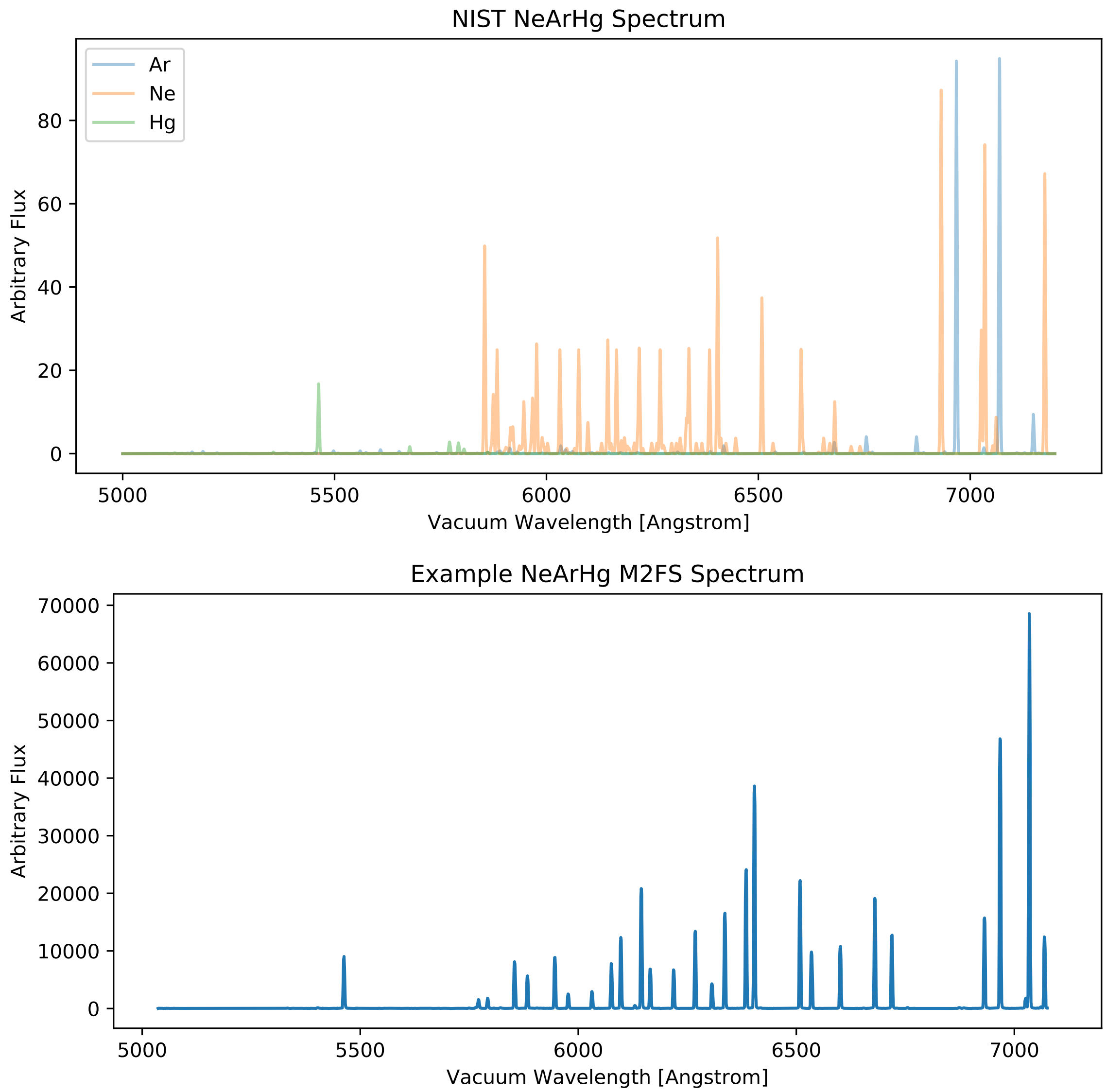

Figure 3.12 Plots of literature (top) and measured (bottom) spectral lines from Neon, Argon, and Mercury lamps. The literature values are taken from The National Institute of Standards and Technology and plotted in vacuum wavelengths. The measured values are from an example M2FS spectrum and already calibrated using the literature lines. Note the NIST lines were modified to remove lines that don't appear in the M2FS spectra.

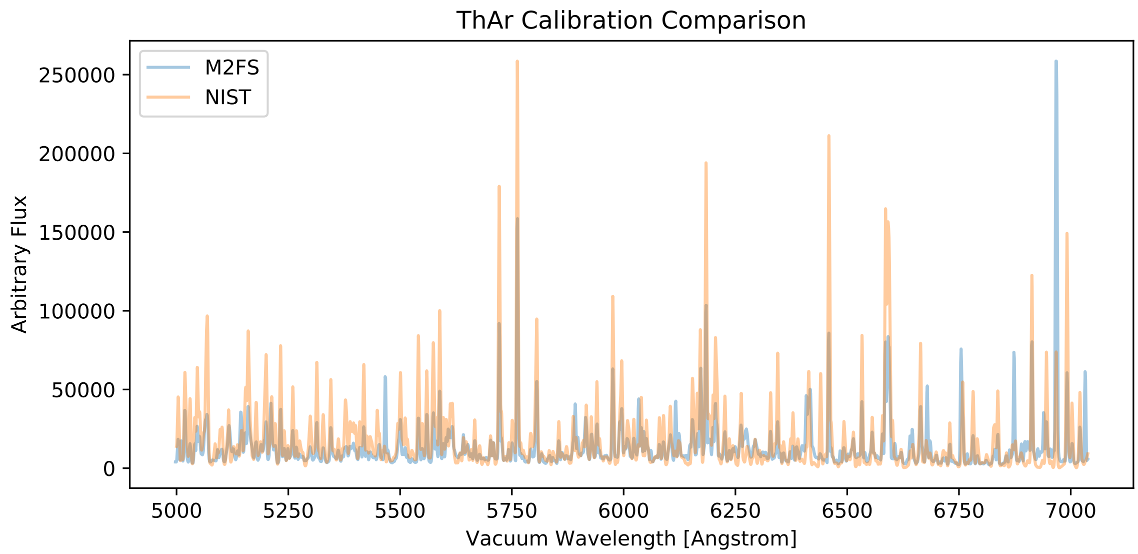

Figure 3.13 A plot showing both a measured M2FS spectrum and literature values of a Thorium-Argon lamp. The literature values are from The National Institute of Standards and Technology, and the measured spectrum was previously calibrated using the literature spectrum. Note the differences in flux values but the clear overlap in lines. Also note the greater density of lines compared to Figure 3.12.

all exposures are calibrated. The root mean squared deviations in the final fifth-order polynomial fits are typically 0.3-0.5Å.

The preliminary and final calibration steps will be discussed in more detail in the sections below.

3.7.2 Data Handling and Line Lists

Unlike the spectral data generated at each step, the calibration files that are saved do not overwrite any files generated from previous runs of the same dataset. A unique time-stamp is given to each file to enable lookup of past calibrations, or to default back to a specific set of calibrations if necessary. This was done primarily because of the non-deterministic nature of the human calibrations and the iterative calibrations, and the fact that human interventions make this step less convenient to rerun in the event of data loss.

Two different sets of line lists for the various lamps are available for use:

1. **SALT Lines**: This set comes from the South Africa Large Telescope, who published flux and wavelength calibrations for their lamps at roughly the same

resolution as that used in the low-resolution mode of M2FS (1 Å per pixel, but the peaks can be identified to 0.01-0.1Å level).

2. **NIST Lines**: This is a set from NIST, which contains all observed lines at finer resolution ($\sim 0.01 - 0.0001$ Å). These lines need to be convolved with the typical line spread function (LSF) of the observed spectra, which we approximate as a Gaussian with widths measured empirically. The typical widths are 1.4-2.2 Å. These are determined by the relation between an observed full width at half maximum and the standard deviation of a Gaussian: FWHM $= (2\sqrt{2\ln 2})\sigma \approx 2.355\sigma$.

The user can specify which set of lines are used. The NIST lines are used by default.

3.7.3 Initial Calibrations: Interactive Method

The setup for the preliminary calibration differs between the SALT and NIST lines. The reason for the difference is that the SALT lines were calibrated and measured using a lower resolution spectrograph whereas the NIST lines were measured at much higher resolution. Because of this the line locations and fluxes are already accurate representations of the resolved and unresolved lines we expect in our spectra. For the NIST lines, the data needs to be convolved to assess where the peaks of unresolved combinations of lines will be. The advantage of using the NIST lines is that you can empirically measure the LSF of the spectral lines and generate the appropriate spectrum for that exact resolution, whereas the SALT lines are approximating a constant LSF. As indicated before this assumption fails with LSF's ranging from anywhere between 1.4 to 2.2Å in the data.

For the NIST lines, the line fluxes are assigned to an array of otherwise zero valued fluxes, which is then convolved with a Gaussian of the appropriate width to reproduce the resolution of the current fiber. The peaks of this spectrum are then found, and it is these wavelength and flux values that are used in the calibration for that particular fiber.

Figures 3.14 and 3.15 show two examples of the interactive GUI for fitting the NeArHgXe data. The GUI plots the current fiber spectrum with some initial guess at the pixel to wavelength transformation, and displays the calibration line locations as color coded lines. The width of the lines corresponds to the flux value of that line and the color indicates which lamp it was generated from. On the right-hand side of the window is a zoomed in view of the left plot that lets you view small features in finer detail. The five sliders give you control over the fit coefficients for the pixel to wavelength transformation of the form:

$$\lambda = a + b\mathrm{p} + c\mathrm{p}^2, \tag{3.3}$$

where p represents the numeric pixel location and λ represents the vacuum wavelength for that pixel, given the fitted coefficients a, b, and c. The GUI identifies these by their conceptual purpose, a being the offset, b being the stretch, and c being the "quad." The top two sliders let you change the offset and stretch respectively over a wide range of their parameter spaces. The next two give you finer control over these same two parameters so that you can make small adjustments. The final, bottom slider lets you set the quadratic term (c). Moving any of these sliders will change the graphs of the fiber spectrum in both plots in real-time. The calibration lines are fixed and so you can manipulate the coefficients until you find good agreement between the peaks of the fiber spectrum and the calibration lines. In the lower right there are a number of options to use. One box lets you select whether to smooth the spectrum or show you the raw pixel values. Another lets you select or deselect specific lamps, in case you find that some lamps aren't noticeably appearing in the measured spectrum. The upper right box lets you select from several potential solutions: historical (if available), default (based on an empirical fit), or cross-correlation which uses a technique similar to that of the automated method given below. The final sets of boxes let you output the current parameters to the terminal for documenting potential options, resetting to the default calibration, flagging the spectra as bad, and saving the current values before exiting.

When things are operating efficiently, each new fiber should be close to fit once the previous is done and the code is able to use it to predict the next. Using this method all fibers must be looked at by eye before being able to proceed to the final calibration steps.

3.7.4 Initial Calibrations: Automated Method

The above manual calibration is perfectly sufficient for a small number of fields, where the number of adjustments and mouse-clicks might be on the order of a few thousand. However, with tens of targeted fields, the number of calibrations can easily surpass tens of thousands. While by no means impossible, it leads one to look for means of automation that will allow the calibrations to proceed with little or no human input. To that end, multiple methods were developed with varying degrees of success. The

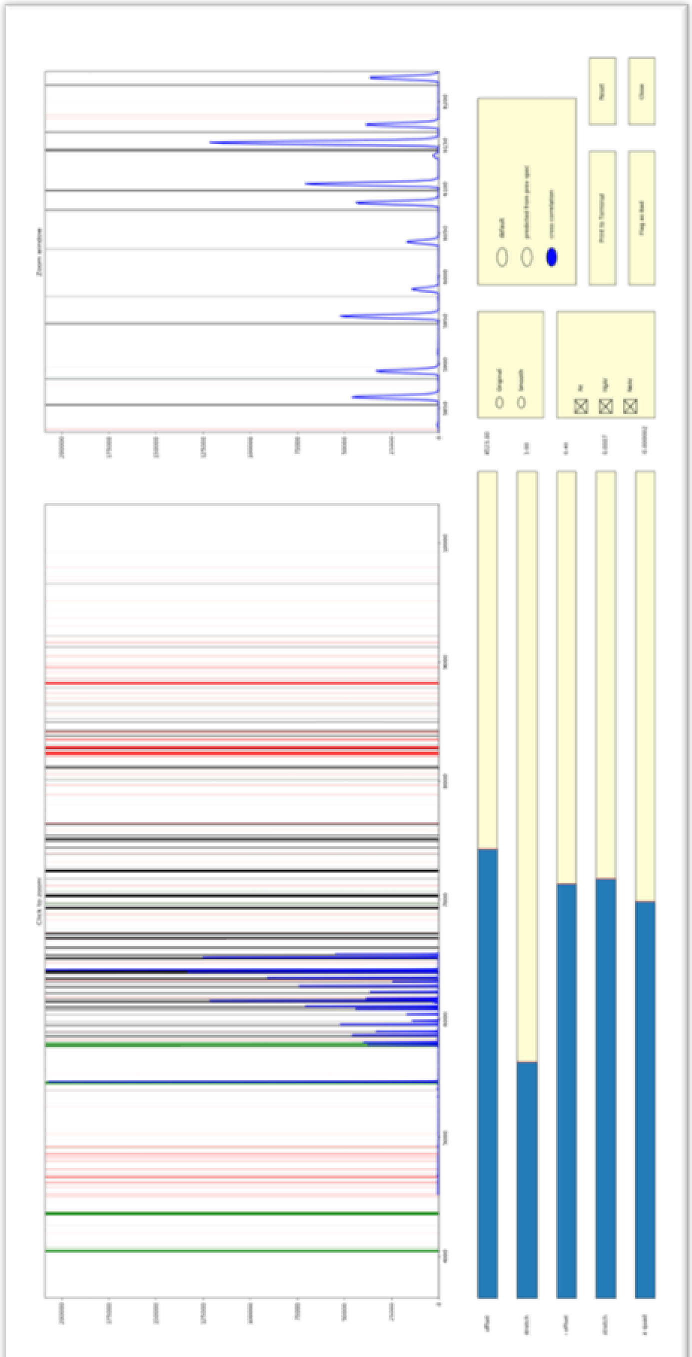

Figure 3.14 Example of the interactive GUI for fitting the NeArHgXe data. The GUI plots the current fiber spectrum with some initial guess at the pixel to wavelength transformation, and displays the calibration line locations as color coded lines. The width of the lines corresponds to the flux value of that line and the color indicates which lamp it was generated from. On the right-hand side of the window is a zoomed in view of the left plot that lets you view small features in finer detail. The five sliders give you control over the fit coefficients of the quadratics.

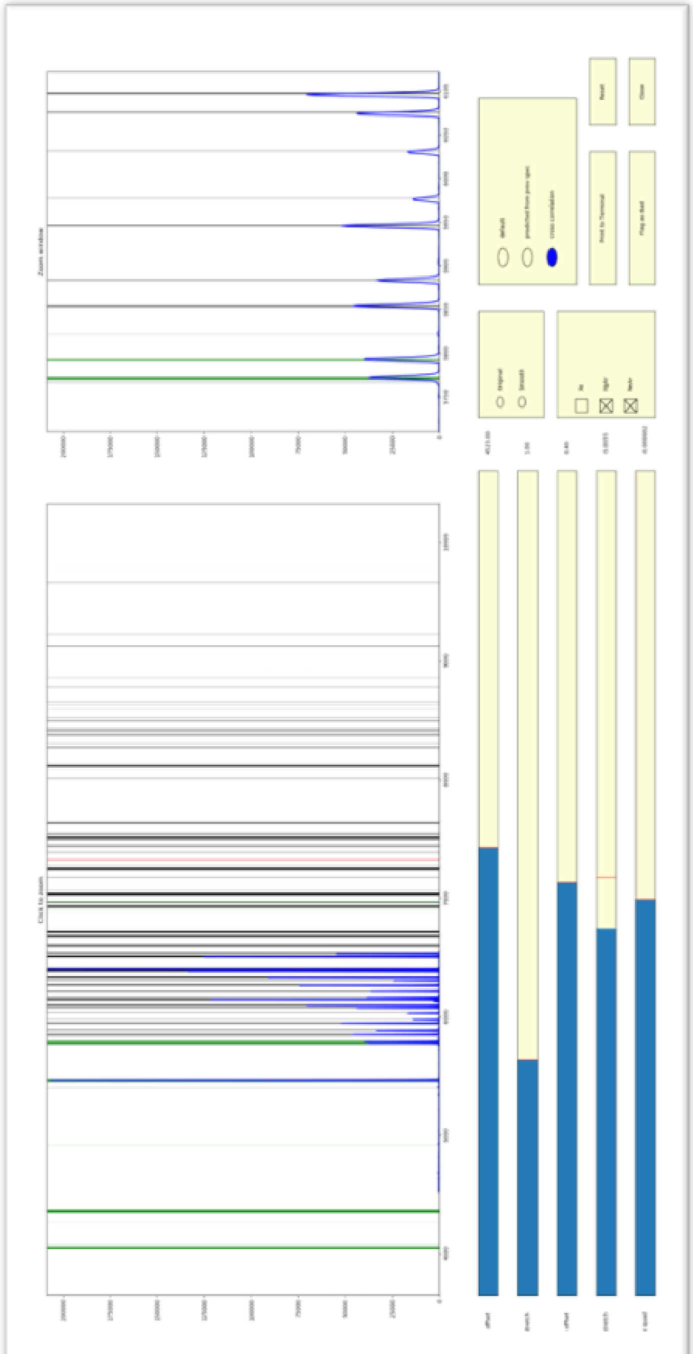

Figure 3.15 Examples of the interactive GUI for fitting the NeArHgXe data. Similar to Figure 3.14, except here we have unchecked Xenon which was previously displayed in red. Note there are no red lines that are coincident with the measured M2FS lamp lines.

most effective solution is the one currently implemented. It eliminates the need for a human to input any information or use any Graphical User Interfaces (GUI's) for this step in the calibration. It instead generates a mock spectrum from the calibration lines and uses an interactive technique to step through potential solutions. It uses a Pearson-r cross-correlation coefficient as the metric for selecting the best solution. The cross correlation coefficient quantifies the amount of overlap between the observed spectrum and the calibration, where the fluxes are binned in wavelength bins. For the spectrum being calibrated, the bins are defined by the guessed solution and the flux in each pixel bin, for the mock spectrum interpolation is used to get the expected flux in those same wavelength bins.

Whether using the NIST or SALT line sets, the flux and wavelength values are formed into a mock spectrum. In the case of the SALT lines, the peaks are generated using Gaussian's centered on the wavelength and with height equal to the quoted flux. For the NIST data, the peaks of the convolved spectrum are used, as described for the interactive method.

Once completed, an initial estimate is made assuming a simple linear relation between pixels and wavelength with a slope (b) set to a fixed value, which is unity by default. Clearly this is the same as Equation 3.3 with the quadratic term (c) set to zero. Since the quadratic term is small, this approximation works for a rough solution and greatly reduces the search space of parameters.

The offset (a) in the relation between pixel and wavelength is then iterated. A Pearson-r cross-correlation coefficient is used to quantify the amount of agreement between the proposed wavelength fluxes of the fiber pixels, and the flux of the mock calibration spectrum interpolated to those same wavelengths. The purpose of this step is to estimate the constant offset, a, which differs by 10's of Angstroms because of the curved manner that the spectra projects onto the CCD.

Leveraging the sparsity of lines in the NeArHgXe spectrum, we can then use our simple linear solution to identify the peaks in our fiber spectrum that are nearest in estimated wavelength to the mock spectral peaks. This is done in a two step process. First in identifying all peaks above a multiplicative threshold of 1.4 times the median flux value in the mock spectrum. Then for each identified peak in the fiber spectrum, the nearest mock (in wavelength) spectral peak is assigned as the true value. We then use a non-linear least squares fit of the pixel values from the fiber spectrum and the corresponding wavelength values of the mock spectrum to fit to Equation 3.3.

This process proceeds iteratively with the offset (a) determined for the previous fiber used as the midpoint of the search space for the next fiber. If the fit of a

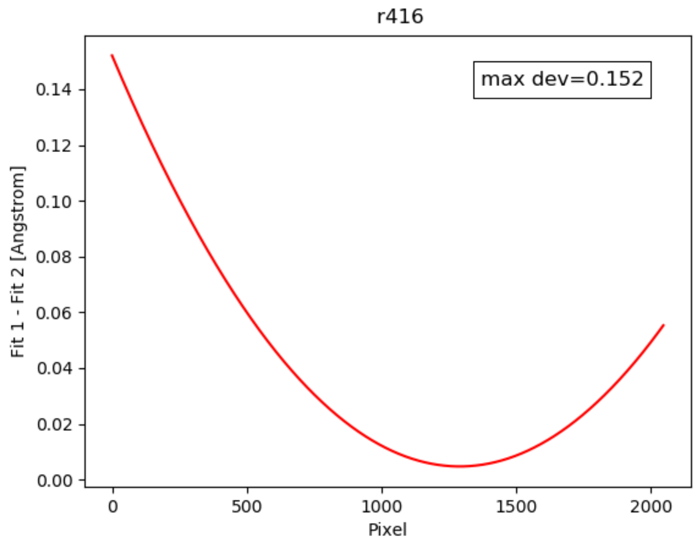

Figure 3.16 The difference between the initial wavelength fits for an example fiber using NeArHg spectral lines determined using two different sets of input fibers for the algorithm to learn from. The difference is less than 0.16Å for all pixels.

fiber was deemed to be poor, the next fiber will be fit using the last known good calibration. Here the goodness of fit is determined by the RMS deviation from the fit to the calibration wavelengths. Poor fits are returned to at the end, using all newly learned calibrations to provide a better fit to those fibers.

When run using multiple cores the code separates the fibers in half and iteratively fits from the outer edge inward from either end of the CCD. Because of this unsupervised machine learning, small differences between calibrations are possible. The two middle fibers are fit by both cores and the differences in the two fits for each of the two fibers are used to quantify the impact that the iterations have on the resulting calibrations. Figure 3.16 shows one such comparison. As can be seen in the figure, the difference between the fits for this fiber is less than 0.16Å for all pixels. In general, the impact is far less than half an Angstrom at any point along the dispersion direction of the CCD.

3.7.5 Final Calibrations

The subset of fibers includes the outermost and central-most spectra on the CCD, where the extrema of wavelengths are found, in addition to four other randomly selected spectra from the remaining tetrises. Figure 3.17 illustrates this on a CCD. This selection of fibers allows the algorithm to identify the complete subset of calibration lines it should expect to see and assign pixel locations to the remaining 120 fibers.

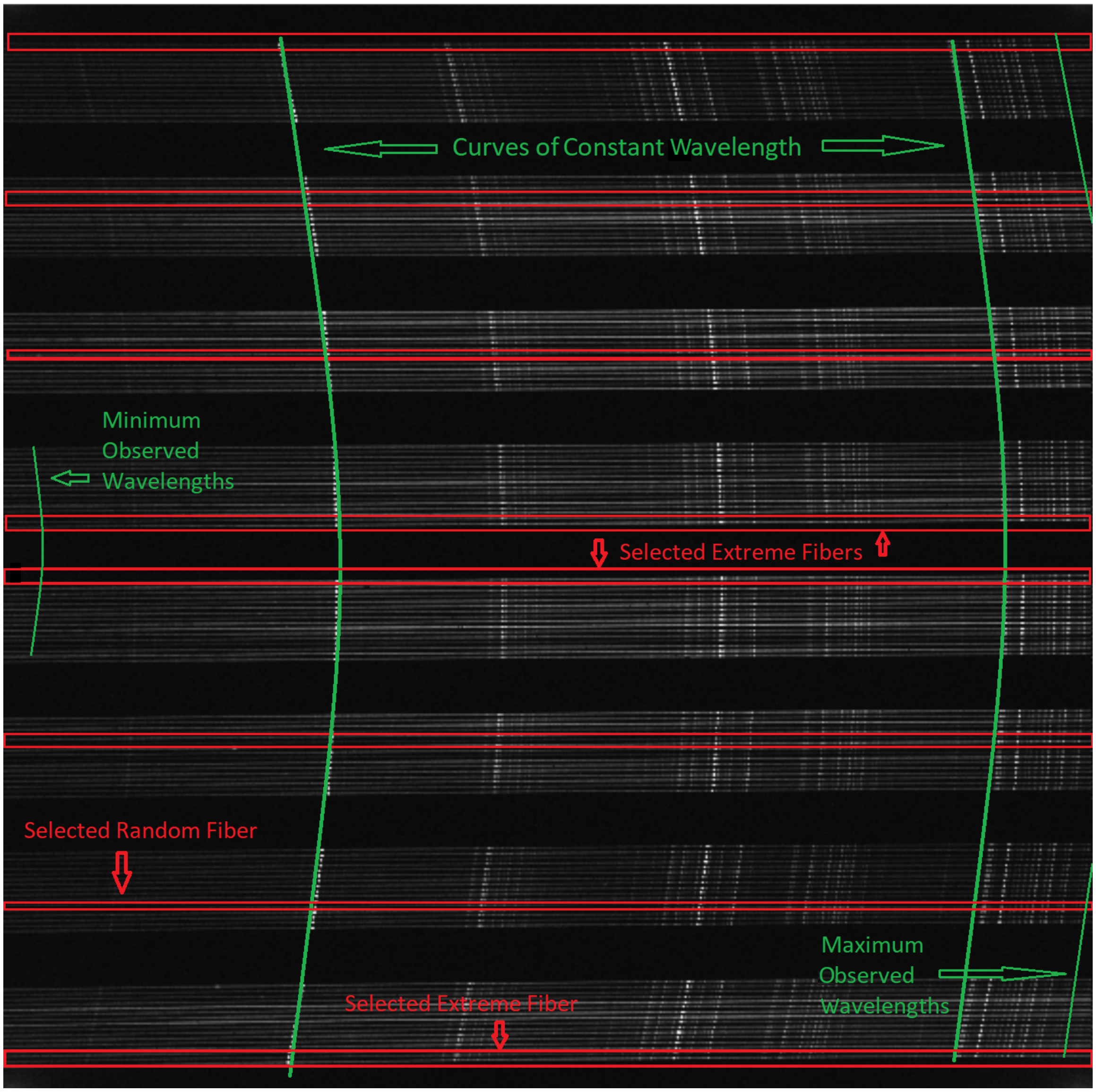

Figure 3.17 Image illustrating the curvature in the lines of constant wavelength on the CCD (green), and the fibers selected to appropriately sample the extremes of the wavelengths on the CCD (red boxes).

For the final calibration, a Thorium-Argon lamp is used. ThAr contains far more lines, especially in the lower half of our range of interest (5000-6000Å). As in the initial calibrations, if NIST lines are used, they are convolved with a Gaussian to produce a representative spectrum at the appropriate resolution. However, unlike the preliminary calibrations, we do not produce a new convolution for every fiber spectrum. This is because we want to be able to cross reference calibration lines between fibers, and to do so appropriately we cannot have different sets of peaks. For this reason, we convolve and fit to a fixed sigma of 1.6 for the NIST lines, which is meant to be representative of the range of LSF's while erring to the side of more resolution for the lower LSF spectra. For the SALT lines, this doesn't occur because it is already at what we assume is a representative resolution.

The process begins by selecting the outermost and innermost fibers, and four random fibers from the remaining four tetrises. These are then displayed in a GUI, where we plot the spectrum in units of wavelength using the calibration coefficients from the preliminary fit and Equation 3.3. An example of the GUI can be seen in Figure 3.18. We also plot the calibration lines as vertical red or gray lines. The red lines are a subset selected because they are prominent or well isolated peaks that are well matched to previously observed fibers. For the red fibers, the flux is shown by red dots along the line, to give an impression of the flux magnitude reported in the calibration files. The purpose of the GUI is to go line-by-line and ensure that the peaks of the spectrum are matched to the appropriate calibration line. With practice and the advanced ability of humans to identify patterns, this can become an efficient way to properly match spectral peaks to calibration lines. The code lets you move forward and backward through the points, highlighting the current line being matched and the corresponding peak is highlighted with a blue circle. You can delete lines that you do not believe appear in the current spectrum and you can undo deletions if done by accident.

Once the lines are matched, the pixel locations of the peaks are fit against the wavelength values of the calibration lines to a fifth order polynomial:

$$\lambda = a + b\mathrm{p} + c\mathrm{p}^2 + d\mathrm{p}^3 + e\mathrm{p}^4 + f\mathrm{p}^5, \tag{3.4}$$

where p represents the numeric pixel location and λ represents the vacuum wavelength for that pixel, given the fitted coefficients a, b, c, d, e and f. The fit uses the same non-linear least-squares technique that is used in the preliminary fitting. The typical root-mean-square deviation between the fit and the calibration wavelengths is roughly 0.3-0.6Å. An example of the summary output provided from an interactive calibration

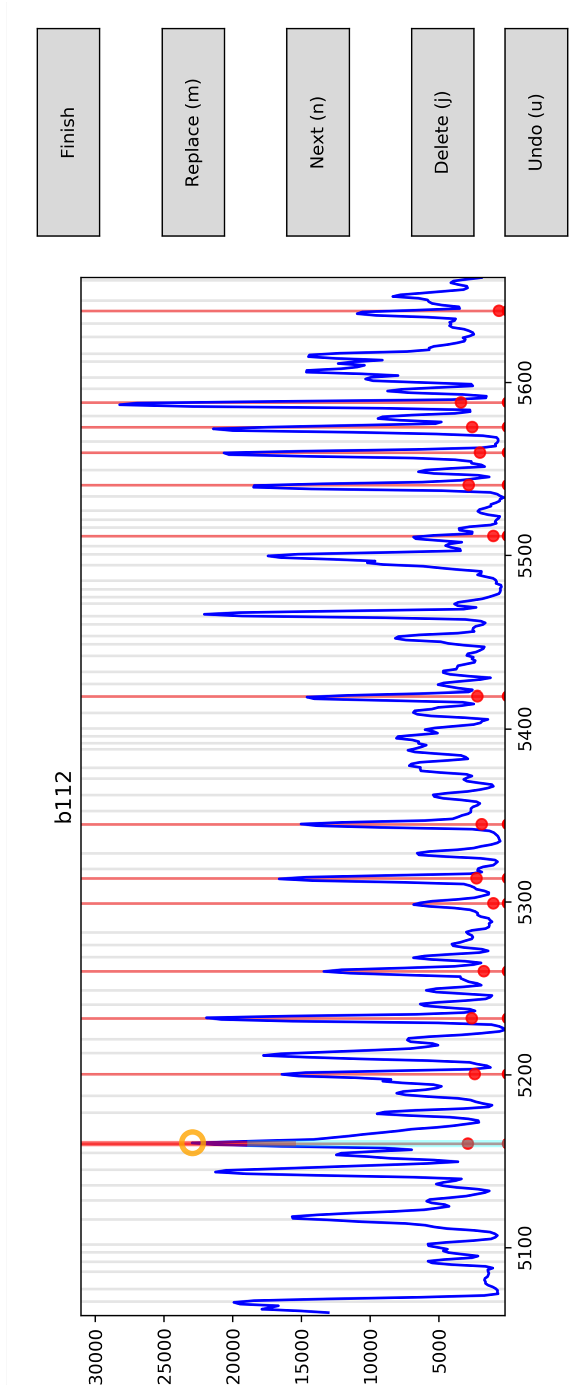

Figure 3.18 GUI used to verify that the identified peaks in a spectrum are matched to appropriate known calibration lines. The red vertical lines are the known spectral lines. The red dots indicate the expected (relative) flux. The gray lines are other known spectral lines not being used for the calibration. The blue spectrum is the M2FS spectrum using a calibration lamp that we are using to calibrate pixels into Wavelengths.

can be seen in Figure 3.19.

Once the initial fibers are fit with human input, the deviations between the preliminary coefficients and the final coefficients for those are determined and used to infer corrections to all of the other fibers. The code then iteratively runs over the fibers, automatically selecting the nearest calibration line to every peak and determining the goodness of fit for that attempt. If the RMS deviation is less than a specific value, that fit is kept as a solution and used to update the corrections of other fibers. If an individual line is found to be skewing the fit, and deemed to be an outlier based on a quantile-based heuristic, that line will be removed from consideration for future iterations of that fiber's fit.

The iterations continue, with each new iteration providing a different initial guess for the fit coefficients based on the updated prediction from all of the previous successful fibers. The fit also differs if lines are removed in a previous iteration. If no new fibers are successfully fit in a given iteration, then the goodness of fit threshold is increased by a small amount (the default being 0.04 Å RMS). This continues up to the maximum allowed deviation of 0.7 Å RMS. Any fiber that isn't fit in this complete process is then presented through the GUI to be hand-fit. An example of the summary output provided from an automated calibration can be seen in Figure 3.20.

If other ThAr exposures have already been calibrated, or historical files exist on disc and we allow historical values to be used, those will be used as the starting guesses for the calibration of the new exposures. In these cases, fewer numbers of hand-fits are required from the user to initiate the fitting as the fits become increasingly good with information from past exposures. The number of hand-fit fibers required decreases from eight to four, then to one and then to zero for all additional exposures. Here again, each new fit will inform new guesses based on deviations seen between past fits and current fits. This enables the predictions to evolve with temporal changes. The initial calibrations are used to try and estimate any systematic offsets in coefficient fits between exposures. These are included in the new guesses, even if the input coefficients are from a previous ThAr calibration.

3.8 Transmission Efficiency Correction

Optical fibers and their lenslits capture light on the focal plane via holes in a plug plate and propagate that light down to the spectrographs. Because of imperfections, damage, focus, or mechanical issues each fiber has a unique efficiency when it comes

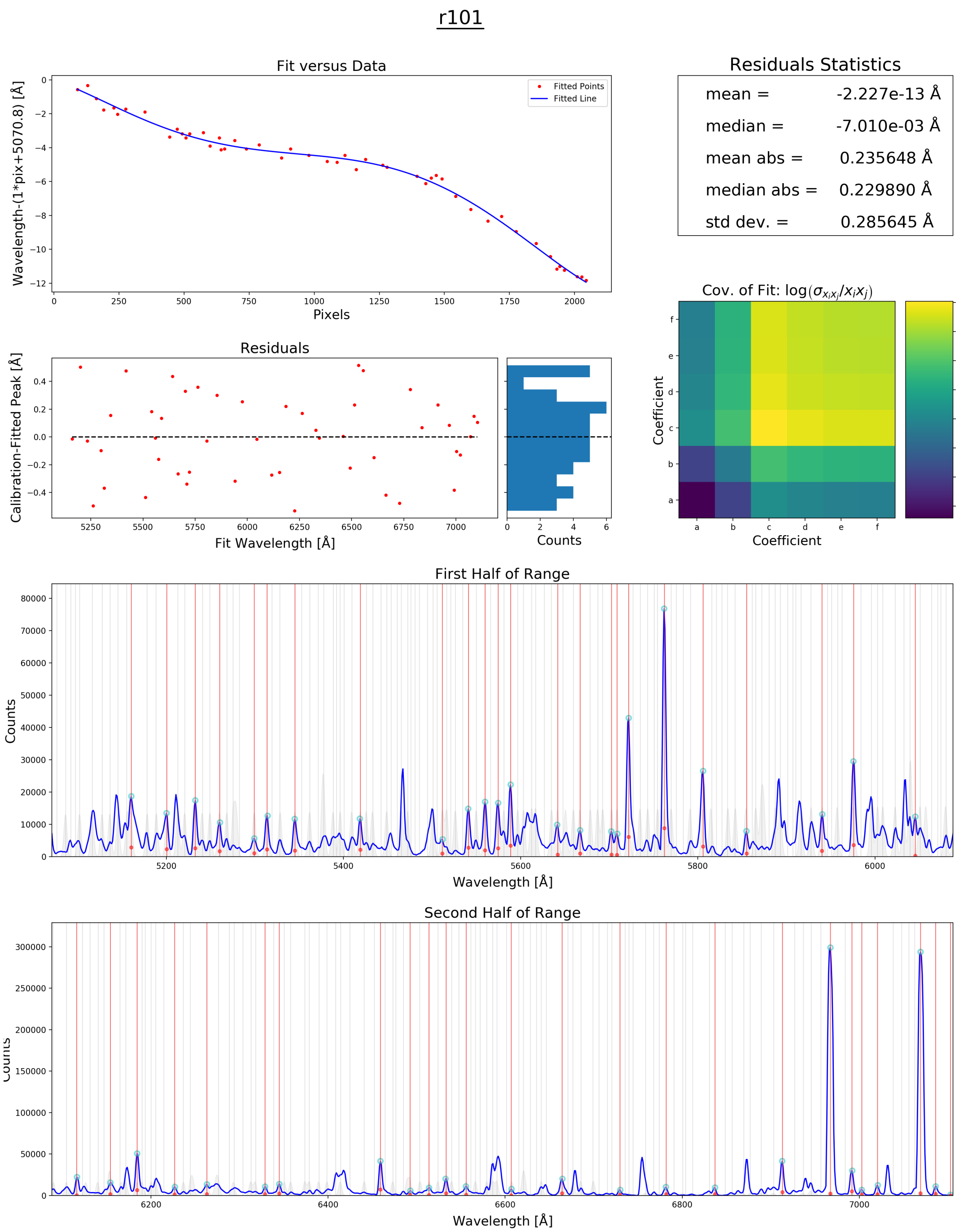

Figure 3.19 An example of a fiber that was fit using human input via the GUI in Figure 3.18. The upper right gives statistics of the fit, with a graphical illustration of the normalized covariance in log-scale below it. The upper left plot shows the wavelengths and identified peak pairs as red points and the fit as a blue line. Here the constant offset and linear component are subtracted to emphasize higher order terms. The plot below shows the residuals of the fit, with a histogram on the right-hand side. The lower two panels show the fitted points and lines directly. The various components are described in Figure 3.18.

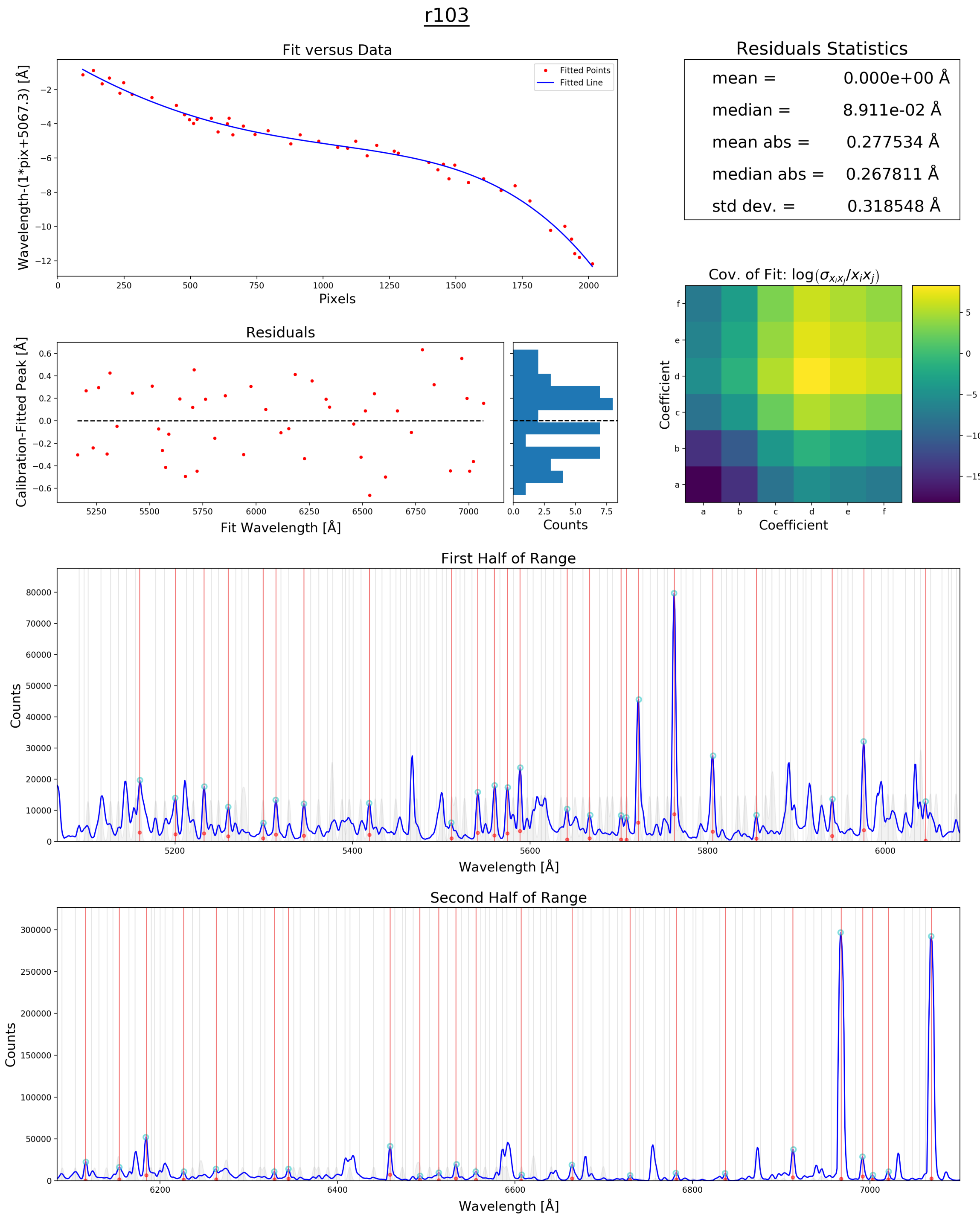

Figure 3.20 The summary graphic generated for an example fiber that was fit using the automatic iterative process. The information is identical to that described for Figure 3.19. Note that the residuals and fit are equally good to that done using human verification.

to transmitting light, both in total flux and to a lesser extent variation in different wavelengths. This needs to be corrected if we wish to properly compare the fluxes of different fibers, to add fluxes from different dates where the physical fibers may have changed, or properly subtract the sky background. Because fiber based spectrographs don't typically capture a sky region in addition to the target like slit-based spectroscopy does, we need to designate specific fibers to observe "blank" patches of sky. To properly utilize these "sky fibers," we need to know how to compare the flux from these fibers with those of the science fibers so that we can subtract out the sky.

To do this, we take observations of the sky during twilight where the sky is dim enough to saturate the camera but bright enough to uniformly illuminate the entire 0.5° focal plate. These so-called "twilight flats," named for their use in "flattening" the data to make it more uniform, give a fixed flux as a function of wavelength for us to compare amongst the 128 fibers on a given camera. To avoid additional factors from the CCDs, we flatten the fibers independently. We then take the ratio of these fibers with respect to the brightest fiber to get the relative efficiencies compared to the best throughput. Because of imperfect wavelength calibrations (at the sub-Angstrom level), directly comparing a complex spectrum like that of the Sun (via its scattering in the twilight sky) becomes difficult. Small deviations can lead to sharp and incorrect jumps in the efficiency curves. To avoid this we first use a Gaussian convolution to smooth the spectra so that only the smooth background is visible. This eliminates the sharp variations and provides a means of creating a smooth approximation of efficiency as a function of wavelength. We interpolate the smoothed data to fit to a uniform grid of wavelengths, where the ratio can be properly taken, before interpolating the resulting ratio back the the original wavelength solution for that particular fiber.

Because of the spectrograph setup, each fiber has a slightly different wavelength span, with those in the middle offset by 10s of Angstroms compared to those at the edges. Because of this, the extreme wavelength regions cannot easily be compared in the same way the wavelengths shared by all the spectra can. For those extreme wavelengths, the efficiency is approximated by a linear ramp that goes from the last valid data point toward the median value for that specific fiber as the value for the endpoint. Examples of the twilight flat spectra (top left), smoothed curves used for creating the flats (top right), the corrected twilight spectra (bottom left) with a corresponding log-scaled version (bottom right) can be seen in Figure 3.21 for the red camera and Figure 3.22 for the blue camera. Note the uniformity in the vertical direction when following along the curves of equal wavelength.

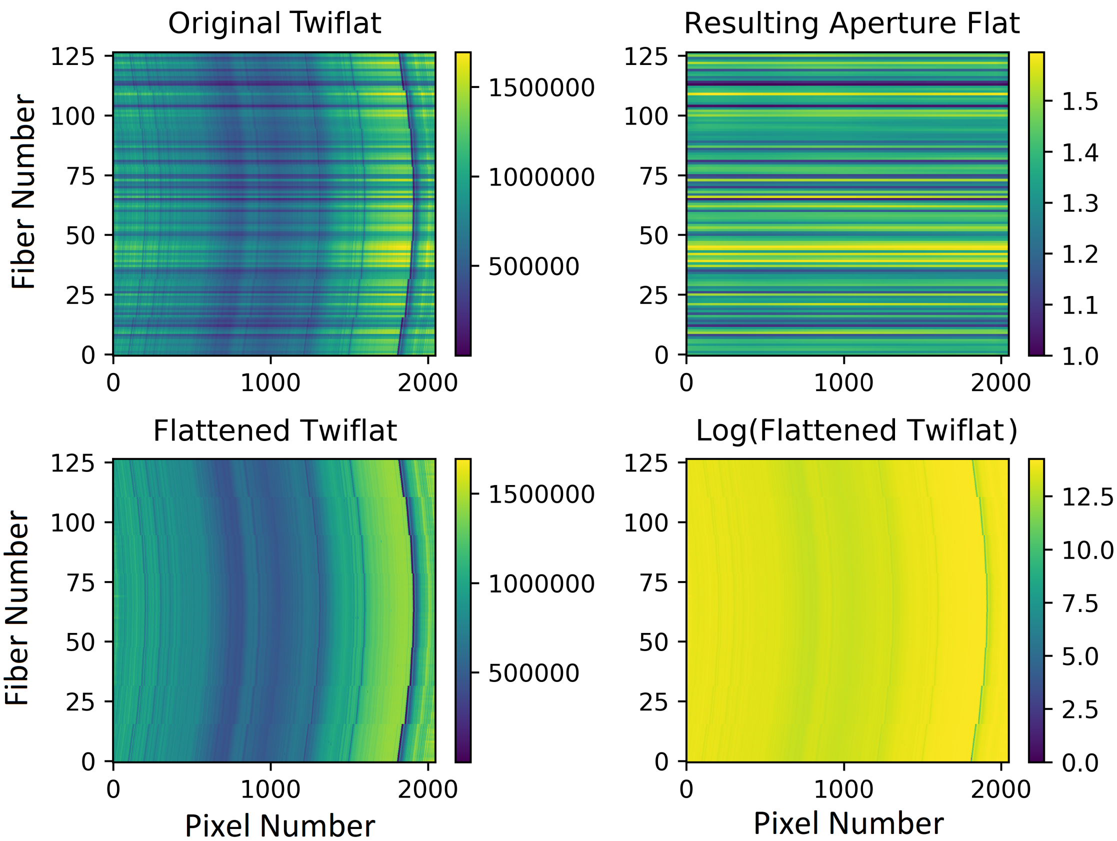

Figure 3.21 The results of the "fiber flattening" reductions using twilight spectra in all fibers of the red camera. The twilight spectra is quite uniform across the focal plane and thus allows us to identify the efficiency as a function of wavelength for each fiber based on the detected flux. The top left shows the data, the top right shows the identified corrections as a function of pixel number (and wavelength) for each of the fibers. The bottom left and right demonstrate the uniformity at fixed wavelength after the corrections. Note this is plotted versus pixel coordinates so lines of constant wavelength are curved.

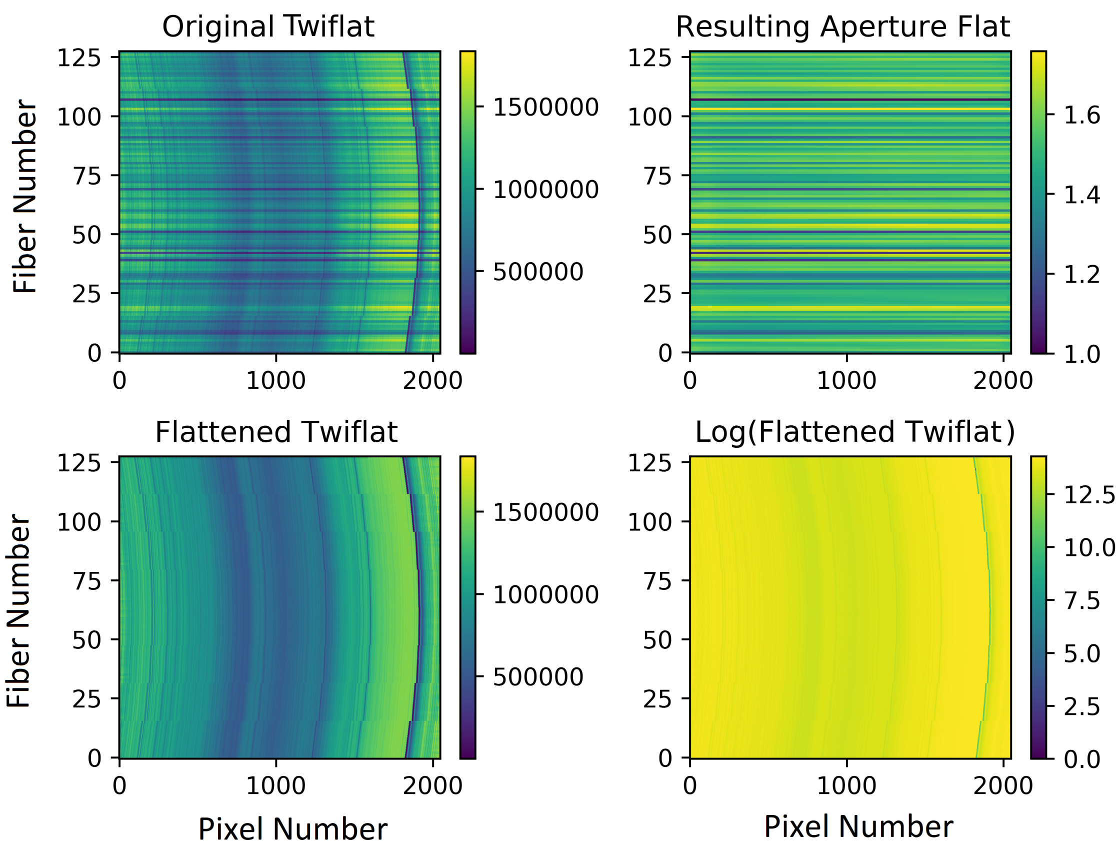

Figure 3.22 The same as Figure 3.21, except for the blue camera in this particular set of example twilight exposures.

3.9 Removal of Atmospheric Light Emission

As was alluded to in Section 3.5, the Earth's atmosphere both absorbs and emits light during the night at count rates far greater than the photons from our targets. This is especially true for our observations at the redder wavelengths of the optical and the near infrared, where vibrational modes from OH molecules in the atmosphere produce multiple sets of emission lines.

In the targeting of objects we assign a minimum of six fibers to observe sky, where no known galaxies or stars (above the photometric limit of the targeting data, roughly an r band magnitude of 22 for our data). These fibers will measure the sky flux in that local region of the focal plane, without the addition of targeting flux. This gives us a template of the sky flux we need to remove from the science targets.

There are two implemented methods for sky removal. The first option is to identify the nearest sky fiber to each target and use that as your sky flux template for subtraction. This is potentially beneficial because it contains more of the local brightness variations that might be present. The second method takes the median of all sky fibers to create a master sky template that all fibers (in that camera) are matched against. The benefits here are the reduction of noise that comes from averaging, in addition to the elimination of very local flux deviations that might not affect neighboring fibers but does affect a particular sky fiber, because of e.g. contamination from a nearby bright star.

The default method, and the method used in our analysis is to create a master template by taking the median of all sky fibers. Once that is obtained, each science fiber is iterated over. First, the continuum of the science target and the sky are fit and subtracted separately. If the continuum flux in the template is greater than that observed from the science spectrum, the sky template is scaled to avoid unphysical negative fluxes. For the remaining sky lines, each peak identified in the sky template is matched to a corresponding peak in the science spectrum. To avoid subtraction issues in the tails of the line distributions, the flux of the sky line is instead integrated and that value is subtracted from the matched peak in the science spectrum using the profile shape of the science spectrum line. Special fail-safes are instituted to ensure that the subtractions of the most substantial lines doesn't leave large positive or negative residuals due to some imperfections in the flattening of the fiber fluxes in the previous step or additional sky brightness in the science or template spectra. The code reduces any skyline with an integrated flux greater than 10% more than the corresponding matched line in the science spectrum to be exactly 10% greater.

It also limits the over or under subtraction from being more than 60 counts. The latter is simply for aesthetic reasons of plotting, as any of the above fail-safes will flag those pixels to be masked from use in any future steps. Finally any residual sky flux that was not identified as a line or as continuum is subtracted in the final step as the subtracted continuum and subtracted peak spectrum are added back together.

There are three important notes, the final two of which are mentioned above but deserve to be reiterated. First, all spectra are oversampled onto a fixed, linear wavelength grid in 0.25 Åincrements going from the minimum wavelength of any sky spectrum to the maximum of any sky spectrum using a Cubic Spline interpolator. The logic behind this choice is that without proper sky flux measurements, any flux values cannot be trusted. So only those wavelength values with known sky flux values can be used moving forward. The oversampling is useful for the next step of combining multiple science exposures, which have slightly different wavelength calibrations and therefore can be more or less accurately sampled at fixed spacings of e.g. 1 Å, which is roughly the original resolution of each spectrum. All wavelengths outside of the calibrated range of a specific fiber are masked. Second, because the code was not developed to work with absolute calibrations of flux, scaling of templates is done to ensure physical results under the assumption that deviations in the flat fielding or sky brightness led to the discrepancy. The second is that somewhat arbitrary cutoffs are made to avoid large over or under subtractions for aesthetic reasons of plotting unmasked spectra. If the masks, which are propagated along with the spectral data are used, these choices will not affect any scientific inferences.

Figures 3.23 and 3.24 show several of these components for two example spectra. The left plot of each shows the continuum of the science target in green, the sky continuum plus the remaining sky flux in orange, and the resulting unmasked galaxy spectrum after subtraction in blue. The right plot shows the original galaxy (gray) and sky spectra before subtraction (orange), and the resulting masked spectrum (blue).

3.10 Combining Science Exposures

As mentioned in the previous section, all of the single exposure spectra are fixed to a linear wavelength grid with a step size of 0.25Å and minimum and maximum wavelengths set by that exposure's sky spectra. If the calibration of a particular exposure allowed for shorter or longer wavelengths, the largest maximum and smallest minimum are selected, and those exposures that have less extreme endpoints would have those outer values masked.

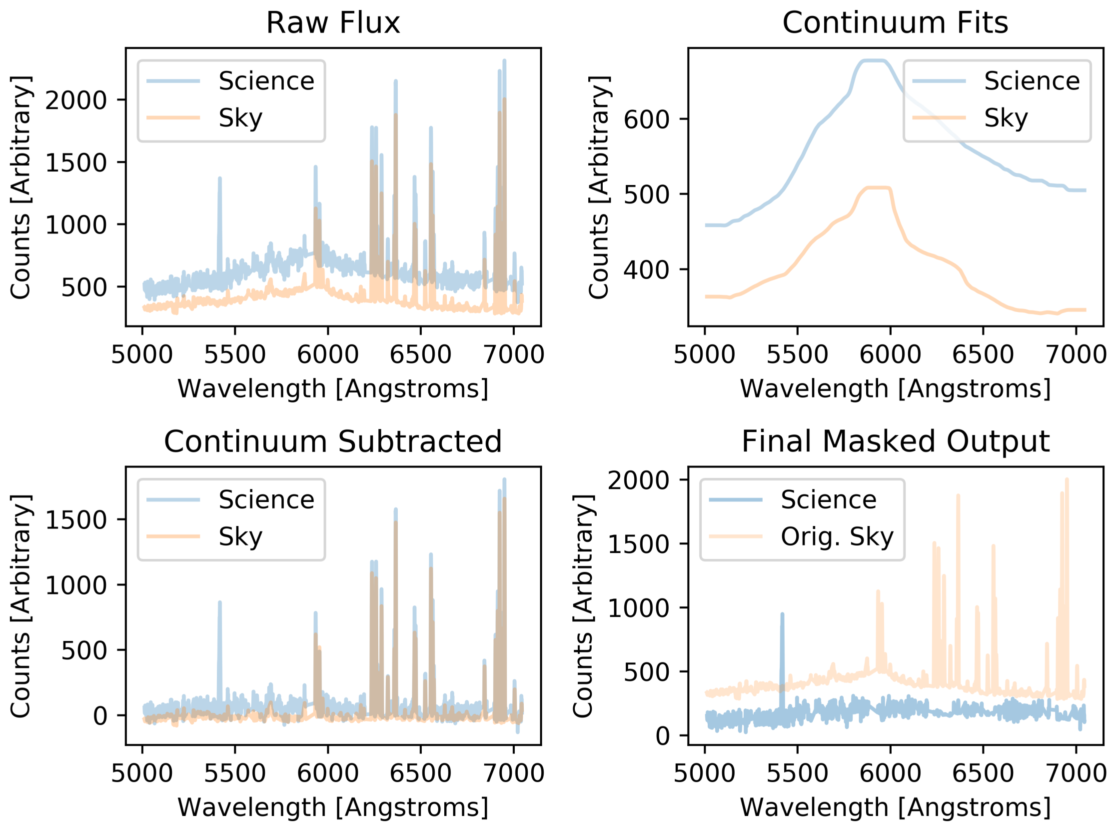

Figure 3.23 Four plots showing the sky subtraction process used in the M2FSreduce pipeline. The top left plot shows the flattened, wavelength calibrated flux of the science target and the sky. The top right shows the fitted continuum for each. The lower left shows the two spectra after subtracting the continua. The lower right shows the final, sky subtracted science target with its continuum added back in versus the original sky flux for reference. Note the removal of the obvious sky lines at the upper wavelengths in addition to the sky continuum. Also note that the emission line in the science spectrum that is not present in the sky is retained.

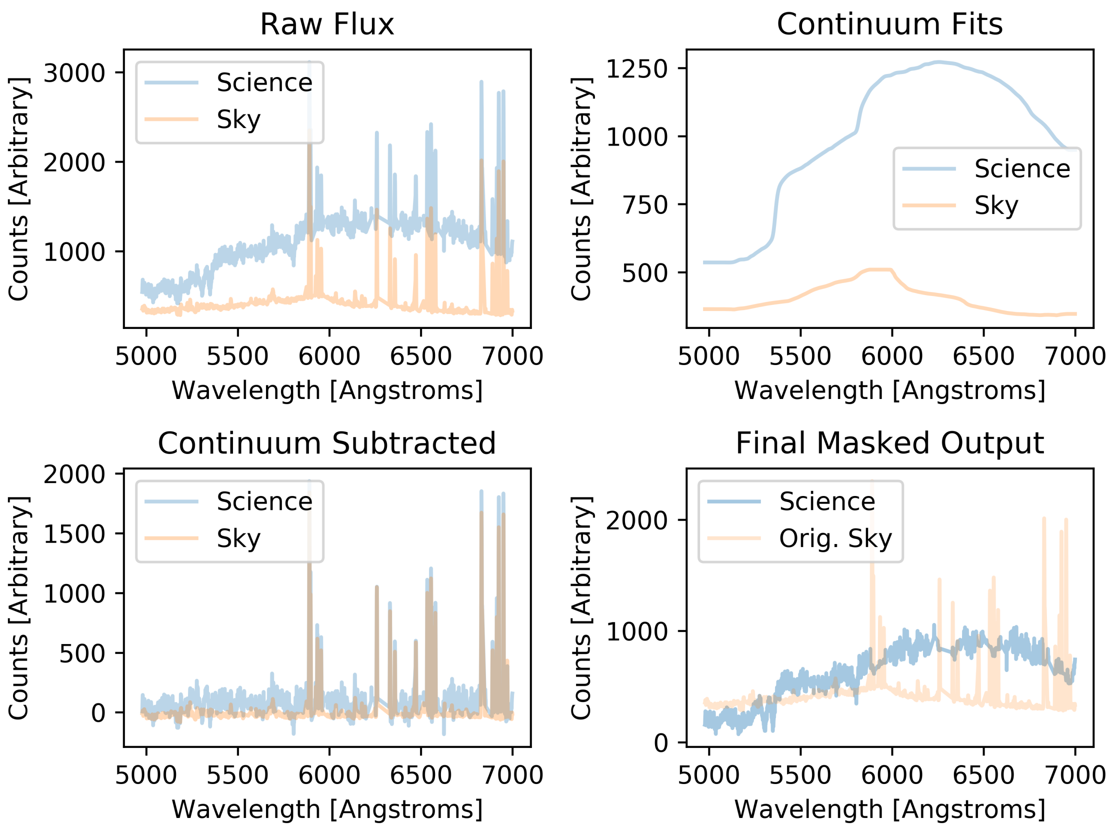

Figure 3.24 A second example of sky subtraction in M2FSreduce. The four plots have the same characteristics as in Figure 3.23, except that the science fiber is different. Note the strong absorption features retained in the final science spectrum and the proper removal and/or masking of the sky lines.

For each target, all exposures are stacked into a two dimensional array. For each wavelength bin, all non-masked values are averaged and multiplied by the total number of exposures. This avoids the addition of masked values, while allowing for consistent flux values across the final spectrum. If more than half of the exposures had that wavelength bin masked, the resulting final spectrum has that bin masked as well. This choice is made to maintain roughly consistent signal-to-noise across wavelengths. Fewer unmasked exposures of a given wavelength means less reduction in Poisson noise.

3.11 Redshift Fitting

This code was designed to analyse the spectra of galaxies. Because of this, the final step within the pipeline allows the user to automatically fit the final spectra for cosmological redshifts. The method uses cross correlation of the spectra with SDSS templates of a range of astronomical objects from large/luminous, red galaxies (LRG's); emission-line galaxies (ELG's); quasars; and stars. The templates were obtained by the SDSS Collaboration from co-adding 2000 commissioning spectra at high signal to noise. Since this pipeline was specifically developed to study galaxies that reside in galaxy clusters, the default template used is "spDR2-023," which is an early-type LRG with almost no discernible emission lines. That spectrum can be seen in Figure 3.25 (Alam et al., 2015).

The redshift fitter works by first removing the continuum of both the science spectrum of interest and the template spectrum. The template is then redshifted and then interpolated to the wavelength grid of the science target being fit. A Pearson-r cross-correlation is performed to find the Pearson-r coefficient, which represents the quantitative agreement between the two data-sets. This is then repeated for an entire range of redshift values set by the user, in redshifts steps also set by the user. The defaults are a minimum redshift of 0.1 to maximum redshift of 0.6, in steps of 1×10^{-5} (roughly 3 km/s). The redshift with the largest Pearson-r coefficient is selected as the redshift of the object. If multiple templates are selected by the user, an additional loop will be performed over all templates before selecting the maximum Pearson-r for the complete set. The template and coefficient are recorded along with the redshift. Figures 3.26 and 3.27 show two example fits. The top panel shows the galaxy spectrum with the template spectrum overlaid at the best-fit redshift. The colored vertical lines indicate common absorption (red and orange), emission (blue and purple), and sky lines (black). The lower panel shows the Pearson-r coefficient as

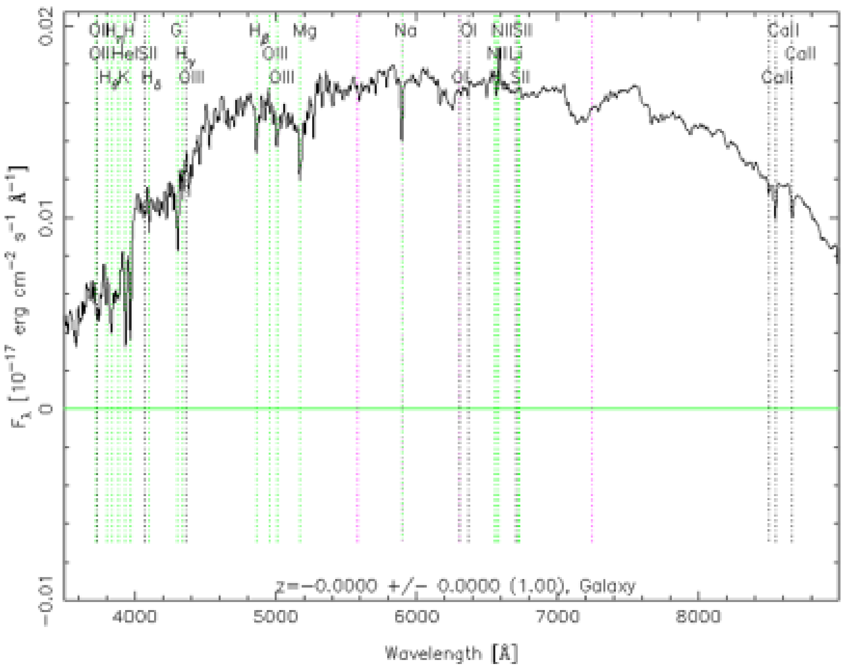

Figure 3.25 A galaxy template spectrum from the Sloan Digital Sky Survey (Alam et al., 2015). Such templates are cross-correlated with the measured spectra to determine redshifting from the rest frame of the object, which in this case is a galaxy.

a function of redshift, with the black dotted line indicating the maximum location.

It is important to note that both the calibrated wavelengths of the spectra in this pipeline and the template spectra are converted into vacuum wavelengths. In addition, no barycentric or heliocentric corrections are performed in this step, though code is available to take these outputs and perform those corrections upon request.

3.12 Summary and Future Work

As multi-object spectrographs like M2FS continue to increase the number of spectra that can be acquired simultaneously, the data reduction software needs continued innovating as well. The boutique single-spectra reductions of the past will become increasingly difficult for small human-power limited teams. There are general purpose software packages such as *IRAF*, but it is beginning to show its age. For these reasons; automated, adaptable, and robust data reduction methods need to be produced in a modern programming language. M2FSreduce is a python-based attempt to do this for M2FS, and potentially for its future successors such as the Integral Field Unit (IFU)

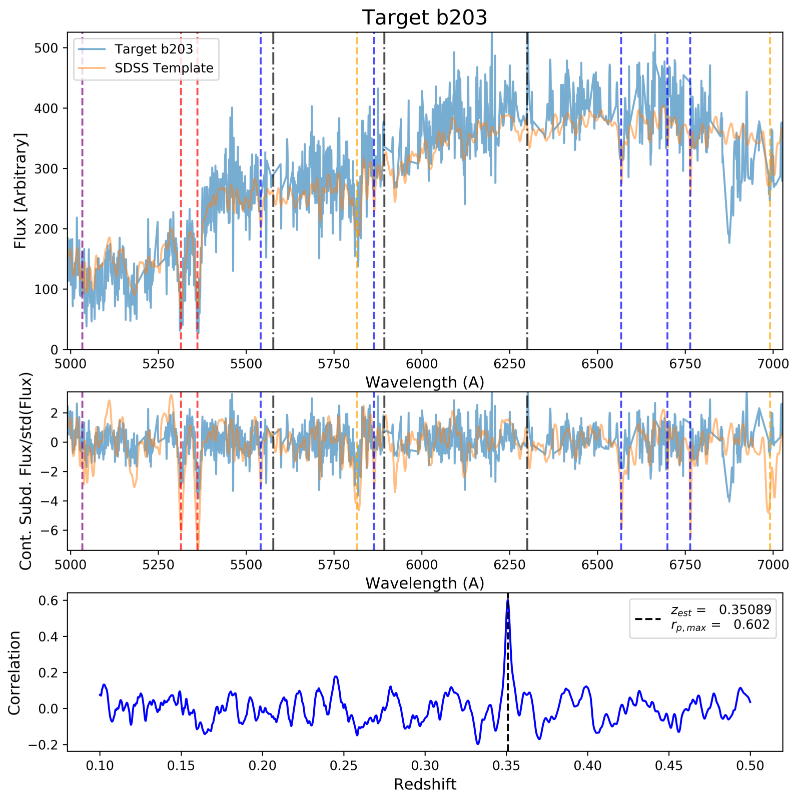

Figure 3.26 An output of the M2FSreduce redshift fitting using zestipy. The continuum of the science spectrum in blue was subtracted and cross-correlated with an SDSS template like that found in Figure 3.25 whose continuum was also removed. The template was redshifted and interpolated to the same wavelength grid as the science spectrum for the range of redshifts shown in the lower panel. The redshift that provided the greatest Pearson-r cross-correlation coefficient was 0.33341, and the SDSS template redshifted to that value is plotted in the upper panel. The black dot-dash lines are sky line locations. The red dashed lines are the Calcium H and K lines. The yellow dashed lines are other prominent absorption lines, and the blue dashed lines are common galactic emission lines.

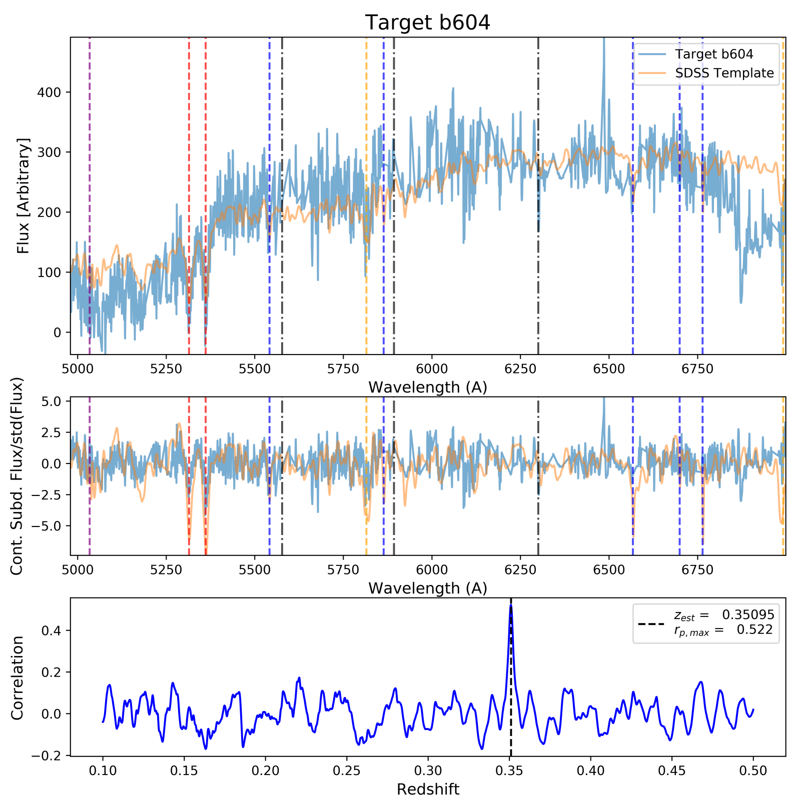

Figure 3.27 Similar to Figure 3.26, except for a lower signal-to-noise spectrum.

version of the instrument. The code can currently bias subtract the spectra, combine the image segments into seamless single images, remove cosmic rays, extract the spectral information from each individual fiber, wavelength calibrate those spectra, flatten them to remove their fiber efficiency dependence, remove the sky contribution, combine multiple observations, and fit the resulting spectrum to a redshift. All of these, with the exception of wavelength calibration, are done without the need for human input.

With all of the features listed above, there are still several areas that could be improved in the future. Potential ares of improvement include:

1. Propagating cosmic ray masks into the final analysis masks.

2. Create a method of fitting and removing scattered light from the CCDs.

3. Improving the sky subtraction to reduce the amount of masked pixels in the final spectra.

4. Include a means of spectro-photometric calibration, including proper treatment of flux throughout.

5. Implement more functionality for high-resolution spectra.

Depending on the applications, these may be useful features or even necessities for an analysis. For the studies relevant to the development of the pipeline, the current implementation has been shown to be sufficient in determining redshifts and identifying galaxy morphologies, which left the remainder relegated to future efforts.

Chapter 4

Target Sample

4.1 Introduction

The power of M2FS and the motivation behind the large amount of work outlined in Chapter 3 is that it can acquire hundreds of spectra at a time over a wide field of view of thirty arcminutes. For studies of mass profiles using dynamics, such large numbers and high number densities near the cores are valuable in properly estimating the radial mass-density profile of the cluster.

There were multiple goals of the "survey," including the investigation of individual galaxy clusters of interest and the aggregation of 20-30 clusters for small population studies. The population was selected using consistent selection rules, and will be used for multiple analyses including the constraint of cosmology using the comparison of phase spaces in future analyses (Stark et al., 2017).

Over the course of five semesters we were awarded a total of ten nights. In that time we were able to acquire up to 240 galaxy spectra per cluster for 21 clusters, and roughly 300 galaxies in two fields of cluster Abell S1063. Abell S1063 will be discussed in depth in Chapter 5. The total on-sky time ranged from as few as two 1800s (30 min.) exposures to as many as three 2400s (40 min.) exposures. The purpose of multiple exposures is to reduce the number of cosmic rays in an individual image. The amount of time needed to reach our target signal-to-noise depended on redshift and target galaxy luminosity. Including overhead, a cluster took roughly 2-3.5 hours to complete.

The remainder of this chapter will proceed as follows. We will first discuss the criteria with which we selected the galaxy clusters to include in our sample, and the properties of the clusters we eventually did select. We follow that with information regarding what galaxies were observed within each cluster. Next we will describe the creation of the target masks and the acquisition of the data. Finally we will summarize the targets, the acquired data, the redshift efficiency, the redshift precision, and several properties of the clusters inferred from the data including the velocity dispersion.

4.2 Target Selection

As mentioned in the introduction, we wished to create a consistent set of selection rules to generate a population of galaxy clusters that could be used for studies of mass estimates and cosmological constraints. Given the demand for telescope time and the size of the analysis team, a larger population was not possible. Because of this, in order to get a representative sample, we needed to narrow the scope from all clusters to a specific mass and redshift range. Because one of M2FS' greatest virtues is its multiplicity, we targeted massive clusters that would provide richnesses (or rather member galaxy counts) greater than 100. With the exception of Abell S1063, which was not part of the sample population, all others were chosen based on the criteria given below.

4.2.1 Cluster Selection

Galaxy clusters were selected based on a set of cuts:

1. Within the RA/DEC limits of the awarded time
2. Within the redshift range 0.2-0.5
3. Availability of photometry of sufficient depth (for red sequence targeting of cluster members)
4. Mass estimates in literature showing that it is a high mass system, M$> 6 \times 10^{14}\, M_{\odot}$. (Two lower mass systems, Abell 315 and RM J010650.5+010411.0 were also allowed in because of published weak lensing, available redshifts, and lack of better matches in that observing period).
5. Published individual weak lensing mass measurements or existence in a known photometric survey of sufficient depth, particularly DES and KiDS Diehl et al. (2016); de Jong et al. (2013).

Another cut that was never needed was to require a star of sufficient brightness ($9 < V < 14$) near the center of the cluster field. Fortunately the availability of field stars was large enough that we were not limited in this regard. A central bright star was used as a Shack-Hartmann star to correct for mirror distortions during the observations by monitoring the shape and point spread function (PSF) of the star. The photometry was taken from SDSS (Alam et al., 2015), DES (Drlica-Wagner et al., 2018) and Pan-STARRS (Kaiser et al., 2010).

The clusters were rank-ordered based on the a combination of its estimated mass (larger mass and lower uncertainty were ranked higher), the consistency of its redshift and sky location with our limits, magnitude limit of the available photometry, the number of member redshifts in the literature, and the availability of weak lensing information (which is required for the cosmological constraints) (Stark et al., 2017). Throughout the observing campaign all clusters that passed the cuts listed above were targeted and observed with one exception. It was lost due to weather and was only visible in the "A" semester. However, it was the lowest priority among all targets. In total, 22 galaxy clusters (and 23 fields) were observed in this campaign over the course of 5 semesters and 10 awarded nights. The clusters are listed in Table 4.1.

4.2.2 Galaxy Selection

As mentioned, a requirement for cluster selection was the availability of sufficient depth photometry. For our redshift range of interest, this meant depths of at least $r < 22$mag, where smaller magnitudes are brighter objects. An additional benefit of leveraging these data-sets is the useful "value-added" information in the catalogs. These included likelihoods of being a galaxy, uncertainties in their magnitudes along with multiple alternative definitions of the total apparent magnitude. Photometric redshifts are also available, though ignored for the purposes of target selection.

To select potential member galaxies, we first used available information on the star/galaxy separation of the survey to remove stellar contamination. We then used color cuts on all optical and near-IR bands. It is a well established empirical result that cluster cores are dominated by passively evolving, early type galaxies that are redder in color compared to a general population (Bower et al., 1992). Here colors are defined as the difference in flux (typically integrated to a total apparent magnitude) between two observations of a target using different wavelength band filters. For example, in the SDSS filter scheme there are u, g, r, i, z, and y bands ranging from the ultraviolet wavelengths to the mid-infrared respectively. If g, r, i,

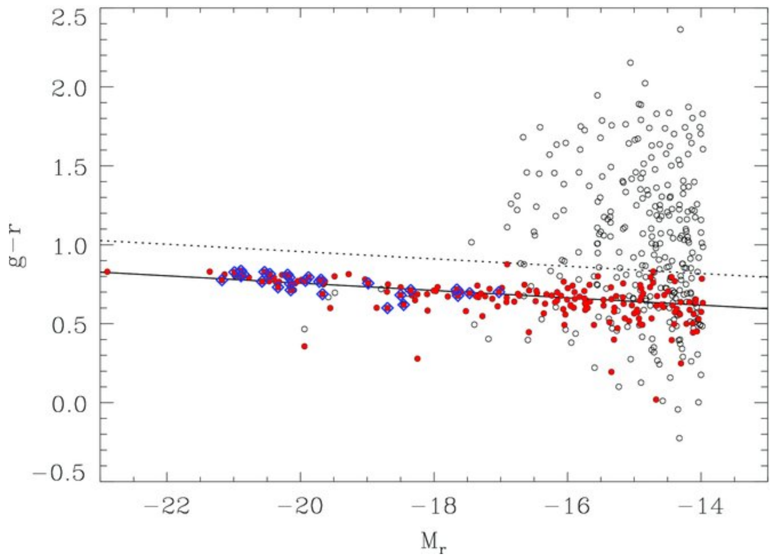

Figure 4.1 Color-magnitude diagram illustrating the tight relationship that galaxy cluster members share in these spaces that allow us to efficiently select them from numerous cluster and field galaxies in the photometric catalogs. Here the circles represent all galaxies and the red circles represent those selected as potential cluster members. Figure is from Méndez-Abreu et al. (2010).

and z bands were observed; we could create $4!/(2!2!) = 6$ "colors" (where we take e.g. r-i to be equivalent to i-r, since the magnitude of the difference is all that is relevant for seeing similarity between objects). Figure 4.1 shows an example color-magnitude diagram of (g-r) versus M_r. By looking at the color-magnitude diagrams we can locate over-densities in the color-magnitude or color-color phase spaces where the redder galaxies are preferentially located (Gladders & Yee, 2000, 2005). There is a clear, tight, relation color-magnitude space ranging across a wide breadth of magnitude space. Because these galaxies are well separated compared to the fiber separation requirements of the M2FS instrument (see Table 2.2), our primary concern was only in attaining the greatest number of potential members given the available photometric information. Thus we selected the n nearest objects to jointly fit set of color-magnitude diagrams, where $n \sim 250 - 300$. This allows for some losses due to spatial densities. 2.4

Figure 4.2 shows an example cluster that we observed, RM J211849.1+003337.2, at $z = 0.28$. The green markers indicate ~ 175 galaxies we targeted based on their colors. The x's without green circles or cyan squares are galaxies not likely to be members based on their colors. We targeted some of these to fill out the cluster phase spaces. The cyan squares represent galaxies with existing spectroscopic redshifts in

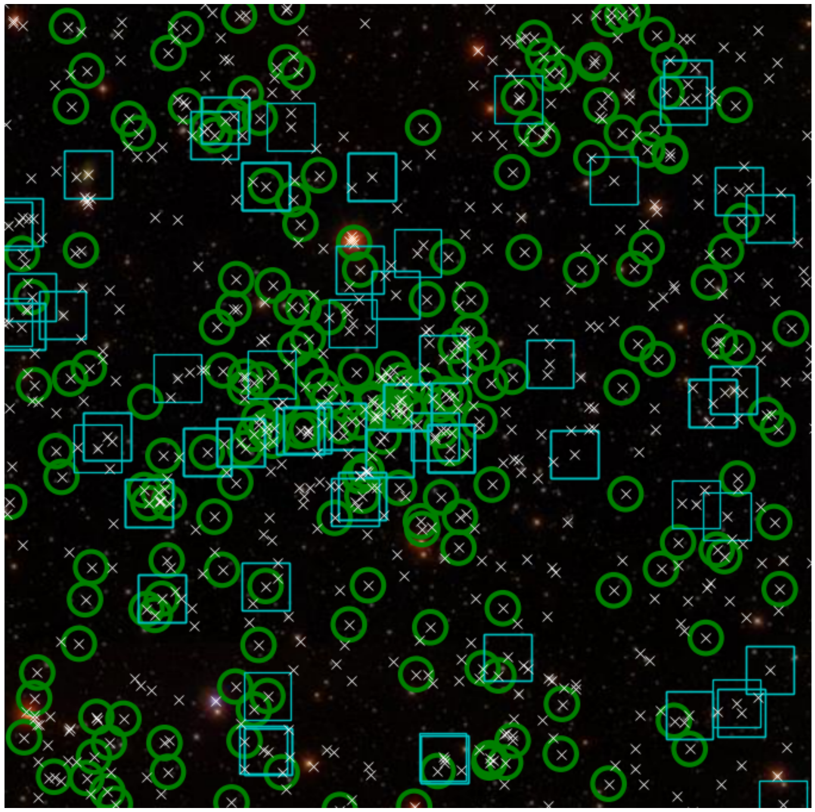

Figure 4.2 An image showing RM J211849.1+003337.2, one of our X-ray selected clusters, at a redshift of $z = 0.28$. The green markers indicate ~ 175 galaxies we targeted based on their colors. The x's are galaxies not likely to be members based on their colors. We targeted some of these to fill out the cluster phase spaces. The cyan squares represent galaxies with existing spectroscopic redshifts in the literature Rykoff et al. (2014); Alam et al. (2015) which we use to ensure high accuracy between the SDSS and M2FS redshifts.

the literature (Rykoff et al., 2014; Alam et al., 2015).

When selecting targets, we check against objects with known redshifts so that we ensure we aren't wasting fibers on galaxies that have already been targeted. However we do purposefully keep a small sample of spectroscopically measured galaxies to use as validation samples for our analysis to ensure high accuracy between our redshifts and literature.

Figure 4.3 shows the magnitude distributions of the galaxies that passed all of the color selections ("All"), those that pass the spatial constraints and were targeted ("Targeted"), those we obtained a valid spectra for ("Recovered"), and those with a confident redshift determined ("Success"). Figures B.1 through B.3 in Appendix B shows the distributions for individual masks. Figures B.4 through B.6 in Appendix B

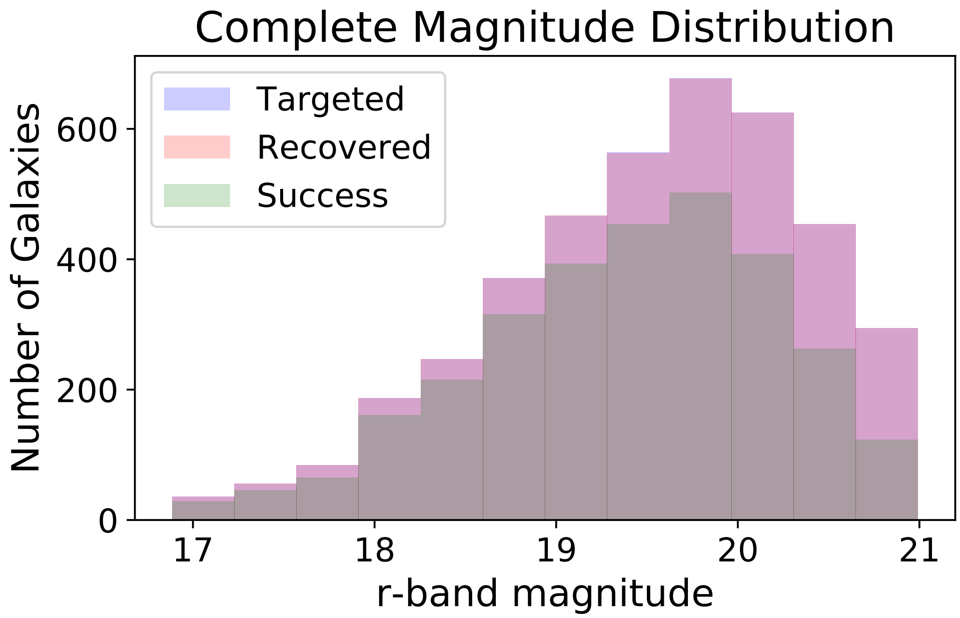

Figure 4.3 r-band magnitude distribution for all targeted, recovered, and successfully recovered redshifts in the complete catalog.

shows the targets on the sky where the color indicated if the galaxy was a potential target, if it was targeted with a fiber, and whether a redshift was successfully recovered for each individual masks.

4.2.3 Mask Creation

Once the targets were selected an iterative process occured to assemble a valid observation ("*field*"). This is composed of a central Shack-Hartmann star, 2-4 guide stars, 2-8 alignment stars, and the galaxy targets. The Shack-Hartmann star, as already mentioned, was used for dynamic mirror corrections during the observations. The 2-4 guide-stars were used to track the field as the Earth rotated. Finally, the 2-8 alignment stars were used to assure the rotational alignment of the instrument with respect to the sky, in addition to small corrections in right ascension and declination.

Regions around the Shack-Hartmann star and guide stars were forced to be devoid of science targets for two important reasons. First, the stars were typically several orders of magnitude brighter than the science targets and therefore residual sky brightness in these areas could contaminate the spectra. Second, each of these objects has special components in the instrument that required additional space compared to a standard optical fiber. The exclusion zone between the Shack-Hartmann star and a science fiber is 25", while this rises to 58" between the Shack-Hartmann star and guide stars. The exclusion between guide stars and science or alignment fibers is 33". The alignment stars used the same type of fiber as the science fibers, and are typically dimmer than the other stars, so the exclusion was the same as between two science fibers, which is 13".

To find stars within the region of the galaxy cluster, the UCAC4 meta catalog was used (Zacharias et al., 2013). Shack-Hartmann candidates were selected based on the angular distance from the cluster center. Because of the exclusion zone, the ideal location was a few arcminutes from the cluster center, such that the core could be observed with science fibers, while still being near enough to the center that a fair radial sampling could be made in all directions. For the largest (in this case most negative) declination objects, this led to some challenges as the number of stars is far more sparse than near the plane of the galaxy. Stars as far as 10 arcminutes from the cluster center had to be selected. For each candidate, the number of displaced science targets is found and the number of available science targets within a radius of 15' (the radius of the field of view) is also determined. The star that allows the most priority-weighted science targets is selected as the Shack-Hartmann star. Here the priorities are a normalized function of the inverse r-band magnitude. By weighting by the inverse magnitude, we prioritize brighter objects. The logic behind this choice is that brighter objects give more photons and thus make it more likely that a successful redshift can be determined.

After the Shack-Hartmann star was selected, all possible guide stars are searched to determine the number of fiber collisions that occur (meaning that if the star were selected some science fibers would no longer be able to be observed). If at least two guide stars can be assigned without collisions, then the process moves on, otherwise the selection proceeds in a similar manner to the Shack-Hartmann case where the stars that displace the fewest fibers are selected. In the event of equal number of displaced fibers, the priorities of displaced fibers are used to select the more ideal star candidates. The alignment stars, having a broader magnitude range, is then selected last from the available stars. Because they can be dimmer and the physical fibers are smaller, these are almost always able to be selected without collision with science targets.

After the stars have been selected, the science targets that pass all exclusions are assigned based on priority. Lower priority objects that are too close to higher priority targets are thus discarded. These are not common in an individual cluster, however, multiple fields are typically drilled on the same aluminum plate for both economic and environmental reasons. It is common for conflicts to arrive when superimposing multiple fields onto the drilled plate and therefore the priorities are used to make decisions about what targets will be drilled and which will not.

The final consideration is the placement of sky fibers. In slit based spectroscopy the small science target is flanked by the spectrum of the sky on either side of the object, making it possible to fit for the sky and target fluxes simultaneously and thus separating the two. For fiber spectroscopy, that is no longer the case. Even if the fibers did have angular diameters larger than the typical target, the spatial information is lost before it reaches the spectrograph. So the additional sky light only reduces the signal-to-noise (S/N) rather than helping to remove the background. The sky fibers were made the lowest priority and were assigned based on locations that wouldn't conflict with science fibers and weren't near known bright objects in the photometry. A minimum of six sky fibers were acquired, with additional fibers used if the number of science targets was less than 250 (the total number of allowed science and sky fibers is 256).

Figure 4.4 shows a computer output showing an example target set (hereafter referred to as a "field" or "mask") of data. The data includes the galaxy targets along with the additional fibers for acquisition, alignment, and guiding. The blue and red lines help to guide the observers about what camera the corresponding fiber belongs to. The green holes are ancillary fibers for guiding and alignment. Examples of each of these are labeled in the lower right. Figure 4.5 shows an image of such a mask, which has been marked for plugging using a diagram similar to Figure 4.4. Figure 4.6 shows an example plate mounted to the telescope and plugged into the instrument.

4.3 Data Acquisition

M2FS is a fiber based plug-plate spectrograph, which requires manual insertion of the fiber tips (metallic ferrules) into an aluminum plate. The fiber holes are pre-drilled and as mentioned, multiple observations are typically drilled on a single piece of material. Because of the additional holes from other fields and the needed accounting of what object is acquired by what fiber, the mapping must be physically drawn onto the plate prior to observing. This is typically done the afternoon prior to observation. The marking consists of 32 lines that are each connect eight drilled fiber holes. These correspond to a half-tetris. The name of said half-tetris is used to label each line. In most circumstances colors are additionally used to differentiate the red and blue fibers

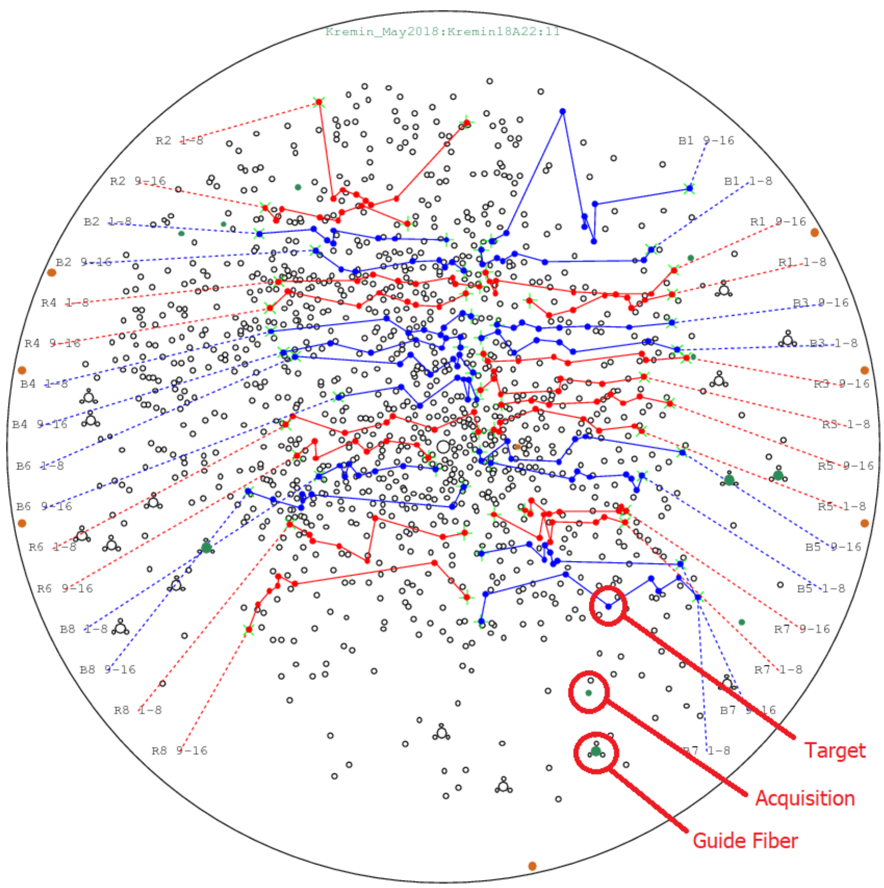

Figure 4.4 An example schematic M2FS plate generated by software to assist observers in drawing the target field onto the aluminum mask shown in Figure 4.5. The blue and red lines help to guide the observers about what camera the corresponding fiber belongs to. The green holes are ancillary fibers for guiding and alignment. Examples of each of these are labeled in the lower right.

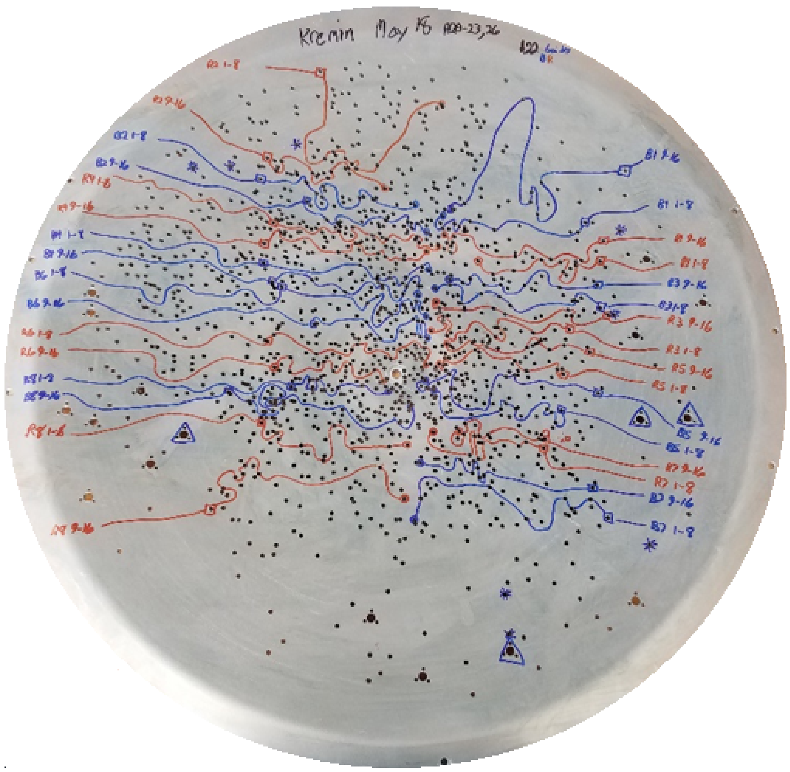

Figure 4.5 An example of an M2FS plate that has been marked for observations. The blue and red lines help to guide the observers. The triangles indicate guide fiber locations. The star patterns indicate acquisition fiber holes. The holes connected by lines are the target holes strung into sets of 8 corresponding to half tetrises.

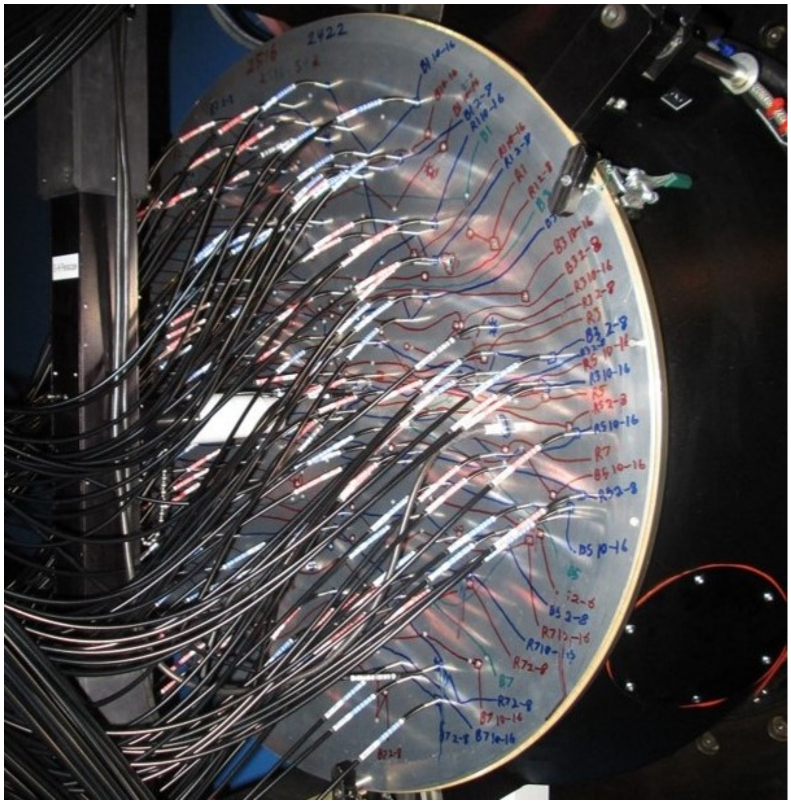

Figure 4.6 A similar plate to that in Figure 4.5 when it is plugged into the instrument. Image courtesy of Mario Mateo.

to assist the observers plugging in the darkness of the night. This was illustrated in the last section in Figure 4.5. For the low-resolution mode, all 256 science fibers are placed into locations regardless of whether they were assigned targets. The unassigned fibers are used as additional sky fiber locations in the analysis. In addition, two guide fibers and up to eight alignment star fibers are also inserted, depending on what was assigned during mask creation. These are unique fibers that don't run to the spectrograph but are instead read out directly to CCD's to get the rotation correct and ensure proper tracking of the sky over the long duration science exposures. An example of a plate that has been mounted to the telescope and plugged into the instrument can be seen in Figure 4.6.

Like most spectroscopic observations, a number of calibration images in addition to the science exposures are needed to properly utilize the data. "Flats" need to be taken to correct the spectra for fiber throughput differences as well as optical throughput variations across the focal plane. For this, M2FS uses the sky at twilight and quartz emission lamps that provide a smooth continuum. Twilight flats are the most ideal and these are used when available. The reason that the sky is preferable is because on the scale of thirty arc-minutes the sky is far more uniform at twilight than what can be achieved using lamps inside a dome. Since our goal is to remove non-uniformities, this is an important factor that we want to mitigate.

In addition to flats, bias exposures are typically taken during the day before and/or after the observations to understand the zero-point offsets in the CCD pixels. Finally, atomic emission lamps are used to project spectral lines from atomic transitions in the visible wavelengths onto the CCD's through the optical fibers. These are used to calibrate the wavelength of light as a function of pixel location along the dispersion axis of the camera. These are typically done immediately before and after the science exposures to reduce the amount of time with which the wavelength solutions might vary due to environmental changes. Some, but not all of the observations, included additional calibration measurements between science exposures as well. The science exposures were initially taken for two hours, which was later reduced to 1.5 hours or even one hour. Typically exposure times for a single image were 1200s (20 minutes), 1800s (30 minutes), and 2400s (40 minutes). Generally three images were taken for a given target, with a fourth taken if time was available. These splits were made to reduce the number of cosmic rays in a given image and help in the identification of cosmic rays (though our particular algorithm didn't utilize such comparisons).

4.4 Summary of Data

M2FS is a queue based instrument. This means that a PI is not designated specific full or half calendar nights, but rather given the equivalent number of hours to be spent on targets during a "run" where the instrument was installed on the telescope. The time and observations of each awarded proposal are combined and observed based on availability and priority. This means that a PI may not be present for a particular observation, and that a PI may take several nights worth of data for others. The time lost to mechanical or weather related issues are shared amongst all users for that semester. This allows for more averaged amounts of time-loss per user.

These observations took place over the course of five semesters, with ten total days awarded. Two days were allotted for each of the semesters 2016A, 2016B, 2017B, 2018A, and 2018B. Because of the queue based system, data was acquired on 34 unique nights of observation. With 23 fields acquired, this averaged to 2.3 targets per night of awarded time. Given the typical efficiency of three targets per night of observing on M2FS, this equates to roughly 30% loss due to factors such as weather and mechanical difficulties. This observing efficiency is consistent with the typical losses for the instrument and telescope during those time periods, which anecdotally ranged from 20-50%.

4.4.1 Final Dataset

The final dataset amounted to 22 galaxy clusters and 23 fields. The clusters are summarized in Table 4.1. For each cluster, roughly 100 to 240 galaxy spectra were taken. All 4427 galaxies are given in Appendix C in Table C.1. Of the 4427 galaxies targeted, redshifts were able to be robustly estimated for 3054. Of that number, 1679 are considered to be cluster members based on radial distance less than 5 Mpc and peculiar velocities less than 6000 $\mathrm{km\,s^{-1}}$with respect to the cluster center.

4.4.2 Example Spectra

Galaxies were cross correlated using a Pearson-r coefficient against SDSS early-type galaxy templates. The correlation value, r, can range from -1 (anticorrelated) to +1 (perfect correlation). For our purposes, a correlation above 0.35 was required to use the resulting redshift in our analyses.

In addition to this correlation statistic, an indication of the signal to noise (SN) is calculated for major absorption lines Ca H, K, and G. The average of these three is another proxy for the confidence of the redshift estimate, as more prominent features should be more easily fit. Unfortunately, at low SN the calculation becomes inaccurate, even when the fitting process can still be performed. For that reason, SN is used only for qualitative studies and it isn't used in selecting data. For that, the correlation value is used instead.

Below we show two plots. Figure 4.7 shows example spectra at different values of maximum fit correlation. Here arbitrary offsets are added vertically to improve visibility. Figure 4.8 shows a similar plot except showing examples of varying signal-to-noise.

In the plots given in Figures 4.9 - 4.11 we show a zoomed in view of multiple examples in each correlation bin to highlight the visibility of the prominent Ca H and K lines. Each spectrum is plotted in its rest frame to make the comparison more apparent. Figures 4.12 and 4.13 again shows the H and K lines in their rest frame except in bins of SN.

Table 4.1. M2FS Cluster Sample Information.

Mask	Object	RA	DEC	z
A21	Abell 907	149.5925	-11.059722	0.167
B09	Abell 315	32.5125	-0.997778	0.1753
B07	Abell 291	30.434167	-2.200833	0.197
A23	Abell 1451	180.820833	-21.522778	0.199
A04	RM J160319.0+031644.6	240.82912	3.27905	0.2198
A10	Abell 2397	329.03577	1.39094	0.2219
A26	Abell 1942	219.59125	3.670278	0.224
A00	RM J132415.1-032446.6	200.999	-3.38192	0.2334
A09	Abell 2355	323.82825	1.42417	0.2509
B05	Abell 2645	355.32	-9.0275	0.251
A02	Abell 1835	210.25864	2.87847	0.252
B10	Abell 68	9.272083	9.153	0.255
B11	RM J010650.5+010411.0	16.702083	1.045	0.255
A07	RM J211849.1+003337.2	319.70447	0.56034	0.2765
A11	RM J230800.7-015543.3	347.00381	-1.92809	0.3208
B01	XMMXCS J234231.5-562106.8	355.63125	-56.351639	0.35
A22	MACS J1115.9+0129	168.96625	1.498639	0.352
B04[a,b]	Abell S1063	342.23917	-44.5038	0.365
B08	Abell 370	39.960417	-1.585556	0.375
B02	XMMXCS J233836.3-543740.3	354.64667	-54.62486	0.38
B06	XMMXCS J022145.4-034617.4	35.438	-3.772	0.429
A20	RM J092636.7+124304.1	141.652917	12.717722	0.489

Note. — 22 clusters were observed in total, in 23 fields. Abell S1063 was observed with two M2FS masks, B04a and B04b. Target identifiers taken from their respective catalogs: RM - Rykoff et al. (2016); Abell - Abell (1958); Abell S - Abell et al. (1989); XMM-XCS - Mehrtens et al. (2012).

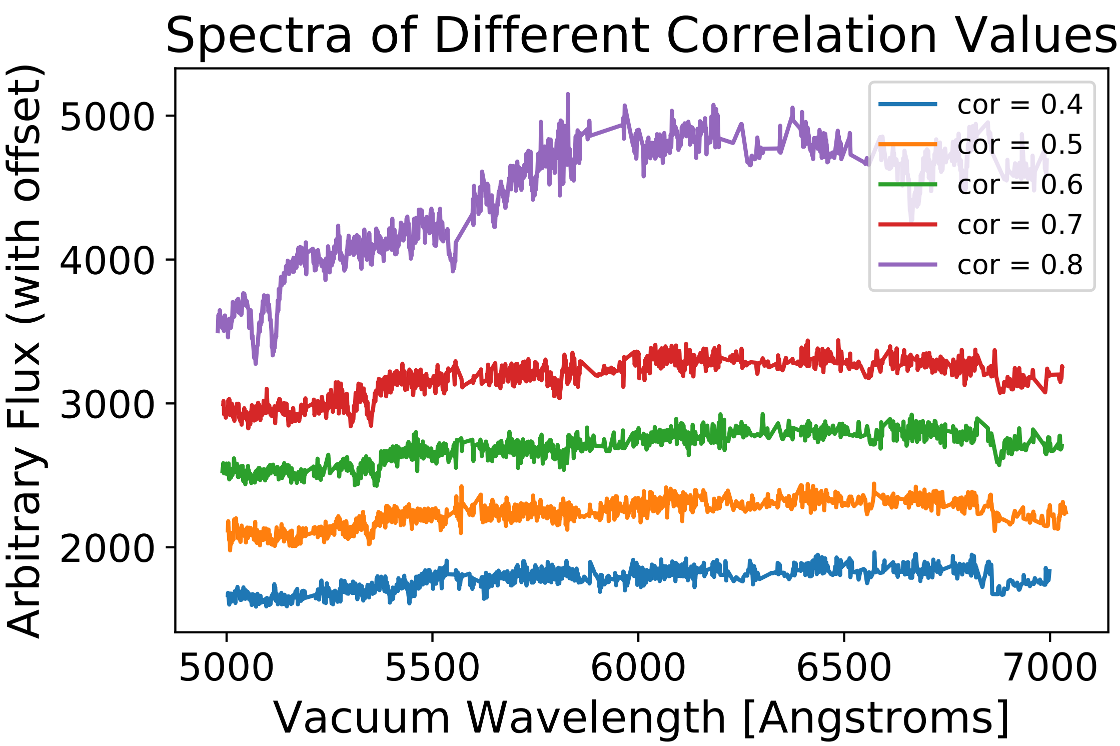

Figure 4.7 Example spectra as a function of recovered Pearson-r cross correlation value. Arbitrary offsets are added to separate them vertically.

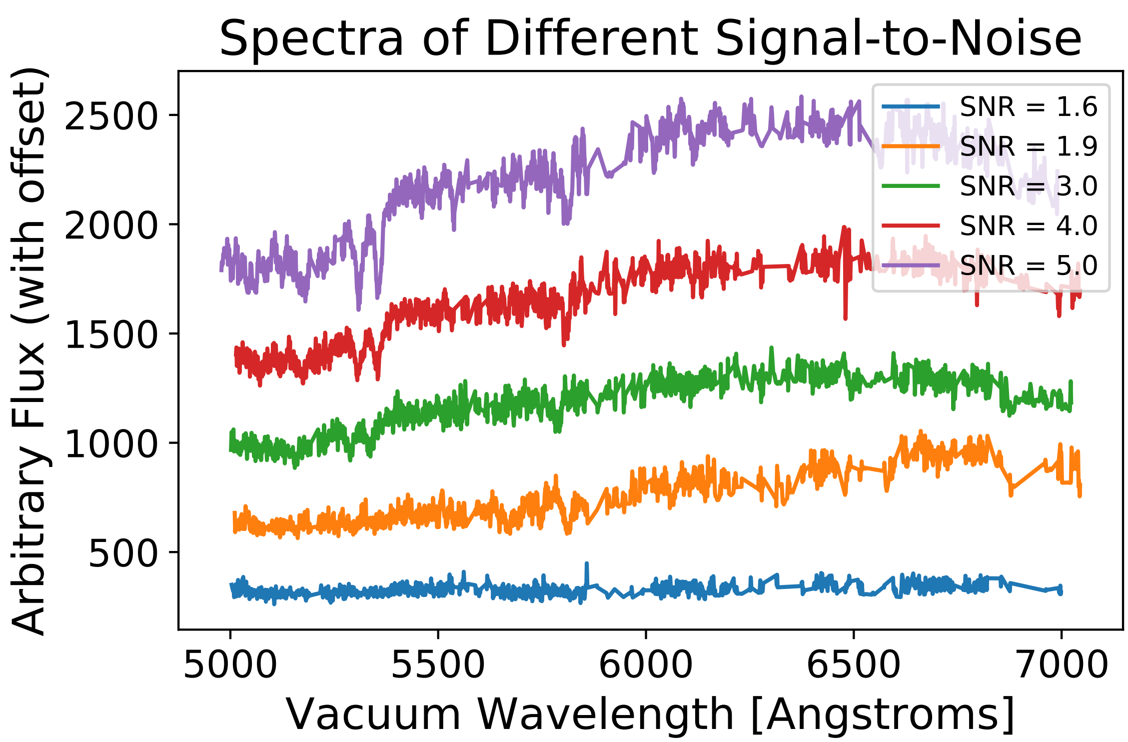

Figure 4.8 Example spectra as a function of signal-to-noise. Arbitrary offsets are added to separate them vertically.

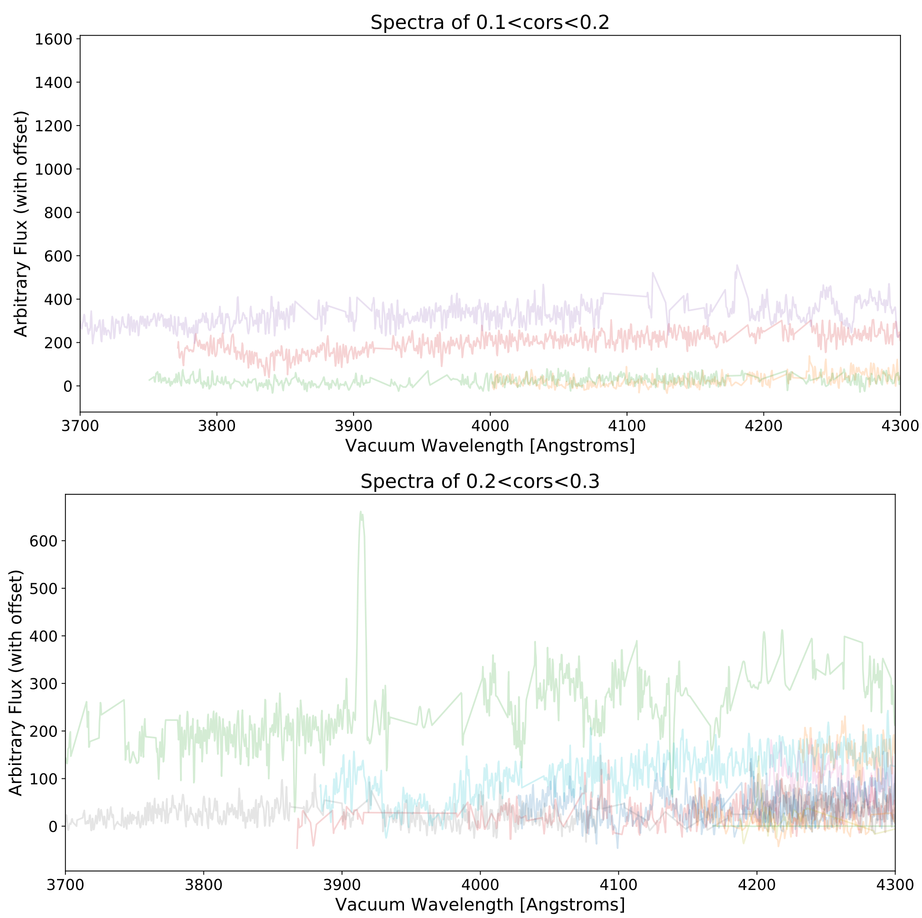

Figure 4.9 : Stacked example spectra in bins of recovered Pearson-r cross correlation value. The galaxies are zoomed in to show the calcium H and K absorption lines. Note the wavelengths are rest-frame wavelengths.

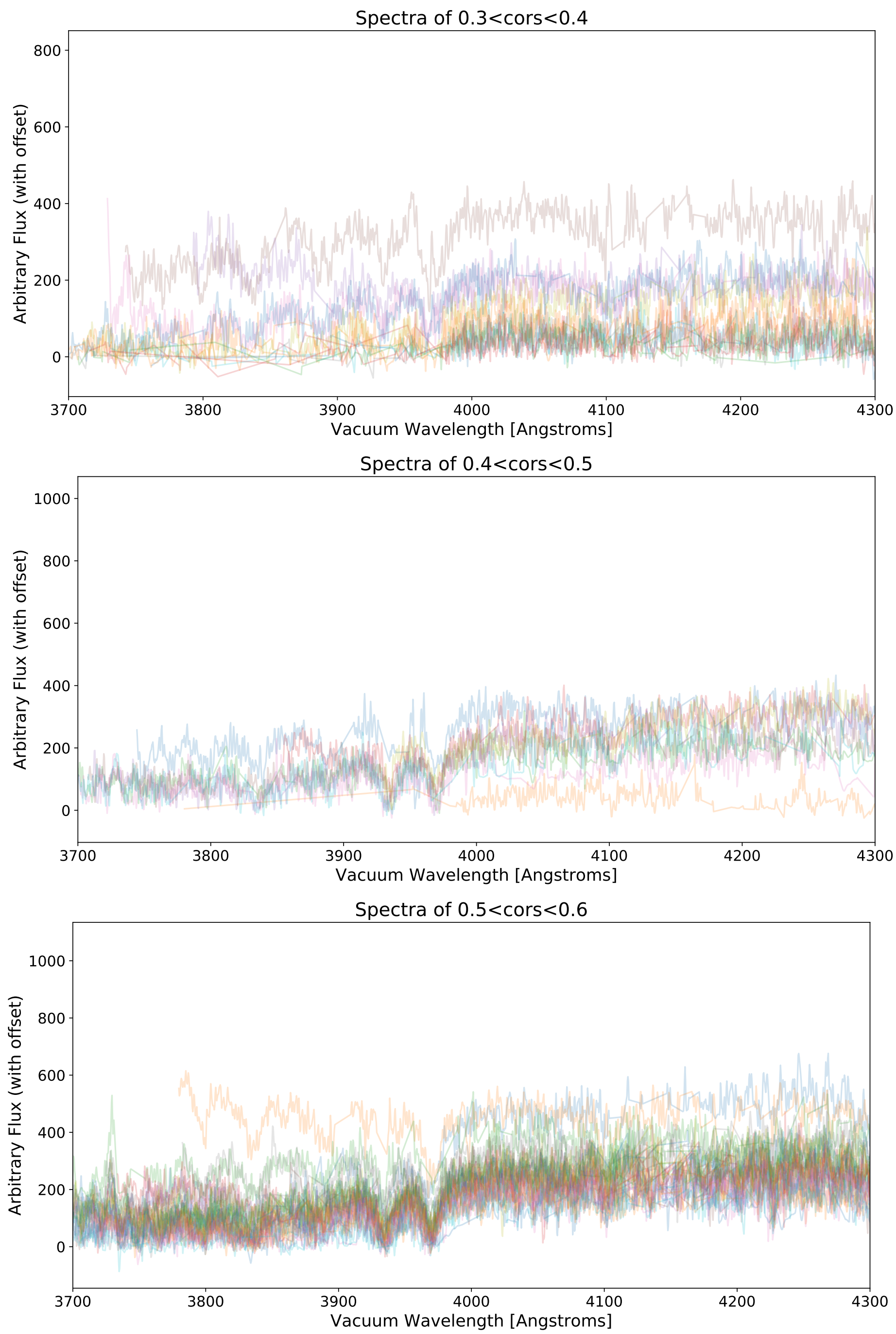

Figure 4.10 : Continuation of 4.9.

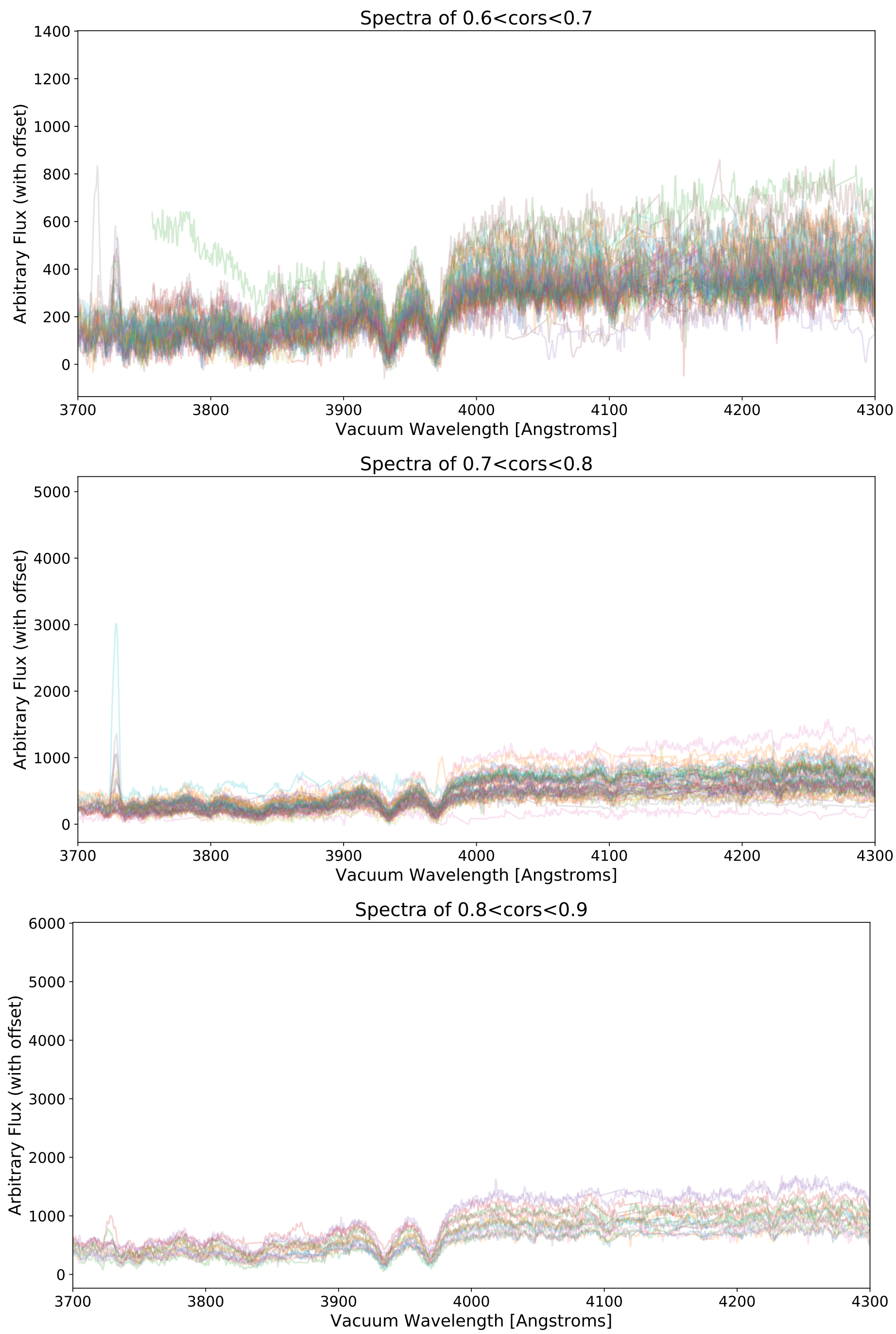

Figure 4.11 Continuation of 4.9.

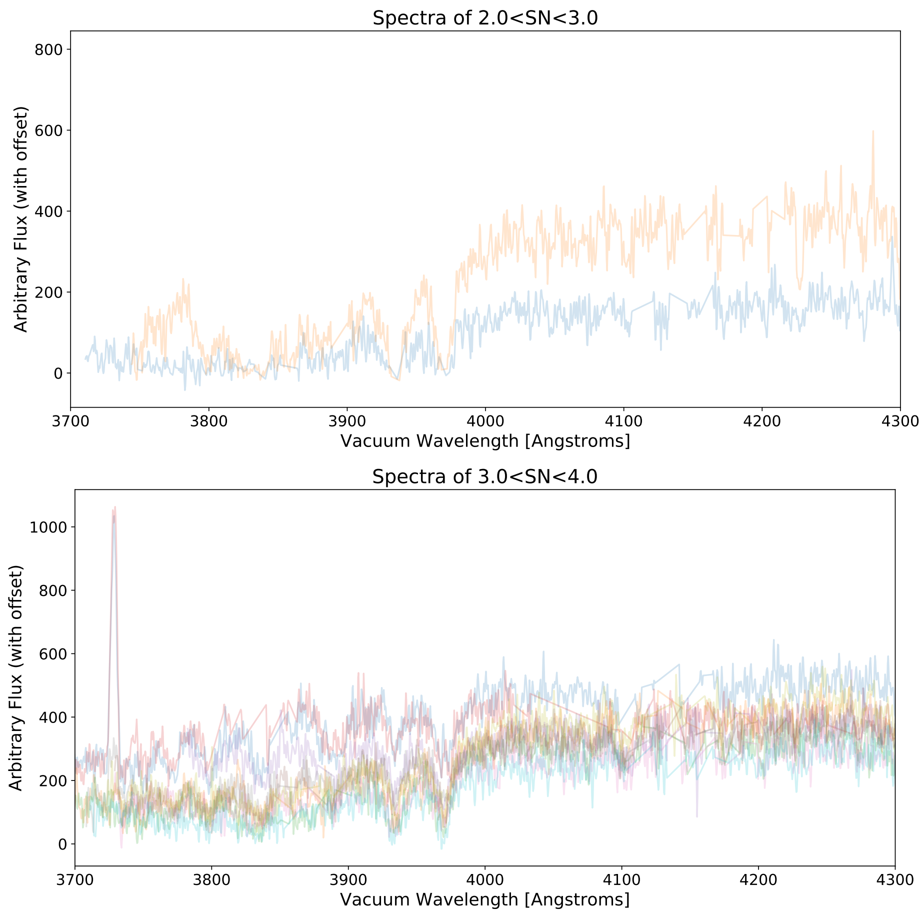

Figure 4.12 : Stacked example spectra in bins of the estimate signal-to-noise value. The galaxies are zoomed in to show the calcium H and K absorption lines. Note the wavelengths are rest-frame wavelengths.

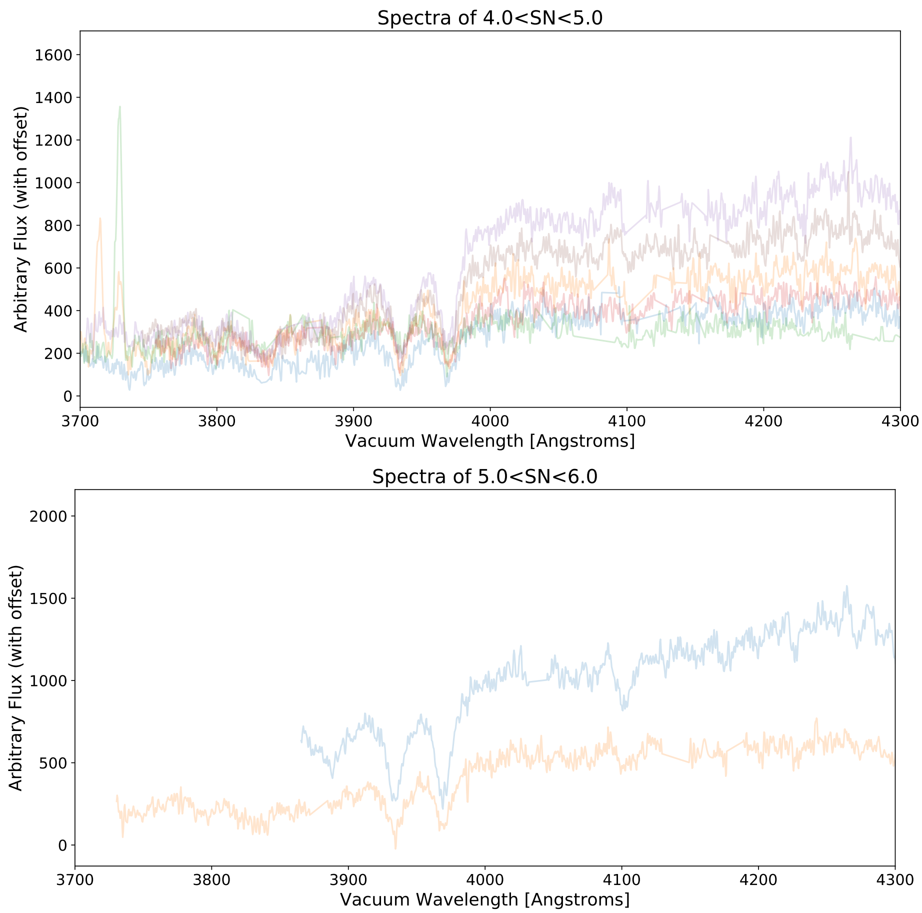

Figure 4.13 Continuation of 4.12.

4.4.3 Signal Strength versus Galaxy Properties

Assuming nominal conditions, we expect a lower apparent magnitude (brighter, higher flux) object to be observed with higher SN and thus higher redshifting fitting efficiency. Figure 4.14 shows that for our masks, this relationship does indeed hold on average. There appear to be two populations, each of which show the expected anticorrelation between the galaxy template correlation coefficient and the magnitude. The first population is lower and centered around 0.3, with a second centered around 0.6 or 0.7. We suspect that the populations differ in the redshift of the objects, the position of skylines with respect to the redshifted spectra, and the morphological type of the target galaxy. Very bright objects were sometimes removed to prevent light from affecting neighboring fibers on the spectrometer's CCD. This may account for the very bright objects that reside at low correlation values. Figures B.7 - B.9 in Appendix B show the distributions for individual masks.

We can also assume that, given a distribution of galaxies, lower redshift objects will have on average greater apparent magnitudes. Figure 4.15 illustrates this general dependence for our datasets. Second we would imagine that higher SN objects would be related to brighter objects and that larger correlations would be related to higher signal-to-noise. Figure 4.16 explores the relationship between apparent magnitude, recovered spectral correlation coefficient and recovered SN for the complete sample. These relationships are seen in the data. Figures B.14 - B.16 in Appendix B show the distributions with redshift for individual masks, and Figures B.11 - B.13 show the distributions for individual masks with respect to SN.

4.4.4 Redshift Success rate

Using the information above, comparisons with the SDSS, and comparisons with human-verified redshifts, we were able to assess the relationship between accurate redshifts and correlation value and select a value to use as our definition of a trustworthy redshift. This value, 0.35, was chosen for the entire dataset. Figure 4.18 shows the percentage of objects that met or exceeded this correlation criteria as a function of the estimated heliocentric redshift for the entire aggregate sample. The evolution with redshift is roughly what is expected with the percentage decreasing with increasing redshift but saturating near peak efficiency at lower redshifts. Regions with no data-points had fewer than four measurements and thus had nothing informative to contribute. The vertical uncertainties are the statistical uncertainties and the horizontal bars indicate the width of the bins in which the data was aggregated. Figure

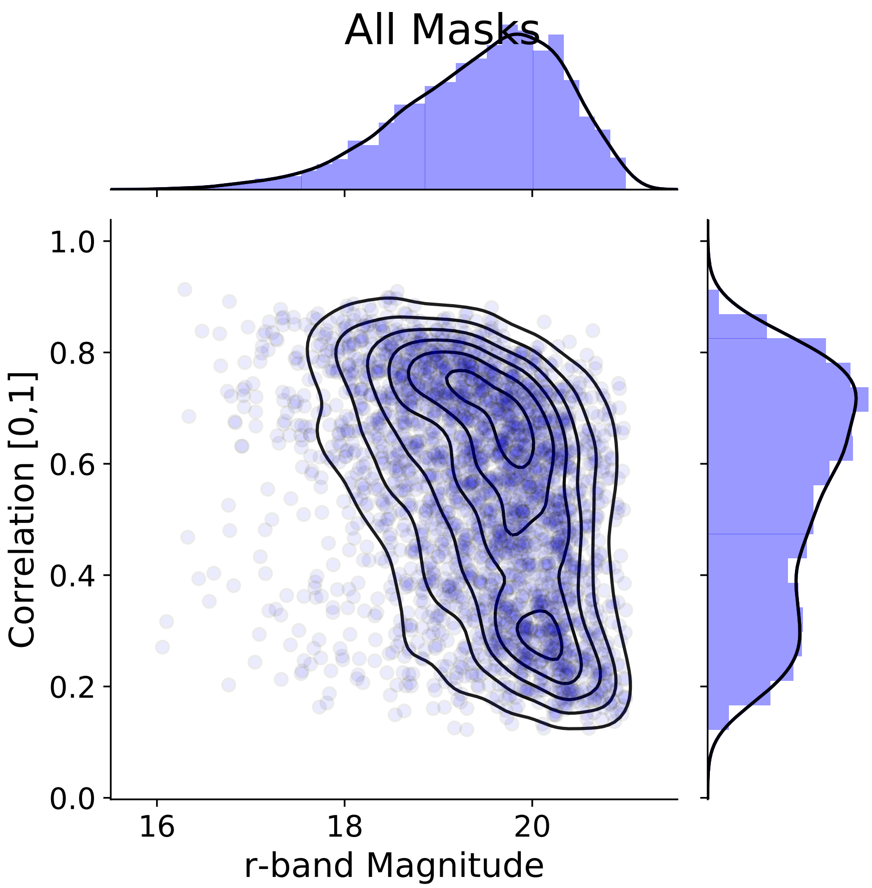

Figure 4.14 Cross correlation Pearson-r coefficient versus r-band magnitude for galaxies in the sample. The coefficient is with respect to one of two SDSS template spectra with early type galaxy forms. The histograms show summations along the given axis, with smoothed fit lines overlaid.

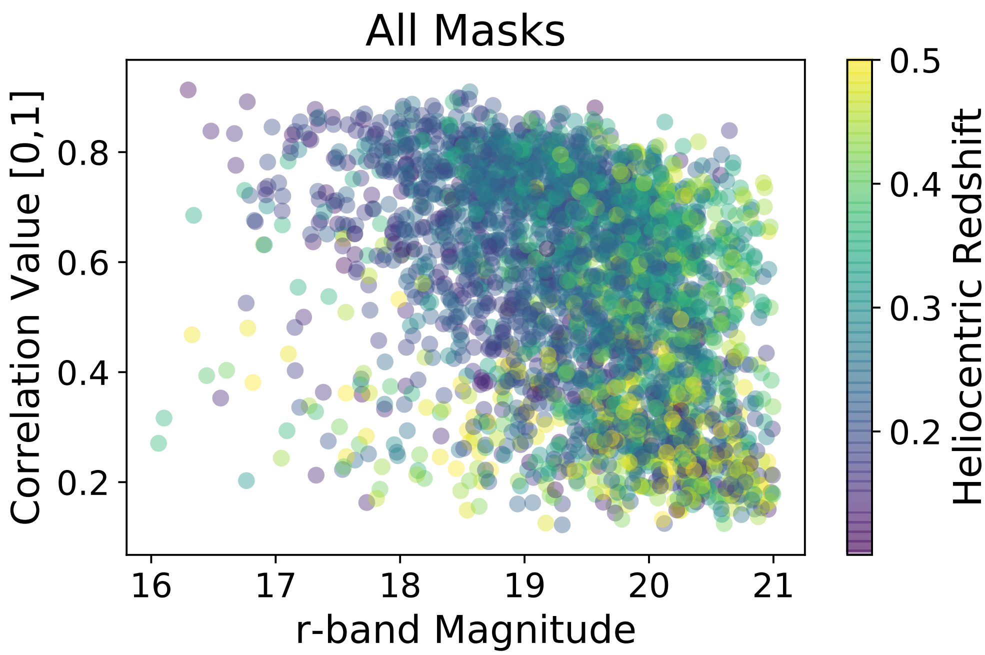

Figure 4.15 Pearson-r cross correlation coefficient versus r-band magnitude for all galaxies in the sample. The color represents the recovered redshift of the galaxy.

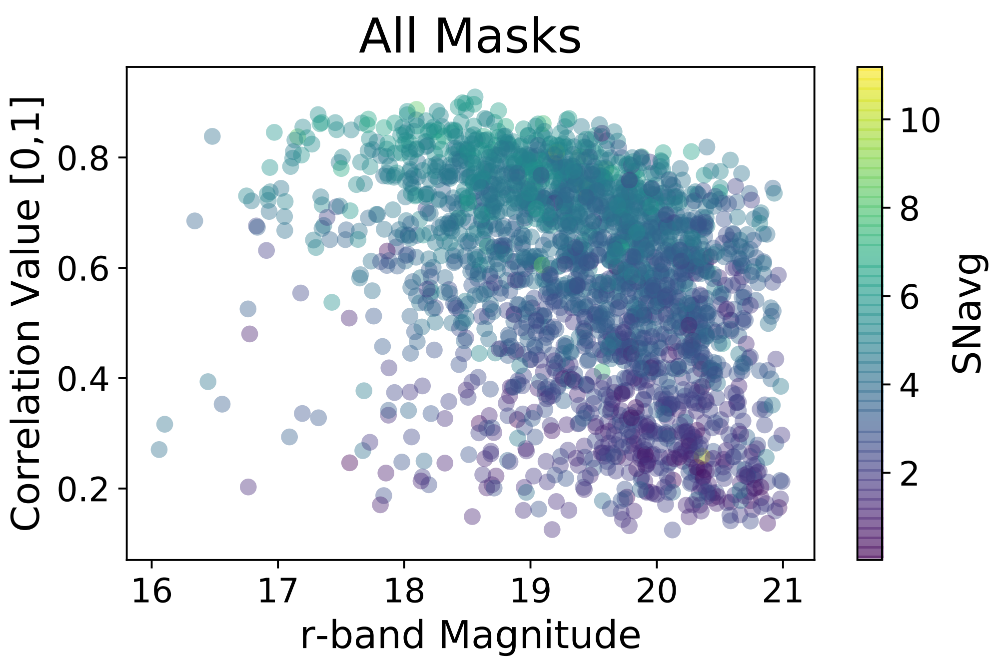

Figure 4.16 Pearson-r cross correlation coefficient versus r-band magnitude for all galaxies in the sample. The color represents the estimated signal-to-noise of the spectrum.

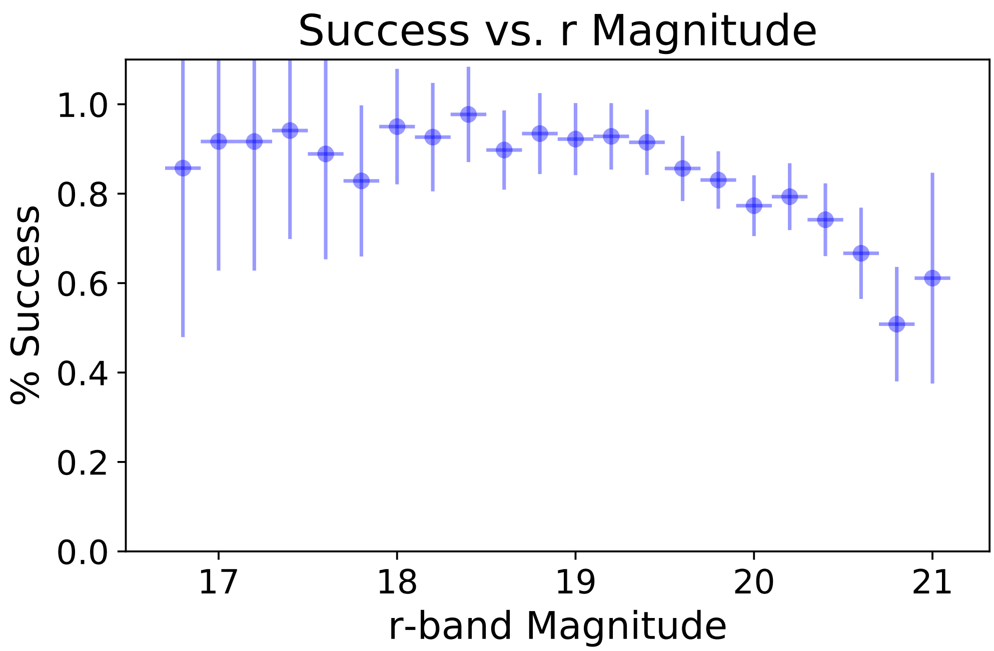

Figure 4.17 Showing redshift success rate as a function of r-band magnitude of the galaxies.

4.17 shows the success rate as a function of r band apparent magnitude. The trend that brighter objects were recovered with higher rates of success is clearly visible with a linear drop-off occuring above r$\sim$19.5. Figures B.20 - B.22 and Figures B.17 - B.19 in Appendix B show these for each mask individually. When viewing the individual masks it is clear that some were more successful than others. This is due to many factors including exposure time, seeing, sky brightness, clouds, etc.

Finally, using the cut criteria, we can look at the distribution of apparent magnitudes and recovered redshifts for successful and unsuccessful spectral measurements. Figures 4.19 - 4.22 show all the masks. The red dots indicate galaxies with recovered redshifts that meet our quality criteria. The gray dots are objects where we recovered redshifts that did not pass the quality cuts. Projection effects are prominent in several masks, particularly A26, which appears to be composed of three distinct clusters.

4.4.5 Redshift Precision and Accuracy Analysis

As mentioned earlier, some of our target clusters overlapped with the Sloan Digital Sky Survey spectroscopic programs. To accumulate more redshifts, we avoided many of these galaxies for re-observation, but we purposefully re-observed some to test

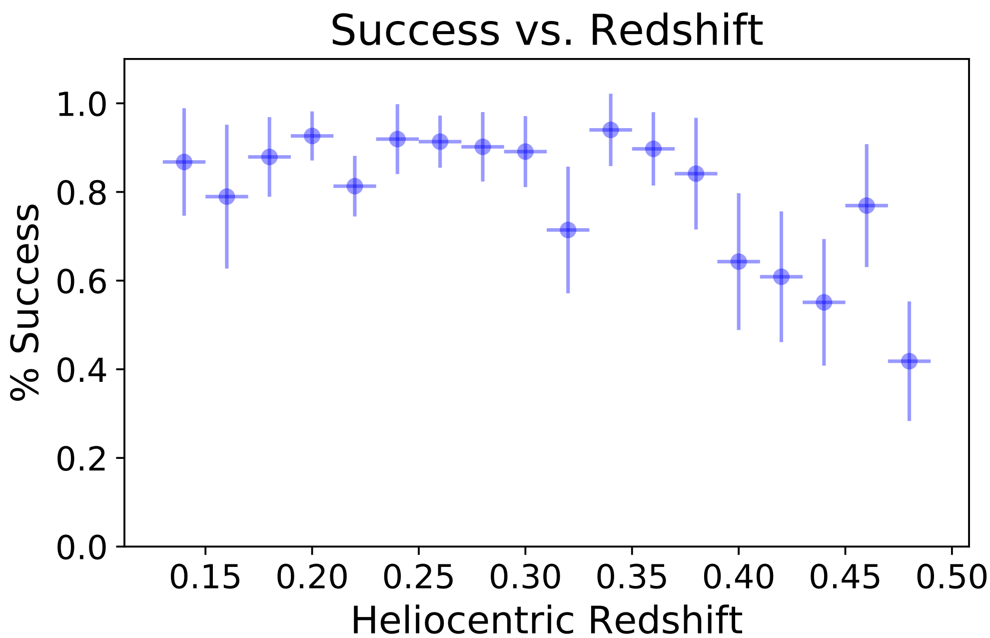

Figure 4.18 Showing redshift success rate as a function of the recovered redshift of the galaxies.

our ability to recover accurate and precise redshifts. Figures 4.23 and 4.24 show a comparison of all redshifts that were determined from the M2FS work given here with the respective redshift determined by SDSS. There is excellent agreement with a scatter of roughly 68 $\mathrm{km\,s^{-1}}$and a small (but non-negligible) systematic bias of ~ 16 $\mathrm{km\,s^{-1}}$. Even assuming comparable scatter for the SDSS sample itself with respect to "Truth," we are within the realm of 100 $\mathrm{km\,s^{-1}}$ uncertainties, which is more than adequate for our studies given the number of cluster members recovered. In running tests, we are able to recover masses to roughly equal precision even with uncertainties as high 150 $\mathrm{km\,s^{-1}}$ thanks to the large sample size for each cluster.

Figure 4.24 shows the deviations as a function of redshift. There is no noticeable change in bias as a function of redshift and the scatter is consistent. There is an added selection effect as some redshifts have galaxy cluster members while other redshift bins only have erroneously targeted field galaxies (and thus low number densities).

4.4.6 Derived Quantities

As a starting point of our future studies, we began with exploratory looks at some derivable properties of each target mask. Appendix B shows three of these derived quantities for each of the 23 masks individually. Note that masks B04a and B04b per-

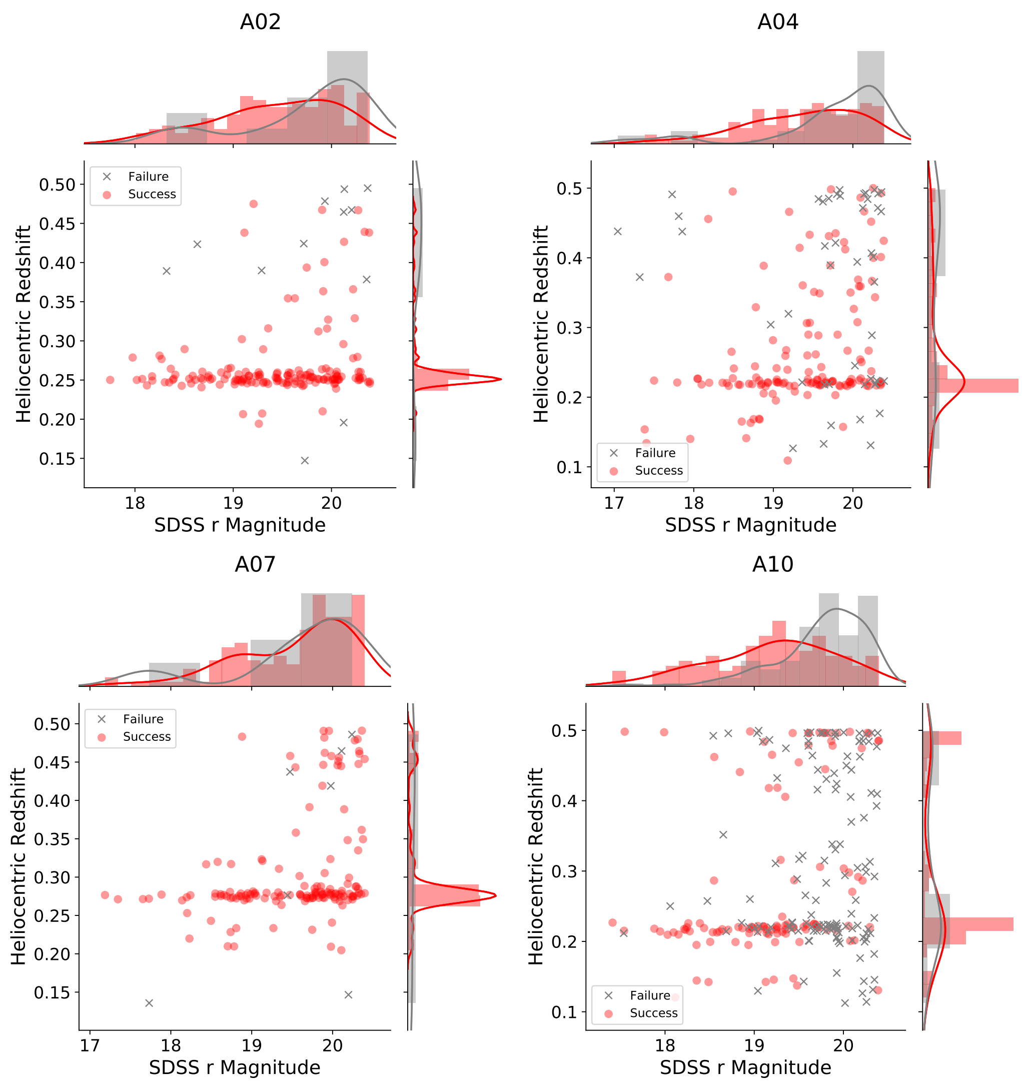

Figure 4.19 Redshift vs. Magnitude for the successful (red) and unsuccessful (gray) recovered redshift samples. Success here is defined as having a correlation value greater than r=0.35. The histograms and corresponding smoothed fits are projections along the corresponding axis.

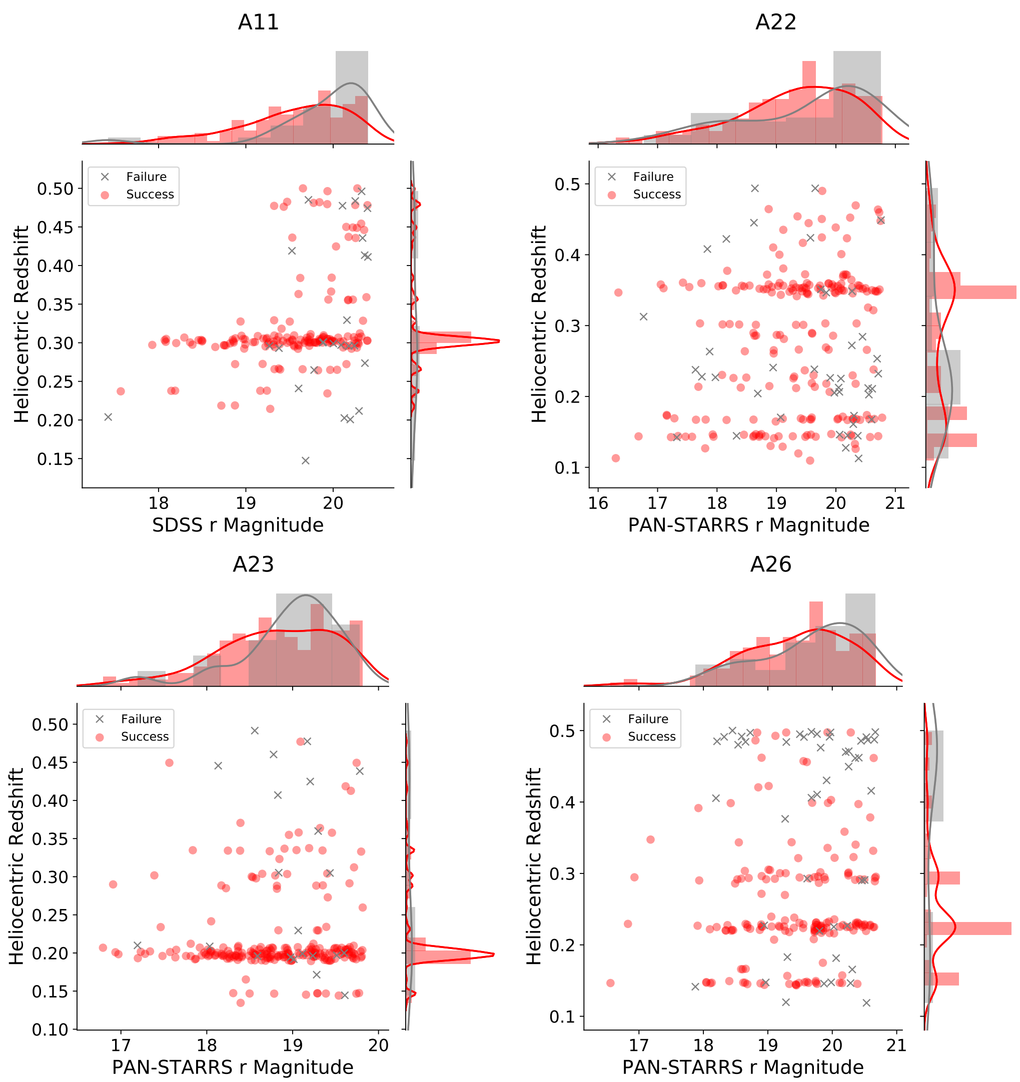

Figure 4.20 A continuation of Figure 4.19.

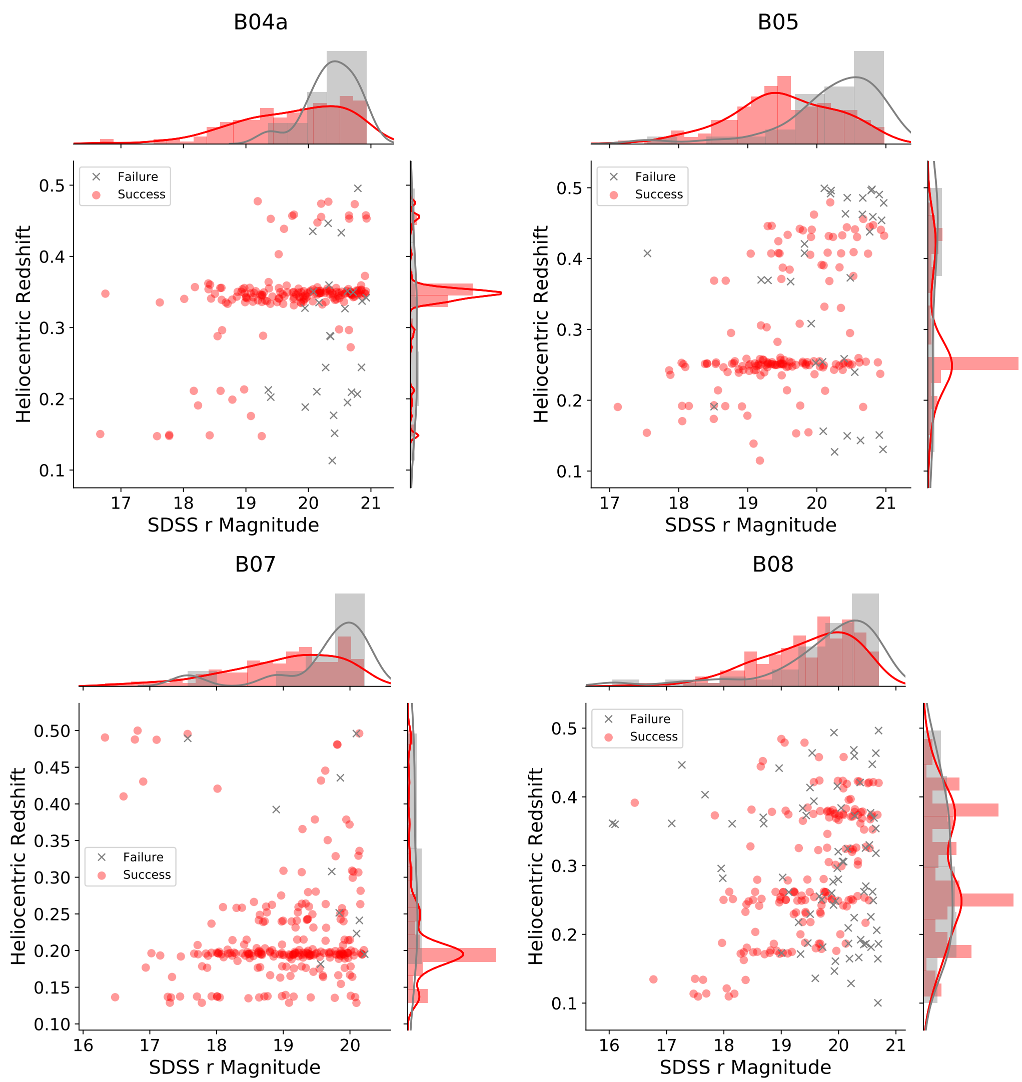

Figure 4.21 A continuation of Figure 4.19.

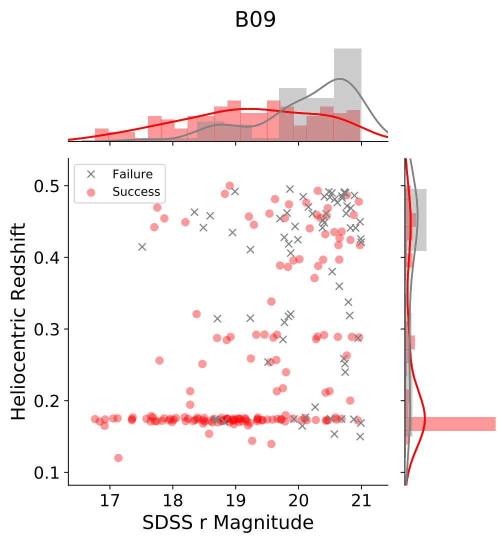

Figure 4.22 A continuation of Figure 4.19.

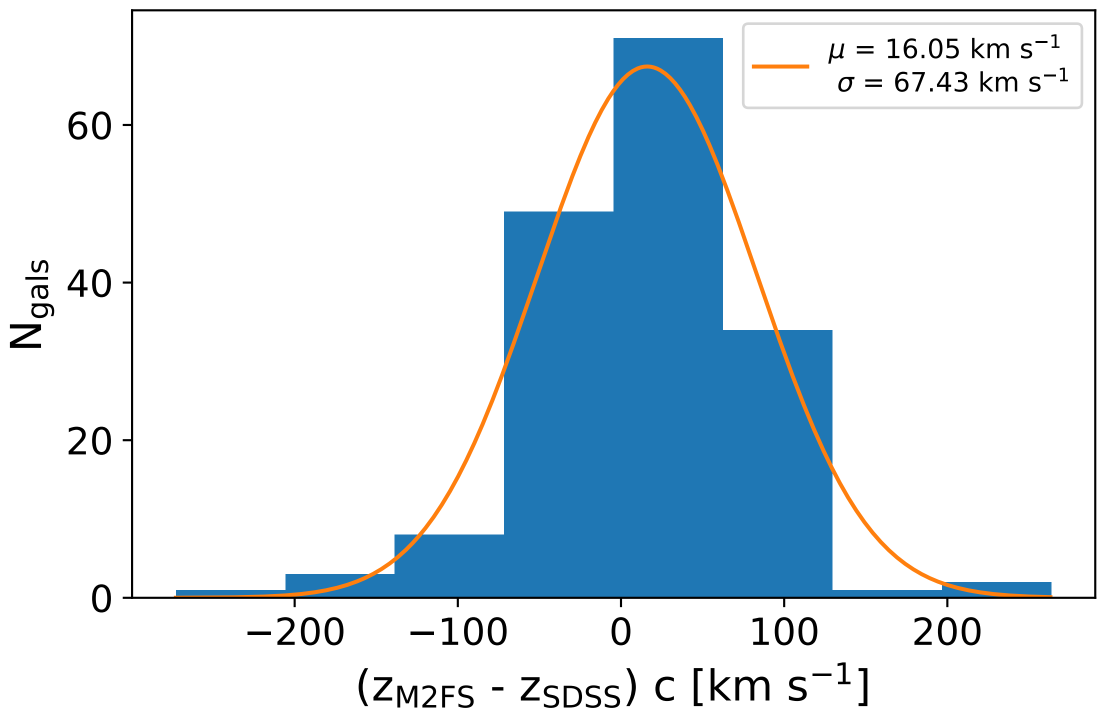

Figure 4.23 Histogram of the differences in all spectra with corresponding redshifts measured by SDSS. Assuming the large survey to be "truth," we can determine out redshift recovery bias of a few tens of km/s and a dispersion that is consistent with other low-resolution measurements.

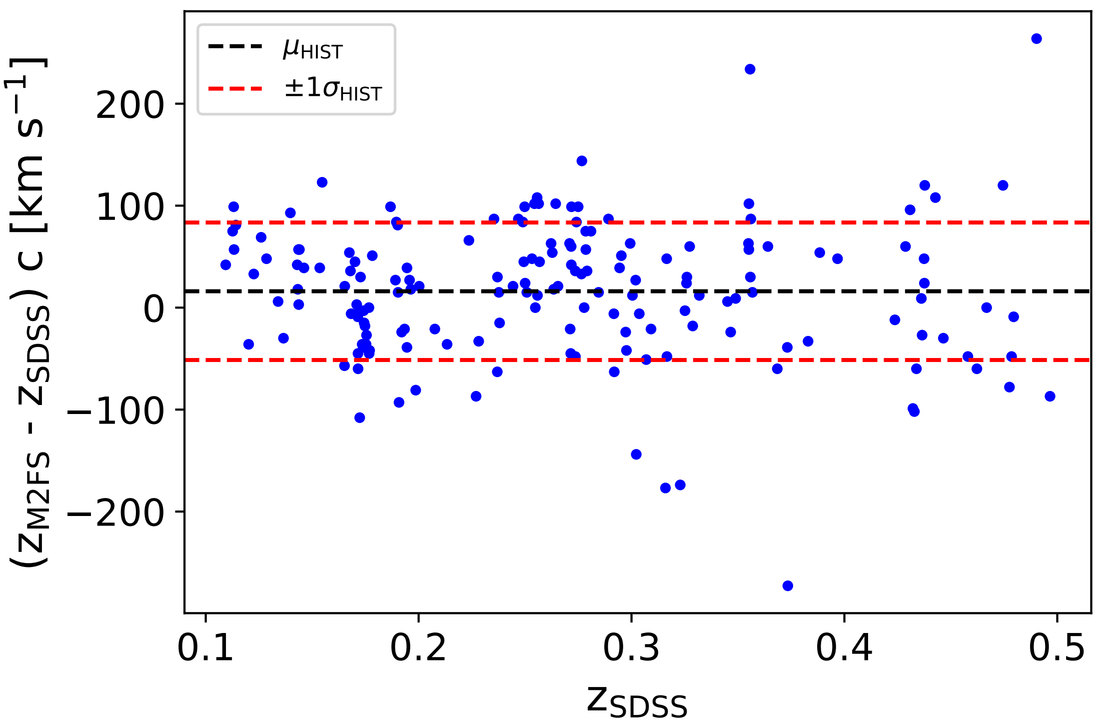

Figure 4.24 Similar to Figure 4.23 except we show the differences as a function of SDSS redshift.

tain to the same cluster, Abell S1063, but are kept separate here as we're interested in looking at the information in individual masks. The two masks are combined and studied as a single dataset in the next chapter. Section B.8 shows the velocity dispersions of each cluster in Figures B.23 - B.25. The blue histograms use all recovered redshifts, while the orange histograms use only the recovered redshifts that exceed the correlation threshold of 0.35 deemed as "successful." A Bi-Weight method is used to identify the center and the dispersion in a manner robust to outliers (Danese et al., 1980; Beers et al., 1990).

Finally, substructure and dynamic equilibrium are important factors governing these recently formed gravitational systems. We leverage the velocity and spatial information to quantitatively assess the substructure in each of the clusters in Section B.9 using a statistic published by Dressler and Shectman (Dressler & Shectman, 1988). The statistic compares the local line of sight velocity dispersions around each galaxy with respect to its nearest 10 neighbors (on the spatially projected sky). Deviations in dispersions are then computed by comparing neighbors. Large deviations result in larger values of the statistic, and are associated with substructure or local deviations from the global velocity field. The value for the cluster is the average of these constituent values. The plots in Figures B.26 - B.28 in the appendix show the individual galaxies with the size of their circle related to the size of their statistic. Larger circles indicate larger deviations in velocity from its neighbors. Multiple large circles in an area indicate a region that is either dynamically disrupted or another gravitationally bound structure being accreted by the larger cluster potential.

Figures B.29 - B.31 show the averaged statistic of each cluster (red vertical line) compared with statistics generated from 1000 randomized samples of that cluster (blue histogram). The randomization is done by shuffling all the redshifts in the sample, and assigning them to random sky locations from the sample. This procedure destroys any real redshift structure. The histograms can be interpreted roughly as random draws from a probability distribution. They therefore givesan indication of the likelihood of the measured value happening only by chance in the given cluster with the given measurements in the absence of true substructure. Note that some clusters do indeed have significant substructure, with values that deviate beyond any of the 1000 samples.

4.4.7 Summary

With these preliminary results achieved, we felt confident in our targeting, acquisition, and resulting data reduction. We have shown good agreement between the recovered redshifts and SDSS values, and have seen reasonable distributions of redshift success versus redshift, magnitude, correlation value, and signal-to-noise. With those aspects understood we were able to proceed in our first analysis, which was studying the massive Galaxy Cluster Abell S1063 (Masks B04a and B04b). The following chapter will discuss this in detail.

Chapter 5

Dynamical Mass Measurements of Abell S1063 and Evidence of Substructure

5.1 Introduction

Galaxy clusters are the largest gravitationally bound objects in the Universe that, due to hierarchical structure formation, reside in some of the largest and therefore rarest dark matter halos. As one of the brightest X-ray objects in the southern sky, Abell S1063, also referred to as RXC J2248.7-4431, is big even among these most massive objects. Having been cataloged by Abell and colleagues in the 1980s and detected by the ROSAT All-Sky Survey (RASS), it has been studied in multiple wavelength bands including the X-ray, UV, optical, infrared, and microwave (Abell et al., 1989; Cruddace et al., 2002). While mass estimates based on X-ray temperature, SZ, weak lensing, strong lensing, richness, and luminosity proxies agree within uncertainties, the dynamical estimates have been found to be discrepantly high.

Gómez and colleagues in their 2012 paper argue that this may indicate that the system is not in hydrostatic equilibrium and that bulk velocities of subregions are causing the additional spread in velocity that gives rise to the erroneously large mass estimate (Gómez et al., 2012). They cite a bimodal spatial distribution of galaxies and an X-ray profile that is ellipsoidal with a similar major axis to the bimodality in the core. In comparing to simulations they claim that a recent merger of two halos with mass ratio 1:4 is the most likely scenario to generate their observed velocity distribution. This velocity distribution and the dispersion estimate, however, were inferred from a relatively smaller dataset of 51 spectroscopically confirmed members that resided only in the inner regions of the cluster. They then use additional simulated studies to extrapolate the measurement to larger radii by correcting for additional baryon bias in the cluster core, among other factors.

Gruen et al. in 2013 gave additional credence to this hypothesis by confirming the bimodal spatial distribution with much deeper, independent photometry (Gruen et al., 2013). They also modeled the system using weak lensing and found multiple mass overdensities that remained after subtracting their best one-halo fit, and found better agreement when allowing a joint fit with two NFW halos. They identified the primary halo and a secondary halo approximately 25% of the mass of the main halo. They also used their color information to identify differences in the metallicity and red galaxy percentages in the sub-regions of the cluster. In the end, the identified haloes were within the R_{200c} radii of one another. As a result, they used the one halo model for their final weak lensing results but stated that additional spectroscopy could show definitive evidence of this substructure and the dynamical state of the system.

Here we report evidence of substructure in the system using 261 galaxy redshifts from the literature and new redshifts taken with the Michigan-Magellan Fiber System (M2FS) multi-fiber spectrograph on the Magellan-Clay telescope. This substructure leads to an over-estimation in the velocity dispersion inferred mass compared to other observable proxies, including dynamical techniques more robust to deviations from hydrostatic equilibrium (Miller et al., 2016). We report a value of $1599 \pm 37\,\mathrm{km\,s^{-1}}$ for the velocity dispersion with a corresponding M_{200c} estimate of $M_{\sigma_v,200c} = 31.9 \pm 5.54 \times 10^{14}\ M_\odot$, in agreement with past velocity dispersion studies. This larger dataset allows us to move beyond the velocity dispersion to measure the mass profile using the radius-velocity escape profile. We use simulations to show that the escape masses can be calculated to be mostly immune to one-to-one mergers and significant sub-structure. We assume a flat ΛCDM Universe with $\Omega_m = 0.27$ and $H_0 = 72\,\mathrm{km\,s^{-1}}$. Under that cosmology we find $M_{\mathrm{caustic},200c} = 19.87^{+7.54}_{-5.17} \times 10^{14}\ M_\odot$. Our velocity dispersion mass agrees with the escape-velocity inferred mass within uncertainties.

5.2 Abell S1063 in the Literature

5.2.1 Overview

Abell S1063 has been the subject of numerous past studies. First identified by Abell et al. in 1989 at the lower estimated redshift of 0.252, the cluster remained mainly unstudied even after its identification in the ROSAT All-Sky Survey in the late 1990s (Abell et al., 1989; Cruddace et al., 2002). The cluster was analyzed in a 2008 X-ray paper (Maughan et al., 2008), where they unfortunately used an erroneous redshift of 0.252 in their X-ray analysis and found a smaller mass than what would be determined at the proper redshift. Comis et al. (2011) and Gómez et al. (2012) independently corrected the X-ray analysis for the proper redshift near 0.347 in 2011 and 2012 respectively. In the Gómez et al. paper they presented new spectroscopic observations in addition to the analysis of the Chandra X-ray data. Using spectroscopy to determine a velocity dispersion, they published mass estimates using both X-ray temperature and velocity dispersion, finding $M_{X,200c} = 26.0^{+3.3}_{-3.3} \times 10^{14}$ $M_\odot$ and $M_{\sigma,200c} = 42.0^{+17.0}_{-9.0} \times 10^{14}$ $M_\odot$ respectively. In that paper they identify evidence of substructure and posit that the cluster is a merging system, but with only low significance. They assert that the higher mass estimate from their velocity dispersion compared to X-ray can also be explained by AS1063 being a merging system.

Gruen et al. in 2014 used deep optical data from the 2.2 meter MPG/ESO telescope in La Silla to perform a weak lensing analysis on the cluster (Gruen et al., 2013). Like the X-ray estimates, they found a lower mass, $M_{200m} = 33.1^{+9.6}_{-6.8} \times 10^{14}$ $M_\odot$, than that estimated by Gómez et al. using dynamics with only a little more than a 1σ significance. Using deep photometry they were able to comment on the substructure, identifying two overdensities outside of the main structure of the cluster, one N-NE and one SW. These are roughly in line with the substructure identified by Gómez et al. (2012). Gruen et al. (2013) emphasize that their photometric redshifts are not accurate enough to explicitly constrain them to the gravitationally bound system of AS1063.

Over this same period of time, Hubble was acquiring data on the cluster as part of the Cluster Lensing And Supernova Survey with Hubble (CLASH). Abell S1063 was selected among 20 massive X-ray clusters (and five strongly lensed clusters) to be part of the weak (and strong) lensing survey (Postman et al., 2012). As part of that was extensive photometry performed in 15 bands of HST down to limiting magnitudes of $\sim$25, with $r_{AB} \sim 26$. From this collection came a wealth of cluster studies of both the aggregate sample and the individual cluster from the CLASH team. Due to the prominence of the sample, AS1063 has received larger attention in the past decade, receiving auxiliary and ancillary observations from the microwave, to the IR through UV, into the X-rays. Below we will briefly summarize the CLASH team's studies, followed by the additional observations and analyses.

5.2.2 CLASH Studies

The two relevant goals of CLASH for this analysis is their desire to map the distribution of dark matter in galaxy clusters and study the structure and evolution of galaxies within the clusters. They did so with a detailed weak lensing analysis which was followed up with strong lensing modeling for those systems that presented multiple images and arcs. To that end they performed increasingly detailed studies, beginning in 2014 and proceeding through 2018 and the present (Umetsu et al., 2014; Merten et al., 2015; Umetsu et al., 2016, 2018). The later analyses utilized auxiliary spectra of background galaxies and arcs from multiple campaigns: Balestra et al. (2013); Monna et al. (2014); Karman et al. (2015, 2017); Bonamigo et al. (2018); Bergamini et al. (2019) and Caminha et al. (2016, 2019) to name just those that involved AS1063. These follow-up papers studied topics from mass-concentration to galaxy kinematics and galaxy evolution, using strong lensing models that leveraged the spectroscopic data. Finally, Rodríguez-Muñoz et al. (2019), acquired Spitzer and IRAC data to study the star formation rates using the wider range of available wavelengths. This enabled a number of the galaxy evolution studies.

In the context of AS1063, Balestra et al. (2013) and Gómez et al. (2012) were the first to report spectroscopic confirmation of strong lensing arcs in the system. These were expanded upon with Monna et al., which led to a number of lens modeling teams participating in complementary analyses, e.g. Johnson et al. (Monna et al., 2014; Johnson et al., 2014). Using extensive VLT time with MUSE (Karman et al., 2015, 2017) and VIMOS (Caminha et al., 2016; Bonamigo et al., 2018; Caminha et al., 2019), upwards of 50 multiple images have been identified in the cluster, as of the most recent analyses (Bergamini et al., 2019). The modeling is consistent with a single massive halo, with no substantial improvements in fit for two or three halo models in the cluster plane, when accounting for the additional degrees of freedom those models provide. Johnson et al. did find marginal evidence for substructures in the N-NE and SW directions in their 2014, consistent with the Gómez study, but emphasized that the single halo model fit equally well (Johnson et al., 2014). Because of the equivalent fits they selected the single halo model for their final results.

Using both weak lensing shear and convergence maps and strong lensing constraints, Umetsu et al. found a mass of $M_{200m} = 30.2^{+12.0}_{-12.0} \times 10^{14}$ $M_\odot$ (Umetsu et al., 2014). They later corrected this with a better study of their systematics and improved strong lens modeling to $M_{200m} = 24.5^{+9.9}_{-9.9} \times 10^{14}$ $M_\odot$ (Umetsu et al., 2016). Both studies used a similar concentration, with the 2016 paper using $c_{200m} = 3.6 \pm 1.4$. Both the masses and the concentrations were consistent with the previous weak lensing, the strong lensing, the SZ, and the X-ray estimates, which will be detailed below. The estimates listed above and those to follow are summarized in Table 5.2.

5.2.3 Weak Lensing Observations

As mentioned above, Gruen et al. performed a weak lensing study using data taken from the 2.2m MPG/ESO telescope at La Silla, finding a mass of $M_{200m} = 33.1^{+9.6}_{-6.8} \times 10^{14}$ $M_\odot$, and identifying what could be substructure, though they claim further spectroscopic studies would be required to confirm the claim of Gómez et al. (Gruen et al., 2013). Gruen et al. does note, however, that their Wwak lensing mass centroid and that identified in more extensive X-ray analyses show no offset from the BCG beyond typical intrinsic scatter.

In 2015 the Dark Energy Survey team used Abell S1063 as one of four massive SPT selected clusters to target and study with their Science Verification optical imaging (Melchior et al., 2015). Their imaging was much wider, allowing them to identify galaxies in the images out to several degrees (10's of Mpc). They note filamentary structure that passes through the cluster at roughly the angle identified by Gómez et al., giving further credence to the hypothesis of additional structure surrounding the halo, but not going so far as to corroborate a recent merger. They give a mass of $M_{200c} = 17.5^{+4.5}_{-3.7} \times 10^{14}$ $M_\odot$, which is consistent with the CLASH and Gruen weak lensing analyses.

5.2.4 CMB-SZ Observations

Abell S1063 is within the original SPT footprint, and was thus observed with both Planck and SPT. Both detected the cluster with signal-to-noise above 10. Using the Planck calibrated SZ-mass scaling relation, they gave a mass estimate of $M_{500c} = 11.5 \pm_{\rm stat} 2.6 \pm_{\rm syst} 0.5 \times 10^{14}$ $M_\odot$ in 2011 (Planck Collaboration et al., 2011). In the same year Williamson et al., used an SPT SZ-mass scaling relation and found a larger mass but with much larger uncertainties, $M_{200m} = 28.2 \pm_{\rm stat} 3.6 \pm_{\rm syst} 9.3 \times 10^{14}$ $M_\odot$ (Williamson et al., 2011). In 2014, Ruel et al. updated that analysis with the new scaling relations of Reichardt et al. and found $M_{500c} = 18.0^{+2.2}_{-2.2} \times 10^{14}$ $M_\odot$ (Reichardt et al., 2013; Ruel et al., 2014), which also found a higher mass than that found by Planck at several standard deviation significance. This is likely explained by underestimated uncertainties, but we leave any such investigations to future works.

5.2.5 X-ray Observations

Having been identified as a highly luminous X-ray source by the ROSAT satellite, it is no surprise that Abell S1063 has been studied extensively in the X-ray (Cruddace et al., 2002). Maughan et al. first presented Chandra data in 2008, but underestimated the mass of the cluster due to a mis-identification of the redshift (Maughan et al., 2008). Comis et al. and Gómez et al. independently reanalyzed that data and found consistent results of $M_{2500c} = 5.3 \pm 2.6 \times 10^{14}$ $M_\odot$ and $M_{200c} = 26.0^{+3.3}_{-3.3} \times 10^{14}$ $M_\odot$ respectively (Comis et al., 2011; Gómez et al., 2012). While difficult to numerically compare, the masses can be seen in Figure 5.10.

Because of its prominent SZ signal in the CMB, the Planck team selected Abell S1063 as a cluster to follow up in the X-ray, receiving observations with the XMM-Newton telescope (Planck Collaboration et al., 2011). This independent dataset agreed remarkably well with the temperature assessed by both ROSAT and Chandra, roughly 12.5keV, with a mass estimate of $M_{X,500c} = 12.25 \pm 0.21 \times 10^{14}$ $M_\odot$ (Planck Collaboration et al., 2011).

Finally, the SPT collaboration chose to target Abell S1063 with new Chandra observations as part of a uniform set of cluster data that they selected to help constrain the SZ - X-ray scaling relation (Ruel et al., 2014). Their estimate of $T_x = 12.37^{+1.01}_{-0.77}$ keV, provides yet another verification of the cluster temperature in agreement with past values. From this, they estimate the mass of the cluster to be $M_{X,500c} = 16.35^{+0.84}_{-0.7} \times 10^{14}$ $M_\odot$ (Ruel et al., 2014). This, once more, disagrees with the Planck value at high significance, like the other X-ray measurements.

5.2.6 Past Spectroscopic Observations

Beyond the strong lensing spectroscopy search, there have been four previous spectroscopic observations of cluster members in Abell S1063, with he first being Gómez et al. (2012). Ruel et al. performed additional spectroscopy using IMACS+GISMO on the Magellan-Baade 6.5m telescope. They did not use the Gómez data, choosing instead to perform a dynamic estimate using their uniform sample (Ruel et al., 2014). They found 15 cluster members and used those 15 to determine a velocity dispersion of $\sigma_{\rm BI} = 1301 \pm 320\,{\rm km\,s^{-1}}$, which is smaller than the measurements presented here and by Gómez, but consistent given their large uncertainties (Ruel et al., 2014).

As part of ongoing CLASH studies, they received time for a large spectroscopic campaign on the VLT telescope. Through this campaign AS1063 was observed using two pointings of the MUSE IFU as well as several VIMOS masks. The MUSE spectra, primarily of the core, were published in the two papers by Karman et al., where they were interested in the spectra relevant to strong lensing and did not investigate cluster dynamics (Karman et al., 2015, 2017). The VIMOS observations have yet to be published.

Of the spectra presented in the literature, we use the matching members in our sample as an additional measurement of our velocity uncertainties. All unmatched galaxies are added to our final sample. Before including the redshifts, we first measure and subtract any offset to avoid bias.

5.3 Spectroscopic Observations

Two observations of AS1063 were attained with the M2FS instrument on the Magellan-Clay 6.5m telescope on November 27 and 29th of 2018. 391 objects were targeted, of which 253 had redshifts obtained with the highest quality flag. These were identified using an automated redshift finder and verified by-eye.

Two fields were observed to both increase the number of targeted objects and to perform validations of our recovered redshifts. By re-observing a subset of the targets, we can assess the reproducibility of the observations. This accounts for variations in inferred redshift from factors such as differences in each fiber's throughput, focal plane location, observing conditions, and location on the CCD. Of those galaxies that passed quality cuts, 68 overlapping redshifts were recovered in both fields. Thus 163 unique galaxy redshifts were identified.

Figure 5.3 shows the comparison between recovered spectra. The differences show a roughly Gaussian distribution with a long tail to lower (more negative) differences. A fit yields a bias of -49 $\,{\rm km\,s^{-1}}$and a scatter of 111 $\,{\rm km\,s^{-1}}$. This is expected for the difference in two distributions each with standard deviations of $\sim 80\,{\rm km\,s^{-1}}$, for which you would expect a factor of $\sqrt{2}$ increase.

Comparing with spectra obtained in the previous dynamical estimate of Gómez et al. and in more recent South Pole Telescope and strong lensing observations, we find a consistent result (Gómez et al., 2012; Ruel et al., 2014; Karman et al., 2015, 2017). Figure 5.4 shows the differences in $\,{\rm km\,s^{-1}}$, along with Gaussian fit parameters of the

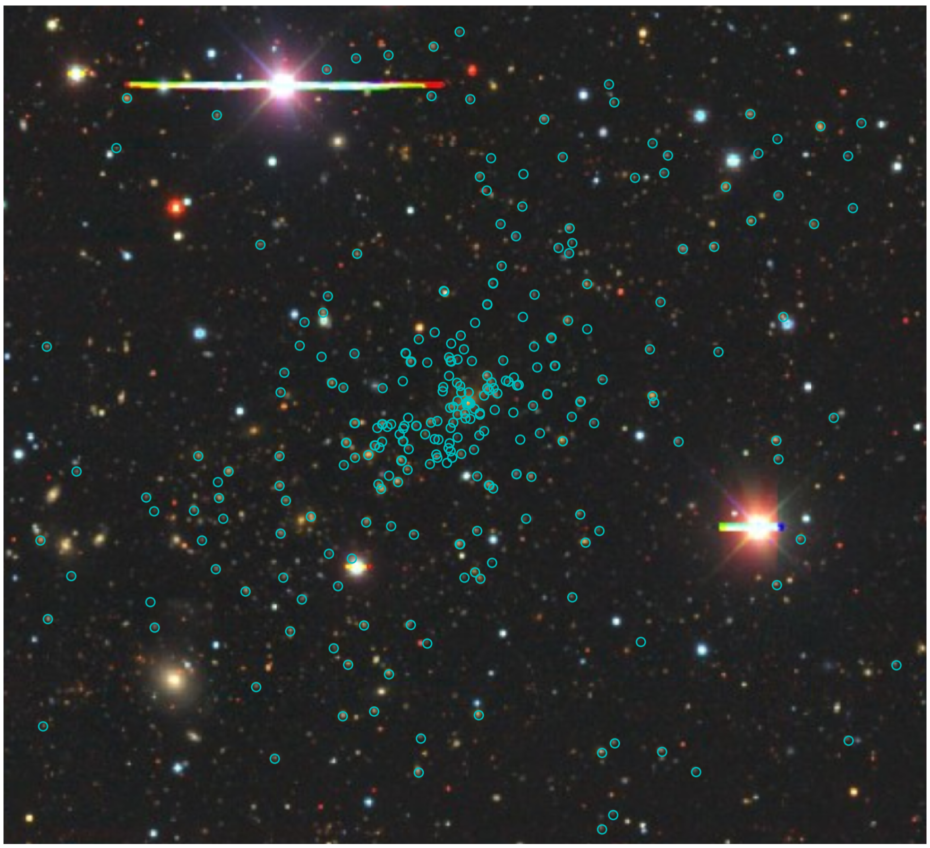

Figure 5.1 DECALs mosaic image of the Abell S1063 cluster with spectroscopic observations overlaid as cyan circles. This includes spectra from this work and those from the literature (Gómez et al., 2012; Ruel et al., 2014; Melchior et al., 2015; Karman et al., 2017).

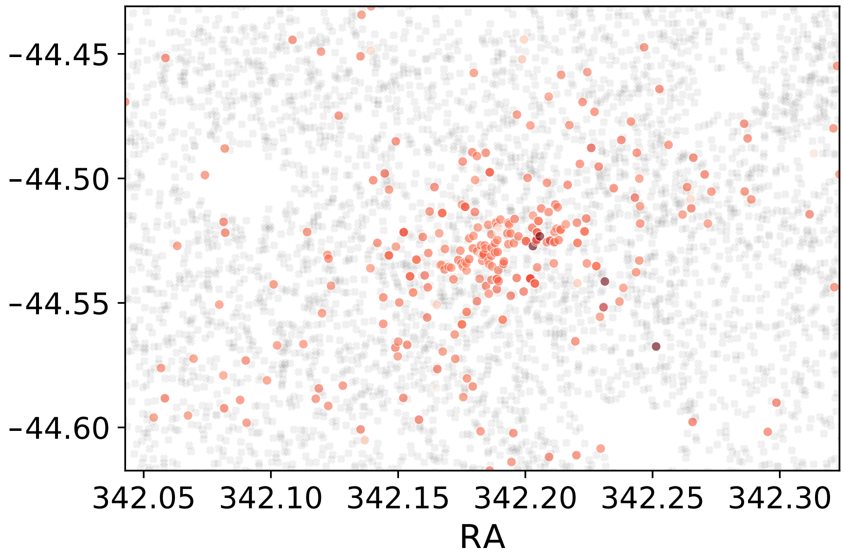

Figure 5.2 The distribution of objects in the vicinity of Abell S1063. The red dots are those spectroscopically confirmed to belong to the cluster while the gray are other objects detected with DES photometry.

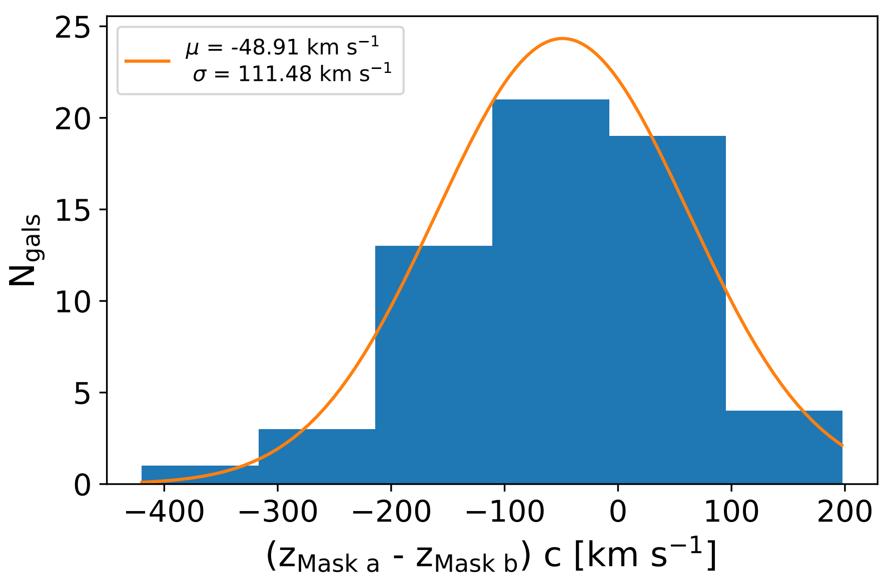

Figure 5.3 Histogram comparing the redshifts that were observed in both M2FS masks for calibration of the redshift uncertainties. We find values consistent with individual redshift uncertainties of $\sim 80\,\mathrm{km\,s^{-1}}$.

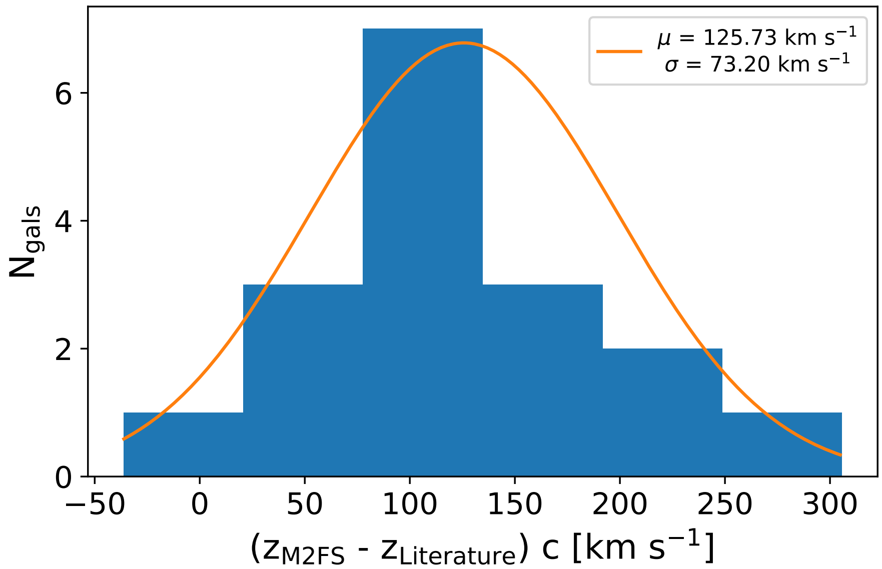

Figure 5.4 Comparison of redshifts recovered in this work compared to those in the literature. We find a significant bias of 126 km s^{-1}, far greater than the bias found with SDSS. The spread in values meets expectations with a standard deviation of 73 km s^{-1}.

distribution. We see a scatter consistent with the measurements vs. SDSS, finding a value of 73 km s^{-1}. The bias increases to 126 km s^{-1}, which we cannot account for. This holds when comparing with individual reference sources, and when comparing to either individual M2FS field.

With these results, we chose to take a conservative value of 150 km s^{-1}as the uncertainty in the individual redshifts. This was also the cut applied to redshifts from the literature for them to be used in the analysis. Given the number of galaxies in the sample, the individual uncertainties showed little impact on the result when different values were tested.

5.4 Dynamical Analyses

5.4.1 Velocity Dispersion Analysis

We perform two dynamical methods to estimate the mass of this system using the redshift information. The first relies on the Velocity Dispersion - Mass relation from Evrard et al. 2008 (Evrard et al., 2008). In that paper they study a number of N-body simulations to fit a power-law relation between the projected line-of-sight velocity of dark matter particles and the corresponding mass of the halo with the form:

$$\sigma_{\mathrm{DM}}(M, z) = \sigma_{\mathrm{DM},15} \left[\frac{h(z) M_{200c}}{10^{15} M_{\odot}} \right]^{\alpha}, \tag{5.1}$$

where $\sigma_{\mathrm{DM},15}$ is the normalization scaling factor for the pivot mass of 10^{15} $\mathrm{M}_{\odot}\mathrm{h}^{-1}$, h(z) is the dimensionless Hubble parameter at redshift z (h(z) = H(z)/(100km/s/Mpc)), and α is the power-law dependence between mass and velocity dispersion. M_{200c} is the mass of the halo in units of $10^{15}\mathrm{M}_{\odot}\mathrm{h}^{-1}$ and σ_{DM}(M, z) is the one dimensional (line-of-sight) velocity dispersion of the dark matter particles associated with the halo. They found best fit model parameters to be $\sigma_{\mathrm{DM},15} = 1082.9 \pm 4.0$ $\mathrm{km\,s^{-1}}$and $\alpha = 0.3361 \pm 0.0026$. In that paper they investigate the bias of using galaxies as tracers of the dark matter distribution and conclude that it is roughly unbiased. For that reason we assign a bias of unity (no bias, $\sigma_{\mathrm{DM}} = 1.0\ \sigma_{\mathrm{gal}}$) (Evrard et al., 2008).

To determine the velocities we first perform a cut of 6000 $\mathrm{km\,s^{-1}}$around the cluster redshift, then use an iterative sigma-clipping method to remove any outliers from the main distribution that deviated by more than four standard deviations. Of the 280 galaxies only 18 failed these cuts.

The redshifts of the cleaned dataset were then used to jointly fit the Bi-weight center and Bi-weight dispersion of the redshifts. Here we follow Beers et al. (1990), where the Bi-weight center and spread are:

$$C_{\mathrm{BI}} = M + \frac{\Sigma_{|u_i|<1} (x_i - M) (1 - u_i^2)^2}{\Sigma_{|u_i|<1} (1 - u_i^2)^2} \tag{5.2}$$

and

$$S_{\mathrm{BI}} = n^{1/2} \frac{\left[\Sigma_{|u_i|<1} (x_i - M)^2 (1 - u_i^2)^4 \right]^{1/2}}{\left| \Sigma_{|u_i|<1} (1 - u_i^2)(1 - 5u_i^2) \right|} \tag{5.3}$$

respectively (Danese et al., 1980; Beers et al., 1990). The u_i are given by

$$u_i = \frac{(x_i - M)}{cMAD}, \tag{5.4}$$

where MAD = median($|x_i - M|$), n is the sample size, and c is a "tuning constant" which we assign be 6 and 9 for the two relations respectively, following Beers et al. (1990). In the first iteration, M is the median of the sample. In subsequent iterations M is replaced with C_{BI} and MAD is replaced with S_{BI}, which continues until the estimates converge.

The value of S_{BI} is our robust estimate of the redshift dispersion given the data.

The velocity dispersion is determined by removing the cosmological redshift of the cluster (C_{BI}), and dividing by ($1+C_{BI}$), which is removing the cosmological redshifting *of the Doppler redshift* that occurs during the propagation to Earth. The final velocities are thus:

$$v_i = \left(\frac{z_{BI,cent} - z_i}{1 + z_{BI,cent}}\right) c\,\mathrm{km\,s^{-1}}, \tag{5.5}$$

and our velocity dispersion is

$$\sigma_v = \left(\frac{S_{BI}}{1 + z_{BI,cent}}\right) c\,\mathrm{km\,s^{-1}}. \tag{5.6}$$

Note that we define the velocities above such that higher redshift objects have negative velocities. The choice does not affect the dispersion. Figure 5.5 shows the velocities of our galaxy sample with respect to our Bi-weight redshift of $z_{BI,cent} = 0.3468$. Here we overlay a Gaussian with μ and σ equal to the Bi-weight center and Bi-weight spread. Our best-fit value for the velocity dispersion was $1599 \pm 37\,\mathrm{km\,s^{-1}}$.

The uncertainties in our estimate come from bootstrap simulations in which we draw from a Gaussian random distribution with standard deviation equal to our redshift uncertainties ($150\,\mathrm{km\,s^{-1}}$) and add these draws to the observed redshifts. We fit the resulting set of mock redshifts with added noise as we did for the true dataset. We repeat this process hundreds of thousands of times and calculate the standard deviation of the resulting distribution of recovered values.

Using the velocity dispersion given above, and using the assumption that our galaxies are unbiased tracers of the dark matter distribution, we find our mass estimate to be $\mathrm{M}_{200c} = 31.9 \pm 2.42 \times 10^{14}\ \mathrm{M}_{\odot}$, where we have used Equation 5.1 (Evrard et al., 2008). The uncertainties are again determined by a bootstrap method in which we draw new fit parameters from distributions according to the uncertainties quoted in Evrard et al. (2008). We simultaneously draw random scatter in our individual velocities and compute new velocity dispersions for each iteration. The distribution of bootstrap recovered masses can be seen in Figure 5.7.

We know our uncertainties to be underestimated by systematic effects such as a complex selection function that we have not accounted for, as well as projection effects, galaxy velocity bias, etc. For this reason we include an additional 10% uncertainty in our uncertainty budget, giving our final result of $\mathrm{M}_{\sigma_v,200c} = 31.9 \pm 5.54 \times 10^{14}\ \mathrm{M}_{\odot}$.

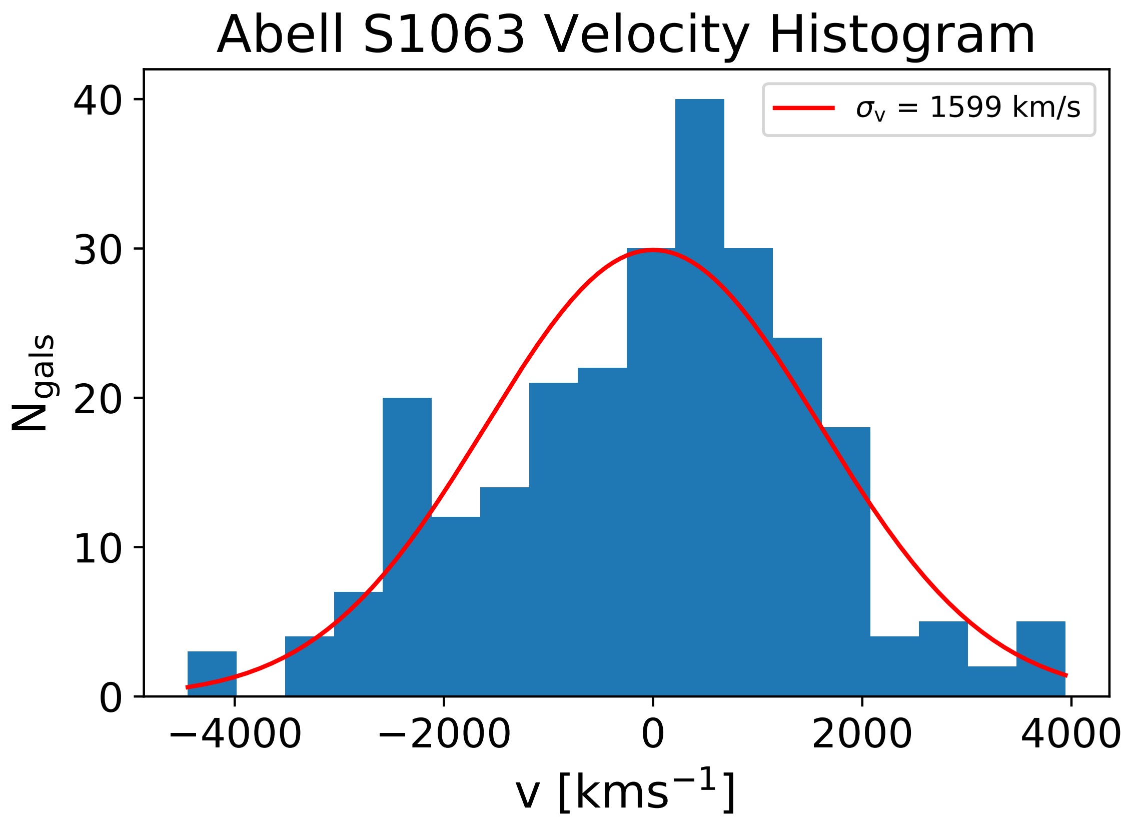

Figure 5.5 Histogram of the recovered velocities derived from the redshifts with respect to the bi-weight redshift center of the cluster. The curve uses the recovered Bi-weight spread parameter used as our velocity dispersion measurement as the sigma parameter of a Gaussian with a mean of zero. While the fit is accurate, there is clear bi-modality that may be due to substructures that a single Gaussian model cannot reproduce.

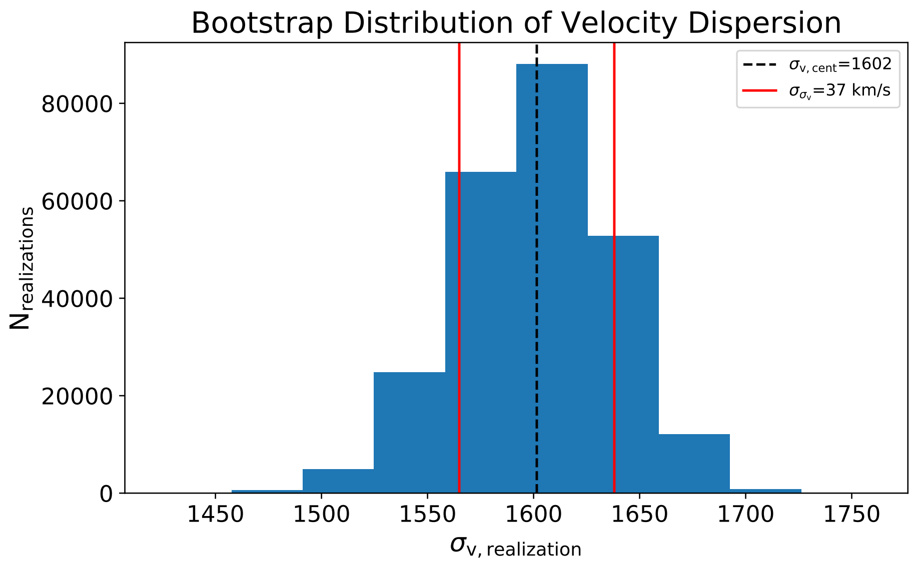

Figure 5.6 Simulated bootstrap velocity dispersions generated by adding Gaussian random noise to the redshifts with variance of $(150\,\mathrm{km\,s^{-1}})^2$ and performing the velocity dispersion bi-weight analysis on the resulting mock redshift catalog.

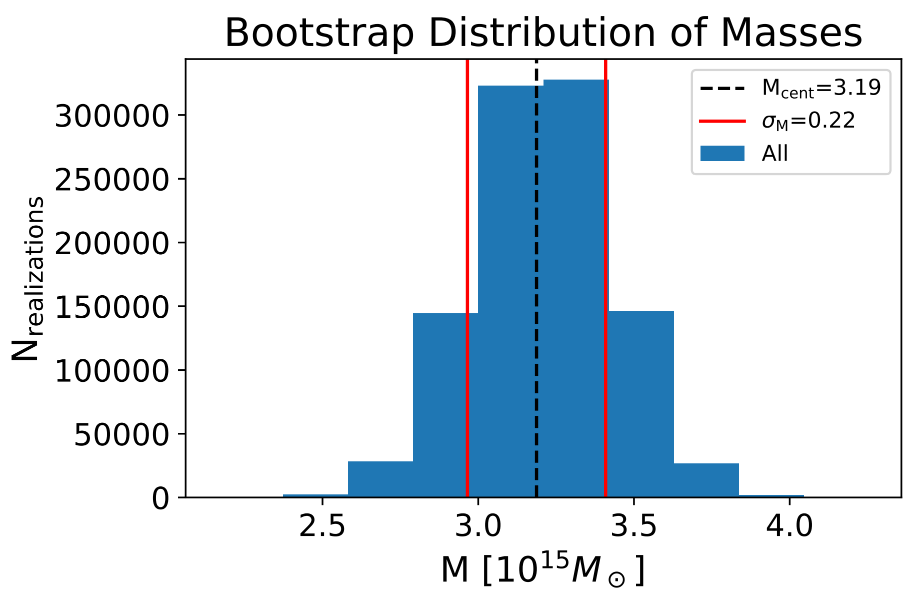

Figure 5.7 Simulated bootstrap cluster Masses generated by adding Gaussian random noise to the redshifts with variance of $(150\,\mathrm{km\,s^{-1}})^2$ and performing the velocity dispersion bi-weight analysis on the resulting mock redshift catalog while simultaneously drawing from the quoted distribution for the scaling relation fit parameters from Evrard et al. (2008).

5.4.2 Escape Velocity Edge (Caustic) Analysis

In a Universe with accelerating expansion, the interplay between dark matter and dark energy lead to regions in space at which the gravitational forces will negate one another. As the largest gravitational systems in the Universe, it is no surprise that galaxy clusters exist at these boundaries. A galaxy cluster is surrounded by an ellipsoid surface of zero potential, outside of which the Hubble flow accelerates matter away and within which the dark matter accretes the matter into the halo. Most recently, Miller et al. drew this connection with the so-called caustic technique in galaxy cluster mass estimation (Miller et al., 2016; Diaferio & Geller, 1997). In the caustic technique, the velocity-radial phase-space is used to constrain the gravitational potential (and thus the mass) of a system. This is directly analogous to velocity dispersion measurements, except taken in many discrete radial bins. The additional information comes at the cost of reduced number counts in each bin, unless massive systems, complete spectroscopy, or cluster stacking is used.

For Abell S1063 we are able to perform a radial escape velocity measurement using the individual measurements in our sample. The technique follows a similar approach to Diaferio and Gellar in 1997, where radial bins are taken, and for each 0.25 arcminute bin a shifting-gapper technique is used to identify outliers and determine the potential boundary (Fadda et al., 1996; Adami et al., 1998). For this cluster, no outliers were identified. The edge identification is calibrated on simulations and maps to roughly the 90th percentile of velocities in the bin. The fit begins at $0.2\mathrm{M}_{200}$ and takes the minimum of the two edges determined in the positive and negative velocity directions. Unlike Diaferio and Gellar, we use the technique of Miller et al. and require that each successive radial bin have a smaller profile than the one before it such that the profile falls monotonically as theory would suggest (Diaferio & Geller, 1997; Miller et al., 2016). The uncertainties we report are the larger of either half the distance between the two maxima or $100\,\mathrm{km\,s^{-1}}$. The technique is able to jointly constrain the two parameters of a density model through its relation to the gravitational potential (ie density-potential pairs). For an NFW profile (Navarro et al., 1996):

$$\rho(r) = \frac{\rho_0}{\frac{r}{R_s}\left(1 + \frac{r}{R_s}\right)^2} \tag{5.7}$$

the two free parameters are generally parametrized as the mass and concentration,

$$c_{\Delta\mathrm{ref}} = \frac{R_{\Delta\mathrm{ref}}}{R_s}, \qquad M_{\Delta\mathrm{ref}} = \Delta\frac{4}{3}\pi R^3_{\Delta\mathrm{ref}}\rho_{\mathrm{ref}}. \tag{5.8}$$

Here $R_{\Delta\mathrm{ref}}$ is defined as the distance from the center of the spherical halo at which the density drops to Δ times the critical (c) or matter (m) density of the Universe. For example $r_{200\mathrm{c}}$ is the radius at which the density reaches 200 times the critical density at the redshift of the halo.

The NFW profile often has problems when trying to model the core and outskirts of a cluster simultaneously using the velocity edge technique (Miller et al., 2016). In that paper they found that the Einasto profile (Einasto, 1969) is a better functional form for fitting both the core and outskirts of the density profile :

$$\rho(r) = \rho_0 \mathrm{exp}\left[-\left(\frac{r}{r_0}\right)^{1/n}\right]. \tag{5.9}$$

For fitting AS1063, both profiles show promising goodness of fits and agree within error bars. Figure 5.9 shows a comparison of three mass profiles based on escape edge fits to the data. The first uses an Einasto profile (blue) with a fixed n of 4. We take an n of 4 from Dutton & Macciò (2014), where a median of their range of best fit is $\sim$1/0.25, as determine in simulations comparing the fits of Einasto and NFW profiles to dark matter halos. With the present dataset we were unable to constrain both the mass and n, which is why we choose to fix n to a value well motivated by the literature.

The second profile is an NFW with the concentration value fixed to a lower value of c = 5.7, closer to values preferred by weak lensing (green) compared to what the fit would do if unconstrained. Finally an NFW fit where we allow both mass and concentration to vary (red) is also given. To show the sensitivity of the escape velocity technique we give both the Einasto fit and the fixed concentration fit in Figure 5.8 on the top and bottom respectively. The data prefers a higher concentration, as in the Einasto case, whereas the weak lensing mass profile agrees with the escape edge only if we allow the concentration to be fixed low. Otherwise it favors values near c = 15.0 and has a form more similar to the Einasto profile. For the Einasto fit we find a mass of $\mathrm{M}_{\mathrm{caustic},200c} = 19.87^{+7.54}_{-5.17}\times10^{14}\ \mathrm{M}_{\odot}$, which is consistent with weak lensing but in slight tension with our velocity dispersion estimate – in conjunction with the Evrard 2008 σ_v-M scaling relation(Evrard et al., 2008; Gruen et al., 2013; Umetsu et al., 2016). The NFW fit in which we fix the concentration at 5.7 gives $\mathrm{M}_{200c} = 19.02^{+8.13}_{-5.35}\times10^{14}\ \mathrm{M}_{\odot}$ for our mass, which agrees with the weak lensing and Einasto profile. Finally, the NFW profile in which we jointly fit for mass and concentration yields $\mathrm{M}_{200c} = 19.25^{+7.81}_{-5.24}\times10^{14}\ \mathrm{M}_{\odot}$ and c$\sim$ 15, which is consistent with the above Einasto fit and weak lensing estimates as well. Once again, however, the caustic

Table 5.1. Comparison of Dynamical Mass Estimates in this Work.

Mass Definition	Mass ($10^{14}\,M_\odot$)	Method
M_{200c}	$31.9^{+5,5}_{-5.5}$	σ_v + Evrard08
M_{200c}	$19.87^{+7.54}_{-5.17}$	Einasto Caustic
M_{200c}	$19.02^{+8.13}_{-5.35}$	NFW (fixed c=5.7) Caustic
M_{200c}	$19.25^{+7.81}_{-5.24}$	NFW (fit c=15.0) Caustic

Note. — Velocity dispersion mass estimate from this work compared with our three escape velocity edge estimates.

disagrees with the velocity dispersion estimate. Table 5.1 shows a summary of our results.

The tendency of the jointly fit NFW to prefer higher concentrations could be explained by a high cooling luminosity, as discussed in Mantz et al. (2016) where they looked at 40 X-ray selected clusters and analyzed their fits to both Einasto and generalized NFW profiles. In that paper they found that the small subset of clusters that held especially high cooling luminosities were also found to have abnormally high concentrations with c's greater than 10. We, however, leave that to a future analysis.

5.5 Discussion

5.5.1 Comparison with the Literature

We select the Einasto fit as our final result for comparison with the literature, as it has been shown to best fit the profile over the entire radial range by Miller et al. (2016).

Figures 5.10 and 5.11 show the mass distributions from the literature detailed in Section 5.2 along with our mass estimates. For plotting the velocity dispersion mass we assumed the best-fit concentration of 3.6 ± 1.4 from the most recent weak lensing results, Umetsu et al. (2016). Where available, we used quoted concentrations for the

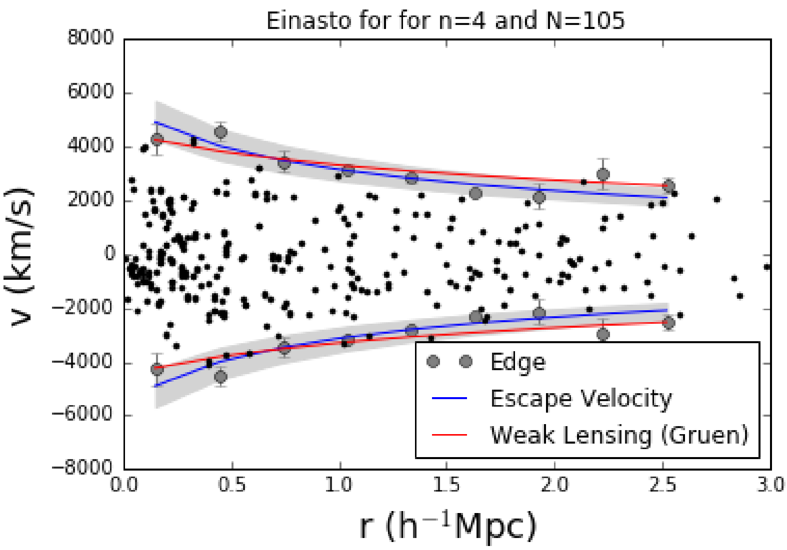

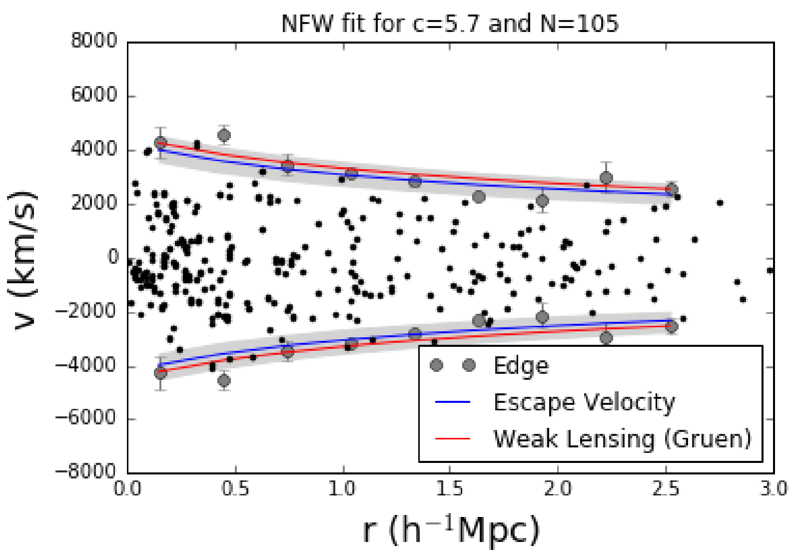

Figure 5.8 Escape velocity edge fit of AS1063 showing the edge overlaid with the data in a plot of velocity versus radial distance from the cluster center. The top plot shows a fit to the data using the Einasto model with n fixed to 4 (see Equation 5.9) in blue. The bottom plot shows an NFW fit to the data where the concentration is fixed to a lower concentration like those favored by weak lensing (c=5.7 in this case), also in blue. For comparison the NFW profile from the Gruen et al. weak lensing measurement is shown in red (Gruen et al., 2013). Note the good agreement in the fit with both the weak lensing measurement and the data at large radii, but see deviations at small radii where weak lensing prefers a smaller concentration than the Einasto profile. If we fix the concentration as we did in the lower plot, we can find excellent agreement in mass profile throughout, however if we allow c to float, it prefers larger values of c$\sim$ 15.

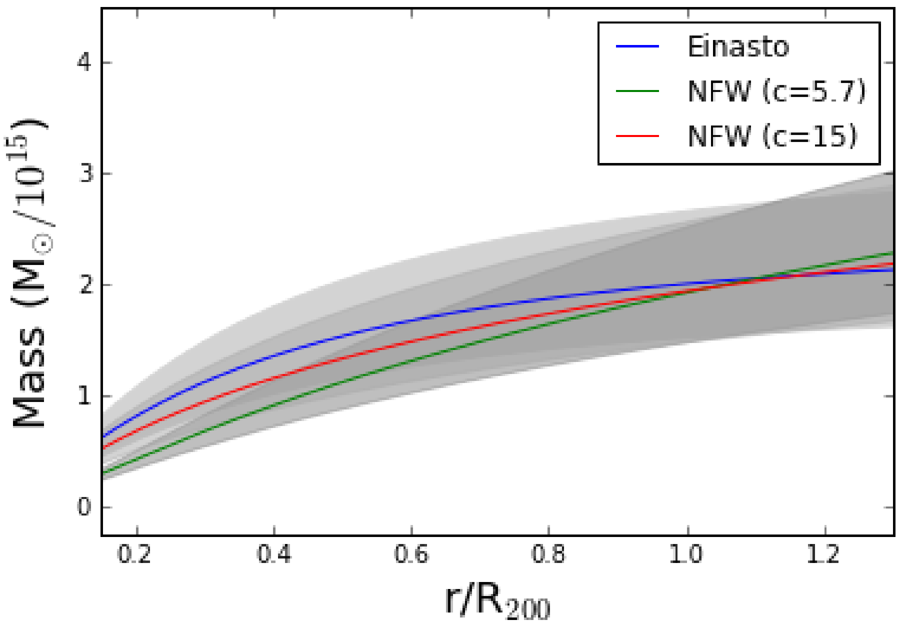

Figure 5.9 Mass profile comparison among three fits to the phase-space data. Here we show an Einasto profile fit with n fixed to 4 (see Equation 5.9) in blue, an NFW fit with c fixed to 5.7 in green, and an NFW fit where c is jointly fit and prefers a higher concentration of 15.0 in red.

literature curves. Where not available we used the c-M relation of Duffy et al. (Duffy et al., 2008).

Table 5.2 summarizes the values in the literature and gives our best fit values for comparison. To convert between mass definitions we assumed the same best-fit concentration of c= 3.6 from Umetsu et al. (2016) for the velocity dispersion. We find that our velocity dispersion estimate is systematically higher than the other probes.

These results lend credence to the idea of an expanded velocity distribution caused by substructure leading to a larger velocity dispersion and therefore an over estimation in mass. We have confirmed Gómez et al.'s assertion that the velocity dispersion mass estimate is high with respect to other mass proxies, confirmed the bi-modality of the velocity distribution, and have now included a new technique (the escape edge) that also favors a lower mass. Since the escape edge has been shown to be robust to dynamical instabilities and substructure in simulations, and it is using the same dataset with identical targeting, systematics, and incompleteness, we found the evidence compelling enough to delve into greater detail.

Table 5.2. Comparison with Mass Estimates in the Literature.

Mass Definition	Our $\sigma_{\rm v}$ Mass ($10^{14}\,M_\odot$)	Our Caustic Mass ($10^{14}\,M_\odot$)	Literature Mass ($10^{14}\,M_\odot$)	Method	Ref.
M_{200m}	$41.3^{+9.1}_{-6.9}$	$27.0^{+11.5}_{-7.9}$	$33.1^{+9.6}_{-6.8}$	WL	(1)
			$24.5^{+9.9}_{-9.9}$	WL+SL	(2)
			$28.2^{+10.0}_{-10.0}$	SZ (Plk)	(3)
M_{101c}	$40.5^{+8.8}_{-6.7}$	$26.4^{+11.0}_{-7.7}$	$19.0^{+6.0}_{-6.0}$	Lum	(3)
M_{200c}	$31.9^{+5.5}_{-5.5}$	$19.9^{+7.5}_{-5.2}$	$42.0^{+17.0}_{-9.0}$	Vel. Disp.	(4)
			$17.5^{+4.5}_{-3.7}$	WL	(5)
			$16.6^{+1.7}_{-1.7}$	WL+SL	(6)
M_{500c}	$21.6^{+3.8}_{-5.0}$	$12.4^{+4.2}_{-5.1}$	$12.2^{+0.2}_{-0.2}$	Xray	(7)
			$11.5^{+2.6}_{-2.6}$	SZ (Plk)	(7)
			$12.6^{+1.5}_{-1.5}$	SZ (SPT)	(8)
			$16.4^{+0.8}_{-0.7}$	Xray	(8)
M_{2500c}	$8.1^{+2.9}_{-3.3}$	—	$5.3^{+2.6}_{-2.6}$	Xray	(9)

Note. — Velocity dispersion mass estimates from this work were converted assuming a concentration taken from Umetsu et al. (2016).(1): Gruen et al. (2013), (2): Umetsu et al. (2016), (3): Williamson et al. (2011), (4): Gómez et al. (2012), (5): Melchior et al. (2015), (6): Merten et al. (2015), (7): Planck Collaboration et al. (2011), (8): Ruel et al. (2014), (9): Comis et al. (2011).

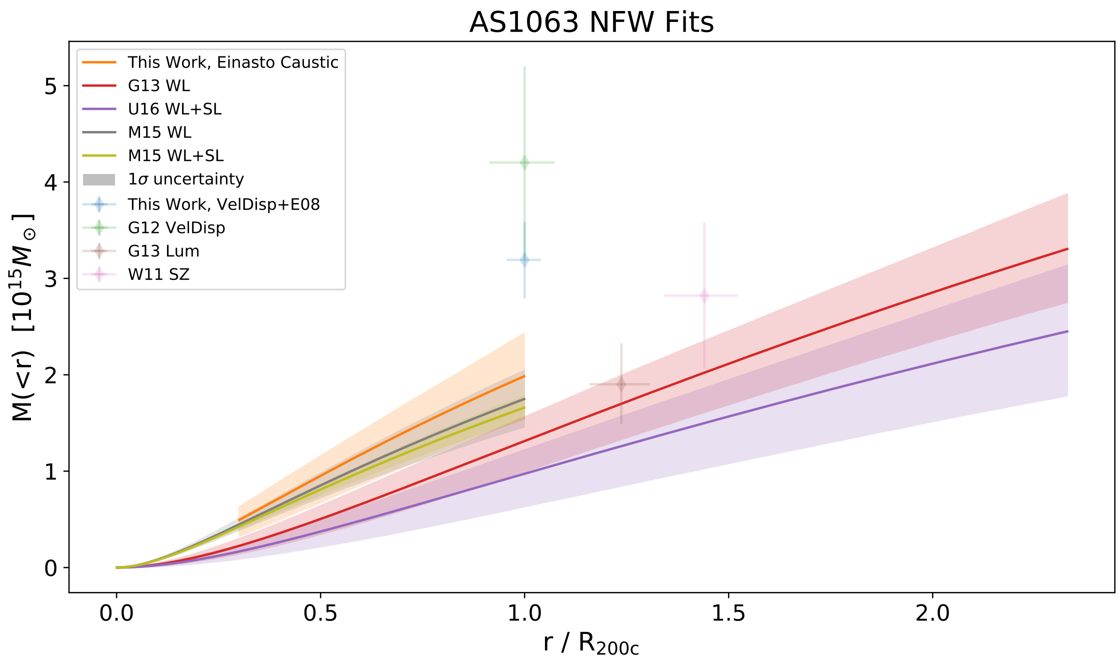

Figure 5.10 Plot showing all available mass estimates for Abell S1063, including the dynamical and escape velocity edge masses produced in this work. For plotting our velocity dispersion measurement we use the concentration reported in the weak lensing analysis of the cluster in Umetsu et al. (2016). Where published, we used the concentrations given with the mass estimates and used the Duffy c-M relation when concentrations were unavailable (Duffy et al., 2008). There is a clear tendency for the velocity dispersion methods to prefer higher values of the mass, in agreement with results found using much lower number counts by Gómez et al. (2012).

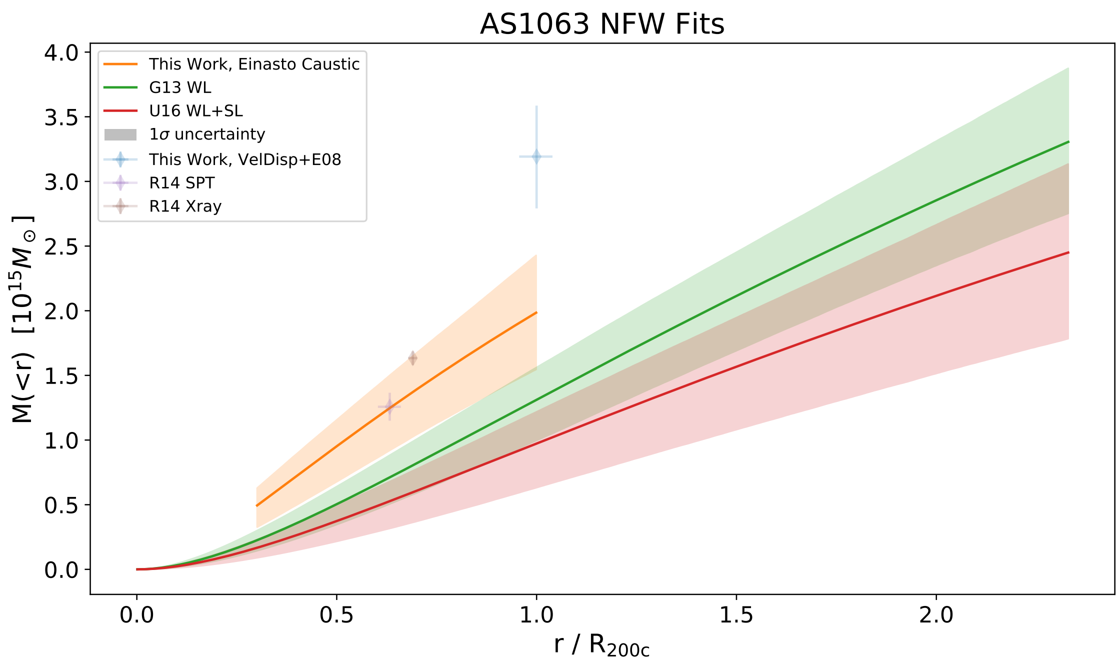

Figure 5.11 A plot similar to Figure 5.10, except where we have removed some mass estimates for visual clarity. We favor the most recent estimates in selecting those to compare.

5.5.2 Dressler-Shectman Statistic

To investigate the existence of substructure we leverage the three dimensional nature of our dataset to look for local overdensities. Visual inspections of the spectroscopic members do not reveal obvious substructure, but it can be observed in the wider photometric sample as reported by Gruen et al. (2013) and Melchior et al. (2015). Melchior et al. went on to claim that they visually identified a filamentary structure running roughly diagonally through the cluster from South-West to North-East.

To quantify the existence of distinct subhalos we use the three dimensional Dressler-Shectman statistic (Dressler & Shectman, 1988). For each galaxy, we calculate the velocity dispersion amongst itself and its nearest neighbors. Following the selection from Dressler and Shectman we select the ten nearest neighbors. We then calculate the individual DS statistic:

$$\delta^2 = \left(11/\sigma^2\right)\left[\left(\bar{v}_{\rm local} - \bar{v}\right)^2 + \left(\sigma_{\rm local} - \sigma\right)^2\right], \tag{5.10}$$

where $\sigma_{\rm local}$ is the velocity dispersion of the ith galaxy and its ten neighbors, $\bar{v}_{\rm local}$ is the mean velocity of the 11 members, $\bar{v}$ is the global average velocity, and σ is the global velocity dispersion. When there are local regions with velocity dispersions that differ significantly from the global value, this quantity will be large. The sum of all individual DS values gives the global level of disagreement between local regions and the global fit. In the original paper they define Δ_{DS} as the sum over the individual δ_i's. Here we modify that slightly to define Δ_{DS} as the mean of the δ_i's:

$$\Delta_{DS} \equiv \frac{1}{n}\sum_i^n \delta_i^2 = \left(\frac{11}{n\sigma^2}\right)\sum_i^n \left[(\bar{v}_{\text{local,i}} - \bar{v})^2 + (\sigma_{\text{local,i}} - \sigma)^2\right]. \tag{5.11}$$

This definition was selected because it is now independent of the number of galaxies. Since the significance of a given statistic is specific to a particular system, we will be determining significance based on Monte Carlo bootstrap techniques with the same number of observables. This renders the factor of n meaningless.

For the Abell S1063 sample, we found a Δ_{DS} value of 1.42. To determine the significance of this we perform a bootstrap technique as mentioned above. We randomly shuffle the velocities in our sample and assign them back to a randomly selected coordinate from the sample list. With this done, all true correlations between velocity and spatial structure should be lost. After each shuffling, we calculate Δ_{DS} and then repeat. The number of simulated clusters that achieved Δ_{DS} values greater than the true value signifies the likelihood of such a value occurring by random chance. For our simulations, we performed 16000 simulations and found three random shufflings that led to a value greater than the true value. This lets us approximate the probability of this occurring at $\sim$3/16000, or $p \lesssim 0.0002$. Assuming Gaussian statistics, which the distribution was, this would be a deviation of greater than 3.5σ.

Figure 5.12 visually represents the individual statistics by plotting them in their sky positions with the size of their marker indicative of the δ_i value for that galaxy. Note the larger values near the core and along the filamentary structure going from the lower left to the upper right. Figure 5.13 shows a zoomed in view of the cluster core. In our plots of the sky we take East to be toward the right and North to be upward.

From these figures and the low probability of this happening from a random distribution, we found strong indications of the existence of substructure within Abell S1063. However, interestingly there doesn't appear to be obvious signs of substructure visually on the sky beyond small overdensities found in the photometry. When investigating in the three dimensional space with redshifts, we don't identify any clear substructure that could be identified by eye or with out-of-the-box k-means clustering techniques.

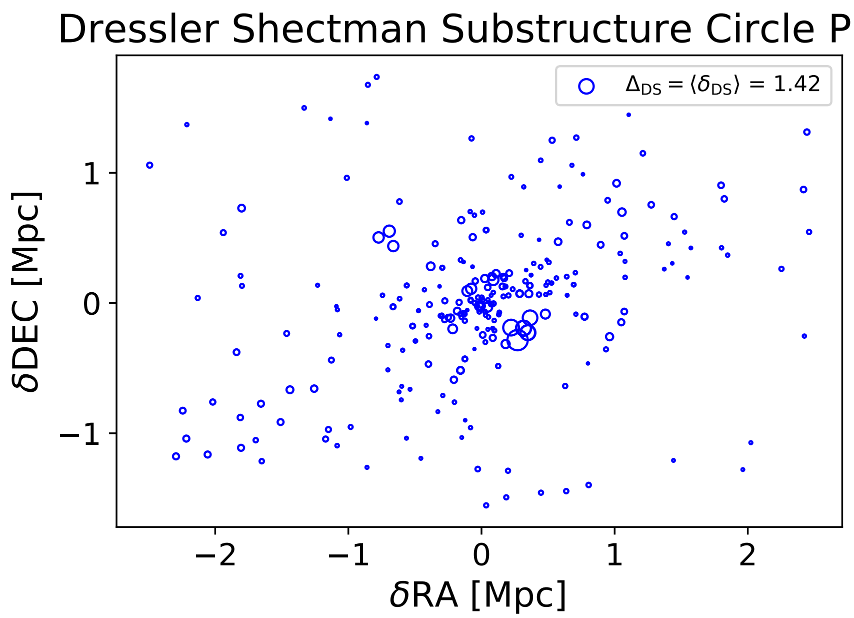

Figure 5.12 Visual representation of the Dressler-Shectman statistics in which the locations correspond to the position of the galaxy on the sky, while the size of the circle marker is related to the DS statistic for that galaxy. The larger the circle, the greater the deviation between the local velocities and the global values.

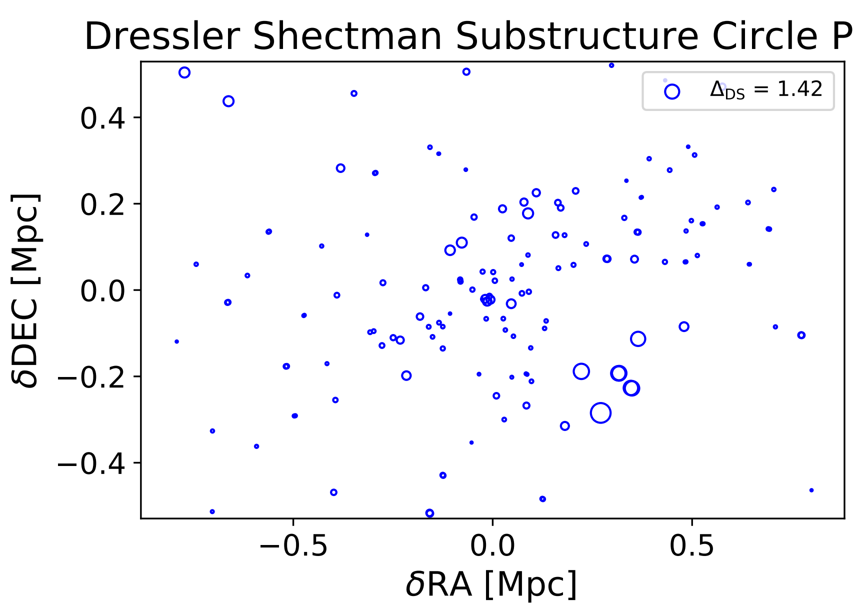

Figure 5.13 Similar to Figure 5.12 but where we have zoomed in to the central region around the core of the cluster.

5.5.3 Velocity Histogram Relation to Substructure

To approach the subject from another perspective, we returned to the bimodal nature of the velocity histogram, which does appear to remain even when deprojected into a phase-space. We performed a purely exploratory search on the data using a best fit Gaussian mixture model to determine the relative shape and sizes of a proposed two halo model. The best fit model is shown in Figure 5.14 where only the relative heights matter in the vertical directions but the widths are in $\mathrm{km\,s^{-1}}$. We then used these fitted distributions as naive likelihoods to split the sample into two halos depending on what distribution is larger at a given location. Figure 5.15 shows the pair-wise plots for the complete cluster dataset, while Figure 5.16 shows the dataset split based on the naive probabilities mentioned above. The distributions don't differ greatly, though it appears that the smaller halo prefers to be aligned with the large scale structure (lower-left to upper-right). So as with the visual and k-means clustering searches, we were unable to determine concrete signs of substructure using this naive approach.

5.5.4 Phase Space Evidence for Substructure

As a final approach, we looked in the radial-velocity phase-space for indications of substructure. There we were able to identify a number of potential clumps, including the cyan and yellow clumps shown in Figure 5.17. Each of these is located near an excess from the one single halo model of the velocity distribution. The cyan dots reside near the prominent bimodality we identified while the yellow dots are near a smaller excess in the opposite velocity direction.

If we focus on those two subclumps on the sky, we see both are concentrated near the core in Figure 5.18. The cyan does appear spatially clustered whereas the yellow does not.

Pursuing the cyan cluster, we see in Figure 5.19 that the clump may be composed of several smaller clumps in red, yellow, and orange. Note here that these are all parts of the cyan clump, and the yellow galaxies here have no relation to the yellow clump above.

If we look at these spatially correlated objects in RA-velocity and DEC-velocity space, we do indeed see that the clustering is retained, especially for the red and orange portions. Figure 5.20 shows the clustering.

If we choose to remove those galaxies from our sample and recalculate our dispersion, we find a shift of roughly $54\,\mathrm{km\,s^{-1}}$, which is significant for our uncertainties.

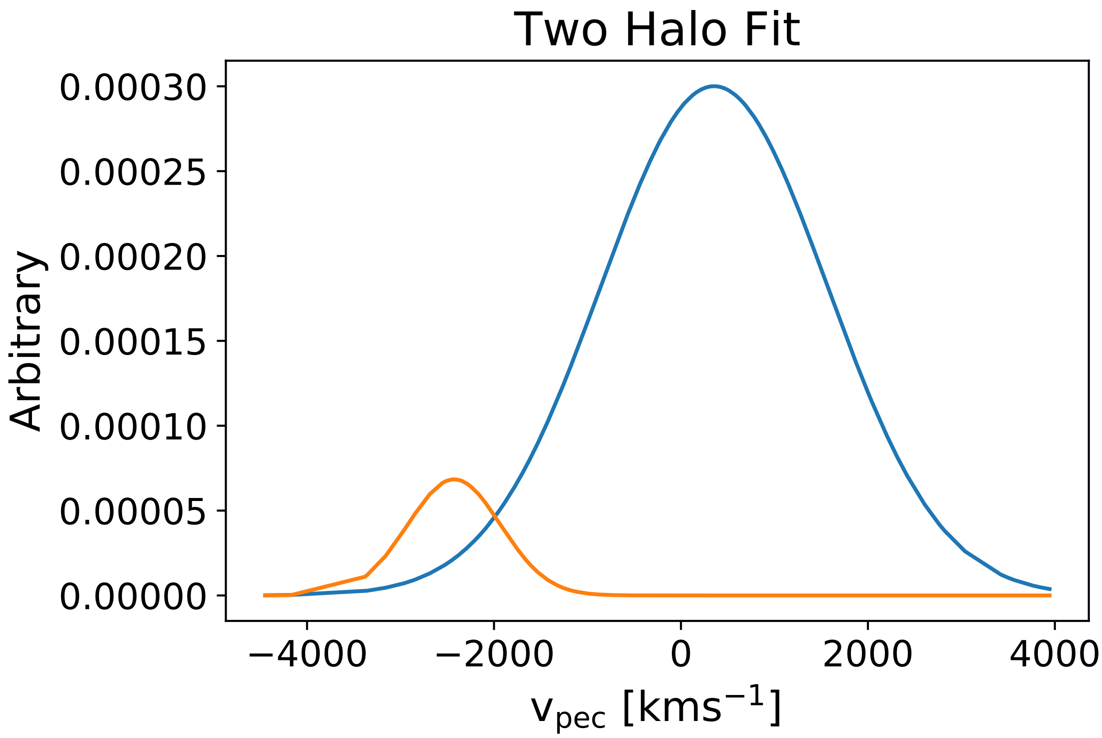

Figure 5.14 Two Gaussian model fit to the velocity histogram of AS1063. The amplitude values are arbitrary but the relative heights are informative as they are related to the relative number counts of galaxies in that velocity bin. The horizontal axis shows the peculiar velocity. The curves in this naive search are meant to represent the likelihood of a galaxy in at that velocity belonging to halo 1 or halo 2.

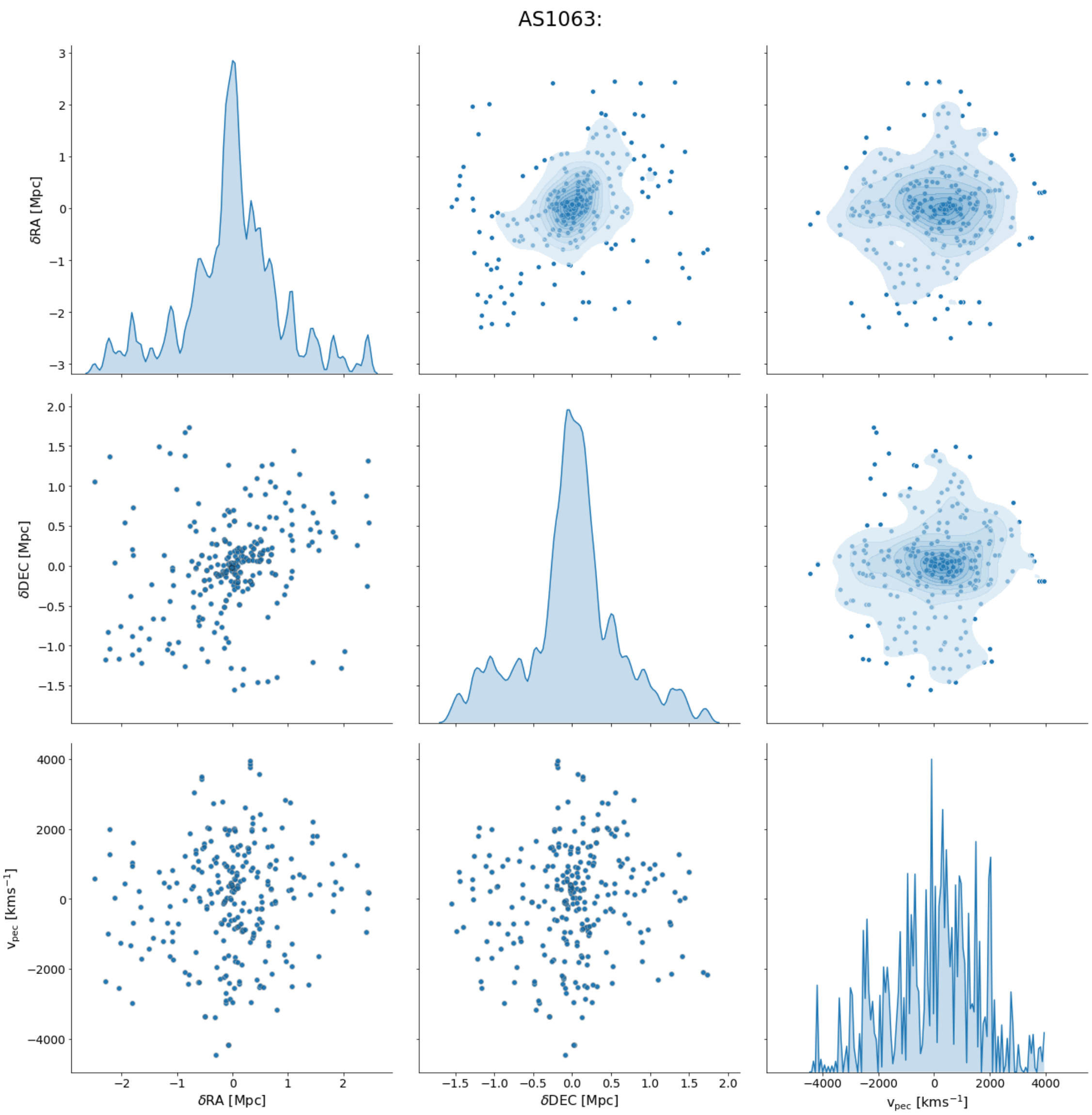

Figure 5.15 Plots showing both scatterplots and smoothed density contours as well as histograms showing the distributions of RA, DEC, and peculiar velocities.

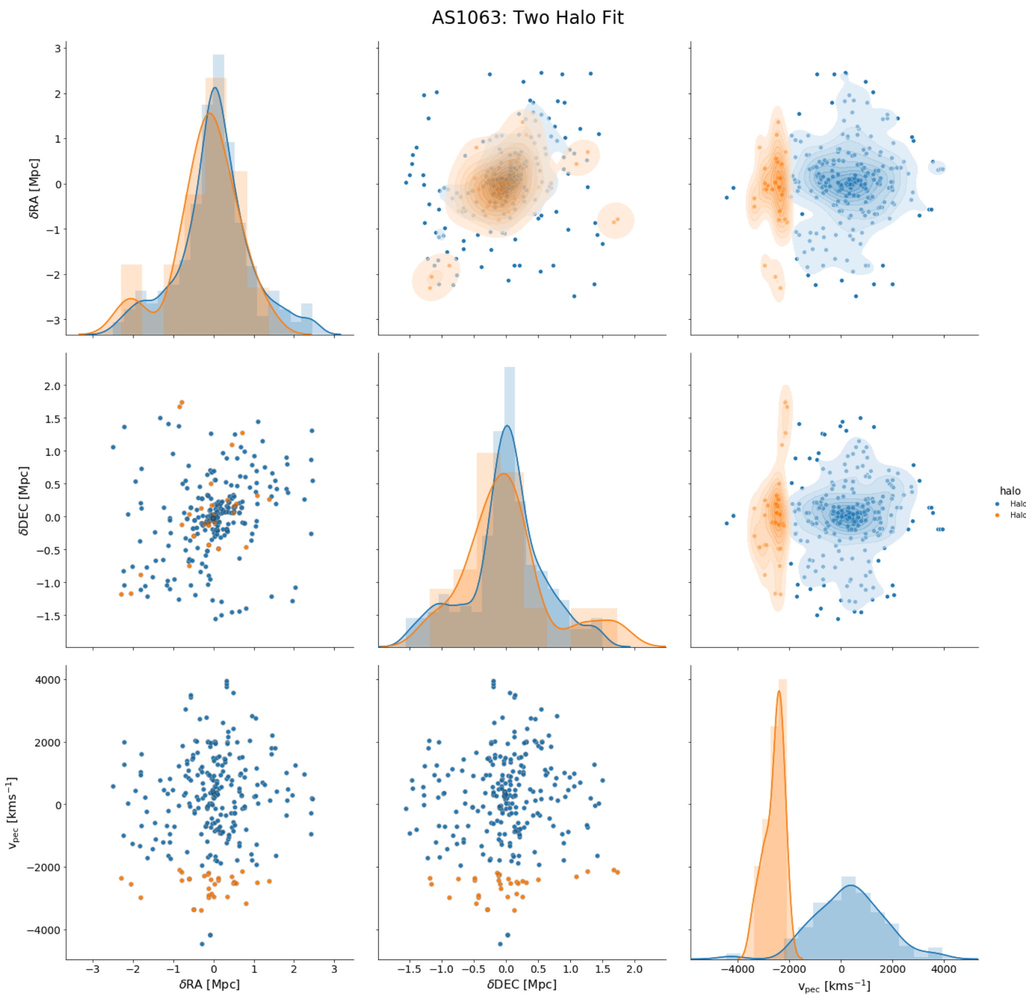

Figure 5.16 Using the two halo fits from Figure 5.14, we selected the halo with the largest amplitude at that galaxy's peculiar velocity and use it to assign the galaxy to either halo one or halo two. We then plot the two subsets against RA, DEC, and velocity.

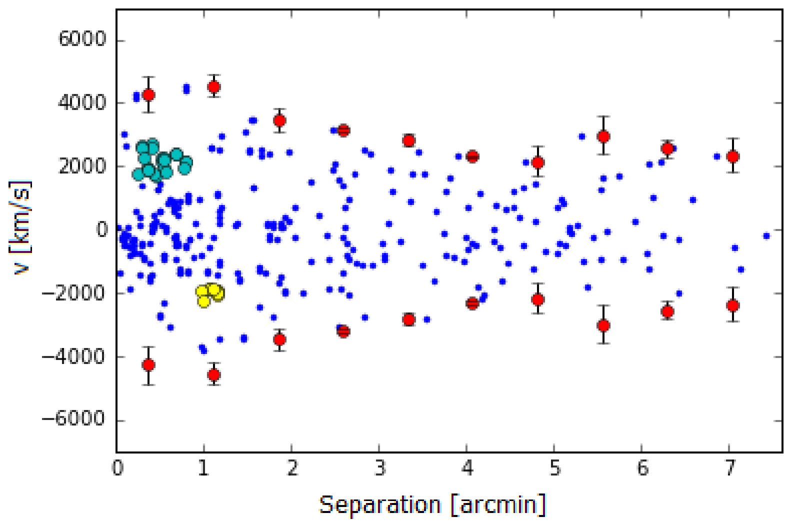

Figure 5.17 Velocity $[\,\mathrm{km\,s^{-1}}]$ versus angular separation [arcmin] on the sky from the center of the cluster. Two resolved clumps can be found in the phase-space, which we have identified with cyan and yellow.

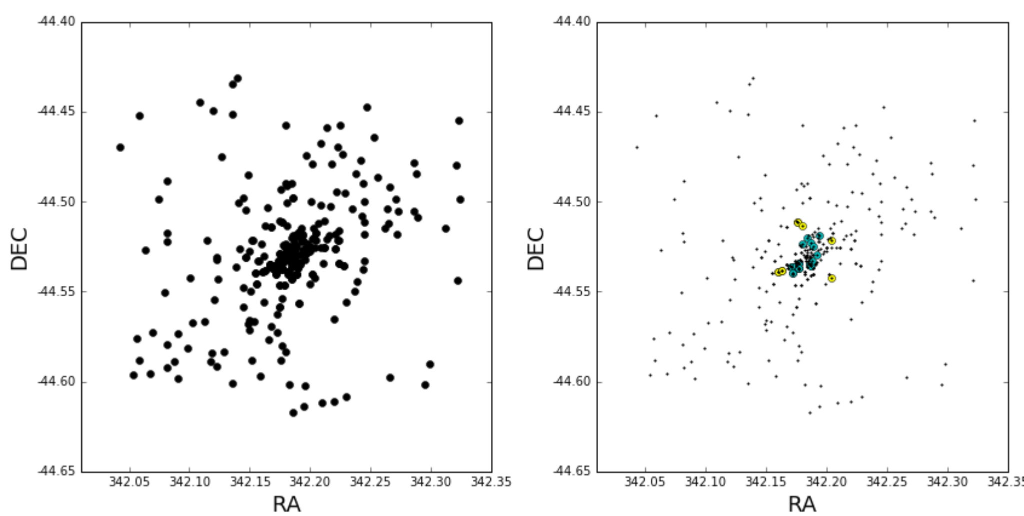

Figure 5.18 Sky plot, RA versus DEC, of the full dataset (black) and two possible subclumps (cyan and yellow) identified in Figure 5.17.

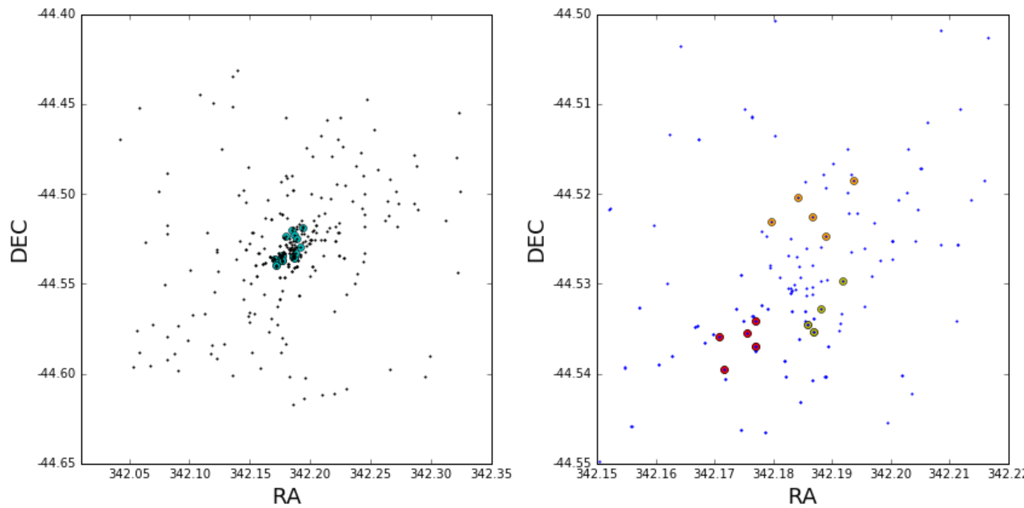

Figure 5.19 Plot of the projected sky, RA versus DEC, showing the full dataset (black), and the subclumps clustered in space (red, orange, yellow). Note the yellow galaxies here are unrelated to those in Figure 5.18.

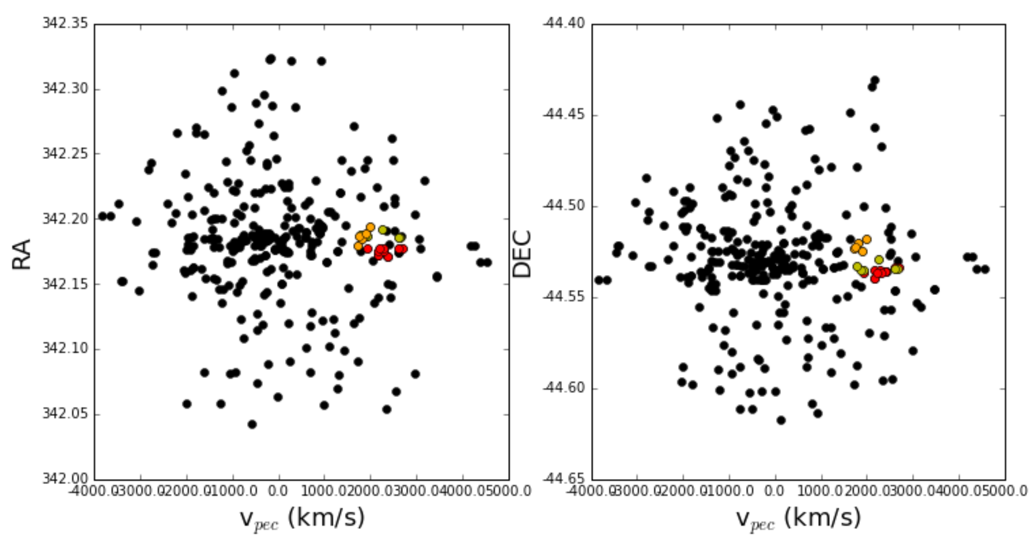

Figure 5.20 RA versus peculiar velocity and DEC versus peculiar velocity for the full dataset (black) and the subclumps (orange,red,and possibly yellow).

The removal of a small random subset does not have such great an impact. Our velocity dispersions changes from $\sigma_v = 1599\,\mathrm{km\,s^{-1}}$ to $\sigma_v = 1545\,\mathrm{km\,s^{-1}}$, which translates into a mass shift of -3.1$\times10^{14}$ $M_\odot$.

While this change in mass cannot explain the entire mass discrepancy, it does provide some proof of the substructure that the DS statistic and velocity dispersion is indicating. With denser spectroscopy, the addition of color and galaxy morphologies, and more sophisticated clustering algorithms, more clumps would likely be identified to help further alleviate the mass discrepancy. We leave such searches to a future work.

5.6 Conclusion

Here we have presented a detailed dynamical study of the massive Abell S1063 system. We have confirmed and corroborated claims made by Gómez et al. regarding structure in the cluster and report a similarly high velocity dispersion and mass estimate (Gómez et al., 2012). We find values of 1599$\pm$37 $\mathrm{km\,s^{-1}}$and $M_{\sigma_v,200c}$ = 31.9$\pm$5.54$\times10^{14}$ $M_\odot$using 261 spectroscopically confirmed cluster members.

We also perform the first escape velocity edge (caustic) mass measurement of the cluster, which found a mass that was consistent with non-dynamical estimates with a value of $M_{\mathrm{caustic},200c} = 19.87^{+7.54}_{-5.17}\times10^{14}$ $M_\odot$. Interestingly the escape velocity edge, which can simultaneously fit for concentration, favors unusually high values of $c_{200c} \sim$ 15 compared with typical weak lensing best fits near 3 to 4 while the mass estimate is in excellent agreement with other estimates. This is due to the low constraining power of the escape velocity edge technique to determine the concentration in this cluster.

In viewing the velocities in Figure 5.5, a clear bi-modality can be observed. We test this theory using the Dressler-Shectman statistic to identify local velocity deviations from the global values. We report a significant value in which we estimate a likelihood of $p \lesssim 0.0002$ of this occurring by chance. We interpret this as a significant indication of substructure. We visually inspect the cluster on the projected sky as well as through its radial velocity phase-space. We try to identify trends in the spatial location of the galaxies in the negative velocity excess in the velocity histogram but find little that can be distinguished from the massive central halo. Finally in looking at the phase-space we are able to identify at least one subclump that is correlated with a particular location in Ra/Dec and velocity, centered near the core. These galaxy tracers are consistent with what was seen in the DS statistics plots with the same areas identified by galaxies in the clump being associated with areas of large individual DS statistics. With physical clumps identified, a significant DS statistic found, and significantly high mass estimate determined from the bi-modal velocity distribution, we can confirm the existence of substructure in the galaxy cluster Abell S1063. We can also report an estimate the mass using a robust dynamical mass proxy, the escape velocity edge, that finds $M_{\mathrm{caustic},200c} = 19.87^{+7.54}_{-5.17}\times10^{14}\ M_{\odot}$.

Chapter 6

Closing Remarks

6.1 Summary

Galaxy clusters stand at the forefront of the gravitational struggle between dark matter and dark energy, making them powerful probes of the relative strengths of these elusive components. While no direct mass measurements are possible, the use of independent probes with differing assumptions and constraints can give complementary information that allow us to produce more precise constraints on mass. This in turn allows us to better understand the halo mass function, leading to stronger constraints on cosmology and a deeper insight into the laws governing our Universe.

This thesis details an attempt to contribute to this great pursuit from the observational and astrophysical perspective. By utilizing spectroscopy we can learn about the galaxies in the cluster environments, and use them as tracers of the underlying gravitational potentials that they reside in. We can estimate the masses of the clusters and provide complimentary information to break degeneracies in assumptions between estimates (e.g. X-ray and SZ). We can also utilize the three dimensional nature of the spectroscopy to investigate the substructure within the halos which can once more inform mass estimates by e.g. confirming deviations from hydrostatic equilibrium or showing spatial correlations between X-ray peaks and subclumps within a cluster, to name just two.

In pursuit of those goals, we undertook an ambitious observational campaign to observe tens of massive clusters with high multiplicity using the Michigan-Magellan Fiber System on the 6.5m Magellan-Clay telescope. We developed a nearly automated pipeline for the reduction of low resolution spectroscopy from that instrument, with the goal of making it both user friendly and equally powerful scientifically compared to its multipurpose predecessors. We observed and reduced 23 fields of M2FS data, each with between 100-240 spectra. The final dataset consists of 4427 galaxies in total among 22 clusters, of which 3054 received robust redshifts and 1679 were identified as cluster members.

We performed an analysis on two of those fields to illustrate the power of this dataset. We observed one cluster, Abell S1063, with two fields and recovered over 163 unique redshifts, which when combined with an additional 117 in the literature allowed us to perform a high resolution dynamical study to investigate and validate open questions regarding the dynamical state of the cluster (Gómez et al., 2012; Gruen et al., 2013). We were also able to provide a more detailed velocity dispersion measurement using an order of magnitude more cluster members than previous studies as well as the first measurement of the cluster mass using the escape velocity edge technique (Gómez et al., 2012; Ruel et al., 2014).

6.2 Future Work

6.2.1 *M2FSreduce*

Chapters 3, 4, and 5 have discussed portions of projects that still have many interesting avenues left to explore within them. In Chapter 3 we discussed the pipeline created to reduce M2FS astronomical data. While the pipeline works without any recently reported bugs and only requires human intervention at one stage (fine adjustments to wavelength calibrations), there are still things that could be improved and investigated. First and foremost are two current drawbacks that should be addressed. The first is the propagation of the masked pixels from the cosmic ray removal stage to the final spectral masks used for redshift fitting and during scientific inference. The code currently saves these files but doesn't use them when collapsing the two dimensional spectra into one dimensional spectra, or at any point further down the reduction chain. This has clear drawbacks as a value replaced with a smoothed flux from neighboring pixels may inherit characteristics of those features, thus smearing them out or worse, disguising them or making them unresolved. To get around this would require the code to identify those pixels and either smartly fit the data around the bad pixels or mask out that entire pixel bin (the several pixels in width the spectrum has in two dimensions on the focal plane before being combined into a one dimensional spectrum).

The second is a useful feature found in the *IRAF* version of the M2FS reduction code. This identifies and tries to remove scattered light that shines on the CCD through either openings in the encasing or bright objects being observed among fainter objects. This requires image recognition in identifying the telltale curved arcs that pass through both spectra and areas between them that are meant to be dark. This is both an interesting and useful problem that should be addressed as *M2FSreduce* matures.

Third would be a preprocessing step in the sky subtraction to leverage the wavelength information of the sky lines to further tweak the wavelength calibrations, while also allowing for more effective and complete sky line removal, because the line wavelengths will be defined with respect to the sky line values. This should reduce the number of mis-centered lines that cause large spikes and noise in the sky subtractions. The result should be more accurate spectra with fewer wavelengths needing to be masked. Not only will this improve redshift efficiencies, the reduction in abrupt spikes and large areas of masked pixels will also improve the catastrophic failure rate – where the redshifts aren't just wrong by a small noise term but are completely wrong because the algorithm picked up something it thought was signal but was actually a subtraction artifact.

Finally, tools for more in-depth spectroscopic analyses beyond recovering redshifts and basic signal to noise estimates should be developed. The first is spectrophotometry which is relevant to anyone who needs to know the meaning of their flux number counts in physical units. This would require a great deal of work to achieve. The second is to increase the support for high-resolution spectral reductions. For single-line spectra the code should be able to adapt with some additional instructions given to it. For high resolution spectra that take the place of several fiber rows, those would again be a challenge left for future work.

6.2.2 Substructure Analysis

Chapter 5 gave a first analysis of data taken as part of the larger cluster sample outline in Chapter 4. Centering around AS1063 we were able to measure the escape velocity edge inferred mass for the first time and confirm a number of statements made with fewer spectra than in 2012 (Gómez et al., 2012). While the mass proxy analysis for the cluster is complete, there are still more investigations that can be done regarding the existence of substructure in the cluster and how much it is influencing the mass proxies. More advanced unsupervised cluster finding techniques could be employed, both using the RA, DEC, and velocity information we used here but also expanding that information to colors and morphological information. Simulations could also be utilized to understand the formation histories that generate clumping, for instance what we observe within the cluster. Finally, updated weak lensing and strong lensing models could be created to further improve the constraints and test the profiles to investigate the discrepancy in preferred concentrations.

6.2.3 Dataset

Finally, in Chapter 4 we described a rich dataset of 22 clusters and thousands of galaxy redshifts and more than 1500 galaxy cluster members taken from a uniform survey with the same instrument, configurations, and data reduction methodology. There are a vast number of research topics that could be addressed using this data by itself or in concert with further spectroscopic or multi-wavelength data. What was shown in Chapter 5 was a testing ground for the analyses to come. We were able to show that M2FS data is capable of creating well constrained caustic masses and velocity dispersions, in addition to investigating the dynamical state of the clusters. With further analysis of colors and morphology, we can do environment studies to identify differences in clustering or substructure for different morphologies, in addition to generating scaling relations between the escape velocity edge technique and X-ray, weak lensing, SZ, richness, and velocity dispersion. We can also investigate the dynamical state of those clusters that deviate from best fit relations. The thousands of spectra can provide a wealth of knowledge for both the astrophysical processes that go on within clusters and also information that can help inform cosmology. The calibration of scaling relations and understanding what assumptions inherent in any mass proxy are failing in a given system are important when trying to use that proxy for cosmology. That is where an additional method, like the escape velocity edge that doesn't require hydrostatic equilibrium, can help break degeneracies and reveal failed assumptions in estimates.

Yet even with all of the possibilities above, the most exciting may be the potential to constrain cosmology using the combination of weak lensing and highly sampled velocity edge mass profiles. By pairing the weak lensing with the velocity edge, instead of comparing them as we did in Chapter 5, we can use one dataset to fix the concentration and gravitational potential, which frees the other dataset to constrain the remaining free parameters which are cosmological parameters (Miller et al., 2016; Stark et al., 2016).

6.3 Future Outlook

As the complexities of the problems in astrophysics and cosmology continue to increase and the size of the telescopes grow ever larger, the movement toward international collaborations has grown with them. The cost of such facilities and the amount of effort required to execute and maintain the instrument and telescopes, as well as to analyze the data, necessitate such an evolution. In this work we have discussed one such instrument, the Dark Energy Spectroscopic Instrument, which is currently running in a preliminary state and nearly ready to begin survey validation. Moving forward these large spectrographs will begin to map the sky to ever increasing depth. Another such instrument is the Prime Focus Spectrograph (PFS) on the 8m Subaru telescope on Mauna Kea, Hawaii (Sugai et al., 2012, 2015; Tamura et al., 2018). PFS consists of 2394 fixed robotic positioners that can re-position optical fibers across the 1.3 deg field of view of the prime focus. Like DESI, it has three cameras designed for optimal sensitivity in the blue, red, and infrared, and will observe in the wavelength range from 380nm to 1260nm at a resolution of roughly 3000, with a "medium resolution" mode in the red camera that can reach a resolution of roughly 5000. With a telescope diameter twice the size of the Mayall, PFS can collect four times more light than DESI. Therefore, while it may have half the fibers of DESI it will be able to reach deeper limiting magnitudes or conversely operate at a faster cadence and make more passes across any given region of the sky within their chosen footprint. While in some ways a competing telescope; the regions, science goals, and spectral quality will be very much complementary. In addition it will fostering competition and push each collaboration to perform at their best.

Yet DESI and PFS are just two of several highly multiplexed spectrographs currently under being built and run. There are several more, not including the future proposals. As the complexities have increased, so too have the lead times between conception and implementation. Two future highly multiplexed multi-object spectrographs are the European Southern Observatory's ELT-MOSAIC, on the soon to be built 39.3m Extremely Large Telescope in Chile, and the MegaMapper spectrograph, planned by the DOE with the proposed site being Las Campanas in Chile on a purpose-built third clone of the Magellan 6.5m telescope (Puech et al., 2018; Schlegel et al., 2019). The MegaMapper will continue in a very similar way to how DESI will operate in the northern hemisphere, except scaling up to 20,000 robotic fibers on a larger telescope. This will enable denser sampling of object rich regions such as clusters as well as setting a faster cadence, which will allow for target-of-opportunity spectroscopic observations of supernova observed with the Large Synoptic Survey Telescope and gravitational wave optical counterparts from LIGO (LSST Science Collaboration et al., 2009; LIGO Scientific Collaboration et al., 2015; Schlegel et al., 2019). ELT-MOSAIC is taking a different approach by using fiber bundles that can either be combined into eight (or 10) IFU's, each of which are 1.9" across, or 80 (100) smaller bundles, which are 19 fibers of width 169 mas that combine to form 0.84" diameter mini-bundles – based on nominal (goal) requirements (Puech et al., 2018). The goal is to observe at resolutions of R$\sim$ 5000 in the optical with a high resolution mode that can reach R$\sim$ 15000.

While the datasets these surveys produce will not be as complete in the dense regions of clusters, the huge number of spectra taken will still open new doors to cluster studies. By stacking sparsely sampled cluster members into ensemble clusters of similar richness, X-ray/SZ signal, redshift, and bcg magnitude, you can begin to unlock population averaged values. The more narrow you draw the bins however, the more detailed the properties you can study once you have the numbers available from these massive surveys to reduce the statistical noise.

When dense cores are desired there will always be a place for instruments like ELT-MOSAIC, other IFU's, or PI instruments like M2FS that allow you to follow-up targets of interest. These are symbiotic in nature, with the large surveys taking the brunt of the data while allowing the detailed instruments to narrow in on targets of interest.

This is an exciting time in cosmology. We are acquiring a surplus of data in an array of different wavelengths and spectral resolutions. The increased computational power and mathematical techniques allow us to pursue more complicated yet precise and illuminating analyses, with the hope of better constraining the parameters of our Universe. I hope that my small contribution to our understanding of galaxy clusters here has been able to inch that pursuit ever further on the endless trail of scientific pursuit. I look forward to the trail ahead. Onward.

Appendix A

Robotic Positioner Collision Avoidance

A.1 Introduction

As described in Chapter 2, the DESI instrument consists of 5000 robotic fiber positioners. Each positioner has the responsibility of moving a single optical fiber to a specific location within its 'patrol radius,' ie the region it can reach using its two arms. To within fabrication variances, each of the two arms is 3mm in length, giving a maximum patrol radius of 6mm, which corresponds to 0.024°or 1.42' on the sky (DESI Collaboration et al., 2016). In order to increase the density of targets that can be acquired during a given configuration of positioners, the patrol radii overlap one another by approximately 1.6 millimeters. The full focal plane is made up of 10 pie-shaped "petals," with each petal containing 500 positioners. Positioners in the central areas of each petal contain six neighbors. The exact layout of positioner locations can be seen in Figure A.2. Therefore, there is a not trivial probability of two positioners attempting to occupy the same space. While simple checks can be done to ensure that targeted locations don't overlap, the same is less clear for the movements required to move from a starting position to a final position. The software and algorithms used to generate the movement paths of positioners, check if collisions would occur, and re-generate new move tables to avoid such spatio-temporal collisions is internally referred to as either "collision avoidance" or "anti-collision." Here I will use the term collision avoidance.

The goal of collision avoidance is to allow for arbitrary configurations of targets, so long as those targets are not physically overlapping, without regard to how the positioners reach those target locations. This requires an adaptable and deterministic method of transport between the initial and final locations. The timing of the reconfiguration is under one minute and therefore the list of moves given to each positioner must be capable of being completed by the robot within that specified time. Any additional time is wasted seconds that could be spent acquiring data. Movements are not the only place where efficiency is required. The movements need to be determined for 5000 fibers, simultaneously, to micron-level precision on an ordinary desktop, in the order of minutes. This is a critical constraint in that it rules out inefficient algorithms while also preventing highly parallelized implementations.

The problem lends itself well to a two factored solution: a mitigation technique where moves are generated in a way that makes collisions less likely, and an avoidance step that creates new paths for those positioners that would collide even given the mitigation step.

Collision mitigation is the first attempt at the software computing machine-readable instructions that can guide a positioner from its initial position to the desired target. The steps are created in theta and phi, which describe the rotation of the central body (theta) and the angular rotation of a secondary arm located 3mm from the center (phi). The exact geometries can be seen in Figure A.1. Using this representation any point can be reached within the patrol radius equal to the sum of the two arms, 6mm. The electric motors operate directly in these coordinates with a specified angular velocity for each of theta and phi, where the velocity is specified by a pulse width modulated signal. That means there are effectively two states, "on" (ie moving) and "off" (ie not moving), for each motor. The constants speeds are a limitation in avoidance but also simplify the problem, though acceleration and deceleration are still important and need to be accounted for. The two-state system makes the machine firmware much simpler, however. A "movetable" is sent to each positioner, which gives instructions to each positioner motor. Because of the two-state system, the table only needs to specify whether a motor is on or off and for what interval of time that state will be held. The collection of such moves should result in the positioner reaching the desired target location, without getting in the way of any neighbors.

The remainder of this appendix will describe the algorithms attempted or used, and to a lesser extent the implementation of them into python for the actual code development. The mitigation technique is described in Section A.2 while the avoidance techniques are described in Section A.3.

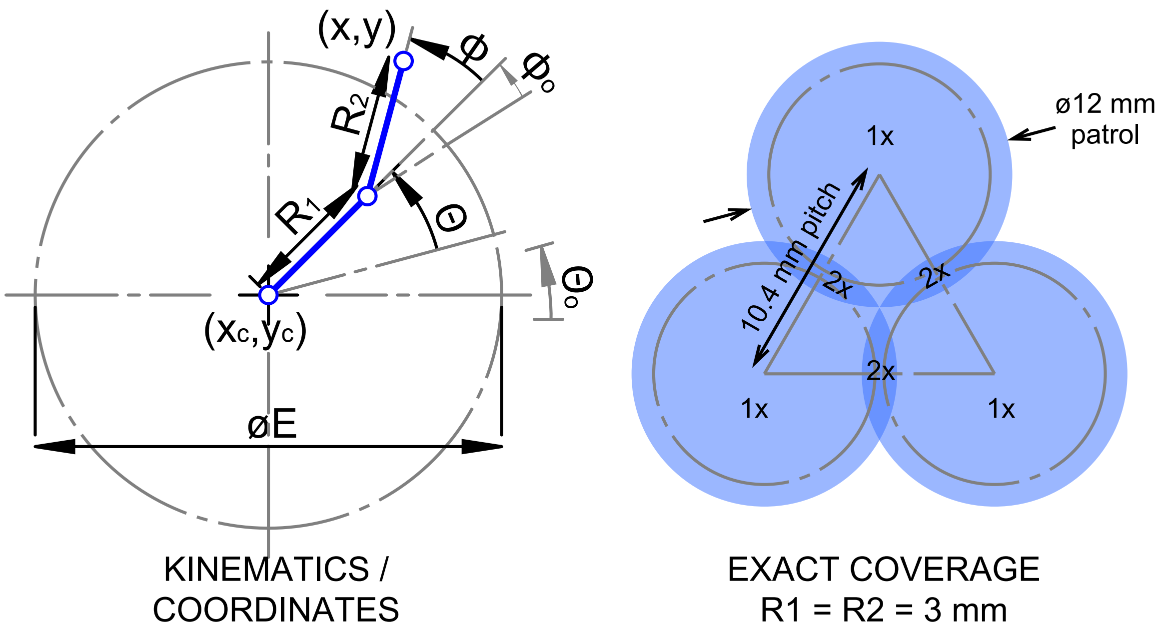

Figure A.1 A schematic top-down view of a fiber positioner in DESI. Left: Shows the coordinates of relevance to the positioner. It has two arms, theta and phi, with radii R1 and R2 respectively. The inner arm rotates in the theta direction 370°. The phi arm is attached to the end of the theta arm, and can rotate by 190°. Neighboring positioners are placed 10.4mm apart, meaning there is up to 1.6mm of overlap between a positioner and it's neighbor (who each have length 6mm). Figure taken from DESI Collaboration et al. (2016).

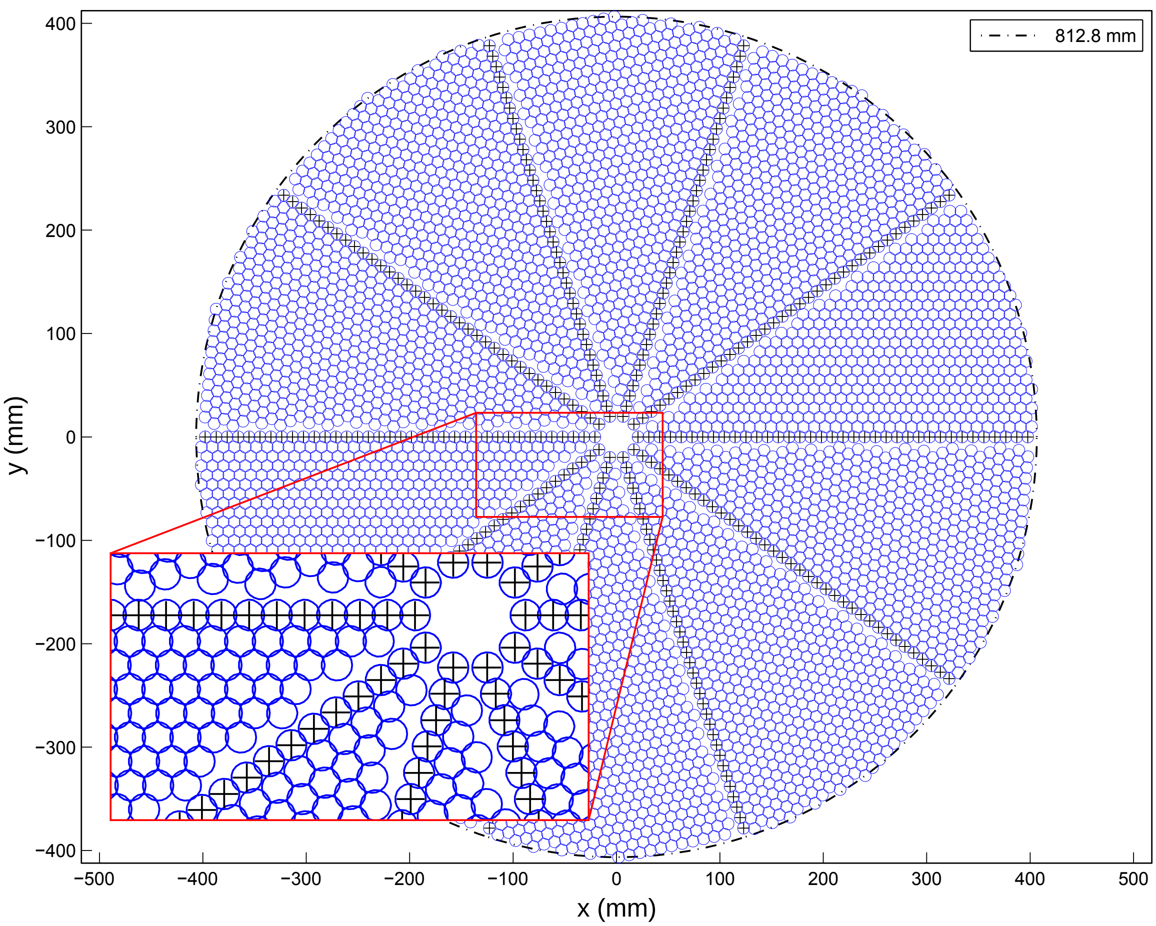

Figure A.2 This diagram shows the layout of the robotic fiber positioners on the focal plane of the DESI instrument. The packing is hexagonal in nature with interior fibers having six neighbors. The "+" symbols indicate that special constraints were placed on those positioners. The focal plate is split into 10 slices, called petals. The straight radial lines of "+" positioners are constrained to smoothly trace the boundary between petals. Figure taken from DESI Collaboration et al. (2016).

A.2 Collision Reduction

A.2.1 Direct Movements

As stated, the collision mitigation is the software's first attempt at making movetables that tell the positioners how to move. As such, the first and most naive approach is to simply calculate how far the positioner must travel in each coordinate, theta and phi. Then, taking the minimum of $(\Delta\theta, \Delta\phi)$, we instruct both motors to run for $t = \Delta\mathrm{x}/\omega_{\mathrm{x}}$; where t is time, x is the smaller angle and ω_{x} is the angular velocity of that motor. After this move, the remaining distance in the larger displacement direction is given why the other motor remains idle.

While this requires the fewest possible commands and is most direct, it allows for increased risk of collisions as it doesn't consider where the positioner is and can therefore spend a large amount of time with the arms fully extended, rotating large distances through neighbor's territory. Therefore this technique is only used for small correction moves where the movements are smaller than a safety envelope calculated to surround each motor so that calculation errors or hardware uncertainties can be negated.

A.2.2 Retract-Rotate-Extend (RRE)

The first and only mitigation technique used was created early on by Jpseph Silber, a Lawrence Berkeley National Lab (LBL) Engineer and collaborator. Coining the term, Retract-Rotate-Extend (RRE), he realized that the majority of collisions occur when the arms are rotating while extended out to lengths ($\sim$ 4.4mm) at which they can reach their neighbor's patrol region. His solution was to have the positions retract inward first, then rotate about their central axis, before finally extending their arms back out to the final location. When in the retracted state, no part of the positioner is more than 4mm from the center and therefore cannot collide with a neighbor. Thus rotations about the center by any number of degrees is free from collision. This significantly reduced the number of collisions, as the only place where they can occur are in the initial retraction and final extension of the arms.

An additional bonus of this technique, which was not initially required, is that only half of the motors are running at any given time. That is due to the fact that the retract and extend motions are purely in the secondary phi arm (and thus only use the phi motor), while the rotation about the center only uses the theta motor. This may seem inefficient but due to electrical constraints from the power supplies, this was actually an important safety feature for the system.

A.3 Collision Avoidance

A.3.1 Introduction

Once preventative measures have attempted to create a set of collision-free movetables, these must be tested virtually to ensure that no collisions would occur. Among 5000 positioners, there will inevitably be some. This is done using accurate representations of the positioner geometries in a locally flattened 2d representation of the focal plane. Using common techniques for the overlap of polygonal objects, and stepping through time to simulate the movements, the simulation determines whether positioners will collide based on the overlap of a positioner with a neighbor. Once these are detected, they are logged as a pair whose tables need to be corrected. The final list of pairs is then passed to the desired version of collision avoidance to produce new movetables for each positioner in the pair. For all of the algorithms below, if an avoidance attempt fails to find a satisfactory path of avoidance for one positioner in the pair, it will attempt to do the same for the other. Certainty situations, coupled with implicit assumptions in the given technique, make it possible to solve for the second even if the first attempt had failed.

The full suite of positioner movetables are then tested once again to ensure that the newly generated movetables made by the avoidance algorithms have not created any other problems. The more advanced algorithms account for these possibilities, such that this step is equivalent to a final sanity check that everything will be safe.

Here we discuss the various algorithms tested as methods to correct for collisions of positioners. They are ordered from simplest to most sophisticated, with the degree of successful collision avoidance and efficiency scaling along with the development.

A.3.2 'Full Stop'

The most obvious and naive approach to avoiding a collision is to stop the positioners from moving. If the code determines that a positioner will collide with a neighbor, it can simply tell that positioner not to execute its moves. The downfall of this situation is that those positioners will never reach their final target, meaning losses of data. There is also the potential of the stopped positioner causing another collision because it now remains in a location that a different neighbor may need to pass through. This causes an iterative cascade. The iterations typically converge within 1-3 iterations after which no collisions occur, however it is clear that this is a non-ideal situation. This method, referred to as 'full stop' is implemented only as a last resort option if the algorithms below fail to create a sufficient solution.

A.3.3 Wait and Shift

This method was also devised by a collaborator at LBL. The premise is to isolate the two positioners that are colliding and force one of them to stop short of the impact location and pause for a period of time before proceeding. This is in the hopes that the other positioner will pass by in the interim and therefore avoid the collision. The method would iterate over many possible stopping distances and waiting periods until one successfully avoids the collision. The advantage of such a method is that it is simple and intuitive. The disadvantages, however, are that it is non-deterministic in nature and in no way ensures optimality/efficiency in computational time or movement time.

A.3.4 Force Law Analog

The term "em avoidance" was coined for this method because of its analogous behavior to the forces in electromagnetism. The positioner in question is assigned a 'charge' while the neighboring positioners are assigned the same 'charge,' and the target location the positioner should go to is assigned a point charge opposite to the positioners. The dynamics of the positioner in question can then be calculated using a $1/r^n$ repulsive and attractive forces caused by $1/r^{n-1}$ potentials to simulate the moves. Several power-laws were attempted including n=1, n=1.5, n=2 (e.g. gravity or electromagnetism), n=4, and n=6. The best behaving were n=1.5 and n=2, with n=2 selected for simplicity in working with the well known force-law. The advantages of this method are that is is again intuitive when conceiving ways to have things avoid one-another, and it easily produces deterministic dynamical paths.

The simulations worked very well for point masses in a Cartesian plane. An example of the generated 'potential field' for a positioner is shown in Figure A.3. The disadvantages arose with realism, however. The true positioners are 3 dimensional objects (though only the 2-dimensional projections are relevant here) and the positioners operate in angular movements about the central axis. Using the naive point mass approach did not work in the realistic simulations because it did not account for the location of the arms as they moved the positioner. The extended object locations were not properly accounted for in the model and collisions with portions of the positioner away from the fiber location occurred. A related issue was in the added complexity of selecting how charge would be distributed across the objects and keeping track of where different parts of the positioner were located at any given time. This led to a high degree of numerical complexity in calculating the movements of the two extended and connected rigid bodies that held the positioner. This was compounded by the need to work in the multiple coordinate systems that the problem naturally required. The positioner moves in a theta-phi space with the rotations being about different axes. In order to create movetables or dynamically move the object while numerically simulating its path, transformations needed to be made for numerous points on each extended body relevant to the problem. While non-trivial, these transformations can be easily programmed. The challenge was in the long computational time. The final challenging realism component was the need to use constant angular velocities in the current implementation of the positioner software. This again is trivial given some heuristic when numerically calculating, but effectively meant using a step function to determine whether a specific motor would run or not. This led to a jagged looking path that traced the smooth solutions but meant very long move tables with short duration movements and many starts and stops of each motor. Each start and stop compounding additional uncertainties, not to mention the need to properly account for acceleration and deceleration in the calculations.

With all of these shortcomings, this algorithm was set aside for an approach that was able to better account for the various shortcomings that were identified in the "em avoidance" technique. The new method utilized the concept of pathfinding. It considered the collisions as constraints to avoid, rather than avoidance with the eventual goal of finding a path.

A.3.5 Pathfinding: Dijkstra and A* Algorithms

With the unprecedented rise of computation over the past decades has come an increased interest in the idea of graphs: a collection of connected edges that meet at vertices (also called nodes). For a range of issues dealing with everything from accessing a website in a server on the other end of the world, to optimizing the storage of data on a supercomputer, to finding the optimal route to drive from one location to another, these can all be viewed as problems in traversing a graph (Cherkassky et al., 1996; Raman, 1997; Zeng & Church, 2009).

The objective of these searches is to begin at a node, traversing edges to other nodes, until the target node has been reached. The simplest approaches are to look

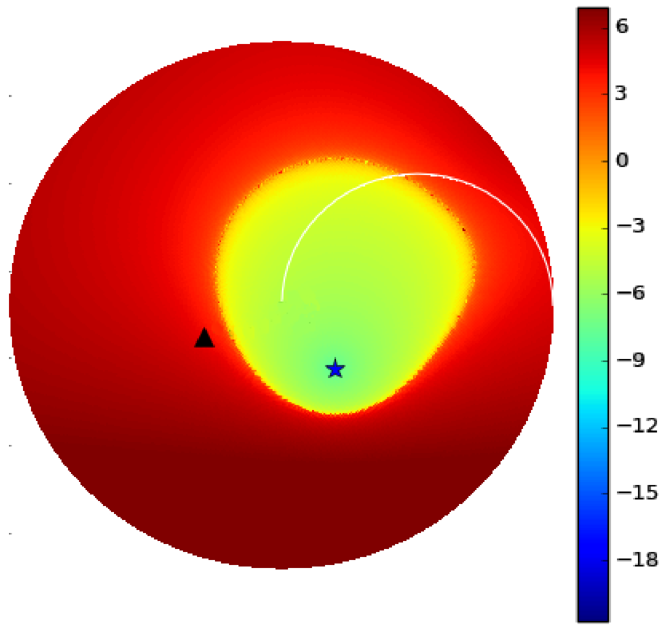

Figure A.3 Example of the force law solution to a realistic simulation of a fiber positioner trying to move from an initial location (green triangle) to a final location (blue star). The color values are of arbitrary scale, but the magnitude is related to the 'potential' of the fictitious force law. Note the global minimum around the target location (blue star) and the repulsive higher potential in the outskirts of the patrol radius.

at all neighboring nodes, then all the nodes neighboring those nodes, and so on until the target is found. That is known as Breadth-First and takes roughly $\mathcal{O}(4^n)$ calculations for a square grid with 4 neighbors, where n is the number of nodes from start to target (n is $\mathcal{O}(100)$ for these circumstances). Another is to keep propagating in a single direction until you can't anymore. Then branching off and continuing onward again. This is Depth-First and while it can get lucky, contains a lot of the same inefficiencies.

Improvements were developed in the second half of the 20th century, particularly by Dijkstra (Dijkstra, 1959), Hart (Hart et al., 1968), Pohl (Pohl, 1969a,b, 1970; Pohl, I., 1970; Pohl, 1973), Sint (Sint & de Champeaux, 1977), and de Champeaux (de Champeaux, 1983). Their contributions were on a class of graphs called weighted graphs, where there is a cost associated with traversing an edge. The costs need not be the same, and typically are not the same, though equal weighting simply results in the graph becoming equivalent to an unweighted graph. The weights (the term being used interchangeably with costs) are meant to illustrate the difficulty of the travel over that edge. A concrete example is in driving. Going 10 miles through a dense city is much more difficult and takes longer than driving 10 miles on a highway. So for navigation, weighted graphs are ideal as they can naturally account for this "ease of travel" when selecting the best path. That was Dijkstra's major insight. By creating a queue of potential paths, we can always look at the path with the smallest current cost to traverse. We then look at the neighbors of the most recent node in the best path and take the edge with the lowest cost. Afterward the queue is checked to see if the current path still has the lowest cost. If not, it is moved to the appropriate location in the queue and the lowest cost path at the top of the queue is selected to be searched in the next iteration. If the lowest cost edge selected reaches a node that has already been reached, the path with the lower cost to reach that node is kept. This continues with the shortest path always getting the first opportunity to explore it's neighbors until it is no longer the shortest (lowest cost). The search terminates when the target is added to a path. Because the current path being searched is by definition the path with the lowest cost, this automatically implies that the path that adds the target is the most optimal (lowest cost). If cost is simply distance, then this is also the shortest path in the geometric sense.

Hart and Pohl improved upon this idea by realizing that the inferred cost of a move could be augmented with an additional heuristic that was dependent on where the current search node was on the graph with respect to the target. If the lowest cost node moved you farther from the target, it may not be the most optimal path to take. While Dijkstra's algorithm naturally de-prioritizes such paths and eventually finds the shorter path, it takes additionally computations that a heuristic could help to eliminate. By providing information about the distance to the target, you effectively augment the cost of traversing an edge. It may be beneficial to move farther away if you can access a highway that will save significant time, but providing a quantitative measure of both pieces of information allows the algorithm to make a more intelligent and informed choice. Generally this heuristic is selected to be a distance measure. Common choices are the euclidean distance ($\sqrt{\Delta x^2 + \Delta y^2}$) from the current node to the final or "Manhattan" distance ($|\Delta x| + |\Delta y|$) which is the distance moving along square gridlines (where you can't take a diagonal movement). Any heuristic can be selected and under the condition that the heuristic does not over-estimate the true distance to the target, this was proven to again provide the optimal path and with greater efficiency de Champeaux (1983).

Finally, Pohl, Sint, and de Champeaux discovered that as long as you use the proper heuristics and termination conditions, you can further speed up the search by doing two searches simultaneously. Using a traditional search from start to target and a second that searches from the target to the start. Once a node is contained in both searches, the job is done. Because each individual search has discovered the lowest cost path to that node, the sum must be the lowest cost from the start to that node and that node to the target. Because that connecting node is abitrary, the two paths must therefore makeup the shortest path from the start to the target. This is contingent on certain specific conditions that were rigorously shown in Sint & de Champeaux (1977) and de Champeaux (1983). Because the number of paths grow exponentially with distance, this can be a vast reduction in search space going from $\mathcal{O}(4^n)$ to $\mathcal{O}(2 \times 4^{n/2})$, where again n is $\mathcal{O}(100)$. Examples comparing the results of the various algorithms and very rough indications of the computational time are shown in Figure A.4.

A.3.6 Modified Bi-directional A* Implementation

After reading Section A.3.5, the reader will hopefully see the applicability of such a technique to the situation of finding a collision-less path around obstacles. The Bi-directional A* algorithm was chosen for efficiency, flexibility, and proof of optimal solutions. The positioner patrol radii was broken into a grid of equal angular width sections. The grids were made in one degree intervals from the measured minimum and maximum values of theta and phi for the individual positioner for which a path is

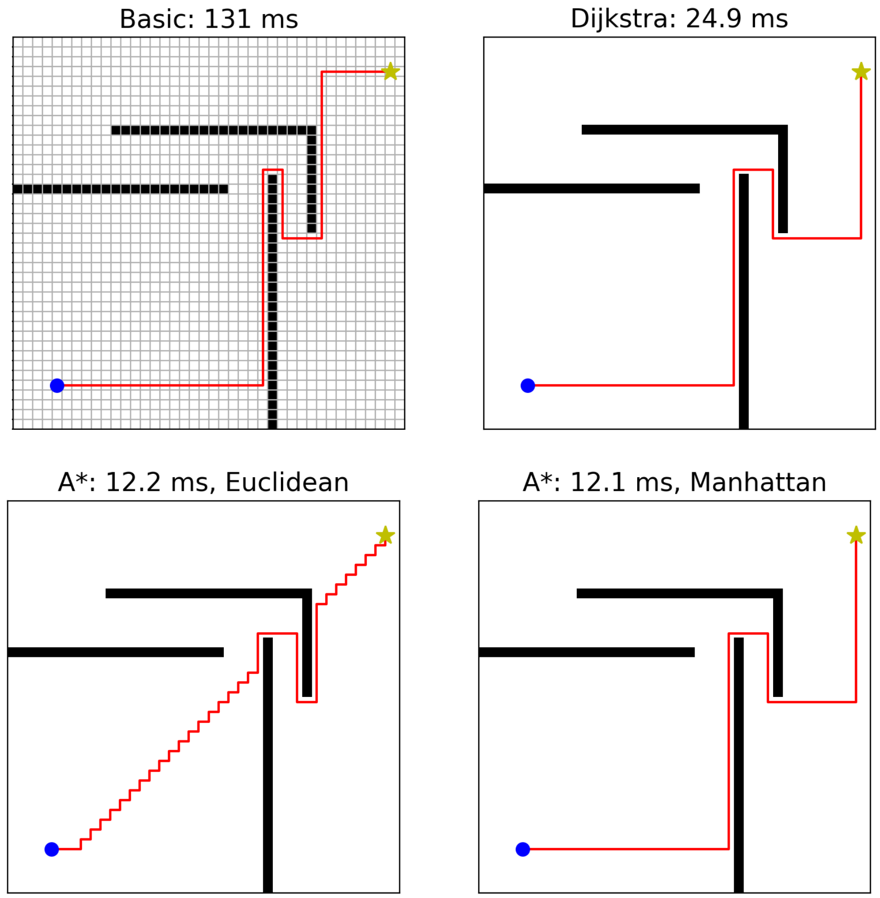

Figure A.4 Examples of the pathfinding solutions to a toy model set on a euclidean grid. The black pixels indicate an inaccessible barrier, white indicates traverse-able area. The red path in the returned 'shortest path' using each algorithm. The blue dot is the given starting location and the yellow star is the final location. The "Basic" pathfinder used is a Breadth-First search, as briefly described in the text. The actual grid of pixels is shown. The pixels are treated as nodes and the edges (not shown) are connections to the top, bottom, left, and right neighboring pixels. This grid was turned off for readability in the other plots. Note that Dijkstra and A* provide increased efficiency in solution time and give equal or better solutions. In the case where the A* heuristic used was the euclidean distance, we see the preference to move along the diagonal between the start and target nodes. Switching to a Manhattan heuristic in which all solutions that move up and to the right have equivalent distance returns the same solution as in Dijkstra.

trying to be found. Note this does not correspond to equal physical area regions and the physical distances between points are highly variable. What it does do, however, is give a natural way of traversing phase-space from the starting to final locations (both of which are given in these angular coordinates), and provide equal time step movements since the motors operate at fixed angular speed. It has the added benefit of being directly relate-able to the movetable that is produced by the collision avoidance algorithms. For example, the movements along phi correspond to constant velocity movements for a given period of time by the phi motor. Multiple heuristics were used, and the best results came from the use of the Euclidean distance, again calculated in angle phase-space (dist= $\sqrt{(\Delta\theta)^2 + (\Delta\phi)^2}$). A modification was introduced to the algorithm, however, that gave an additional cost to changing direction. This I termed an 'inertial' component and corresponded to the real cost associated with the acceleration and deceleration times of the positioner motors, the associated uncertainties in the final positions that come from starting and stopping, and the added complexity and size of the movetables with many direction changes. So the final movement costs were chosen based on: the edge weight (which was distance one for all steps), the heuristic weight (based on the phase-space distance to the target), and the inertial penalty which was zero if the movement was in the same direction as the previous movement in that path, or a calibrated positive value if the direction was different). This is similar in nature to the original heuristic concept except that it is path-dependent and requires accessing the history of the current path being expanded on.

The implementation was written in python as a submodule to the larger *poscollider* module developed for moving the positioners. It utilizes hash based heap-queues to hold and optimally sort the paths such that the shortest is always at the top of the queue. The graph is a dictionary with nodes as keys and a list of (neighbor,cost) tuples as the values of each key. When a path is being searched the most recent node is used as the key to the dictionary, which thus yields all candidates for the next step and the cost to move there. The nodes are defined as a (θ, ϕ) such that the identifier can be used to calculate the numerical heuristic cost. The inertial component is found by finding the direction of movement from the previous node to the current.

The most computationally challenging step is the generation of the graph itself. This requires an understanding of how the angles map to Cartesian space, where the neighboring positioners are, what space the positioner in question would occupy at any given (θ,ϕ), and when that would be a collision with one of the neighbors. Thankfully this can be greatly vectorized and mapped and only requires a Boolean decision of whether a collision will or won't occur. Additional speedups were gained by knowing where a collision could never occur. Once the Boolean map is created, connections are made to all neighboring fibers (including those on the diagonal $\{\theta \pm 1, \phi \pm 1\}$) such that at each node there are eight potential edges to follow. An example of the Boolean map with an overlay of the positioners is shown in Figure A.5.

The inertial cost parameter was tuned to give results that were efficient in both angular distance traveled and number of direction changes required. The Euclidean distance heuristic was selected by the same criteria.

As of writing, the current implementation of this technique holds the neighboring positioners fixed by having them pause for the duration of time required for the current positioner who is avoiding collisions to move to its final, safe location. The code does not allow two neighboring positioners to be given new movetables, which means that all modified movements can be executed at once while the fixed neighbors are paused. The full set of remaining positioners are then able to move to their final locations after their pauses without the issue of running into that original set of positioners who had collisions (or one another as by definition they didn't collide when first checked and still moving in unison). Prior to this a second iteration is done to correct further collisions (that may take place after an earlier collision with a different positioner). Afterward any remaining collisions are solved with the 'Full Stop' algorithm already described such that the pauses may actually last for two or three sets of avoidance moves until the original subset of collisionless movetables is executed.

A final note is that all of the descriptions above refer to corrections for the "retract" phase of the RRE method. The rotate method give no possibility of collision by construction. In the "extend" phase, all starting positions and targets are switched and moves calculated as though it were a "retract" step as described above. The moves are then reversed, with all time reversals and negatives accounted for, and pauses prior to movements turning into post-movement pauses, etc.

A.4 Summary

A.4.1 Future Outlook

In this appendix, I have described the work done to enable a revolutionary instrument to take unprecedented amounts of astronomical spectra over the course of the coming years. The technical challenges have been immense and this is only one tiny

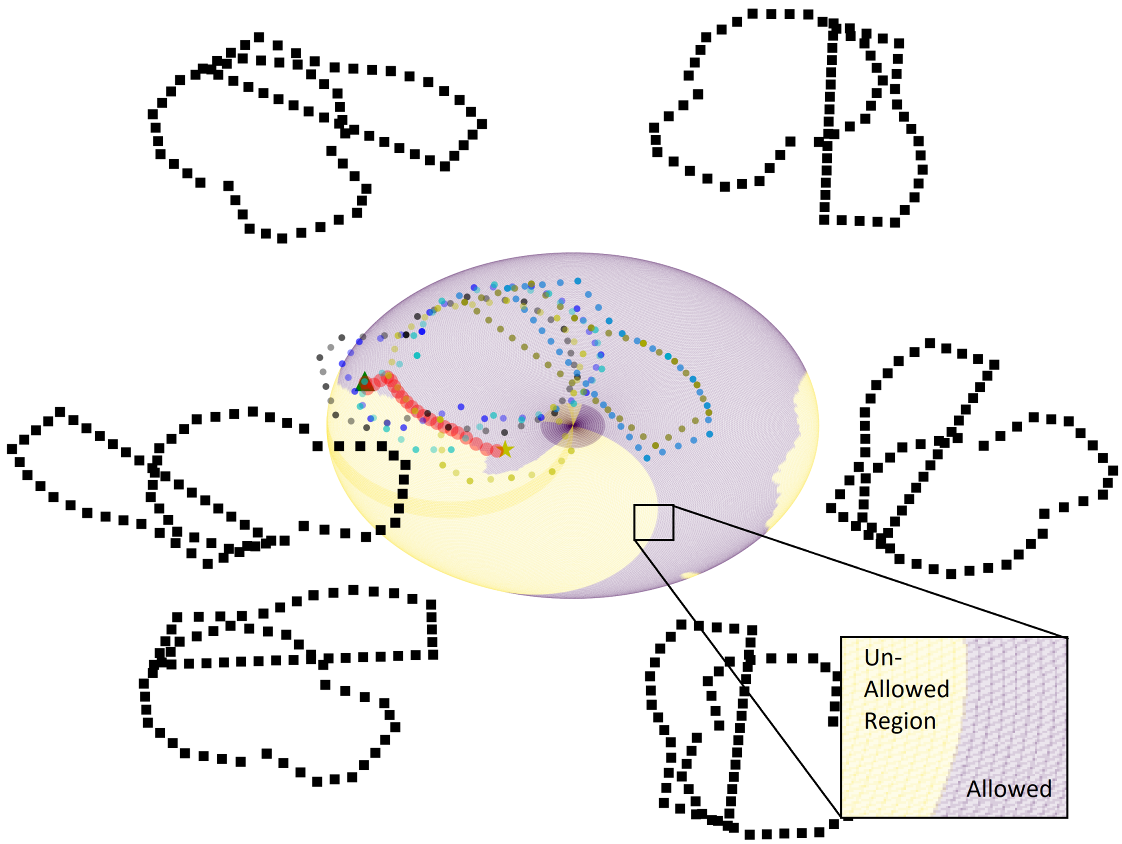

Figure A.5 Example of the A* algorithm's solution to a realistic simulation of a fiber positioner trying to move from an initial location (green triangle) to a final location (gold star). The red dots show the path taken. The purple and cream colored circle is the grid that the pathfinding algorithm traversed, with cream being regions that it was not allowed to enter and purple being the allowed regions. The black dotted figures are representations of the neighboring positioners. The colored, dotted figures are "time snapshots" of the central positioner at several points in its movement from the start to the target. Note that all of the exclusions are based on the fiber location. The exclusion of the region at the bottom of the figure in cream is because the location would require the inner theta body of the moving positioner to collide with the neighbor on the left who is paused within the patrol region.

part. However, without any of those pieces, the system could not work. What has been completed so far is sufficient but not optimal. The A* algorithm coupled with RRE is the an excellent approach, but the implementation could use additional optimization. In order to speed up calculations, some approximations of the positioner geometry were taken and that led to less-than-ideal outcomes in which corrected paths still failed subsequent tests. These are especially visible near boundaries where the boundary conditions need to be better incorporated. The computational time needed to compute the new move tables is within specifications for one petal of 500 positioners, but would either need to be run on 10 processors in parallel or further optimized to complete in the $\mathcal{O}$(mins) desired for the computations. Finally, the total move times with multiple pausing steps exceeds the specifications for total move times of all positioners between exposures. Thus work needs to be done to aggregate pauses and movements after all collisions are avoided to reduce time in which only a few positioners are moving and all others are forced to wait. These avenues plus additional features such as allowing for the simultaneously movement of the neighbors while the avoidance A* paths are being made are areas of current research for colleagues at LBL. While some are more pressing than others, each would have distinct benefits to the efficiency of the survey.

A.4.2 Closing Remarks

The Dark Energy Spectroscopic Instrument went on sky in the Fall of 2019, with current commissioning tasks already being performed at the Mayall Telescope and in the laboratories at LBL. The collision avoidance is deeply embedded in the instrument's infrastructure as the software that generates the move-readable code that allows the positioners to move from one location to another. Moving fibers smaller than a human hair from pointing at one speck of light in the sky to another, as the celestial sphere rotates above. The complexity and inter-connectivity are immense, but hopefully this has given a self-contained understanding of how the collision avoidance system operates.

Appendix B

M2FS Dataset: Derived Quantities

B.1 Target Histograms

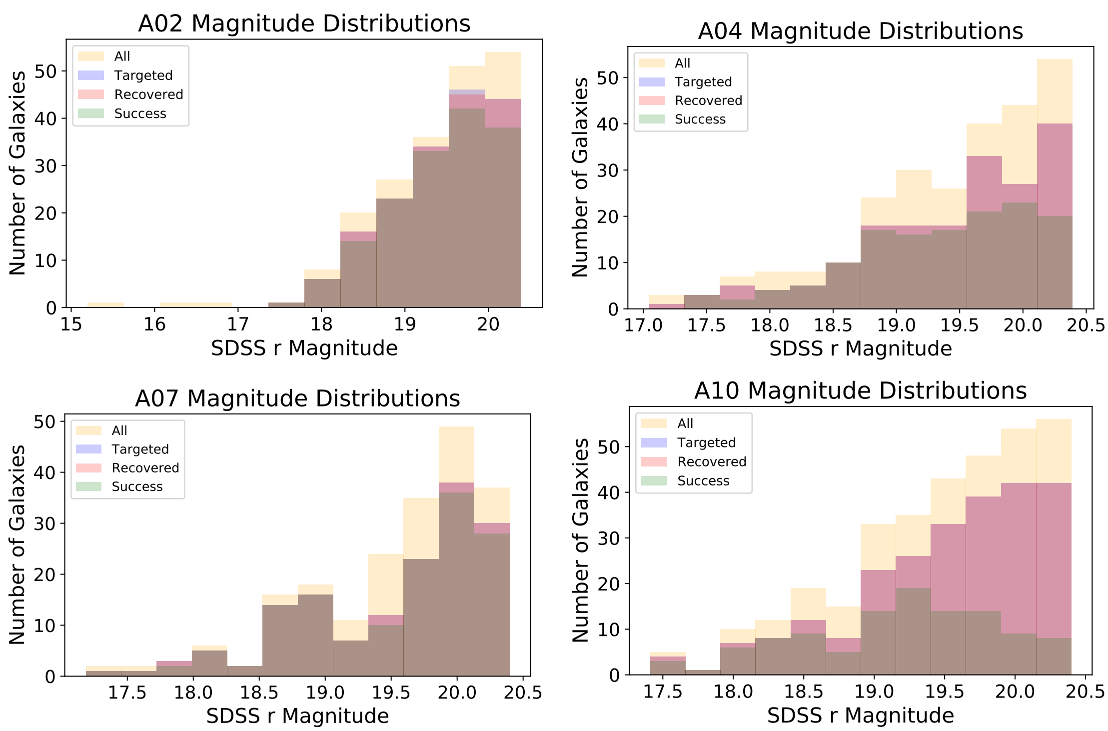

Figure B.1 Histograms showing the magnitude distributions of the selected, targeted, recovered redshift, and successfully recovered redshift samples.

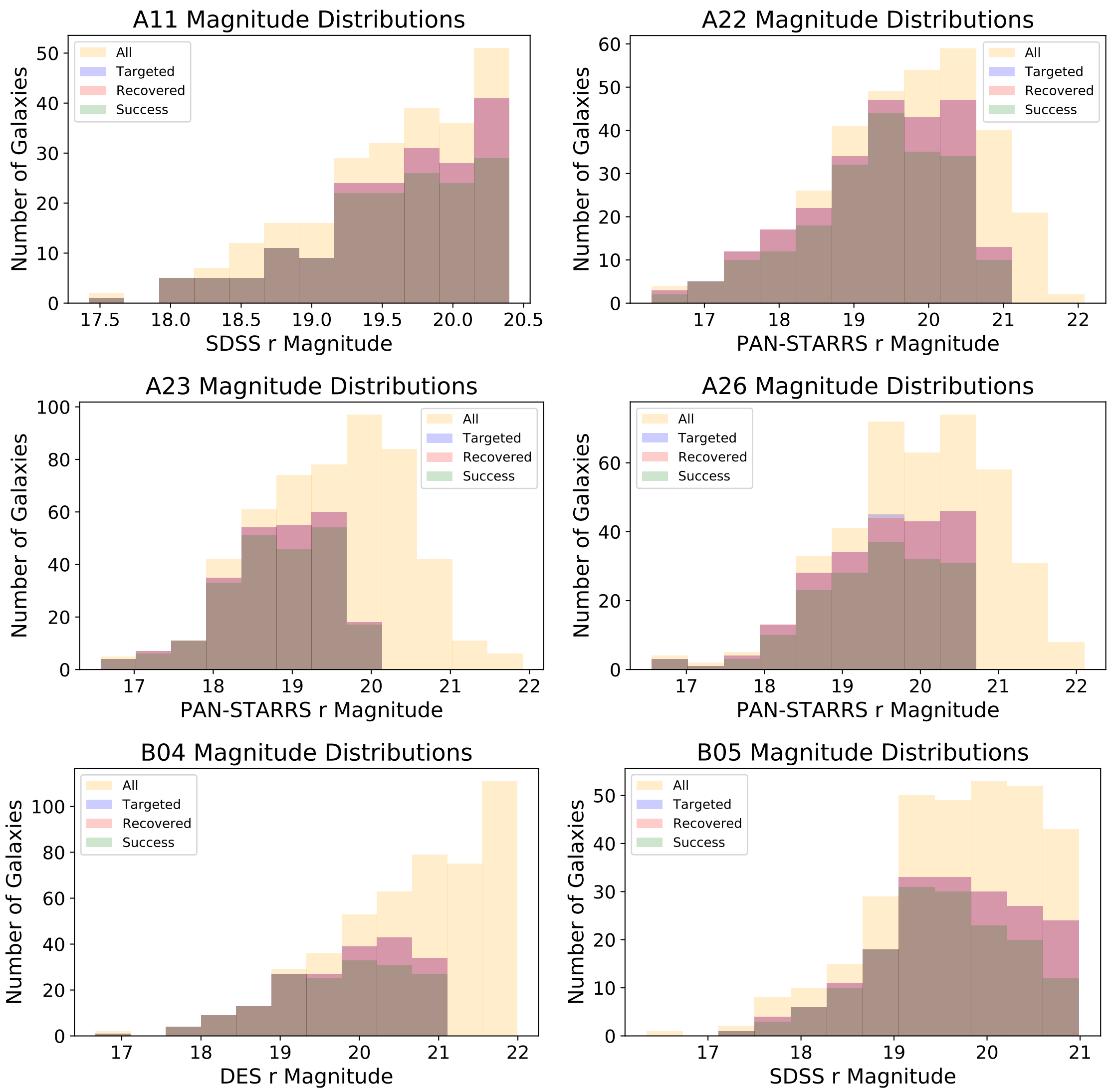

Figure B.2 A continuation of Figure B.1.

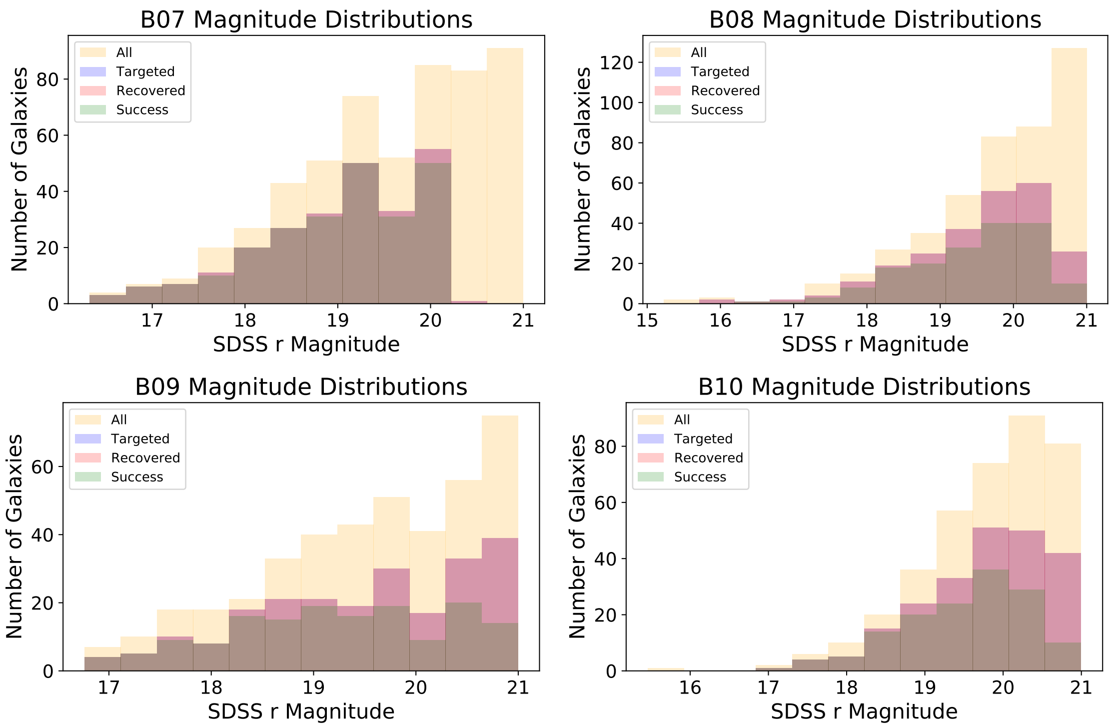

Figure B.3 A continuation of Figure B.1.

B.2 Sky Positions

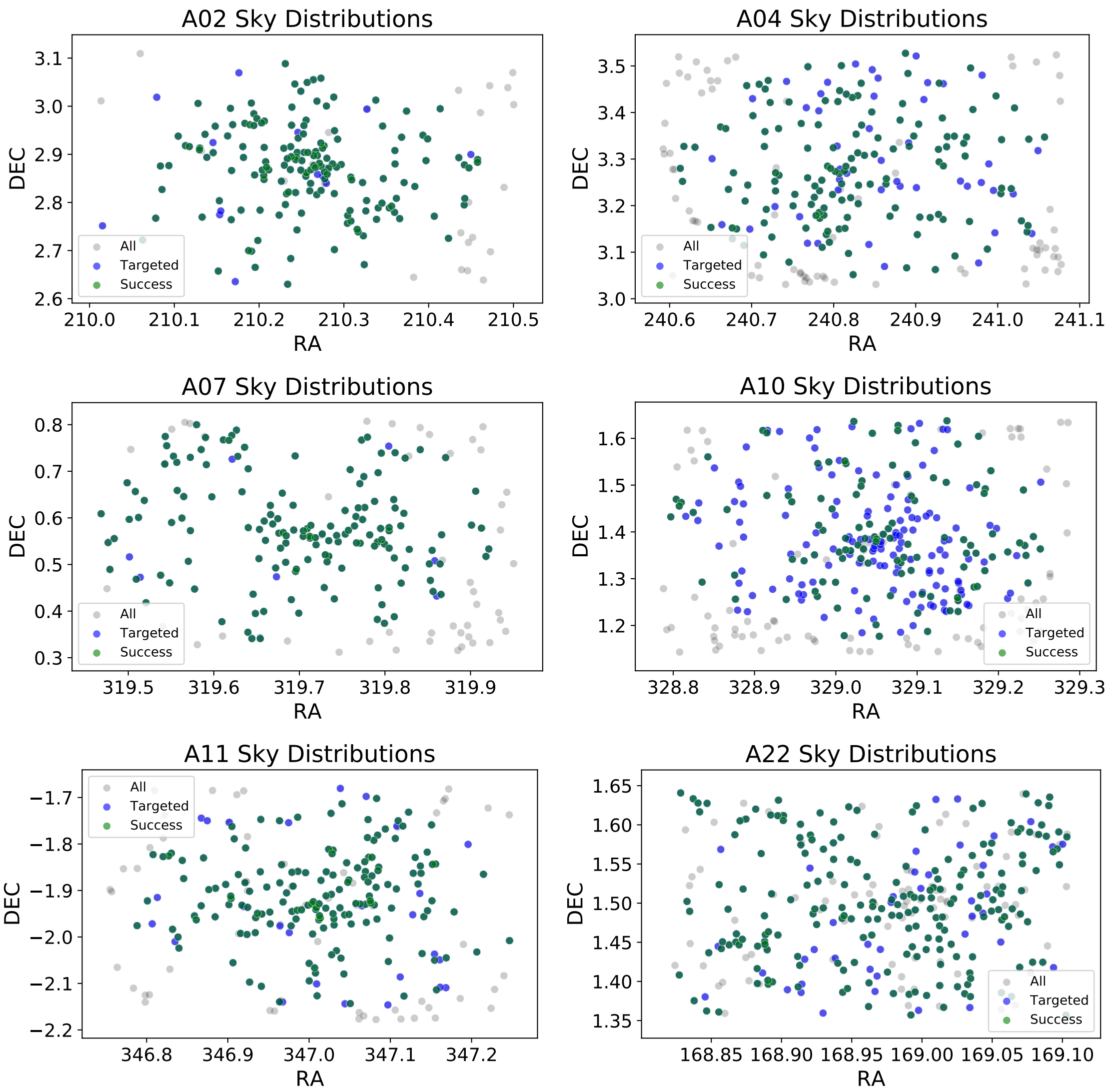

Figure B.4 Sky positions of the selected sample, targeted sample, and successfully recovered redshift sample.

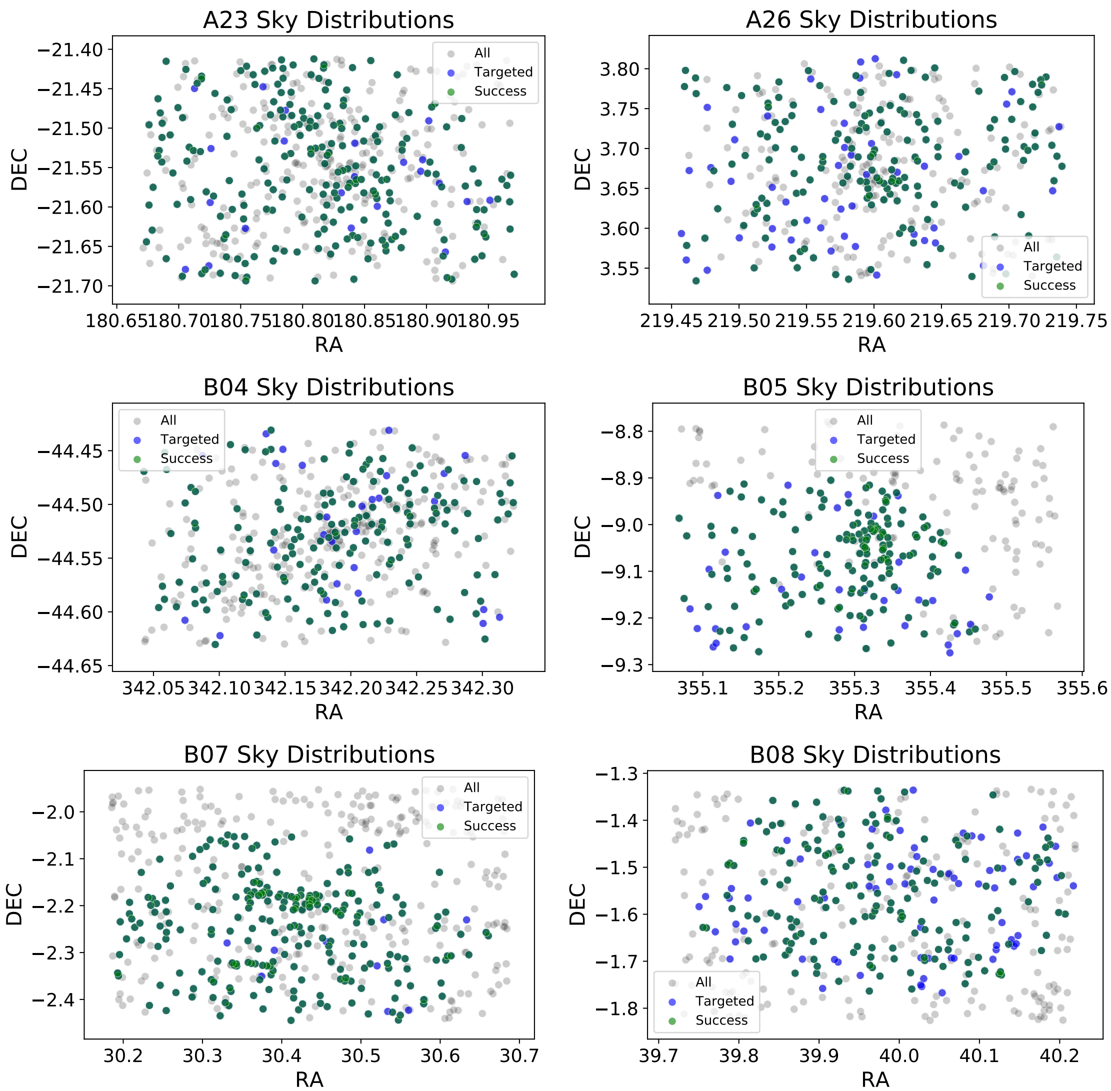

Figure B.5 A continuation of Figure B.4.

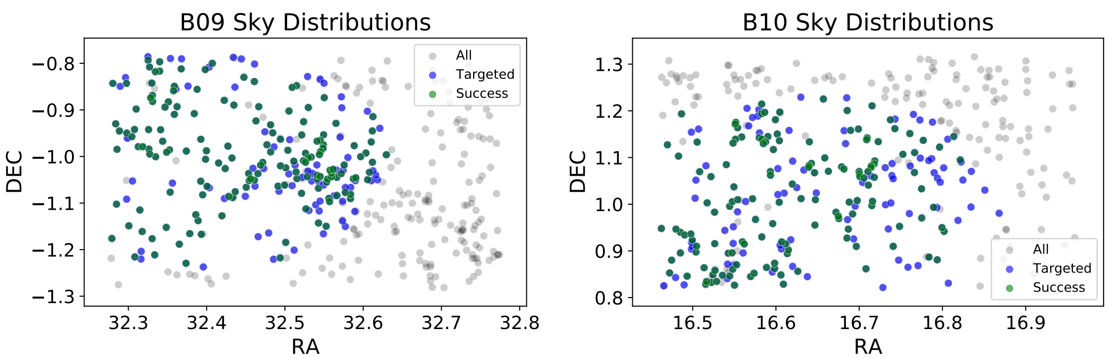

Figure B.6 A continuation of Figure B.4.

B.3 Correlations versus Magnitude

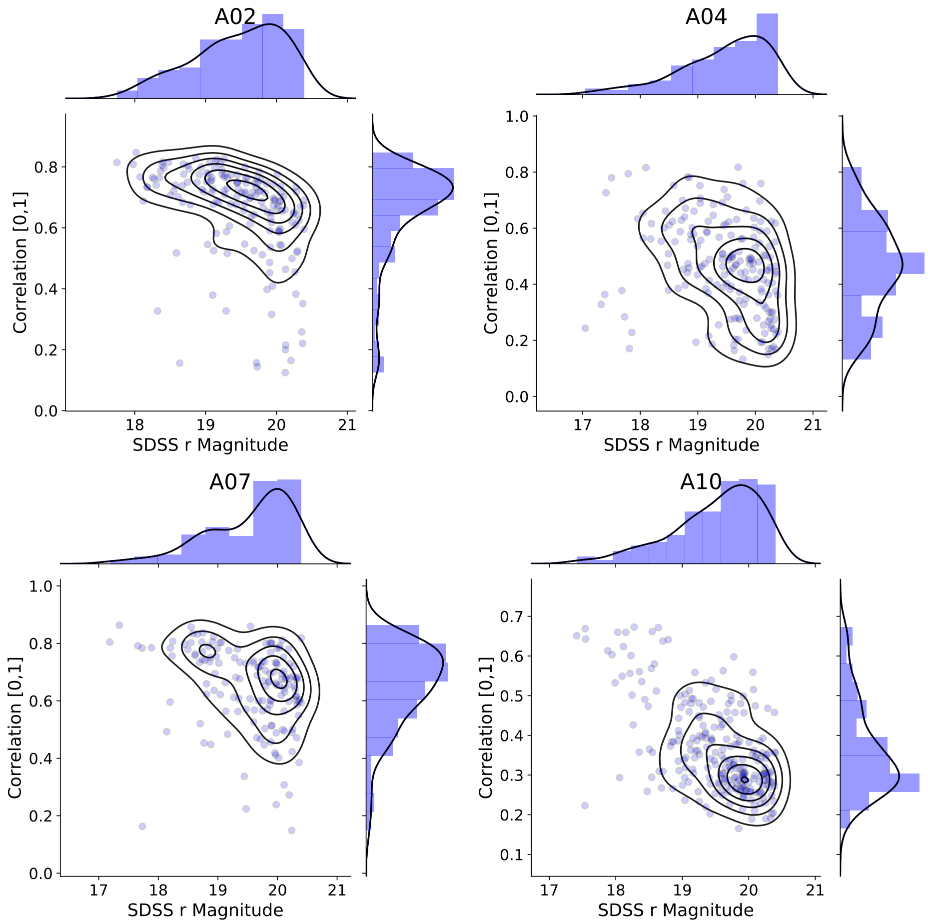

Figure B.7 Cross correlation Pearson-r coefficient versus r-band magnitude for galaxies in the sample. The coefficient is with respect to one of two SDSS template spectra with early type galaxy forms. The histograms show summations along the given axis, with smoothed fit lines overlaid.

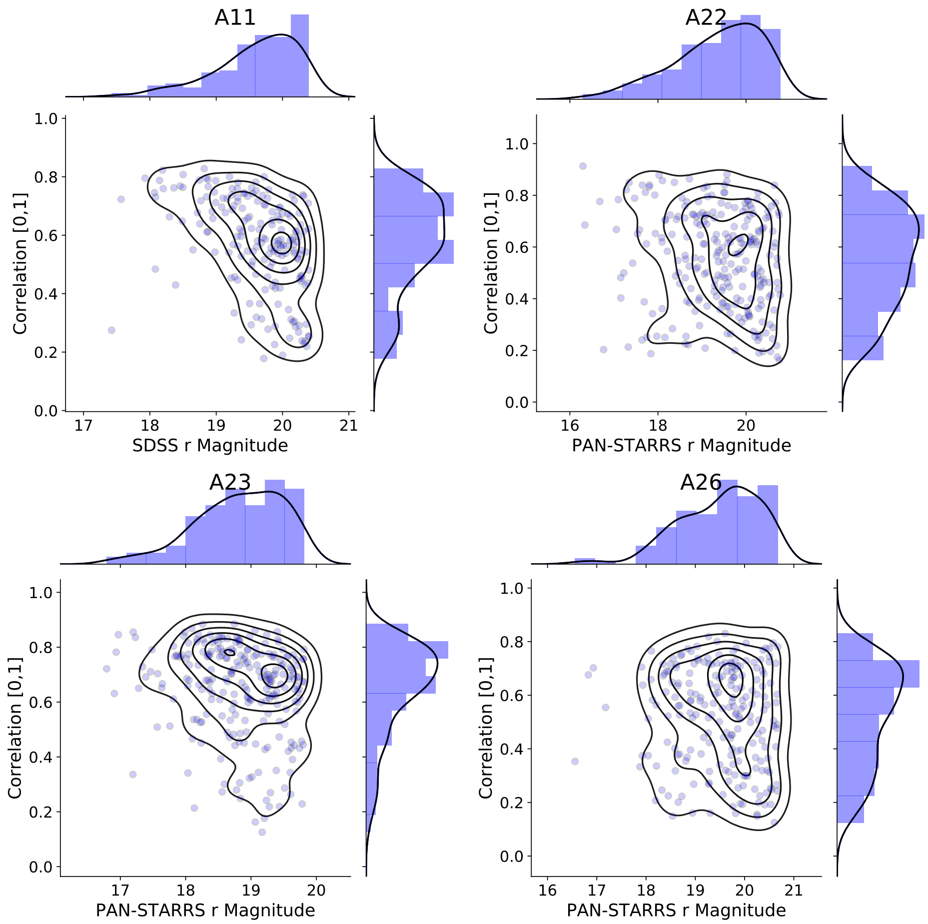

Figure B.8 A continuation of Figure B.7.

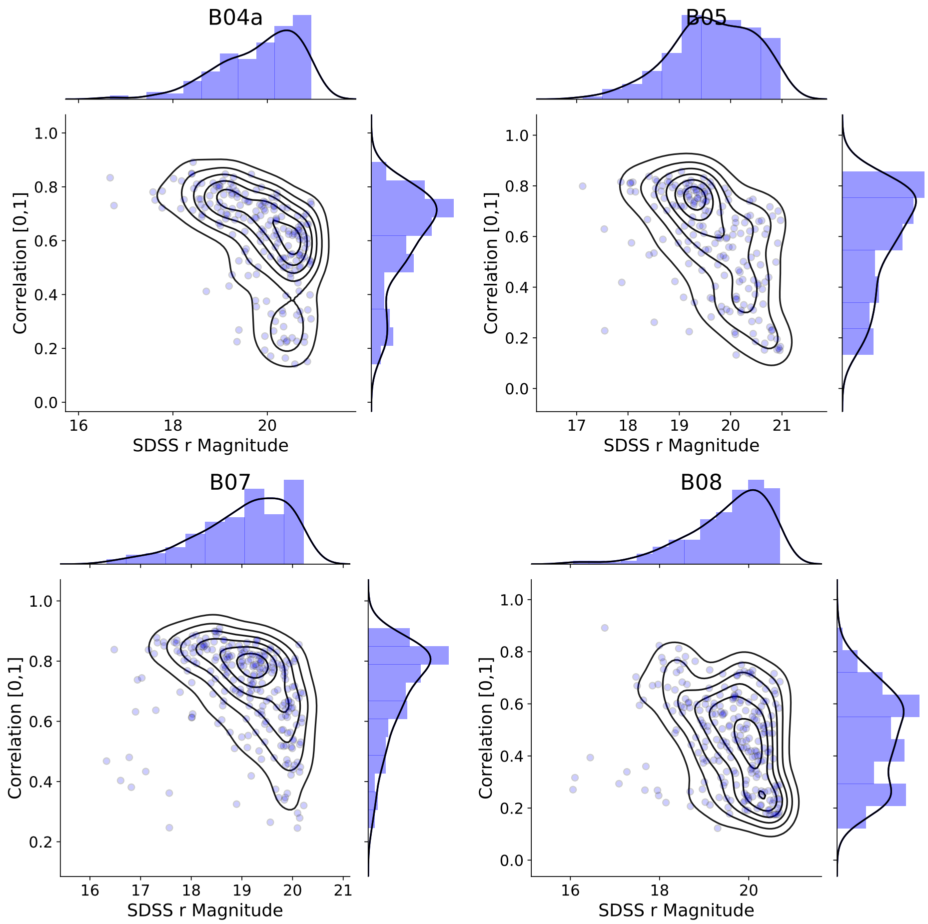

Figure B.9 A continuation of Figure B.7.

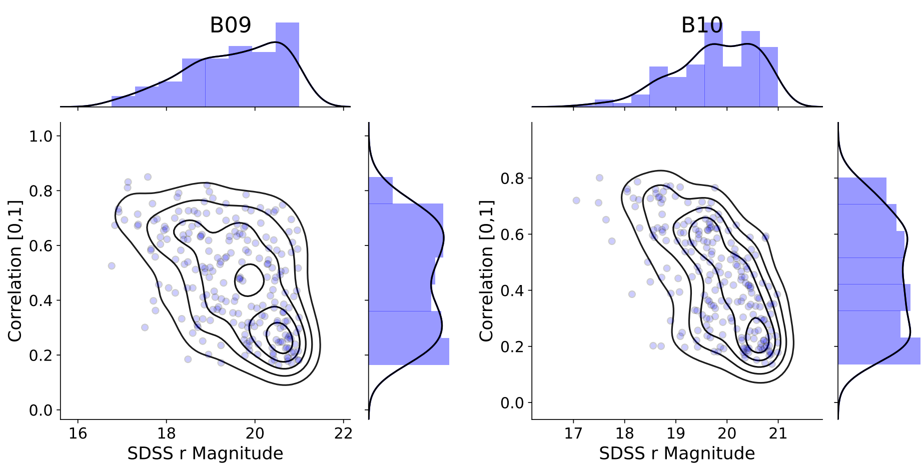

Figure B.10 A continuation of Figure B.7.

B.4 Correlations versus Magnitude versus S/N

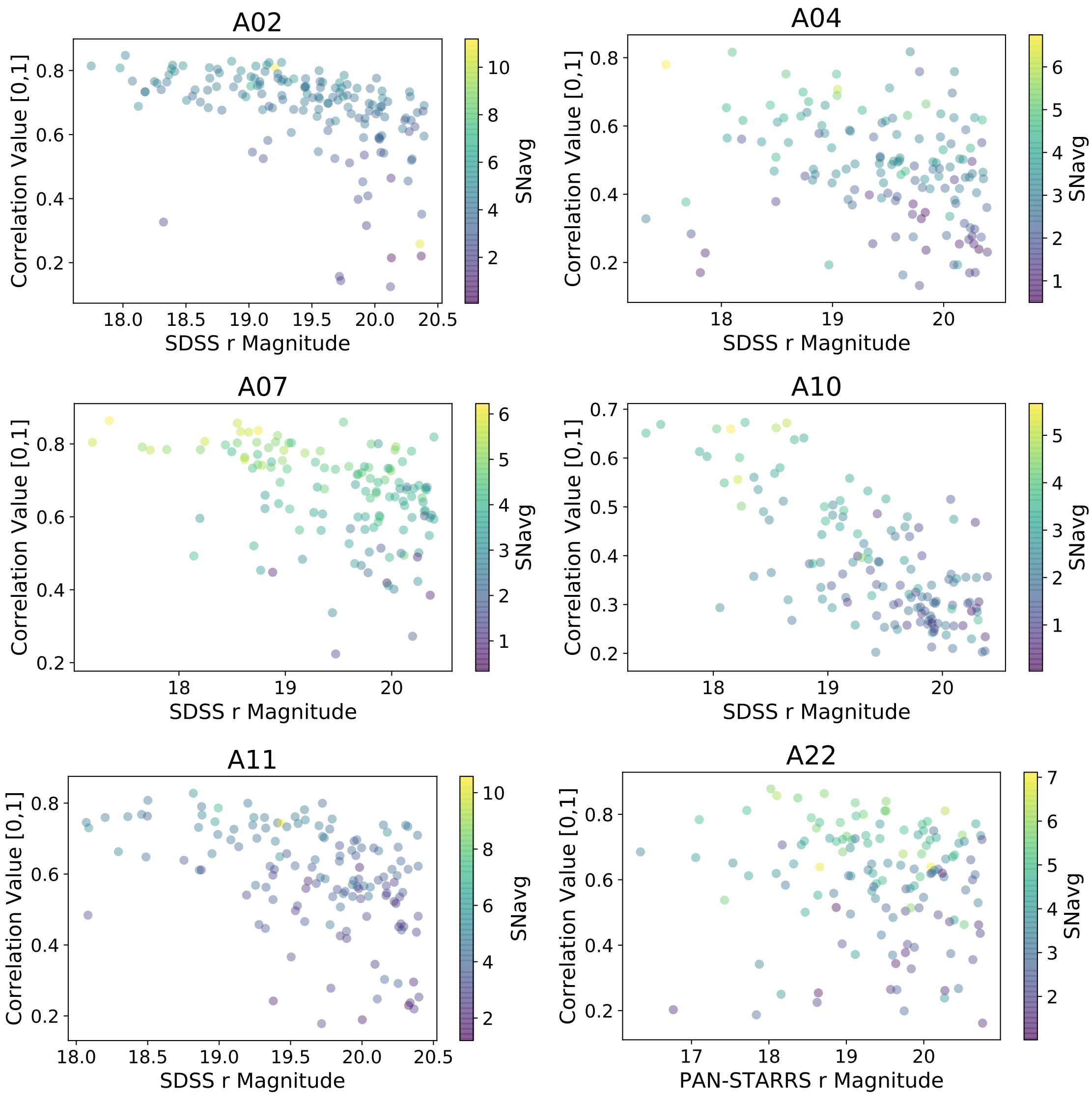

Figure B.11 Pearson-r cross correlation coefficient versus r-band magnitude for all galaxies in the sample. The color represents an estimate of signal-to-noise based on the average of three prominant absorption lines in early type galaxies (Calcium H, K, and G lines).

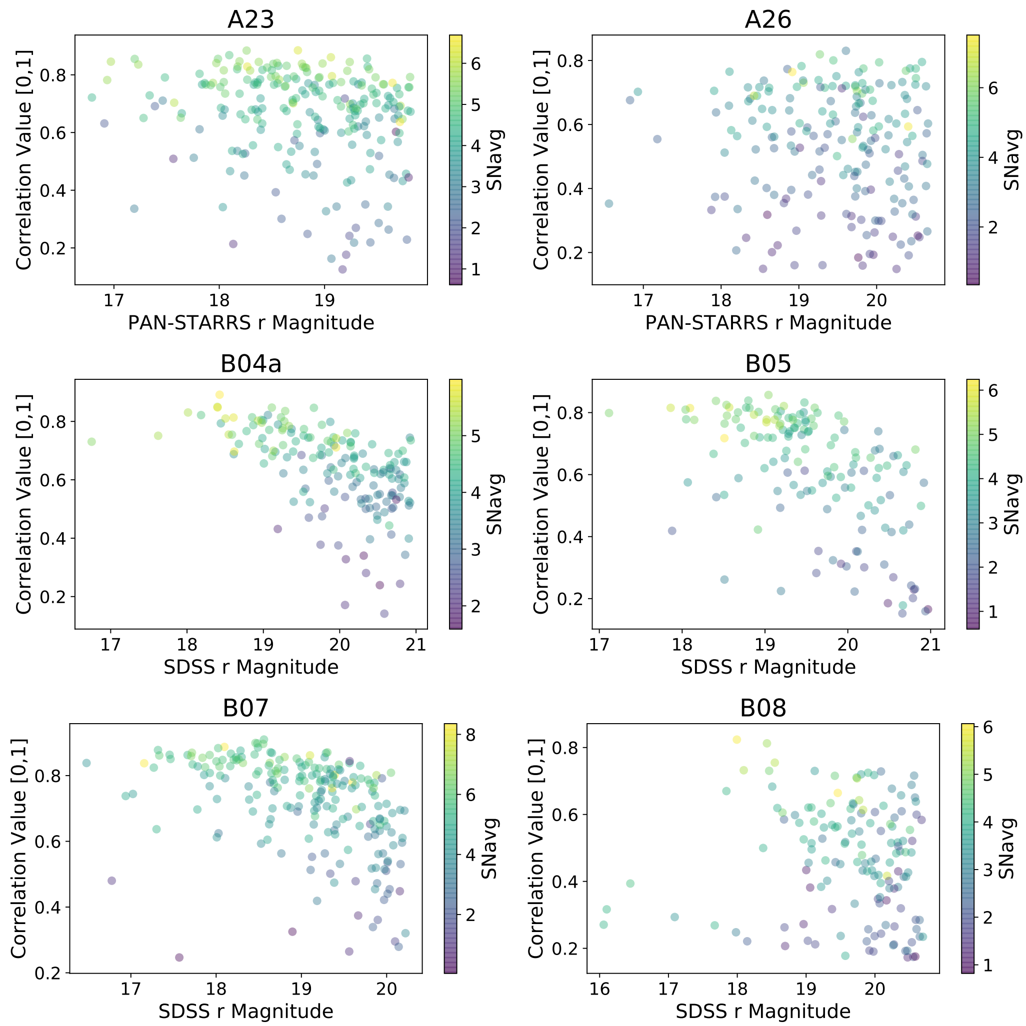

Figure B.12 A continuation of Figure B.11.

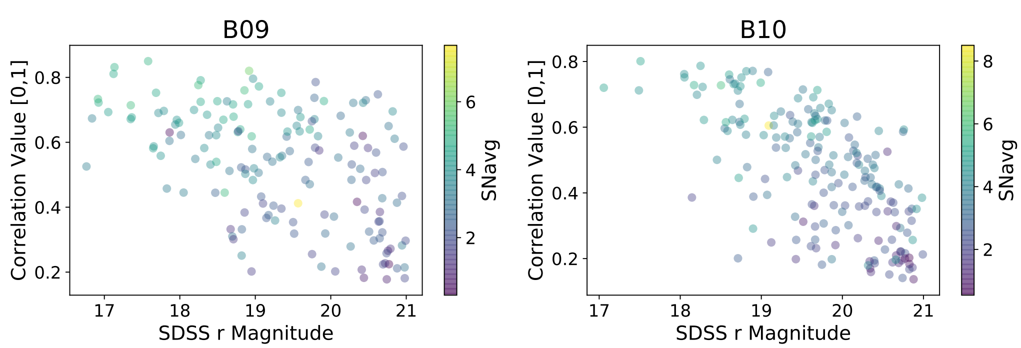

Figure B.13 A continuation of Figure B.11.

B.5 Correlations versus Magnitude versus z

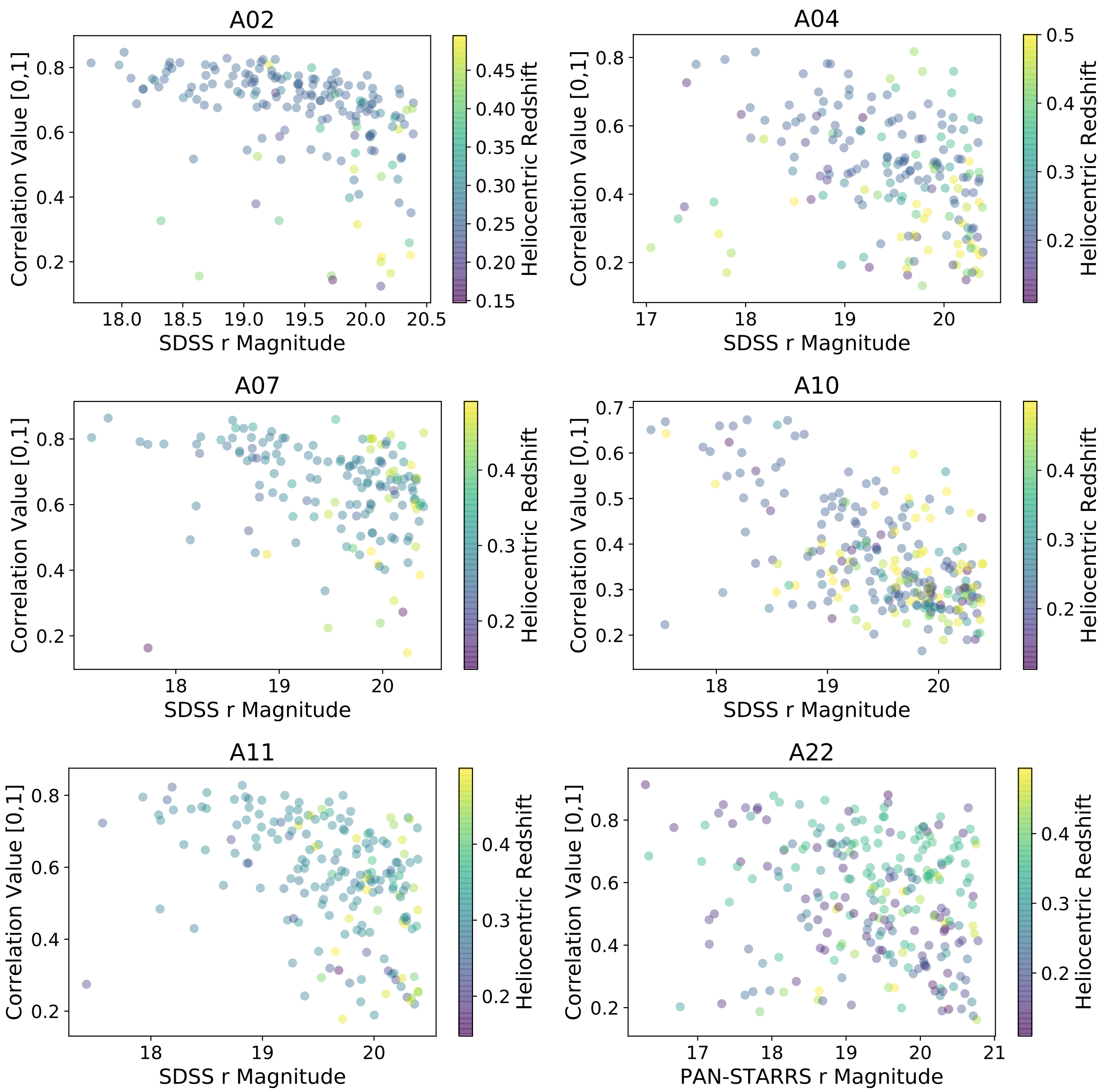

Figure B.14 Pearson-r cross correlation coefficient versus r-band magnitude for all galaxies in the sample. The color represents the heliocentric redshift estimate of each galaxy.

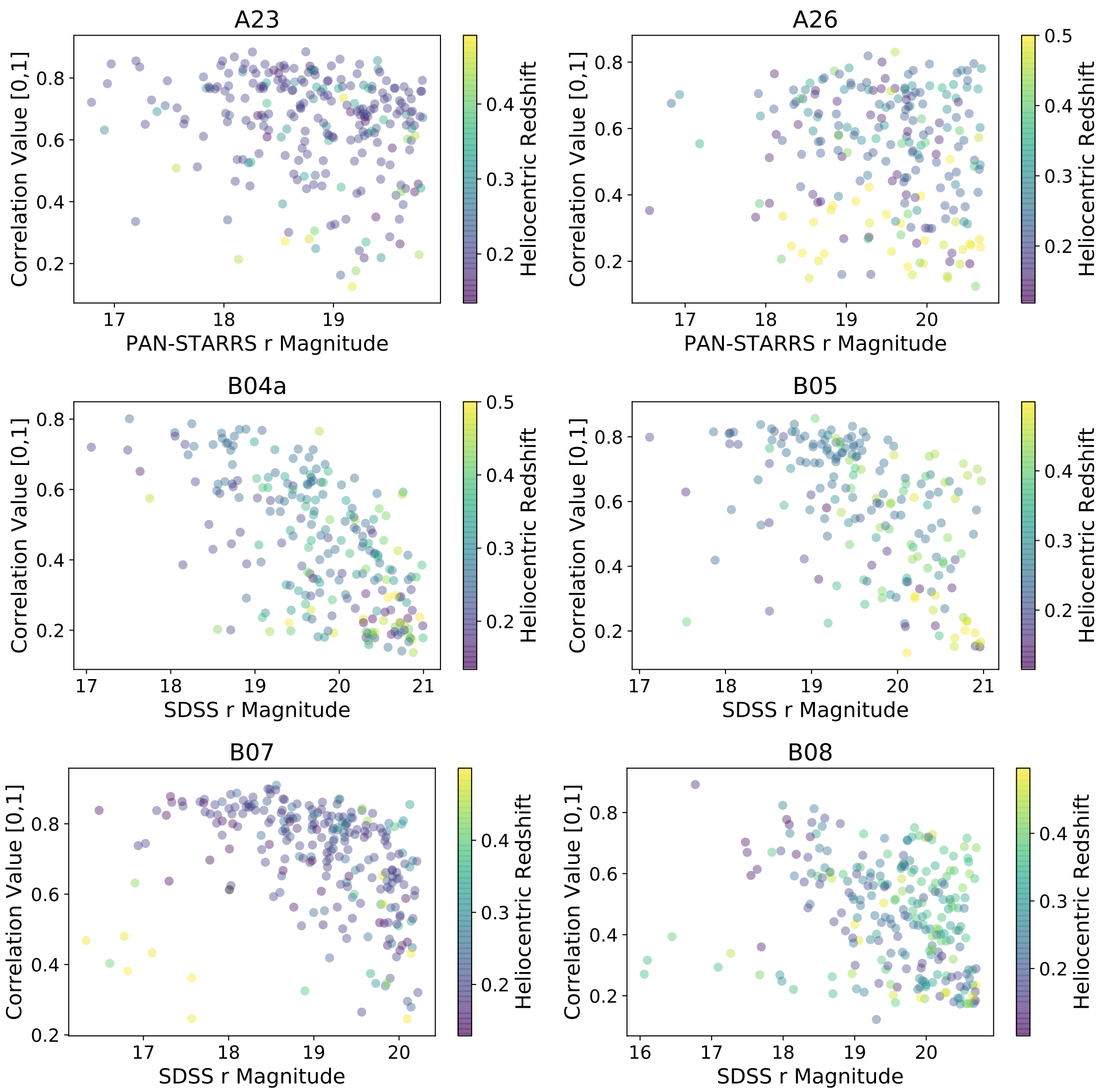

Figure B.15 A continuation of Figure B.14.

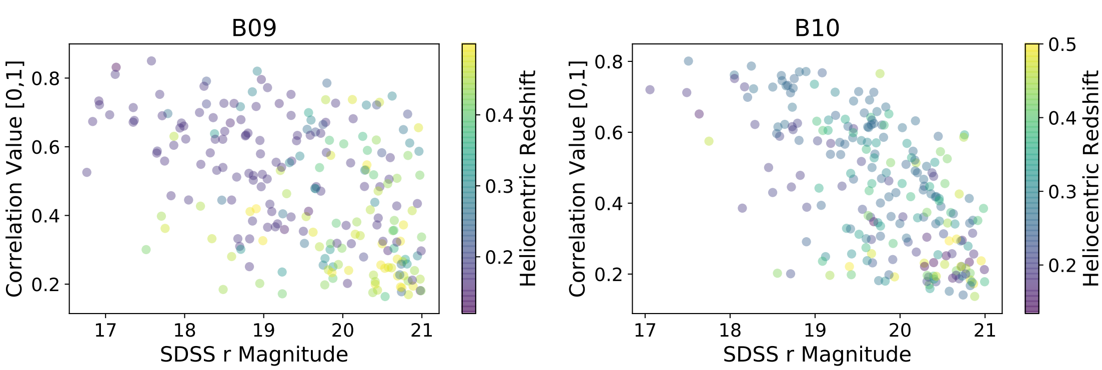

Figure B.16 A continuation of Figure B.14.

B.6 Redshift Success versus Magnitude

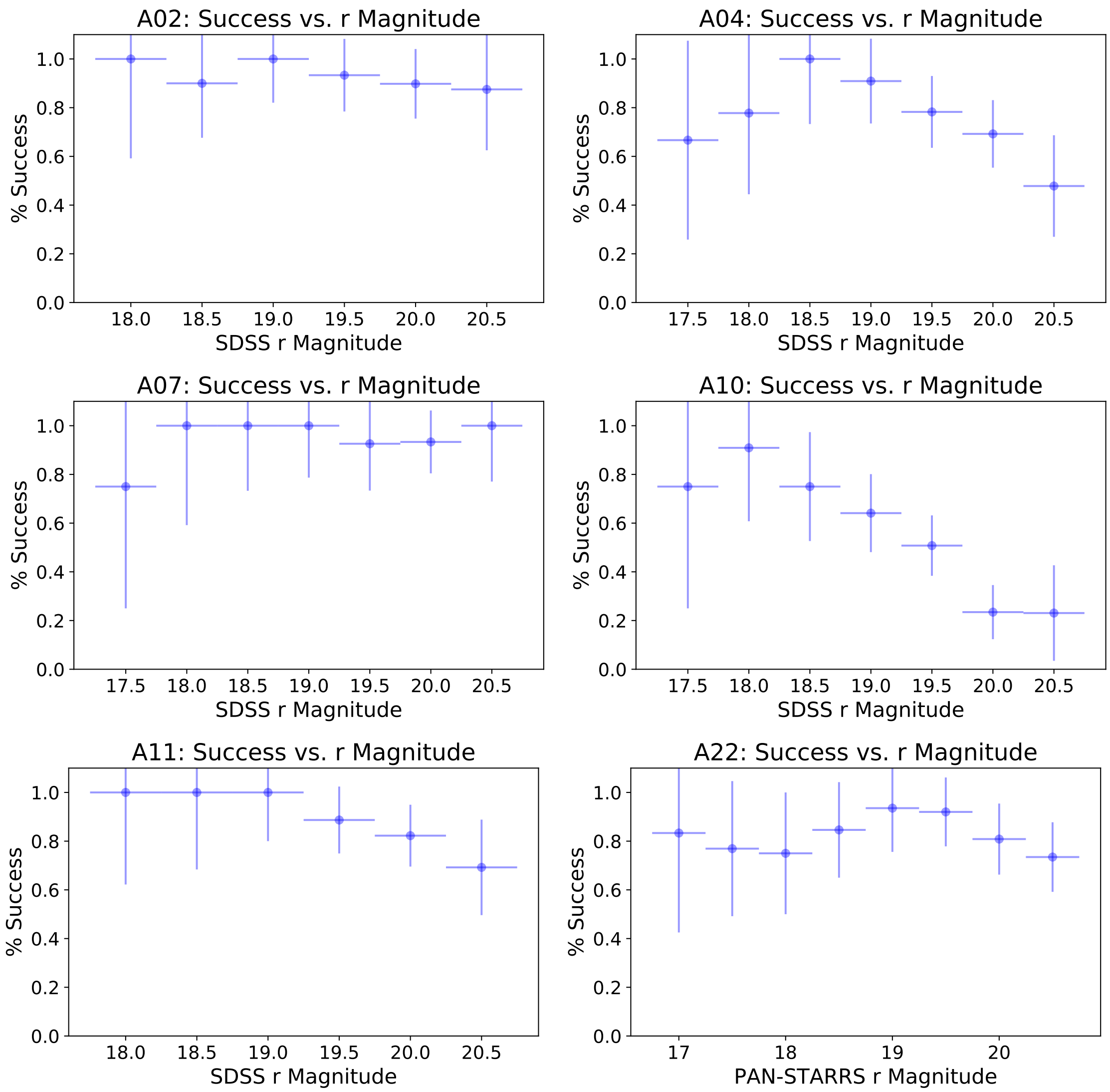

Figure B.17 Showing redshift success rate as a function of r-band magnitude of the galaxies.

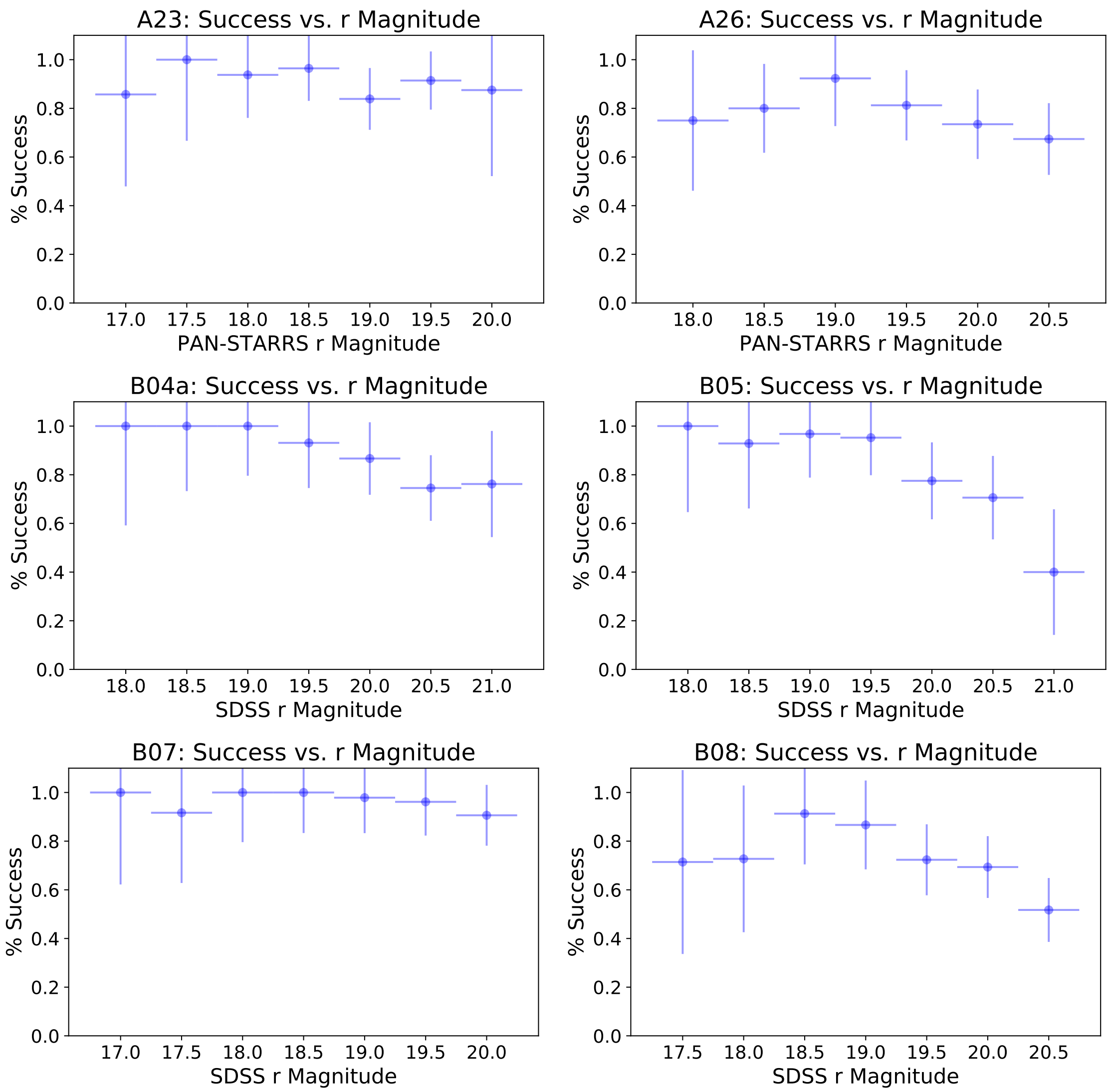

Figure B.18 A continuation of Figure B.17.

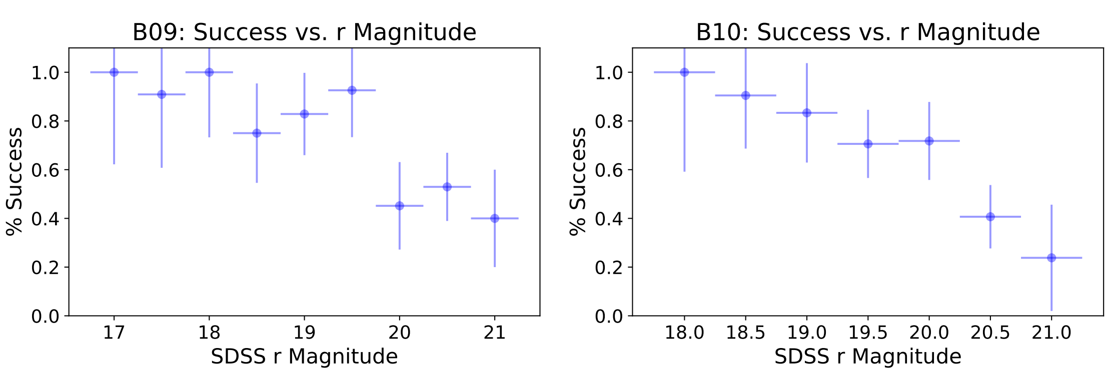

Figure B.19 A continuation of Figure B.17.

B.7 Redshift Success versus Redshift

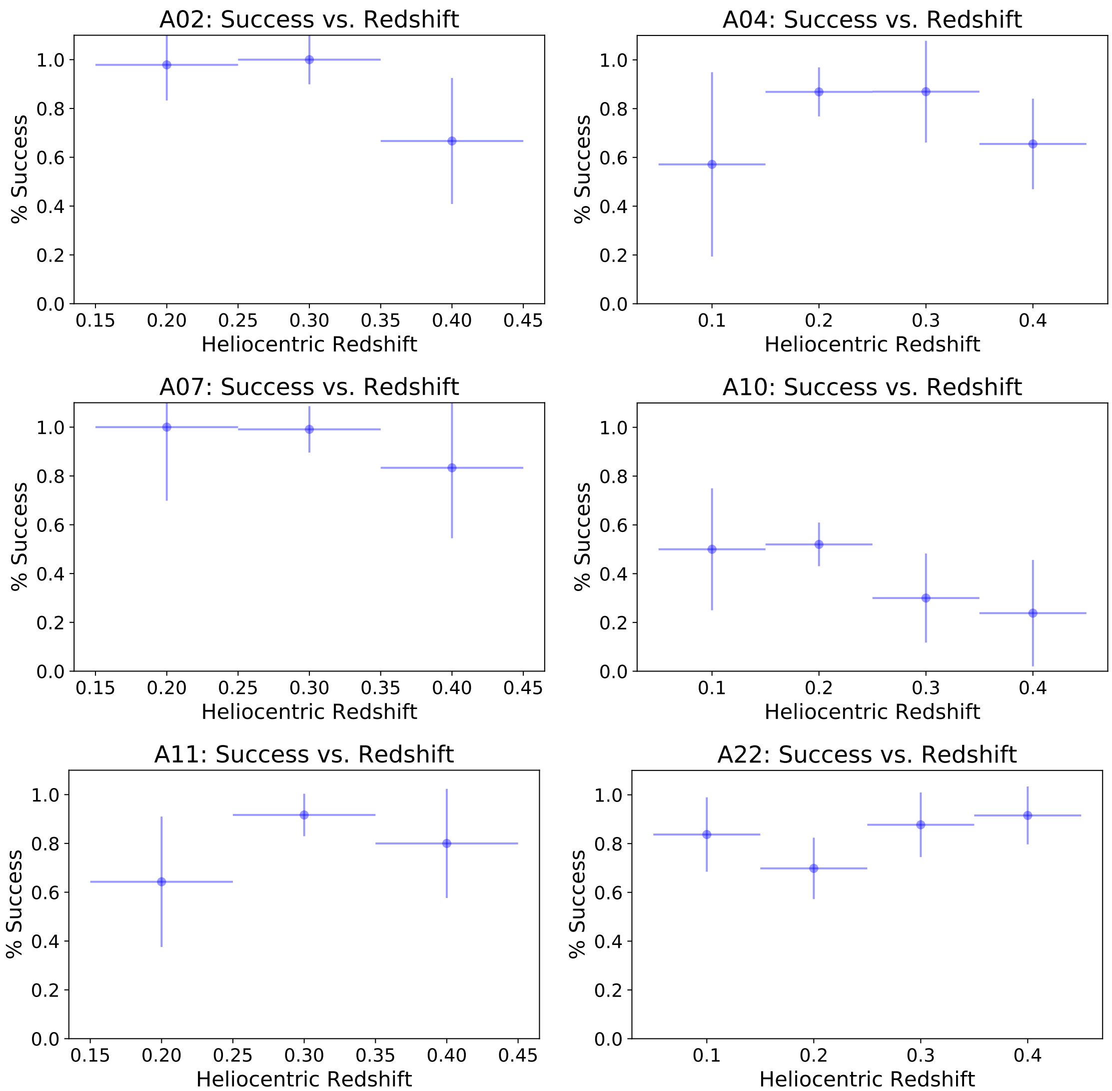

Figure B.20 Showing redshift success rate as a function of the recovered redshift of the galaxies.

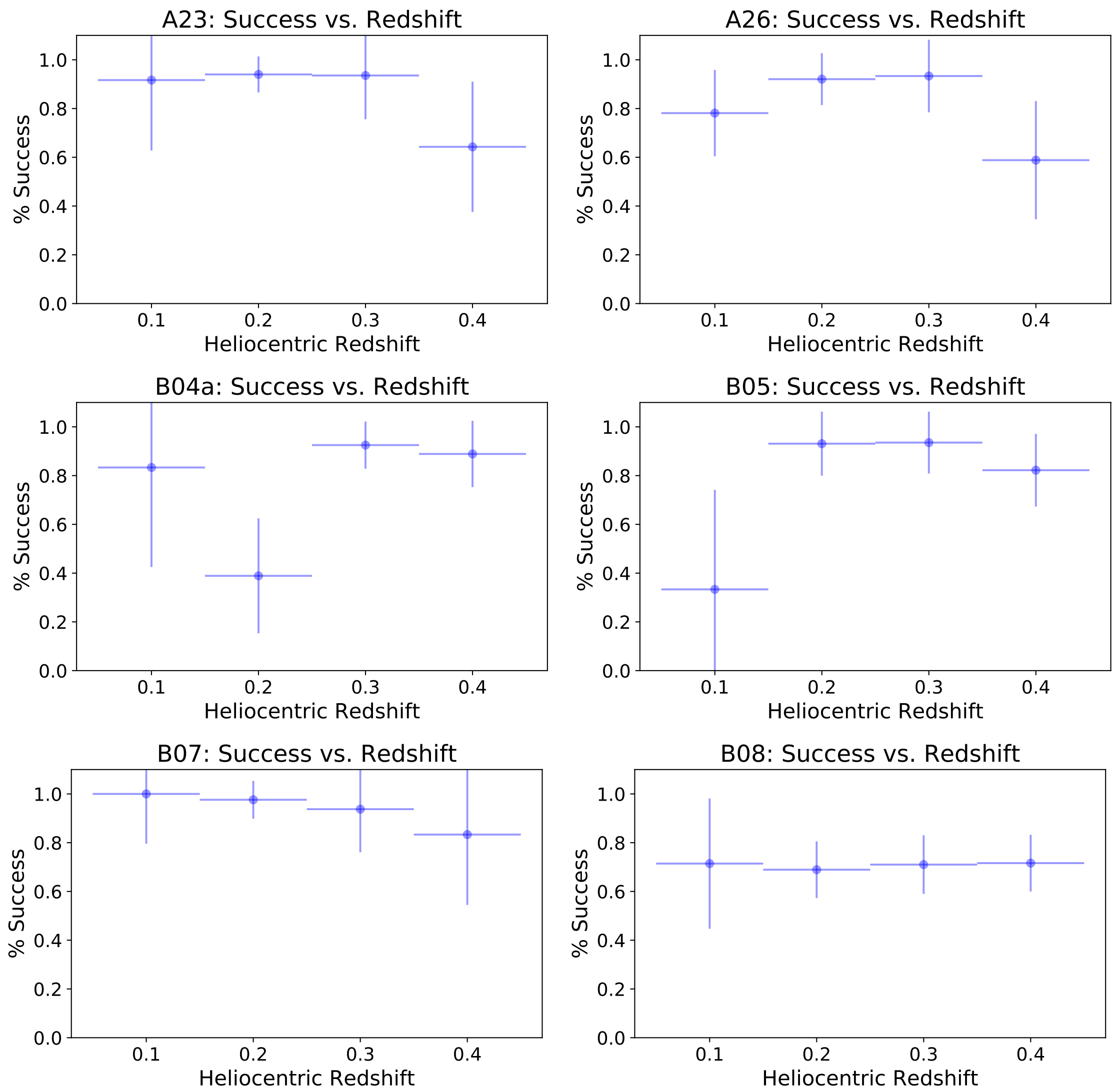

Figure B.21 A continuation of Figure B.20.

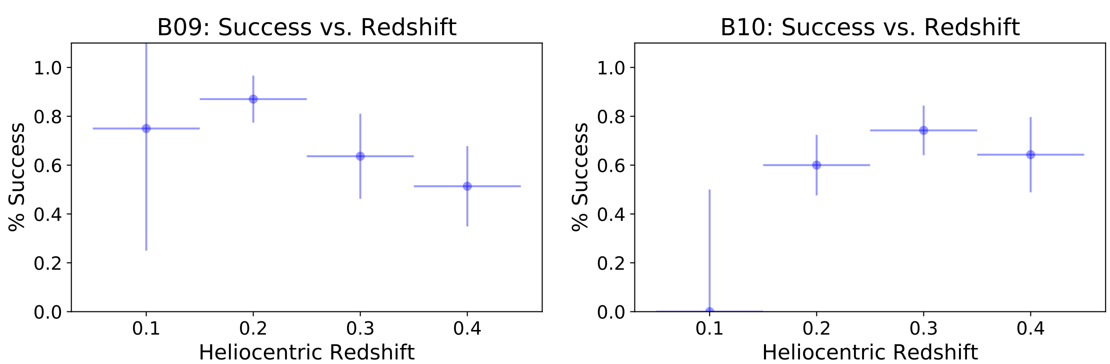

Figure B.22 A continuation of Figure B.20.

B.8 Velocity Dispersions

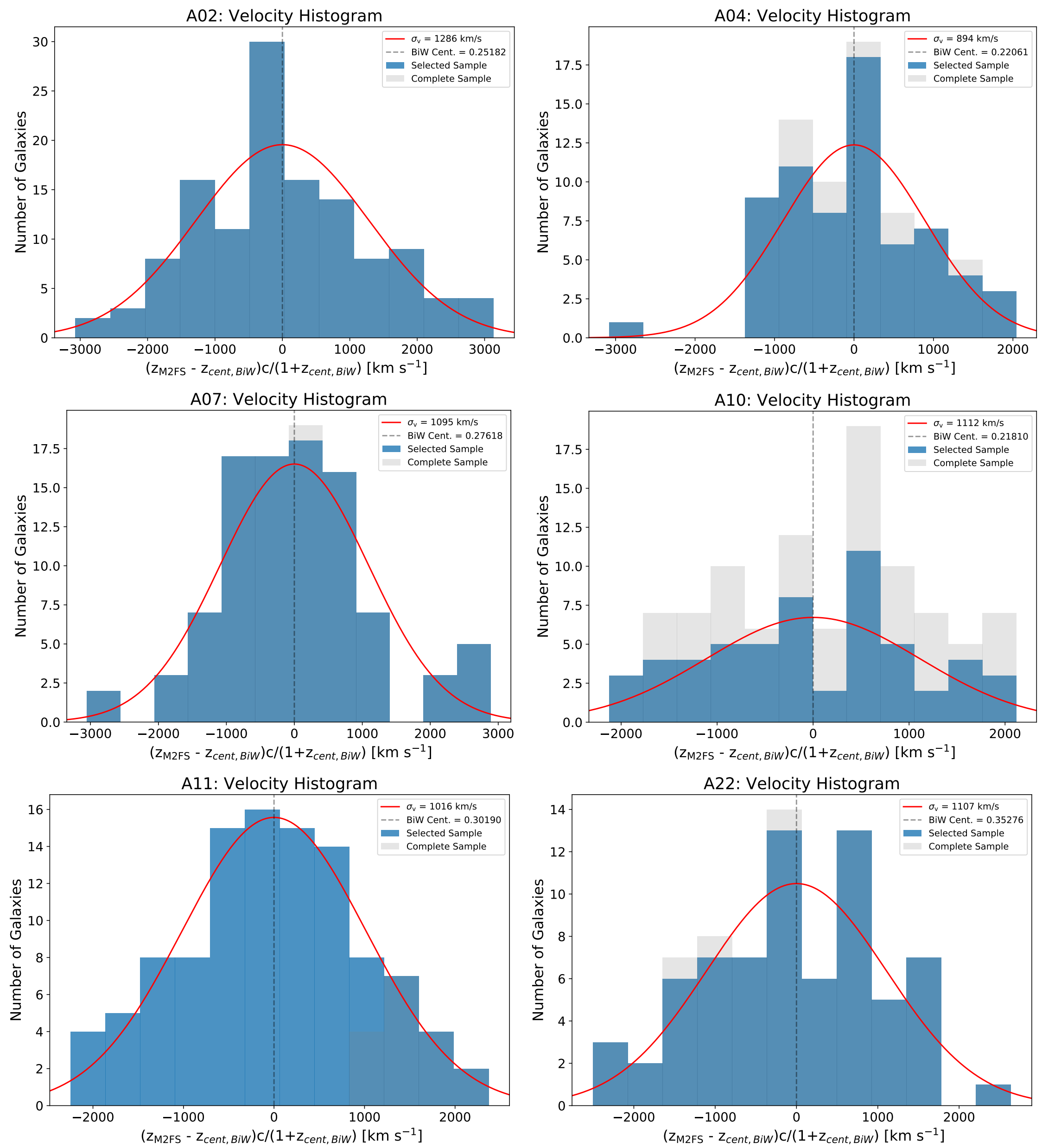

Figure B.23 The velocity histograms for all masks in the sample. The zero velocity is the biweight central value calculated given the distributions of velocities. This is robust to outliers, but is still inevitably affected by outliers (projected field galaxies) and substructure.

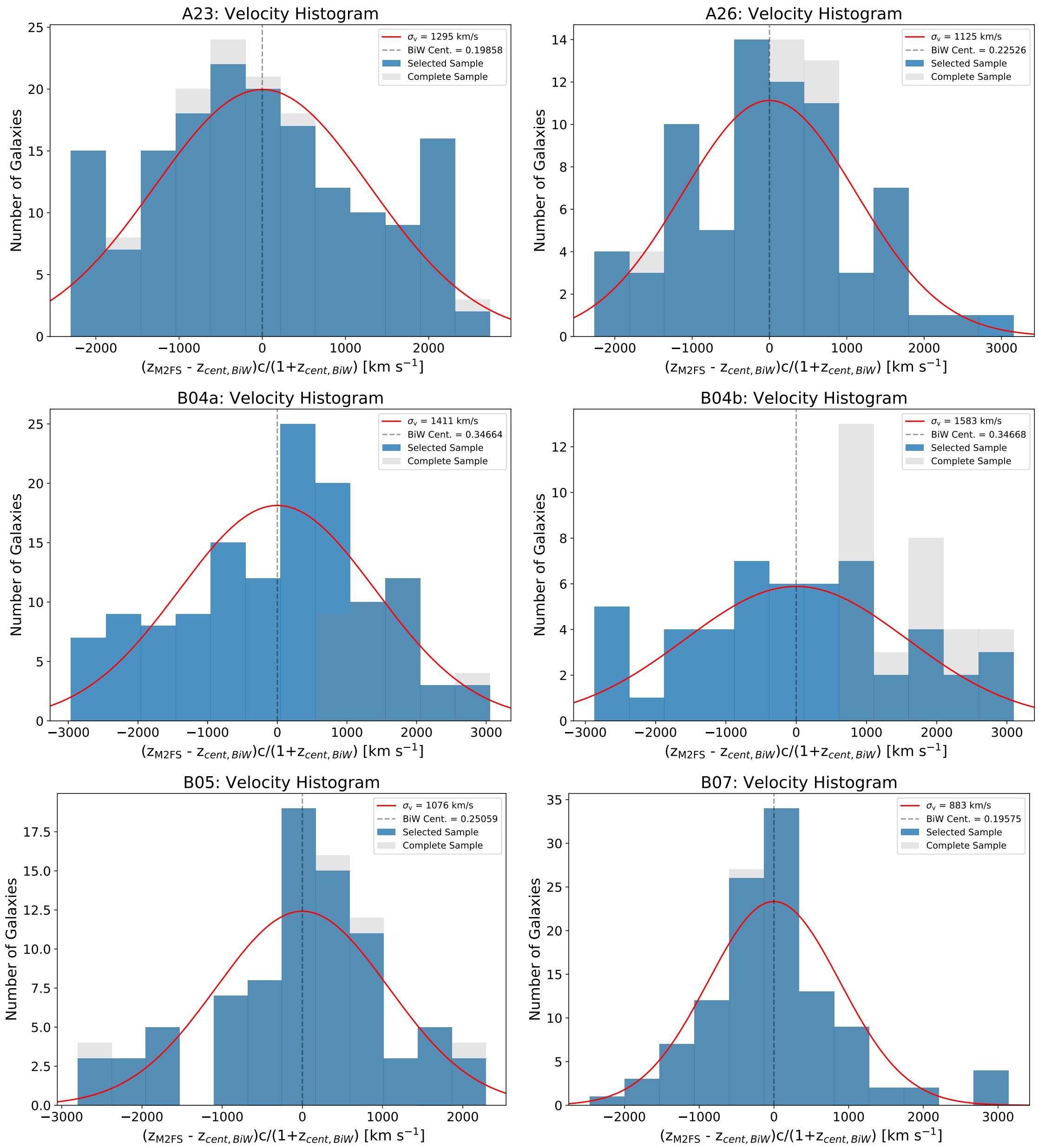

Figure B.24 A continuation of Figure B.23.

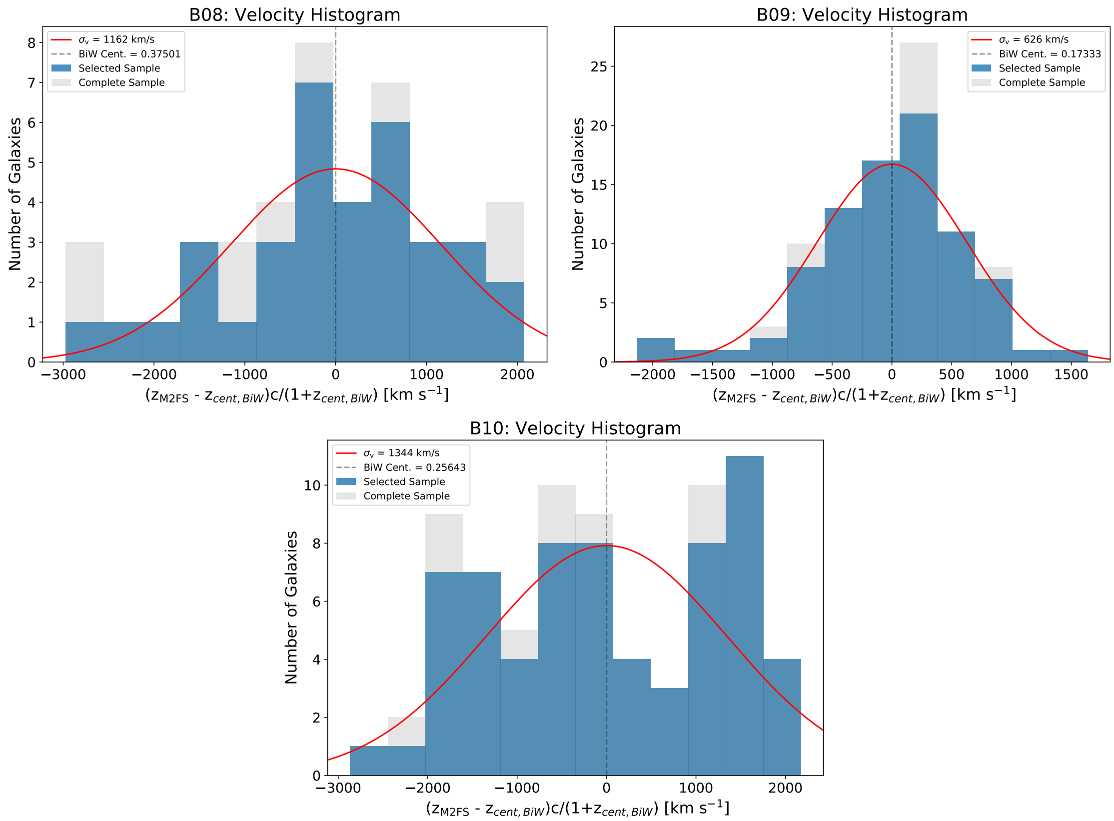

Figure B.25 A continuation of Figure B.23.

B.9 Dressler-Shectman Statistics

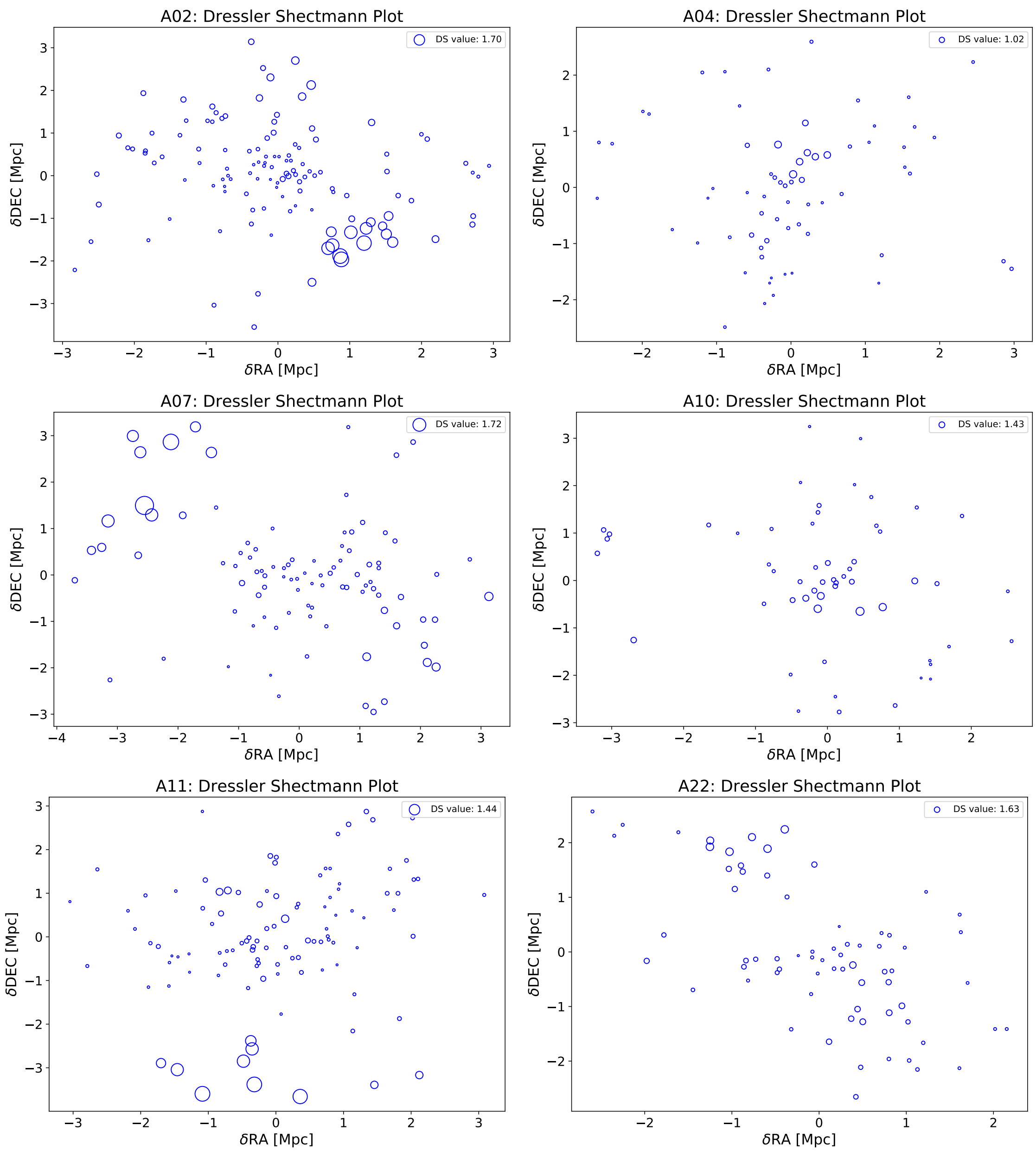

Figure B.26 Visual representation of the Dressler-Shectman substructure statistic. Increasing size of the circle indicates increasing deviations of the point from its nearest neighbors.

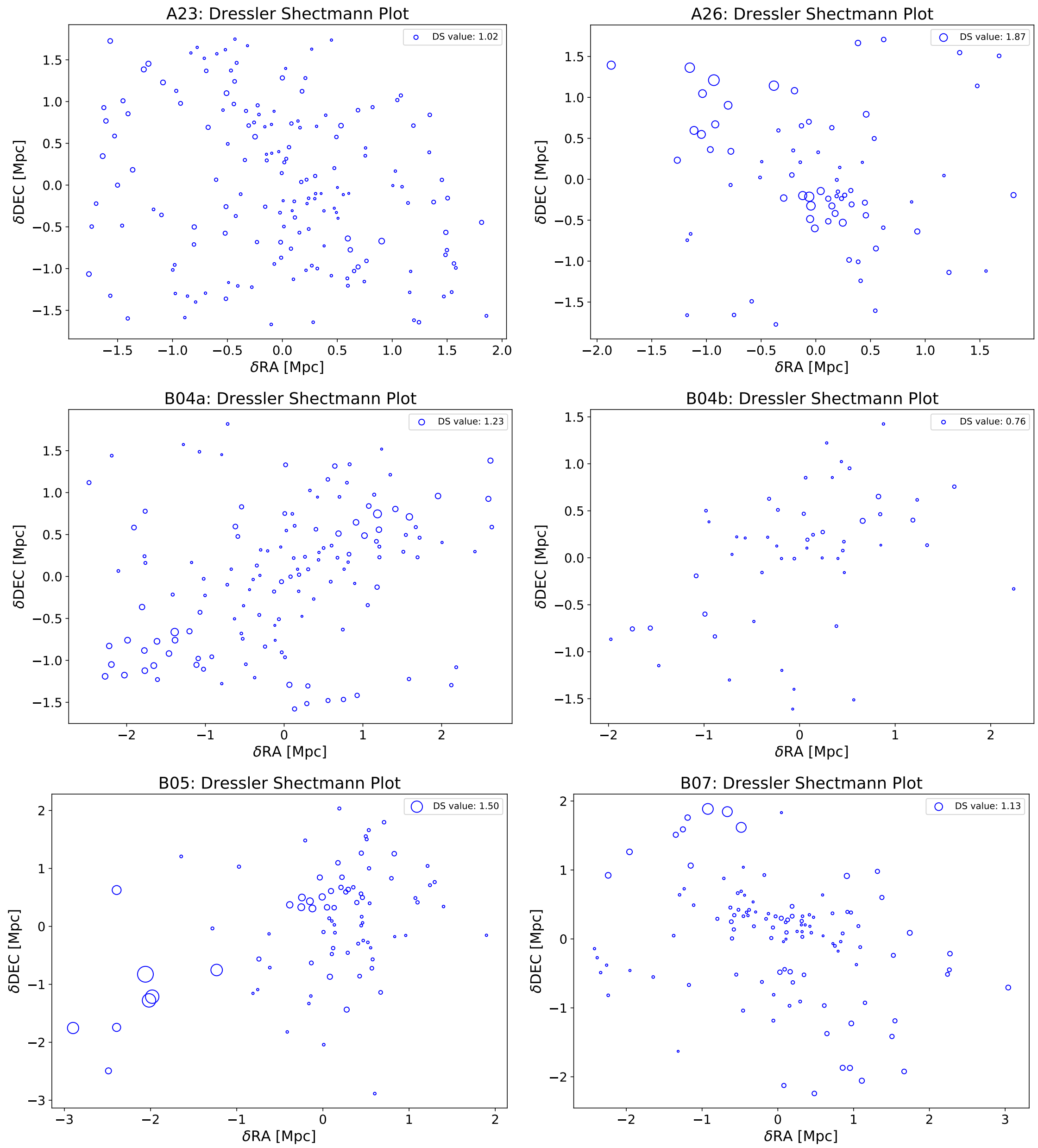

Figure B.27 A continuation of Figure B.26.

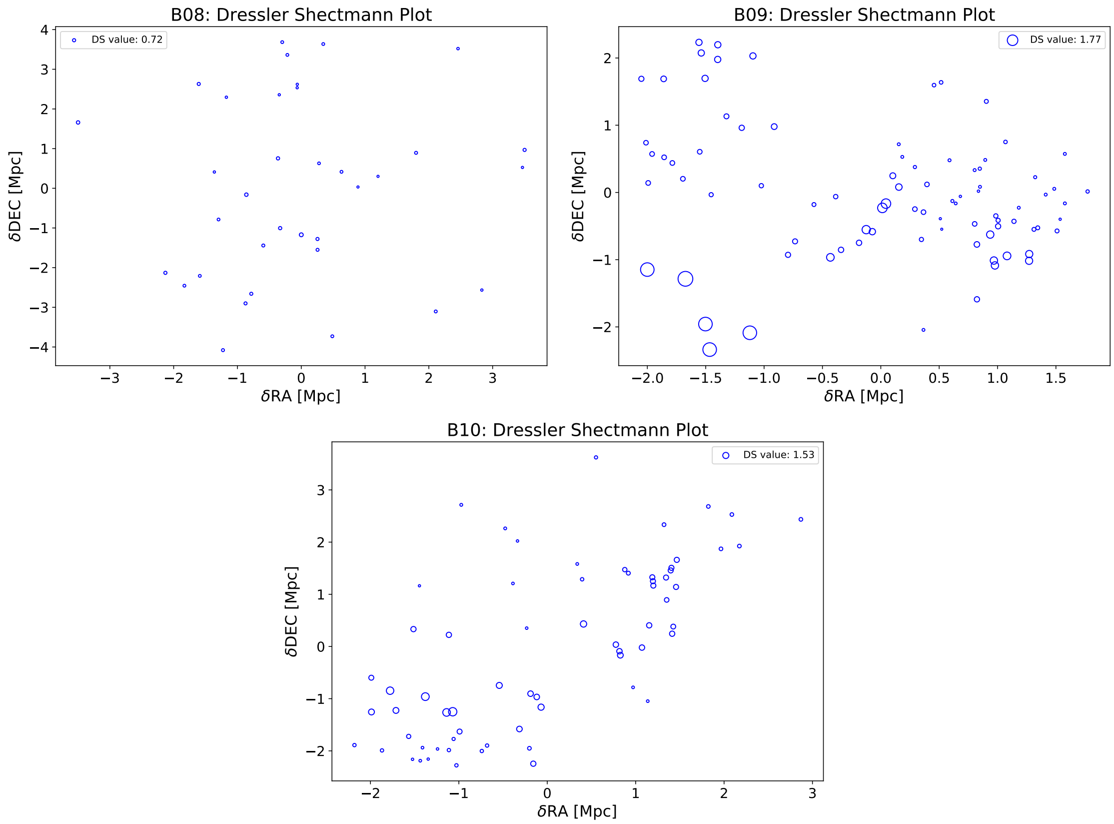

Figure B.28 A continuation of Figure B.26.

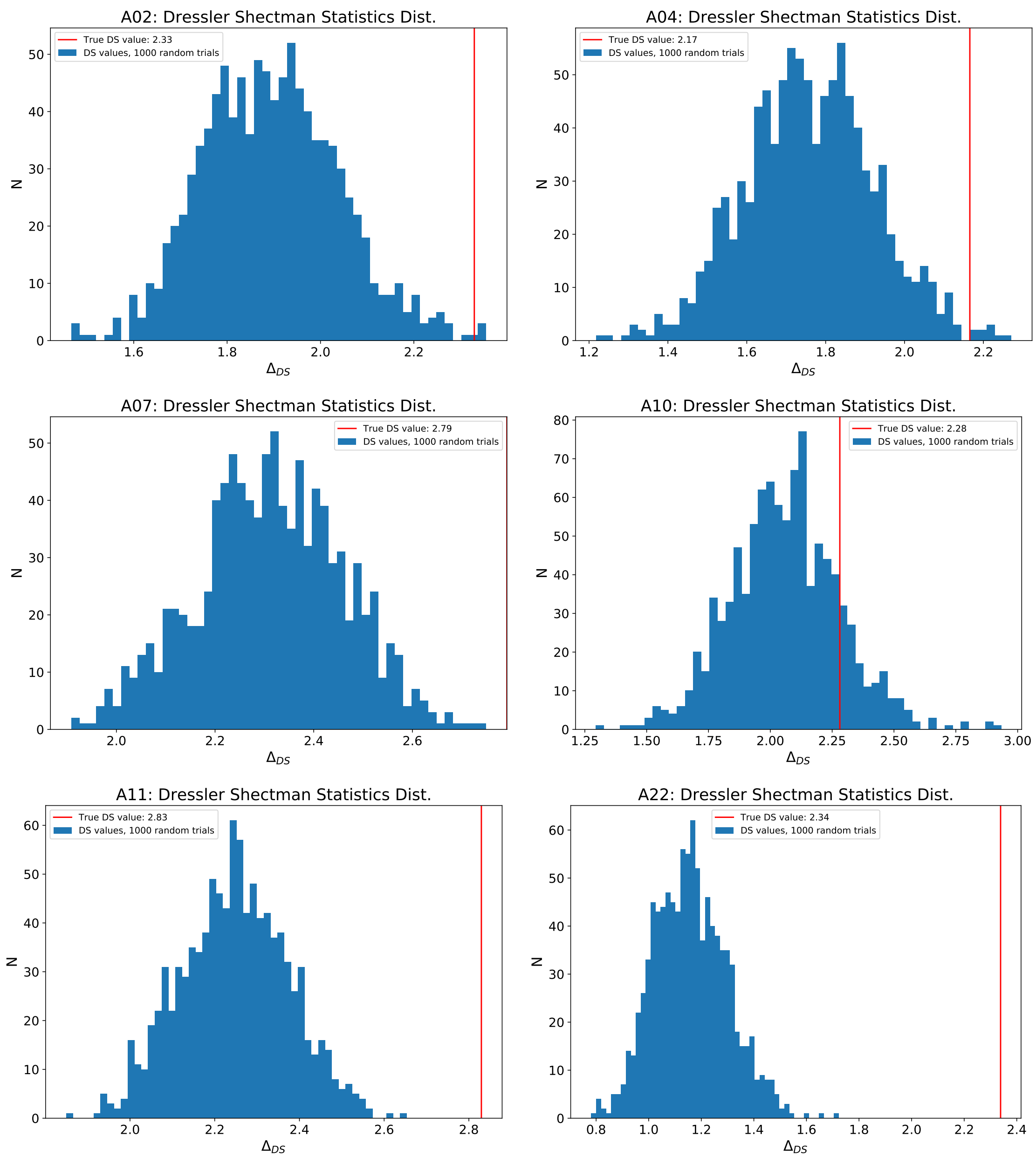

Figure B.29 Shows the calculated Dressler-Shectman statistic against a distribution of randomized trials. The trials were done by randomly shuffling the velocities of the sample and assigning them to random coordinates in the sample.

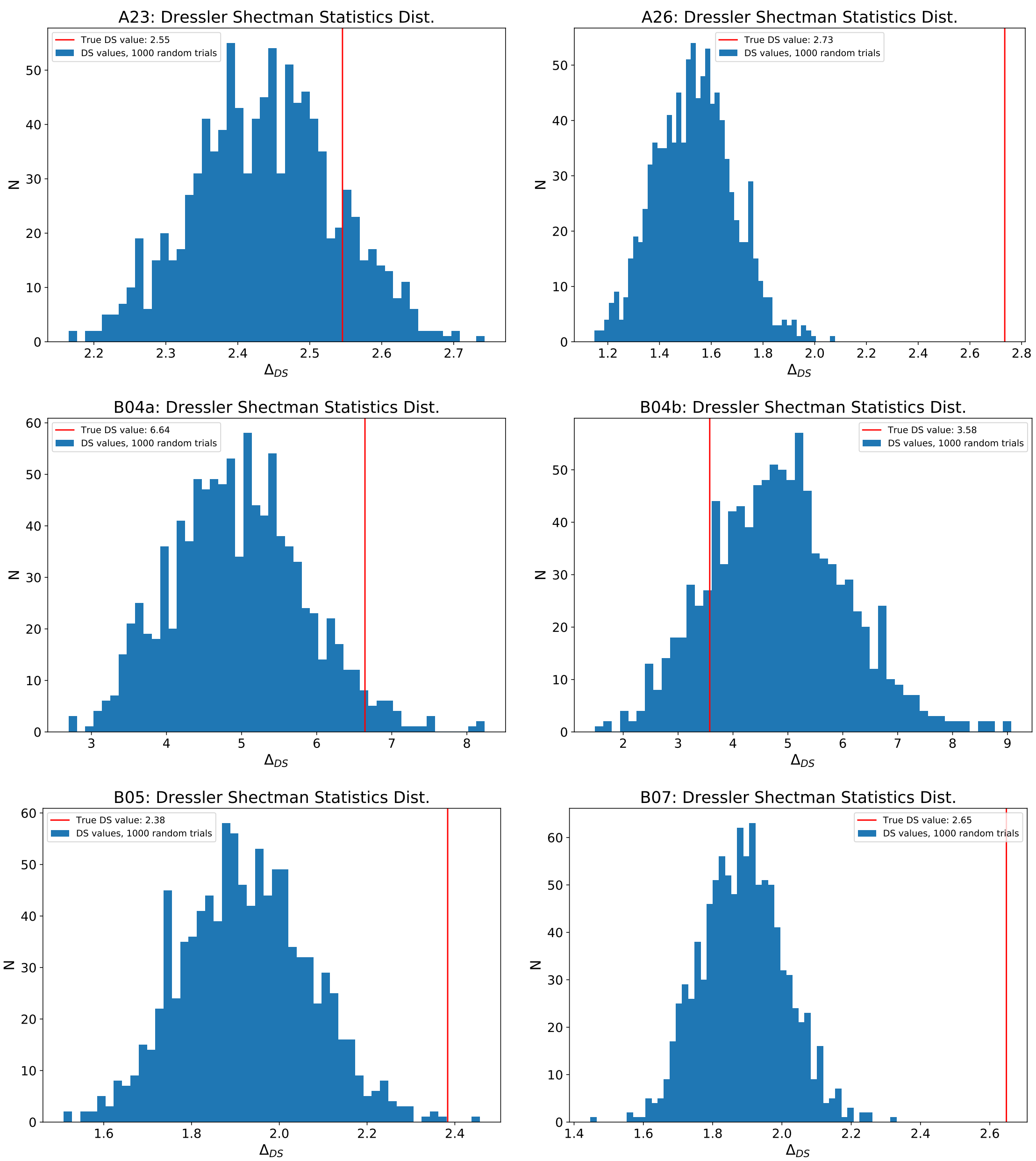

Figure B.30 A continuation of Figure B.29.

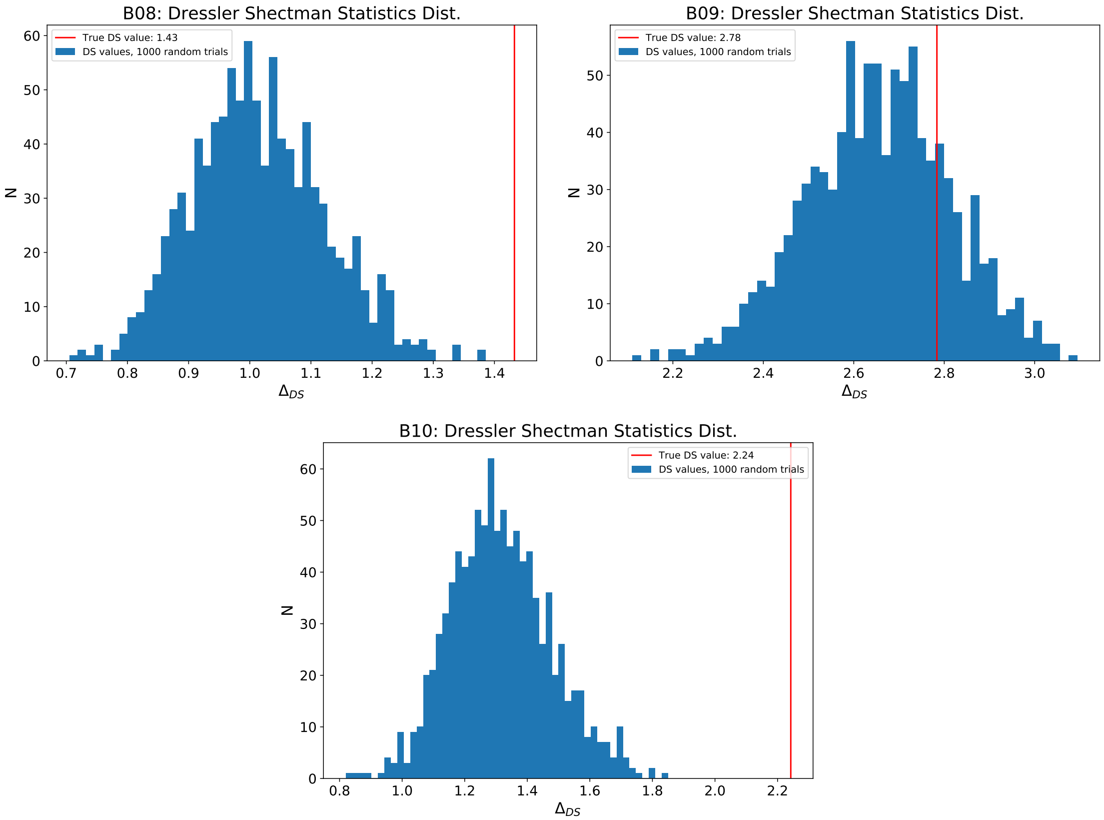

Figure B.31 A continuation of Figure B.29.

Appendix C

M2FS Dataset: Object Table

C.1 M2FS Cluster Target Sample

Table C.1: Complete M2FS Galaxy Cluster Target Catalog

Target ID	RA	DEC	r-band mag.	z	Corr.	FiberID
A02-000	210.2113	2.8677	19.78	0.25947	0.72	r516
A02-001	210.3045	2.7729	19.26	0.19422	0.72	r104
A02-002	210.3042	2.7566	19.50	0.24640	0.71	r102
A02-003	210.1808	2.9160	19.72	0.24370	0.76	b815
A02-004	210.1816	2.8935	19.57	0.25109	0.75	b816
A02-005	210.2729	3.0583	20.01	0.25037	0.66	b209
A02-006	210.2728	2.9235	19.26	0.25993	0.83	r402
A02-007	210.1688	2.9617	19.86	0.25161	0.74	b813
A02-008	210.2607	2.8396	19.64	0.24824	0.64	b304
A02-009	210.0781	2.7672	20.08	0.25061	0.65	b704
A02-010	210.1974	2.9744	20.07	0.25036	0.54	r610
A02-011	210.0153	2.7515	19.93	0.47841	0.32	b703
A02-012	210.1985	2.7210	20.22	0.27789	0.62	r510
A02-013	210.3932	2.9397	19.94	0.26489	0.41	r211
A02-014	210.2914	2.8733	20.01	0.25156	0.78	b208
A02-015	210.1280	3.0059	20.05	0.25454	0.60	r811
A02-016	210.1300	2.9131	18.39	0.25008	0.81	r805
A02-017	210.1297	2.9095	19.68	0.25729	0.53	r806
A02-018	210.2236	2.7737	20.13	0.42647	0.46	r301
A02-019	210.4136	2.9948	20.38	0.43827	0.67	r201
A02-020	210.2291	2.9126	20.06	0.25537	0.74	r601
A02-021	210.1362	2.9416	19.96	0.25372	0.67	r802
A02-022	210.2298	2.8773	19.46	0.24943	0.73	b415
A02-023	210.1383	2.8937	18.91	0.25118	0.77	r808
A02-025	210.2309	3.0884	18.74	0.25354	0.75	b409
A02-026	210.1459	2.9035	20.03	0.25099	0.59	r807
A02-027	210.2379	2.8950	18.39	0.25162	0.82	b413
A02-028	210.1456	2.9244	20.37	0.49502	0.22	r804
A02-029	210.2387	2.9981	20.32	0.25269	0.62	b403

Continued on next page

Target ID	RA	DEC	r-band mag.	z	Corr.	FiberID
A02-030	210.2383	2.9605	19.21	0.47489	0.81	b411
A02-032	210.1328	2.7695	18.55	0.25155	0.72	b705
A02-033	210.4066	2.7713	18.77	0.25056	0.79	b111
A02-034	210.3988	2.9321	18.95	0.26449	0.73	r213
A02-035	210.3968	2.8870	20.24	0.32887	0.64	r215
A02-037	210.1548	2.7822	19.29	0.38986	0.33	r505
A02-038	210.0626	2.7218	20.27	0.24983	0.38	b702
A02-039	210.1535	2.7745	20.12	0.19571	0.12	b706
A02-040	210.2440	2.8940	19.96	0.24956	0.74	b407
A02-041	210.1518	2.6574	18.27	0.27678	0.76	b701
A02-042	210.1531	2.8036	20.29	0.25039	0.52	b707
A02-043	210.2447	2.7429	18.50	0.28947	0.71	b301
A02-044	210.2461	2.9336	18.02	0.25011	0.85	b405
A02-045	210.2449	2.9039	20.05	0.25712	0.69	b406
A02-047	210.2262	2.8441	19.45	0.25215	0.75	r316
A02-049	210.1177	2.9161	20.06	0.25089	0.71	r814
A02-050	210.2088	2.8732	20.29	0.25201	0.64	r616
A02-051	210.4498	2.8996	20.36	0.37842	0.26	r203
A02-052	210.3535	2.7886	19.75	0.39363	0.72	b103
A02-053	210.2372	2.9159	19.15	0.24978	0.58	b412
A02-055	210.2369	2.8682	19.98	0.26133	0.69	b416
A02-056	210.2346	2.8214	19.36	0.31597	0.77	r314
A02-057	210.2373	2.6834	19.10	0.25064	0.73	r310
A02-058	210.1762	3.0694	20.20	0.46719	0.16	b809
A02-059	210.2640	3.0551	20.27	0.46681	0.61	r409
A02-060	210.0836	2.8757	19.78	0.24952	0.76	r816
A02-061	210.2645	2.8974	18.69	0.26065	0.81	r405
A02-062	210.0854	2.8269	19.92	0.25050	0.63	b708
A02-063	210.1787	2.7841	19.10	0.20645	0.38	r506
A02-064	210.3271	2.9939	18.32	0.38927	0.33	b203
A02-065	210.2332	2.8909	20.25	0.25250	0.65	b414
A02-066	210.2323	2.8181	19.34	0.24733	0.61	r312
A02-067	210.3268	2.8040	20.39	0.24809	0.60	r114
A02-068	210.3259	2.7823	19.36	0.24499	0.68	r113
A02-069	210.2337	2.6300	18.88	0.25973	0.75	r309
A02-070	210.0793	3.0186	18.64	0.42336	0.16	r810
A02-071	210.2664	2.8725	19.59	0.25881	0.76	r408
A02-072	210.1719	2.6355	19.73	0.14723	0.14	r501
A02-073	210.2682	3.0106	19.11	0.43816	0.53	r401
A02-074	210.2668	2.9057	19.02	0.24834	0.78	r403
A02-075	210.2687	2.8974	20.28	0.25425	0.72	r404
A02-076	210.1046	2.9378	18.61	0.25021	0.70	r812
A02-077	210.1947	2.8571	18.57	0.24566	0.74	r514
A02-078	210.2866	2.8802	20.27	0.26047	0.73	b214
A02-079	210.1954	2.6652	18.12	0.24316	0.69	r509
A02-080	210.2880	3.0189	19.03	0.25068	0.55	b201
A02-081	210.2889	2.9491	20.10	0.25441	0.70	b205
A02-082	210.2492	3.0312	18.36	0.26442	0.79	b402
A02-083	210.2500	2.7777	19.05	0.24984	0.78	b302
A02-084	210.2504	2.8870	18.86	0.24415	0.83	r416
A02-085	210.2492	2.8672	19.26	0.25599	0.77	b307
A02-086	210.3230	2.7306	19.92	0.36335	0.54	r110
A02-087	210.3220	2.8413	19.80	0.25405	0.51	r115

Continued on next page

Target ID	RA	DEC	r-band mag.	z	Corr.	FiberID
A02-088	210.1892	2.9614	19.27	0.25385	0.71	b814
A02-089	210.1908	3.0065	19.63	0.35437	0.61	b810
A02-091	210.0936	2.8766	19.30	0.20726	0.59	r815
A02-092	210.2820	2.8712	20.05	0.23900	0.54	b216
A02-093	210.3739	2.9899	19.87	0.31210	0.40	r209
A02-094	210.1131	2.9180	19.09	0.24861	0.77	r813
A02-095	210.2060	2.9144	19.23	0.25510	0.79	r614
A02-096	210.2062	2.9691	19.44	0.25232	0.70	r611
A02-097	210.2054	2.8560	18.17	0.25476	0.73	r513
A02-098	210.2058	2.8477	19.74	0.25626	0.75	r512
A02-099	210.2078	2.8845	19.43	0.25332	0.68	r615
A02-100	210.1482	2.9584	20.12	0.29588	0.66	r801
A02-101	210.2421	3.0462	19.13	0.26044	0.80	b401
A02-102	210.4355	2.8931	18.69	0.25067	0.78	r204
A02-103	210.2431	2.8890	18.75	0.25583	0.80	b408
A02-104	210.1629	2.9382	19.87	0.25091	0.65	r803
A02-105	210.2554	2.9711	19.16	0.25539	0.82	r411
A02-106	210.2551	2.8545	19.81	0.25321	0.66	b305
A02-107	210.2559	2.8617	19.72	0.25230	0.73	b306
A02-108	210.2574	2.9038	20.30	0.26029	0.52	r415
A02-109	210.2567	3.0494	19.56	0.35435	0.80	r410
A02-110	210.3457	2.9588	18.67	0.25228	0.74	r210
A02-111	210.3449	2.7985	19.23	0.24627	0.78	b106
A02-112	210.3465	2.8496	20.34	0.43920	0.67	b108
A02-113	210.1662	2.9956	19.55	0.25585	0.68	b811
A02-114	210.1675	2.8663	20.04	0.24597	0.59	r508
A02-115	210.1671	2.7641	19.09	0.30217	0.72	r504
A02-116	210.2732	2.8750	19.69	0.24488	0.64	b215
A02-117	210.2731	2.8248	19.69	0.25290	0.75	b311
A02-118	210.1832	2.9643	19.93	0.40050	0.62	b812
A02-119	210.2749	2.9128	19.97	0.32713	0.69	b212
A02-120	210.2752	2.8544	20.13	0.49375	0.22	b314
A02-121	210.2765	2.9178	20.03	0.24505	0.67	b211
A02-122	210.4577	2.8891	18.07	0.25136	0.77	r205
A02-123	210.2029	2.9654	19.92	0.25081	0.65	r612
A02-124	210.2037	2.8673	18.30	0.24713	0.74	r515
A02-125	210.3168	2.7388	19.31	0.24626	0.52	r111
A02-126	210.3157	2.7441	18.68	0.24072	0.68	r112
A02-128	210.1877	2.7000	19.91	0.46728	0.49	r503
A02-129	210.2794	3.0004	19.57	0.25967	0.77	b210
A02-130	210.2799	2.8918	20.05	0.26065	0.69	b213
A02-131	210.2793	2.8398	19.72	0.42423	0.16	b312
A02-134	210.2803	2.8586	20.26	0.27953	0.46	r108
A02-135	210.3562	2.7922	19.31	0.24775	0.76	b105
A02-137	210.2609	2.8678	19.14	0.24580	0.82	b308
A02-138	210.1938	2.9843	19.05	0.25729	0.81	r609
A02-139	210.1937	2.9599	19.79	0.25390	0.69	r613
A02-140	210.1911	2.6986	18.25	0.28121	0.77	r502
A02-141	210.3681	2.9356	18.98	0.26546	0.72	r212
A02-142	210.3376	3.0126	19.91	0.21003	0.59	b202
A02-143	210.2310	2.7956	18.94	0.25684	0.80	r311
A02-144	210.3385	2.7649	20.39	0.24555	0.69	b101
A02-145	210.4234	2.7254	20.22	0.36588	0.50	b109

Continued on next page

Target ID	RA	DEC	r-band mag.	z	Corr.	FiberID
A02-146	210.2011	2.7840	18.41	0.25672	0.80	r511
A02-147	210.2926	2.9313	19.63	0.24502	0.70	b206
A02-148	210.3072	2.7831	19.45	0.24851	0.75	r105
A02-149	210.3082	2.8525	18.35	0.24689	0.76	r107
A02-150	210.3083	2.7613	19.09	0.24705	0.76	r103
A02-151	210.3091	2.8469	19.71	0.24236	0.71	r116
A02-152	210.3404	2.7886	19.19	0.24723	0.68	b104
A02-153	210.3240	2.6708	17.98	0.27873	0.81	r109
A02-154	210.2531	2.9040	18.18	0.24925	0.73	r414
A02-155	210.2523	2.9424	19.90	0.26373	0.45	r413
A02-156	210.2528	2.9599	19.67	0.26232	0.72	r412
A02-158	210.3601	2.9079	19.45	0.25955	0.77	r214
A02-159	210.3604	2.8800	19.16	0.25535	0.69	r216
A02-160	210.3597	2.7795	19.56	0.24744	0.71	b102
A02-161	210.2887	2.8184	19.55	0.25608	0.72	r106
A02-162	210.2888	2.7020	18.48	0.24266	0.82	r101
A02-163	210.2598	2.8241	19.95	0.31576	0.70	b303
A02-164	210.3619	2.8085	20.04	0.25063	0.59	b107
A02-165	210.2711	2.8814	19.02	0.24450	0.75	r406
A02-166	210.2969	2.8788	19.76	0.25655	0.79	b207
A02-167	210.2645	2.8767	18.79	0.25182	0.68	r407
A02-168	210.4422	2.8781	19.63	0.25234	0.70	r207
A02-169	210.4419	2.7948	19.07	0.25032	0.75	b112
A02-170	210.4426	2.8083	20.37	0.24753	0.35	b114
A02-171	210.2430	2.8205	19.27	0.25701	0.77	r313
A02-172	210.3837	2.8332	18.59	0.25536	0.52	b115
A02-173	210.4475	2.8718	19.11	0.25168	0.68	r208
A02-175	210.2680	2.8161	19.44	0.25795	0.75	b310
A02-176	210.2689	2.8584	20.12	0.46456	0.20	b315
A02-177	210.3658	2.7664	19.54	0.24593	0.66	b110
A02-178	210.2774	2.8487	17.75	0.25014	0.81	b313
A02-180	210.2770	2.8636	19.55	0.24371	0.55	b316
A02-181	210.3710	2.8413	19.84	0.24676	0.71	b116
A02-182	210.4576	2.8835	19.30	0.28928	0.73	r206
A04-000	240.6637	3.1591	20.12	0.47156	0.19	b705
A04-001	240.8051	3.4235	20.39	0.42444	0.36	r612
A04-002	240.7334	3.2652	19.74	0.22307	0.44	r707
A04-003	240.8055	3.2336	20.28	0.21797	0.30	b514
A04-004	240.8727	3.3217	19.90	0.21751	0.49	r415
A04-005	240.8138	3.1512	19.50	0.22124	0.40	r501
A04-006	240.7455	3.0786	19.54	0.21864	0.62	r701
A04-007	240.7455	3.4225	18.84	0.21737	0.46	b811
A04-008	240.8876	3.5272	19.73	0.49825	0.37	r409
A04-009	240.6717	3.2350	18.48	0.26513	0.47	b706
A04-010	240.8149	3.2844	19.61	0.22892	0.46	r614
A04-011	240.7246	3.1324	19.43	0.20306	0.51	b711
A04-012	240.7963	3.2799	19.05	0.22517	0.71	b808
A04-013	240.9385	3.3481	20.35	0.22255	0.44	b212
A04-014	240.9377	3.3264	20.08	0.35912	0.70	b213
A04-015	240.6504	3.1531	18.88	0.38860	0.58	b704
A04-016	240.7948	3.1213	20.14	0.22177	0.50	b509
A04-017	240.7202	3.4688	19.70	0.43113	0.82	r801
A04-018	240.6518	3.3007	19.25	0.12653	0.19	r815

Continued on next page

Target ID	RA	DEC	r-band mag.	z	Corr.	FiberID
A04-019	240.8642	3.2578	18.90	0.21556	0.60	r315
A04-020	240.8637	3.2463	19.20	0.46596	0.41	r314
A04-021	240.7831	3.1728	18.58	0.21773	0.75	b503
A04-022	240.9240	3.0627	18.66	0.14113	0.38	r101
A04-023	240.7843	3.4402	20.26	0.40158	0.28	b802
A04-024	240.8542	3.4739	19.65	0.41699	0.20	b610
A04-025	240.7829	3.2318	20.30	0.21678	0.40	b507
A04-026	240.7824	3.1852	19.75	0.22302	0.56	b505
A04-027	240.8541	3.3454	19.57	0.28865	0.38	b614
A04-028	240.8237	3.0517	18.75	0.16841	0.45	r509
A04-029	240.8227	3.4323	20.23	0.23721	0.45	r604
A04-030	240.8906	3.4839	20.07	0.36869	0.55	r410
A04-031	240.7527	3.2243	18.49	0.49517	0.38	r704
A04-032	240.6778	3.2705	19.88	0.15735	0.42	b708
A04-033	240.8238	3.2768	20.35	0.21717	0.62	r516
A04-034	240.8914	3.3348	20.16	0.49304	0.22	r414
A04-035	240.8921	3.3274	19.14	0.22089	0.38	r407
A04-036	240.9603	3.3064	19.03	0.19520	0.46	r215
A04-037	240.9020	3.1378	18.10	0.21819	0.82	r103
A04-038	240.9698	3.4064	19.33	0.41436	0.40	r211
A04-039	240.8132	3.2739	19.55	0.22514	0.50	r507
A04-040	240.7426	3.4667	20.23	0.22642	0.27	b810
A04-042	240.8155	3.4393	20.28	0.34335	0.62	r611
A04-043	240.6816	3.1499	18.78	0.32905	0.40	b702
A04-044	240.8890	3.0664	17.96	0.14007	0.63	r102
A04-045	240.7505	3.1995	19.97	0.21833	0.64	r703
A04-046	240.6905	3.1145	18.82	0.16895	0.44	b710
A04-047	240.8336	3.4629	18.93	0.22045	0.66	r602
A04-048	240.6920	3.2099	18.86	0.21922	0.78	b715
A04-049	240.9050	3.1753	19.56	0.22447	0.45	r105
A04-050	240.8341	3.3729	20.26	0.39996	0.46	r605
A04-051	240.9037	3.3749	20.14	0.46653	0.42	r405
A04-052	240.8067	3.1498	19.96	0.22178	0.45	b512
A04-053	240.8073	3.4470	19.45	0.23603	0.61	r610
A04-054	240.8068	3.2689	20.20	0.21590	0.45	b515
A04-055	240.8071	3.2561	20.34	0.17671	0.27	r505
A04-056	240.8076	3.2782	20.28	0.21961	0.17	r508
A04-058	240.8771	3.2519	20.22	0.13095	0.15	r108
A04-059	240.9471	3.3491	18.60	0.16498	0.55	r212
A04-060	240.7145	3.0942	19.60	0.24320	0.50	b709
A04-061	240.7860	3.1103	19.27	0.20807	0.68	b501
A04-062	240.7855	3.2545	17.79	0.22102	0.79	b508
A04-063	240.9278	3.1811	20.36	0.49269	0.38	r113
A04-064	240.9278	3.3208	19.84	0.21570	0.66	b214
A04-065	240.9948	3.2326	17.05	0.43792	0.24	b105
A04-066	240.7928	3.1448	17.50	0.22384	0.78	b511
A04-067	240.8620	3.0693	20.14	0.49169	0.25	r309
A04-068	240.7226	3.4214	18.36	0.22071	0.55	r804
A04-069	240.7926	3.4648	20.19	0.48423	0.31	b801
A04-070	240.9325	3.3882	20.34	0.22155	0.55	b211
A04-071	240.9338	3.4618	20.30	0.22370	0.30	b210
A04-072	240.9338	3.2853	18.82	0.22392	0.78	b216
A04-073	240.7925	3.2846	19.48	0.21971	0.61	b807

Continued on next page

Target ID	RA	DEC	r-band mag.	z	Corr.	FiberID
A04-074	240.9334	3.1704	19.81	0.28970	0.42	r112
A04-075	240.7910	3.1379	19.66	0.22038	0.47	b510
A04-076	240.7898	3.4255	18.19	0.22072	0.62	b803
A04-077	240.7178	3.1919	19.61	0.21800	0.51	b714
A04-078	240.8465	3.4011	19.42	0.30622	0.49	b612
A04-079	240.8470	3.4919	20.31	0.47164	0.18	b609
A04-080	240.7771	3.2421	20.10	0.48638	0.44	r715
A04-081	240.7765	3.2179	19.72	0.38906	0.52	r714
A04-082	240.9177	3.1743	18.77	0.24428	0.64	r104
A04-083	240.7662	3.1517	18.56	0.21813	0.62	r710
A04-084	240.9767	3.0769	19.83	0.49739	0.35	b101
A04-085	240.6940	3.4577	20.25	0.50002	0.50	r809
A04-086	240.9006	3.5214	19.63	0.13299	0.16	r401
A04-087	240.6174	3.3273	18.05	0.22657	0.56	r813
A04-088	240.7605	3.3764	20.00	0.22036	0.53	b813
A04-089	240.9009	3.2386	19.72	0.38934	0.34	r106
A04-091	241.0379	3.3427	17.68	0.37240	0.38	r205
A04-092	240.7807	3.1190	20.15	0.21832	0.32	b502
A04-093	240.7092	3.4606	20.35	0.40112	0.46	r802
A04-094	240.7819	3.4036	19.84	0.48884	0.24	b804
A04-095	240.7813	3.3736	20.06	0.30754	0.48	b805
A04-096	240.8492	3.4351	19.70	0.21861	0.20	b611
A04-097	240.7786	3.1788	19.16	0.26751	0.58	r712
A04-098	240.8497	3.3104	19.07	0.22123	0.46	b615
A04-100	240.7292	3.2705	19.46	0.43302	0.74	r708
A04-101	240.7292	3.2316	19.53	0.26134	0.49	r705
A04-102	240.8043	3.3279	19.19	0.31969	0.22	r613
A04-103	240.8687	3.1773	19.37	0.36045	0.57	r311
A04-105	241.0048	3.3417	20.24	0.36691	0.53	r206
A04-106	241.0048	3.2373	19.04	0.24159	0.69	b106
A04-107	240.9479	3.0919	19.00	0.28170	0.43	r109
A04-108	240.8094	3.5007	19.18	0.10908	0.62	r609
A04-109	240.8809	3.3838	19.66	0.22230	0.47	r412
A04-110	240.6684	3.3655	19.12	0.21921	0.47	r812
A04-111	240.8100	3.2119	18.70	0.21922	0.59	r503
A04-112	240.8097	3.2469	19.43	0.22538	0.46	r504
A04-114	240.8810	3.2416	20.39	0.22307	0.23	r107
A04-115	240.8294	3.4363	19.46	0.30674	0.43	r603
A04-116	241.0205	3.4098	20.23	0.45184	0.36	r202
A04-117	240.6130	3.2800	18.99	0.20475	0.54	r816
A04-118	240.8303	3.2438	18.73	0.21864	0.70	r514
A04-119	240.8294	3.3134	20.10	0.22693	0.38	r607
A04-121	240.8299	3.2041	19.05	0.22102	0.56	r512
A04-122	240.9620	3.3472	19.51	0.35095	0.71	r213
A04-123	240.7153	3.1629	19.78	0.20293	0.56	b713
A04-124	240.9966	3.1416	20.24	0.28890	0.30	b103
A04-125	240.7165	3.4505	19.18	0.23937	0.37	r803
A04-126	240.9288	3.4630	20.10	0.35909	0.76	b209
A04-127	240.9980	3.4355	18.93	0.22139	0.58	r201
A04-128	240.7162	3.3590	18.71	0.16312	0.63	r806
A04-129	240.7156	3.3270	19.90	0.41211	0.47	r807
A04-130	240.7882	3.1949	19.04	0.22208	0.75	b506
A04-131	240.7881	3.1795	20.20	0.26672	0.59	b504

Continued on next page

Target ID	RA	DEC	r-band mag.	z	Corr.	FiberID
A04-132	240.8580	3.2971	19.36	0.22133	0.26	r416
A04-133	240.8580	3.2341	20.36	0.46648	0.17	r313
A04-134	240.9285	3.2939	20.17	0.21663	0.50	b215
A04-135	241.0571	3.3472	20.11	0.25034	0.37	r204
A04-136	240.7329	3.3655	19.15	0.25931	0.59	b814
A04-137	240.6621	3.3690	20.08	0.22410	0.59	r811
A04-138	240.8020	3.2734	19.68	0.22012	0.63	b516
A04-139	240.9670	3.4956	19.97	0.35018	0.57	r209
A04-140	240.8977	3.3494	19.59	0.21674	0.49	r406
A04-141	240.9657	3.1660	17.41	0.13401	0.73	r111
A04-142	241.0289	3.1673	19.93	0.21583	0.49	b112
A04-143	241.0039	3.2258	20.01	0.32668	0.42	b104
A04-144	240.9146	3.4641	20.05	0.39412	0.34	r402
A04-145	240.9810	3.4801	19.80	0.49134	0.33	r210
A04-146	240.6309	3.3255	18.44	0.21621	0.66	r814
A04-147	240.7016	3.3932	18.18	0.45575	0.56	r805
A04-148	240.8446	3.2460	19.74	0.22173	0.48	r515
A04-149	241.0491	3.3181	17.32	0.37229	0.33	r207
A04-150	240.8429	3.1165	20.09	0.16790	0.19	r511
A04-151	240.9874	3.1066	18.50	0.24119	0.61	b102
A04-152	240.7011	3.4297	20.23	0.40669	0.17	r810
A04-153	240.7727	3.2026	19.43	0.22131	0.69	r713
A04-154	240.8435	3.3655	17.81	0.45968	0.17	b613
A04-155	240.9892	3.2896	20.36	0.49448	0.22	r216
A04-156	240.7681	3.1192	19.64	0.21792	0.28	r709
A04-157	240.7666	3.4103	17.86	0.43769	0.23	b812
A04-158	240.7686	3.4983	19.44	0.28969	0.39	b809
A04-159	240.9100	3.4279	20.27	0.49754	0.25	r404
A04-160	240.6953	3.2441	18.88	0.20532	0.56	b716
A04-161	240.7683	3.3234	19.83	0.21696	0.44	b816
A04-162	240.7682	3.2597	19.27	0.21625	0.65	r716
A04-163	240.8375	3.3080	18.49	0.22719	0.51	b616
A04-164	240.7586	3.1763	20.27	0.36534	0.24	r711
A04-165	240.8267	3.5042	19.73	0.15947	0.27	r601
A04-166	240.6157	3.2521	19.96	0.22193	0.48	b707
A04-167	240.8274	3.3535	19.98	0.22609	0.60	r606
A04-168	240.9630	3.2416	20.32	0.49227	0.24	r114
A04-171	240.7283	3.2522	18.79	0.22827	0.67	r706
A04-172	240.7285	3.1979	19.70	0.48513	0.28	r702
A04-173	240.8751	3.1952	19.58	0.34898	0.39	r312
A04-174	240.7986	3.2238	19.58	0.21804	0.57	b513
A04-175	240.7996	3.3243	20.36	0.21945	0.45	b806
A04-177	241.0166	3.2363	20.09	0.25416	0.62	b116
A04-178	240.6765	3.1285	17.38	0.15369	0.36	b701
A04-179	240.6764	3.1520	19.93	0.26671	0.49	b703
A04-180	240.8181	3.0973	18.83	0.16792	0.47	r510
A04-181	240.8840	3.4190	19.78	0.43524	0.76	r411
A04-182	240.9546	3.2527	19.78	0.42149	0.13	r115
A04-183	240.6978	3.1496	19.57	0.48440	0.27	b712
A04-184	241.0359	3.1435	19.89	0.42246	0.49	b110
A04-185	240.9800	3.2496	18.97	0.30403	0.19	b107
A04-186	241.0371	3.1571	19.20	0.21621	0.49	b111
A04-187	240.8216	3.3013	18.05	0.22644	0.65	r608

Continued on next page

Target ID	RA	DEC	r-band mag.	z	Corr.	FiberID
A04-188	240.8208	3.2170	18.41	0.22026	0.60	r513
A04-189	240.9586	3.3339	20.22	0.22308	0.40	r214
A04-190	241.0190	3.2251	20.03	0.24529	0.28	b115
A04-191	240.8160	3.2693	19.62	0.48055	0.18	r506
A04-192	240.8167	3.1746	19.43	0.25992	0.51	r502
A04-193	241.0417	3.1400	17.73	0.49099	0.28	b109
A07-000	319.8413	0.7464	18.86	0.27861	0.74	r201
A07-001	319.5378	0.4770	19.75	0.23132	0.57	b703
A07-002	319.4764	0.5471	19.55	0.35796	0.86	b706
A07-003	319.4785	0.4894	20.31	0.47991	0.60	b704
A07-005	319.5426	0.7154	20.36	0.36158	0.60	b813
A07-006	319.5432	0.7747	20.36	0.49095	0.38	b809
A07-007	319.8044	0.7539	20.11	0.46444	0.31	b201
A07-008	319.8644	0.5012	18.14	0.26968	0.49	r113
A07-009	319.8189	0.4601	19.48	0.45799	0.57	r104
A07-010	319.5567	0.7191	20.14	0.38845	0.68	b812
A07-011	319.6214	0.7259	19.47	0.43721	0.22	r811
A07-012	319.5572	0.6588	19.78	0.28514	0.45	b814
A07-013	319.7495	0.4921	19.75	0.27296	0.67	b311
A07-014	319.7994	0.3739	20.25	0.27446	0.50	b101
A07-015	319.6094	0.3773	18.23	0.21985	0.76	r301
A07-016	319.5449	0.7548	19.65	0.28848	0.47	b810
A07-017	319.7922	0.4500	18.77	0.27348	0.45	r103
A07-018	319.6583	0.3993	19.90	0.48189	0.80	b510
A07-019	319.6589	0.5932	19.04	0.27942	0.62	r815
A07-020	319.7092	0.5769	19.94	0.28027	0.70	b308
A07-021	319.7920	0.6970	18.44	0.31668	0.80	r210
A07-022	319.7912	0.5483	20.26	0.27561	0.69	b104
A07-023	319.7965	0.4137	19.90	0.30528	0.51	b102
A07-024	319.7958	0.7389	20.19	0.29115	0.66	b203
A07-025	319.5977	0.6452	19.74	0.27565	0.74	b808
A07-026	319.7045	0.5603	17.19	0.27660	0.80	r314
A07-027	319.7047	0.5723	18.66	0.27674	0.83	r416
A07-028	319.6486	0.3948	19.99	0.24069	0.73	b502
A07-029	319.5187	0.6374	20.35	0.27762	0.55	b816
A07-030	319.7436	0.5623	17.89	0.27717	0.78	r315
A07-031	319.6934	0.5740	20.12	0.26319	0.63	b307
A07-032	319.7878	0.5396	18.87	0.27489	0.75	r106
A07-033	319.8604	0.4322	19.44	0.27630	0.34	r109
A07-034	319.8562	0.4421	18.20	0.27372	0.60	r111
A07-035	319.8109	0.3880	20.02	0.27372	0.40	b109
A07-036	319.8118	0.7398	20.19	0.34820	0.78	b202
A07-037	319.7727	0.7670	19.68	0.27590	0.60	b209
A07-038	319.5140	0.4725	20.24	0.48591	0.15	b702
A07-039	319.5775	0.4473	19.78	0.28046	0.74	b710
A07-040	319.7408	0.4263	20.32	0.33491	0.62	b309
A07-042	319.6543	0.3411	20.33	0.46438	0.59	b509
A07-044	319.5903	0.7725	20.06	0.44582	0.62	b801
A07-045	319.8238	0.4927	19.75	0.27274	0.60	b111
A07-046	319.6398	0.3546	20.33	0.46096	0.68	b709
A07-047	319.5798	0.7999	19.13	0.32109	0.56	r809
A07-048	319.7796	0.7732	18.20	0.25307	0.78	r209
A07-049	319.8236	0.7283	18.62	0.27777	0.76	r203

Continued on next page

Target ID	RA	DEC	r-band mag.	z	Corr.	FiberID
A07-050	319.6906	0.4245	19.37	0.27640	0.68	r309
A07-051	319.8656	0.4358	18.69	0.27489	0.73	r110
A07-052	319.5483	0.4605	19.87	0.41913	0.80	b711
A07-053	319.6732	0.4736	19.98	0.41896	0.24	b511
A07-054	319.6723	0.4927	19.16	0.27246	0.48	r304
A07-055	319.8531	0.4659	19.35	0.27393	0.61	r112
A07-056	319.6459	0.4363	20.32	0.28470	0.68	b503
A07-057	319.5120	0.6009	18.95	0.27898	0.69	r814
A07-058	319.6993	0.3955	19.80	0.27989	0.65	b301
A07-059	319.6534	0.5753	18.73	0.28072	0.80	r816
A07-060	319.6527	0.5126	19.30	0.26874	0.68	r305
A07-061	319.7949	0.5773	19.33	0.28009	0.78	r214
A07-062	319.7121	0.5602	19.98	0.20927	0.65	b306
A07-063	319.6688	0.5869	19.97	0.27773	0.73	b616
A07-064	319.6264	0.7882	19.89	0.44639	0.77	b609
A07-065	319.8582	0.5081	17.73	0.13577	0.16	r114
A07-066	319.6445	0.3411	19.71	0.39121	0.47	b501
A07-067	319.7291	0.4505	19.87	0.27689	0.69	b310
A07-068	319.6279	0.7320	20.24	0.27470	0.49	b611
A07-069	319.8519	0.5013	19.83	0.27297	0.57	b112
A07-070	319.6111	0.7674	19.98	0.27621	0.49	b802
A07-071	319.4836	0.5556	19.47	0.27680	0.73	r307
A07-072	319.6760	0.5672	20.10	0.27408	0.75	b515
A07-073	319.7195	0.5423	20.11	0.27876	0.56	b304
A07-074	319.6955	0.4852	20.20	0.29920	0.73	b302
A07-075	319.6964	0.4899	19.02	0.28128	0.73	r310
A07-076	319.7593	0.7035	19.97	0.32351	0.66	b210
A07-077	319.5093	0.4684	18.88	0.48312	0.45	r303
A07-078	319.5725	0.7298	20.38	0.34943	0.60	b805
A07-079	319.6359	0.7515	19.27	0.23349	0.61	r810
A07-080	319.6950	0.7329	18.75	0.31703	0.84	r410
A07-081	319.5726	0.5726	20.27	0.47827	0.72	b714
A07-082	319.7365	0.5823	19.66	0.26868	0.69	b316
A07-083	319.5913	0.7142	20.40	0.45397	0.82	b806
A07-084	319.4682	0.6089	20.32	0.44757	0.47	b708
A07-085	319.7453	0.5486	17.66	0.27131	0.79	r312
A07-086	319.7099	0.5106	19.72	0.27216	0.72	b303
A07-087	319.7879	0.6354	19.06	0.27580	0.80	r212
A07-088	319.6661	0.6267	19.95	0.49067	0.42	b613
A07-089	319.6664	0.6070	19.85	0.28097	0.66	b614
A07-090	319.7962	0.5533	18.81	0.27227	0.66	r216
A07-093	319.7267	0.5654	19.61	0.27520	0.57	b315
A07-094	319.7710	0.5457	17.73	0.27186	0.78	r107
A07-095	319.8185	0.5831	18.78	0.20964	0.74	r206
A07-096	319.7706	0.6734	20.04	0.27888	0.79	b212
A07-097	319.9128	0.5780	19.12	0.32322	0.66	r207
A07-098	319.6603	0.5517	19.90	0.27278	0.51	b514
A07-099	319.7994	0.5440	19.68	0.27307	0.72	b103
A07-100	319.7573	0.5733	19.80	0.27573	0.71	b107
A07-101	319.8049	0.5724	20.30	0.27580	0.62	b106
A07-102	319.8049	0.5351	20.11	0.28207	0.49	b116
A07-103	319.8049	0.5792	20.14	0.27501	0.67	b108
A07-104	319.7534	0.6158	18.50	0.24299	0.78	r401

Continued on next page

Target ID	RA	DEC	r-band mag.	z	Corr.	FiberID
A07-105	319.7134	0.5839	19.28	0.27494	0.75	r415
A07-106	319.7124	0.5566	20.40	0.27899	0.59	b305
A07-107	319.7536	0.5653	20.33	0.27924	0.67	b105
A07-108	319.6748	0.5983	19.68	0.27259	0.72	b615
A07-109	319.7186	0.5575	19.18	0.27954	0.78	r313
A07-110	319.7688	0.6216	19.81	0.28804	0.80	b214
A07-111	319.5528	0.7323	20.29	0.28754	0.65	b811
A07-112	319.6176	0.7664	20.07	0.45107	0.69	b803
A07-113	319.6812	0.5685	20.19	0.27005	0.60	b516
A07-114	319.7644	0.5827	18.93	0.27628	0.82	r402
A07-115	319.8103	0.6393	18.74	0.22831	0.77	r211
A07-116	319.6800	0.6531	18.58	0.31988	0.83	r412
A07-118	319.9214	0.5332	18.74	0.27253	0.74	r116
A07-119	319.5506	0.5900	19.86	0.28794	0.67	b715
A07-120	319.8109	0.5140	19.88	0.27332	0.60	b114
A07-121	319.8119	0.6212	19.98	0.27926	0.73	b207
A07-122	319.7764	0.6223	19.89	0.27829	0.60	b206
A07-123	319.5702	0.5069	19.59	0.30140	0.73	b712
A07-126	319.7753	0.6886	19.99	0.45785	0.78	b211
A07-127	319.7343	0.5178	19.79	0.27832	0.50	b312
A07-128	319.6926	0.6270	20.03	0.27088	0.78	b213
A07-129	319.7343	0.5510	20.09	0.26879	0.50	b314
A07-130	319.7822	0.5635	19.03	0.27807	0.80	r215
A07-132	319.6403	0.5791	19.60	0.27749	0.53	b504
A07-133	319.6402	0.7054	20.11	0.20464	0.64	b612
A07-134	319.8662	0.5637	18.24	0.27635	0.81	r208
A07-136	319.8709	0.7294	18.70	0.20984	0.52	r202
A07-138	319.8284	0.5325	18.97	0.27188	0.75	r105
A07-139	319.5013	0.5163	20.20	0.14658	0.27	b705
A07-140	319.5012	0.5968	19.87	0.27755	0.59	b707
A07-141	319.5648	0.6458	19.97	0.28446	0.41	b807
A07-142	319.7303	0.5207	20.08	0.27701	0.68	b313
A07-143	319.9060	0.6572	20.11	0.44475	0.70	b205
A07-144	319.5627	0.5996	19.90	0.46203	0.80	b716
A07-145	319.4987	0.6753	19.34	0.31085	0.56	r812
A07-146	319.8221	0.6098	18.55	0.27865	0.86	r205
A07-147	319.9181	0.5174	19.89	0.49069	0.46	b115
A07-148	319.5082	0.6565	20.08	0.45602	0.81	b815
A07-149	319.7324	0.5057	18.55	0.27441	0.80	r311
A07-150	319.6329	0.6559	18.99	0.27752	0.78	r813
A07-151	319.6842	0.5460	20.21	0.27817	0.68	b513
A07-152	319.6845	0.5618	18.91	0.26973	0.81	r308
A07-153	319.6840	0.5046	20.03	0.27797	0.65	b512
A07-154	319.7738	0.5964	18.84	0.27551	0.79	r213
A07-155	319.5207	0.4180	19.37	0.26369	0.73	r302
A07-156	319.7911	0.3821	18.62	0.27527	0.76	r101
A07-157	319.5852	0.7465	20.30	0.28796	0.64	b804
A07-158	319.6210	0.7770	19.54	0.44311	0.61	b610
A07-159	319.6779	0.5350	17.35	0.27111	0.86	r306
A07-160	319.7667	0.5464	18.94	0.27213	0.64	r108
A07-161	319.8551	0.5303	18.81	0.23346	0.62	r115
A07-162	319.7661	0.6029	19.60	0.27737	0.74	b215
A07-163	319.9012	0.5844	20.25	0.27095	0.42	b208

Continued on next page

Target ID	RA	DEC	r-band mag.	z	Corr.	FiberID
A09-000	323.6235	1.3316	19.24	0.35632	0.77	r705
A09-001	323.6230	1.2780	20.17	0.21650	0.52	r702
A09-002	323.8227	1.4401	19.51	0.22997	0.72	r415
A09-003	323.7610	1.2068	19.59	0.34969	0.64	r301
A09-004	323.6314	1.3211	19.89	0.11388	0.26	r704
A09-006	323.6168	1.3192	19.16	0.17448	0.50	r703
A09-007	323.6818	1.4295	16.92	0.45048	0.67	r807
A09-008	323.7471	1.2564	18.29	0.11851	0.71	r302
A09-009	323.8755	1.4006	20.31	0.22698	0.36	r107
A09-010	323.9406	1.3924	20.34	0.22815	0.45	r115
A09-012	323.8312	1.3480	19.09	0.49869	0.15	r314
A09-013	323.7075	1.2898	20.05	0.50000	0.78	r508
A09-014	323.8362	1.4165	19.37	0.23910	0.67	r416
A09-015	323.6711	1.2670	20.26	0.38588	0.74	r709
A09-016	323.8589	1.2942	19.83	0.38845	0.32	r105
A09-017	323.8589	1.2538	20.01	0.48154	0.37	r103
A09-019	323.8406	1.5190	19.21	0.11193	0.57	r404
A09-020	323.8393	1.6286	19.51	0.30307	0.31	r409
A09-021	323.7913	1.2798	19.86	0.26242	0.67	r303
A09-022	323.6053	1.3614	20.15	0.49801	0.26	r707
A09-023	323.9922	1.2853	20.33	0.23530	0.14	r111
A09-024	323.7335	1.2114	20.03	0.12139	0.34	r503
A09-025	323.7882	1.4065	20.36	0.26141	0.65	r607
A09-026	323.7243	1.2340	18.77	0.23649	0.51	r504
A09-027	323.8538	1.2557	20.26	0.14282	0.20	r104
A09-030	323.6832	1.2918	16.48	0.12618	0.38	r711
A09-031	323.8082	1.3272	19.69	0.47839	0.75	r307
A09-032	323.7457	1.1958	19.68	0.49897	0.19	r502
A09-033	323.8085	1.2374	19.10	0.11306	0.33	r310
A09-034	323.8727	1.1929	19.95	0.25855	0.62	r101
A09-035	323.9531	1.2998	19.71	0.34393	0.73	r112
A09-036	323.6972	1.1886	20.35	0.45981	0.20	r501
A09-037	323.7623	1.4958	19.27	0.42296	0.17	r613
A09-038	323.6489	1.3516	19.04	0.12615	0.46	r714
A09-040	323.7929	1.4045	18.20	0.14829	0.66	r608
A09-041	323.6016	1.4789	18.39	0.12831	0.43	r815
A09-042	323.9180	1.5428	20.29	0.23212	0.64	r212
A09-043	323.8951	1.4021	18.70	0.44909	0.44	r108
A09-044	323.8948	1.5622	20.34	0.36601	0.70	r402
A09-045	323.8333	1.3774	20.26	0.24218	0.66	r315
A09-046	324.0336	1.4643	19.95	0.17155	0.29	r207
A09-047	323.8989	1.1887	20.32	0.21243	0.26	r109
A09-048	323.8343	1.2477	20.01	0.11410	0.35	r311
A09-049	323.7707	1.6005	15.17	0.36878	0.35	r604
A09-050	323.6381	1.5484	19.83	0.18123	0.35	r809
A09-051	323.6750	1.2988	20.26	0.40681	0.52	r712
A09-052	323.8026	1.3120	19.93	0.22434	0.53	r305
A09-053	323.6317	1.5229	18.98	0.16245	0.56	r810
A09-054	323.6943	1.5064	20.36	0.13363	0.28	r803
A09-055	323.8478	1.3302	19.89	0.22996	0.74	r313
A09-056	323.9792	1.3291	18.61	0.17999	0.46	r113
A09-057	323.9782	1.4566	19.68	0.23461	0.24	r208
A09-058	323.8481	1.2358	20.32	0.11373	0.18	r309

Continued on next page

Target ID	RA	DEC	r-band mag.	z	Corr.	FiberID
A09-059	323.5914	1.5204	17.57	0.12843	0.56	r811
A09-060	323.6782	1.3983	19.92	0.11227	0.31	r716
A09-061	323.7448	1.4161	19.03	0.10398	0.48	r616
A09-062	323.8792	1.5480	20.11	0.19425	0.46	r403
A09-063	323.8916	1.4701	17.80	0.44439	0.23	r407
A09-064	323.8907	1.5702	20.39	0.45176	0.37	r401
A09-066	323.8194	1.3268	19.08	0.23633	0.67	r312
A09-067	323.8831	1.2968	19.11	0.13469	0.15	r106
A09-068	323.8104	1.5393	19.63	0.22819	0.43	r412
A09-069	323.8106	1.5577	18.56	0.22321	0.35	r411
A09-070	323.5925	1.3498	19.45	0.49732	0.31	r706
A09-071	323.8492	1.2156	20.17	0.24560	0.21	r102
A09-072	324.0202	1.5097	19.90	0.12919	0.26	r204
A09-073	323.6517	1.3439	18.02	0.13928	0.71	r713
A09-074	323.7798	1.3059	18.77	0.14818	0.25	r304
A09-075	323.7799	1.6051	20.02	0.35465	0.62	r603
A09-076	323.7383	1.5104	18.79	0.11099	0.52	r612
A09-077	323.9193	1.4889	19.60	0.18053	0.30	r214
A09-078	323.6327	1.3700	20.21	0.13953	0.37	r715
A09-079	323.7656	1.3247	17.72	0.45782	0.35	r306
A09-080	323.7007	1.2363	17.61	0.12626	0.57	r505
A09-081	323.7655	1.5560	19.88	0.25424	0.66	r610
A09-082	323.6799	1.2770	19.18	0.22609	0.54	r710
A09-083	323.9232	1.3986	17.39	0.15245	0.59	r116
A09-084	323.8058	1.5704	20.21	0.45046	0.41	r410
A09-085	323.9886	1.5227	20.38	0.42677	0.69	r202
A09-086	323.5953	1.4939	19.98	0.50000	0.29	r813
A09-087	323.8931	1.4754	19.91	0.15255	0.39	r406
A09-088	323.7820	1.3994	18.86	0.22312	0.74	r308
A09-089	323.7173	1.4565	20.18	0.25483	0.67	r806
A09-090	323.5895	1.4914	19.50	0.12848	0.23	r814
A09-091	323.7173	1.5072	20.11	0.22685	0.57	r802
A09-092	323.9062	1.5771	20.09	0.43624	0.14	r211
A09-093	323.7697	1.6207	19.80	0.28924	0.66	r602
A09-094	323.6243	1.2574	18.93	0.12268	0.35	r701
A09-095	323.9339	1.4714	19.45	0.14961	0.32	r206
A09-096	323.7328	1.5847	19.88	0.11175	0.32	r609
A09-097	323.8717	1.4872	19.23	0.28915	0.76	r405
A09-098	323.7957	1.6272	19.63	0.44553	0.37	r601
A09-099	323.7995	1.5966	18.63	0.49210	0.13	r605
A09-100	323.6829	1.6015	20.39	0.44732	0.32	r801
A09-101	323.7446	1.4605	15.35	0.40611	0.23	r614
A09-102	323.6783	1.4903	19.56	0.45170	0.62	r804
A09-103	323.8183	1.4802	20.18	0.29335	0.61	r414
A09-104	323.5932	1.4614	18.37	0.11233	0.45	r816
A09-105	323.9165	1.6156	20.13	0.22956	0.34	r209
A09-106	323.6752	1.4834	20.26	0.47377	0.62	r805
A09-108	323.9295	1.5376	18.14	0.49320	0.16	r201
A09-109	323.9950	1.5178	20.40	0.34325	0.57	r203
A09-110	323.9247	1.5835	19.99	0.45105	0.75	r210
A09-111	323.9236	1.5411	20.32	0.16669	0.39	r213
A09-112	323.9238	1.4669	19.92	0.22824	0.64	r215
A09-114	323.9934	1.4807	20.39	0.43548	0.74	r205

Continued on next page

Target ID	RA	DEC	r-band mag.	z	Corr.	FiberID
A10-001	329.1154	1.4401	18.94	0.22070	0.34	b214
A10-002	328.8754	1.4648	20.35	0.29229	0.20	r806
A10-003	329.0647	1.4070	19.25	0.22232	0.48	b405
A10-004	329.0837	1.4041	19.91	0.49156	0.30	r413
A10-005	328.9756	1.3980	19.93	0.21608	0.25	r616
A10-006	328.9741	1.5794	20.09	0.44377	0.23	r611
A10-007	329.1004	1.4280	20.25	0.30627	0.32	b216
A10-008	328.7970	1.4322	19.82	0.21623	0.40	r815
A10-009	328.9841	1.4034	18.21	0.21759	0.56	r608
A10-010	328.8805	1.5065	19.67	0.21500	0.27	r804
A10-011	329.0043	1.5527	20.26	0.20343	0.19	r601
A10-012	328.9416	1.4924	20.35	0.23343	0.31	b803
A10-013	328.9417	1.4774	19.35	0.40549	0.40	b805
A10-014	329.0676	1.4749	19.59	0.49590	0.35	b402
A10-015	329.1111	1.4339	20.33	0.13143	0.19	b215
A10-016	329.0498	1.5218	19.62	0.20059	0.30	b410
A10-017	329.1756	1.6044	19.50	0.45452	0.36	r209
A10-019	329.0495	1.2015	18.82	0.22040	0.37	r502
A10-020	329.0494	1.3794	19.71	0.21997	0.44	b416
A10-022	329.0937	1.4306	19.74	0.49624	0.27	r407
A10-023	329.0949	1.4039	19.91	0.41587	0.24	r408
A10-024	329.0930	1.4765	19.35	0.22288	0.53	r404
A10-025	329.1648	1.4941	20.38	0.40954	0.28	r212
A10-026	328.8037	1.4698	18.15	0.20981	0.66	r809
A10-027	328.8662	1.4477	19.31	0.23516	0.42	r807
A10-028	329.1825	1.4824	18.36	0.14441	0.56	r213
A10-029	329.0638	1.4500	19.95	0.20022	0.31	b403
A10-030	329.0310	1.4980	18.97	0.22073	0.50	b603
A10-031	329.0322	1.5092	19.26	0.22015	0.40	b602
A10-032	328.8099	1.4630	19.16	0.21017	0.39	r810
A10-033	328.9993	1.4357	20.39	0.49614	0.27	r607
A10-034	329.1240	1.4303	19.87	0.22207	0.32	b206
A10-035	329.0252	1.4799	19.14	0.21172	0.49	b604
A10-037	328.8355	1.2926	19.36	0.21106	0.39	b704
A10-038	328.8075	1.4553	19.26	0.21144	0.44	r812
A10-039	328.9381	1.4352	20.35	0.14547	0.28	b808
A10-040	329.0012	1.4651	20.25	0.29841	0.23	r605
A10-041	329.1907	1.5308	17.99	0.49725	0.53	r201
A10-042	329.1897	1.4140	19.85	0.21755	0.29	r205
A10-043	328.9954	1.4491	19.79	0.49639	0.46	r606
A10-044	328.9951	1.5219	19.85	0.22344	0.17	r604
A10-045	329.1838	1.4922	17.54	0.21514	0.67	r203
A10-046	329.1202	1.5157	19.80	0.44477	0.38	b212
A10-047	329.1210	1.5739	19.96	0.33822	0.26	b204
A10-048	328.9790	1.4143	19.04	0.21514	0.48	r615
A10-049	328.9794	1.5377	18.95	0.26016	0.31	r613
A10-050	329.0415	1.4166	18.95	0.21795	0.44	b412
A10-051	329.2521	1.5063	19.19	0.22024	0.34	r202
A10-054	328.9969	1.3635	19.70	0.21476	0.33	r716
A10-057	329.0584	1.3950	20.06	0.22226	0.35	b406
A10-058	329.0535	1.1769	19.73	0.22003	0.37	r501
A10-059	328.9914	1.5496	20.39	0.13053	0.46	r603
A10-060	328.9912	1.3286	18.69	0.21431	0.27	r715

Continued on next page

Target ID	RA	DEC	r-band mag.	z	Corr.	FiberID
A10-061	328.8507	1.5368	20.09	0.23933	0.21	r802
A10-062	328.9151	1.4778	18.25	0.22002	0.50	b804
A10-063	328.9779	1.5463	18.49	0.14227	0.47	r612
A10-064	329.0970	1.4671	19.11	0.22108	0.51	b213
A10-065	329.0387	1.4341	19.77	0.49608	0.33	b605
A10-066	329.0399	1.4435	19.48	0.28863	0.34	b411
A10-067	329.0979	1.5906	20.29	0.49581	0.47	b210
A10-068	328.9818	1.4714	19.04	0.22178	0.50	r614
A10-069	329.1069	1.5425	20.28	0.21730	0.27	b211
A10-070	328.8315	1.4619	20.23	0.37580	0.29	r811
A10-071	328.9577	1.2544	19.36	0.47450	0.22	r701
A10-072	328.9583	1.2869	19.79	0.31495	0.33	r704
A10-073	329.0205	1.3794	19.93	0.42419	0.24	b616
A10-074	328.8154	1.4333	19.90	0.22084	0.30	r814
A10-075	328.8792	1.2328	19.93	0.15517	0.29	b701
A10-076	328.8817	1.4207	18.06	0.25017	0.29	r808
A10-077	328.8827	1.4974	19.00	0.21926	0.27	r805
A10-078	328.9458	1.4644	18.98	0.21971	0.47	b806
A10-079	329.0694	1.4187	18.71	0.21658	0.64	b404
A10-080	329.0698	1.5426	19.44	0.21991	0.54	b401
A10-081	329.1358	1.5059	19.19	0.21619	0.56	b205
A10-082	329.1977	1.4074	20.37	0.39258	0.20	r206
A10-083	329.0082	1.3434	20.06	0.29795	0.56	b503
A10-084	328.9465	1.3415	20.10	0.27051	0.47	b715
A10-085	329.1356	1.2301	19.58	0.22623	0.26	r102
A10-086	328.9738	1.3509	18.87	0.21878	0.38	r707
A10-087	329.0360	1.3859	19.11	0.22144	0.46	b607
A10-088	328.8427	1.5604	18.11	0.12031	0.62	r801
A10-089	329.0281	1.5307	19.64	0.22088	0.29	b601
A10-090	329.0890	1.4688	19.78	0.21755	0.29	r405
A10-091	329.1480	1.4083	19.73	0.22273	0.31	r214
A10-092	328.8247	1.4417	19.23	0.19896	0.36	r813
A10-093	329.0125	1.5461	19.25	0.21722	0.45	b612
A10-094	329.0744	1.5005	20.16	0.30451	0.28	r411
A10-095	329.0739	1.3985	20.03	0.22165	0.26	r414
A10-096	329.0120	1.3865	18.26	0.22583	0.43	b614
A10-097	329.0120	1.3616	20.08	0.20059	0.36	b507
A10-098	329.0199	1.6249	19.04	0.12975	0.24	b610
A10-099	329.0876	1.5226	17.88	0.21808	0.61	r402
A10-100	329.0886	1.5187	19.57	0.26551	0.30	r403
A10-101	329.0884	1.4469	20.16	0.22268	0.25	r406
A10-102	329.0797	1.1855	18.65	0.35163	0.31	r301
A10-103	329.0793	1.4243	19.49	0.21501	0.25	r412
A10-104	329.1501	1.5877	18.51	0.19936	0.37	r210
A10-105	329.1732	1.5008	19.16	0.41791	0.49	r211
A10-106	329.2308	1.4896	19.73	0.49716	0.50	r204
A10-107	328.8564	1.3697	20.26	0.11406	0.34	b708
A10-108	329.0285	1.4094	18.28	0.21443	0.67	b606
A10-109	328.9677	1.6008	19.71	0.41573	0.32	r610
A10-110	329.0305	1.3841	19.61	0.48462	0.30	b608
A10-111	329.1047	1.2383	19.41	0.22054	0.29	b302
A10-112	329.0289	1.3337	19.55	0.14298	0.28	b514
A10-113	329.0103	1.1783	18.95	0.21180	0.41	b501

Continued on next page

Target ID	RA	DEC	r-band mag.	z	Corr.	FiberID
A10-114	329.0112	1.5516	19.62	0.49625	0.56	r602
A10-115	328.8864	1.4599	18.54	0.49228	0.29	b814
A10-117	328.8865	1.3889	19.54	0.32190	0.28	b816
A10-118	329.0503	1.3846	19.35	0.21707	0.41	b414
A10-119	328.8303	1.4243	19.73	0.22297	0.34	r816
A10-120	328.8899	1.5815	19.82	0.49649	0.28	b812
A10-121	329.0149	1.3844	19.81	0.43066	0.29	b615
A10-122	328.9718	1.2926	20.10	0.21847	0.26	r705
A10-123	329.0340	1.3636	20.30	0.22046	0.36	b516
A10-125	329.0947	1.2663	20.19	0.17628	0.30	r312
A10-126	328.9637	1.3725	19.43	0.22627	0.28	r708
A10-127	328.8975	1.2639	20.00	0.49701	0.28	b711
A10-129	329.0921	1.3416	20.18	0.48447	0.23	r314
A10-130	329.0926	1.3177	19.43	0.49614	0.49	r313
A10-131	329.1540	1.2755	20.34	0.18211	0.25	r112
A10-133	329.2262	1.3765	19.11	0.48376	0.38	b116
A10-134	329.0925	1.6206	20.21	0.12631	0.27	r401
A10-135	329.0550	1.3730	19.04	0.21323	0.29	r515
A10-136	329.0557	1.3635	20.05	0.46315	0.19	r514
A10-138	329.0557	1.3793	20.24	0.19951	0.30	r516
A10-139	329.1199	1.2408	20.22	0.48497	0.30	b310
A10-140	329.1236	1.2854	20.18	0.49581	0.26	b312
A10-141	328.9223	1.2774	19.09	0.48391	0.28	b712
A10-143	328.9840	1.2932	19.22	0.14560	0.39	r714
A10-144	328.9857	1.2172	19.65	0.46423	0.32	r709
A10-145	329.0467	1.3640	19.05	0.22165	0.34	r507
A10-146	329.1129	1.1873	18.61	0.21413	0.51	b301
A10-147	329.0466	1.2136	20.08	0.40533	0.29	r503
A10-148	329.0479	1.3698	19.81	0.28315	0.26	r508
A10-149	329.0477	1.3895	19.67	0.22450	0.39	b413
A10-150	329.1740	1.2834	19.74	0.30593	0.49	b102
A10-152	329.1607	1.3545	18.95	0.49843	0.40	r116
A10-153	329.0322	1.1844	19.71	0.44378	0.23	b509
A10-154	329.0308	1.3430	19.59	0.22415	0.44	b515
A10-156	329.0951	1.1997	19.91	0.49690	0.31	r309
A10-157	329.1614	1.2451	20.31	0.41101	0.27	r110
A10-158	328.9603	1.2659	20.02	0.29385	0.26	r702
A10-159	329.1391	1.3833	19.05	0.49956	0.32	r216
A10-160	329.0837	1.3456	20.27	0.49637	0.35	r306
A10-161	329.0221	1.6361	18.03	0.20947	0.66	b609
A10-162	329.0041	1.3569	19.69	0.22363	0.48	b505
A10-163	328.8809	1.2903	20.26	0.21161	0.30	b703
A10-164	329.0672	1.2636	19.77	0.49626	0.60	r509
A10-165	329.0670	1.3865	19.67	0.22522	0.46	b408
A10-166	329.1926	1.3465	20.21	0.28646	0.39	b105
A10-167	329.1928	1.3959	19.26	0.41841	0.35	r207
A10-168	329.1318	1.6194	19.61	0.47781	0.25	b202
A10-169	328.8765	1.2563	19.20	0.46522	0.36	b702
A10-170	328.8756	1.3076	19.30	0.31586	0.40	b705
A10-171	329.0020	1.2371	18.54	0.21305	0.57	r710
A10-172	329.1289	1.3167	19.17	0.48640	0.30	b313
A10-173	329.1281	1.3616	17.54	0.21170	0.22	b316
A10-175	328.9773	1.2621	20.16	0.29167	0.39	r711

Continued on next page

Target ID	RA	DEC	r-band mag.	z	Corr.	FiberID
A10-176	329.0398	1.3333	18.79	0.19911	0.64	b513
A10-177	329.1573	1.3834	17.95	0.21408	0.60	r215
A10-179	329.1575	1.3250	20.39	0.48477	0.36	r114
A10-180	329.2115	1.3572	19.51	0.19919	0.52	b107
A10-181	329.2114	1.2578	19.50	0.31695	0.33	b109
A10-182	328.9769	1.6185	20.18	0.46249	0.26	r609
A10-183	328.9152	1.6119	19.61	0.47933	0.36	b811
A10-184	329.1181	1.3493	18.86	0.22630	0.27	b314
A10-185	329.1825	1.3357	19.92	0.20601	0.32	b104
A10-186	329.1833	1.3171	19.45	0.28683	0.39	b103
A10-187	328.9308	1.6147	19.43	0.22715	0.34	b801
A10-188	329.1701	1.2821	19.32	0.21352	0.47	b101
A10-189	329.0412	1.3838	20.10	0.20169	0.35	b415
A10-190	329.2339	1.3498	19.44	0.14736	0.39	b113
A10-191	328.9160	1.6171	19.90	0.43906	0.28	b809
A10-192	329.1167	1.2619	18.35	0.19497	0.36	b304
A10-193	329.0544	1.3279	19.82	0.22419	0.32	r504
A10-194	329.1165	1.2440	19.69	0.25841	0.26	b303
A10-195	329.2364	1.2908	19.13	0.21749	0.48	b111
A10-196	329.1029	1.6320	20.29	0.48422	0.30	b209
A10-197	328.9997	1.2923	17.55	0.49807	0.64	r713
A10-198	329.0600	1.3276	20.02	0.11241	0.27	r512
A10-199	329.2516	1.3636	20.40	0.48552	0.36	b114
A10-200	329.0708	1.2755	19.91	0.33052	0.26	r510
A10-201	329.1346	1.2783	19.92	0.22568	0.30	r106
A10-202	329.1344	1.3505	20.14	0.25862	0.34	b315
A10-203	329.0281	1.2314	19.92	0.22200	0.27	b510
A10-204	329.0272	1.3721	18.23	0.21641	0.60	b508
A10-205	328.9746	1.2728	20.00	0.30371	0.38	r712
A10-206	329.0997	1.3456	17.41	0.22670	0.65	r315
A10-207	329.0380	1.2576	19.55	0.22053	0.45	b511
A10-208	329.1008	1.2264	19.61	0.49611	0.43	r310
A10-209	329.1659	1.3713	19.93	0.49612	0.46	b108
A10-210	329.2324	1.3710	19.58	0.21702	0.42	b115
A10-211	328.9103	1.6169	19.88	0.47820	0.48	b810
A10-212	328.9390	1.2556	20.20	0.47457	0.36	b710
A10-213	328.9432	1.2997	19.03	0.49597	0.34	b713
A10-214	328.9446	1.3525	19.42	0.21678	0.20	b716
A10-215	329.0757	1.3388	18.39	0.22581	0.54	r305
A10-216	329.1328	1.2487	19.16	0.21307	0.31	b311
A10-217	329.1336	1.2331	20.23	0.14349	0.30	b309
A10-218	329.1337	1.3878	18.44	0.21898	0.49	b207
A10-219	329.0767	1.3260	19.87	0.33811	0.26	r303
A10-220	329.1333	1.3807	19.91	0.22030	0.27	b208
A10-221	329.0763	1.6167	18.64	0.21734	0.67	r410
A10-222	329.0766	1.6277	18.55	0.28648	0.66	r409
A10-223	328.8844	1.3164	20.18	0.48457	0.34	b706
A10-224	329.1404	1.2315	19.37	0.22437	0.37	r103
A10-225	329.0738	1.3930	19.88	0.21861	0.27	r415
A10-226	329.0745	1.3129	19.91	0.21970	0.21	r511
A10-227	329.1637	1.2426	19.93	0.20466	0.30	r109
A10-228	329.1634	1.3422	20.09	0.36982	0.30	r115
A10-229	329.0455	1.3589	18.48	0.25744	0.26	r506

Continued on next page

Target ID	RA	DEC	r-band mag.	z	Corr.	FiberID
A10-230	329.1062	1.2671	18.93	0.19495	0.39	b305
A10-231	329.0460	1.3374	20.30	0.21166	0.28	r505
A10-232	329.1066	1.2706	20.03	0.44993	0.24	b306
A10-233	329.1724	1.3545	20.07	0.49789	0.52	b106
A10-234	329.0450	1.6108	20.12	0.20143	0.35	b409
A10-235	329.0708	1.3504	19.38	0.22215	0.32	r513
A10-236	329.0714	1.3871	19.94	0.21856	0.30	b407
A10-237	329.1373	1.6187	19.96	0.19732	0.26	b203
A10-238	329.1367	1.6376	19.48	0.13730	0.42	b201
A10-239	329.0163	1.3897	18.71	0.49577	0.31	b613
A10-241	328.9544	1.2675	20.37	0.47696	0.23	r703
A10-242	329.0172	1.3520	19.63	0.49723	0.34	b504
A10-243	329.1505	1.2535	18.58	0.21268	0.58	r104
A10-245	329.0800	1.3342	18.84	0.44068	0.38	r304
A10-246	329.1510	1.2907	19.24	0.31093	0.26	r107
A10-247	329.1504	1.2298	19.92	0.21587	0.50	r101
A10-248	329.0806	1.3111	19.84	0.49625	0.38	r302
A10-249	329.0806	1.3775	19.80	0.21471	0.27	r308
A10-250	329.1506	1.2943	20.25	0.49463	0.29	r108
A10-251	329.2225	1.3493	19.70	0.22029	0.29	b112
A10-252	328.8913	1.2296	19.91	0.49612	0.34	b709
A10-253	329.0182	1.3599	19.44	0.21954	0.39	b506
A10-254	329.1497	1.2595	18.10	0.21279	0.55	r105
A10-255	329.0781	1.3646	20.32	0.49637	0.31	r307
A10-256	329.0785	1.3919	19.77	0.22370	0.33	r416
A10-257	328.9610	1.3383	19.13	0.14240	0.36	r706
A10-258	329.0231	1.2741	19.61	0.20101	0.29	b502
A10-259	329.0886	1.3736	18.55	0.46209	0.36	r316
A10-260	329.0872	1.2512	20.30	0.31318	0.29	r311
A10-261	329.1546	1.2659	19.26	0.43229	0.23	r111
A10-262	329.2148	1.2691	19.95	0.21264	0.29	b110
A10-264	329.1150	1.3170	19.64	0.23760	0.28	b308
A10-265	329.1151	1.3123	20.22	0.20557	0.24	b307
A10-266	329.2430	1.3900	19.86	0.48476	0.39	r208
A11-000	346.9674	-2.1400	20.24	0.29625	0.27	r709
A11-001	346.8305	-1.8197	19.93	0.49631	0.54	r810
A11-003	346.9013	-1.9306	19.43	0.47610	0.74	b716
A11-004	346.9679	-1.9248	20.17	0.35507	0.57	r716
A11-005	347.0774	-1.8287	19.88	0.30689	0.55	b213
A11-006	347.0773	-1.8686	20.20	0.29667	0.61	b214
A11-007	347.0385	-1.6805	19.72	0.48509	0.18	r409
A11-008	346.8272	-1.8256	19.65	0.26573	0.62	r812
A11-009	346.8974	-1.8870	19.39	0.29787	0.61	r805
A11-011	347.0373	-1.8980	19.23	0.30487	0.74	r416
A11-012	347.0380	-1.9372	19.55	0.30959	0.74	r308
A11-013	347.1687	-2.0449	19.32	0.32910	0.45	b111
A11-014	347.1684	-2.1091	19.27	0.29585	0.33	b109
A11-015	346.8387	-2.0002	19.97	0.26493	0.56	b703
A11-016	346.9779	-1.9762	19.89	0.30756	0.42	r713
A11-017	347.0835	-1.9616	19.77	0.30042	0.73	r103
A11-018	346.9790	-1.9451	18.75	0.29690	0.79	b504
A11-020	346.9789	-1.8609	19.68	0.30264	0.57	r614
A11-021	347.0462	-1.8404	20.27	0.44879	0.64	r412

Continued on next page

Target ID	RA	DEC	r-band mag.	z	Corr.	FiberID
A11-022	347.0307	-1.9742	18.86	0.30027	0.61	r305
A11-023	346.9641	-1.9762	20.34	0.43563	0.24	r712
A11-024	346.9637	-2.1396	18.65	0.29454	0.55	r710
A11-025	346.9636	-1.7499	19.23	0.29518	0.45	b802
A11-026	346.9639	-1.8836	18.88	0.30582	0.77	b806
A11-027	346.8069	-1.9717	20.36	0.41338	0.30	b706
A11-028	346.9522	-1.9718	20.08	0.30110	0.67	r714
A11-029	346.8080	-1.8228	19.78	0.48113	0.46	r811
A11-030	346.9517	-1.9465	19.55	0.29694	0.51	r715
A11-031	346.8398	-2.0241	19.19	0.27255	0.54	b701
A11-032	346.9802	-1.8907	20.17	0.30820	0.54	r615
A11-033	347.0489	-1.8775	18.36	0.30049	0.76	r407
A11-034	347.0477	-1.8824	19.85	0.30126	0.65	r415
A11-035	347.0491	-1.9515	18.82	0.29919	0.83	r311
A11-036	347.1168	-2.1272	20.27	0.29354	0.46	r110
A11-037	346.8350	-2.0101	20.11	0.47747	0.25	b702
A11-038	347.0392	-2.0456	20.38	0.35900	0.44	r303
A11-039	346.9051	-1.7622	20.34	0.32853	0.43	b809
A11-040	346.9040	-1.9172	19.32	0.47728	0.72	b815
A11-041	346.9722	-1.9052	20.39	0.30280	0.62	b808
A11-042	347.1121	-2.0861	20.20	0.20065	0.29	r111
A11-043	347.2466	-2.0079	17.57	0.23713	0.72	b114
A11-044	347.0405	-1.7135	19.39	0.26533	0.69	r410
A11-045	346.8319	-1.9834	20.05	0.26497	0.54	b704
A11-046	346.9018	-1.7534	19.88	0.30010	0.23	r803
A11-047	346.9036	-1.9121	19.96	0.29977	0.70	r808
A11-048	346.9748	-1.7542	19.78	0.26469	0.28	r610
A11-049	347.0428	-2.0797	20.17	0.35574	0.55	r302
A11-050	347.1096	-1.7500	19.85	0.30230	0.51	r210
A11-051	346.8589	-1.9547	19.41	0.31819	0.74	b707
A11-053	346.8132	-1.9151	20.39	0.47424	0.26	r816
A11-054	346.8848	-1.8953	19.65	0.49998	0.37	r806
A11-055	346.8843	-1.9566	19.50	0.32742	0.66	b712
A11-057	346.9399	-1.8598	18.95	0.30909	0.66	b805
A11-058	347.0120	-1.9631	19.50	0.30170	0.37	r503
A11-059	346.9063	-2.0554	19.95	0.35593	0.69	b709
A11-060	346.9756	-1.9907	19.53	0.41908	0.29	r711
A11-061	347.0442	-2.1437	19.60	0.24086	0.32	r301
A11-062	346.9079	-1.7889	20.28	0.49995	0.44	b810
A11-063	347.0438	-1.9524	19.74	0.31115	0.59	r307
A11-064	347.0831	-1.7021	20.03	0.42471	0.48	b209
A11-065	346.9338	-1.9908	19.60	0.29747	0.47	r704
A11-066	347.0001	-2.0569	20.15	0.45003	0.74	b502
A11-067	347.0002	-2.0945	20.11	0.29390	0.58	b501
A11-068	346.9987	-1.9317	20.32	0.30798	0.61	b507
A11-069	347.0306	-1.9610	19.74	0.30776	0.70	r306
A11-070	346.8203	-1.8272	19.38	0.26666	0.53	r813
A11-071	347.0295	-1.8132	18.86	0.30204	0.73	r411
A11-072	347.0294	-1.8668	19.33	0.30942	0.73	r414
A11-073	347.0294	-1.9500	19.93	0.23438	0.36	r506
A11-075	346.9129	-1.8658	18.75	0.29665	0.64	b812
A11-076	347.0507	-2.1433	18.98	0.29239	0.54	r309
A11-077	347.0178	-1.9808	20.29	0.30693	0.46	r502

Continued on next page

Target ID	RA	DEC	r-band mag.	z	Corr.	FiberID
A11-078	347.0733	-1.8286	19.70	0.30658	0.74	b212
A11-079	347.0337	-2.0295	18.39	0.29749	0.43	r304
A11-083	346.9662	-1.8446	19.87	0.30485	0.54	b804
A11-084	346.9413	-2.1062	20.29	0.30002	0.55	r701
A11-085	347.0093	-2.1010	20.36	0.27364	0.22	b510
A11-086	347.0098	-2.1266	19.81	0.29984	0.49	b509
A11-087	346.9405	-1.7472	19.47	0.48253	0.66	b801
A11-088	346.8010	-1.9224	20.39	0.47816	0.48	b708
A11-089	346.9419	-1.9506	20.26	0.29953	0.54	r706
A11-091	347.0089	-1.9367	19.74	0.30042	0.41	b515
A11-093	346.9343	-1.9585	19.84	0.30493	0.64	r705
A11-094	347.0043	-1.9937	19.25	0.29866	0.57	b513
A11-095	346.8673	-1.7443	20.09	0.29706	0.35	r801
A11-096	346.8672	-1.9329	19.84	0.48202	0.68	b714
A11-097	347.0031	-1.9287	18.07	0.30335	0.75	b508
A11-098	346.7883	-1.9756	18.88	0.27232	0.79	b705
A11-099	346.8611	-1.9632	19.32	0.29789	0.60	b711
A11-100	346.9236	-1.9947	18.94	0.32752	0.68	r703
A11-103	346.9243	-1.9363	19.98	0.30244	0.56	r708
A11-104	346.9268	-2.0972	19.56	0.29521	0.54	r702
A11-106	346.9267	-1.9016	20.32	0.45424	0.73	b814
A11-107	346.9957	-1.8618	19.88	0.30019	0.58	r605
A11-109	347.0797	-1.7921	18.72	0.21863	0.68	b211
A11-110	347.0802	-1.9310	19.60	0.29215	0.78	r105
A11-111	346.9156	-1.9924	19.36	0.30340	0.62	b710
A11-112	346.9839	-1.9613	20.31	0.31220	0.74	b503
A11-113	347.0518	-1.9721	19.67	0.30006	0.64	r310
A11-114	346.8439	-1.8354	19.33	0.26583	0.56	r814
A11-115	346.8456	-1.8744	19.96	0.30476	0.42	r815
A11-116	346.9854	-1.9425	19.72	0.30386	0.71	b505
A11-117	347.1225	-1.7316	19.98	0.38431	0.62	r209
A11-119	347.0269	-1.7340	19.83	0.26426	0.56	r601
A11-120	347.0275	-1.9083	19.38	0.30798	0.60	r607
A11-121	347.0278	-2.0382	19.62	0.38392	0.58	r501
A11-122	347.1608	-2.0493	17.42	0.20386	0.27	b103
A11-123	347.1613	-2.1082	20.18	0.29586	0.31	b110
A11-124	347.1014	-1.9380	18.99	0.29773	0.79	r116
A11-125	347.0283	-1.8209	19.61	0.29621	0.56	r603
A11-128	346.9211	-1.8831	20.18	0.43710	0.72	b813
A11-129	346.9906	-1.9415	18.50	0.30285	0.81	b506
A11-130	346.9219	-1.8085	19.98	0.36631	0.59	b811
A11-131	347.1391	-2.0357	19.24	0.30619	0.76	b105
A11-132	347.2064	-2.0323	20.26	0.43571	0.45	b112
A11-135	347.1785	-1.9461	18.15	0.23774	0.79	b116
A11-136	346.9860	-1.7424	20.23	0.35586	0.58	r609
A11-137	346.9173	-1.9317	20.06	0.30662	0.56	b715
A11-138	346.9863	-1.8589	19.71	0.30207	0.59	r613
A11-139	347.0067	-2.0665	17.93	0.29719	0.80	b512
A11-140	347.0079	-2.0776	18.77	0.29653	0.72	b511
A11-141	346.8747	-1.7500	20.40	0.41113	0.25	r802
A11-142	347.0083	-1.9410	18.08	0.30117	0.48	b514
A11-143	347.0725	-1.7474	19.24	0.23797	0.69	b210
A11-144	347.0211	-1.8598	19.14	0.30871	0.68	r604

Continued on next page

Target ID	RA	DEC	r-band mag.	z	Corr.	FiberID
A11-145	347.0205	-1.9381	19.80	0.30027	0.54	r507
A11-146	347.0209	-1.9116	19.53	0.30409	0.62	r608
A11-147	347.0137	-1.9594	20.25	0.30282	0.60	r504
A11-148	346.8766	-1.8981	20.25	0.47838	0.68	r807
A11-149	347.0241	-1.8114	19.53	0.30311	0.50	r602
A11-150	347.1061	-1.7881	20.36	0.44604	0.54	b204
A11-151	347.1080	-1.7616	19.89	0.30091	0.29	b201
A11-152	347.1074	-1.8967	20.39	0.30269	0.71	b208
A11-153	346.8701	-1.8299	18.49	0.30363	0.65	r804
A11-154	346.9364	-1.9493	18.20	0.29959	0.76	r707
A11-155	347.0052	-1.9241	20.12	0.30188	0.67	b516
A11-156	347.0704	-1.9687	18.99	0.30439	0.71	r102
A11-157	347.0703	-1.6977	20.25	0.48360	0.29	r401
A11-158	347.0824	-1.8931	20.21	0.29229	0.61	b215
A11-159	347.0843	-1.7810	19.72	0.30043	0.80	b203
A11-160	347.0848	-1.8573	19.94	0.30475	0.58	b206
A11-161	347.0122	-1.9287	19.08	0.30070	0.70	r508
A11-162	347.0128	-1.9542	19.85	0.30324	0.43	r505
A11-163	347.1507	-1.7589	19.42	0.30234	0.65	r201
A11-164	347.1519	-1.8439	19.10	0.30097	0.73	r205
A11-165	347.1512	-1.9222	19.33	0.29448	0.78	b108
A11-166	346.9197	-1.9348	20.13	0.20259	0.31	b713
A11-168	346.9479	-1.8927	19.53	0.43618	0.76	b807
A11-169	347.1545	-2.0500	20.23	0.44929	0.52	b102
A11-170	347.0975	-2.0529	20.01	0.30168	0.57	r112
A11-171	347.0970	-2.1462	20.33	0.49610	0.23	r109
A11-172	347.1543	-2.0369	20.16	0.32933	0.30	b104
A11-173	347.1154	-1.7615	18.50	0.30175	0.76	r211
A11-174	347.1306	-1.8291	19.96	0.30157	0.65	r212
A11-175	347.0596	-1.8513	20.15	0.27231	0.59	r404
A11-176	347.0990	-2.0023	18.30	0.30676	0.66	r113
A11-177	347.0630	-1.9292	18.46	0.30338	0.77	r312
A11-178	347.1282	-1.8629	19.26	0.30077	0.70	r214
A11-179	347.1276	-1.9523	19.38	0.29303	0.24	r115
A11-180	347.1957	-1.8008	20.00	0.29899	0.19	r202
A11-181	347.0719	-1.7862	18.88	0.21882	0.61	r402
A11-182	347.1412	-1.9564	18.19	0.23793	0.82	b106
A11-183	347.0726	-1.8816	18.97	0.30495	0.75	r408
A11-184	347.1370	-1.8473	19.93	0.47949	0.57	r213
A11-185	347.0692	-1.9299	18.09	0.30497	0.73	r106
A11-186	347.0693	-1.8592	19.60	0.36310	0.75	r405
A11-187	347.1378	-1.8629	19.47	0.29988	0.73	r206
A11-188	347.1568	-2.1137	19.73	0.29603	0.52	b101
A11-190	347.0761	-1.9269	19.32	0.30170	0.76	r107
A11-191	347.0752	-1.9222	19.99	0.30298	0.53	r108
A11-192	347.0576	-1.9280	19.63	0.30392	0.72	r313
A11-193	347.0650	-1.9331	20.30	0.21166	0.24	r104
A11-194	347.1457	-1.9435	19.16	0.23785	0.73	b107
A11-195	347.0857	-1.8498	19.79	0.30063	0.76	b205
A11-196	347.1363	-1.9064	19.68	0.14741	0.31	r216
A11-197	347.0742	-1.9119	19.89	0.30969	0.44	b216
A11-198	347.0969	-1.8871	19.20	0.30537	0.80	b207
A11-199	347.1556	-1.8431	20.29	0.29866	0.45	r204

Continued on next page

Target ID	RA	DEC	r-band mag.	z	Corr.	FiberID
A11-200	347.1454	-1.8176	20.00	0.30163	0.67	r203
A11-201	347.2146	-1.8652	20.15	0.29586	0.58	r207
A11-202	347.0146	-1.8783	18.85	0.30408	0.80	r606
A11-203	347.0938	-1.7677	19.93	0.30523	0.67	b202
A11-204	347.1341	-1.8860	19.47	0.30685	0.55	r215
A11-205	347.0685	-1.8381	20.24	0.30729	0.52	r403
A11-206	347.0681	-1.8715	19.28	0.21438	0.46	r406
A20-002	141.5084	12.6722	15.74	0.21320	0.34	b706
A20-003	141.5195	12.6926	16.17	0.29730	0.27	b716
A20-004	141.5466	12.7140	16.41	0.45343	0.67	b816
A20-005	141.7786	12.5993	16.57	0.22868	0.21	b110
A20-006	141.5190	12.7317	16.59	0.43270	0.25	r805
A20-007	141.5498	12.6980	16.73	0.45371	0.51	b808
A20-008	141.5146	12.7261	16.94	0.18713	0.79	r816
A20-009	141.6223	12.7790	17.16	0.37581	0.51	b414
A20-010	141.6363	12.6844	17.31	0.16747	0.44	r316
A20-011	141.6000	12.8029	17.31	0.15606	0.58	b613
A20-012	141.6054	12.8094	17.36	0.15637	0.58	b612
A20-013	141.6325	12.6496	17.56	0.21757	0.77	r315
A20-014	141.6942	12.6608	17.81	0.44979	0.31	b314
A20-015	141.5411	12.8090	17.89	0.11683	0.36	b810
A20-016	141.7139	12.6505	17.92	0.11443	0.47	b312
A20-017	141.5457	12.7898	17.92	0.24984	0.68	b812
A20-018	141.6138	12.7972	18.02	0.43330	0.26	b605
A20-019	141.6139	12.8423	18.05	0.48113	0.39	b602
A20-020	141.7453	12.7000	18.21	0.38189	0.50	r216
A20-021	141.6410	12.7660	18.22	0.18232	0.43	b406
A20-022	141.5957	12.7965	18.27	0.24378	0.41	b614
A20-023	141.7025	12.7343	18.35	0.11491	0.27	b207
A20-024	141.6831	12.8335	18.36	0.20722	0.38	b209
A20-025	141.6789	12.7178	18.37	0.34063	0.49	b216
A20-027	141.6765	12.7508	18.38	0.11400	0.52	b212
A20-028	141.6862	12.7968	18.40	0.34862	0.49	b202
A20-030	141.5394	12.6194	18.54	0.17646	0.46	b710
A20-031	141.6862	12.5859	18.54	0.46023	0.14	b302
A20-032	141.7343	12.5851	18.55	0.35617	0.76	r110
A20-034	141.5358	12.8570	18.64	0.33829	0.14	r801
A20-035	141.6584	12.5841	18.70	0.35669	0.61	r309
A20-036	141.6361	12.8044	18.77	0.15767	0.51	b412
A20-037	141.5272	12.6291	18.82	0.16746	0.56	b711
A20-038	141.6152	12.6276	18.84	0.49117	0.65	r304
A20-039	141.7704	12.5819	18.86	0.17506	0.78	b101
A20-040	141.5366	12.8429	18.89	0.27506	0.22	b809
A20-041	141.5269	12.6554	18.92	0.48215	0.56	b713
A20-042	141.6470	12.7442	18.99	0.16181	0.50	r414
A20-043	141.7620	12.6265	18.99	0.43240	0.30	b104
A20-044	141.5478	12.7533	18.99	0.18723	0.74	b814
A20-045	141.6041	12.6405	19.00	0.43451	0.23	r513
A20-046	141.5682	12.6517	19.00	0.32901	0.57	r505
A20-047	141.7203	12.5783	19.02	0.35613	0.31	r101
A20-048	141.7520	12.5931	19.04	0.17732	0.64	b102
A20-051	141.5091	12.5915	19.09	0.12884	0.70	b702
A20-052	141.6254	12.6001	19.09	0.18639	0.50	r302

Continued on next page

Target ID	RA	DEC	r-band mag.	z	Corr.	FiberID
A20-053	141.6442	12.8294	19.09	0.27470	0.42	r410
A20-054	141.6727	12.5975	19.12	0.35929	0.52	b303
A20-055	141.5854	12.6176	19.15	0.43760	0.81	r504
A20-056	141.7165	12.7521	19.16	0.48895	0.64	r213
A20-058	141.5668	12.6994	19.24	0.31886	0.63	r615
A20-059	141.5559	12.7905	19.25	0.45300	0.31	b804
A20-060	141.6699	12.8231	19.25	0.39225	0.25	r402
A20-061	141.6042	12.7622	19.32	0.11306	0.29	b615
A20-062	141.6663	12.8394	19.32	0.15312	0.30	r401
A20-063	141.5810	12.6145	19.33	0.44028	0.51	r503
A20-065	141.6921	12.6150	19.33	0.28696	0.47	b309
A20-066	141.7660	12.5960	19.33	0.12939	0.60	b103
A20-067	141.6325	12.8489	19.35	0.18567	0.42	b409
A20-068	141.7305	12.6353	19.39	0.32870	0.47	r114
A20-070	141.5286	12.5923	19.42	0.45335	0.57	b709
A20-072	141.5912	12.7294	19.42	0.18279	0.13	r608
A20-074	141.6154	12.6372	19.47	0.43649	0.53	r305
A20-075	141.5599	12.8432	19.50	0.35207	0.24	b801
A20-076	141.6670	12.6450	19.51	0.46044	0.77	r313
A20-077	141.7169	12.6127	19.53	0.35643	0.54	r105
A20-078	141.6218	12.7356	19.54	0.21252	0.28	b608
A20-079	141.5535	12.6107	19.56	0.34004	0.52	r704
A20-080	141.5228	12.7684	19.59	0.24789	0.29	r803
A20-081	141.5674	12.8565	19.59	0.31826	0.25	r609
A20-082	141.5874	12.6308	19.63	0.32886	0.64	r511
A20-083	141.7867	12.6034	19.63	0.12965	0.51	b111
A20-084	141.7812	12.6898	19.63	0.11341	0.57	b115
A20-085	141.5530	12.6919	19.63	0.45405	0.59	r708
A20-086	141.5392	12.7472	19.64	0.46495	0.57	b815
A20-087	141.5417	12.6901	19.65	0.41670	0.15	r707
A20-088	141.6286	12.7628	19.67	0.15729	0.70	b415
A20-089	141.6742	12.7463	19.71	0.45580	0.65	r404
A20-090	141.6820	12.7264	19.73	0.34203	0.39	b215
A20-091	141.6778	12.7872	19.73	0.11393	0.48	b211
A20-092	141.7650	12.7298	19.77	0.30761	0.23	r205
A20-093	141.5876	12.8054	19.78	0.35788	0.34	r604
A20-094	141.5848	12.7831	19.79	0.30474	0.31	r612
A20-096	141.5510	12.7350	19.81	0.34533	0.24	b807
A20-098	141.7220	12.6164	19.84	0.35849	0.37	r106
A20-099	141.6289	12.6594	19.85	0.35706	0.60	r307
A20-100	141.6417	12.7067	19.85	0.12871	0.82	b408
A20-101	141.6693	12.7477	19.86	0.42919	0.61	r403
A20-102	141.7456	12.5809	19.87	0.32790	0.65	r109
A20-103	141.7784	12.7008	19.88	0.46475	0.42	r207
A20-104	141.5092	12.5964	19.88	0.21673	0.51	b703
A20-105	141.5465	12.7586	19.90	0.27338	0.47	b813
A20-106	141.6691	12.7428	19.92	0.49830	0.56	r405
A20-107	141.6862	12.7743	19.93	0.33987	0.50	b204
A20-108	141.6249	12.6142	19.93	0.33986	0.50	r303
A20-109	141.5467	12.6011	19.94	0.34020	0.54	r702
A20-110	141.6504	12.7201	19.95	0.28828	0.70	r415
A20-111	141.6837	12.6534	19.96	0.18625	0.58	b305
A20-112	141.6896	12.7451	19.97	0.15751	0.54	b206

Continued on next page

Target ID	RA	DEC	r-band mag.	z	Corr.	FiberID
A20-113	141.6715	12.6658	19.98	0.15167	0.26	b308
A20-114	141.5892	12.6969	19.98	0.22321	0.33	r516
A20-115	141.7868	12.6505	19.99	0.48625	0.46	b113
A20-116	141.5579	12.7828	20.01	0.33361	0.20	b806
A20-117	141.6952	12.7568	20.05	0.33578	0.24	b205
A20-118	141.6851	12.6636	20.06	0.33934	0.49	b307
A20-119	141.6145	12.6909	20.07	0.33273	0.17	r515
A20-120	141.6757	12.7296	20.08	0.44964	0.59	b214
A20-121	141.7271	12.6001	20.09	0.35559	0.75	r103
A20-122	141.6094	12.8294	20.14	0.15696	0.73	b610
A20-123	141.7429	12.7834	20.16	0.38665	0.28	r211
A20-124	141.7129	12.8125	20.17	0.35734	0.26	b201
A20-125	141.6490	12.5949	20.18	0.43838	0.73	r310
A20-126	141.5804	12.6985	20.18	0.18761	0.39	r616
A20-127	141.7346	12.8051	20.21	0.32922	0.42	r210
A20-128	141.7723	12.7543	20.21	0.39267	0.20	r203
A20-129	141.7509	12.6291	20.23	0.20644	0.23	b105
A20-130	141.5953	12.8055	20.23	0.11346	0.79	r603
A20-131	141.5399	12.6268	20.23	0.48998	0.55	r706
A20-132	141.5902	12.8288	20.31	0.33590	0.27	r601
A20-134	141.6906	12.6230	20.34	0.18450	0.48	b310
A20-136	141.5768	12.5767	20.35	0.28462	0.56	r501
A20-137	141.6138	12.8351	20.36	0.36059	0.40	b603
A20-138	141.7227	12.7434	20.37	0.27445	0.65	r214
A20-139	141.7777	12.6568	20.37	0.32853	0.47	b107
A20-141	141.6552	12.8057	20.42	0.27454	0.51	r411
A20-142	141.6826	12.6570	20.44	0.33978	0.60	b306
A20-143	141.6231	12.5816	20.48	0.43350	0.51	r301
A20-144	141.7654	12.7717	20.51	0.16807	0.55	r201
A20-146	141.7225	12.5925	20.54	0.22012	0.38	r102
A20-147	141.7825	12.5815	20.54	0.48292	0.44	b109
A20-149	141.5922	12.8012	20.58	0.11365	0.46	r605
A20-150	141.7804	12.6953	20.59	0.22798	0.28	b116
A20-151	141.7907	12.6391	20.59	0.36136	0.20	b112
A20-152	141.5283	12.6456	20.61	0.38363	0.40	b712
A20-153	141.6661	12.7320	20.61	0.12926	0.49	r406
A20-154	141.6364	12.8424	20.62	0.12622	0.38	b401
A20-155	141.6473	12.7479	20.63	0.35797	0.22	r413
A20-156	141.5643	12.8244	20.64	0.48917	0.65	b802
A20-157	141.5229	12.7078	20.64	0.18780	0.30	r807
A20-158	141.7506	12.7517	20.66	0.28837	0.38	r204
A20-159	141.5936	12.7586	20.66	0.39235	0.32	r606
A20-160	141.6314	12.8257	20.67	0.32945	0.31	b410
A20-161	141.5802	12.7050	20.69	0.44035	0.63	r614
A20-162	141.6755	12.7148	20.70	0.15582	0.21	r408
A20-163	141.6187	12.7638	20.70	0.15923	0.24	b606
A20-164	141.7475	12.6045	20.70	0.49391	0.66	r112
A20-165	141.6259	12.6625	20.71	0.47165	0.35	r308
A20-166	141.6799	12.6343	20.72	0.36040	0.28	b304
A20-167	141.6439	12.7162	20.74	0.48428	0.49	r416
A20-168	141.5341	12.6586	20.74	0.28432	0.51	b714
A20-169	141.6809	12.8129	20.76	0.20378	0.31	b210
A20-170	141.7218	12.6845	20.76	0.49182	0.51	r108

Continued on next page

Target ID	RA	DEC	r-band mag.	z	Corr.	FiberID
A20-171	141.5895	12.5965	20.78	0.14958	0.29	r509
A20-172	141.5611	12.5776	20.78	0.49246	0.58	r502
A20-173	141.5467	12.6244	20.81	0.32826	0.36	r705
A20-174	141.6459	12.7640	20.81	0.35769	0.37	r412
A20-177	141.5538	12.5831	20.86	0.23109	0.23	r701
A20-181	141.7188	12.6503	20.91	0.45632	0.27	r107
A20-182	141.6189	12.8049	20.93	0.46045	0.70	b604
A20-183	141.5101	12.8413	20.93	0.27510	0.51	r810
A20-184	141.7483	12.7616	20.93	0.35787	0.28	r202
A20-185	141.5885	12.8212	20.94	0.37580	0.46	r602
A20-186	141.6443	12.6496	20.98	0.15159	0.32	r314
A20-187	141.6076	12.6360	20.99	0.44544	0.23	r512
A20-188	141.7662	12.6967	21.00	0.16751	0.52	r208
A20-189	141.5623	12.6597	21.02	0.43753	0.70	r506
A20-190	141.7677	12.6567	21.03	0.19975	0.18	b106
A20-191	141.5862	12.8167	21.03	0.11394	0.22	r611
A20-192	141.7426	12.6302	21.04	0.37319	0.45	r113
A20-193	141.5509	12.7903	21.05	0.21413	0.43	b805
A20-195	141.6125	12.6515	21.12	0.48486	0.32	r514
A20-196	141.6130	12.7562	21.15	0.31870	0.38	b607
A20-197	141.6702	12.6027	21.15	0.20569	0.20	r311
A20-198	141.5224	12.6720	21.18	0.10643	0.56	b715
A20-199	141.5245	12.7000	21.18	0.49231	0.50	r808
A20-200	141.7132	12.6623	21.18	0.47123	0.55	b315
A20-201	141.7358	12.7563	21.23	0.28887	0.43	r212
A20-202	141.7464	12.6398	21.24	0.13821	0.58	r115
A20-203	141.7297	12.6456	21.25	0.49384	0.64	r116
A20-204	141.7454	12.5884	21.26	0.23489	0.24	r111
A20-205	141.6087	12.8231	21.27	0.26645	0.32	b611
A20-206	141.6494	12.8311	21.31	0.40287	0.31	r409
A20-207	141.5607	12.6105	21.34	0.31870	0.33	r703
A20-208	141.5509	12.8029	21.37	0.20794	0.42	b803
A20-210	141.6345	12.8108	21.40	0.11409	0.25	b411
A20-211	141.6343	12.7034	21.41	0.48888	0.64	b416
A20-212	141.6421	12.7984	21.47	0.25979	0.27	b403
A20-214	141.5769	12.7640	21.49	0.36526	0.51	r613
A20-215	141.7016	12.6825	21.50	0.48600	0.54	b316
A20-216	141.5143	12.7620	21.52	0.21117	0.20	r814
A20-217	141.5440	12.8032	21.54	0.34027	0.16	b811
A20-220	141.5982	12.7120	21.56	0.10648	0.63	b616
A20-221	141.6085	12.8586	21.59	0.11847	0.22	b609
A20-222	141.5162	12.8489	21.60	0.27393	0.36	r809
A20-223	141.7173	12.8100	21.60	0.21282	0.28	r209
A20-224	141.6365	12.8353	21.61	0.20334	0.25	b402
A20-225	141.6377	12.7913	21.61	0.34682	0.31	b404
A20-226	141.6422	12.7598	21.65	0.12819	0.64	b407
A20-227	141.6416	12.7891	21.70	0.11349	0.80	b405
A20-229	141.6995	12.6246	21.75	0.47415	0.68	b311
A20-230	141.6174	12.6489	21.76	0.43477	0.19	r306
A20-231	141.6780	12.7388	21.76	0.44972	0.57	b213
A20-232	141.5105	12.7640	21.81	0.12916	0.40	r813
A20-234	141.6938	12.7305	21.90	0.13824	0.59	b208
A20-235	141.7693	12.6672	22.01	0.12932	0.79	b108

Continued on next page

Target ID	RA	DEC	r-band mag.	z	Corr.	FiberID
A21-001	149.4841	-11.0914	16.16	0.48798	0.29	b715
A21-002	149.6408	-11.1807	16.41	0.43536	0.32	b310
A21-003	149.4900	-11.0767	16.53	0.48968	0.35	b716
A21-004	149.5433	-11.1500	16.64	0.28648	0.35	b504
A21-005	149.4983	-11.0902	16.69	0.49156	0.27	r706
A21-006	149.5515	-10.9702	16.73	0.16367	0.23	r603
A21-007	149.7351	-10.9179	16.74	0.31853	0.47	r201
A21-009	149.5645	-10.9344	16.80	0.49077	0.28	b602
A21-010	149.6685	-11.1189	16.85	0.43565	0.39	r116
A21-011	149.5918	-11.0261	16.94	0.17181	0.44	b405
A21-012	149.6095	-11.0829	17.00	0.49907	0.26	r314
A21-013	149.5425	-11.1557	17.05	0.36482	0.27	r710
A21-014	149.6261	-10.9224	17.10	0.49258	0.22	r401
A21-016	149.4937	-11.0739	17.19	0.37655	0.26	r707
A21-017	149.5962	-11.0611	17.23	0.15455	0.64	r307
A21-018	149.6309	-11.0647	17.32	0.19688	0.39	b316
A21-019	149.5695	-11.1329	17.34	0.16203	0.46	b510
A21-021	149.5341	-10.9590	17.37	0.16433	0.28	b805
A21-022	149.6028	-11.0370	17.45	0.32613	0.26	r416
A21-023	149.6105	-11.0622	17.48	0.16426	0.66	r316
A21-024	149.5957	-11.1099	17.48	0.16580	0.83	r303
A21-025	149.6928	-11.0645	17.61	0.39743	0.18	b107
A21-026	149.6355	-11.0270	17.63	0.25311	0.29	b213
A21-027	149.5800	-11.0482	17.65	0.16205	0.65	b414
A21-028	149.5790	-11.1246	17.77	0.47842	0.27	r504
A21-029	149.5277	-10.9212	17.80	0.17168	0.31	b801
A21-030	149.6661	-11.1458	17.80	0.16368	0.75	r104
A21-031	149.6842	-11.1744	17.82	0.38179	0.35	r110
A21-032	149.6199	-11.1543	17.83	0.39471	0.33	b302
A21-033	149.5568	-10.9703	17.91	0.35459	0.35	b611
A21-034	149.6023	-11.0319	17.92	0.39913	0.23	r415
A21-035	149.5883	-11.1464	17.93	0.38341	0.25	r511
A21-036	149.5342	-10.9488	17.98	0.13377	0.47	b803
A21-037	149.5639	-11.0530	17.98	0.47957	0.37	b608
A21-038	149.5513	-11.0715	17.99	0.16378	0.49	b508
A21-039	149.4620	-11.0943	18.01	0.21273	0.39	b704
A21-040	149.6846	-11.0122	18.01	0.26642	0.59	r214
A21-041	149.5820	-11.0174	18.02	0.15999	0.53	b411
A21-042	149.5828	-11.1139	18.02	0.40571	0.20	r506
A21-043	149.5431	-10.9537	18.05	0.16465	0.35	r612
A21-044	149.5308	-11.1116	18.06	0.42794	0.25	r714
A21-045	149.5136	-11.0134	18.08	0.16280	0.46	b814
A21-046	149.5540	-10.9436	18.09	0.13338	0.67	r601
A21-047	149.6270	-11.0046	18.10	0.34140	0.29	b212
A21-048	149.6018	-11.1068	18.11	0.16359	0.71	r304
A21-049	149.6013	-11.0870	18.11	0.16813	0.76	r305
A21-050	149.6612	-11.0080	18.11	0.31298	0.33	b204
A21-051	149.4919	-11.1581	18.11	0.48971	0.26	r703
A21-052	149.6460	-11.0859	18.13	0.16581	0.73	r107
A21-053	149.4601	-10.9210	18.15	0.16092	0.78	r809
A21-054	149.4769	-11.0922	18.15	0.40156	0.22	b714
A21-055	149.6005	-11.0175	18.17	0.16088	0.29	r414
A21-056	149.5342	-10.9422	18.19	0.13385	0.59	r611

Continued on next page

Target ID	RA	DEC	r-band mag.	z	Corr.	FiberID
A21-057	149.5389	-10.9392	18.19	0.13381	0.26	r610
A21-059	149.5668	-11.0845	18.20	0.41385	0.29	b515
A21-060	149.4858	-10.9401	18.21	0.16189	0.73	r803
A21-061	149.6227	-11.1223	18.23	0.34930	0.26	b304
A21-062	149.5893	-11.0610	18.25	0.16583	0.40	r515
A21-063	149.5929	-11.1382	18.27	0.45375	0.30	r512
A21-065	149.6153	-10.9376	18.28	0.39785	0.22	r409
A21-066	149.6145	-11.1478	18.33	0.16251	0.74	r311
A21-067	149.5905	-10.9943	18.34	0.49985	0.24	b403
A21-069	149.5541	-10.9510	18.41	0.13378	0.49	b610
A21-070	149.6044	-10.9623	18.41	0.39524	0.22	r410
A21-071	149.4529	-11.0814	18.42	0.44146	0.23	b705
A21-072	149.6395	-11.1526	18.43	0.47528	0.29	b312
A21-073	149.5828	-10.9922	18.43	0.13115	0.25	b402
A21-074	149.5967	-11.1717	18.44	0.34154	0.35	r301
A21-075	149.6624	-11.0187	18.45	0.25301	0.45	b206
A21-076	149.5471	-11.0090	18.46	0.42656	0.18	r606
A21-077	149.5819	-11.0521	18.47	0.16410	0.54	b416
A21-078	149.5553	-11.0877	18.48	0.28846	0.53	b514
A21-079	149.6008	-11.0638	18.48	0.43747	0.25	r306
A21-080	149.5356	-11.1205	18.49	0.21536	0.24	r713
A21-082	149.5782	-11.1147	18.53	0.29062	0.62	r505
A21-083	149.4802	-11.1566	18.54	0.30419	0.26	b712
A21-084	149.5774	-11.0260	18.54	0.21281	0.50	b412
A21-085	149.7068	-11.0540	18.55	0.15778	0.81	r208
A21-087	149.4635	-11.0552	18.57	0.21899	0.51	b708
A21-088	149.6603	-11.1243	18.57	0.16386	0.60	r106
A21-089	149.4587	-11.1804	18.57	0.28165	0.30	b702
A21-091	149.5969	-10.9979	18.61	0.17167	0.57	b404
A21-092	149.6511	-11.0810	18.63	0.16053	0.63	r108
A21-094	149.4621	-11.0325	18.64	0.44441	0.20	r815
A21-095	149.5116	-11.1840	18.67	0.28720	0.33	r702
A21-096	149.4882	-11.1975	18.67	0.48599	0.27	b709
A21-097	149.6405	-11.1715	18.67	0.16116	0.58	b311
A21-098	149.5576	-11.0563	18.67	0.32628	0.30	b516
A21-099	149.5547	-11.1278	18.68	0.16302	0.57	b506
A21-100	149.5067	-10.9428	18.68	0.31466	0.28	r804
A21-101	149.5227	-11.0188	18.68	0.16358	0.67	b815
A21-102	149.5082	-11.1869	18.69	0.50003	0.38	r701
A21-103	149.6174	-11.0941	18.69	0.16142	0.38	b308
A21-104	149.6718	-11.1498	18.70	0.16270	0.64	r113
A21-105	149.6465	-11.0351	18.71	0.43681	0.22	b215
A21-106	149.5414	-11.0933	18.71	0.46170	0.22	r715
A21-107	149.6081	-11.0044	18.72	0.39514	0.25	r412
A21-108	149.5634	-11.0472	18.73	0.49383	0.26	b615
A21-109	149.5002	-11.1240	18.73	0.40825	0.23	r704
A21-110	149.5977	-11.0478	18.75	0.15834	0.27	b407
A21-111	149.6167	-11.0504	18.76	0.44519	0.19	r408
A21-112	149.6494	-10.9984	18.77	0.30266	0.20	b202
A21-114	149.5796	-11.0002	18.78	0.16532	0.32	b410
A21-115	149.5291	-11.0202	18.80	0.44771	0.23	b808
A21-116	149.6316	-10.9446	18.80	0.42573	0.19	b211
A21-117	149.6006	-10.9926	18.81	0.40313	0.26	r411

Continued on next page

Target ID	RA	DEC	r-band mag.	z	Corr.	FiberID
A21-118	149.5885	-11.0810	18.81	0.16154	0.32	r513
A21-119	149.6787	-11.1710	18.82	0.32485	0.19	r111
A21-120	149.7368	-11.0347	18.82	0.43341	0.31	r207
A21-121	149.4728	-11.1623	18.82	0.34147	0.36	b711
A21-122	149.6571	-11.1677	18.83	0.16296	0.66	r102
A21-123	149.6243	-11.1029	18.83	0.15982	0.55	b307
A21-125	149.5549	-11.0048	18.85	0.49471	0.26	b614
A21-126	149.5803	-11.1577	18.85	0.17129	0.35	r502
A21-127	149.4557	-11.0726	18.86	0.43942	0.31	b707
A21-128	149.5464	-11.0352	18.88	0.16424	0.67	r616
A21-129	149.7310	-11.1717	18.89	0.30371	0.22	b111
A21-130	149.5138	-10.9321	18.89	0.32982	0.34	b810
A21-131	149.5503	-10.9602	18.90	0.30898	0.26	r602
A21-133	149.5758	-11.0489	18.92	0.15729	0.62	b415
A21-134	149.5529	-11.0463	18.93	0.16172	0.50	r608
A21-136	149.6271	-11.1253	18.96	0.45671	0.28	b313
A21-137	149.5519	-10.9916	18.98	0.43864	0.26	r605
A21-138	149.6353	-11.0692	18.99	0.48088	0.25	b315
A21-139	149.5940	-11.1199	19.01	0.15835	0.68	r302
A21-141	149.6988	-11.0644	19.03	0.45450	0.35	b108
A21-142	149.5553	-11.1432	19.05	0.48045	0.50	b505
A21-144	149.5743	-11.1058	19.08	0.45881	0.26	r507
A21-145	149.5601	-10.9213	19.09	0.45605	0.35	b609
A21-146	149.7209	-10.9434	19.09	0.38813	0.18	r203
A21-147	149.5827	-10.9333	19.10	0.34313	0.28	b409
A21-148	149.4879	-11.0210	19.13	0.44584	0.68	r806
A21-149	149.5582	-11.0484	19.16	0.44409	0.25	b616
A21-150	149.5220	-11.1425	19.17	0.36496	0.20	r711
A21-151	149.6937	-11.1002	19.17	0.15674	0.28	b105
A21-152	149.6711	-11.1824	19.17	0.40114	0.27	r109
A21-153	149.5310	-11.1696	19.18	0.39513	0.22	r709
A21-154	149.5784	-11.0560	19.19	0.25264	0.42	r508
A21-155	149.5640	-11.1209	19.19	0.38842	0.37	b511
A21-159	149.4519	-10.9337	19.23	0.16372	0.80	r812
A21-160	149.5957	-11.0557	19.24	0.16994	0.55	r308
A21-162	149.4807	-11.1791	19.25	0.39427	0.32	b710
A21-163	149.5135	-11.1207	19.26	0.16211	0.71	r705
A21-164	149.5305	-10.9501	19.27	0.16436	0.54	b804
A21-165	149.5728	-11.1481	19.28	0.32427	0.24	r503
A21-166	149.6908	-11.1121	19.28	0.15673	0.30	b104
A21-167	149.4685	-11.1888	19.29	0.44157	0.26	b701
A21-168	149.4701	-10.9224	19.29	0.27872	0.69	r810
A21-169	149.5730	-11.0419	19.30	0.45692	0.24	b606
A21-170	149.6689	-11.0118	19.30	0.15529	0.71	r213
A21-172	149.5140	-10.9481	19.31	0.31442	0.21	b811
A21-173	149.5077	-11.0473	19.32	0.16849	0.53	r808
A21-174	149.6662	-11.0279	19.32	0.32728	0.59	r215
A21-175	149.5275	-10.9628	19.33	0.13343	0.36	b806
A21-176	149.5414	-11.0314	19.34	0.16349	0.78	r615
A21-177	149.5769	-11.0341	19.35	0.15881	0.41	b413
A21-178	149.6554	-11.1813	19.35	0.15905	0.54	r101
A21-180	149.6732	-11.1683	19.36	0.15905	0.72	r112
A21-181	149.5733	-11.0181	19.36	0.49980	0.67	b605

Continued on next page

Target ID	RA	DEC	r-band mag.	z	Corr.	FiberID
A21-182	149.6098	-11.0143	19.38	0.37633	0.37	r413
A21-183	149.4886	-11.1540	19.38	0.16362	0.29	b713
A21-185	149.6259	-11.1377	19.38	0.43572	0.31	b303
A21-186	149.5375	-11.0003	19.38	0.36088	0.53	r614
A21-187	149.6977	-11.0879	19.39	0.47242	0.30	b106
A21-188	149.5603	-10.9981	19.39	0.41079	0.24	b613
A21-189	149.5523	-11.0149	19.41	0.15806	0.71	r607
A21-190	149.5353	-10.9919	19.42	0.23643	0.63	r613
A21-192	149.5106	-11.0193	19.44	0.21283	0.25	b816
A21-194	149.5605	-11.1009	19.45	0.28956	0.19	b512
A21-195	149.6205	-11.1120	19.46	0.15957	0.75	b306
A21-196	149.6929	-11.1884	19.46	0.49198	0.38	b101
A21-197	149.6900	-11.1271	19.46	0.34861	0.69	r115
A21-198	149.5656	-10.9281	19.47	0.16289	0.36	b601
A21-199	149.4514	-11.0455	19.48	0.35859	0.79	r816
A21-200	149.5515	-10.9874	19.49	0.39500	0.27	r604
A21-201	149.4946	-10.9377	19.50	0.18508	0.73	r802
A21-202	149.7003	-11.1213	19.51	0.47210	0.14	b103
A21-203	149.5252	-11.0834	19.52	0.16781	0.31	r716
A21-204	149.5309	-10.9799	19.52	0.13280	0.39	b807
A21-205	149.4518	-10.9287	19.52	0.34099	0.71	r811
A21-206	149.5466	-11.1878	19.53	0.45755	0.33	b501
A21-207	149.5385	-11.1407	19.54	0.35542	0.19	r712
A21-208	149.6663	-11.1247	19.56	0.16503	0.30	r105
A21-209	149.5742	-11.1684	19.58	0.50003	0.25	r501
A21-211	149.7175	-11.0958	19.60	0.45240	0.25	b114
A21-214	149.5919	-11.0435	19.62	0.16258	0.43	b406
A21-215	149.6059	-11.1735	19.64	0.16476	0.46	r310
A21-216	149.5878	-11.0550	19.65	0.36027	0.25	r516
A21-218	149.5545	-11.1846	19.67	0.48908	0.26	b502
A21-219	149.6030	-11.0756	19.67	0.42651	0.25	r315
A21-220	149.7334	-10.9429	19.70	0.34342	0.37	r202
A21-221	149.5830	-11.2019	19.70	0.21388	0.37	r509
A21-222	149.6566	-11.0193	19.71	0.15987	0.34	b207
A21-224	149.6962	-10.9358	19.72	0.47425	0.27	r210
A21-225	149.5895	-11.1643	19.74	0.49574	0.18	r510
A21-226	149.6199	-11.0094	19.76	0.16854	0.46	r406
A21-227	149.5723	-11.1594	19.77	0.43980	0.26	b509
A21-229	149.6480	-10.9425	19.77	0.45771	0.29	b210
A21-230	149.5710	-11.0457	19.78	0.15804	0.28	b607
A21-232	149.5015	-11.0472	19.80	0.25524	0.79	r807
A21-233	149.6209	-10.9784	19.81	0.27808	0.56	r405
A21-234	149.6261	-10.9595	19.81	0.48442	0.22	r402
A21-235	149.5239	-10.9488	19.82	0.42928	0.55	b812
A21-236	149.7259	-11.1099	19.82	0.16290	0.32	b113
A21-237	149.6889	-11.0029	19.82	0.26725	0.26	r212
A21-238	149.6504	-11.0336	19.84	0.35883	0.44	b208
A21-239	149.6172	-11.1140	19.86	0.15927	0.33	b305
A21-240	149.6044	-11.1433	19.86	0.49630	0.45	r312
A21-241	149.5692	-11.0930	19.86	0.16458	0.46	b513
A21-243	149.6211	-11.1725	19.87	0.15214	0.51	b301
A21-244	149.5207	-11.0119	19.90	0.42860	0.45	b813
A21-245	149.5318	-10.9241	19.90	0.17127	0.34	b802

Continued on next page

Target ID	RA	DEC	r-band mag.	z	Corr.	FiberID
A21-246	149.5692	-10.9643	19.90	0.48884	0.32	b603
A21-251	149.7372	-11.0571	19.94	0.47768	0.43	b116
A21-252	149.5436	-11.0762	19.96	0.15443	0.58	b507
A21-253	149.7073	-11.0944	19.97	0.46828	0.36	b115
A21-254	149.4791	-10.9994	19.97	0.33914	0.78	r805
A21-255	149.6334	-10.9377	19.97	0.49810	0.25	b209
A21-256	149.5712	-10.9973	19.97	0.49871	0.31	b604
A21-257	149.7013	-11.0389	19.99	0.16121	0.48	r216
A21-258	149.4547	-11.0248	19.99	0.42165	0.16	r814
A21-260	149.5147	-11.0670	20.01	0.41399	0.24	r708
A21-261	149.6154	-11.1893	20.02	0.41959	0.21	r309
A21-262	149.5906	-11.0726	20.02	0.43527	0.23	r514
A21-263	149.7370	-10.9640	20.03	0.44269	0.29	r204
A21-264	149.5838	-10.9432	20.04	0.33013	0.34	b401
A21-266	149.6825	-11.1342	20.06	0.49875	0.23	r114
A21-267	149.6168	-10.9732	20.06	0.16138	0.74	r404
A21-268	149.5205	-10.9207	20.06	0.13196	0.41	b809
A21-269	149.6650	-10.9347	20.06	0.46826	0.29	b201
A21-270	149.6599	-11.1459	20.07	0.49550	0.22	r103
A21-271	149.5382	-10.9325	20.09	0.16057	0.36	r609
A21-273	149.6249	-11.0232	20.11	0.25262	0.76	r407
A21-274	149.6456	-11.1840	20.13	0.42251	0.24	b309
A21-275	149.5480	-11.1677	20.13	0.28613	0.40	b503
A21-276	149.6267	-10.9686	20.13	0.49077	0.32	r403
A21-277	149.7306	-11.1173	20.14	0.49442	0.27	b112
A21-279	149.4786	-10.9310	20.15	0.44157	0.25	r801
A21-280	149.6521	-11.0139	20.15	0.31999	0.22	b205
A21-283	149.7151	-11.1834	20.16	0.44859	0.76	b109
A21-284	149.6055	-11.0944	20.16	0.45042	0.25	r313
A21-285	149.7011	-11.1736	20.18	0.44785	0.69	b110
A21-290	149.6378	-11.0435	20.23	0.45620	0.21	b216
A22-000	168.8272	1.4082	16.30	0.11289	0.91	b705
A22-001	169.0130	1.5177	16.34	0.34661	0.69	b406
A22-002	169.0505	1.5043	16.68	0.14368	0.78	b216
A22-003	169.0434	1.4873	16.77	0.31259	0.20	r115
A22-004	168.9868	1.5087	17.05	0.35800	0.67	b606
A22-005	168.9786	1.4845	17.10	0.35270	0.78	r307
A22-006	169.0495	1.4898	17.15	0.17388	0.48	r116
A22-007	169.0400	1.4940	17.16	0.17286	0.40	r408
A22-008	168.8747	1.6074	17.23	0.14263	0.50	r802
A22-009	169.0682	1.5909	17.28	0.16914	0.82	b204
A22-010	169.0353	1.5029	17.32	0.14226	0.21	r416
A22-011	169.0347	1.4038	17.34	0.14419	0.85	r111
A22-012	168.9945	1.5074	17.43	0.36062	0.54	b607
A22-013	168.8378	1.3754	17.47	0.14327	0.79	b703
A22-014	168.9840	1.4840	17.53	0.35440	0.65	r306
A22-015	168.9130	1.4205	17.58	0.14311	0.67	b505
A22-016	169.0513	1.5858	17.64	0.23765	0.24	b210
A22-017	168.9996	1.5065	17.65	0.16714	0.84	b416
A22-018	169.0635	1.6027	17.69	0.21363	0.39	b209
A22-019	168.8880	1.4510	17.71	0.30308	0.81	r706
A22-020	169.0226	1.5054	17.74	0.35983	0.61	b407
A22-021	168.9976	1.3631	17.75	0.22785	0.25	b301

Continued on next page

Target ID	RA	DEC	r-band mag.	z	Corr.	FiberID
A22-022	169.0704	1.5952	17.80	0.12682	0.83	b203
A22-023	168.9538	1.5518	17.81	0.16736	0.84	r605
A22-024	169.0436	1.5483	17.84	0.40801	0.19	r404
A22-025	168.8549	1.4447	17.88	0.26335	0.34	b711
A22-026	168.9620	1.3679	17.93	0.14637	0.80	r509
A22-027	168.9952	1.4913	17.94	0.14320	0.65	r316
A22-028	168.8568	1.5686	17.97	0.22700	0.25	r805
A22-029	168.8417	1.6166	18.02	0.35549	0.88	r814
A22-030	168.9623	1.3982	18.09	0.23035	0.64	r511
A22-031	168.8882	1.4474	18.09	0.30163	0.62	r713
A22-032	168.9784	1.5044	18.09	0.35663	0.36	b613
A22-033	168.9964	1.4317	18.10	0.35686	0.86	b303
A22-034	168.8866	1.4108	18.16	0.42227	0.25	r702
A22-035	169.0204	1.4995	18.16	0.16683	0.70	b408
A22-036	168.9259	1.5279	18.17	0.37734	0.71	r616
A22-037	168.9345	1.5360	18.21	0.30213	0.58	r615
A22-038	168.8675	1.4503	18.28	0.22608	0.72	b713
A22-039	169.0081	1.5198	18.32	0.34961	0.65	b405
A22-040	169.0358	1.4833	18.33	0.14446	0.28	r114
A22-041	168.8828	1.3973	18.37	0.30152	0.85	r701
A22-042	168.8668	1.5874	18.40	0.21253	0.49	r804
A22-044	168.9684	1.4797	18.42	0.35622	0.71	r305
A22-045	169.0752	1.4762	18.45	0.14599	0.55	b115
A22-046	168.9932	1.4443	18.46	0.35515	0.72	r313
A22-047	168.8973	1.6117	18.47	0.26377	0.50	b813
A22-049	168.8830	1.4450	18.49	0.22666	0.46	r704
A22-050	168.9431	1.4944	18.55	0.35648	0.79	r608
A22-051	169.0569	1.4785	18.61	0.14318	0.71	b105
A22-052	169.0830	1.5876	18.61	0.28966	0.76	r213
A22-053	169.0161	1.4655	18.61	0.16732	0.57	b314
A22-054	169.0885	1.5854	18.62	0.14456	0.48	r214
A22-055	168.9780	1.5009	18.62	0.44516	0.23	b615
A22-056	169.0909	1.6354	18.63	0.28561	0.55	r209
A22-057	169.1002	1.5752	18.64	0.49371	0.25	r204
A22-059	169.0060	1.4928	18.65	0.14678	0.39	b308
A22-060	168.8554	1.3609	18.65	0.30109	0.78	b709
A22-061	169.0345	1.3807	18.66	0.28600	0.64	r110
A22-062	168.9615	1.4474	18.69	0.20419	0.22	r514
A22-064	168.8627	1.4467	18.71	0.14314	0.53	b712
A22-065	168.9608	1.5338	18.71	0.14536	0.38	b611
A22-066	168.8619	1.4922	18.71	0.35197	0.86	b716
A22-067	169.0546	1.4917	18.75	0.14689	0.44	b107
A22-068	169.0067	1.5067	18.79	0.35116	0.73	b415
A22-069	168.8905	1.3965	18.81	0.14382	0.73	r709
A22-071	168.9651	1.5014	18.84	0.35142	0.56	b614
A22-072	168.9423	1.5840	18.84	0.37190	0.35	r603
A22-073	169.0643	1.4927	18.87	0.46438	0.52	b108
A22-074	169.0341	1.4108	18.87	0.35805	0.72	r105
A22-075	169.0638	1.3808	18.88	0.21462	0.69	b101
A22-077	169.0696	1.4180	18.90	0.13018	0.52	b111
A22-078	168.8726	1.5180	18.92	0.34682	0.78	r807
A22-079	168.9827	1.4981	18.92	0.35462	0.39	b608
A22-081	169.0341	1.3666	18.94	0.24080	0.30	r101

Continued on next page

Target ID	RA	DEC	r-band mag.	z	Corr.	FiberID
A22-082	168.9371	1.5559	18.95	0.41022	0.40	r614
A22-083	168.8936	1.3994	18.95	0.26063	0.72	r710
A22-084	168.9908	1.3835	18.95	0.26527	0.69	r310
A22-085	169.1026	1.3569	18.96	0.14113	0.65	b109
A22-086	169.0428	1.6273	18.99	0.16467	0.55	r401
A22-087	169.0268	1.5208	19.00	0.28678	0.73	r415
A22-089	169.0208	1.4475	19.03	0.35586	0.61	r107
A22-090	168.9449	1.5236	19.04	0.14377	0.83	r606
A22-091	168.9961	1.6244	19.05	0.40003	0.70	b409
A22-092	168.9643	1.4592	19.05	0.36012	0.50	r515
A22-094	168.8467	1.3623	19.06	0.28681	0.61	b702
A22-095	169.0931	1.5720	19.07	0.17047	0.21	r215
A22-096	168.9168	1.5637	19.07	0.34336	0.72	b806
A22-097	168.9616	1.4792	19.10	0.12915	0.50	r516
A22-098	169.0979	1.5490	19.11	0.16843	0.69	r207
A22-100	168.9217	1.5809	19.11	0.35634	0.84	b804
A22-101	168.9182	1.5230	19.11	0.43511	0.37	b808
A22-102	169.0588	1.4826	19.11	0.38059	0.73	b106
A22-103	168.9138	1.5744	19.12	0.28117	0.79	b805
A22-105	168.9479	1.6229	19.22	0.34778	0.80	r601
A22-106	169.0253	1.3932	19.25	0.35247	0.74	r103
A22-107	169.0701	1.4861	19.27	0.14380	0.43	b116
A22-108	168.9563	1.4975	19.28	0.34938	0.71	r607
A22-109	168.9493	1.5557	19.28	0.35883	0.63	r604
A22-110	169.0132	1.4218	19.29	0.22549	0.45	b311
A22-111	168.9436	1.3861	19.30	0.22808	0.47	r501
A22-112	168.9519	1.4242	19.33	0.35377	0.65	r504
A22-113	168.9299	1.5689	19.33	0.30104	0.57	r613
A22-114	168.8879	1.4839	19.33	0.21182	0.41	r708
A22-115	168.9431	1.4805	19.34	0.34147	0.62	r507
A22-116	168.8346	1.4895	19.35	0.45409	0.58	b707
A22-117	168.8898	1.4404	19.37	0.11961	0.49	r712
A22-118	168.8482	1.4366	19.38	0.26617	0.54	b706
A22-119	168.9298	1.4939	19.39	0.35274	0.59	b516
A22-120	169.0364	1.6211	19.41	0.16899	0.36	r410
A22-121	169.0304	1.3843	19.43	0.34831	0.73	r102
A22-122	169.0145	1.4823	19.43	0.35295	0.77	b316
A22-123	169.0278	1.5362	19.44	0.41672	0.49	r414
A22-124	169.0298	1.5421	19.45	0.16738	0.38	r413
A22-125	168.8974	1.4593	19.45	0.30102	0.43	r714
A22-126	168.9754	1.4119	19.46	0.35408	0.60	r302
A22-127	168.8580	1.4506	19.48	0.23684	0.44	b714
A22-128	169.0154	1.3669	19.48	0.37233	0.54	b309
A22-129	169.0813	1.5416	19.49	0.14298	0.38	r216
A22-130	169.0788	1.4245	19.50	0.35258	0.81	b113
A22-131	168.9015	1.6118	19.51	0.34511	0.84	b812
A22-132	169.0100	1.4815	19.51	0.35991	0.51	b307
A22-133	168.9131	1.5836	19.52	0.34651	0.81	b803
A22-134	168.9887	1.5469	19.52	0.14540	0.48	b602
A22-135	168.9649	1.4957	19.54	0.34427	0.65	b616
A22-136	168.9115	1.4319	19.54	0.44457	0.57	b507
A22-138	169.0129	1.4407	19.55	0.35740	0.37	b312
A22-139	169.0022	1.5936	19.57	0.10952	0.88	b410

Continued on next page

Target ID	RA	DEC	r-band mag.	z	Corr.	FiberID
A22-140	169.0058	1.5164	19.57	0.16765	0.86	b414
A22-141	168.9958	1.5662	19.57	0.42385	0.26	b411
A22-142	168.9797	1.3845	19.58	0.14613	0.46	r301
A22-143	168.9918	1.5111	19.59	0.16770	0.61	b605
A22-144	169.0963	1.5693	19.59	0.17029	0.76	r205
A22-145	169.0438	1.5752	19.59	0.21880	0.64	r402
A22-146	169.0974	1.5909	19.60	0.28960	0.37	r202
A22-147	169.0420	1.5362	19.60	0.28863	0.48	r405
A22-148	168.8929	1.5119	19.62	0.22988	0.45	b815
A22-149	168.9042	1.3894	19.64	0.23831	0.34	b502
A22-150	169.0828	1.6282	19.64	0.21353	0.62	r210
A22-151	169.0272	1.5742	19.65	0.49370	0.26	r411
A22-152	168.8885	1.4595	19.66	0.14319	0.53	r715
A22-154	168.9903	1.4881	19.70	0.35276	0.64	r315
A22-155	168.9951	1.3865	19.73	0.35639	0.68	r311
A22-156	169.0566	1.3856	19.74	0.35082	0.75	b102
A22-157	169.0100	1.6324	19.75	0.35115	0.20	b401
A22-158	168.8327	1.5022	19.76	0.45040	0.38	r816
A22-159	169.1032	1.5846	19.76	0.42439	0.50	r203
A22-160	168.8571	1.4419	19.77	0.49001	0.57	b710
A22-162	168.9250	1.4727	19.79	0.34241	0.40	b513
A22-164	168.8721	1.4538	19.82	0.30307	0.57	r707
A22-166	169.0852	1.5998	19.83	0.26917	0.51	r212
A22-167	168.9992	1.5187	19.84	0.34655	0.33	b413
A22-168	168.9538	1.6185	19.84	0.21803	0.63	r602
A22-170	168.8282	1.6407	19.88	0.35936	0.63	r810
A22-171	168.9445	1.4840	19.88	0.35954	0.39	r508
A22-172	168.8406	1.6279	19.88	0.26599	0.58	r812
A22-173	169.0033	1.3821	19.89	0.20650	0.62	b302
A22-174	168.9145	1.3965	19.90	0.22625	0.31	b504
A22-175	169.0440	1.4827	19.92	0.14697	0.45	r113
A22-176	168.9372	1.6037	19.93	0.35351	0.74	r610
A22-177	168.9892	1.4348	19.94	0.35812	0.51	r312
A22-179	169.0326	1.3961	19.95	0.28571	0.61	r104
A22-180	169.0125	1.4710	19.97	0.35531	0.68	b315
A22-181	168.9166	1.4284	19.98	0.20520	0.32	b506
A22-182	168.9663	1.5880	19.98	0.34692	0.77	b609
A22-184	168.9206	1.5870	20.00	0.34572	0.75	b802
A22-185	168.9066	1.5044	20.00	0.43842	0.55	b816
A22-186	169.0715	1.5503	20.03	0.16766	0.37	b207
A22-187	169.0127	1.3947	20.03	0.35589	0.70	b310
A22-188	169.0934	1.5656	20.04	0.16882	0.78	r206
A22-191	168.9382	1.4297	20.05	0.21253	0.35	b511
A22-192	168.8816	1.6201	20.05	0.34889	0.78	r801
A22-194	168.9680	1.4068	20.06	0.20657	0.34	r512
A22-195	168.9795	1.5083	20.06	0.14614	0.33	b612
A22-196	168.9818	1.5264	20.08	0.35245	0.72	b604
A22-197	169.0561	1.4503	20.08	0.22527	0.33	b103
A22-199	168.8470	1.6275	20.09	0.35911	0.62	r813
A22-200	168.8978	1.6315	20.09	0.40082	0.64	b810
A22-201	169.0709	1.5159	20.09	0.14236	0.76	b208
A22-203	169.0574	1.5208	20.11	0.34984	0.62	b213
A22-204	169.0481	1.5644	20.12	0.17151	0.40	r403

Continued on next page

Target ID	RA	DEC	r-band mag.	z	Corr.	FiberID
A22-205	169.0903	1.6245	20.12	0.36926	0.61	r211
A22-206	168.8372	1.6333	20.13	0.37184	0.75	r811
A22-207	168.9013	1.6056	20.14	0.34927	0.63	b814
A22-208	168.9583	1.4561	20.16	0.37229	0.73	r505
A22-210	169.0775	1.6040	20.17	0.12752	0.27	b202
A22-211	169.0741	1.6395	20.18	0.37164	0.63	b201
A22-212	168.8705	1.6052	20.19	0.42324	0.49	r803
A22-213	169.0113	1.5308	20.19	0.16677	0.50	b404
A22-214	169.0462	1.5117	20.20	0.14496	0.25	r406
A22-217	168.8855	1.5633	20.24	0.45234	0.62	r806
A22-218	169.0030	1.4407	20.25	0.14620	0.78	b304
A22-219	169.0358	1.5608	20.26	0.36466	0.61	r412
A22-220	168.8827	1.4164	20.26	0.14413	0.49	r703
A22-221	168.9704	1.4408	20.27	0.27209	0.24	r304
A22-222	168.9233	1.4407	20.27	0.34853	0.26	b512
A22-223	168.9237	1.4925	20.27	0.35404	0.81	b515
A22-225	168.9470	1.3909	20.28	0.22972	0.36	r502
A22-226	168.9224	1.4864	20.28	0.34545	0.66	b508
A22-227	169.0717	1.5612	20.28	0.16841	0.52	b206
A22-228	169.0497	1.5766	20.29	0.16872	0.66	b211
A22-229	168.9140	1.3859	20.29	0.16092	0.19	b501
A22-230	169.0307	1.4604	20.30	0.17291	0.25	r108
A22-231	168.9497	1.4799	20.32	0.13296	0.44	r506
A22-233	168.8556	1.5236	20.33	0.12607	0.45	r815
A22-234	169.0360	1.4314	20.33	0.21792	0.40	r112
A22-235	168.8679	1.4607	20.33	0.46957	0.47	b715
A22-237	169.0564	1.5121	20.34	0.16822	0.51	b215
A22-238	168.8698	1.4467	20.35	0.30304	0.37	r705
A22-239	169.0937	1.4177	20.37	0.14456	0.31	b110
A22-240	168.9713	1.4929	20.37	0.35688	0.67	r308
A22-241	168.9296	1.3596	20.38	0.11258	0.19	b509
A22-242	168.8907	1.4634	20.39	0.35247	0.48	r716
A22-243	168.9921	1.3572	20.40	0.35612	0.68	r309
A22-244	169.0094	1.5415	20.41	0.16699	0.46	b403
A22-246	169.0254	1.6330	20.45	0.28425	0.27	r409
A22-247	168.9135	1.6007	20.45	0.35165	0.71	b801
A22-250	168.9958	1.4706	20.50	0.35288	0.74	b306
A22-252	168.8903	1.4014	20.52	0.17373	0.41	r711
A22-253	169.0529	1.5170	20.52	0.26576	0.46	b214
A22-254	168.9369	1.5770	20.52	0.34816	0.72	r612
A22-255	168.8923	1.6125	20.54	0.32544	0.57	b811
A22-256	168.9368	1.4752	20.54	0.21193	0.30	b514
A22-257	168.9949	1.5397	20.55	0.20258	0.20	b603
A22-258	169.0045	1.4555	20.56	0.16814	0.41	b305
A22-259	169.0418	1.5097	20.58	0.14275	0.76	r407
A22-261	169.0048	1.5361	20.60	0.16740	0.24	b412
A22-262	169.0567	1.5382	20.61	0.34991	0.66	b212
A22-263	168.8456	1.3803	20.61	0.21083	0.29	b704
A22-265	168.9442	1.4143	20.63	0.32167	0.60	r503
A22-266	168.9119	1.3930	20.63	0.23796	0.36	b503
A22-267	169.0767	1.5907	20.65	0.16827	0.84	b205
A22-268	169.0860	1.4245	20.66	0.34894	0.62	b112
A22-270	168.9275	1.6152	20.67	0.34800	0.77	r609

Continued on next page

Target ID	RA	DEC	r-band mag.	z	Corr.	FiberID
A22-271	168.9203	1.5447	20.69	0.25329	0.22	b807
A22-272	169.0246	1.4316	20.70	0.34821	0.53	r106
A22-273	169.0121	1.4542	20.71	0.46373	0.46	b313
A22-274	168.9906	1.4679	20.71	0.14397	0.56	r314
A22-275	168.9631	1.4155	20.71	0.23218	0.17	r513
A22-277	168.9401	1.4233	20.73	0.45970	0.44	b510
A22-278	169.0617	1.4703	20.73	0.35088	0.73	b104
A22-279	168.9932	1.6165	20.75	0.44773	0.72	b601
A22-280	168.9666	1.3872	20.76	0.44885	0.16	r510
A22-281	169.0187	1.5558	20.78	0.17007	0.41	b402
A23-000	180.7842	-21.4367	16.79	0.20687	0.72	b611
A23-001	180.6831	-21.5355	16.91	0.28991	0.63	r816
A23-002	180.7391	-21.4643	16.94	0.20093	0.78	b804
A23-003	180.8101	-21.6938	16.97	0.19837	0.85	b509
A23-004	180.8419	-21.5616	17.19	0.20995	0.34	r308
A23-005	180.9708	-21.6853	17.20	0.19318	0.86	b109
A23-006	180.7933	-21.4983	17.23	0.20156	0.84	b605
A23-007	180.8199	-21.5345	17.28	0.19884	0.65	r416
A23-008	180.8587	-21.5096	17.34	0.20206	0.73	b205
A23-009	180.9465	-21.6036	17.39	0.30175	0.69	b106
A23-010	180.6865	-21.5118	17.46	0.23391	0.71	r807
A23-011	180.7293	-21.4560	17.48	0.19605	0.79	b803
A23-012	180.8328	-21.4715	17.56	0.44937	0.51	r402
A23-013	180.8331	-21.4647	17.57	0.20125	0.70	r401
A23-014	180.7501	-21.4270	17.63	0.19422	0.65	b802
A23-015	180.7782	-21.6526	17.64	0.20414	0.67	b504
A23-016	180.7184	-21.4376	17.76	0.19608	0.51	b810
A23-017	180.7856	-21.5357	17.81	0.21208	0.80	b616
A23-018	180.6760	-21.5976	17.81	0.19594	0.61	b705
A23-019	180.8132	-21.4369	17.84	0.33473	0.77	b402
A23-020	180.8209	-21.4423	17.86	0.19169	0.77	r410
A23-021	180.8053	-21.4995	17.87	0.19237	0.77	b414
A23-022	180.7800	-21.4443	17.92	0.20705	0.76	r603
A23-023	180.9167	-21.6896	17.94	0.19670	0.77	r110
A23-024	180.7149	-21.4432	17.97	0.20055	0.84	b811
A23-025	180.7912	-21.4840	17.99	0.19795	0.86	b603
A23-026	180.7536	-21.6717	18.01	0.20430	0.76	r711
A23-027	180.7610	-21.6630	18.02	0.19588	0.69	b503
A23-028	180.6842	-21.5284	18.03	0.19729	0.66	r815
A23-029	180.8816	-21.5434	18.03	0.20866	0.34	r215
A23-030	180.8749	-21.4833	18.04	0.20325	0.77	b203
A23-031	180.7758	-21.4238	18.04	0.20113	0.82	r602
A23-032	180.7653	-21.4967	18.05	0.24151	0.68	r613
A23-033	180.8105	-21.5255	18.06	0.20222	0.74	b407
A23-034	180.7385	-21.6634	18.09	0.19642	0.87	r702
A23-035	180.7695	-21.4278	18.10	0.19743	0.47	r609
A23-036	180.8213	-21.5310	18.12	0.20032	0.54	r415
A23-037	180.7538	-21.6272	18.13	0.44556	0.21	r713
A23-038	180.8091	-21.4122	18.17	0.28855	0.82	b409
A23-039	180.8368	-21.5750	18.17	0.19877	0.54	r515
A23-040	180.7475	-21.6659	18.18	0.19670	0.83	r712
A23-041	180.8257	-21.5820	18.19	0.19596	0.85	r514
A23-042	180.8380	-21.5698	18.19	0.20729	0.73	r306

Continued on next page

Target ID	RA	DEC	r-band mag.	z	Corr.	FiberID
A23-043	180.7851	-21.6559	18.20	0.19740	0.66	b511
A23-044	180.6760	-21.4958	18.22	0.28493	0.53	r814
A23-045	180.9281	-21.5247	18.24	0.19248	0.45	r206
A23-046	180.8643	-21.6421	18.25	0.33424	0.53	b303
A23-047	180.8572	-21.5402	18.25	0.20264	0.65	b207
A23-048	180.6739	-21.6442	18.26	0.19457	0.88	b703
A23-049	180.6899	-21.6656	18.27	0.19850	0.78	b702
A23-050	180.8316	-21.5005	18.27	0.19281	0.83	r404
A23-051	180.8234	-21.5196	18.29	0.19602	0.81	r414
A23-053	180.7336	-21.6841	18.31	0.14734	0.68	r701
A23-054	180.8550	-21.4143	18.32	0.19435	0.56	b201
A23-055	180.9204	-21.6916	18.33	0.19709	0.77	r109
A23-056	180.8248	-21.6193	18.34	0.19686	0.77	r504
A23-057	180.8361	-21.6405	18.34	0.19610	0.68	r510
A23-058	180.7281	-21.5862	18.36	0.19094	0.77	r707
A23-059	180.7380	-21.6353	18.36	0.20739	0.65	r704
A23-060	180.9448	-21.6620	18.36	0.20224	0.77	b101
A23-061	180.9413	-21.6207	18.37	0.20924	0.67	b105
A23-062	180.7029	-21.6879	18.38	0.19431	0.84	b701
A23-063	180.8528	-21.6657	18.39	0.33415	0.78	r309
A23-064	180.6786	-21.6294	18.39	0.37057	0.72	b704
A23-065	180.7175	-21.5298	18.39	0.13458	0.61	b815
A23-066	180.8796	-21.6516	18.41	0.19614	0.63	b309
A23-067	180.8622	-21.4984	18.41	0.19445	0.68	b204
A23-068	180.8673	-21.6093	18.41	0.20023	0.82	b304
A23-069	180.7085	-21.5242	18.45	0.16524	0.83	b813
A23-070	180.7923	-21.4199	18.49	0.19635	0.79	b601
A23-071	180.6833	-21.4627	18.50	0.14684	0.82	r812
A23-072	180.8102	-21.4972	18.51	0.20209	0.84	b405
A23-073	180.7365	-21.6402	18.52	0.19054	0.77	r703
A23-074	180.7096	-21.5907	18.52	0.30020	0.61	b715
A23-075	180.8572	-21.5796	18.54	0.20026	0.80	r315
A23-076	180.9609	-21.5649	18.54	0.29925	0.39	b115
A23-077	180.6931	-21.5086	18.55	0.19916	0.84	r806
A23-078	180.8494	-21.5822	18.55	0.20538	0.77	r314
A23-079	180.7852	-21.5164	18.56	0.49157	0.27	b615
A23-080	180.8587	-21.5838	18.56	0.19776	0.55	r313
A23-081	180.8508	-21.4882	18.56	0.19033	0.83	b211
A23-083	180.7548	-21.4215	18.57	0.19757	0.78	b801
A23-084	180.8764	-21.4323	18.57	0.29785	0.64	b202
A23-085	180.9104	-21.5702	18.59	0.19600	0.30	r105
A23-086	180.8496	-21.6166	18.61	0.20466	0.68	r312
A23-087	180.8403	-21.4233	18.62	0.19906	0.76	b209
A23-088	180.7776	-21.5164	18.63	0.20777	0.76	r608
A23-089	180.7973	-21.4953	18.64	0.19040	0.49	b604
A23-090	180.7031	-21.4868	18.64	0.19936	0.67	r804
A23-091	180.8067	-21.5326	18.64	0.19555	0.83	b416
A23-092	180.8062	-21.4912	18.65	0.30378	0.79	b413
A23-093	180.7630	-21.5001	18.67	0.19924	0.47	r614
A23-095	180.6851	-21.4808	18.68	0.18984	0.53	r813
A23-097	180.9375	-21.5517	18.70	0.20247	0.71	r208
A23-098	180.8300	-21.4939	18.70	0.19838	0.70	r403
A23-099	180.8432	-21.5652	18.70	0.19308	0.70	r307

Continued on next page

Target ID	RA	DEC	r-band mag.	z	Corr.	FiberID
A23-100	180.9285	-21.4879	18.71	0.20335	0.79	r203
A23-101	180.7222	-21.5808	18.71	0.19396	0.57	b716
A23-102	180.8311	-21.6036	18.73	0.20612	0.72	r511
A23-103	180.8439	-21.4991	18.73	0.19374	0.79	b212
A23-104	180.7907	-21.4546	18.73	0.33342	0.48	b602
A23-105	180.7956	-21.6571	18.74	0.19508	0.60	b510
A23-106	180.8381	-21.6000	18.74	0.19221	0.63	r304
A23-107	180.8669	-21.6485	18.75	0.20361	0.88	b302
A23-108	180.8190	-21.5722	18.75	0.19763	0.44	r508
A23-109	180.9672	-21.5935	18.76	0.20722	0.55	b111
A23-110	180.8122	-21.4843	18.77	0.20636	0.82	b404
A23-111	180.7243	-21.6746	18.78	0.46031	0.28	b712
A23-112	180.7119	-21.5285	18.79	0.14667	0.84	b814
A23-113	180.9042	-21.4733	18.79	0.19092	0.75	r202
A23-114	180.9575	-21.5900	18.80	0.30161	0.83	b113
A23-115	180.8172	-21.4197	18.82	0.28812	0.83	r409
A23-116	180.7389	-21.5104	18.82	0.28420	0.73	b807
A23-117	180.9135	-21.6622	18.82	0.19729	0.46	r101
A23-118	180.7762	-21.6685	18.83	0.19501	0.82	b502
A23-119	180.9153	-21.6572	18.83	0.40703	0.31	r112
A23-120	180.8805	-21.5203	18.83	0.19562	0.81	r212
A23-121	180.9675	-21.6281	18.83	0.22976	0.49	b110
A23-122	180.8969	-21.5401	18.84	0.30526	0.25	r214
A23-123	180.7186	-21.6846	18.85	0.32322	0.77	b709
A23-126	180.7689	-21.5516	18.86	0.19746	0.67	r616
A23-128	180.8171	-21.6130	18.89	0.19756	0.76	r505
A23-129	180.9314	-21.5735	18.89	0.19425	0.45	r116
A23-130	180.8068	-21.4323	18.91	0.33676	0.76	b410
A23-131	180.7999	-21.4785	18.91	0.19479	0.53	b411
A23-132	180.8273	-21.5728	18.91	0.20664	0.65	r516
A23-133	180.8445	-21.6388	18.92	0.19790	0.74	r311
A23-134	180.7994	-21.6128	18.93	0.20662	0.49	b513
A23-135	180.8322	-21.5223	18.94	0.30351	0.64	r405
A23-136	180.8175	-21.6282	18.94	0.20388	0.62	r503
A23-137	180.8166	-21.5839	18.94	0.19916	0.79	r507
A23-138	180.8639	-21.5662	18.95	0.20014	0.74	b307
A23-139	180.6866	-21.4938	18.95	0.19033	0.79	r805
A23-140	180.8365	-21.5515	18.96	0.19841	0.61	r406
A23-141	180.9086	-21.6195	18.96	0.35484	0.60	r102
A23-143	180.7254	-21.5944	18.98	0.19447	0.32	b714
A23-145	180.7830	-21.4134	18.98	0.19403	0.73	b609
A23-146	180.9078	-21.5585	18.98	0.18962	0.84	r107
A23-147	180.7757	-21.6041	18.99	0.18990	0.61	b505
A23-149	180.6987	-21.5967	19.00	0.19107	0.61	b706
A23-150	180.8313	-21.5821	19.01	0.19180	0.33	r513
A23-152	180.8287	-21.5557	19.05	0.33489	0.77	r408
A23-155	180.9405	-21.6033	19.06	0.20764	0.86	b107
A23-156	180.9512	-21.5915	19.07	0.22944	0.16	b112
A23-157	180.9649	-21.5727	19.07	0.35798	0.45	b114
A23-158	180.8595	-21.5592	19.07	0.20012	0.80	b308
A23-159	180.8404	-21.6360	19.08	0.19729	0.77	r302
A23-160	180.7721	-21.5697	19.09	0.47705	0.74	b508
A23-161	180.8954	-21.5547	19.11	0.19916	0.34	r216

Continued on next page

Target ID	RA	DEC	r-band mag.	z	Corr.	FiberID
A23-162	180.8252	-21.4963	19.12	0.19683	0.71	r413
A23-164	180.7511	-21.5836	19.16	0.14532	0.69	r716
A23-165	180.7741	-21.4831	19.16	0.20029	0.77	r607
A23-166	180.9418	-21.5696	19.16	0.19705	0.60	b108
A23-167	180.8603	-21.5992	19.17	0.47753	0.13	b305
A23-168	180.7213	-21.6796	19.19	0.33746	0.72	b710
A23-169	180.8720	-21.6413	19.19	0.20450	0.53	b310
A23-170	180.7054	-21.6792	19.20	0.42483	0.18	b711
A23-171	180.7066	-21.5419	19.21	0.18939	0.43	b816
A23-172	180.8599	-21.5894	19.22	0.20216	0.81	b306
A23-173	180.9122	-21.5744	19.22	0.20762	0.69	r104
A23-175	180.8414	-21.6916	19.23	0.20487	0.60	r301
A23-176	180.9328	-21.5932	19.24	0.19641	0.24	r115
A23-177	180.8278	-21.5887	19.24	0.19854	0.65	r512
A23-178	180.7836	-21.5872	19.24	0.20103	0.84	b514
A23-179	180.8606	-21.5171	19.24	0.21218	0.70	b206
A23-180	180.7424	-21.4766	19.25	0.19495	0.68	b805
A23-181	180.8803	-21.5280	19.25	0.19518	0.43	r213
A23-182	180.8691	-21.6204	19.26	0.20078	0.56	b313
A23-183	180.7827	-21.4550	19.27	0.19970	0.70	r604
A23-184	180.7526	-21.5980	19.27	0.20499	0.63	r715
A23-185	180.8858	-21.4803	19.27	0.19567	0.69	r210
A23-186	180.8169	-21.4239	19.27	0.28833	0.78	b401
A23-187	180.9019	-21.4907	19.28	0.17152	0.22	r204
A23-188	180.8226	-21.6598	19.28	0.22970	0.61	r501
A23-189	180.7337	-21.6118	19.29	0.14710	0.67	r705
A23-190	180.7542	-21.6938	19.29	0.14713	0.66	r709
A23-191	180.7127	-21.4498	19.30	0.35989	0.27	b812
A23-192	180.7408	-21.5666	19.30	0.22957	0.68	r708
A23-194	180.7767	-21.4665	19.31	0.20626	0.68	r605
A23-195	180.6793	-21.5750	19.32	0.19943	0.62	b707
A23-196	180.8714	-21.5509	19.32	0.36384	0.77	b208
A23-198	180.9028	-21.5431	19.34	0.19463	0.70	r207
A23-199	180.7648	-21.5403	19.35	0.33441	0.63	r615
A23-200	180.8199	-21.4721	19.35	0.28868	0.77	r412
A23-201	180.8267	-21.6494	19.35	0.19655	0.76	r509
A23-202	180.8550	-21.6458	19.37	0.19092	0.70	r310
A23-203	180.8749	-21.6372	19.38	0.20031	0.62	b311
A23-204	180.9142	-21.6417	19.38	0.19337	0.72	r113
A23-205	180.7433	-21.6031	19.39	0.14681	0.35	r706
A23-206	180.7184	-21.4341	19.39	0.23419	0.64	b809
A23-207	180.8184	-21.4515	19.40	0.19038	0.59	r411
A23-208	180.7841	-21.4857	19.40	0.30412	0.86	b614
A23-210	180.7842	-21.4243	19.41	0.27291	0.83	b610
A23-212	180.8473	-21.5651	19.42	0.19020	0.82	r316
A23-213	180.7615	-21.4446	19.43	0.20005	0.47	r611
A23-214	180.8179	-21.5451	19.43	0.18965	0.53	b408
A23-215	180.8421	-21.5191	19.43	0.30488	0.22	b215
A23-216	180.8426	-21.5702	19.45	0.19057	0.75	r305
A23-217	180.9679	-21.5598	19.46	0.35767	0.66	b116
A23-218	180.8065	-21.5266	19.46	0.19979	0.73	b415
A23-219	180.8124	-21.6344	19.48	0.20543	0.79	b512
A23-220	180.7524	-21.6152	19.49	0.20656	0.74	r714

Continued on next page

Target ID	RA	DEC	r-band mag.	z	Corr.	FiberID
A23-221	180.9402	-21.6254	19.49	0.19238	0.70	r114
A23-223	180.8393	-21.6268	19.51	0.19689	0.29	r303
A23-224	180.9163	-21.4984	19.52	0.20644	0.52	r205
A23-225	180.8680	-21.5650	19.52	0.20170	0.65	b316
A23-226	180.7058	-21.4255	19.54	0.14413	0.57	r802
A23-227	180.7980	-21.5093	19.55	0.20387	0.77	b606
A23-229	180.9465	-21.6339	19.56	0.19844	0.77	b104
A23-231	180.8812	-21.6313	19.57	0.20678	0.42	b312
A23-232	180.7763	-21.5780	19.58	0.19888	0.68	b507
A23-234	180.7681	-21.4476	19.60	0.20000	0.34	r612
A23-235	180.9479	-21.6382	19.60	0.20043	0.73	b103
A23-236	180.8325	-21.5538	19.61	0.19419	0.69	r407
A23-237	180.7260	-21.5259	19.61	0.14452	0.26	b808
A23-238	180.8356	-21.4517	19.62	0.20454	0.45	b210
A23-239	180.8841	-21.5130	19.62	0.41856	0.43	r211
A23-240	180.8926	-21.6119	19.62	0.20414	0.72	r103
A23-241	180.7904	-21.5322	19.64	0.20438	0.39	b608
A23-243	180.6953	-21.5569	19.64	0.20539	0.77	b708
A23-244	180.8195	-21.5976	19.65	0.19788	0.71	r506
A23-245	180.8157	-21.5240	19.66	0.20136	0.44	b406
A23-246	180.8129	-21.6528	19.66	0.29134	0.68	r502
A23-247	180.8009	-21.4875	19.66	0.20770	0.65	b412
A23-249	180.8701	-21.5820	19.68	0.41262	0.60	b315
A23-250	180.8429	-21.5479	19.69	0.20101	0.75	b216
A23-252	180.6994	-21.4740	19.70	0.19635	0.57	r803
A23-253	180.7456	-21.6870	19.70	0.19394	0.66	r710
A23-255	180.9390	-21.6663	19.71	0.19278	0.69	r111
A23-256	180.8056	-21.5781	19.71	0.19916	0.73	b515
A23-257	180.7873	-21.5657	19.71	0.20952	0.60	b516
A23-260	180.6864	-21.5430	19.71	0.31227	0.64	r808
A23-261	180.9009	-21.5573	19.72	0.19891	0.69	r108
A23-264	180.9069	-21.4688	19.74	0.19181	0.65	r201
A23-265	180.8708	-21.5922	19.74	0.14662	0.43	b314
A23-266	180.7897	-21.4701	19.75	0.44933	0.61	b612
A23-271	180.7550	-21.6890	19.77	0.14746	0.46	b501
A23-272	180.7861	-21.4775	19.78	0.43845	0.23	b613
A23-274	180.7822	-21.4772	19.79	0.20189	0.68	r606
A23-275	180.6898	-21.4152	19.80	0.19397	0.76	r801
A23-276	180.7708	-21.6028	19.80	0.33293	0.44	b506
A23-278	180.7601	-21.4323	19.80	0.19558	0.76	r610
A23-280	180.8673	-21.6557	19.81	0.20373	0.79	b301
A23-281	180.8493	-21.5164	19.82	0.25960	0.67	b214
A26-000	219.7021	3.7365	16.56	0.14654	0.35	b211
A26-001	219.6097	3.7208	16.83	0.22935	0.68	b414
A26-002	219.7318	3.7040	16.93	0.29459	0.70	r205
A26-003	219.5966	3.7443	17.18	0.34741	0.55	b603
A26-004	219.7371	3.7273	17.88	0.14143	0.33	r204
A26-005	219.7087	3.7588	17.91	0.22681	0.71	b204
A26-006	219.4612	3.5785	17.92	0.39153	0.37	b704
A26-007	219.4813	3.6721	17.93	0.29020	0.64	b715
A26-008	219.6052	3.7320	18.05	0.14789	0.51	b413
A26-009	219.7175	3.7804	18.05	0.14712	0.37	r211
A26-010	219.5159	3.7183	18.10	0.22185	0.66	b813

Continued on next page

Target ID	RA	DEC	r-band mag.	z	Corr.	FiberID
A26-011	219.6315	3.7425	18.11	0.14626	0.76	r411
A26-012	219.5804	3.6651	18.13	0.14702	0.58	r507
A26-013	219.5945	3.6673	18.20	0.40533	0.21	r307
A26-014	219.5113	3.6185	18.21	0.22494	0.56	r706
A26-015	219.5212	3.7407	18.21	0.48500	0.34	b812
A26-016	219.6297	3.5926	18.32	0.49120	0.25	b312
A26-017	219.6226	3.6637	18.34	0.22030	0.72	b307
A26-018	219.5941	3.7262	18.35	0.22001	0.67	b606
A26-019	219.6130	3.6586	18.37	0.22763	0.68	r313
A26-020	219.6679	3.6958	18.40	0.14927	0.61	r406
A26-021	219.6323	3.6843	18.42	0.39844	0.69	r415
A26-023	219.5210	3.7147	18.43	0.21983	0.42	b814
A26-024	219.6305	3.6893	18.45	0.22111	0.52	r414
A26-025	219.5863	3.5771	18.45	0.50001	0.22	r510
A26-026	219.5391	3.7412	18.46	0.22051	0.69	b804
A26-027	219.7354	3.5640	18.49	0.28593	0.72	b110
A26-028	219.5206	3.6313	18.53	0.29169	0.65	r713
A26-029	219.5755	3.6241	18.54	0.48014	0.15	r504
A26-030	219.5402	3.7545	18.55	0.34348	0.74	b803
A26-031	219.6112	3.7941	18.59	0.16600	0.40	b410
A26-032	219.7193	3.7194	18.59	0.29269	0.59	r215
A26-033	219.6374	3.6778	18.59	0.49176	0.32	r108
A26-034	219.5867	3.7912	18.61	0.16585	0.70	b609
A26-035	219.6194	3.7483	18.62	0.14714	0.71	b405
A26-036	219.6190	3.5935	18.64	0.30351	0.64	b301
A26-037	219.6226	3.7437	18.64	0.14709	0.38	b406
A26-038	219.6215	3.6006	18.65	0.22931	0.56	b302
A26-039	219.4764	3.5474	18.65	0.48425	0.20	b710
A26-040	219.6219	3.8106	18.66	0.16644	0.64	b401
A26-041	219.6640	3.6533	18.68	0.22811	0.53	r114
A26-042	219.5907	3.7312	18.68	0.14502	0.38	b605
A26-043	219.6293	3.5816	18.68	0.22443	0.56	b311
A26-044	219.5474	3.6453	18.70	0.29358	0.75	b515
A26-046	219.5130	3.7754	18.73	0.22248	0.75	b809
A26-047	219.5531	3.7872	18.73	0.49702	0.22	r610
A26-048	219.6893	3.7362	18.81	0.48624	0.35	b212
A26-049	219.6975	3.6993	18.84	0.49716	0.37	b215
A26-050	219.7176	3.7521	18.85	0.42055	0.77	r214
A26-051	219.6860	3.6773	18.88	0.22091	0.64	b108
A26-052	219.5966	3.6412	18.89	0.14605	0.68	r305
A26-053	219.6073	3.6562	18.90	0.22858	0.53	r312
A26-054	219.6120	3.7539	18.90	0.27153	0.40	b411
A26-055	219.4747	3.5876	18.90	0.46201	0.58	b712
A26-056	219.6275	3.7978	18.90	0.22562	0.61	b402
A26-057	219.6673	3.6707	18.91	0.29630	0.58	r116
A26-058	219.5899	3.6591	18.91	0.22538	0.76	r515
A26-060	219.5781	3.5900	18.94	0.22729	0.16	r503
A26-061	219.6777	3.7719	18.95	0.14396	0.52	r402
A26-062	219.4765	3.7515	18.97	0.14742	0.27	r804
A26-063	219.7393	3.6777	18.98	0.29177	0.72	b116
A26-064	219.5976	3.5482	19.01	0.30533	0.60	r302
A26-066	219.5812	3.5362	19.01	0.42241	0.53	r509
A26-067	219.6040	3.6595	19.03	0.30475	0.78	r314

Continued on next page

Target ID	RA	DEC	r-band mag.	z	Corr.	FiberID
A26-068	219.5975	3.6896	19.05	0.23951	0.74	b608
A26-069	219.6185	3.6594	19.06	0.22562	0.73	b305
A26-070	219.4682	3.7688	19.10	0.20724	0.58	r813
A26-071	219.5901	3.7703	19.11	0.29248	0.59	b602
A26-072	219.6597	3.6569	19.12	0.49266	0.38	r115
A26-073	219.7147	3.5905	19.17	0.22659	0.44	b105
A26-074	219.7235	3.7861	19.18	0.22512	0.72	r210
A26-075	219.4948	3.6804	19.19	0.30035	0.56	r808
A26-076	219.6120	3.6429	19.25	0.22576	0.74	r310
A26-077	219.4603	3.7979	19.27	0.26984	0.46	r809
A26-078	219.6329	3.6412	19.27	0.23429	0.52	b314
A26-079	219.5347	3.6329	19.27	0.37640	0.27	b506
A26-080	219.6331	3.7330	19.27	0.21974	0.82	r412
A26-082	219.5410	3.6070	19.28	0.30036	0.72	b505
A26-083	219.6173	3.6702	19.28	0.11969	0.27	b308
A26-084	219.5215	3.7569	19.29	0.49735	0.42	b810
A26-085	219.6009	3.8126	19.29	0.48397	0.32	b409
A26-086	219.6971	3.7107	19.30	0.15658	0.64	b214
A26-087	219.6168	3.7925	19.30	0.18288	0.16	b403
A26-088	219.5703	3.7590	19.33	0.21792	0.53	r602
A26-089	219.6247	3.7103	19.33	0.14528	0.71	b407
A26-090	219.4951	3.7304	19.37	0.34369	0.57	r805
A26-092	219.6679	3.6265	19.40	0.22390	0.60	r112
A26-093	219.6894	3.5892	19.41	0.23816	0.67	b104
A26-094	219.7216	3.7702	19.43	0.14436	0.72	r213
A26-095	219.5035	3.6035	19.44	0.14458	0.63	r705
A26-096	219.7275	3.7897	19.44	0.14331	0.80	r209
A26-098	219.5268	3.7326	19.47	0.32143	0.61	b806
A26-099	219.6046	3.7487	19.48	0.14679	0.75	b412
A26-101	219.5949	3.6378	19.49	0.23091	0.50	r304
A26-102	219.7108	3.6850	19.49	0.29435	0.66	b208
A26-103	219.5737	3.6787	19.50	0.49496	0.34	r608
A26-104	219.5046	3.6913	19.55	0.22358	0.67	r807
A26-105	219.5770	3.6569	19.55	0.22891	0.55	r506
A26-106	219.5195	3.5876	19.55	0.45725	0.71	r710
A26-108	219.5838	3.6279	19.56	0.49101	0.23	r512
A26-109	219.7356	3.6903	19.57	0.14760	0.44	r208
A26-110	219.5514	3.7976	19.60	0.14839	0.72	r609
A26-111	219.5526	3.6607	19.61	0.45597	0.83	b516
A26-112	219.5247	3.5995	19.61	0.29278	0.32	r711
A26-113	219.6212	3.7649	19.63	0.14680	0.46	b404
A26-114	219.5715	3.7103	19.64	0.29319	0.69	r605
A26-117	219.4609	3.5602	19.68	0.49825	0.31	b702
A26-118	219.5002	3.5880	19.68	0.40597	0.28	r703
A26-119	219.4909	3.7763	19.69	0.39896	0.56	r801
A26-120	219.4678	3.7884	19.71	0.20794	0.44	r811
A26-121	219.5734	3.7183	19.72	0.22178	0.64	r604
A26-122	219.5136	3.6242	19.72	0.22504	0.45	r707
A26-123	219.6232	3.6511	19.73	0.21757	0.38	b315
A26-124	219.6381	3.7894	19.73	0.29483	0.72	r409
A26-125	219.6386	3.7110	19.73	0.21967	0.72	r404
A26-127	219.5890	3.7225	19.74	0.21976	0.66	b612
A26-128	219.6475	3.6897	19.74	0.14726	0.69	r408

Continued on next page

Target ID	RA	DEC	r-band mag.	z	Corr.	FiberID
A26-129	219.5932	3.7410	19.75	0.14937	0.40	b604
A26-130	219.5552	3.5629	19.75	0.23101	0.70	b511
A26-131	219.6447	3.6299	19.75	0.22817	0.58	r106
A26-132	219.6139	3.6626	19.75	0.23150	0.45	b306
A26-133	219.6376	3.7242	19.76	0.14539	0.59	r413
A26-134	219.4791	3.6761	19.76	0.49511	0.18	b716
A26-135	219.5387	3.5853	19.77	0.41049	0.34	b504
A26-136	219.5981	3.6293	19.77	0.22278	0.67	r303
A26-137	219.5943	3.6581	19.77	0.22785	0.76	r514
A26-139	219.5993	3.6930	19.78	0.29579	0.56	b416
A26-140	219.7112	3.7024	19.79	0.28683	0.67	b206
A26-141	219.5831	3.6916	19.80	0.21952	0.30	b615
A26-143	219.7334	3.6595	19.81	0.22635	0.70	b115
A26-144	219.5806	3.7110	19.82	0.30168	0.73	b613
A26-145	219.6393	3.5544	19.82	0.22483	0.53	r101
A26-146	219.5780	3.7316	19.82	0.47612	0.16	r603
A26-148	219.6276	3.5989	19.83	0.22167	0.62	b313
A26-149	219.5882	3.6894	19.83	0.22703	0.53	b616
A26-150	219.6151	3.6847	19.83	0.21690	0.78	b408
A26-153	219.5621	3.6832	19.85	0.17491	0.39	r607
A26-154	219.5217	3.7518	19.86	0.21998	0.71	b811
A26-155	219.6450	3.8010	19.86	0.22377	0.47	r401
A26-156	219.6629	3.6901	19.87	0.14573	0.25	r407
A26-157	219.5462	3.6890	19.88	0.29497	0.35	r616
A26-158	219.5205	3.6128	19.89	0.29140	0.52	r712
A26-159	219.5270	3.7009	19.91	0.22378	0.51	b808
A26-160	219.4968	3.7110	19.91	0.43031	0.20	r806
A26-161	219.5955	3.6498	19.91	0.23091	0.71	r306
A26-162	219.4682	3.5341	19.93	0.49749	0.40	b709
A26-163	219.5454	3.5708	19.93	0.33573	0.55	b503
A26-164	219.7043	3.7965	19.93	0.39870	0.63	b201
A26-166	219.6073	3.6357	19.95	0.23258	0.67	r309
A26-167	219.5408	3.6687	19.96	0.21650	0.58	b508
A26-168	219.6810	3.6471	19.96	0.49128	0.19	r113
A26-169	219.4573	3.5934	19.97	0.49743	0.26	b705
A26-171	219.5296	3.7834	19.98	0.40283	0.56	b801
A26-172	219.5895	3.7882	19.98	0.14755	0.30	b610
A26-173	219.5606	3.7489	20.02	0.22525	0.30	r612
A26-174	219.5294	3.7640	20.03	0.21602	0.59	b802
A26-175	219.6098	3.6497	20.03	0.23570	0.79	r311
A26-176	219.5485	3.5743	20.04	0.32191	0.73	b512
A26-178	219.4631	3.6723	20.06	0.18143	0.30	b708
A26-179	219.5019	3.7663	20.11	0.14693	0.52	r802
A26-181	219.5609	3.6755	20.12	0.22535	0.50	r508
A26-182	219.7242	3.7796	20.15	0.14651	0.57	r212
A26-183	219.7141	3.6976	20.16	0.15728	0.62	b207
A26-184	219.5410	3.6993	20.17	0.22781	0.42	r614
A26-186	219.6889	3.6832	20.19	0.35842	0.72	b216
A26-187	219.6375	3.5846	20.21	0.46987	0.25	r103
A26-189	219.5304	3.7239	20.23	0.22492	0.37	b807
A26-190	219.6445	3.6004	20.23	0.22684	0.33	r104
A26-192	219.5398	3.5625	20.25	0.29990	0.70	b502
A26-193	219.5169	3.6376	20.25	0.29720	0.66	r714

Continued on next page

Target ID	RA	DEC	r-band mag.	z	Corr.	FiberID
A26-194	219.5985	3.6729	20.25	0.30135	0.60	r308
A26-195	219.6811	3.5532	20.25	0.44952	0.16	b103
A26-196	219.7022	3.7711	20.26	0.47112	0.15	b203
A26-197	219.6967	3.7891	20.27	0.22485	0.46	b209
A26-198	219.5982	3.7062	20.28	0.14647	0.20	b607
A26-199	219.5342	3.7338	20.29	0.49736	0.51	b805
A26-200	219.5901	3.8085	20.31	0.16555	0.22	b601
A26-201	219.5599	3.7788	20.33	0.32292	0.73	r611
A26-202	219.5620	3.6899	20.33	0.22017	0.35	r615
A26-204	219.5425	3.6439	20.36	0.29104	0.43	b507
A26-205	219.6455	3.5816	20.36	0.46133	0.32	r102
A26-206	219.5223	3.6858	20.36	0.34030	0.69	b816
A26-207	219.6004	3.6985	20.36	0.23079	0.63	b415
A26-208	219.6021	3.6632	20.36	0.22861	0.47	r315
A26-209	219.5834	3.7001	20.38	0.22663	0.77	b614
A26-211	219.6473	3.7018	20.39	0.14539	0.68	r405
A26-212	219.6322	3.6527	20.39	0.23144	0.55	b316
A26-213	219.6494	3.5746	20.41	0.39711	0.59	r110
A26-214	219.5782	3.7012	20.41	0.46211	0.19	r606
A26-215	219.5431	3.5505	20.41	0.22970	0.41	b501
A26-217	219.6861	3.7258	20.43	0.29202	0.78	b213
A26-218	219.6020	3.5413	20.45	0.48556	0.24	r301
A26-219	219.5716	3.5419	20.46	0.22791	0.56	r501
A26-220	219.5246	3.6514	20.46	0.29007	0.32	r715
A26-222	219.5112	3.5503	20.48	0.22510	0.36	r702
A26-223	219.7194	3.7022	20.50	0.29156	0.72	r216
A26-225	219.6172	3.6344	20.50	0.22873	0.77	b303
A26-226	219.5503	3.6100	20.50	0.29084	0.31	b514
A26-227	219.6397	3.6110	20.50	0.22705	0.74	r105
A26-229	219.5843	3.7545	20.52	0.21942	0.64	b611
A26-230	219.5244	3.5765	20.53	0.49083	0.25	r709
A26-231	219.4941	3.6588	20.53	0.11881	0.19	b714
A26-234	219.6983	3.7556	20.55	0.48675	0.25	b210
A26-236	219.6131	3.6734	20.58	0.22695	0.80	r316
A26-237	219.6473	3.7342	20.59	0.37840	0.49	r403
A26-238	219.6163	3.6564	20.59	0.22806	0.50	b304
A26-239	219.7324	3.6470	20.60	0.41568	0.12	b113
A26-241	219.4596	3.7777	20.64	0.22477	0.41	r812
A26-242	219.7090	3.6171	20.64	0.33173	0.72	b106
A26-243	219.6977	3.5429	20.64	0.46163	0.57	b102
A26-244	219.5825	3.6778	20.65	0.22503	0.48	r516
A26-245	219.5606	3.6005	20.65	0.48728	0.27	b513
A26-247	219.4842	3.6245	20.66	0.28904	0.60	b713
A26-249	219.6726	3.5396	20.66	0.29379	0.49	r109
A26-250	219.5682	3.5715	20.67	0.49789	0.24	r502
A26-251	219.5127	3.6298	20.68	0.29540	0.78	r708
B02-000	354.7158	-54.6048	16.78	0.16842	0.81	b508
B02-001	354.6197	-54.5838	17.61	0.32766	0.86	r314
B02-002	354.7619	-54.5920	17.95	0.33133	0.81	b415
B02-003	354.7215	-54.6121	18.07	0.26097	0.32	r715
B02-004	354.4837	-54.7200	18.09	0.16726	0.73	r608
B02-005	354.6442	-54.7200	18.19	0.21053	0.56	b201
B02-006	354.6590	-54.6237	18.37	0.21989	0.65	b402

Continued on next page

Target ID	RA	DEC	r-band mag.	z	Corr.	FiberID
B02-007	354.6020	-54.5530	18.44	0.32769	0.84	b607
B02-008	354.7194	-54.5603	18.50	0.29164	0.81	b304
B02-009	354.7017	-54.6397	18.63	0.10593	0.58	b504
B02-010	354.6680	-54.6147	18.92	0.43463	0.81	r607
B02-011	354.5684	-54.5687	19.06	0.20246	0.26	r605
B02-012	354.6377	-54.6295	19.09	0.33149	0.39	b608
B02-014	354.4756	-54.5603	19.24	0.20284	0.27	b313
B02-015	354.6481	-54.5846	19.27	0.32610	0.44	b406
B02-016	354.6219	-54.5381	19.35	0.28286	0.73	r805
B02-017	354.5431	-54.7179	19.40	0.36757	0.82	r112
B02-018	354.5413	-54.5361	19.41	0.32910	0.62	r514
B02-019	354.6960	-54.6606	19.49	0.34713	0.78	b408
B02-020	354.6250	-54.6359	19.51	0.33960	0.30	r302
B02-021	354.7098	-54.5292	19.51	0.42143	0.44	b209
B02-022	354.5922	-54.6485	19.54	0.47278	0.65	r101
B02-023	354.7468	-54.6627	19.56	0.33113	0.68	r604
B02-025	354.6437	-54.5498	19.67	0.29129	0.55	b510
B02-026	354.6204	-54.5734	19.67	0.38782	0.82	r406
B02-027	354.6884	-54.6460	19.71	0.20299	0.24	b615
B02-028	354.7675	-54.5669	19.73	0.33292	0.82	b612
B02-029	354.6562	-54.5256	19.74	0.33048	0.58	r612
B02-030	354.6511	-54.6238	19.75	0.32791	0.74	b308
B02-032	354.7349	-54.5543	19.79	0.32970	0.67	r512
B02-033	354.4902	-54.5742	19.80	0.32837	0.66	r304
B02-035	354.6411	-54.6253	19.83	0.46301	0.77	r713
B02-036	354.7925	-54.6669	19.84	0.32822	0.56	r509
B02-038	354.6852	-54.5607	19.87	0.32819	0.57	r507
B02-039	354.5759	-54.6194	19.88	0.14423	0.38	b503
B02-040	354.6977	-54.6737	19.89	0.35531	0.24	r113
B02-041	354.6219	-54.7236	19.93	0.34650	0.70	r108
B02-042	354.7703	-54.6097	19.95	0.33384	0.68	b407
B02-043	354.6529	-54.6947	19.95	0.19419	0.49	b811
B02-044	354.7745	-54.5856	19.96	0.43448	0.70	r102
B02-045	354.6152	-54.5508	19.97	0.32895	0.62	r506
B02-046	354.7402	-54.5596	19.98	0.32310	0.65	r408
B02-047	354.7249	-54.5861	20.01	0.38900	0.31	r603
B02-049	354.5415	-54.6095	20.05	0.37829	0.70	b401
B02-050	354.6230	-54.6404	20.07	0.45919	0.78	b808
B02-052	354.7780	-54.6432	20.15	0.17981	0.30	r707
B02-053	354.6239	-54.5904	20.16	0.29166	0.65	r311
B02-055	354.6339	-54.6125	20.17	0.47243	0.67	r712
B02-056	354.5591	-54.5625	20.18	0.44927	0.26	b505
B02-057	354.7393	-54.5281	20.20	0.47018	0.77	b414
B02-058	354.5599	-54.6430	20.21	0.41422	0.54	b604
B02-059	354.6699	-54.6456	20.22	0.38728	0.76	b216
B02-061	354.5199	-54.6690	20.25	0.38777	0.74	r116
B02-062	354.8041	-54.6827	20.26	0.30446	0.32	b813
B02-063	354.7127	-54.5872	20.27	0.32969	0.57	r307
B02-066	354.5279	-54.5555	20.32	0.46299	0.74	b310
B02-067	354.6439	-54.6336	20.33	0.25443	0.29	r710
B02-068	354.5842	-54.5292	20.34	0.38712	0.83	b214
B02-069	354.7279	-54.6363	20.35	0.33233	0.23	b613
B02-070	354.7501	-54.6203	20.36	0.32837	0.56	r316

Continued on next page

Target ID	RA	DEC	r-band mag.	z	Corr.	FiberID
B02-071	354.6357	-54.6992	20.36	0.29902	0.59	b206
B02-072	354.8157	-54.5656	20.36	0.26233	0.16	r803
B02-073	354.5937	-54.7179	20.39	0.20584	0.28	b506
B02-074	354.6509	-54.5907	20.44	0.38145	0.23	b809
B02-076	354.7534	-54.5262	20.54	0.38658	0.40	r103
B02-078	354.6045	-54.5860	20.56	0.41549	0.71	b301
B02-079	354.6459	-54.5302	20.57	0.16906	0.42	r614
B02-081	354.5272	-54.6707	20.64	0.46051	0.40	b807
B02-082	354.6529	-54.6311	20.64	0.41388	0.52	b404
B02-083	354.6413	-54.6140	20.65	0.10588	0.50	r705
B02-084	354.6792	-54.6184	20.65	0.28544	0.38	r409
B02-086	354.5288	-54.6141	20.68	0.33050	0.41	r515
B02-087	354.6476	-54.6753	20.69	0.28565	0.24	b806
B02-089	354.6015	-54.5667	20.70	0.32298	0.63	r709
B02-090	354.4953	-54.5772	20.75	0.33055	0.46	r305
B02-091	354.5618	-54.6596	20.75	0.32723	0.45	b307
B02-092	354.5682	-54.7200	20.76	0.44940	0.21	r510
B02-094	354.5490	-54.5814	20.77	0.20618	0.21	r209
B02-095	354.5795	-54.5739	20.83	0.36707	0.56	b205
B02-098	354.5964	-54.6935	20.87	0.33068	0.71	b616
B02-099	354.7201	-54.6482	20.88	0.21412	0.41	b311
B02-101	354.6036	-54.6262	20.92	0.35292	0.25	b208
B02-102	354.7701	-54.5427	20.95	0.13940	0.22	b410
B02-103	354.7933	-54.6316	20.95	0.38842	0.68	b203
B02-104	354.6660	-54.7136	20.96	0.18422	0.19	b305
B02-105	354.6637	-54.6069	20.96	0.33372	0.20	b611
B02-108	354.6169	-54.6449	21.01	0.22023	0.44	r401
B02-109	354.6349	-54.6945	21.02	0.16765	0.31	r616
B02-111	354.6466	-54.6708	21.06	0.37817	0.66	b314
B02-112	354.8179	-54.5545	21.07	0.12746	0.22	b515
B02-113	354.7347	-54.6038	21.10	0.18495	0.19	b306
B02-114	354.6731	-54.5527	21.10	0.32861	0.36	r613
B02-115	354.7858	-54.6406	21.11	0.32584	0.59	r313
B02-116	354.4979	-54.5378	21.13	0.45981	0.55	r411
B02-118	354.6697	-54.6972	21.14	0.33871	0.19	b316
B02-120	354.6685	-54.6400	21.18	0.33338	0.43	r416
B02-121	354.5306	-54.5285	21.18	0.30426	0.23	r711
B02-122	354.4986	-54.6072	21.19	0.13966	0.24	b816
B02-123	354.5499	-54.7103	21.19	0.45942	0.73	r609
B02-124	354.6632	-54.7002	21.21	0.32216	0.16	b601
B02-125	354.7250	-54.7210	21.23	0.33440	0.21	r516
B02-126	354.6063	-54.5470	21.23	0.18218	0.17	r706
B02-128	354.7935	-54.7041	21.26	0.32777	0.47	r303
B02-129	354.7023	-54.5424	21.27	0.33535	0.29	r414
B02-130	354.7044	-54.5680	21.28	0.33271	0.38	b405
B02-132	354.7117	-54.5426	21.31	0.33848	0.23	r611
B02-133	354.7426	-54.6982	21.31	0.49490	0.26	b411
B02-134	354.7496	-54.6030	21.33	0.10715	0.32	r704
B02-135	354.5327	-54.7081	21.33	0.31554	0.19	b507
B02-136	354.6047	-54.5421	21.34	0.18642	0.25	r504
B02-137	354.6972	-54.5310	21.34	0.36785	0.70	r115
B02-138	354.5417	-54.5944	21.34	0.46684	0.47	b814
B02-139	354.6506	-54.6423	21.36	0.20762	0.18	r111

Continued on next page

Target ID	RA	DEC	r-band mag.	z	Corr.	FiberID
B02-140	354.6921	-54.5981	21.38	0.43533	0.44	b309
B02-141	354.6050	-54.5917	21.38	0.33466	0.24	b609
B02-142	354.8186	-54.6105	21.39	0.43466	0.54	b605
B02-144	354.5674	-54.6463	21.42	0.35443	0.18	r114
B02-145	354.7551	-54.6619	21.42	0.32936	0.33	b614
B02-148	354.7704	-54.6465	21.45	0.42681	0.46	b210
B02-151	354.5206	-54.6733	21.53	0.33794	0.28	r308
B02-152	354.5470	-54.6152	21.53	0.17056	0.27	r310
B02-153	354.6248	-54.5308	21.54	0.41475	0.40	r413
B02-154	354.5096	-54.5271	21.54	0.21272	0.15	r801
B02-155	354.8090	-54.6890	21.55	0.19704	0.32	b512
B02-156	354.7717	-54.6336	21.56	0.36069	0.14	b509
B02-157	354.5784	-54.5324	21.57	0.47277	0.71	b514
B02-159	354.7254	-54.6441	21.58	0.14443	0.41	b513
B02-160	354.5229	-54.6561	21.58	0.46183	0.51	r610
B02-162	354.5197	-54.5282	21.59	0.33276	0.35	r716
B02-163	354.6724	-54.5597	21.60	0.40653	0.30	b211
B02-164	354.6464	-54.6996	21.61	0.15428	0.21	b303
B02-165	354.7511	-54.6583	21.61	0.33035	0.48	b413
B02-166	354.7262	-54.7167	21.62	0.22461	0.36	b511
B02-167	354.7503	-54.5856	21.63	0.20702	0.19	r107
B02-169	354.7795	-54.6014	21.64	0.33093	0.30	b412
B02-170	354.6586	-54.6366	21.65	0.33272	0.43	b516
B02-171	354.7292	-54.5447	21.68	0.32678	0.36	r315
B02-172	354.5930	-54.6551	21.69	0.33931	0.15	r808
B02-173	354.5938	-54.7067	21.72	0.33696	0.21	r601
B02-174	354.7469	-54.7077	21.75	0.32829	0.35	r407
B02-175	354.6166	-54.6584	21.78	0.33027	0.32	b803
B02-176	354.6766	-54.5444	21.80	0.33793	0.31	r309
B02-178	354.6581	-54.6184	21.81	0.40689	0.44	r306
B02-179	354.8021	-54.6626	21.81	0.35774	0.20	b805
B02-180	354.7343	-54.5400	21.84	0.34050	0.25	r701
B02-182	354.6983	-54.7070	21.85	0.26754	0.24	b802
B02-184	354.6650	-54.5891	21.86	0.41194	0.23	b204
B02-186	354.4851	-54.6703	21.88	0.43426	0.19	r301
B02-187	354.6162	-54.5356	21.89	0.17832	0.25	r109
B02-189	354.6085	-54.5597	21.90	0.13814	0.18	r802
B02-190	354.8017	-54.6154	21.90	0.33376	0.16	b815
B02-191	354.6649	-54.5453	21.91	0.47157	0.72	b302
B02-193	354.5321	-54.5807	21.95	0.42712	0.16	r703
B02-194	354.5685	-54.7032	21.95	0.31108	0.24	r615
B02-195	354.4831	-54.5744	21.96	0.33696	0.20	r606
B02-196	354.5413	-54.6286	21.97	0.25503	0.18	b207
B02-197	354.5715	-54.5894	21.97	0.26529	0.20	r104
B02-199	354.5499	-54.6557	21.98	0.34699	0.26	r505
B02-200	354.8177	-54.6313	21.98	0.41321	0.50	b403
B02-201	354.6913	-54.5411	22.00	0.35537	0.23	b804
B04a-000	342.3196	-44.5089	16.67	0.15055	0.83	r707
B04a-001	342.1832	-44.5308	16.75	0.34768	0.73	b614
B04a-002	342.2116	-44.4628	17.58	0.14758	0.78	r301
B04a-003	342.2159	-44.5184	17.62	0.33535	0.75	r515
B04a-004	342.2790	-44.4984	17.77	0.14784	0.72	r713
B04a-005	342.2970	-44.5317	17.77	0.14946	0.78	r807

Continued on next page

Target ID	RA	DEC	r-band mag.	z	Corr.	FiberID
B04a-006	342.0985	-44.5811	18.01	0.34032	0.83	b211
B04a-007	342.2754	-44.6069	18.17	0.21118	0.72	b809
B04a-008	342.2118	-44.5105	18.18	0.35691	0.82	r305
B04a-009	342.2865	-44.5820	18.23	0.19075	0.75	b812
B04a-010	342.1521	-44.5217	18.40	0.36208	0.85	b316
B04a-011	342.2062	-44.5121	18.40	0.35394	0.85	r306
B04a-012	342.3148	-44.4980	18.42	0.14877	0.71	r705
B04a-013	342.1447	-44.4980	18.43	0.36036	0.89	b314
B04a-014	342.0797	-44.5507	18.44	0.34078	0.79	b207
B04a-015	342.3235	-44.4984	18.50	0.34745	0.81	r706
B04a-016	342.1393	-44.4488	18.55	0.28796	0.75	b311
B04a-017	342.1861	-44.4975	18.59	0.35562	0.75	r313
B04a-018	342.3020	-44.6253	18.59	0.21123	0.73	r801
B04a-019	342.2347	-44.5039	18.61	0.35585	0.81	r507
B04a-020	342.0904	-44.5981	18.61	0.33902	0.69	b202
B04a-021	342.1995	-44.4442	18.62	0.29634	0.70	r309
B04a-022	342.0674	-44.5952	18.68	0.33524	0.72	r211
B04a-023	342.1027	-44.5724	18.71	0.33342	0.41	b212
B04a-024	342.2717	-44.5181	18.78	0.33934	0.77	r716
B04a-025	342.3096	-44.5653	18.78	0.19888	0.74	r806
B04a-026	342.1798	-44.4576	18.85	0.34342	0.81	b301
B04a-027	342.1441	-44.5584	18.87	0.35022	0.79	r413
B04a-028	342.1227	-44.5322	18.93	0.35036	0.80	r407
B04a-029	342.0820	-44.5218	18.94	0.35394	0.72	b208
B04a-030	342.0969	-44.6303	18.97	0.21318	0.67	b209
B04a-031	342.1764	-44.5114	18.97	0.35568	0.81	b305
B04a-032	342.2233	-44.5213	18.98	0.34799	0.80	r516
B04a-033	342.2618	-44.5145	18.99	0.33570	0.74	b508
B04a-034	342.1024	-44.5670	19.00	0.34198	0.80	b213
B04a-035	342.2296	-44.6085	19.01	0.34313	0.66	b801
B04a-036	342.1128	-44.5665	19.02	0.34124	0.71	b214
B04a-037	342.1582	-44.5969	19.06	0.35591	0.82	b401
B04a-038	342.2953	-44.6018	19.08	0.34807	0.77	b810
B04a-039	342.1688	-44.6087	19.08	0.17589	0.73	b409
B04a-040	342.2092	-44.4672	19.11	0.33638	0.85	r302
B04a-041	342.1945	-44.6139	19.12	0.34257	0.68	r601
B04a-042	342.2196	-44.5654	19.13	0.34859	0.70	r613
B04a-043	342.2225	-44.4693	19.16	0.35114	0.70	r510
B04a-044	342.2741	-44.4677	19.19	0.47745	0.43	r710
B04a-045	342.2173	-44.4786	19.19	0.33827	0.79	r511
B04a-046	342.1504	-44.5498	19.23	0.34644	0.81	b405
B04a-047	342.2141	-44.4584	19.25	0.34377	0.77	r509
B04a-048	342.2956	-44.4787	19.25	0.14765	0.47	r702
B04a-049	342.1499	-44.5714	19.25	0.33602	0.78	b403
B04a-050	342.1955	-44.5260	19.26	0.34619	0.72	r607
B04a-051	342.0901	-44.5731	19.26	0.34565	0.62	b206
B04a-052	342.2649	-44.5083	19.27	0.28857	0.80	b507
B04a-053	342.2451	-44.5181	19.29	0.34952	0.84	b516
B04a-054	342.2448	-44.5001	19.31	0.33810	0.68	b513
B04a-055	342.2244	-44.4573	19.34	0.33704	0.78	r502
B04a-058	342.3131	-44.6050	19.36	0.21245	0.22	r803
B04a-059	342.2020	-44.5403	19.36	0.36399	0.76	r606
B04a-061	342.1792	-44.4895	19.37	0.35504	0.77	b303

Continued on next page

Target ID	RA	DEC	r-band mag.	z	Corr.	FiberID
B04a-062	342.2030	-44.5149	19.39	0.33343	0.70	r307
B04a-063	342.2424	-44.5322	19.40	0.45271	0.52	b808
B04a-064	342.0739	-44.6078	19.40	0.20242	0.27	b201
B04a-065	342.1176	-44.5885	19.43	0.34365	0.73	r402
B04a-067	342.1391	-44.5361	19.50	0.33580	0.68	r415
B04a-068	342.2020	-44.4787	19.52	0.34122	0.63	r303
B04a-069	342.2307	-44.5517	19.52	0.40304	0.56	b805
B04a-070	342.2166	-44.5026	19.53	0.35560	0.75	r514
B04a-071	342.2205	-44.5259	19.53	0.34074	0.77	r616
B04a-073	342.1624	-44.5133	19.55	0.34978	0.57	b307
B04a-076	342.2467	-44.4473	19.59	0.34690	0.74	b509
B04a-077	342.0813	-44.5791	19.60	0.33334	0.47	b205
B04a-078	342.2514	-44.5675	19.61	0.43869	0.52	b813
B04a-079	342.1854	-44.5186	19.62	0.34409	0.75	r316
B04a-081	342.2430	-44.5077	19.65	0.35912	0.68	b514
B04a-082	342.2563	-44.4865	19.66	0.34954	0.85	b502
B04a-083	342.0785	-44.4843	19.74	0.45700	0.69	r113
B04a-084	342.0427	-44.4693	19.75	0.34931	0.38	r112
B04a-086	342.1465	-44.5045	19.76	0.33984	0.71	b315
B04a-087	342.1881	-44.5260	19.77	0.35007	0.68	b616
B04a-088	342.1557	-44.5459	19.77	0.33132	0.35	b406
B04a-089	342.3211	-44.4799	19.77	0.34250	0.79	r703
B04a-090	342.2084	-44.5900	19.77	0.45866	0.47	r611
B04a-091	342.1824	-44.6016	19.80	0.34669	0.50	b601
B04a-094	342.1953	-44.6023	19.84	0.34917	0.62	r602
B04a-096	342.2657	-44.5978	19.84	0.35477	0.73	b811
B04a-098	342.1722	-44.5627	19.86	0.34361	0.60	b412
B04a-099	342.1933	-44.5178	19.86	0.34255	0.69	r315
B04a-100	342.2451	-44.5112	19.88	0.33546	0.80	b515
B04a-101	342.1769	-44.5341	19.88	0.33457	0.64	b607
B04a-102	342.2527	-44.4641	19.89	0.34982	0.73	b501
B04a-104	342.0819	-44.4880	19.92	0.34359	0.63	r114
B04a-105	342.1803	-44.5006	19.92	0.33592	0.75	b304
B04a-106	342.1673	-44.5140	19.93	0.35131	0.72	b308
B04a-107	342.1197	-44.4491	19.93	0.33937	0.56	r104
B04a-108	342.1794	-44.5282	19.95	0.32741	0.19	b608
B04a-109	342.2289	-44.4310	19.95	0.18842	0.25	r501
B04a-110	342.2009	-44.4998	19.95	0.34510	0.71	r314
B04a-111	342.0696	-44.5724	19.95	0.34101	0.74	r214
B04a-112	342.1283	-44.5832	19.98	0.34349	0.61	r412
B04a-113	342.1188	-44.5843	19.98	0.34829	0.38	r403
B04a-116	342.1520	-44.5881	20.02	0.35021	0.66	b402
B04a-117	342.2438	-44.4897	20.03	0.35187	0.74	b512
B04a-118	342.1394	-44.4309	20.07	0.33695	0.54	b309
B04a-119	342.3006	-44.6108	20.07	0.43527	0.17	r802
B04a-120	342.1546	-44.5393	20.07	0.35382	0.67	b407
B04a-121	342.2214	-44.4942	20.08	0.35059	0.33	r512
B04a-123	342.2415	-44.4772	20.10	0.34780	0.76	b511
B04a-124	342.3010	-44.5979	20.14	0.21001	0.26	r804
B04a-125	342.0814	-44.5174	20.14	0.35140	0.62	r116
B04a-126	342.2279	-44.5352	20.14	0.34641	0.71	r614
B04a-127	342.1883	-44.5913	20.14	0.44760	0.73	b610
B04a-128	342.2660	-44.4917	20.14	0.35662	0.73	b503

Continued on next page

Target ID	RA	DEC	r-band mag.	z	Corr.	FiberID
B04a-131	342.1891	-44.5295	20.17	0.34815	0.58	b615
B04a-132	342.1857	-44.5346	20.17	0.33509	0.30	b613
B04a-134	342.2731	-44.5053	20.18	0.34860	0.64	r714
B04a-135	342.1654	-44.5766	20.19	0.35174	0.67	b410
B04a-137	342.3117	-44.5144	20.19	0.35099	0.68	r708
B04a-138	342.1793	-44.5835	20.19	0.34839	0.68	b603
B04a-140	342.1800	-44.5673	20.20	0.47403	0.76	b605
B04a-141	342.2443	-44.5732	20.20	0.45541	0.78	b803
B04a-142	342.0741	-44.4986	20.21	0.34873	0.62	r115
B04a-144	342.2293	-44.5556	20.22	0.33251	0.59	b804
B04a-145	342.2888	-44.5084	20.27	0.34888	0.61	r715
B04a-146	342.2710	-44.4712	20.28	0.24402	0.22	r711
B04a-147	342.0539	-44.5960	20.28	0.33617	0.53	r210
B04a-148	342.2860	-44.4780	20.28	0.35128	0.52	r712
B04a-149	342.2705	-44.4984	20.30	0.35475	0.69	b505
B04a-150	342.1816	-44.5890	20.32	0.44658	0.34	b602
B04a-151	342.2961	-44.5656	20.32	0.47680	0.72	b814
B04a-153	342.2085	-44.5018	20.33	0.35972	0.33	r304
B04a-155	342.2240	-44.5161	20.34	0.35326	0.54	r508
B04a-156	342.0632	-44.5271	20.34	0.34682	0.50	r216
B04a-157	342.1489	-44.5680	20.34	0.35155	0.64	b404
B04a-158	342.2869	-44.4545	20.34	0.28859	0.28	r709
B04a-160	342.1430	-44.4619	20.35	0.28767	0.24	b312
B04a-162	342.1142	-44.5215	20.38	0.34875	0.53	r408
B04a-163	342.1006	-44.6221	20.38	0.11330	0.16	b210
B04a-166	342.1352	-44.4510	20.39	0.34652	0.50	r105
B04a-167	342.0568	-44.5761	20.40	0.34225	0.40	r213
B04a-168	342.1817	-44.5118	20.40	0.17682	0.22	b306
B04a-172	342.2636	-44.4970	20.42	0.15164	0.23	b504
B04a-173	342.1236	-44.5431	20.43	0.33887	0.72	r406
B04a-175	342.0583	-44.5883	20.44	0.35567	0.58	r212
B04a-176	342.2370	-44.5495	20.45	0.33961	0.64	b806
B04a-177	342.2093	-44.6118	20.45	0.35017	0.62	r609
B04a-178	342.2112	-44.5341	20.48	0.34416	0.51	r615
B04a-181	342.1369	-44.6051	20.49	0.29753	0.48	r410
B04a-182	342.2201	-44.6112	20.49	0.34900	0.46	r610
B04a-184	342.1225	-44.5914	20.50	0.34132	0.55	r401
B04a-185	342.1571	-44.5327	20.52	0.34574	0.55	b408
B04a-186	342.2272	-44.4732	20.53	0.43326	0.24	r503
B04a-189	342.2027	-44.5198	20.54	0.35043	0.62	r308
B04a-191	342.1911	-44.5568	20.57	0.33613	0.63	r604
B04a-192	342.2636	-44.5035	20.58	0.34726	0.63	b506
B04a-194	342.2056	-44.5827	20.59	0.32658	0.14	r612
B04a-195	342.1418	-44.5259	20.59	0.34807	0.49	r416
B04a-198	342.2288	-44.4953	20.61	0.35165	0.52	r506
B04a-199	342.2042	-44.5252	20.62	0.35113	0.32	r608
B04a-200	342.2163	-44.4954	20.62	0.19490	0.23	r513
B04a-201	342.1614	-44.5559	20.64	0.35420	0.69	b413
B04a-203	342.1987	-44.4522	20.65	0.29656	0.62	r310
B04a-204	342.1286	-44.6216	20.65	0.45746	0.44	r409
B04a-205	342.1136	-44.5040	20.65	0.45301	0.64	r108
B04a-206	342.3225	-44.4549	20.66	0.34759	0.65	r701
B04a-207	342.1491	-44.4851	20.67	0.35046	0.64	b313

Continued on next page

Target ID	RA	DEC	r-band mag.	z	Corr.	FiberID
B04a-208	342.1085	-44.4444	20.68	0.35013	0.55	r103
B04a-209	342.3134	-44.4900	20.68	0.27243	0.41	r704
B04a-210	342.1619	-44.5300	20.68	0.34740	0.50	b415
B04a-211	342.1597	-44.5235	20.69	0.34785	0.60	b416
B04a-213	342.1895	-44.5739	20.69	0.20930	0.34	b611
B04a-214	342.1860	-44.6174	20.69	0.34614	0.56	b609
B04a-215	342.1717	-44.5405	20.69	0.34806	0.55	b414
B04a-217	342.1201	-44.5541	20.70	0.34574	0.51	r405
B04a-219	342.2025	-44.5588	20.72	0.34970	0.31	r603
B04a-220	342.1967	-44.4744	20.72	0.34279	0.66	r311
B04a-221	342.1725	-44.5724	20.74	0.34351	0.63	b411
B04a-222	342.0600	-44.4675	20.74	0.47333	0.53	r111
B04a-225	342.1352	-44.6008	20.77	0.35221	0.69	r411
B04a-227	342.0816	-44.5923	20.77	0.35092	0.60	b203
B04a-228	342.0872	-44.4544	20.78	0.20665	0.22	r106
B04a-229	342.1751	-44.5586	20.79	0.34630	0.54	b606
B04a-230	342.1889	-44.5404	20.79	0.34847	0.62	b612
B04a-231	342.1484	-44.4487	20.79	0.49561	0.24	b310
B04a-232	342.0586	-44.4516	20.80	0.35243	0.57	r110
B04a-233	342.0879	-44.5890	20.83	0.34774	0.70	b204
B04a-234	342.2377	-44.4846	20.84	0.35937	0.66	r504
B04a-235	342.2987	-44.5901	20.85	0.35229	0.61	r805
B04a-236	342.1993	-44.5454	20.85	0.35325	0.59	r605
B04a-237	342.1631	-44.4636	20.85	0.24418	0.15	b302
B04a-238	342.1356	-44.4343	20.86	0.33733	0.34	r101
B04a-239	342.1010	-44.5425	20.87	0.34403	0.66	b216
B04a-242	342.2435	-44.5377	20.90	0.34790	0.53	b807
B04a-243	342.2259	-44.4877	20.91	0.37257	0.40	r505
B04a-244	342.1844	-44.4897	20.91	0.34763	0.51	r312
B04a-246	342.2483	-44.4710	20.92	0.45765	0.74	b510
B04a-247	342.1771	-44.5803	20.92	0.35098	0.52	b604
B04a-248	342.1414	-44.5425	20.93	0.34198	0.31	r414
B04a-249	342.2790	-44.5245	20.93	0.45320	0.74	b816
B04b-000	342.2116	-44.4628	17.58	0.14765	0.67	r509
B04b-001	342.2159	-44.5184	17.62	0.36381	0.46	r505
B04b-002	342.2118	-44.5105	18.18	0.35758	0.81	r504
B04b-003	342.1521	-44.5217	18.40	0.36228	0.38	b312
B04b-004	342.2062	-44.5121	18.40	0.35454	0.43	r513
B04b-005	342.1447	-44.4980	18.43	0.36057	0.72	r105
B04b-006	342.3235	-44.4984	18.50	0.24998	0.15	r705
B04b-007	342.1393	-44.4488	18.55	0.28774	0.53	r103
B04b-008	342.1861	-44.4975	18.59	0.33577	0.44	r311
B04b-009	342.3020	-44.6253	18.59	0.21046	0.58	b809
B04b-010	342.2347	-44.5039	18.61	0.35519	0.78	b505
B04b-011	342.1995	-44.4442	18.62	0.29604	0.63	r301
B04b-012	342.2717	-44.5181	18.78	0.33929	0.65	r707
B04b-013	342.1441	-44.5584	18.87	0.35081	0.57	r413
B04b-014	342.1764	-44.5114	18.97	0.45617	0.18	b305
B04b-015	342.2233	-44.5213	18.98	0.34859	0.73	b515
B04b-016	342.1024	-44.5670	19.00	0.34172	0.61	b214
B04b-017	342.2296	-44.6085	19.01	0.34311	0.52	r609
B04b-018	342.1128	-44.5665	19.02	0.34102	0.51	b215
B04b-019	342.1582	-44.5969	19.06	0.35589	0.66	b403

Continued on next page

Target ID	RA	DEC	r-band mag.	z	Corr.	FiberID
B04b-020	342.1945	-44.6139	19.12	0.34306	0.52	b609
B04b-021	342.2196	-44.5654	19.13	0.34885	0.47	r606
B04b-022	342.2225	-44.4693	19.16	0.35111	0.71	b510
B04b-023	342.2173	-44.4786	19.19	0.33870	0.55	r502
B04b-024	342.2141	-44.4584	19.25	0.34383	0.63	r501
B04b-025	342.1499	-44.5714	19.25	0.33632	0.57	b405
B04b-026	342.1955	-44.5260	19.26	0.34612	0.55	r306
B04b-027	342.0901	-44.5731	19.26	0.34538	0.48	b205
B04b-028	342.2451	-44.5181	19.29	0.34995	0.65	b506
B04b-029	342.2448	-44.5001	19.31	0.33872	0.71	b502
B04b-030	342.1810	-44.4910	19.34	0.34472	0.45	r310
B04b-032	342.3131	-44.6050	19.36	0.21143	0.14	b811
B04b-033	342.2020	-44.5403	19.36	0.36411	0.61	b616
B04b-035	342.2030	-44.5149	19.39	0.33379	0.52	r514
B04b-036	342.2424	-44.5322	19.40	0.45249	0.51	b508
B04b-037	342.0739	-44.6078	19.40	0.21097	0.19	b202
B04b-038	342.1176	-44.5885	19.43	0.34355	0.49	b211
B04b-039	342.1391	-44.5361	19.50	0.33576	0.36	r416
B04b-040	342.2020	-44.4787	19.52	0.34132	0.40	r510
B04b-041	342.2166	-44.5026	19.53	0.12345	0.18	r503
B04b-042	342.2205	-44.5259	19.53	0.34111	0.51	r507
B04b-044	342.1624	-44.5133	19.55	0.34622	0.54	b311
B04b-045	342.2115	-44.5256	19.56	0.33542	0.69	r506
B04b-046	342.2467	-44.4473	19.59	0.34711	0.39	r709
B04b-047	342.2514	-44.5675	19.61	0.43888	0.42	b804
B04b-048	342.1854	-44.5186	19.62	0.34443	0.59	r314
B04b-051	342.1465	-44.5045	19.76	0.34001	0.47	r107
B04b-052	342.1881	-44.5260	19.77	0.35059	0.48	r315
B04b-053	342.1557	-44.5459	19.77	0.19961	0.21	b406
B04b-054	342.2084	-44.5900	19.77	0.45814	0.36	r604
B04b-055	342.1824	-44.6016	19.80	0.34651	0.25	b601
B04b-057	342.1953	-44.6023	19.84	0.34886	0.66	b610
B04b-058	342.1802	-44.5135	19.84	0.35553	0.67	r313
B04b-060	342.1722	-44.5627	19.86	0.34353	0.36	b413
B04b-061	342.1933	-44.5178	19.86	0.34221	0.35	r305
B04b-062	342.1769	-44.5341	19.88	0.33464	0.47	b308
B04b-063	342.2527	-44.4641	19.89	0.35064	0.26	r710
B04b-064	342.3215	-44.5437	19.90	0.34549	0.39	b815
B04b-065	342.1803	-44.5006	19.92	0.35236	0.29	r312
B04b-066	342.1673	-44.5140	19.93	0.35172	0.63	b306
B04b-067	342.1794	-44.5282	19.95	0.32795	0.40	r316
B04b-068	342.2289	-44.4310	19.95	0.20638	0.21	b509
B04b-069	342.2009	-44.4998	19.95	0.36025	0.35	r511
B04b-070	342.1283	-44.5832	19.98	0.34379	0.27	r403
B04b-071	342.1188	-44.5843	19.98	0.49087	0.19	b212
B04b-073	342.1520	-44.5881	20.02	0.35070	0.33	b404
B04b-074	342.2438	-44.4897	20.03	0.35163	0.53	b501
B04b-075	342.1394	-44.4309	20.07	0.33709	0.28	r101
B04b-076	342.3006	-44.6108	20.07	0.34096	0.18	b810
B04b-077	342.1546	-44.5393	20.07	0.35460	0.30	b407
B04b-078	342.2214	-44.4942	20.08	0.35094	0.28	b512
B04b-080	342.3010	-44.5979	20.14	0.20570	0.14	b812
B04b-081	342.1883	-44.5913	20.14	0.36026	0.39	b611

Continued on next page

Target ID	RA	DEC	r-band mag.	z	Corr.	FiberID
B04b-082	342.2660	-44.4917	20.14	0.35744	0.44	r713
B04b-083	342.2242	-44.5341	20.16	0.34611	0.50	b516
B04b-085	342.1891	-44.5295	20.17	0.33776	0.24	r307
B04b-086	342.1857	-44.5346	20.17	0.20899	0.20	b608
B04b-088	342.1654	-44.5766	20.19	0.35126	0.24	b411
B04b-090	342.1800	-44.5673	20.20	0.47452	0.58	b605
B04b-092	342.2293	-44.5556	20.22	0.33742	0.23	r613
B04b-093	342.2710	-44.4712	20.28	0.49629	0.18	r712
B04b-094	342.2085	-44.5018	20.33	0.34542	0.23	r512
B04b-095	342.2240	-44.5161	20.34	0.35355	0.53	b514
B04b-096	342.1489	-44.5680	20.34	0.49636	0.30	r412
B04b-101	342.1784	-44.5888	20.41	0.21119	0.19	b602
B04b-102	342.2370	-44.5495	20.45	0.33952	0.28	r614
B04b-103	342.2093	-44.6118	20.45	0.33755	0.22	r602
B04b-104	342.2112	-44.5341	20.48	0.34430	0.25	r508
B04b-105	342.1369	-44.6051	20.49	0.33952	0.24	r409
B04b-106	342.2201	-44.6112	20.49	0.20648	0.20	r603
B04b-107	342.1225	-44.5914	20.50	0.34081	0.31	r402
B04b-108	342.1571	-44.5327	20.52	0.34588	0.31	b316
B04b-109	342.2272	-44.4732	20.53	0.35064	0.36	b511
B04b-112	342.2027	-44.5198	20.54	0.35034	0.41	r515
B04b-114	342.2636	-44.5035	20.58	0.34767	0.52	r714
B04b-115	342.2056	-44.5827	20.59	0.33862	0.22	r605
B04b-116	342.1418	-44.5259	20.59	0.18320	0.15	r108
B04b-118	342.2288	-44.4953	20.61	0.35160	0.17	b513
B04b-119	342.2042	-44.5252	20.62	0.35073	0.33	r516
B04b-121	342.1286	-44.6216	20.65	0.45886	0.33	r401
B04b-122	342.1597	-44.5235	20.69	0.34780	0.37	b313
B04b-123	342.1717	-44.5405	20.69	0.34792	0.19	b416
B04b-124	342.2025	-44.5588	20.72	0.25730	0.16	r607
B04b-125	342.1967	-44.4744	20.72	0.34303	0.30	r302
B04b-126	342.0600	-44.4675	20.74	0.47357	0.39	b104
B04b-129	342.0872	-44.4544	20.78	0.35416	0.14	b103
B04b-130	342.1751	-44.5586	20.79	0.34657	0.23	b606
B04b-131	342.1993	-44.5454	20.85	0.24994	0.15	b614
B04b-132	342.1631	-44.4636	20.85	0.43250	0.14	b309
B04b-133	342.1356	-44.4343	20.86	0.27122	0.19	r102
B04b-134	342.1015	-44.5442	20.88	0.42357	0.13	b216
B04b-136	342.2483	-44.4710	20.92	0.45799	0.54	r711
B04b-137	342.1771	-44.5803	20.92	0.33978	0.19	b603
B04b-138	342.1414	-44.5425	20.93	0.33768	0.22	r415
B04b-139	342.0943	-44.5850	20.93	0.40609	0.12	b204
B04b-140	342.1467	-44.5291	20.94	0.21169	0.22	b314
B04b-141	342.1981	-44.4916	20.95	0.22482	0.21	r304
B04b-142	342.1626	-44.6232	20.95	0.34388	0.21	b409
B04b-143	342.0741	-44.5562	20.96	0.42494	0.14	b207
B04b-144	342.2257	-44.5678	20.98	0.33834	0.22	r612
B04b-145	342.0832	-44.4490	20.99	0.25600	0.17	b102
B04b-146	342.2647	-44.5460	20.99	0.45616	0.32	b814
B04b-147	342.2545	-44.5818	21.00	0.35641	0.26	b802
B04b-148	342.1294	-44.5587	21.00	0.33755	0.24	r407
B04b-150	342.2862	-44.5052	21.03	0.34509	0.34	r706
B04b-152	342.1304	-44.5673	21.05	0.24330	0.21	r406

Continued on next page

Target ID	RA	DEC	r-band mag.	z	Corr.	FiberID
B04b-153	342.1866	-44.5408	21.08	0.33938	0.15	b615
B04b-154	342.1264	-44.5267	21.10	0.25338	0.17	r115
B04b-156	342.1616	-44.5437	21.12	0.35149	0.17	b415
B04b-157	342.1512	-44.5346	21.17	0.34861	0.19	b408
B04b-159	342.2386	-44.5440	21.19	0.25819	0.22	b807
B04b-160	342.2386	-44.6175	21.20	0.35728	0.28	b801
B04b-161	342.2413	-44.5028	21.23	0.39412	0.16	b504
B04b-162	342.1180	-44.5079	21.23	0.17787	0.26	r112
B04b-163	342.2335	-44.5810	21.24	0.33747	0.21	r610
B04b-164	342.1252	-44.4495	21.25	0.20687	0.25	r109
B04b-166	342.1705	-44.4589	21.34	0.15616	0.23	b302
B04b-168	342.2652	-44.5120	21.39	0.35394	0.28	r715
B04b-169	342.1754	-44.4932	21.40	0.35124	0.30	b303
B04b-170	342.1315	-44.5771	21.41	0.34142	0.30	r405
B04b-171	342.1496	-44.6300	21.47	0.13265	0.29	b401
B04b-172	342.1643	-44.5035	21.47	0.35900	0.31	b304
B04b-173	342.1588	-44.5099	21.48	0.21412	0.12	b310
B04b-174	342.1402	-44.5875	21.49	0.33751	0.19	r411
B04b-175	342.1676	-44.4433	21.51	0.34197	0.22	b301
B04b-176	342.2153	-44.6266	21.52	0.33798	0.23	r601
B04b-180	342.2168	-44.5378	21.56	0.20961	0.21	r608
B04b-181	342.2538	-44.5171	21.57	0.49613	0.19	r716
B04b-182	342.1441	-44.5478	21.58	0.32947	0.15	r414
B04b-183	342.2455	-44.5771	21.59	0.47642	0.51	b803
B04b-184	342.1327	-44.6015	21.60	0.33737	0.18	r410
B04b-185	342.1856	-44.5754	21.62	0.45729	0.12	b612
B04b-186	342.1111	-44.4979	21.65	0.45390	0.53	b106
B04b-187	342.1043	-44.5891	21.65	0.24547	0.16	b210
B04b-188	342.2294	-44.5005	21.66	0.39053	0.16	b503
B04b-189	342.2632	-44.5358	21.69	0.25695	0.20	b816
B04b-190	342.2908	-44.4580	21.70	0.11408	0.13	r701
B04b-191	342.1680	-44.5511	21.71	0.23824	0.16	b414
B04b-193	342.1915	-44.5333	21.72	0.33794	0.20	r308
B04b-194	342.3016	-44.5296	21.72	0.24554	0.12	r708
B04b-195	342.1882	-44.4496	21.74	0.33741	0.25	r309
B04b-196	342.2371	-44.5248	21.75	0.25575	0.19	b507
B04b-197	342.1744	-44.5290	21.77	0.37377	0.11	b307
B04b-198	342.0923	-44.4756	21.77	0.30490	0.14	b105
B04b-199	342.1676	-44.5660	21.78	0.11510	0.13	b412
B04b-201	342.0657	-44.5898	21.80	0.19621	0.14	b203
B04b-202	342.2491	-44.5626	21.80	0.25934	0.24	b805
B04b-203	342.1031	-44.5786	21.80	0.34010	0.17	b213
B04b-204	342.1329	-44.4608	21.81	0.26975	0.23	r104
B04b-206	342.3151	-44.4627	21.82	0.28922	0.15	r702
B04b-207	342.1103	-44.5303	21.83	0.20385	0.14	b108
B04b-209	342.2874	-44.4840	21.88	0.34733	0.60	r704
B04b-210	342.1101	-44.5966	21.89	0.18060	0.15	b209
B04b-211	342.2570	-44.5569	21.91	0.47814	0.56	b806
B04b-212	342.3175	-44.4736	21.92	0.49665	0.37	r703
B04b-213	342.1927	-44.5545	21.92	0.20918	0.21	b613
B04b-214	342.0887	-44.5592	21.93	0.49127	0.20	b206
B04b-215	342.1267	-44.4748	21.93	0.34883	0.28	r111
B04b-218	342.0789	-44.5272	21.95	0.13945	0.21	b107

Continued on next page

Target ID	RA	DEC	r-band mag.	z	Corr.	FiberID
B04b-219	342.1531	-44.6066	21.99	0.34112	0.22	b402
B04b-220	342.1999	-44.4835	21.99	0.33955	0.25	r303
B05-000	355.2159	-9.1673	17.12	0.19048	0.80	r305
B05-001	355.4144	-9.0366	17.54	0.15405	0.63	r203
B05-002	355.3584	-9.0805	17.55	0.40739	0.23	b208
B05-003	355.1703	-9.1387	17.86	0.24225	0.82	r707
B05-004	355.2778	-9.2424	17.88	0.23591	0.42	b301
B05-005	355.2800	-9.0297	18.04	0.25279	0.81	r605
B05-006	355.1227	-9.2286	18.05	0.19200	0.78	b703
B05-007	355.2410	-8.9270	18.05	0.17048	0.81	b802
B05-008	355.3136	-9.0881	18.07	0.25087	0.57	b608
B05-009	355.2923	-8.9534	18.09	0.24689	0.81	b609
B05-010	355.1119	-9.1065	18.15	0.19189	0.78	r808
B05-011	355.2545	-9.1303	18.38	0.25130	0.67	r314
B05-012	355.3154	-9.0331	18.41	0.25156	0.84	b603
B05-013	355.3478	-9.2537	18.41	0.25200	0.53	r109
B05-014	355.2055	-8.9511	18.51	0.17362	0.53	b811
B05-015	355.2089	-9.1509	18.51	0.19293	0.72	r306
B05-016	355.1082	-9.0958	18.51	0.19082	0.26	r815
B05-017	355.1545	-9.2421	18.51	0.36882	0.76	r702
B05-018	355.2981	-9.0340	18.54	0.25122	0.82	b615
B05-019	355.3146	-9.0811	18.54	0.25336	0.79	b607
B05-020	355.3167	-9.0266	18.57	0.21399	0.82	b414
B05-021	355.3156	-9.0535	18.65	0.24651	0.78	b415
B05-022	355.1653	-9.0254	18.67	0.19167	0.80	b814
B05-023	355.2801	-9.1775	18.68	0.36882	0.59	b305
B05-024	355.2183	-9.0577	18.71	0.23980	0.75	b805
B05-025	355.1773	-8.9469	18.76	0.29501	0.70	b810
B05-026	355.2969	-9.1379	18.77	0.25163	0.82	b316
B05-027	355.3115	-9.0457	18.80	0.25235	0.84	b604
B05-028	355.3725	-9.0660	18.81	0.25507	0.81	b206
B05-030	355.3370	-9.0543	18.87	0.24366	0.79	r415
B05-031	355.2507	-9.1348	18.87	0.23890	0.72	r313
B05-032	355.2311	-9.1497	18.91	0.19124	0.42	r312
B05-033	355.3380	-9.0211	18.92	0.24816	0.80	r404
B05-034	355.1649	-9.1121	18.94	0.24275	0.72	b816
B05-035	355.3059	-9.0204	18.98	0.25854	0.57	b613
B05-036	355.1584	-9.0842	18.99	0.17815	0.62	b815
B05-037	355.2961	-9.0255	19.02	0.24909	0.77	b614
B05-038	355.1934	-8.9723	19.02	0.24140	0.78	b812
B05-039	355.3120	-9.1151	19.04	0.25105	0.72	r108
B05-040	355.2551	-8.9326	19.04	0.40701	0.86	r609
B05-041	355.3365	-8.9284	19.08	0.13873	0.36	r409
B05-043	355.1419	-9.1751	19.09	0.24238	0.72	r705
B05-044	355.3455	-9.1050	19.10	0.25202	0.64	b216
B05-045	355.3446	-9.0807	19.12	0.24271	0.78	r408
B05-046	355.3263	-9.0866	19.12	0.24823	0.81	b408
B05-047	355.3071	-9.1956	19.15	0.25134	0.55	b311
B05-048	355.3819	-9.0268	19.15	0.24932	0.79	r214
B05-049	355.3414	-8.9520	19.18	0.25809	0.76	r402
B05-050	355.1737	-9.2723	19.18	0.11480	0.58	r301
B05-051	355.3152	-9.2656	19.18	0.23499	0.49	r101
B05-052	355.3900	-8.9836	19.18	0.25000	0.76	r210

Continued on next page

Target ID	RA	DEC	r-band mag.	z	Corr.	FiberID
B05-053	355.3441	-8.9990	19.19	0.30564	0.80	b211
B05-054	355.2477	-9.0603	19.19	0.36989	0.22	r613
B05-055	355.2395	-8.9845	19.22	0.25735	0.74	b803
B05-056	355.3307	-9.0089	19.23	0.25692	0.82	b405
B05-057	355.4369	-9.0658	19.24	0.23939	0.65	r205
B05-058	355.3254	-9.1540	19.26	0.24972	0.68	r104
B05-059	355.2687	-8.9050	19.27	0.30304	0.61	r601
B05-060	355.4027	-9.0318	19.28	0.24658	0.73	r202
B05-061	355.3637	-9.0675	19.28	0.25370	0.72	b207
B05-062	355.3802	-9.0217	19.29	0.25081	0.78	b204
B05-063	355.2053	-8.9785	19.29	0.44588	0.80	b813
B05-064	355.1176	-9.2542	19.29	0.36927	0.34	b702
B05-065	355.2217	-9.1070	19.30	0.25218	0.74	b807
B05-066	355.3069	-9.0620	19.33	0.25099	0.78	b606
B05-067	355.2980	-9.0012	19.34	0.40727	0.78	b612
B05-069	355.2532	-9.0845	19.35	0.44623	0.57	r615
B05-070	355.2953	-9.1469	19.35	0.25376	0.75	b314
B05-071	355.3266	-9.0115	19.36	0.25091	0.75	b406
B05-073	355.3247	-9.0145	19.39	0.25028	0.77	b407
B05-074	355.3433	-8.9864	19.40	0.24964	0.64	r403
B05-075	355.3371	-8.9684	19.42	0.24980	0.79	r410
B05-076	355.4590	-9.2239	19.43	0.28245	0.53	b111
B05-077	355.1327	-9.1153	19.44	0.42454	0.73	r708
B05-078	355.4305	-9.2149	19.44	0.40781	0.47	b112
B05-079	355.4097	-9.1008	19.46	0.40723	0.64	r208
B05-081	355.3461	-9.0944	19.47	0.25103	0.80	b215
B05-082	355.3129	-9.0134	19.47	0.26012	0.75	b601
B05-083	355.3098	-9.0327	19.48	0.25682	0.83	b602
B05-084	355.3040	-8.9973	19.48	0.25216	0.61	b611
B05-085	355.2560	-9.1639	19.49	0.37127	0.68	b307
B05-086	355.3431	-8.9411	19.49	0.25085	0.78	b210
B05-087	355.4038	-9.0950	19.49	0.23515	0.77	r206
B05-088	355.2918	-9.0880	19.51	0.38724	0.70	r607
B05-089	355.3919	-9.0064	19.51	0.25144	0.55	r213
B05-090	355.2972	-9.0987	19.52	0.25038	0.74	b616
B05-092	355.2892	-9.0326	19.53	0.25672	0.74	r606
B05-093	355.3217	-8.9970	19.56	0.24686	0.78	b412
B05-094	355.3277	-9.0030	19.57	0.21407	0.55	b404
B05-095	355.2201	-9.0915	19.58	0.43352	0.70	b806
B05-096	355.3346	-9.0758	19.59	0.24786	0.76	r416
B05-097	355.3209	-9.0091	19.60	0.25457	0.82	b413
B05-098	355.1543	-8.9131	19.61	0.38439	0.36	b809
B05-099	355.1197	-8.9375	19.62	0.36750	0.28	r802
B05-100	355.2897	-9.0210	19.63	0.25332	0.80	r604
B05-101	355.2641	-9.1042	19.64	0.24761	0.35	r608
B05-103	355.3196	-8.9154	19.70	0.24988	0.57	b409
B05-104	355.4174	-9.0397	19.70	0.15324	0.40	r204
B05-105	355.2394	-9.2350	19.75	0.30806	0.49	r310
B05-106	355.3936	-9.1680	19.75	0.44200	0.61	b106
B05-107	355.3203	-9.1270	19.76	0.19244	0.60	r107
B05-108	355.3136	-9.0489	19.79	0.25252	0.59	b605
B05-109	355.3956	-9.0027	19.80	0.25434	0.69	r212
B05-111	355.2941	-9.1949	19.80	0.43985	0.52	b312

Continued on next page

Target ID	RA	DEC	r-band mag.	z	Corr.	FiberID
B05-112	355.4527	-9.2138	19.82	0.40767	0.30	b113
B05-113	355.4234	-9.2578	19.82	0.42072	0.32	b103
B05-114	355.3423	-9.0743	19.84	0.25144	0.62	r407
B05-115	355.3374	-9.0438	19.84	0.24936	0.72	r413
B05-116	355.3386	-9.0721	19.86	0.25377	0.53	r406
B05-117	355.4130	-9.0174	19.88	0.15470	0.45	r201
B05-118	355.3369	-9.0166	19.89	0.24969	0.79	r411
B05-119	355.2220	-9.0111	19.90	0.40538	0.51	b804
B05-121	355.0788	-9.0242	19.91	0.43053	0.59	r814
B05-122	355.1168	-9.2232	19.92	0.30815	0.31	b704
B05-123	355.3119	-9.2023	19.93	0.44081	0.60	b310
B05-125	355.3335	-9.0270	19.95	0.25509	0.77	r412
B05-126	355.3711	-9.1993	19.96	0.46211	0.74	r111
B05-127	355.3200	-9.1887	19.97	0.23672	0.56	r102
B05-128	355.4029	-9.1628	19.98	0.25254	0.30	b107
B05-132	355.2780	-9.1805	20.04	0.25503	0.56	b304
B05-133	355.1419	-9.0122	20.04	0.24750	0.61	r804
B05-134	355.1120	-9.0230	20.07	0.39111	0.63	r813
B05-135	355.4353	-9.2338	20.08	0.25418	0.22	b109
B05-136	355.3161	-9.0628	20.09	0.24644	0.67	b416
B05-137	355.4776	-9.1550	20.09	0.15628	0.21	b116
B05-138	355.1107	-9.0038	20.10	0.39039	0.65	r812
B05-139	355.3525	-9.1336	20.10	0.24943	0.35	r115
B05-140	355.4256	-9.2747	20.11	0.49923	0.13	b102
B05-141	355.2092	-9.1743	20.11	0.33207	0.36	r304
B05-142	355.4000	-9.1096	20.12	0.21337	0.35	r216
B05-143	355.1933	-9.1200	20.16	0.40838	0.47	r308
B05-144	355.4026	-9.0690	20.17	0.43174	0.42	r215
B05-145	355.1742	-9.2086	20.18	0.36827	0.46	r303
B05-146	355.1404	-9.2642	20.19	0.47940	0.61	r701
B05-147	355.2773	-8.9641	20.20	0.49170	0.30	r603
B05-149	355.1572	-9.2189	20.21	0.49610	0.31	r704
B05-150	355.1505	-9.0599	20.23	0.43053	0.43	r806
B05-151	355.2554	-9.0940	20.25	0.24296	0.50	r616
B05-152	355.4461	-9.0976	20.26	0.12709	0.33	r207
B05-153	355.2635	-9.0642	20.27	0.25078	0.65	r614
B05-154	355.3358	-9.1143	20.32	0.24888	0.48	r116
B05-155	355.3455	-9.0419	20.33	0.38765	0.68	b213
B05-156	355.0753	-9.1583	20.35	0.33034	0.59	b708
B05-157	355.4514	-9.2298	20.35	0.40743	0.39	b110
B05-158	355.0687	-8.9863	20.37	0.43286	0.74	r810
B05-159	355.1678	-9.1431	20.37	0.24282	0.62	r706
B05-160	355.3552	-8.9317	20.38	0.25179	0.68	b209
B05-161	355.3251	-8.9821	20.39	0.25845	0.32	b403
B05-162	355.3437	-9.0279	20.40	0.25327	0.52	r405
B05-164	355.3573	-8.9383	20.41	0.46318	0.26	b201
B05-165	355.3150	-8.9212	20.43	0.44418	0.75	b410
B05-166	355.3664	-9.2166	20.44	0.14965	0.22	r110
B05-167	355.0831	-9.1806	20.44	0.48591	0.31	b706
B05-168	355.1354	-9.2267	20.45	0.25292	0.43	r703
B05-169	355.1071	-9.1759	20.47	0.25023	0.63	b707
B05-170	355.1508	-8.9408	20.48	0.29485	0.37	r803
B05-171	355.3117	-9.2200	20.48	0.37282	0.19	b309

Continued on next page

Target ID	RA	DEC	r-band mag.	z	Corr.	FiberID
B05-172	355.3634	-8.9691	20.51	0.25052	0.53	b202
B05-173	355.3917	-9.2343	20.53	0.37541	0.41	b105
B05-174	355.4320	-9.2107	20.53	0.40910	0.41	b114
B05-175	355.2122	-8.9156	20.55	0.23963	0.27	b801
B05-176	355.3130	-9.1373	20.55	0.44130	0.66	r106
B05-179	355.3462	-9.0625	20.58	0.43042	0.49	b214
B05-180	355.3611	-8.9983	20.60	0.25956	0.66	b203
B05-181	355.3407	-8.9484	20.62	0.25337	0.39	r401
B05-182	355.3388	-9.1627	20.63	0.14322	0.33	r113
B05-183	355.2798	-9.2254	20.66	0.46242	0.15	b303
B05-184	355.1295	-9.0591	20.66	0.48565	0.18	r805
B05-185	355.1319	-9.0940	20.67	0.19051	0.42	r807
B05-186	355.1359	-8.9285	20.67	0.45597	0.61	r801
B05-188	355.3185	-8.9799	20.71	0.25441	0.63	b411
B05-191	355.2569	-8.9626	20.74	0.40695	0.44	r611
B05-193	355.3127	-9.1411	20.77	0.43781	0.24	r105
B05-194	355.3043	-8.9746	20.77	0.44483	0.72	b610
B05-195	355.1137	-9.2622	20.79	0.49600	0.20	b701
B05-196	355.3573	-9.1412	20.80	0.49785	0.23	r114
B05-198	355.2038	-9.1387	20.81	0.45895	0.23	r307
B05-199	355.2597	-8.9468	20.82	0.44719	0.68	r610
B05-202	355.3381	-9.0511	20.88	0.25349	0.50	r414
B05-203	355.0927	-9.2227	20.90	0.49038	0.19	b705
B05-204	355.2300	-9.1124	20.90	0.15086	0.15	b808
B05-205	355.3380	-9.1823	20.92	0.23726	0.57	r112
B05-206	355.3080	-9.1462	20.93	0.44069	0.70	b315
B05-207	355.2915	-8.9358	20.94	0.45403	0.16	r602
B05-209	355.3847	-9.1616	20.96	0.13060	0.15	b108
B05-210	355.2798	-9.1396	20.97	0.47861	0.17	b308
B05-211	355.3775	-9.0614	20.97	0.43233	0.66	b205
B06-000	35.5076	-3.5539	15.87	0.27698	0.18	r402
B06-001	35.5181	-3.6721	17.71	0.27874	0.52	b213
B06-002	35.5078	-3.6024	18.11	0.27924	0.71	r411
B06-003	35.3939	-3.5782	18.16	0.27432	0.55	b612
B06-004	35.5100	-3.9469	18.20	0.18206	0.45	b309
B06-005	35.3998	-3.5563	18.23	0.16503	0.58	b610
B06-006	35.2430	-3.6829	18.30	0.27504	0.67	b810
B06-007	35.6247	-3.8770	18.33	0.29169	0.43	b109
B06-008	35.6549	-3.7511	18.40	0.26137	0.69	r208
B06-009	35.3856	-3.6633	18.41	0.24067	0.72	r605
B06-010	35.6319	-3.6826	18.42	0.22002	0.69	r213
B06-011	35.4406	-3.7719	18.46	0.43254	0.57	r305
B06-012	35.4926	-3.8604	18.63	0.43303	0.25	b313
B06-013	35.4382	-3.7673	18.63	0.43119	0.61	r306
B06-014	35.4922	-3.9405	18.67	0.14865	0.54	b310
B06-015	35.4415	-3.7039	18.67	0.16532	0.61	b411
B06-016	35.4676	-3.6892	18.68	0.14229	0.50	b405
B06-017	35.6534	-3.8240	18.68	0.16487	0.30	b112
B06-018	35.1955	-3.7568	18.69	0.32755	0.58	b708
B06-019	35.3233	-3.8882	18.73	0.31648	0.39	b504
B06-020	35.5064	-3.8514	18.74	0.14777	0.45	b314
B06-021	35.3133	-3.8337	18.78	0.42891	0.80	r715
B06-022	35.2807	-3.6021	18.82	0.36829	0.79	b802

Continued on next page

Target ID	RA	DEC	r-band mag.	z	Corr.	FiberID
B06-023	35.2024	-3.6746	18.86	0.31355	0.67	r811
B06-024	35.3992	-3.5712	18.86	0.24056	0.53	b611
B06-025	35.4707	-3.7425	18.89	0.18306	0.56	b408
B06-026	35.2171	-3.6848	18.92	0.32592	0.72	r812
B06-027	35.2214	-3.6945	18.92	0.32511	0.74	r806
B06-028	35.3979	-3.6579	18.95	0.23993	0.58	b613
B06-029	35.3552	-3.7790	18.95	0.18287	0.63	b515
B06-030	35.5185	-3.6024	18.97	0.43186	0.63	b211
B06-031	35.2523	-3.6838	18.98	0.32231	0.63	b811
B06-032	35.2655	-3.7602	18.98	0.18187	0.52	b715
B06-033	35.3263	-3.8971	18.99	0.31536	0.43	b503
B06-034	35.3378	-3.6760	19.02	0.28969	0.37	r612
B06-035	35.2442	-3.8671	19.08	0.29151	0.44	b710
B06-036	35.2463	-3.6845	19.11	0.27753	0.52	b812
B06-037	35.4718	-3.6105	19.12	0.16863	0.42	b403
B06-038	35.2791	-3.7796	19.17	0.32611	0.79	r706
B06-040	35.5583	-3.6147	19.19	0.25423	0.52	b202
B06-041	35.2681	-3.7075	19.21	0.16435	0.49	b806
B06-042	35.3918	-3.5584	19.23	0.16489	0.70	r601
B06-043	35.4717	-3.6628	19.23	0.17236	0.42	b404
B06-044	35.2723	-3.5821	19.27	0.21091	0.27	b801
B06-045	35.5046	-3.7736	19.29	0.48805	0.32	b316
B06-046	35.2340	-3.7814	19.30	0.26420	0.67	b707
B06-047	35.5108	-3.6302	19.31	0.26256	0.40	r406
B06-048	35.3331	-3.7435	19.32	0.43766	0.61	r616
B06-049	35.3162	-3.9463	19.39	0.37264	0.60	r709
B06-050	35.4469	-3.7822	19.40	0.20026	0.33	r312
B06-051	35.6496	-3.8249	19.41	0.21893	0.35	b111
B06-052	35.3531	-3.8041	19.44	0.22202	0.46	b513
B06-053	35.3840	-3.9474	19.44	0.39757	0.79	r501
B06-054	35.2905	-3.6038	19.45	0.16702	0.32	b803
B06-056	35.2643	-3.8827	19.50	0.29042	0.56	b709
B06-057	35.3931	-3.7434	19.50	0.22811	0.56	b616
B06-058	35.3840	-3.9063	19.50	0.15938	0.33	r502
B06-059	35.5468	-3.9051	19.53	0.23798	0.56	r111
B06-060	35.3211	-3.8415	19.53	0.18228	0.37	r714
B06-061	35.3138	-3.9276	19.53	0.22090	0.27	r710
B06-062	35.2537	-3.7405	19.53	0.18057	0.48	b815
B06-063	35.6046	-3.7405	19.54	0.26195	0.34	r216
B06-064	35.6259	-3.6379	19.55	0.40901	0.47	r211
B06-065	35.5519	-3.7634	19.56	0.16942	0.48	r115
B06-066	35.4708	-3.8097	19.58	0.42737	0.51	b306
B06-067	35.5279	-3.9319	19.62	0.40343	0.20	r102
B06-069	35.5914	-3.8168	19.67	0.21811	0.42	b105
B06-070	35.4396	-3.6722	19.67	0.43441	0.54	b602
B06-071	35.4570	-3.9214	19.67	0.49995	0.43	r310
B06-073	35.5606	-3.6860	19.69	0.27947	0.32	b205
B06-074	35.6241	-3.7928	19.72	0.23731	0.33	b107
B06-075	35.5085	-3.7204	19.73	0.34945	0.59	r408
B06-076	35.5710	-3.9359	19.74	0.45749	0.28	r110
B06-077	35.4087	-3.8251	19.75	0.42679	0.49	r515
B06-079	35.3549	-3.7680	19.75	0.43642	0.45	b516
B06-080	35.3729	-3.6041	19.77	0.40428	0.34	r603

Continued on next page

Target ID	RA	DEC	r-band mag.	z	Corr.	FiberID
B06-081	35.2465	-3.7035	19.77	0.32582	0.28	b813
B06-083	35.5695	-3.7547	19.79	0.40701	0.46	r116
B06-085	35.3013	-3.7629	19.82	0.43472	0.62	r716
B06-086	35.4147	-3.6817	19.84	0.43201	0.67	b614
B06-087	35.3699	-3.8437	19.85	0.42980	0.57	r504
B06-088	35.6013	-3.6991	19.85	0.16971	0.26	b207
B06-089	35.3652	-3.8334	19.86	0.43085	0.43	r506
B06-090	35.4641	-3.7534	19.88	0.42977	0.42	b416
B06-091	35.4754	-3.6046	19.89	0.27924	0.50	b402
B06-092	35.4515	-3.7365	19.92	0.27509	0.51	b413
B06-093	35.5389	-3.6455	19.92	0.43118	0.45	b212
B06-094	35.5847	-3.8613	19.92	0.49638	0.23	r112
B06-095	35.3073	-3.9101	19.92	0.21943	0.55	r711
B06-096	35.2701	-3.7548	19.92	0.25341	0.45	b716
B06-097	35.6565	-3.7680	19.93	0.26109	0.41	b115
B06-098	35.4777	-3.7234	19.93	0.37178	0.53	r414
B06-099	35.2972	-3.7869	19.93	0.43095	0.47	r705
B06-100	35.2348	-3.6520	19.93	0.26514	0.68	r802
B06-101	35.2968	-3.8411	19.95	0.32662	0.48	r703
B06-102	35.4865	-3.5683	19.97	0.43387	0.55	r409
B06-103	35.6232	-3.6196	19.99	0.49641	0.40	r210
B06-104	35.5398	-3.8381	19.99	0.23932	0.33	r106
B06-105	35.3227	-3.8459	20.00	0.38401	0.62	b505
B06-106	35.4783	-3.9426	20.01	0.43140	0.43	b302
B06-107	35.5119	-3.5319	20.02	0.23927	0.22	r401
B06-108	35.4241	-3.7629	20.03	0.43066	0.64	r308
B06-109	35.3404	-3.7737	20.05	0.43288	0.56	b507
B06-110	35.4249	-3.8042	20.06	0.42585	0.45	r302
B06-111	35.3301	-3.6558	20.06	0.28980	0.31	r611
B06-112	35.3133	-3.8866	20.06	0.43694	0.49	r713
B06-113	35.5591	-3.7222	20.07	0.29809	0.33	b215
B06-114	35.5412	-3.7656	20.08	0.34935	0.36	r108
B06-115	35.5919	-3.8224	20.12	0.40308	0.22	b103
B06-116	35.4832	-3.7538	20.13	0.43623	0.54	r416
B06-117	35.4608	-3.8627	20.13	0.13878	0.30	b303
B06-118	35.4728	-3.8249	20.13	0.24144	0.52	b305
B06-119	35.4663	-3.9560	20.14	0.43086	0.35	b301
B06-120	35.4052	-3.9328	20.14	0.27966	0.20	r509
B06-121	35.4508	-3.5763	20.17	0.18258	0.26	b409
B06-122	35.5256	-3.7673	20.17	0.42856	0.51	r107
B06-124	35.3774	-3.7037	20.19	0.43656	0.45	r607
B06-125	35.4495	-3.9052	20.20	0.28951	0.28	r311
B06-126	35.2749	-3.7591	20.22	0.32709	0.50	r708
B06-128	35.5132	-3.5904	20.23	0.28045	0.46	r405
B06-129	35.2850	-3.8756	20.24	0.29177	0.49	r701
B06-130	35.4014	-3.5238	20.24	0.17273	0.28	b609
B06-131	35.4361	-3.7470	20.25	0.43454	0.68	b604
B06-132	35.4475	-3.7768	20.26	0.42947	0.60	r313
B06-133	35.3951	-3.7091	20.27	0.43301	0.43	b615
B06-134	35.4963	-3.6342	20.27	0.27920	0.37	r412
B06-135	35.4541	-3.6114	20.28	0.42255	0.56	b410
B06-136	35.3523	-3.5612	20.28	0.28112	0.20	r602
B06-137	35.2242	-3.7020	20.28	0.32498	0.52	r807

Continued on next page

Target ID	RA	DEC	r-band mag.	z	Corr.	FiberID
B06-139	35.2418	-3.6865	20.30	0.32583	0.25	r804
B06-140	35.5407	-3.8667	20.30	0.34206	0.38	r105
B06-141	35.2688	-3.8191	20.30	0.24552	0.28	b712
B06-142	35.6606	-3.7109	20.31	0.24602	0.43	r203
B06-143	35.2090	-3.6718	20.31	0.32771	0.69	r810
B06-144	35.6427	-3.6465	20.32	0.11400	0.22	r201
B06-145	35.5102	-3.5673	20.33	0.43364	0.51	r404
B06-146	35.5244	-3.5519	20.34	0.21542	0.27	b209
B06-147	35.3968	-3.8572	20.34	0.26732	0.19	r512
B06-148	35.5112	-3.8300	20.35	0.49995	0.30	b315
B06-149	35.2109	-3.8251	20.35	0.43256	0.32	b702
B06-150	35.4159	-3.7494	20.36	0.43188	0.43	b605
B06-151	35.6257	-3.6802	20.36	0.26170	0.27	r212
B06-152	35.2877	-3.7881	20.37	0.37772	0.20	r704
B06-154	35.6150	-3.7758	20.39	0.21113	0.18	b108
B06-155	35.6249	-3.7549	20.41	0.30570	0.27	b116
B06-156	35.2716	-3.7617	20.41	0.32648	0.39	r707
B06-157	35.4041	-3.8265	20.42	0.39730	0.47	r514
B06-158	35.2104	-3.6889	20.42	0.32416	0.57	r813
B06-159	35.2540	-3.7169	20.42	0.41920	0.48	b814
B06-160	35.3612	-3.8016	20.42	0.22235	0.42	b514
B06-161	35.2163	-3.8125	20.43	0.20295	0.47	b703
B06-162	35.4392	-3.7825	20.43	0.42300	0.55	r304
B06-163	35.3724	-3.8413	20.43	0.43043	0.36	r505
B06-164	35.3882	-3.6749	20.44	0.43015	0.69	r606
B06-165	35.2824	-3.6235	20.44	0.30889	0.25	b804
B06-167	35.2104	-3.7537	20.46	0.30610	0.22	r816
B06-168	35.5440	-3.9461	20.47	0.40232	0.29	r101
B06-169	35.2194	-3.7224	20.47	0.18290	0.26	r815
B06-170	35.3456	-3.5854	20.48	0.43161	0.66	r609
B06-171	35.5103	-3.5630	20.49	0.37020	0.40	r403
B06-172	35.5146	-3.6456	20.50	0.20380	0.28	r407
B06-173	35.4473	-3.7427	20.50	0.43173	0.44	b414
B06-174	35.3701	-3.7834	20.52	0.28952	0.16	r508
B06-175	35.4188	-3.5808	20.54	0.16717	0.24	b601
B06-176	35.4437	-3.7280	20.55	0.43605	0.63	b412
B06-177	35.2573	-3.8137	20.55	0.43117	0.51	b713
B06-178	35.4298	-3.7633	20.55	0.43404	0.40	r307
B06-179	35.3829	-3.7413	20.55	0.20328	0.16	r608
B06-180	35.5347	-3.9302	20.56	0.29784	0.15	r103
B06-181	35.4492	-3.7544	20.57	0.43819	0.43	r316
B06-182	35.3346	-3.9148	20.58	0.43205	0.28	b502
B06-183	35.3996	-3.7565	20.60	0.43063	0.46	r516
B06-184	35.3274	-3.5982	20.61	0.36917	0.27	r610
B06-185	35.4860	-3.6779	20.61	0.20140	0.23	r413
B06-186	35.4538	-3.9317	20.61	0.43510	0.30	r309
B06-187	35.4876	-3.9230	20.61	0.26674	0.22	b311
B06-188	35.6551	-3.7371	20.62	0.26209	0.45	r206
B06-189	35.6335	-3.8756	20.62	0.26777	0.23	b110
B06-190	35.4211	-3.8087	20.62	0.38411	0.57	r301
B06-191	35.3654	-3.7875	20.63	0.43502	0.40	r507
B06-193	35.2131	-3.7820	20.63	0.27161	0.40	b706
B06-194	35.4415	-3.7655	20.63	0.42503	0.50	r315

Continued on next page

Target ID	RA	DEC	r-band mag.	z	Corr.	FiberID
B06-195	35.5184	-3.9099	20.64	0.43210	0.31	b312
B06-196	35.2330	-3.6202	20.64	0.19841	0.15	r801
B06-197	35.5588	-3.7732	20.64	0.34862	0.25	r114
B06-198	35.2209	-3.6518	20.64	0.19921	0.26	r809
B06-199	35.6011	-3.5839	20.65	0.43059	0.32	r209
B06-200	35.3220	-3.7100	20.65	0.42389	0.51	r613
B06-201	35.3217	-3.8952	20.66	0.43730	0.35	r712
B06-202	35.4790	-3.7440	20.66	0.42938	0.47	r415
B06-204	35.3509	-3.9024	20.67	0.42976	0.47	b511
B06-205	35.3244	-3.7916	20.67	0.45843	0.54	b506
B06-206	35.1941	-3.7967	20.68	0.29079	0.36	b704
B06-207	35.4635	-3.8605	20.68	0.24165	0.25	b304
B06-208	35.3671	-3.6095	20.71	0.20131	0.23	r604
B06-209	35.6054	-3.7969	20.71	0.49576	0.31	b106
B06-211	35.5248	-3.8948	20.72	0.39782	0.23	r104
B06-212	35.5647	-3.5669	20.72	0.29520	0.31	b201
B06-213	35.2898	-3.7288	20.72	0.43457	0.56	r615
B06-214	35.2931	-3.8608	20.73	0.32557	0.28	r702
B06-215	35.3655	-3.9693	20.74	0.21039	0.24	b509
B06-216	35.4871	-3.5830	20.75	0.17121	0.28	r410
B06-217	35.4324	-3.6879	20.75	0.43520	0.45	b603
B06-218	35.2610	-3.7869	20.76	0.33486	0.22	b714
B06-219	35.5424	-3.6900	20.77	0.21546	0.22	b214
B06-221	35.3340	-3.7604	20.77	0.43228	0.39	b508
B06-223	35.5641	-3.6911	20.79	0.13887	0.32	b206
B06-225	35.6220	-3.6973	20.79	0.32247	0.19	r214
B06-226	35.2147	-3.8573	20.80	0.29157	0.34	b701
B06-227	35.3558	-3.8849	20.81	0.43304	0.35	b512
B06-228	35.5419	-3.7517	20.81	0.12953	0.24	b216
B06-229	35.6138	-3.7228	20.81	0.49590	0.20	r215
B06-230	35.2099	-3.7937	20.82	0.21171	0.20	b705
B06-231	35.3351	-3.9552	20.83	0.37738	0.24	b501
B06-232	35.3512	-3.9293	20.83	0.14081	0.54	b510
B06-233	35.6318	-3.8116	20.85	0.29754	0.23	b114
B06-235	35.2590	-3.8483	20.86	0.32668	0.40	b711
B06-238	35.4738	-3.7209	20.87	0.29465	0.42	b407
B06-239	35.5675	-3.6460	20.89	0.36574	0.26	b204
B06-240	35.6422	-3.7257	20.89	0.43231	0.24	r205
B06-241	35.4458	-3.7723	20.89	0.43150	0.41	r314
B06-242	35.4196	-3.8871	20.90	0.27248	0.22	r511
B06-243	35.2566	-3.6874	20.91	0.30428	0.24	b805
B06-244	35.4774	-3.7084	20.91	0.21247	0.25	b406
B06-245	35.2415	-3.6571	20.91	0.36634	0.23	r803
B06-246	35.5585	-3.9368	20.91	0.17473	0.21	r109
B06-247	35.5997	-3.8806	20.92	0.29065	0.20	b102
B06-248	35.3781	-3.8503	20.92	0.42683	0.20	r503
B06-249	35.6273	-3.8148	20.92	0.26601	0.20	b113
B06-250	35.5858	-3.6187	20.93	0.30001	0.21	b203
B06-251	35.4275	-3.7856	20.95	0.28132	0.21	r303
B06-252	35.3201	-3.7224	20.95	0.42286	0.53	r614
B06-253	35.4622	-3.7711	20.95	0.42337	0.32	b307
B06-254	35.2418	-3.7039	20.97	0.43364	0.49	r808
B06-255	35.2071	-3.7165	20.98	0.40427	0.59	r814

Continued on next page

Target ID	RA	DEC	r-band mag.	z	Corr.	FiberID
B06-256	35.4670	-3.7601	20.99	0.43451	0.31	b308
B07-000	30.3345	-2.3753	16.33	0.49056	0.47	r712
B07-001	30.4489	-2.4084	16.48	0.13642	0.84	r310
B07-002	30.3288	-2.4067	16.61	0.41024	0.40	r711
B07-003	30.3333	-2.4133	16.78	0.48780	0.48	r710
B07-004	30.4263	-2.4095	16.82	0.49995	0.38	r302
B07-005	30.2419	-2.1955	16.90	0.43046	0.63	r806
B07-006	30.5557	-2.3130	16.94	0.17684	0.74	r115
B07-007	30.4296	-2.1967	17.02	0.19639	0.74	r414
B07-008	30.2080	-2.1930	17.10	0.48748	0.43	r811
B07-009	30.4452	-2.1983	17.16	0.19331	0.84	r406
B07-010	30.3866	-2.3474	17.27	0.13690	0.82	r503
B07-011	30.4600	-2.3004	17.30	0.12888	0.64	b307
B07-012	30.4117	-2.4446	17.32	0.13609	0.88	r509
B07-013	30.3236	-2.0620	17.33	0.16403	0.86	b802
B07-014	30.3890	-2.3385	17.45	0.13735	0.86	r504
B07-015	30.3603	-2.1944	17.46	0.19195	0.85	r607
B07-016	30.3915	-2.0643	17.57	0.49538	0.36	b601
B07-017	30.5109	-2.0817	17.57	0.48943	0.25	b202
B07-018	30.3842	-2.1733	17.66	0.19583	0.86	b605
B07-019	30.3756	-2.2283	17.71	0.13734	0.86	b616
B07-020	30.2466	-2.2437	17.72	0.20755	0.87	b715
B07-021	30.4623	-2.3197	17.72	0.19500	0.83	b306
B07-022	30.5246	-2.1672	17.78	0.12881	0.70	r212
B07-023	30.6138	-2.3071	17.78	0.17858	0.83	b112
B07-024	30.5005	-2.3764	17.84	0.19598	0.85	b311
B07-025	30.5464	-2.3089	17.86	0.17657	0.80	r116
B07-026	30.5039	-2.2826	17.87	0.19299	0.83	b314
B07-027	30.3578	-2.3210	17.92	0.23675	0.86	b514
B07-028	30.3319	-2.0493	17.92	0.19702	0.77	r609
B07-029	30.3193	-2.3184	17.93	0.13761	0.81	r715
B07-030	30.4430	-2.1767	18.00	0.19703	0.84	r409
B07-031	30.2399	-2.2141	18.01	0.13733	0.61	r808
B07-032	30.2348	-2.1995	18.01	0.13749	0.73	r812
B07-033	30.4258	-2.2089	18.01	0.42079	0.61	b407
B07-034	30.4151	-2.3821	18.02	0.19625	0.88	r511
B07-035	30.3646	-2.1506	18.03	0.19608	0.62	r603
B07-036	30.3982	-2.1753	18.04	0.19837	0.83	b411
B07-037	30.4574	-2.4153	18.05	0.13617	0.80	r309
B07-038	30.4485	-2.3917	18.07	0.19497	0.85	r311
B07-039	30.2545	-2.2569	18.10	0.25930	0.89	b714
B07-040	30.4159	-2.2423	18.11	0.19095	0.79	r308
B07-041	30.4171	-2.1858	18.17	0.20128	0.83	b404
B07-042	30.4330	-2.2811	18.17	0.19585	0.87	r313
B07-043	30.5367	-2.3043	18.21	0.19653	0.85	r108
B07-044	30.2228	-2.2736	18.23	0.19310	0.86	b706
B07-045	30.6362	-2.3047	18.24	0.21422	0.85	b113
B07-046	30.3163	-2.1651	18.26	0.19718	0.85	b807
B07-047	30.3707	-2.1195	18.29	0.19602	0.88	b610
B07-048	30.2579	-2.2372	18.30	0.25821	0.86	b716
B07-049	30.4123	-2.1808	18.31	0.18591	0.84	b413
B07-050	30.2369	-2.1848	18.38	0.25846	0.77	r804
B07-051	30.3131	-2.1175	18.39	0.19613	0.73	b804

Continued on next page

Target ID	RA	DEC	r-band mag.	z	Corr.	FiberID
B07-052	30.2968	-2.0804	18.41	0.20828	0.84	b811
B07-053	30.3684	-2.1484	18.43	0.19311	0.69	b611
B07-054	30.6091	-2.3073	18.45	0.21484	0.86	b111
B07-055	30.3060	-2.1454	18.46	0.19803	0.90	b806
B07-056	30.4745	-2.2204	18.47	0.19565	0.80	b216
B07-057	30.4150	-2.3968	18.48	0.13498	0.74	r510
B07-058	30.3630	-2.2487	18.48	0.19520	0.90	b516
B07-059	30.4774	-2.2090	18.49	0.19578	0.89	b213
B07-060	30.4347	-2.1842	18.50	0.18974	0.81	r411
B07-061	30.3684	-2.0715	18.53	0.19615	0.59	b609
B07-062	30.2145	-2.2463	18.55	0.19252	0.90	b708
B07-063	30.6260	-2.2611	18.56	0.26631	0.91	b115
B07-064	30.3608	-2.1772	18.60	0.20331	0.60	r605
B07-066	30.2595	-2.1580	18.62	0.17652	0.83	r803
B07-067	30.2078	-2.2175	18.62	0.19766	0.65	r813
B07-068	30.3758	-2.1776	18.63	0.19597	0.84	b606
B07-069	30.3399	-2.3269	18.63	0.24138	0.78	b503
B07-070	30.3705	-2.2920	18.64	0.19948	0.87	b515
B07-071	30.3764	-2.4203	18.64	0.13610	0.67	r501
B07-072	30.5415	-2.0687	18.65	0.24871	0.81	r201
B07-073	30.5350	-2.3334	18.65	0.17734	0.87	r104
B07-074	30.4371	-2.2489	18.66	0.19780	0.70	r316
B07-075	30.3112	-2.2612	18.66	0.19492	0.79	r706
B07-076	30.4795	-2.3608	18.68	0.19550	0.78	b302
B07-077	30.3532	-2.0526	18.68	0.19410	0.75	r610
B07-078	30.3431	-2.3288	18.70	0.23895	0.81	b502
B07-079	30.4213	-2.4219	18.72	0.13743	0.81	r301
B07-080	30.3428	-2.3243	18.72	0.23996	0.76	b505
B07-081	30.3654	-2.1707	18.73	0.20307	0.82	b613
B07-082	30.2543	-2.2131	18.74	0.25999	0.85	r807
B07-083	30.5132	-2.2349	18.75	0.25211	0.81	r216
B07-084	30.3223	-2.4348	18.77	0.13779	0.56	r709
B07-085	30.4180	-2.1980	18.80	0.19905	0.82	b405
B07-086	30.4886	-2.1740	18.80	0.19759	0.86	b205
B07-087	30.3422	-2.0729	18.80	0.16643	0.79	r613
B07-089	30.3646	-2.3917	18.83	0.26236	0.71	b509
B07-090	30.4987	-2.2156	18.83	0.20068	0.74	b207
B07-091	30.4353	-2.2033	18.86	0.19197	0.51	r416
B07-092	30.3494	-2.1329	18.88	0.19555	0.70	r614
B07-093	30.6333	-2.2304	18.89	0.39236	0.33	r208
B07-095	30.4061	-2.1786	18.95	0.19482	0.85	b412
B07-096	30.3399	-2.0531	18.95	0.16316	0.69	r611
B07-097	30.5093	-2.4308	18.97	0.27515	0.71	b309
B07-098	30.3618	-2.3233	18.98	0.23970	0.78	b513
B07-099	30.4886	-2.4076	18.98	0.13786	0.70	b310
B07-100	30.4688	-2.2114	18.98	0.19682	0.84	b214
B07-101	30.3046	-2.0739	18.98	0.20815	0.82	b810
B07-102	30.3956	-2.1816	18.98	0.19442	0.80	b414
B07-103	30.5794	-2.4003	18.98	0.17858	0.74	b103
B07-104	30.3891	-2.3194	19.00	0.24070	0.55	r508
B07-106	30.4808	-2.3541	19.00	0.30884	0.83	b304
B07-107	30.3565	-2.1680	19.01	0.19392	0.80	r604
B07-108	30.3133	-2.3960	19.04	0.13950	0.78	r701

Continued on next page

Target ID	RA	DEC	r-band mag.	z	Corr.	FiberID
B07-109	30.5951	-2.3161	19.05	0.17808	0.83	b106
B07-110	30.4955	-2.2230	19.09	0.12888	0.61	b208
B07-111	30.4350	-2.1970	19.09	0.19483	0.84	r415
B07-112	30.3937	-2.1289	19.09	0.19103	0.76	b410
B07-113	30.2720	-2.2516	19.10	0.19362	0.86	r707
B07-114	30.2886	-2.3771	19.11	0.16540	0.51	r703
B07-115	30.4241	-2.1665	19.12	0.18821	0.80	b401
B07-116	30.4905	-2.2807	19.12	0.23974	0.55	b315
B07-117	30.3911	-2.2575	19.14	0.19443	0.65	r515
B07-118	30.4875	-2.3610	19.15	0.19476	0.69	b301
B07-119	30.3131	-2.2084	19.16	0.13728	0.72	b808
B07-120	30.4242	-2.1784	19.16	0.19458	0.82	b402
B07-121	30.6025	-2.3932	19.16	0.17566	0.68	b109
B07-122	30.4036	-2.3041	19.17	0.19828	0.74	r512
B07-123	30.3742	-2.1737	19.18	0.19610	0.81	b614
B07-124	30.2107	-2.2283	19.18	0.19652	0.70	r814
B07-125	30.3813	-2.0947	19.18	0.23153	0.42	b602
B07-126	30.2534	-2.1886	19.20	0.24091	0.72	r805
B07-128	30.2538	-2.2711	19.21	0.21497	0.82	b713
B07-130	30.5497	-2.4336	19.22	0.25217	0.78	r110
B07-131	30.3583	-2.2052	19.23	0.19222	0.73	r608
B07-132	30.1941	-2.3498	19.23	0.25929	0.75	b702
B07-133	30.5176	-2.1245	19.23	0.19698	0.79	r210
B07-134	30.4476	-2.1797	19.24	0.20069	0.76	r403
B07-135	30.5350	-2.2255	19.27	0.19423	0.86	r214
B07-136	30.4741	-2.3356	19.27	0.17838	0.56	b305
B07-137	30.4553	-2.2078	19.28	0.30694	0.79	r408
B07-138	30.2331	-2.4128	19.28	0.26394	0.78	b701
B07-139	30.4733	-2.1281	19.29	0.36568	0.87	b210
B07-140	30.4213	-2.2862	19.30	0.19707	0.82	r305
B07-141	30.4174	-2.2060	19.30	0.19050	0.71	b406
B07-142	30.3759	-2.3274	19.30	0.21504	0.87	r507
B07-143	30.4039	-2.2729	19.31	0.19467	0.63	r514
B07-144	30.3112	-2.3577	19.34	0.26417	0.81	r704
B07-146	30.5473	-2.4439	19.34	0.17641	0.50	r109
B07-147	30.4945	-2.2367	19.34	0.19745	0.82	b316
B07-148	30.1953	-2.3045	19.35	0.24197	0.77	b704
B07-149	30.3376	-2.3221	19.36	0.24253	0.76	b506
B07-150	30.6608	-2.2643	19.36	0.19630	0.75	b114
B07-151	30.5583	-2.3349	19.37	0.24306	0.70	r114
B07-152	30.3575	-2.1217	19.37	0.27971	0.80	r602
B07-153	30.3721	-2.1532	19.37	0.19976	0.80	b612
B07-155	30.5970	-2.2235	19.39	0.19535	0.47	r207
B07-156	30.2041	-2.2708	19.39	0.26003	0.63	b707
B07-157	30.4147	-2.2090	19.39	0.19265	0.80	b408
B07-160	30.3097	-2.0597	19.40	0.19492	0.62	b801
B07-161	30.2211	-2.2373	19.40	0.19300	0.73	r816
B07-162	30.3142	-2.3629	19.41	0.13612	0.65	r713
B07-163	30.4343	-2.1889	19.42	0.19399	0.77	r412
B07-164	30.5625	-2.3710	19.44	0.24951	0.82	r112
B07-165	30.4014	-2.2047	19.44	0.20186	0.83	b416
B07-166	30.6011	-2.3650	19.45	0.17108	0.53	b105
B07-167	30.2665	-2.3853	19.45	0.23148	0.59	b710

Continued on next page

Target ID	RA	DEC	r-band mag.	z	Corr.	FiberID
B07-168	30.4031	-2.1920	19.45	0.19344	0.82	b415
B07-169	30.3626	-2.0782	19.47	0.37878	0.60	r601
B07-170	30.4575	-2.1528	19.48	0.19558	0.77	r401
B07-171	30.5520	-2.2162	19.49	0.28039	0.67	r206
B07-172	30.5943	-2.2484	19.51	0.19686	0.78	b107
B07-173	30.6069	-2.2139	19.54	0.17550	0.67	r205
B07-174	30.3770	-2.1708	19.55	0.19142	0.57	b604
B07-176	30.3748	-2.3507	19.56	0.18161	0.26	b511
B07-177	30.4192	-2.1828	19.56	0.19859	0.84	b403
B07-178	30.5446	-2.1820	19.57	0.43188	0.84	r203
B07-179	30.4516	-2.2692	19.59	0.16611	0.76	r315
B07-180	30.5095	-2.1294	19.60	0.16396	0.78	b203
B07-181	30.4220	-2.2453	19.61	0.19671	0.80	r307
B07-182	30.2438	-2.2870	19.63	0.44538	0.81	b705
B07-183	30.2875	-2.0950	19.63	0.21343	0.77	b812
B07-184	30.2869	-2.3948	19.64	0.26343	0.48	r702
B07-185	30.3360	-2.3829	19.64	0.23111	0.70	b501
B07-187	30.3852	-2.2326	19.67	0.35059	0.37	b608
B07-188	30.5468	-2.3652	19.68	0.19751	0.65	r113
B07-189	30.4795	-2.1991	19.69	0.19575	0.83	b212
B07-191	30.3423	-2.1815	19.70	0.19053	0.79	r615
B07-192	30.4594	-2.2859	19.71	0.19772	0.70	r312
B07-193	30.3907	-2.2951	19.73	0.30785	0.35	r513
B07-195	30.4251	-2.3584	19.77	0.13556	0.52	r303
B07-196	30.4355	-2.1784	19.78	0.19933	0.79	r410
B07-197	30.5530	-2.1984	19.78	0.19480	0.61	r204
B07-198	30.3575	-2.2749	19.79	0.32871	0.57	b507
B07-199	30.4841	-2.1300	19.80	0.19445	0.78	b211
B07-200	30.2542	-2.4237	19.81	0.48114	0.65	b709
B07-201	30.3839	-2.3788	19.81	0.48081	0.57	r502
B07-203	30.4835	-2.1190	19.82	0.16633	0.52	b209
B07-204	30.3708	-2.1784	19.83	0.18877	0.75	b615
B07-205	30.5204	-2.3284	19.84	0.25147	0.34	r105
B07-206	30.3009	-2.1527	19.84	0.19467	0.66	b815
B07-207	30.4684	-2.1749	19.85	0.19469	0.76	r402
B07-209	30.4560	-2.2766	19.86	0.43563	0.35	r314
B07-210	30.5199	-2.1985	19.86	0.25093	0.78	r213
B07-211	30.5117	-2.3240	19.86	0.24272	0.64	r106
B07-212	30.4890	-2.3074	19.86	0.19276	0.74	b313
B07-213	30.5044	-2.3332	19.86	0.15456	0.45	b312
B07-214	30.4384	-2.1889	19.86	0.19967	0.62	r413
B07-215	30.5963	-2.2429	19.87	0.19703	0.52	b108
B07-216	30.1929	-2.3436	19.88	0.25779	0.80	b703
B07-217	30.4710	-2.2142	19.89	0.19607	0.47	b215
B07-218	30.4124	-2.0538	19.90	0.20745	0.36	b409
B07-219	30.2945	-2.2018	19.90	0.19499	0.61	b816
B07-220	30.3667	-2.3239	19.90	0.24001	0.56	b512
B07-221	30.3576	-2.1850	19.90	0.19544	0.71	r606
B07-223	30.5330	-2.0717	19.91	0.25142	0.46	r209
B07-224	30.4249	-2.2581	19.92	0.19342	0.63	r306
B07-225	30.3448	-2.2249	19.92	0.21478	0.67	r616
B07-226	30.1962	-2.2345	19.92	0.17642	0.67	r815
B07-227	30.4580	-2.2020	19.92	0.18915	0.65	r407

Continued on next page

Target ID	RA	DEC	r-band mag.	z	Corr.	FiberID
B07-228	30.5398	-2.4272	19.95	0.37864	0.79	r101
B07-230	30.4847	-2.1732	19.96	0.19718	0.56	b204
B07-231	30.2461	-2.1010	19.97	0.19658	0.42	r801
B07-232	30.3814	-2.1612	19.97	0.19685	0.66	b603
B07-233	30.3349	-2.2543	19.98	0.21409	0.64	b508
B07-234	30.4108	-2.2458	19.98	0.19000	0.51	r516
B07-235	30.5990	-2.1291	19.99	0.37190	0.51	r202
B07-236	30.3723	-2.3578	20.00	0.16675	0.71	b510
B07-237	30.6579	-2.2571	20.00	0.21449	0.65	b116
B07-238	30.6071	-2.3161	20.01	0.17834	0.54	b110
B07-239	30.3813	-2.3284	20.01	0.13831	0.44	r506
B07-240	30.4436	-2.1905	20.01	0.20017	0.54	r405
B07-242	30.2466	-2.3698	20.03	0.30900	0.80	b711
B07-243	30.3289	-2.0680	20.04	0.16424	0.45	r612
B07-244	30.4617	-2.2758	20.04	0.29929	0.72	b308
B07-245	30.5430	-2.3974	20.05	0.30767	0.81	r103
B07-247	30.2994	-2.3409	20.06	0.19324	0.63	r705
B07-249	30.5224	-2.1559	20.07	0.19839	0.69	r211
B07-250	30.3854	-2.3288	20.08	0.13656	0.59	r505
B07-251	30.5288	-2.2300	20.10	0.49591	0.25	r215
B07-252	30.4742	-2.3568	20.10	0.12871	0.46	b303
B07-253	30.5339	-2.4256	20.10	0.22321	0.30	r102
B07-254	30.4856	-2.0579	20.13	0.30662	0.68	b201
B07-255	30.2711	-2.3437	20.13	0.32938	0.85	b712
B07-256	30.2315	-2.1825	20.14	0.49612	0.43	r810
B07-257	30.5600	-2.4229	20.14	0.24115	0.28	r111
B07-258	30.3113	-2.2513	20.14	0.33593	0.52	r708
B07-260	30.4156	-2.3301	20.16	0.26328	0.45	r304
B07-262	30.5792	-2.4093	20.16	0.28157	0.70	b102
B07-264	30.2228	-2.1292	20.16	0.19636	0.53	r809
B07-266	30.3823	-2.1905	20.18	0.19457	0.60	b607
B07-267	30.5335	-2.3231	20.19	0.19488	0.61	r107
B07-270	30.4967	-2.1903	20.21	0.20063	0.69	b206
B07-274	30.3311	-2.2796	20.22	0.19511	0.32	r716
B08-000	39.9626	-1.5404	16.06	0.36162	0.27	b616
B08-001	39.9068	-1.5653	16.10	0.36008	0.32	b516
B08-002	40.1262	-1.7224	16.45	0.39149	0.39	r110
B08-003	39.9049	-1.5528	16.77	0.13452	0.89	r616
B08-004	40.0266	-1.6277	17.09	0.36139	0.29	r314
B08-005	39.7963	-1.6210	17.27	0.44650	0.34	b713
B08-006	39.8476	-1.6043	17.47	0.11362	0.70	r707
B08-007	39.9084	-1.5857	17.50	0.13533	0.67	b514
B08-008	40.1245	-1.7271	17.55	0.10953	0.59	r109
B08-010	39.9729	-1.5552	17.64	0.13390	0.61	b608
B08-011	40.1480	-1.6454	17.67	0.40312	0.27	b112
B08-012	40.1228	-1.5923	17.69	0.11397	0.36	r116
B08-013	39.9714	-1.5822	17.84	0.37306	0.67	r516
B08-014	39.7881	-1.5659	17.95	0.29588	0.27	b707
B08-015	40.0489	-1.6749	17.97	0.18753	0.67	b314
B08-016	39.9877	-1.5310	17.98	0.28167	0.25	b416
B08-017	39.9312	-1.3360	17.99	0.25017	0.82	r601
B08-018	39.7854	-1.5599	18.05	0.12134	0.78	r816
B08-019	40.1273	-1.7294	18.09	0.10969	0.76	b102

Continued on next page

Target ID	RA	DEC	r-band mag.	z	Corr.	FiberID
B08-020	39.8659	-1.6274	18.09	0.26198	0.73	r714
B08-021	40.0219	-1.4772	18.14	0.36087	0.22	r410
B08-022	39.9521	-1.5611	18.16	0.25134	0.59	r508
B08-023	39.7595	-1.6290	18.18	0.11364	0.66	b703
B08-024	40.1227	-1.5016	18.29	0.17195	0.57	b206
B08-025	39.8317	-1.5307	18.35	0.17398	0.65	r808
B08-026	40.1834	-1.6449	18.35	0.16268	0.49	b111
B08-027	40.0440	-1.5337	18.38	0.23277	0.50	r415
B08-028	39.9377	-1.5395	18.38	0.13367	0.72	r608
B08-029	39.8978	-1.7108	18.39	0.24362	0.60	b503
B08-030	39.7915	-1.5879	18.40	0.18062	0.77	b705
B08-031	40.1883	-1.4516	18.43	0.24795	0.81	r202
B08-032	39.9261	-1.4632	18.46	0.32798	0.73	r606
B08-033	40.1169	-1.3460	18.48	0.38145	0.59	b201
B08-034	40.0156	-1.7591	18.51	0.25019	0.68	r309
B08-035	39.8876	-1.4154	18.51	0.17396	0.57	b803
B08-036	39.8719	-1.6161	18.55	0.26183	0.75	r715
B08-037	39.8306	-1.6910	18.55	0.20352	0.59	r701
B08-038	40.1415	-1.5310	18.58	0.17459	0.78	b208
B08-039	40.1848	-1.4844	18.58	0.27943	0.62	r204
B08-040	39.8936	-1.6960	18.62	0.24154	0.67	b504
B08-041	39.8969	-1.7257	18.64	0.44419	0.60	b502
B08-042	40.0709	-1.6176	18.66	0.25166	0.61	r108
B08-043	39.7553	-1.6280	18.68	0.45212	0.59	b704
B08-044	40.0739	-1.5346	18.69	0.37034	0.26	r408
B08-045	40.1189	-1.5439	18.70	0.36111	0.21	b216
B08-046	40.0845	-1.4335	18.71	0.17108	0.44	b210
B08-047	39.7865	-1.4945	18.80	0.17311	0.76	r812
B08-048	39.9361	-1.3378	18.82	0.17667	0.47	r602
B08-049	39.9854	-1.3930	18.84	0.37821	0.60	b410
B08-050	40.1854	-1.4379	18.87	0.18622	0.41	r201
B08-051	40.1150	-1.6062	18.90	0.26178	0.58	r115
B08-052	40.1725	-1.5321	18.92	0.17616	0.54	r215
B08-053	39.7706	-1.6373	18.96	0.44186	0.27	b702
B08-054	39.8424	-1.3578	18.96	0.24655	0.53	r801
B08-055	40.0705	-1.4424	18.97	0.17179	0.39	r402
B08-056	39.8113	-1.6033	18.98	0.25043	0.37	b715
B08-057	40.1988	-1.5964	18.99	0.25428	0.52	b114
B08-058	39.9583	-1.4044	19.00	0.48426	0.43	b609
B08-059	40.1458	-1.6627	19.01	0.17293	0.30	b110
B08-060	40.0432	-1.5698	19.02	0.28274	0.22	b308
B08-061	40.1496	-1.4893	19.03	0.17307	0.60	b205
B08-062	40.0314	-1.4398	19.03	0.26131	0.62	r409
B08-063	39.8223	-1.6104	19.04	0.26161	0.46	b714
B08-064	39.9667	-1.3884	19.06	0.47897	0.38	b603
B08-065	39.9853	-1.3975	19.08	0.37989	0.62	b411
B08-066	39.9645	-1.6911	19.08	0.25001	0.51	r512
B08-067	40.0859	-1.7026	19.08	0.25035	0.50	r103
B08-068	39.9885	-1.4365	19.11	0.17225	0.66	b414
B08-069	39.8635	-1.4910	19.11	0.27848	0.58	b813
B08-070	40.0825	-1.4831	19.12	0.37450	0.73	r404
B08-071	40.0649	-1.6929	19.13	0.26138	0.21	b312
B08-073	40.2022	-1.5178	19.18	0.17443	0.56	r206

Continued on next page

Target ID	RA	DEC	r-band mag.	z	Corr.	FiberID
B08-074	39.8116	-1.6564	19.22	0.26172	0.38	b711
B08-075	40.1773	-1.6772	19.22	0.22934	0.59	b109
B08-076	39.8591	-1.6572	19.22	0.26244	0.60	r704
B08-077	39.9660	-1.6712	19.24	0.26095	0.53	r513
B08-078	39.9117	-1.4713	19.26	0.23184	0.56	r612
B08-079	39.9241	-1.3979	19.28	0.24907	0.46	r610
B08-080	40.1208	-1.6755	19.30	0.21748	0.12	r113
B08-081	39.9919	-1.6720	19.31	0.32553	0.40	r303
B08-082	39.8398	-1.5973	19.34	0.20004	0.38	r708
B08-083	40.0905	-1.4331	19.34	0.17132	0.24	b209
B08-084	39.8653	-1.6622	19.36	0.24907	0.63	r711
B08-085	39.8475	-1.4632	19.36	0.25635	0.59	b811
B08-086	39.8522	-1.4067	19.37	0.21788	0.44	b809
B08-087	39.9708	-1.5454	19.38	0.38352	0.32	b607
B08-088	39.9430	-1.6812	19.38	0.36520	0.57	r504
B08-089	39.9639	-1.4543	19.41	0.47887	0.50	b611
B08-090	39.9627	-1.7634	19.42	0.18788	0.56	r501
B08-091	39.9664	-1.7135	19.42	0.24993	0.72	r510
B08-092	40.0301	-1.4868	19.42	0.23254	0.56	r411
B08-093	40.0845	-1.6222	19.43	0.23049	0.46	r107
B08-094	39.9608	-1.4943	19.44	0.37295	0.29	b613
B08-095	39.8212	-1.6950	19.46	0.27973	0.56	b709
B08-096	39.9731	-1.3375	19.46	0.38452	0.66	b601
B08-097	40.0269	-1.6925	19.46	0.18730	0.30	r312
B08-099	39.9936	-1.6947	19.50	0.26154	0.45	r302
B08-100	39.7889	-1.6952	19.50	0.41360	0.24	b701
B08-101	40.1431	-1.6680	19.50	0.22944	0.34	b103
B08-102	39.7937	-1.4963	19.51	0.21782	0.44	r813
B08-103	39.9192	-1.6964	19.54	0.46393	0.20	b511
B08-104	39.9246	-1.7427	19.56	0.37522	0.51	b509
B08-105	40.0279	-1.6155	19.57	0.42153	0.52	b307
B08-106	40.0188	-1.4586	19.57	0.39381	0.18	b404
B08-107	40.2069	-1.5996	19.57	0.25420	0.42	b113
B08-108	40.0364	-1.6939	19.59	0.13608	0.23	b304
B08-109	40.1083	-1.5402	19.60	0.17979	0.39	b215
B08-111	39.8861	-1.4602	19.65	0.32261	0.62	b806
B08-112	40.0629	-1.6590	19.66	0.18649	0.62	b315
B08-113	39.9841	-1.4318	19.66	0.45783	0.58	b413
B08-114	39.9884	-1.4986	19.67	0.25557	0.34	b415
B08-115	39.8606	-1.5274	19.67	0.42379	0.54	b815
B08-116	39.8531	-1.4650	19.68	0.23254	0.48	b812
B08-117	40.0019	-1.5965	19.68	0.37940	0.63	r306
B08-118	40.0442	-1.6953	19.68	0.18648	0.66	b311
B08-119	40.0038	-1.6046	19.69	0.23028	0.63	r315
B08-120	39.8985	-1.4642	19.70	0.17883	0.46	b807
B08-121	39.8705	-1.3651	19.70	0.24233	0.62	b802
B08-122	39.9514	-1.7302	19.70	0.25042	0.33	r502
B08-123	39.8765	-1.4824	19.72	0.18143	0.29	b808
B08-124	39.9634	-1.7087	19.73	0.24989	0.71	r511
B08-126	39.8641	-1.6100	19.74	0.28047	0.71	r706
B08-127	39.8701	-1.7255	19.74	0.26207	0.46	r709
B08-128	39.8713	-1.6467	19.77	0.26138	0.64	r712
B08-129	39.8246	-1.4022	19.77	0.26163	0.55	r802

Continued on next page

Target ID	RA	DEC	r-band mag.	z	Corr.	FiberID
B08-130	39.9246	-1.4571	19.80	0.32601	0.72	r611
B08-131	39.9477	-1.6685	19.80	0.37848	0.60	r505
B08-132	39.9425	-1.6148	19.80	0.34612	0.51	b513
B08-133	39.9209	-1.5708	19.81	0.37975	0.48	b515
B08-134	39.8345	-1.4242	19.82	0.25591	0.43	r805
B08-135	39.9695	-1.5931	19.83	0.30516	0.61	r515
B08-137	40.0140	-1.7245	19.84	0.37013	0.75	r311
B08-138	40.1364	-1.6637	19.86	0.37847	0.45	b105
B08-139	40.0161	-1.5338	19.88	0.25119	0.50	b407
B08-140	39.7585	-1.5622	19.88	0.26001	0.22	b708
B08-142	39.9279	-1.4299	19.89	0.25035	0.43	r605
B08-143	40.0031	-1.4969	19.90	0.38096	0.72	b405
B08-144	40.0279	-1.7538	19.90	0.27638	0.26	b301
B08-145	40.0144	-1.5040	19.91	0.24272	0.23	b406
B08-146	40.1168	-1.6958	19.92	0.49354	0.19	r112
B08-147	40.1213	-1.6663	19.93	0.14658	0.29	r114
B08-148	39.9056	-1.6450	19.93	0.37518	0.57	b506
B08-150	40.1714	-1.4793	19.94	0.37600	0.51	r212
B08-151	40.0535	-1.7672	19.94	0.16099	0.31	b309
B08-152	40.1128	-1.5068	19.95	0.24845	0.25	b213
B08-153	39.8983	-1.4423	19.95	0.30111	0.46	b804
B08-154	39.9696	-1.4904	19.96	0.36864	0.43	b606
B08-155	40.1826	-1.4575	19.96	0.17596	0.52	r210
B08-156	39.8144	-1.4059	19.98	0.29631	0.25	r803
B08-157	40.0304	-1.7370	19.98	0.41568	0.19	b302
B08-158	39.9662	-1.6038	19.99	0.42327	0.72	r514
B08-159	39.9760	-1.7316	19.99	0.24897	0.42	r509
B08-160	40.0798	-1.4272	19.99	0.32027	0.23	r401
B08-161	40.1870	-1.4913	20.00	0.28011	0.24	r205
B08-162	39.9772	-1.3543	20.00	0.36628	0.61	b602
B08-163	39.9273	-1.4100	20.01	0.37296	0.47	r604
B08-167	39.7887	-1.4913	20.03	0.20008	0.72	r811
B08-169	40.0988	-1.5355	20.04	0.38386	0.35	b214
B08-170	40.0318	-1.6985	20.05	0.29920	0.42	b303
B08-171	39.9832	-1.3784	20.07	0.30605	0.33	b409
B08-172	39.8058	-1.4485	20.07	0.42334	0.35	r810
B08-173	40.0987	-1.6918	20.08	0.37529	0.71	r105
B08-174	39.9639	-1.5211	20.08	0.24199	0.36	b614
B08-175	40.1751	-1.4892	20.08	0.41239	0.39	r213
B08-176	40.0350	-1.5281	20.09	0.37360	0.55	r414
B08-177	39.8419	-1.4107	20.09	0.45798	0.73	r804
B08-178	40.1476	-1.4272	20.09	0.30568	0.24	b203
B08-179	39.8579	-1.6868	20.12	0.32437	0.63	r702
B08-180	40.0311	-1.6920	20.12	0.18658	0.54	b305
B08-181	39.9886	-1.5910	20.13	0.38296	0.57	r307
B08-182	39.9961	-1.4009	20.14	0.24065	0.40	b412
B08-183	40.0609	-1.6756	20.14	0.41894	0.42	b313
B08-184	40.1281	-1.6177	20.16	0.32464	0.27	b108
B08-185	40.1673	-1.5414	20.17	0.20933	0.34	r216
B08-186	40.2171	-1.5395	20.17	0.18664	0.32	r208
B08-187	39.8969	-1.3616	20.18	0.24973	0.54	b801
B08-188	40.1610	-1.5735	20.18	0.39571	0.42	b116
B08-189	40.0010	-1.4216	20.19	0.16460	0.20	b403

Continued on next page

Target ID	RA	DEC	r-band mag.	z	Corr.	FiberID
B08-190	40.0194	-1.6400	20.20	0.32481	0.40	r313
B08-191	39.8512	-1.5373	20.21	0.39691	0.38	b816
B08-192	39.8930	-1.6579	20.22	0.37120	0.46	b505
B08-193	39.9237	-1.7018	20.22	0.12864	0.33	b510
B08-194	40.1064	-1.7203	20.22	0.25120	0.57	r111
B08-195	39.9082	-1.4746	20.24	0.31997	0.51	r613
B08-198	39.9175	-1.5083	20.25	0.37149	0.68	r615
B08-199	40.0821	-1.7478	20.25	0.24957	0.56	r101
B08-200	39.8826	-1.4514	20.25	0.32347	0.40	b805
B08-202	39.7958	-1.6588	20.27	0.46839	0.21	b710
B08-204	40.0174	-1.3358	20.27	0.22429	0.25	b401
B08-205	40.1401	-1.6627	20.28	0.45925	0.21	b106
B08-206	39.9437	-1.5382	20.28	0.37807	0.38	b615
B08-207	40.0071	-1.5353	20.28	0.37263	0.27	b408
B08-208	39.9576	-1.6051	20.29	0.38201	0.59	r507
B08-209	39.9725	-1.4761	20.31	0.32616	0.48	b605
B08-210	39.9896	-1.5757	20.33	0.25567	0.52	r308
B08-211	39.9009	-1.5700	20.34	0.42282	0.61	b507
B08-212	40.1252	-1.4192	20.34	0.30146	0.38	b202
B08-213	40.0831	-1.6505	20.34	0.30636	0.43	r106
B08-214	40.0215	-1.5081	20.34	0.37380	0.51	r413
B08-215	39.8317	-1.6341	20.35	0.16639	0.26	r705
B08-216	39.8943	-1.5661	20.36	0.42241	0.49	b508
B08-217	40.0268	-1.7505	20.38	0.42089	0.32	r310
B08-218	40.0020	-1.6107	20.38	0.36137	0.66	r305
B08-219	40.1475	-1.4832	20.39	0.19224	0.18	b204
B08-220	39.8775	-1.6410	20.39	0.37785	0.61	r713
B08-222	39.8060	-1.4432	20.41	0.36875	0.52	r806
B08-224	40.0066	-1.3400	20.42	0.37862	0.41	b402
B08-225	40.1398	-1.6539	20.44	0.18527	0.27	b107
B08-226	39.8792	-1.6955	20.44	0.26203	0.19	r710
B08-227	39.9403	-1.4859	20.44	0.35242	0.49	b612
B08-228	40.0192	-1.5462	20.45	0.25339	0.41	r416
B08-229	40.0422	-1.5045	20.47	0.32560	0.19	r412
B08-230	40.0103	-1.5661	20.47	0.21680	0.36	r316
B08-231	40.0683	-1.5231	20.48	0.27019	0.17	r407
B08-232	39.8733	-1.5734	20.48	0.18656	0.23	r716
B08-233	39.9336	-1.4982	20.48	0.32771	0.43	r607
B08-234	40.0545	-1.7110	20.51	0.41982	0.55	b310
B08-236	39.8628	-1.6764	20.53	0.24955	0.49	r703
B08-237	40.0321	-1.6327	20.53	0.42105	0.69	b306
B08-239	40.1289	-1.5025	20.54	0.33003	0.22	b207
B08-240	40.0867	-1.7272	20.54	0.32547	0.52	r102
B08-241	39.9706	-1.4067	20.55	0.36748	0.39	b604
B08-242	40.0617	-1.5138	20.56	0.37681	0.17	r405
B08-243	39.8062	-1.6358	20.56	0.22549	0.27	b712
B08-245	40.1022	-1.4360	20.57	0.18140	0.23	b211
B08-246	40.1696	-1.5024	20.57	0.37163	0.72	r214
B08-248	39.9048	-1.3925	20.58	0.37410	0.65	r609
B08-249	39.9258	-1.4047	20.59	0.44755	0.18	r603
B08-250	40.1950	-1.4555	20.59	0.26197	0.29	r203
B08-251	39.9154	-1.5000	20.59	0.35254	0.64	r614
B08-252	40.1966	-1.5220	20.60	0.24931	0.26	r207

Continued on next page

Target ID	RA	DEC	r-band mag.	z	Corr.	FiberID
B08-253	40.0739	-1.4529	20.61	0.42146	0.60	r403
B08-254	40.1792	-1.4145	20.62	0.36933	0.17	r209
B08-257	39.8115	-1.5654	20.65	0.35401	0.28	b716
B08-258	39.7907	-1.5452	20.65	0.46365	0.20	r815
B08-259	39.9044	-1.7579	20.65	0.31808	0.24	b501
B08-260	40.0683	-1.6937	20.67	0.20597	0.18	r104
B08-262	40.0514	-1.5141	20.68	0.37393	0.58	r406
B08-263	40.1586	-1.4755	20.68	0.16446	0.21	r211
B08-264	39.9663	-1.4187	20.69	0.10034	0.18	b610
B08-265	39.8601	-1.4428	20.70	0.18617	0.29	b810
B08-266	39.7504	-1.5838	20.70	0.49646	0.23	b706
B08-267	40.0498	-1.6340	20.70	0.42035	0.68	b316
B09-000	32.5562	-1.0901	16.76	0.17436	0.53	b312
B09-001	32.5757	-1.0183	16.84	0.17092	0.67	r116
B09-002	32.3336	-1.2112	16.91	0.16499	0.73	r703
B09-003	32.3271	-0.8079	16.92	0.17390	0.72	b810
B09-004	32.5429	-1.0682	17.05	0.17519	0.69	b304
B09-005	32.3044	-0.9575	17.12	0.17543	0.81	r805
B09-006	32.3286	-0.8740	17.13	0.12004	0.83	b813
B09-007	32.6081	-1.0340	17.35	0.17281	0.67	b115
B09-008	32.5300	-1.0029	17.35	0.17414	0.71	r406
B09-009	32.5533	-1.0548	17.36	0.17666	0.68	b314
B09-011	32.5294	-1.0314	17.51	0.41466	0.30	r316
B09-012	32.3348	-1.0006	17.58	0.17474	0.85	b808
B09-013	32.4995	-1.0615	17.65	0.17115	0.58	r515
B09-014	32.5149	-0.8479	17.65	0.17841	0.59	r401
B09-015	32.5719	-1.0368	17.68	0.17661	0.75	r114
B09-016	32.4237	-1.0259	17.71	0.44206	0.40	b516
B09-017	32.4610	-1.0509	17.72	0.17135	0.69	r503
B09-018	32.4365	-1.0756	17.75	0.17137	0.56	b512
B09-019	32.4349	-0.8897	17.75	0.46949	0.36	b604
B09-020	32.4073	-0.7999	17.79	0.25602	0.70	b601
B09-021	32.5570	-1.0968	17.83	0.17197	0.46	r101
B09-022	32.5441	-0.9958	17.86	0.17548	0.60	b215
B09-023	32.4476	-0.8299	17.86	0.45436	0.63	b412
B09-024	32.5143	-1.0333	17.94	0.17264	0.65	r306
B09-025	32.4506	-1.0660	17.96	0.17470	0.67	b513
B09-027	32.5038	-0.9866	17.99	0.17027	0.66	r415
B09-028	32.5885	-0.9768	18.01	0.17337	0.62	r213
B09-029	32.5838	-1.0905	18.05	0.17591	0.45	b103
B09-030	32.5595	-1.0436	18.19	0.17695	0.70	r104
B09-031	32.3526	-0.9859	18.20	0.44914	0.43	r615
B09-032	32.6296	-0.9962	18.20	0.17147	0.55	r207
B09-033	32.3588	-0.9097	18.25	0.17479	0.78	r614
B09-034	32.3933	-1.1671	18.28	0.21324	0.79	b502
B09-035	32.5491	-0.9748	18.28	0.19438	0.72	b207
B09-036	32.4944	-0.9630	18.32	0.17165	0.58	r412
B09-037	32.4729	-1.0259	18.34	0.46306	0.33	r506
B09-038	32.6035	-0.9926	18.36	0.17316	0.68	r214
B09-039	32.5527	-1.1499	18.38	0.32093	0.64	b310
B09-040	32.6118	-1.0124	18.39	0.17630	0.62	r208
B09-041	32.5154	-1.0475	18.41	0.17435	0.53	r304
B09-042	32.4940	-1.2176	18.47	0.25122	0.44	r510

Continued on next page

Target ID	RA	DEC	r-band mag.	z	Corr.	FiberID
B09-043	32.3303	-1.1765	18.48	0.16810	0.62	r705
B09-044	32.2976	-0.8431	18.48	0.17271	0.54	r812
B09-045	32.5222	-1.0447	18.49	0.44147	0.18	r313
B09-046	32.2838	-0.9299	18.50	0.17587	0.73	r814
B09-047	32.4818	-0.9902	18.51	0.17112	0.64	b407
B09-048	32.3439	-0.9673	18.58	0.15389	0.67	b807
B09-049	32.5736	-1.1385	18.59	0.45799	0.28	r109
B09-050	32.2886	-0.9452	18.59	0.17198	0.44	r815
B09-053	32.4943	-1.0202	18.62	0.16973	0.73	r516
B09-054	32.5429	-1.1429	18.66	0.17479	0.51	b301
B09-055	32.6159	-1.0397	18.67	0.17410	0.33	b114
B09-056	32.4860	-0.9794	18.70	0.17381	0.31	r414
B09-057	32.4630	-0.9237	18.70	0.28739	0.72	b402
B09-058	32.4855	-1.2207	18.71	0.31441	0.30	r509
B09-059	32.5595	-1.0355	18.71	0.16991	0.68	r105
B09-060	32.4771	-0.9749	18.77	0.17195	0.63	b406
B09-061	32.3741	-0.9884	18.77	0.17610	0.63	r608
B09-062	32.5653	-0.9289	18.80	0.17144	0.64	b204
B09-063	32.4005	-1.0640	18.81	0.17296	0.52	b507
B09-064	32.5705	-0.9586	18.82	0.17055	0.25	b206
B09-065	32.6103	-1.0517	18.82	0.17088	0.33	b110
B09-066	32.3006	-1.1488	18.83	0.48857	0.41	b710
B09-067	32.3345	-0.8180	18.86	0.28460	0.76	b803
B09-068	32.3651	-1.1883	18.86	0.17536	0.38	r711
B09-069	32.3675	-0.8119	18.87	0.17447	0.50	r602
B09-070	32.6057	-1.0499	18.87	0.17474	0.52	b112
B09-071	32.4282	-1.0858	18.90	0.17006	0.72	b510
B09-072	32.3183	-0.9791	18.91	0.49995	0.42	r808
B09-073	32.3489	-0.9909	18.92	0.28901	0.82	r616
B09-074	32.6125	-1.0307	18.95	0.43463	0.20	b116
B09-075	32.2802	-0.8430	18.95	0.17330	0.62	r811
B09-076	32.5263	-1.0125	18.96	0.17227	0.58	r408
B09-077	32.5665	-1.0838	18.97	0.17507	0.48	r111
B09-078	32.2848	-1.1024	18.97	0.16717	0.80	b711
B09-079	32.4817	-0.9320	18.98	0.17281	0.52	b403
B09-080	32.2963	-0.8306	18.99	0.49199	0.33	r809
B09-082	32.5876	-1.0477	19.04	0.17449	0.51	b108
B09-083	32.4717	-1.0128	19.05	0.17528	0.77	b408
B09-084	32.4689	-1.0186	19.05	0.17026	0.37	r508
B09-085	32.5906	-1.0456	19.08	0.17455	0.43	b113
B09-086	32.5968	-1.0005	19.10	0.17106	0.41	r215
B09-088	32.5577	-1.0295	19.15	0.17556	0.37	r106
B09-089	32.5215	-0.9538	19.16	0.17404	0.55	r403
B09-090	32.5503	-0.8737	19.18	0.17141	0.38	b203
B09-091	32.3147	-1.1150	19.20	0.16538	0.73	r708
B09-092	32.2789	-1.1761	19.21	0.45700	0.53	b709
B09-093	32.5011	-1.0243	19.23	0.16906	0.54	r307
B09-094	32.4924	-1.0745	19.23	0.31516	0.24	r513
B09-095	32.5290	-0.8285	19.23	0.41078	0.17	b209
B09-096	32.5213	-1.0791	19.24	0.25878	0.40	r311
B09-097	32.3083	-1.2156	19.26	0.14402	0.36	r702
B09-098	32.3891	-1.1378	19.29	0.44544	0.46	r713
B09-100	32.3484	-1.1522	19.33	0.29208	0.55	r707

Continued on next page

Target ID	RA	DEC	r-band mag.	z	Corr.	FiberID
B09-101	32.4562	-1.0481	19.34	0.17142	0.75	r504
B09-102	32.3253	-0.7935	19.35	0.17394	0.40	b809
B09-103	32.3300	-0.8425	19.35	0.17412	0.69	b811
B09-104	32.5411	-0.9672	19.35	0.17659	0.56	b213
B09-105	32.4845	-0.9492	19.41	0.17315	0.62	r411
B09-107	32.2855	-0.9847	19.43	0.17254	0.63	r816
B09-108	32.5114	-1.0100	19.46	0.29224	0.57	r416
B09-109	32.6118	-0.9451	19.50	0.17367	0.35	r205
B09-110	32.4341	-0.7871	19.52	0.25392	0.32	b409
B09-112	32.5269	-1.1125	19.54	0.46111	0.40	r310
B09-113	32.4226	-0.8795	19.55	0.25367	0.65	b603
B09-114	32.3534	-1.0767	19.57	0.13957	0.41	r715
B09-115	32.3998	-0.9878	19.57	0.33834	0.70	b615
B09-116	32.2980	-0.9498	19.59	0.17359	0.63	r804
B09-117	32.5335	-1.0013	19.60	0.28803	0.68	b216
B09-118	32.5286	-1.0435	19.62	0.48124	0.35	r314
B09-119	32.3983	-0.8134	19.65	0.25674	0.48	b611
B09-120	32.3986	-1.0060	19.65	0.21312	0.64	b616
B09-121	32.6125	-0.9145	19.66	0.29206	0.48	r202
B09-122	32.5412	-1.0403	19.66	0.17482	0.48	b307
B09-123	32.5093	-1.0627	19.70	0.45407	0.31	r303
B09-124	32.5412	-1.0486	19.71	0.38866	0.54	b306
B09-125	32.5237	-1.0092	19.72	0.17398	0.64	r407
B09-126	32.3399	-0.8167	19.72	0.17361	0.47	b802
B09-128	32.4655	-1.0368	19.75	0.21736	0.66	r505
B09-129	32.6182	-1.0501	19.75	0.28543	0.26	b111
B09-130	32.5894	-1.1180	19.77	0.42791	0.20	b109
B09-131	32.5341	-1.0528	19.77	0.30931	0.27	r312
B09-132	32.5487	-0.9826	19.78	0.45475	0.74	b208
B09-133	32.4323	-1.0032	19.78	0.17102	0.67	b607
B09-134	32.5093	-0.8517	19.79	0.17973	0.58	r409
B09-135	32.3306	-0.8690	19.80	0.23972	0.79	b812
B09-136	32.4444	-0.7906	19.82	0.46199	0.24	b410
B09-137	32.5300	-0.8949	19.83	0.38664	0.62	b211
B09-138	32.5450	-0.8340	19.84	0.31776	0.30	b201
B09-139	32.4793	-1.1642	19.84	0.41876	0.32	r512
B09-140	32.5663	-1.0448	19.85	0.47398	0.57	r103
B09-141	32.5355	-1.0366	19.86	0.49527	0.23	r315
B09-142	32.5500	-0.8427	19.88	0.32079	0.25	b202
B09-143	32.3053	-1.0527	19.88	0.40593	0.22	b713
B09-144	32.3259	-0.9422	19.91	0.17509	0.73	b814
B09-145	32.3785	-1.1656	19.92	0.39562	0.38	r712
B09-147	32.3608	-0.8557	19.93	0.17446	0.32	r604
B09-148	32.5450	-1.0958	19.94	0.44317	0.26	b311
B09-149	32.3762	-0.8490	19.99	0.42459	0.30	r603
B09-150	32.3412	-0.9427	20.01	0.39736	0.61	b806
B09-152	32.5453	-0.9899	20.04	0.17287	0.37	b214
B09-154	32.3164	-1.2037	20.06	0.16486	0.20	r704
B09-155	32.5118	-1.2011	20.07	0.48463	0.24	r301
B09-156	32.5494	-0.9534	20.10	0.17540	0.55	b205
B09-157	32.5630	-1.0842	20.11	0.17674	0.32	r102
B09-158	32.5450	-1.0430	20.12	0.47644	0.74	b316
B09-159	32.3950	-1.0824	20.13	0.17285	0.68	b505

Continued on next page

Target ID	RA	DEC	r-band mag.	z	Corr.	FiberID
B09-161	32.6213	-0.9395	20.16	0.47030	0.35	r204
B09-163	32.4537	-1.0365	20.18	0.44046	0.38	b515
B09-164	32.6054	-0.9029	20.22	0.46092	0.34	r201
B09-165	32.3926	-0.9631	20.25	0.37112	0.63	b614
B09-166	32.5408	-1.0182	20.26	0.19108	0.28	b308
B09-167	32.3127	-0.9790	20.27	0.17310	0.48	r807
B09-168	32.5052	-0.9024	20.28	0.28586	0.53	r410
B09-169	32.6103	-0.9689	20.29	0.45901	0.53	r206
B09-170	32.3273	-0.9947	20.30	0.28951	0.72	b816
B09-172	32.5264	-0.9931	20.30	0.49294	0.55	r405
B09-173	32.4272	-0.9778	20.31	0.38796	0.59	b606
B09-175	32.5545	-1.0488	20.35	0.45490	0.42	b315
B09-176	32.5657	-1.0290	20.38	0.44132	0.18	r107
B09-177	32.5841	-1.0664	20.39	0.45177	0.23	b106
B09-178	32.4544	-1.0517	20.39	0.39667	0.52	b514
B09-179	32.4912	-1.0637	20.41	0.29162	0.44	r514
B09-180	32.4612	-0.8015	20.41	0.48494	0.20	b411
B09-181	32.4361	-0.8511	20.41	0.44834	0.21	b414
B09-182	32.3310	-0.8820	20.42	0.43220	0.62	b804
B09-183	32.3100	-0.8982	20.43	0.21122	0.72	r802
B09-184	32.4153	-1.0140	20.43	0.17216	0.37	b608
B09-185	32.4226	-1.0904	20.44	0.46092	0.18	b504
B09-186	32.3177	-1.1611	20.45	0.45776	0.47	r706
B09-187	32.3400	-0.7967	20.45	0.17312	0.39	b801
B09-188	32.4609	-0.8391	20.46	0.46865	0.73	b413
B09-189	32.5452	-0.9652	20.47	0.17258	0.48	b212
B09-191	32.5737	-1.0962	20.48	0.49132	0.26	r110
B09-192	32.3924	-1.0532	20.49	0.21319	0.58	b508
B09-194	32.5721	-0.8719	20.50	0.48391	0.32	r210
B09-195	32.2986	-0.9607	20.51	0.17482	0.32	r806
B09-196	32.5900	-1.0520	20.53	0.48983	0.25	b107
B09-197	32.5307	-1.1160	20.54	0.38007	0.16	r309
B09-198	32.3622	-0.8931	20.57	0.43527	0.49	r605
B09-199	32.4035	-1.0673	20.57	0.15345	0.30	b506
B09-200	32.5492	-1.1661	20.58	0.48129	0.25	b309
B09-201	32.5011	-1.1844	20.59	0.17654	0.51	r302
B09-202	32.5839	-1.0813	20.60	0.17369	0.57	b105
B09-203	32.5061	-0.9639	20.62	0.47634	0.25	r413
B09-204	32.3078	-0.9421	20.62	0.28904	0.75	r803
B09-205	32.5772	-1.0773	20.63	0.41709	0.36	r112
B09-206	32.3862	-1.1251	20.65	0.39683	0.36	r714
B09-207	32.4032	-0.8082	20.65	0.35978	0.30	b610
B09-208	32.3577	-0.8588	20.65	0.42682	0.39	r611
B09-209	32.3842	-0.9080	20.68	0.17473	0.43	r606
B09-210	32.2896	-0.8495	20.68	0.17442	0.32	r813
B09-211	32.4334	-1.0882	20.68	0.43591	0.51	b509
B09-212	32.5727	-0.8954	20.69	0.48570	0.27	r211
B09-213	32.5773	-1.0665	20.69	0.48264	0.22	r113
B09-215	32.4618	-1.0639	20.72	0.25854	0.23	r502
B09-217	32.3162	-1.2203	20.73	0.48986	0.32	r701
B09-218	32.4659	-1.1722	20.73	0.49108	0.19	r501
B09-219	32.5129	-1.0188	20.74	0.25165	0.26	r308
B09-220	32.2978	-1.0917	20.74	0.23985	0.18	b712

Continued on next page

Target ID	RA	DEC	r-band mag.	z	Corr.	FiberID
B09-223	32.5394	-1.1040	20.75	0.48996	0.19	b303
B09-224	32.5744	-1.0297	20.76	0.46122	0.27	r115
B09-225	32.3511	-0.8828	20.77	0.26303	0.65	r612
B09-226	32.5616	-1.0276	20.77	0.48667	0.37	r108
B09-227	32.5805	-1.0022	20.77	0.47163	0.22	r216
B09-228	32.5494	-1.0615	20.79	0.33759	0.27	b313
B09-229	32.3538	-0.7897	20.81	0.31882	0.26	r609
B09-230	32.5239	-0.9253	20.82	0.20015	0.70	r402
B09-231	32.3737	-1.2293	20.82	0.42429	0.57	r709
B09-232	32.5050	-1.0373	20.83	0.44113	0.21	r305
B09-233	32.4495	-1.0855	20.83	0.46881	0.17	b511
B09-234	32.3878	-0.8558	20.85	0.28899	0.61	b612
B09-235	32.4196	-1.1274	20.88	0.45923	0.41	b503
B09-236	32.3250	-0.7859	20.88	0.17409	0.21	r801
B09-238	32.4744	-0.9470	20.89	0.48632	0.19	b405
B09-239	32.3563	-1.0572	20.91	0.44105	0.24	r716
B09-241	32.3468	-0.8941	20.94	0.17245	0.43	r613
B09-242	32.5438	-1.1170	20.94	0.28738	0.28	b302
B09-243	32.4666	-0.8932	20.96	0.47776	0.66	b401
B09-244	32.3587	-0.8492	20.96	0.28829	0.59	r610
B09-245	32.3262	-0.9842	20.97	0.41711	0.52	b815
B09-246	32.5772	-1.1504	20.98	0.44971	0.21	b102
B09-247	32.3958	-1.2372	20.98	0.14989	0.18	b501
B09-248	32.3679	-0.7904	20.99	0.42577	0.18	r601
B09-249	32.5434	-1.0549	20.99	0.16883	0.30	b305
B09-251	32.4592	-1.0254	21.00	0.42119	0.34	r507
B10-000	16.5832	1.1393	17.06	0.18981	0.72	r611
B10-001	16.5515	1.1392	17.49	0.18920	0.71	b815
B10-002	16.7105	1.0697	17.51	0.25342	0.80	r413
B10-003	16.7485	0.9525	17.64	0.15510	0.65	r114
B10-004	16.7057	1.0562	17.75	0.46024	0.57	r415
B10-006	16.6426	1.0873	18.05	0.26297	0.76	b605
B10-007	16.5485	1.1309	18.05	0.18971	0.75	r802
B10-009	16.6630	1.0705	18.14	0.19041	0.39	b416
B10-010	16.5984	0.8622	18.17	0.19466	0.73	r510
B10-011	16.7008	1.0593	18.21	0.24441	0.70	b406
B10-012	16.5243	0.8494	18.25	0.25697	0.79	r712
B10-013	16.5526	0.8702	18.28	0.26553	0.72	b510
B10-014	16.6046	1.1973	18.29	0.19585	0.62	r601
B10-015	16.5588	1.1440	18.45	0.19157	0.50	b814
B10-016	16.4866	1.1936	18.50	0.20346	0.43	r809
B10-017	16.6817	1.0754	18.50	0.25723	0.73	b415
B10-018	16.5502	0.8265	18.55	0.24857	0.60	b509
B10-019	16.4653	0.8254	18.56	0.42639	0.20	b701
B10-020	16.7152	0.9970	18.56	0.26287	0.62	r105
B10-021	16.8020	0.9418	18.58	0.20312	0.59	b110
B10-022	16.7005	1.0650	18.60	0.25602	0.76	b405
B10-023	16.7141	1.0789	18.61	0.25655	0.75	r412
B10-024	16.7429	1.1618	18.64	0.26352	0.62	b210
B10-025	16.6150	0.9018	18.66	0.26472	0.73	r312
B10-026	16.7090	1.1382	18.68	0.24904	0.73	r410
B10-028	16.6474	1.0096	18.71	0.25350	0.71	b308
B10-029	16.5636	1.0057	18.71	0.21577	0.20	r508

Continued on next page

Target ID	RA	DEC	r-band mag.	z	Corr.	FiberID
B10-030	16.7179	1.0863	18.72	0.19199	0.45	r405
B10-031	16.6302	1.0119	18.73	0.19439	0.62	b616
B10-032	16.7839	0.8867	18.73	0.26875	0.67	b103
B10-033	16.5849	1.1299	18.74	0.19957	0.61	r613
B10-034	16.6790	1.0800	18.74	0.25421	0.72	b414
B10-035	16.5539	1.1639	18.75	0.24847	0.75	b813
B10-036	16.5084	1.0696	18.79	0.20035	0.63	r806
B10-037	16.5137	0.8640	18.81	0.24971	0.58	r704
B10-038	16.4723	0.8527	18.82	0.26053	0.77	b703
B10-039	16.7749	1.0330	18.82	0.19100	0.48	b208
B10-040	16.5969	1.1171	18.89	0.26243	0.77	r614
B10-041	16.5486	0.9160	18.90	0.24149	0.29	b513
B10-042	16.8214	1.0949	18.90	0.19961	0.39	r204
B10-044	16.4830	1.1030	18.99	0.33641	0.74	r814
B10-045	16.5962	0.9583	19.02	0.38283	0.63	r515
B10-046	16.6587	1.0991	19.03	0.20418	0.58	b413
B10-047	16.4978	0.9361	19.05	0.35479	0.44	b716
B10-049	16.6570	1.2253	19.07	0.24890	0.39	b601
B10-050	16.5903	1.1450	19.08	0.23697	0.77	r610
B10-051	16.6201	1.0923	19.09	0.37450	0.24	b611
B10-052	16.7770	1.1367	19.09	0.39289	0.61	b204
B10-053	16.6485	1.0241	19.12	0.30095	0.25	b608
B10-055	16.5829	1.1940	19.15	0.36427	0.61	b803
B10-056	16.7965	1.1223	19.16	0.31528	0.63	r210
B10-057	16.6860	0.9670	19.17	0.44711	0.20	b312
B10-058	16.6060	0.8486	19.18	0.24946	0.54	r509
B10-059	16.6016	1.1503	19.18	0.18936	0.57	r604
B10-060	16.4747	0.8801	19.24	0.29578	0.71	b704
B10-061	16.6116	0.9151	19.24	0.24671	0.65	r313
B10-062	16.5226	0.8325	19.29	0.25540	0.57	r702
B10-063	16.6921	0.9790	19.30	0.25266	0.54	b315
B10-064	16.7995	0.9499	19.32	0.19883	0.45	b111
B10-065	16.6721	0.9828	19.35	0.25409	0.57	b307
B10-066	16.5511	1.1717	19.36	0.35284	0.64	r801
B10-067	16.8224	1.0904	19.37	0.32593	0.33	r205
B10-068	16.7182	1.0575	19.39	0.25578	0.62	r408
B10-069	16.5956	0.8546	19.40	0.49540	0.22	r503
B10-070	16.8015	1.0778	19.42	0.26704	0.33	r213
B10-071	16.4697	1.1272	19.42	0.33679	0.48	r813
B10-072	16.7381	1.0027	19.43	0.40251	0.20	r116
B10-073	16.7939	1.0561	19.43	0.31511	0.26	r215
B10-074	16.4851	0.9400	19.44	0.26285	0.58	b706
B10-075	16.6042	1.1361	19.45	0.36748	0.60	r605
B10-076	16.5286	0.8346	19.45	0.24934	0.47	r709
B10-077	16.5800	1.1425	19.45	0.18934	0.61	b806
B10-078	16.5481	0.8606	19.45	0.26106	0.69	b502
B10-079	16.5265	0.9155	19.51	0.25477	0.71	r714
B10-080	16.8681	0.9806	19.52	0.33883	0.31	b114
B10-081	16.6401	1.1337	19.55	0.29458	0.58	b604
B10-082	16.5054	1.1330	19.55	0.20055	0.52	r812
B10-083	16.4624	0.9480	19.56	0.21606	0.38	b708
B10-084	16.7110	1.0408	19.58	0.25432	0.65	r416
B10-085	16.6850	1.2279	19.60	0.37540	0.27	b409

Continued on next page

Target ID	RA	DEC	r-band mag.	z	Corr.	FiberID
B10-086	16.6023	1.0762	19.60	0.29115	0.30	r606
B10-087	16.6856	1.2006	19.60	0.37480	0.55	b401
B10-088	16.5672	1.1678	19.61	0.30490	0.24	b812
B10-089	16.5933	1.0698	19.61	0.30168	0.57	r615
B10-090	16.5445	0.9955	19.62	0.26231	0.62	b507
B10-091	16.5619	0.9148	19.62	0.42084	0.37	r505
B10-092	16.5830	0.9300	19.63	0.26256	0.61	r506
B10-093	16.6870	0.9466	19.64	0.38560	0.44	b311
B10-094	16.5934	1.0621	19.64	0.25754	0.69	r616
B10-095	16.7154	1.2107	19.65	0.21352	0.36	r401
B10-096	16.6991	1.1610	19.66	0.37348	0.64	b402
B10-097	16.6965	0.9096	19.66	0.25201	0.62	r103
B10-098	16.4985	0.9038	19.66	0.20181	0.30	b711
B10-099	16.6201	0.8668	19.66	0.47556	0.26	b303
B10-100	16.5994	1.1809	19.67	0.36339	0.46	r602
B10-101	16.5875	1.1334	19.67	0.25440	0.63	r612
B10-102	16.7666	1.1105	19.67	0.26167	0.50	b205
B10-103	16.8343	0.9940	19.68	0.23012	0.23	b116
B10-105	16.8064	1.1392	19.69	0.13472	0.35	r202
B10-106	16.5174	1.0029	19.69	0.25175	0.71	r708
B10-107	16.5984	0.8735	19.69	0.26048	0.62	r511
B10-108	16.5541	1.0096	19.70	0.33188	0.53	b816
B10-109	16.4853	0.8956	19.70	0.25655	0.54	b705
B10-110	16.5719	1.0116	19.72	0.33192	0.57	b808
B10-111	16.6394	1.0791	19.73	0.27112	0.66	b612
B10-112	16.7871	1.0975	19.74	0.32127	0.34	r211
B10-113	16.5160	1.0824	19.75	0.27849	0.18	r804
B10-114	16.6137	0.8941	19.76	0.45014	0.77	r311
B10-115	16.6976	1.0078	19.77	0.25064	0.40	r108
B10-116	16.6837	1.1297	19.77	0.24839	0.31	b412
B10-117	16.8071	0.8308	19.77	0.33741	0.34	b109
B10-118	16.7608	1.1513	19.78	0.25052	0.47	b203
B10-119	16.7146	1.0823	19.79	0.24848	0.62	r406
B10-120	16.5358	0.8477	19.81	0.26105	0.59	r711
B10-121	16.5755	0.9674	19.81	0.38195	0.62	r507
B10-122	16.7351	0.9469	19.82	0.31873	0.18	r113
B10-123	16.5445	0.8462	19.83	0.26321	0.67	b501
B10-125	16.7096	1.1422	19.84	0.29954	0.49	r409
B10-126	16.5865	1.1968	19.87	0.36494	0.65	r609
B10-127	16.6749	0.9743	19.87	0.25717	0.42	b314
B10-128	16.4799	0.9465	19.87	0.20100	0.46	b707
B10-129	16.8510	1.0302	19.87	0.24633	0.20	r208
B10-131	16.7375	1.1808	19.89	0.42368	0.51	r402
B10-132	16.7160	1.0062	19.89	0.25105	0.36	r107
B10-133	16.6065	0.9043	19.91	0.21526	0.24	r512
B10-134	16.7313	1.0783	19.92	0.39225	0.29	r407
B10-135	16.8246	1.0517	19.93	0.48384	0.19	r207
B10-136	16.8136	1.1451	19.95	0.25632	0.43	r201
B10-137	16.5416	0.8406	20.00	0.25577	0.34	r710
B10-138	16.6263	0.8563	20.02	0.35314	0.46	b302
B10-139	16.5040	0.8976	20.03	0.26495	0.61	r706
B10-140	16.7752	0.9706	20.03	0.19022	0.36	b105
B10-142	16.6756	0.9691	20.07	0.24983	0.51	b313

Continued on next page

Target ID	RA	DEC	r-band mag.	z	Corr.	FiberID
B10-143	16.5782	1.1886	20.07	0.26671	0.30	b804
B10-144	16.5495	1.0371	20.08	0.33074	0.57	r808
B10-145	16.4795	0.8429	20.09	0.21902	0.29	b702
B10-147	16.7894	0.9934	20.12	0.37460	0.42	b107
B10-148	16.4903	0.9343	20.14	0.35338	0.53	b715
B10-149	16.5167	0.8343	20.15	0.25849	0.55	r703
B10-150	16.5696	0.8450	20.17	0.25928	0.52	r501
B10-151	16.5220	1.0590	20.18	0.26192	0.49	r807
B10-152	16.6090	0.8286	20.18	0.26108	0.63	r309
B10-153	16.6468	0.9553	20.19	0.45226	0.51	b306
B10-154	16.7431	1.1822	20.19	0.19511	0.26	b209
B10-155	16.7000	1.0700	20.20	0.25641	0.49	b404
B10-156	16.7229	1.1339	20.21	0.32827	0.36	r403
B10-159	16.6853	0.9275	20.27	0.25601	0.44	b310
B10-160	16.7187	1.0926	20.28	0.25159	0.36	r404
B10-161	16.6069	0.9193	20.28	0.26370	0.47	r514
B10-162	16.7602	0.9799	20.28	0.47856	0.23	r115
B10-163	16.6463	1.0675	20.29	0.25008	0.45	b607
B10-164	16.6158	1.1580	20.29	0.13412	0.22	r603
B10-166	16.4933	0.8458	20.31	0.26167	0.50	b710
B10-167	16.7393	1.0612	20.32	0.16146	0.30	b215
B10-168	16.5404	1.0847	20.32	0.42230	0.37	r803
B10-169	16.7316	0.9989	20.32	0.21144	0.18	r106
B10-170	16.6024	1.0207	20.32	0.41611	0.20	r608
B10-171	16.5719	1.1858	20.34	0.21511	0.19	b810
B10-172	16.7934	0.9929	20.34	0.42186	0.17	b106
B10-173	16.5518	1.1754	20.35	0.35337	0.45	b811
B10-174	16.5420	0.8716	20.35	0.33420	0.16	b504
B10-175	16.5268	0.8581	20.36	0.26840	0.43	r713
B10-176	16.5046	0.9100	20.38	0.20257	0.49	r707
B10-178	16.5606	0.8956	20.39	0.39514	0.19	b511
B10-179	16.6397	1.0829	20.39	0.19045	0.48	b606
B10-180	16.4897	0.8273	20.39	0.13947	0.23	b709
B10-181	16.7880	1.1758	20.40	0.35226	0.19	r209
B10-182	16.5476	1.0054	20.41	0.33210	0.52	b508
B10-183	16.7938	0.8810	20.41	0.26935	0.42	b102
B10-184	16.7042	1.0466	20.42	0.25466	0.34	b407
B10-185	16.8347	1.0703	20.42	0.21459	0.18	r206
B10-186	16.6050	0.9122	20.43	0.46770	0.19	r513
B10-187	16.5427	0.8950	20.43	0.26284	0.42	b505
B10-189	16.7900	1.0675	20.45	0.32455	0.25	r214
B10-190	16.6040	1.0042	20.45	0.25032	0.59	r516
B10-191	16.5829	1.2144	20.46	0.36544	0.41	b801
B10-192	16.7663	1.0679	20.46	0.32684	0.41	b207
B10-193	16.5539	0.9837	20.46	0.29434	0.35	b516
B10-194	16.5598	0.9193	20.48	0.42215	0.55	b514
B10-195	16.7525	1.1069	20.48	0.25386	0.39	b211
B10-196	16.6335	1.0731	20.51	0.21795	0.31	b613
B10-198	16.5653	1.2054	20.52	0.46269	0.23	b809
B10-199	16.6897	1.1581	20.53	0.41238	0.46	b403
B10-200	16.6299	1.2292	20.54	0.15065	0.25	b609
B10-201	16.7409	0.9098	20.55	0.41945	0.53	r112
B10-203	16.8187	0.9653	20.56	0.44426	0.34	b113

Continued on next page

Target ID	RA	DEC	r-band mag.	z	Corr.	FiberID
B10-204	16.7587	0.8650	20.58	0.50002	0.29	r109
B10-205	16.4985	1.1543	20.58	0.26106	0.15	r811
B10-206	16.7082	0.8617	20.60	0.37940	0.37	r102
B10-208	16.5802	1.1527	20.61	0.18994	0.26	b805
B10-209	16.6819	1.1575	20.62	0.16021	0.19	b411
B10-210	16.5737	0.8521	20.63	0.25924	0.37	r502
B10-211	16.5795	1.2023	20.65	0.31636	0.34	b802
B10-212	16.7836	1.0935	20.66	0.19380	0.20	r212
B10-213	16.4987	0.9181	20.66	0.42361	0.21	b713
B10-214	16.5039	1.0516	20.66	0.49195	0.30	r815
B10-215	16.7729	1.1804	20.70	0.19667	0.19	b202
B10-216	16.6196	1.0432	20.70	0.46784	0.43	b614
B10-217	16.5485	0.8688	20.71	0.26113	0.29	b503
B10-218	16.6099	1.0237	20.71	0.47477	0.22	r607
B10-219	16.6952	0.9958	20.72	0.23702	0.22	r104
B10-220	16.7408	1.0545	20.73	0.16052	0.30	b216
B10-221	16.7735	1.0987	20.73	0.29003	0.19	b206
B10-222	16.7475	0.8801	20.74	0.24861	0.14	r111
B10-223	16.5157	0.8284	20.75	0.45108	0.59	r701
B10-224	16.5887	0.8645	20.76	0.35298	0.59	r504
B10-225	16.5386	0.9439	20.77	0.20428	0.20	r715
B10-226	16.6933	0.9257	20.77	0.45756	0.22	b309
B10-227	16.7614	1.0818	20.80	0.32497	0.28	b214
B10-228	16.5474	0.8959	20.81	0.26402	0.41	b506
B10-229	16.7652	1.1924	20.82	0.14396	0.23	b201
B10-230	16.7395	1.0871	20.82	0.25152	0.34	b213
B10-231	16.7974	1.0472	20.82	0.41897	0.20	r216
B10-232	16.7141	1.0604	20.83	0.25433	0.17	r414
B10-233	16.4999	0.9087	20.83	0.47298	0.18	b712
B10-234	16.5029	1.0129	20.85	0.31863	0.18	r816
B10-235	16.5070	1.1610	20.85	0.19596	0.32	r810
B10-236	16.4995	0.9232	20.86	0.26260	0.35	b714
B10-237	16.6250	1.0355	20.86	0.48647	0.17	b615
B10-238	16.7285	0.8215	20.87	0.17872	0.26	r101
B10-240	16.7707	0.8684	20.88	0.44649	0.14	r110
B10-241	16.5263	0.9829	20.91	0.39125	0.35	r716
B10-242	16.6378	0.8448	20.95	0.49246	0.24	b301
B10-245	16.6881	1.0045	20.98	0.38555	0.39	b316
B10-246	16.5488	0.9516	20.99	0.16212	0.21	b515
B10-247	16.6178	0.9239	21.00	0.37441	0.18	b304
B11-001	9.2785	9.1567	16.89	0.24956	0.68	r714
B11-002	9.4856	9.0335	18.06	0.16156	0.62	r101
B11-003	9.5135	9.0479	18.17	0.24620	0.49	r111
B11-004	9.2869	9.1564	18.20	0.25543	0.67	r713
B11-005	9.2630	9.1974	18.46	0.25587	0.77	b716
B11-006	9.3510	9.0678	18.50	0.24973	0.49	r509
B11-007	9.3580	9.3592	18.52	0.25168	0.54	r611
B11-008	9.2846	9.1812	18.53	0.25179	0.74	r716
B11-009	9.5132	9.3963	18.61	0.16972	0.49	r210
B11-010	9.4021	9.1754	18.62	0.22572	0.36	r315
B11-011	9.2607	9.1402	18.62	0.25386	0.72	b710
B11-012	9.2994	9.3060	18.63	0.49395	0.46	r804
B11-013	9.5072	9.0208	18.65	0.24985	0.37	r109

Continued on next page

Target ID	RA	DEC	r-band mag.	z	Corr.	FiberID
B11-014	9.3274	9.1121	18.70	0.25034	0.64	r504
B11-015	9.2972	9.1725	18.70	0.25482	0.62	b507
B11-016	9.4748	9.3183	18.74	0.22961	0.69	b605
B11-017	9.2881	9.1710	18.75	0.25423	0.76	b506
B11-018	9.4944	9.2896	18.77	0.18909	0.57	r415
B11-019	9.5206	9.0854	18.79	0.29080	0.56	b102
B11-020	9.3788	9.1178	18.80	0.25376	0.56	r302
B11-021	9.3163	9.2076	18.80	0.24697	0.69	b516
B11-022	9.4439	9.2232	18.84	0.34895	0.65	b616
B11-023	9.4531	9.1227	18.88	0.24873	0.69	b314
B11-024	9.2285	9.2472	18.92	0.49104	0.34	r815
B11-025	9.3238	9.2422	18.92	0.29602	0.56	b808
B11-026	9.2891	9.1021	18.94	0.15123	0.23	r709
B11-027	9.2762	9.2703	18.94	0.25660	0.52	r805
B11-028	9.2745	9.1513	18.96	0.25226	0.69	r702
B11-029	9.3135	9.1483	18.96	0.24555	0.58	b514
B11-030	9.2570	9.1779	18.98	0.25147	0.65	b713
B11-031	9.4444	9.3228	19.01	0.22856	0.57	b604
B11-033	9.2495	9.1876	19.04	0.24745	0.62	b705
B11-034	9.4847	9.0949	19.09	0.25360	0.56	r104
B11-035	9.4218	9.3967	19.09	0.29092	0.48	r601
B11-036	9.4996	9.0683	19.09	0.29288	0.65	r112
B11-037	9.2923	9.2385	19.11	0.26003	0.53	r808
B11-038	9.4420	9.0349	19.17	0.19305	0.29	b301
B11-039	9.4443	9.2713	19.18	0.33018	0.54	b612
B11-040	9.2976	9.1022	19.19	0.25377	0.41	b501
B11-041	9.4832	9.2970	19.20	0.49571	0.24	r414
B11-042	9.2654	9.1755	19.20	0.26573	0.76	r706
B11-043	9.3413	9.3140	19.21	0.25082	0.53	b804
B11-045	9.3095	9.2348	19.27	0.24779	0.60	b815
B11-046	9.4504	9.1075	19.29	0.25222	0.58	b313
B11-048	9.5104	9.2591	19.29	0.37252	0.41	r216
B11-049	9.3977	9.0842	19.30	0.24470	0.46	r310
B11-050	9.3237	9.0809	19.33	0.28123	0.57	r501
B11-051	9.3755	9.3906	19.35	0.39694	0.57	r609
B11-052	9.2639	9.1583	19.36	0.24074	0.61	b711
B11-053	9.3013	9.3277	19.36	0.25052	0.58	r802
B11-054	9.4928	9.3482	19.39	0.28989	0.48	r410
B11-055	9.2796	9.1670	19.39	0.24845	0.38	r715
B11-056	9.3128	9.2509	19.39	0.49330	0.41	b814
B11-058	9.3039	9.1408	19.42	0.49201	0.33	b511
B11-059	9.3765	9.1421	19.43	0.37595	0.16	r303
B11-060	9.4877	9.3296	19.44	0.37323	0.52	r411
B11-061	9.3258	9.2105	19.44	0.29596	0.24	r508
B11-062	9.3150	9.2310	19.46	0.22865	0.52	b816
B11-063	9.4202	9.0887	19.46	0.25381	0.51	r311
B11-065	9.4029	9.0430	19.47	0.29583	0.59	r309
B11-066	9.3028	9.3171	19.47	0.23047	0.34	r803
B11-067	9.3233	9.1376	19.49	0.37176	0.32	r505
B11-068	9.4272	9.3090	19.51	0.22964	0.51	b610
B11-069	9.3396	9.1983	19.51	0.19245	0.50	r516
B11-070	9.4275	9.1374	19.51	0.36853	0.46	b305
B11-071	9.4176	9.3835	19.53	0.28941	0.41	r603

Continued on next page

Target ID	RA	DEC	r-band mag.	z	Corr.	FiberID
B11-072	9.5212	9.1017	19.54	0.29223	0.46	b103
B11-073	9.3101	9.1981	19.54	0.24952	0.64	b515
B11-074	9.4723	9.0919	19.57	0.39823	0.58	r102
B11-075	9.2986	9.1500	19.58	0.25010	0.59	b502
B11-076	9.4609	9.0942	19.64	0.23791	0.33	b311
B11-077	9.2998	9.1379	19.64	0.25526	0.67	b510
B11-078	9.3929	9.1563	19.64	0.18314	0.34	r314
B11-079	9.4423	9.0395	19.65	0.24838	0.43	b302
B11-080	9.5069	9.2830	19.69	0.37062	0.46	r214
B11-081	9.3235	9.3019	19.73	0.44308	0.56	b805
B11-082	9.5172	9.1017	19.74	0.29447	0.42	b105
B11-084	9.3508	9.3006	19.75	0.33008	0.46	b806
B11-085	9.4934	9.1693	19.75	0.37023	0.32	r107
B11-086	9.3632	9.3318	19.78	0.36246	0.57	r612
B11-087	9.2673	9.2573	19.80	0.25975	0.52	r814
B11-088	9.2481	9.1689	19.80	0.23965	0.26	b702
B11-089	9.3675	9.3052	19.80	0.39786	0.61	r613
B11-090	9.5299	9.3651	19.82	0.16099	0.36	r211
B11-091	9.3880	9.3150	19.82	0.44474	0.51	r606
B11-092	9.2866	9.2608	19.84	0.15450	0.25	r807
B11-093	9.3299	9.3908	19.85	0.49792	0.47	b801
B11-094	9.2881	9.1618	19.85	0.24633	0.47	b505
B11-095	9.2393	9.1859	19.89	0.24376	0.51	b704
B11-096	9.3797	9.1951	19.89	0.36344	0.51	r306
B11-097	9.4535	9.2827	19.90	0.36312	0.70	b606
B11-098	9.3854	9.3945	19.90	0.41991	0.63	r602
B11-099	9.2848	9.3871	19.93	0.33128	0.50	r801
B11-100	9.5051	9.0834	19.98	0.29140	0.22	r113
B11-101	9.4981	9.0348	19.98	0.39909	0.36	r110
B11-102	9.3430	9.1043	20.01	0.21295	0.16	r512
B11-103	9.4389	9.2009	20.01	0.35214	0.50	b308
B11-104	9.4797	9.1395	20.02	0.15091	0.22	r106
B11-106	9.4538	9.3513	20.08	0.48281	0.20	b602
B11-107	9.4375	9.0736	20.09	0.37519	0.65	b304
B11-109	9.2360	9.3562	20.10	0.25402	0.48	r811
B11-110	9.3399	9.0840	20.10	0.37229	0.57	r511
B11-111	9.5120	9.2663	20.11	0.36208	0.30	r215
B11-112	9.2757	9.1214	20.12	0.40923	0.12	r710
B11-113	9.2284	9.2871	20.13	0.28996	0.40	r813
B11-114	9.5197	9.2990	20.16	0.49296	0.39	r212
B11-115	9.3643	9.2500	20.18	0.25109	0.32	r615
B11-116	9.3157	9.2926	20.19	0.41976	0.58	b811
B11-117	9.4266	9.1022	20.19	0.36916	0.52	r312
B11-118	9.2741	9.1636	20.19	0.24452	0.39	r704
B11-119	9.2568	9.1456	20.22	0.25888	0.33	b701
B11-120	9.4761	9.3229	20.23	0.22875	0.32	b603
B11-121	9.4256	9.3205	20.23	0.49702	0.36	b609
B11-122	9.5309	9.2810	20.24	0.40595	0.29	r201
B11-123	9.4991	9.1423	20.25	0.35952	0.15	r115
B11-124	9.4772	9.0923	20.25	0.24957	0.30	r103
B11-125	9.3622	9.2241	20.28	0.24930	0.37	r616
B11-126	9.3155	9.2818	20.29	0.33177	0.51	b812
B11-127	9.4643	9.1351	20.30	0.39706	0.31	b315

Continued on next page

Target ID	RA	DEC	r-band mag.	z	Corr.	FiberID
B11-128	9.3022	9.1470	20.30	0.25835	0.22	b513
B11-129	9.3540	9.2948	20.31	0.25132	0.47	b807
B11-130	9.2971	9.1785	20.31	0.25392	0.45	b508
B11-131	9.2653	9.1818	20.31	0.26355	0.42	r707
B11-132	9.4241	9.2695	20.32	0.36952	0.24	b613
B11-133	9.2945	9.1536	20.33	0.25349	0.28	b504
B11-134	9.3571	9.1899	20.34	0.28863	0.30	r514
B11-136	9.4099	9.3640	20.35	0.36495	0.44	r604
B11-137	9.3813	9.3830	20.35	0.18293	0.28	r610
B11-138	9.2652	9.2111	20.36	0.24572	0.46	r708
B11-139	9.2300	9.2187	20.38	0.25422	0.42	b707
B11-140	9.3361	9.1859	20.39	0.37101	0.48	r507
B11-141	9.3089	9.0939	20.39	0.25059	0.26	b509
B11-142	9.3886	9.1048	20.42	0.27337	0.45	r313
B11-143	9.3188	9.2990	20.43	0.25089	0.24	b810
B11-144	9.3249	9.1569	20.44	0.37158	0.41	r506
B11-145	9.3874	9.1647	20.46	0.12249	0.17	r304
B11-146	9.3306	9.0907	20.48	0.49998	0.31	r503
B11-147	9.4427	9.1717	20.48	0.36853	0.33	b316
B11-148	9.4954	9.1320	20.49	0.25355	0.32	r114
B11-149	9.3343	9.0808	20.51	0.44152	0.27	r502
B11-150	9.2752	9.1283	20.52	0.46140	0.17	r711
B11-151	9.2669	9.2365	20.52	0.41238	0.30	r816
B11-152	9.3720	9.0806	20.53	0.23768	0.24	r301
B11-154	9.2251	9.3116	20.56	0.46866	0.38	r812
B11-155	9.2680	9.1695	20.57	0.25268	0.30	r705
B11-156	9.2624	9.1329	20.58	0.25290	0.50	b709
B11-157	9.2476	9.2199	20.58	0.49268	0.25	b708
B11-158	9.3633	9.1962	20.60	0.25903	0.25	r515
B11-159	9.4274	9.2256	20.62	0.49605	0.26	b615
B11-160	9.4790	9.4064	20.62	0.35974	0.39	b601
B11-161	9.2743	9.1600	20.65	0.43666	0.20	r703
B11-162	9.4333	9.1928	20.65	0.39694	0.27	b306
B11-163	9.4337	9.0720	20.66	0.49965	0.24	b303
B11-164	9.4590	9.0412	20.67	0.39795	0.23	b309
B11-165	9.4206	9.2790	20.67	0.24863	0.28	r607
B11-166	9.2893	9.1510	20.70	0.25094	0.33	b503
B11-169	9.2506	9.3618	20.71	0.24963	0.28	r810
B11-170	9.2634	9.1699	20.72	0.26082	0.26	b712
B11-171	9.3478	9.3745	20.74	0.37309	0.41	b802
B11-173	9.4536	9.2484	20.76	0.13287	0.44	b608
B11-174	9.2419	9.1923	20.76	0.43151	0.15	b706
B11-175	9.3599	9.1719	20.76	0.24672	0.37	r513
B11-177	9.4619	9.0457	20.80	0.36752	0.31	b310
B11-179	9.2601	9.1879	20.82	0.49705	0.35	b715
B11-180	9.3079	9.2718	20.82	0.27315	0.36	b813
B11-181	9.4876	9.3139	20.83	0.28961	0.40	r412
B11-182	9.4768	9.1809	20.84	0.15729	0.18	r108
B11-183	9.4439	9.1046	20.84	0.48337	0.27	b312
B11-184	9.4421	9.2291	20.85	0.35166	0.24	b614
B11-186	9.3273	9.3420	20.87	0.49728	0.31	b803
B11-187	9.4785	9.1181	20.88	0.36695	0.37	r105
B11-188	9.4392	9.2892	20.89	0.49613	0.22	b611

Continued on next page

Target ID	RA	DEC	r-band mag.	z	Corr.	FiberID
B11-189	9.2618	9.1817	20.90	0.39237	0.18	b714
B11-190	9.2397	9.3711	20.90	0.49892	0.34	r809
B11-191	9.3658	9.2153	20.90	0.40637	0.16	r307
B11-193	9.5174	9.1535	20.91	0.36254	0.58	b106
B11-194	9.4353	9.2002	20.92	0.48779	0.21	b307
B11-195	9.2810	9.1317	20.93	0.25244	0.21	r712
B11-196	9.4137	9.3177	20.94	0.39694	0.23	r605
B11-197	9.2394	9.1768	20.94	0.49736	0.36	b703
B11-198	9.2705	9.1328	20.97	0.24593	0.28	r701
B11-199	9.3612	9.2960	20.99	0.49998	0.23	r614

Bibliography

Abell, G. O. 1958, ApJS, 3, 211, doi: 10.1086/190036

Abell, G. O., Corwin, Harold G., J., & Olowin, R. P. 1989, ApJS, 70, 1, doi: 10.1086/191333

Adami, C., Biviano, A., & Mazure, A. 1998, A&A, 331, 439. https://arxiv.org/abs/astro-ph/9709268

Alam, S., Albareti, F. D., Prieto, C. A., et al. 2015, The Astrophysical Journal Supplement Series, 219, 12, doi: 10.1088/0067-0049/219/1/12

Allington-Smith, J. 2006, New Astron. Rev., 50, 244, doi: 10.1016/j.newar.2006.02.024

Ashman, K. M., Bird, C. M., & Zepf, S. E. 1994, AJ, 108, 2348, doi: 10.1086/117248

Athreya, R. M., Mellier, Y., van Waerbeke, L., et al. 2002, A&A, 384, 743, doi: 10.1051/0004-6361:20011779

Baier, F. W., & Ziener, R. 1977, Astronomische Nachrichten, 298, 87, doi: 10.1002/asna.19772980205

Bailey, J. I., Mateo, M. L., & Crane, J. D. 2014, in (International Society for Optics and Photonics), 91476P. http://dx.doi.org/10.1117/12.2055536

Balestra, I., Vanzella, E., Rosati, P., et al. 2013, A&A, 559, L9, doi: 10.1051/0004-6361/201322620

Beers, T. C., Flynn, K., & Gebhardt, K. 1990, AJ, 100, 32, doi: 10.1086/115487

Bekki, K., Owers, M. S., & Couch, W. J. 2010, ApJL, 718, L27, doi: 10.1088/2041-8205/718/1/L27

Bergamini, P., Rosati, P., Mercurio, A., et al. 2019, A&A, 631, A130, doi: 10.1051/0004-6361/201935974

Binney, J., & Tremaine, S. 1987, Galactic dynamics

Bird, C. 1994, ApJ, 422, 480, doi: 10.1086/173743

Bird, C. M., & Beers, T. C. 1993, AJ, 105, 1596, doi: 10.1086/116540

Biviano, A. 2020, arXiv e-prints, arXiv:2001.00800. https://arxiv.org/abs/2001.00800

Bonamigo, M., Grillo, C., Ettori, S., et al. 2018, ApJ, 864, 98, doi: 10.3847/1538-4357/aad4a7

Bower, R. G., Lucey, J. R., & Ellis, R. S. 1992, MNRAS, 254, 589, doi: 10.1093/mnras/254.4.589

Caldwell, N., & Rose, J. A. 1997, AJ, 113, 492, doi: 10.1086/118271

Caminha, G. B., Grillo, C., Rosati, P., et al. 2016, A&A, 587, A80, doi: 10.1051/0004-6361/201527670

Caminha, G. B., Rosati, P., Grillo, C., et al. 2019, A&A, 632, A36, doi: 10.1051/0004-6361/201935454

Cherkassky, B. V., Goldberg, A. V., & Radzik, T. 1996, Mathematical Programming, 73, 129, doi: 10.1007/BF02592101

Clowe, D., Bradač, M., Gonzalez, A. H., et al. 2006, ApJL, 648, L109, doi: 10.1086/508162

Cohen, S. A., Hickox, R. C., Wegner, G. A., Einasto, M., & Vennik, J. 2014, ApJ, 783, 136, doi: 10.1088/0004-637X/783/2/136

Colberg, J. M., White, S. M. D., Macfarland, T. J., et al. 1998, in Wide Field Surveys in Cosmology, ed. S. Colombi, Y. Mellier, & B. Raban, Vol. 14, 247

Comis, B., de Petris, M., Conte, A., Lamagna, L., & de Gregori, S. 2011, MNRAS, 418, 1089, doi: 10.1111/j.1365-2966.2011.19562.x

Cruddace, R., Voges, W., Böhringer, H., et al. 2002, ApJS, 140, 239, doi: 10.1086/324519

Czoske, O., Moore, B., Kneib, J. P., & Soucail, G. 2002, A&A, 386, 31, doi: 10.1051/0004-6361:20020230

Danese, L., de Zotti, G., & di Tullio, G. 1980, A&A, 82, 322

Dawson, K. S., Schlegel, D. J., Ahn, C. P., et al. 2013, AJ, 145, 10, doi: 10.1088/0004-6256/145/1/10

de Champeaux, D. 1983, J. ACM, 30, 22, doi: 10.1145/322358.322360

de Haan, T., Benson, B. A., Bleem, L. E., et al. 2016, ApJ, 832, 95, doi: 10.3847/0004-637X/832/1/95 de Jong, J. T. A., Verdoes Kleijn, G. A., Kuijken, K. H., & Valentijn, E. A. 2013, Experimental Astronomy, 35, 25, doi: 10.1007/s10686-012-9306-1

DESI Collaboration, Aghamousa, A., Aguilar, J., et al. 2016, arXiv e-prints, arXiv:1611.00037. https://arxiv.org/abs/1611.00037

Diaferio, A., & Geller, M. J. 1997, The Astrophysical Journal, 481, 633, doi: 10.1086/304075

Diehl, H., Neilsen, E., Gruendl, R., et al. 2016, in Proceedings of SPIE - The International Society for Optical Engineering, Vol. 9910

Dijkstra, E. W. 1959, Numerische Mathematik, 1, 269, doi: 10.1007/BF01386390

Dressler, A., & Gunn, J. E. 1983, ApJ, 270, 7, doi: 10.1086/161093

Dressler, A., Oemler, Augustus, J., Poggianti, B. M., et al. 2013, ApJ, 770, 62, doi: 10.1088/0004-637X/770/1/62

Dressler, A., & Shectman, S. A. 1988, AJ, 95, 985, doi: 10.1086/114694

Drlica-Wagner, A., Sevilla-Noarbe, I., Rykoff, E. S., et al. 2018, ApJS, 235, 33, doi: 10.3847/1538-4365/aab4f5

Duffy, A. R., Schaye, J., Kay, S. T., & Dalla Vecchia, C. 2008, MNRAS, 390, L64, doi: 10.1111/j.1745-3933.2008.00537.x

Dutton, A. A., & Macciò, A. V. 2014, MNRAS, 441, 3359, doi: 10.1093/mnras/stu742

Einasto, J. 1969, Astronomische Nachrichten, 291, 97, doi: 10.1002/asna.19682910303

Escalera, E., & MacGillivray, H. T. 1995, A&A, 298, 1

Evrard, A. E., Bialek, J., Busha, M., et al. 2008, ApJ, 672, 122, doi: 10.1086/521616

Fabricant, D., Fata, R., Roll, J., Hertz, E., et al. 2005, Publications of the Astronomical Society of the Pacific, 117, 1411, doi: 10.1086/497385

Fadda, D., Girardi, M., Giuricin, G., Mardirossian, F., & Mezzetti, M. 1996, ApJ, 473, 670, doi: 10.1086/178180

Fasano, G., & Franceschini, A. 1987, MNRAS, 225, 155, doi: 10.1093/mnras/225.1.155

Fasano, G., Poggianti, B. M., Bettoni, D., et al. 2015, MNRAS, 449, 3927, doi: 10.1093/mnras/stv500

Feretti, L., Gioia, I. M., & Giovannini, G. 2002, Merging Processes in Galaxy Clusters, Vol. 272, doi: 10.1007/0-306-48096-4

Ferrari, C., Benoist, C., Maurogordato, S., Cappi, A., & Slezak, E. 2005, A&A, 430, 19, doi: 10.1051/0004-6361:20041811

Flin, P., & Krywult, J. 2006, A&A, 450, 9, doi: 10.1051/0004-6361:20041635

Fujita, Y., Takizawa, M., Nagashima, M., & Enoki, M. 1999, PASJ, 51, L1, doi: 10.1093/pasj/51.3.L1

Geller, M. J., & Beers, T. C. 1982, PASP, 94, 421, doi: 10.1086/131003

Geller, M. J., Diaferio, A., Rines, K. J., & Serra, A. L. 2013, ApJ, 764, 58, doi: 10.1088/0004-637X/764/1/58

Gerken, B., Ziegler, B., Balogh, M., et al. 2004, A&A, 421, 59, doi: 10.1051/0004-6361:20041222

Girardi, M., & Biviano, A. 2002, Astrophysics and Space Science Library, Vol. 272, Optical Analysis of Cluster Mergers, ed. L. Feretti, I. M. Gioia, & G. Giovannini, 39–77

Girardi, M., Escalera, E., Fadda, D., et al. 1997, ApJ, 482, 41, doi: 10.1086/304113

Girardi, M., Fadda, D., Giuricin, G., et al. 1996, ApJ, 457, 61, doi: 10.1086/176711

Girardi, M., Mercurio, A., et al. 2015, AAp, 579, A4, doi: 10.1051/0004-6361/201425599

Gladders, M. D., & Yee, H. K. C. 2000, AJ, 120, 2148, doi: 10.1086/301557

—. 2005, ApJS, 157, 1, doi: 10.1086/427327

Gómez, P. L., Valkonen, L. E., Romer, A. K., et al. 2012, AJ, 144, 79, doi: 10.1088/0004-6256/144/3/79

Grillo, C., Gobat, R., Presotto, V., et al. 2014, ApJ, 786, 11, doi: 10.1088/0004-637X/786/1/11

Gruen, D., Brimioulle, F., Seitz, S., et al. 2013, MNRAS, 432, 1455, doi: 10.1093/mnras/stt566

Gunn, J. E., Siegmund, W. A., Mannery, E. J., et al. 2006, The Astronomical Journal, 131, 2332, doi: 10.1086/500975

Hart, P. E., Nilsson, N. J., & Raphael, B. 1968, IEEE Transactions on Systems Science and Cybernetics, 4, 100, doi: 10.1109/TSSC.1968.300136

Hill, J. M. 1988, in Astronomical Society of the Pacific Conference Series, Vol. 3, Fiber Optics in Astronomy, ed. S. C. Barden, 77

Hoekstra, H. 2003, MNRAS, 339, 1155, doi: 10.1046/j.1365-8711.2003.06264.x

Hoekstra, H., Franx, M., & Kuijken, K. 2000, ApJ, 532, 88, doi: 10.1086/308556

Jeltema, T. E., Canizares, C. R., Bautz, M. W., & Buote, D. A. 2005, ApJ, 624, 606, doi: 10.1086/428940

Johnson, T. L., Sharon, K., Bayliss, M. B., et al. 2014, ApJ, 797, 48, doi: 10.1088/0004-637X/797/1/48

Jones, C., & Forman, W. 1999, ApJ, 511, 65, doi: 10.1086/306646

Kaiser, N., Burgett, W., Chambers, K., et al. 2010, in Society of Photo-Optical Instrumentation Engineers (SPIE) Conference Series, Vol. 7733, Ground-based and Airborne Telescopes III, 77330E

Karman, W., Caputi, K. I., Grillo, C., et al. 2015, A&A, 574, A11, doi: 10.1051/0004-6361/201424962

Karman, W., Caputi, K. I., Caminha, G. B., et al. 2017, A&A, 599, A28, doi: 10.1051/0004-6361/201629055

Kneib, J. P., Ellis, R. S., Smail, I., Couch, W. J., & Sharples, R. M. 1996, ApJ, 471, 643, doi: 10.1086/177995

Kriessler, J. R., & Beers, T. C. 1997, AJ, 113, 80, doi: 10.1086/118235

Kruskal, W. H., & Wallis, W. A. 1952, Journal of the American Statistical Association, 47, 583, doi: 10.1080/01621459.1952.10483441

Lesser, M. 2015, PASP, 127, 1097, doi: 10.1086/684054

Lewis, I. J., Cannon, R. D., Taylor, K., et al. 2002, MNRAS, 333, 279, doi: 10.1046/j.1365-8711.2002.05333.x

LIGO Scientific Collaboration, Aasi, J., Abbott, B. P., et al. 2015, Classical and Quantum Gravity, 32, 074001, doi: 10.1088/0264-9381/32/7/074001

LSST Science Collaboration, Abell, P. A., Allison, J., et al. 2009, arXiv e-prints, arXiv:0912.0201. https://arxiv.org/abs/0912.0201

Ma, C. J., Ebeling, H., Marshall, P., & Schrabback, T. 2010, MNRAS, 406, 121, doi: 10.1111/j.1365-2966.2010.16673.x

Mantz, A. B., Allen, S. W., & Morris, R. G. 2016, MNRAS, 462, 681, doi: 10.1093/mnras/stw1707

Mao, S., & Schneider, P. 1998, MNRAS, 295, 587, doi: 10.1046/j.1365-8711.1998.01319.x

Mateo, M., Bailey, J. I., Crane, J., et al. 2012, in Ground-based and Airborne Instrumentation for Astronomy IV, Vol. 8446 (International Society for Optics and Photonics), 84464Y–84464Y–19. http://dx.doi.org/10.1117/12.926448

Maughan, B. J., Jones, C., Forman, W., & Van Speybroeck, L. 2008, ApJS, 174, 117, doi: 10.1086/521225

McCleary, J., dell'Antonio, I., & Huwe, P. 2015, ApJ, 805, 40, doi: 10.1088/0004-637X/805/1/40

Mehrtens, N., Romer, A. K., Hilton, M., et al. 2012, MNRAS, 423, 1024, doi: 10.1111/j.1365-2966.2012.20931.x

Melchior, P., Suchyta, E., Huff, E., et al. 2015, MNRAS, 449, 2219, doi: 10.1093/mnras/stv398

Méndez-Abreu, J., Sánchez-Janssen, R., & Aguerri, J. A. L. 2010, ApJL, 711, L61, doi: 10.1088/2041-8205/711/2/L61

Mercurio, A., Busarello, G., Merluzzi, P., et al. 2004, A&A, 424, 79, doi: 10.1051/0004-6361:20040324

Mercurio, A., La Barbera, F., Haines, C. P., et al. 2008, MNRAS, 387, 1374, doi: 10.1111/j.1365-2966.2008.13253.x

Merten, J., Meneghetti, M., Postman, M., et al. 2015, ApJ, 806, 4, doi: 10.1088/0004-637X/806/1/4

Miller, C. J., Stark, A., Gifford, D., & Kern, N. 2016, ApJ, 822, 41, doi: 10.3847/0004-637X/822/1/41

Mohr, J. J., Evrard, A. E., Fabricant, D. G., & Geller, M. J. 1995, ApJ, 447, 8, doi: 10.1086/175852

Monna, A., Seitz, S., Greisel, N., et al. 2014, MNRAS, 438, 1417, doi: 10.1093/mnras/stt2284

Munari, E., Biviano, A., & Mamon, G. A. 2014, A&A, 566, A68, doi: 10.1051/0004-6361/201322450

Muzzin, A., van der Burg, R. F. J., McGee, S. L., et al. 2014, ApJ, 796, 65, doi: 10.1088/0004-637X/796/1/65

Navarro, J. F., Frenk, C. S., & White, S. D. M. 1996, ApJ, 462, 563, doi: 10.1086/177173

Oemler, Augustus, J., Dressler, A., Kelson, D., et al. 2009, ApJ, 693, 152, doi: 10.1088/0004-637X/693/1/152

Oguri, M., Schrabback, T., Jullo, E., et al. 2013, MNRAS, 429, 482, doi: 10.1093/mnras/sts351

Okabe, N., Takada, M., Umetsu, K., Futamase, T., & Smith, G. P. 2010, PASJ, 62, 811, doi: 10.1093/pasj/62.3.811

Owen, F. N., Ledlow, M. J., Keel, W. C., Wang, Q. D., & Morrison, G. E. 2005, AJ, 129, 31, doi: 10.1086/426323

Owers, M. S., Randall, S. W., Nulsen, P. E. J., et al. 2011, ApJ, 728, 27, doi: 10.1088/0004-637X/728/1/27

Pasquini, L., Avila, G., Blecha, A., et al. 2002, The Messenger, 110, 1

Pinkney, J., Roettiger, K., Burns, J. O., & Bird, C. M. 1996, ApJS, 104, 1, doi: 10.1086/192290

Pisani, A. 1993, MNRAS, 265, 706, doi: 10.1093/mnras/265.3.706

—. 1996, MNRAS, 278, 697, doi: 10.1093/mnras/278.3.697

Planck Collaboration, Ade, P. A. R., Aghanim, N., et al. 2011, A&A, 536, A11, doi: 10.1051/0004-6361/201116458

Poggianti, B. M., & Barbaro, G. 1996, A&A, 314, 379. https://arxiv.org/abs/astro-ph/9604066

—. 1997, A&A, 325, 1025. https://arxiv.org/abs/astro-ph/9703067

Poggianti, B. M., Smail, I., Dressler, A., et al. 1999, ApJ, 518, 576, doi: 10.1086/307322

Pohl, I. 1969a, in Machine Intelligence 5 (Edinburgh, Scotland: Edinburgh University Press), 219–236

—. 1969b, PhD thesis, Stanford Universty Computer Sci. Dept., Stanford, CA

—. 1970, AI, 1, 193

Pohl, I. 1973, in Proc. of the IJCAI-73 (Stanford, CA: SRI International, Menlo Park, CA)

Pohl, I. 1970, in Machine Intelligence 5 (American Elsevier), 219–236

Postman, M., Coe, D., Benítez, N., et al. 2012, ApJS, 199, 25, doi: 10.1088/0067-0049/199/2/25

Puech, M., Evans, C. J., Disseau, K., et al. 2018, in Society of Photo-Optical Instrumentation Engineers (SPIE) Conference Series, Vol. 10702, Proceedings of the SPIE, 107028R

Raman, R. 1997, SIGACT News, 28, 81, doi: 10.1145/261342.261352

Reichardt, C. L., Stalder, B., Bleem, L. E., et al. 2013, ApJ, 763, 127, doi: 10.1088/0004-637X/763/2/127

Richstone, D., Loeb, A., & Turner, E. L. 1992, ApJ, 393, 477, doi: 10.1086/171521

Rodríguez-Muñoz, L., Rodighiero, G., Mancini, C., et al. 2019, MNRAS, 485, 586, doi: 10.1093/mnras/sty3335

Rubin, V. C., & Ford, Jr., W. K. 1970, ApJ, 159, 379, doi: 10.1086/150317

Rubin, V. C., Ford, Jr., W. K., & Thonnard, N. 1980, ApJ, 238, 471, doi: 10.1086/158003

Ruel, J., Bazin, G., Bayliss, M., et al. 2014, The Astrophysical Journal, 792, 45, doi: 10.1088/0004-637X/792/1/45

Rykoff, E. S., Rozo, E., Hollowood, D., et al. 2016, 20

Rykoff, E. S., Rozo, E., Busha, M. T., et al. 2014, The Astrophysical Journal, 785, 104, doi: 10.1088/0004-637X/785/2/104

Sarazin, C. L. 1988, X-ray emission from clusters of galaxies

Saro, A., Mohr, J. J., Bazin, G., & Dolag, K. 2013, ApJ, 772, 47, doi: 10.1088/0004-637X/772/1/47

Schlegel, D. J., Kollmeier, J. A., Aldering, G., et al. 2019, arXiv e-prints, arXiv:1907.11171. https://arxiv.org/abs/1907.11171

Sharp, R., Saunders, W., Smith, G., et al. 2006, in Society of Photo-Optical Instrumentation Engineers (SPIE) Conference Series, Vol. 6269, Society of Photo-Optical Instrumentation Engineers (SPIE) Conference Series, 62690G

Shectman, S. A., & Johns, M. 2003, in Society of Photo-Optical Instrumentation Engineers (SPIE) Conference Series, Vol. 4837, Large Ground-based Telescopes, ed. J. M. Oschmann & L. M. Stepp, 910–918

Sint, L., & de Champeaux, D. 1977, J. ACM, 24, 177, doi: 10.1145/322003.322004

Slezak, E., Bijaoui, A., & Mars, G. 1990, A&A, 227, 301

Smee, S. A., Gunn, J. E., Uomoto, A., et al. 2013, The Astronomical Journal, 146, 32, doi: 10.1088/0004-6256/146/2/32

Smith, A., He, J.-h., Cole, S., et al. 2018, ArXiv e-prints. https://arxiv.org/abs/1809.07355

Smith, G. A., Saunders, W., Bridges, T., Churilov, V., et al. 2004, in Society of Photo-Optical Instrumentation Engineers (SPIE) Conference Series, Vol. 5492, Ground-based Instrumentation for Astronomy, ed. A. F. M. Moorwood & M. Iye, 410–420

Stark, A., Miller, C. J., & Huterer, D. 2017, Phys. Rev. D, 96, 023543, doi: 10.1103/PhysRevD.96.023543

Stark, A., Miller, C. J., Kern, N., et al. 2016, Physical Review D, 93, 084036, doi: 10.1103/PhysRevD.93.084036

Strauss, M. A., Weinberg, D. H., Lupton, R. H., et al. 2002, AJ, 124, 1810, doi: 10.1086/342343

Sugai, H., Karoji, H., Takato, N., et al. 2012, Society of Photo-Optical Instrumentation Engineers (SPIE) Conference Series, Vol. 8446, Prime focus spectrograph: Subaru's future, 84460Y

Sugai, H., Tamura, N., Karoji, H., et al. 2015, Journal of Astronomical Telescopes, Instruments, and Systems, 1, 035001, doi: 10.1117/1.JATIS.1.3.035001

Tamura, N., Takato, N., Shimono, A., et al. 2018, in Society of Photo-Optical Instrumentation Engineers (SPIE) Conference Series, Vol. 10702, Proceedings of the SPIE, 107021C

Treu, T., Ellis, R. S., Kneib, J.-P., et al. 2003, ApJ, 591, 53, doi: 10.1086/375314

Umetsu, K., Zitrin, A., Gruen, D., et al. 2016, ApJ, 821, 116, doi: 10.3847/0004-637X/821/2/116

Umetsu, K., Medezinski, E., Nonino, M., et al. 2014, ApJ, 795, 163, doi: 10.1088/0004-637X/795/2/163

Umetsu, K., Sereno, M., Tam, S.-I., et al. 2018, ApJ, 860, 104, doi: 10.3847/1538-4357/aac3d9

van Dokkum, P. G. 2001, PASP, 113, 1420, doi: 10.1086/323894

Vikhlinin, A., Kravtsov, A. V., Burenin, R. A., et al. 2009, ApJ, 692, 1060, doi: 10.1088/0004-637X/692/2/1060

Wen, Z. L., & Han, J. L. 2013, MNRAS, 436, 275, doi: 10.1093/mnras/stt1581

West, M. J., & Bothun, G. D. 1990, ApJ, 350, 36, doi: 10.1086/168360

West, M. J., Oemler, Augustus, J., & Dekel, A. 1988, ApJ, 327, 1, doi: 10.1086/166163

Williamson, R., Benson, B. A., High, F. W., et al. 2011, ApJ, 738, 139, doi: 10.1088/0004-637X/738/2/139

York, D. G., Adelman, J., Anderson, Jr., J. E., et al. 2000, AJ, 120, 1579, doi: 10.1086/301513

Yu, L., Nelson, K., & Nagai, D. 2015, 9

Zacharias, N., Finch, C. T., Girard, T. M., et al. 2013, AJ, 145, 44, doi: 10.1088/0004-6256/145/2/44

Zeng, W., & Church, R. L. 2009, International Journal of Geographical Information Science, 23, 531, doi: 10.1080/13658810801949850

Zwicky, F. 1933, Helvetica Physica Acta, 6, 110